

HaloTag-Based Tools for Live-Cell Imaging and Elucidation of Organellar Redox Biology

Présentée le 21 juin 2024

Faculté des sciences de base
Groupe SCI SB SG
Programme doctoral en chimie et génie chimique

pour l'obtention du grade de Docteur ès Sciences

par

Sarah EMMERT

Acceptée sur proposition du jury

Prof. C. Heinis, président du jury
Prof. S. Gerber, Prof. P. Rivera Fuentes, directeurs de thèse
Dr C. Deo, rapporteuse
Prof. S. Matile, rapporteur
Prof. K. Johnsson, rapporteur

Acknowledgements

Without the incredible support of my supervisors, colleagues, family, and friends, this work would not have been possible. I want to express my sincere gratitude for their contributions.

First and foremost, I would like to especially thank Prof. Dr. Pablo Rivera-Fuentes for the opportunity to work in his research group, where I was always encouraged to learn and offered the guidance that I needed. Thank you for your enthusiasm, your optimism, and for always suggesting a solution when things did not go as expected.

I also want to express my appreciation to Prof. Dr. Sandrine Gerber for agreeing to be the supervisor of my thesis when our lab moved to UZH. Thank you for your guidance in completing my thesis and your support for my future plans.

Many thanks to the jury members for my thesis, Prof. Dr. Christian Heinis, Prof. Dr. Kai Johnsson, Dr. Claire Deo, and Prof. Dr. Stefan Matile, for their time and efforts.

Further, I would like to thank the collaborators involved in this work for their invaluable help. Thanks to Dr. Sebastian Thallmair for the MD simulations, which helped us understand our systems. I want to thank the PTPSP at EPFL, especially Dr. Florence Pojer, Dr. Kelvin Lau and Amédé Larabi, for introducing me to protein crystallography as well as Beat Blattmann from the PCC at UZH and Dr. Peer Mittl who supported my protein crystallography experiments at UZH. I am grateful to BIOP at EPFL and the Center for Microscopy and Image Analysis at UZH for their guidance regarding microscopy experiments. Moreover, I am thankful to the NMR and MS facilities of EPFL and UZH for enabling the characterization of my compounds as well as the flow cytometry facility and the Science IT at UZH.

Thanks must also go to my students, Gianluca, Tatjana, and Jevon, for their dedication. I had a lot of fun during our common projects, and I truly appreciate your valuable contributions.

Importantly, I want to extend big thanks to all my colleagues for making my PhD such an enjoyable time. Thank you for sharing the lab, your wisdom, and great times after work! I am also very grateful that I had such attentive proofreaders in you.

Thank you, Zach, for welcoming me into the lab, passing on your knowledge about fluorophores, and helping me to send my first turquoise boulder at Totem.

Acknowledgements

Thank you, Jade, for taking me in on the redox/phosphine project, for your caring nature, and the great spirit you created in the group.

Thank you, Adam, for sharing your expertise in microscopy, physical chemistry and many things that had nothing to do with work. I really enjoyed every guessing game and, of course, our adventurous ski touring.

Thank you, Gina, for trying to teach us chemists some molecular biology, for fixing the LC-MS together with me, and for your everlasting positivity.

Thank you, Salome, for sharing Montelly with me as my almost neighbor (maybe again in Boston?), for keeping the bouldering gang and SoLa runners motivated, and for being such a respectful and honest person.

Thank, you, Annabell, for so much advice in the lab, for many late GNTM evenings, for giving me shelter and all the other things you have done being such a considerate and thoughtful friend.

Thank you, Carla, for being my redox companion, for joining me in jubilation and ranting, and for being critical, when necessary. You are a role model for me in many ways, and I hope to enjoy our friendship until long after our PhDs.

Thank you, Krzysztof, for so much fun you brought into the lab, for initiating all those social activities, and for your tasty creations (sandwiches and booze).

Thank you, Set, for the cheerfulness you spread every day and for teaching us about your culture, especially with amazing Thai dinners.

Thank you, Hen, for happily joining the most daring mountaineering trips, for setting the baking standards in the lab very high and for simply being such a pleasant person.

Thank you, Léa, for synthesizing all these compounds and for sharing your open and kind spirit.

Thank you, Doro, for organizing so many great parties with the most amazing shots. Your excitement inside and outside the lab was absolutely contagious.

Thank you, Anna, for sharing the COUPY dyes with me and for always being in a good mood. I really enjoyed working with you, but even more hanging out with you.

Thank you, Juan, for being so encouraging, kind and helpful. It was a pleasure being around you, enjoying treats from Mexico, and being able to admire your dance moves.

Thank you, Gianluca, for teaching me some python (it must have been hard) and for taking good care of my hood and my apartment.

Thank you, Beccs, for bringing a new perspective and your humor to the lab. I wish you a lot of joy and success during your new and exciting project.

Thank you, Miu, for always being so friendly and for making the lab more youthful and dynamic. I hope you will have a great time continuing your apprenticeship and doing whatever comes next.

I also want to express my deepest gratitude to my parents and my sister who are accompanying me in all my endeavors. It gives me so much comfort that I can always rely on you. I am thankful to my friends outside the lab who I can always have a great time with, who keep in touch even over distance, and who I share music and laughter with.

Finally, Chrisi, your unconditional support carried me through any difficulty. You bring out the best in me because making you proud motivates me every day. Thank you for being at my side.

Abstract

Redox homeostasis is a key factor in maintaining cellular function and health. The main determinant of the intracellular redox potential is ubiquitous glutathione (GSH) together with its oxidized dimer (GSSG). Importantly, both the redox equilibrium and GSH homeostasis are highly compartmentalized. Thus, tools with subcellular resolution are required to gain a detailed understanding of cellular redox chemistry, as well as the related signaling pathways and stress responses.

In this thesis, we present a novel GSH sensor for live-cell imaging in mammalian cells. By combining a spirocyclizing, GSH-sensitive synthetic fluorophore and the self-labeling protein HaloTag (HT), we created a sensor with a fluorescence and reactivity turn-on mechanism. Structural biology revealed the ligand-protein interactions that facilitate this unique feature. Localized expression of HT as a fluorescent fusion protein enabled straightforward targeting and a robust ratiometric read-out. In live-cell experiments, this sensor was able to report reliably on changes in subcellular GSH. Calibration of the sensor allowed the determination of the absolute GSH concentration in various organelles. Our results clearly suggested separated GSH pools in the cytosol, the endoplasmic reticulum (ER) and the nucleus. A second-generation sensor ought to improve slow equilibration kinetics with GSH and finetune the dynamic range for organelles with low GSH concentrations. Therefore, we established a pipeline for the generation of site-saturation mutagenesis libraries to screen for HT mutants that enhance the desired characteristics.

Besides measuring GSH, another goal of this work was the controlled and targeted manipulation of the GSH/GSSG equilibrium. As redox homeostasis and stress responses are compartment-specific, to probe the cellular reaction to redox perturbations, tools with subcellular selectivity are needed too. In this context, reductive stress is way less explored than oxidative stress but could be especially interesting in organelles with an oxidizing environment like the ER.

To probe subcellular reductive stress, we wanted to create a stress inducer that could release a phosphine upon binding to HT. The released phosphine could reduce GSSG, hence impacting redox homeostasis. Again, by expressing HT in the compartment of interest, targeted activation can be achieved. Successful release is indicated by fluorescence turn-on if the phosphine is carried by a fluorogenic scaffold. We considered rhodamine-, hybrid

coumarin- and cyanine-based probes and different substitution patterns were tested to obtain a stable phosphonium that is selectively released. But despite promising preliminary results, these probes still need further optimization to become a robust tool for probing reductive stress in living cells.

Lastly, we explored how multiplexed fluorescence lifetime imaging with self-labeling proteins can be used to observe several subcellular compartments concurrently. We adapted the environment sensitive COUPY dye scaffold to bind HT. Even subtle changes such as mutations in the protein affected the local environment of the dye, which was reflected in altered fluorescence lifetimes. A screening of only 10 mutants identified two versions of HT, which yielded separable signals by lifetime unmixing. With the unbound dye accumulating in mitochondria and the HT variants being expressed in the nucleus and the Golgi apparatus, three organelles could be simultaneously observed.

Keywords: Redox biology, glutathione, reductive stress, compartmentalization, fluorescence microscopy, HaloTag, chemigenetic tools

Zusammenfassung

Die Redoxhomöostase ist entscheidend für Funktion und Gesundheit aller Zellen. Das intrazelluläre Redoxpotential wird hauptsächlich vom ubiquitären Glutathion (GSH) und seinem oxidierten Dimer (GSSG) bestimmt. Das Redoxgleichgewicht im Allgemeinen und die GSH-Homöostase im Besonderen sind stark kompartmentalisiert. Daher sind Methoden mit subzellulärer Auflösung erforderlich, um ein detailliertes Verständnis der zellulären Redoxchemie sowie der damit verbundenen Signalwege und Stressantworten zu erlangen.

In dieser Arbeit präsentieren wir einen GSH-Sensor für Fluoreszenzmikroskopie in lebenden Säugerzellen, bestehend aus der Kombination eines spirozyklischen, GSH-sensitiven synthetischen Fluorophors mit dem Protein HaloTag (HT). Dies ermöglichte selektives Anschalten von Fluoreszenz und Reaktivität. Strukturbiologische Daten zeigten die Ligand-Protein-Interaktionen, die diesen Mechanismus unterstützen. Durch lokalisierte Expression von HT und Fusion mit einem fluoreszierenden Protein, die ein internes Referenzsignal integriert, konnte der Sensor zuverlässig die Veränderungen von subzellulären GSH-Konzentrationen detektieren. Mit einer Kalibrierung des Sensors konnten auch die absoluten GSH-Konzentrationen bestimmt werden. Unsere Ergebnisse deuteten klar auf einen getrennten GSH-Haushalt des Zytoplasmas, des endoplasmatischen Retikulums (ER) und des Zellkerns hin. Ein Sensor zweiter Generation sollte die langsame Equilibrierung des Sensors mit GSH verbessern und seinen Messbereich für Organellen mit geringen GSH-Konzentrationen anpassen. Daher etablierten wir einen Prozess für die Generierung und Charakterisierung von HT-Mutanten, um Varianten zu finden, die diese Verbesserungen erreichen.

Neben der Messung von GSH, wollten wir das GSH/GSSG-Gleichgewicht auch Kompartiment-spezifisch manipulieren. In diesem Zusammenhang ist reduktiver Stress viel weniger erforscht als oxidativer Stress, könnte aber insbesondere in einer oxidierenden Umgebung wie der des ER besonders interessant sein.

Wir wollten ein Molekül entwickeln, das reduktiven Stress auslöst, indem es bei Bindung an HT ein Phosphin freisetzt. Das Phosphin kann GSSG reduzieren und würde dadurch das Redoxgleichgewicht verändern. HT ermöglicht dabei wieder eine lokalisierte Aktivierung. Mit einem fluorogenen Trägermolekül für das Phosphin wird eine erfolgreiche Abspaltung durch Fluoreszenz messbar. Sowohl Rhodamin-, Hybrid-Cumarin- als auch Cyanin-

basierte Moleküle wurden evaluiert. Durch unterschiedliche Substitutionsmuster sollte die Balance aus einem stabilen Phosphonium und selektiver Freisetzung erreicht werden. Trotz einiger vielversprechender Resultate benötigt dieses System aber noch Optimierungen, um ein robustes Werkzeug zur Untersuchung von reduktivem Stress in lebenden Zellen zu werden.

Zuletzt untersuchten wir, wie Fluoreszenzlebensdauer-mikroskopie mit HaloTag dazu verwendet werden kann, mehrere Kompartimente gleichzeitig zu visualisieren. Wir modifizierten COUPY-Farbstoffe, damit sie HT binden. Veränderungen in der näheren Umgebung dieser Farbstoffe, spiegeln sich in veränderter Fluoreszenzlebensdauer wider. Mit nur 10 getesteten HT-Mutanten wurden zwei identifiziert, die aufgrund der Fluoreszenzlebensdauer trennbare Signale lieferten. Mit dem ungebundenen Farbstoff, der in Mitochondrien akkumulierte, und den HT-Varianten, die im Zellkern und im Golgi-Apparat exprimiert wurden, konnten drei Organellen gleichzeitig beobachtet werden.

Keywords: Redoxbiologie, Glutathion, reduktiver Stress, Kompartimentalisierung, Fluoreszenzmikroskopie, HaloTag, Chemigenetische Methoden

Table of contents

Acknowledgements.....	I
Abstract.....	V
Zusammenfassung.....	VII
Table of contents.....	IX
List of abbreviations	XIII
1 Introduction.....	1
1.1 Cellular redox chemistry.....	1
1.2 Glutathione.....	2
1.3 ER stress.....	5
1.4 Fluorescence microscopy.....	8
1.5 HaloTag.....	11
1.6 Outline.....	15
2 Design, characterization and structural analysis of TRaQ-G.....	17
2.1 Objective.....	17
2.2 Design.....	18
2.3 Glutathione sensitivity of an HT-bound QG3.0 derivative.....	18
2.4 Synthesis of spirocyclic SiR-based HT ligands for GSH sensing.....	21
2.5 <i>In vitro</i> characterization.....	22
2.6 Structural analysis.....	25
2.7 Conclusion and outlook.....	27
3 Live-cell GSH imaging with TRaQ-G.....	29
3.1 Objective.....	29
3.2 Construct for live-cell imaging.....	29
3.3 Compatibility of the sensor with live cells.....	32
3.4 Calibration.....	37

3.5	Validation of the sensor in mammalian cells.....	38
3.6	Long-term GSH monitoring with TRaQ-G.....	39
3.7	Compatibility with roGFP	41
3.8	Spectral flexibility.....	42
3.9	Conclusion and outlook	43
4	Toward improving TRaQ-G by protein engineering	45
4.1	Objective	45
4.2	Identification of mutation sites	46
4.3	Initial screening with site-saturation mutagenesis and protein expression.....	46
4.4	<i>In vitro</i> characterization of mutants	48
4.5	Conclusion and outlook	49
5	Subcellularly probing reductive stress with HT-releasable phosphines	51
5.1	Objective	51
5.2	General principle.....	52
5.3	Rhodamine-based scaffolds	53
5.4	Hybrid coumarin-based scaffolds	55
5.5	Cy7-based scaffolds	63
5.6	Conclusion and outlook	70
6	FLIM multiplexing with COUPY dyes	73
6.1	Objective	73
6.2	Synthesis and characterization of COUPY-based HT ligands.....	74
6.3	HT mutants suitable for COUPY dyes.....	76
6.4	Lifetime multiplexing with free and HT-bound COUPY dye	78
6.5	Lifetime multiplexing with different HT mutants	78
6.6	Lifetime multiplexing with different dehalogenases	79
6.7	Conclusion and outlook	80

7	General conclusion and outlook.....	83
8	Experimental.....	87
8.1	General remarks.....	87
8.2	General methods.....	87
8.3	Experimental procedures for chapter 2.....	90
8.4	Experimental procedures for chapter 3.....	99
8.5	Experimental procedures for chapter 4.....	104
8.6	Experimental procedures for chapter 5.....	107
8.7	Experimental procedures for chapter 6.....	137
9	References.....	141
10	Appendix.....	i
10.1	NMR spectra.....	i
10.2	Cartesian coordinates for modeled compounds.....	lx
	Curriculum vitae.....	lxxxv

List of abbreviations

- ATF6 α – Activating transcription factor 6 α
ATP – Adenosine triphosphate
BiP – Immunoglobulin heavy-chain binding protein
BODIPY – Boron dipyrrolomethene
BSO – Buthionine sulfoximine
CA – Chloroalkane
cAMP – Cyclic adenosine monophosphate
CAT – Catalase
CI – Confidence interval
DFT – Density functional theory
DhaA – Dehalogenase from *Rhodococcus*
DIPEA – *N,N*-Diisopropylethylamine
DMAP – 4-Dimethylaminopyridine
DMEM – Dulbecco's modified Eagle medium
DMF – *N,N*-Dimethyl formamide
DMSO – Dimethylsulfoxide
DNA – Deoxyribonucleic acid
DR – Dynamic range
 E_{GSH}° – Standard reductive potential of GSH/GSSG
EGFR – Epidermal growth factor receptor
EI – Electron ionization
eIF2 α – Eukaryotic initiation factor 2 α
ER – Endoplasmic reticulum
ESI – Electrospray ionization
ESIPT – Excited-state intramolecular proton transfer
EtGSH – Glutathione ethyl ester
EtOAc – Ethyl acetate
F – Faraday constant
FBS – Fetal bovine serum
FLIM – Fluorescence lifetime imaging microscopy
FOV – Field of view

FP – Fluorescent protein
FRET – Förster resonance energy transfer
GAPDH – Glyceraldehyde-3-phosphate dehydrogenase
GFP – Green fluorescent protein
GOI – Gene of interest
GPx – Glutathione peroxidase
GR – Glutathione reductase
Grx – Glutaredoxin
GS – Glutathione synthetase
GSH – Glutathione
GSSG – Oxidized glutathione dimer
HPLC – High-performance liquid chromatography
HRMS – High-resolution mass spectrometry
HT – HaloTag
IPTG – Isopropyl β -D-1-thiogalactopyranoside
IRE1 α – Inositol requiring enzyme 1 α
K_d – Dissociation constant
LB – Lysogeny broth
LC-MS – Liquid chromatography-mass spectrometry
MALDI – Matrix-assisted laser desorption/ionization
MAM – Mitochondria-associated membranes
MD – Molecular dynamics
MES – 2-(*N*-Morpholino)ethanesulfonic acid
mRNA – Messenger ribonucleic acid
MS – Mass spectrometry
MTT – 3-[4,5-Dimethylthiazol-2-yl]-2,5-diphenyl tetrazolium bromide
MWCO – Molecular weight cut-off
NA – Numerical aperture
NADPH – Nicotinamide adenine dinucleotide phosphate
NBS – *N*-Bromosuccinimide
*n*BuLi – *n*-Butyl lithium
NEM – *N*-Ethylmaleimide
NIR – Near infrared

NMR – Nuclear magnetic resonance
NO – Nitric oxide
OD – Optical density
PBS – Phosphate-buffered saline
PCR – Polymerase chain reaction
PEG – Polyethylene glycol
PERK – Protein kinase R-like ER kinase
PeT – Photo-induced electron transfer
PKA – Protein kinase A
POI – Protein of interest
Prx – Peroxiredoxin
PTM – Post-translational modification
PTP – Protein tyrosine phosphatases
PTPSP – Protein Production and Structure Core Facility
PyBOP – Benzotriazole-1-yl-oxy-tris-pyrrolidino-phosphonium hexafluorophosphate
qRT-PCR – Quantitative reverse transcriptase polymerase chain reaction
QY – Quantum yield
R – Gas constant
roGFP – Redox-sensitive GFP
ROI – Region of interest
ROS – Reactive oxygen species
rxYFP – Redox-sensitive yellow fluorescent protein
S/N – Signal-to-noise ratio
SD – Standard deviation
SiR – Silicon rhodamine
SOD – Superoxide dismutase
T – Temperature
TBHP – *tert*-Butyl hydrogenperoxide
*t*BuLi – *tert*-Butyl lithium
TEA – Triethylamine
TERS – Transmissible ER stress
TFA – Trifluoroacetic acid
THF – Tetrahydrofuran

TLC – Thin-layer chromatography

TMR – Tetramethyl rhodamine

Tris – Tris(hydroxymethyl)aminomethane

UHPLC – Ultra-high performance liquid chromatography

UPR^{ER} – Unfolded protein response in the ER

XBP1 – X-box binding protein 1

γ -GCS – γ -Glutamylcysteine synthetase

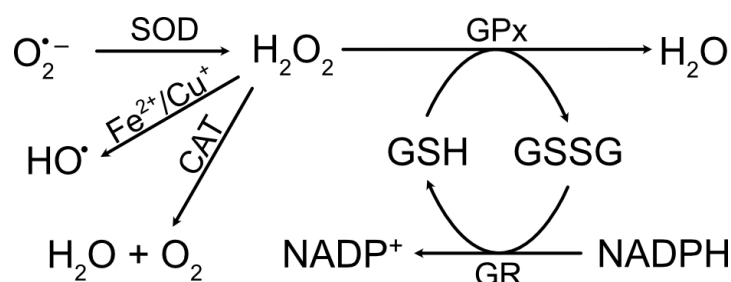
ε – Extinction coefficient

$\tau_{1/2}$ – Half-life

1 Introduction

1.1 Cellular redox chemistry

In any cell, uncountable chemical processes happen simultaneously, each one requiring a very particular environment. The optimal state for all these processes to function and intertwine as needed is generally referred to as homeostasis. Cellular homeostasis comprises many physico-chemical properties, among others ion concentration, pH, and redox potential.¹⁻³ Zooming in on the cellular redox state, it is itself composed of the equilibria of several redox pairs. A large part of the oxidizing power in cells originates from reactive oxygen species (ROS) including superoxide ($O_2^{\bullet-}$), hydrogen peroxide (H_2O_2), and the hydroxyl radical (HO^{\bullet}). The main source of intracellular $O_2^{\bullet-}$ in mammalian cells are electrons from the electron transport chain in mitochondria that are captured by O_2 . $O_2^{\bullet-}$ is rapidly transformed to H_2O_2 by superoxide dismutases (SOD). H_2O_2 can then either react with transition metal ions to form HO^{\bullet} or it is converted to H_2O by catalases (CAT), glutathione peroxidases (GPx) or peroxiredoxins (Prx).⁴⁻⁶ Nicotinamide adenine dinucleotide phosphate (NADPH), on the contrary, is an important reducing agent, which functions as a co-factor for many enzymatic reductions.⁷ Glutathione (GSH) together with its oxidized dimer (GSSG) interconnects with H_2O_2 reduction and NADPH oxidation. GSH is co-substrate for the removal of excess H_2O_2 by GPx and is regenerated by glutathione reductase (GR) with NADPH as the electron donor (Scheme 1).⁸ Together, these redox-active molecules are part of a tightly controlled network, which defines cellular redox homeostasis.



Scheme 1. Redox-active molecules and enzymes involved in cellular redox homeostasis.

Cellular redox homeostasis is not only required to maintain the appropriate conditions for metabolism but has also gained more and more attention for its role in cellular signaling in recent years.⁹ The redox regulation of certain signaling pathways can control metabolism, transcriptional programs, circadian rhythm, proliferation and differentiation.^{4,10,11} For

example, oxidation of reactive cysteine residues in protein tyrosine phosphatases (PTPs) inactivates these enzymes and, consequently, protein tyrosine kinase (PTK) activity is promoted.¹² Many PTKs are known cell surface receptors for growth factors and cytokines.¹¹ The epidermal growth factor receptor (EGFR) is one of these PTKs and the key player in one of the most prominent cellular signaling pathways regulating growth and survival. Notably, the activity of EGFR as well is directly modulated by oxidation with H₂O₂ in a similar manner as for PTPs.^{13,14} Unsurprisingly, due to the important regulatory function of the redox environment, redox imbalances are a biochemical hallmark of many diseases like type-2 diabetes,¹⁵ cancer¹⁶ and neurodegeneration.¹⁷

1.2 Glutathione

The tripeptide GSH (L- γ -glutamyl-L-cysteinyl glycine) has a cytosolic concentration in the order of 1–10 mM.¹⁸ Because of its high abundance, it is typically considered the main intracellular redox buffer, stabilizing and regulating redox homeostasis. Thus, it is often studied representatively to correlate redox chemistry with certain cellular events. Oxidation and reduction between GSH and GSSG are reversible and generally enzymatically controlled. The corresponding redox potential E_{GSH} is defined according to the Nernst equation dependent on the ratio between reduced and oxidized form as follows:¹⁹

$$E_{GSH} = E_{GSH}^{\circ'} - \frac{RT}{2F} \ln \left(\frac{[GSH]^2}{[GSSG]} \right)$$

with the gas constant R (J K⁻¹ mol⁻¹), the temperature T (K), the Faraday constant F (C mol⁻¹) and the standard potential $E_{GSH}^{\circ'}$ (V). However, neither the concentration of GSH nor the GSH/GSSG ratio are homogenous within the whole cell (Figure 1). Both are adapted to fulfill the specific requirements of the processes that take place in a given subcellular compartment.²⁰

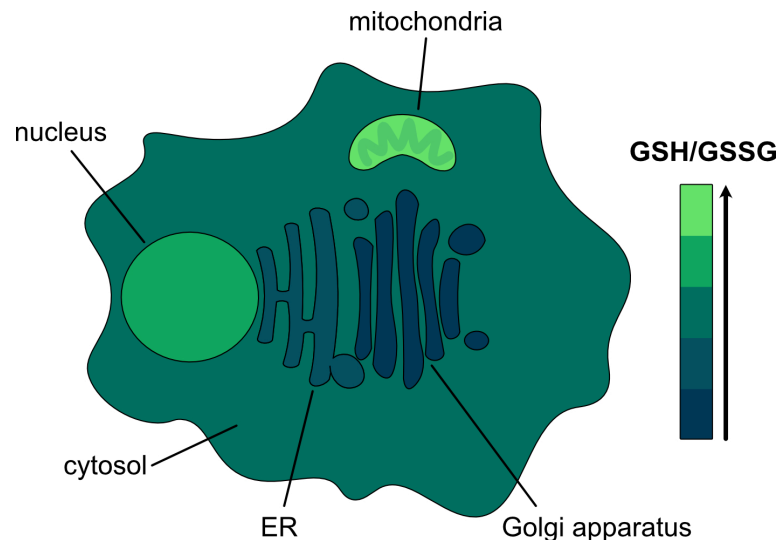
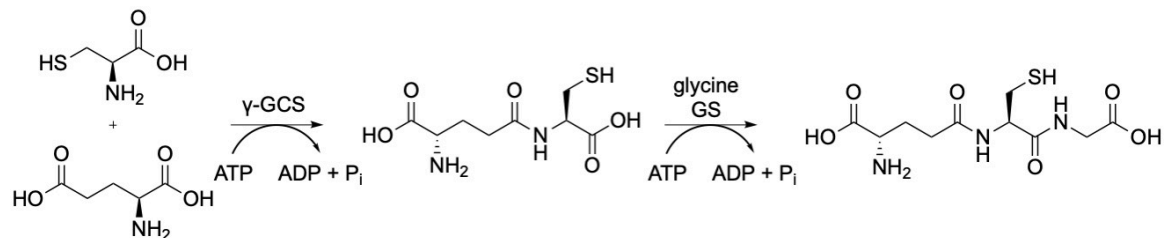


Figure 1. Schematic representation of the compartmentalization of the GSH/GSSG redox potential.

GSH is synthesized from its amino acid building blocks in the cytosol in two enzymatic steps requiring adenosine triphosphate (ATP) (Scheme 2). First, γ -glutamylcysteine synthetase (γ -GCS) forms a peptide bond between the amine group of cysteine and the γ -carboxyl group of glutamic acid. Then, the intermediate is transformed by GSH synthetase (GS) into GSH through condensation with glycine.²¹



Scheme 2. Enzymatic GSH synthesis in the cytosol.

From the cytosol, GSH is distributed to other subcellular localizations. Due to its negative charge at physiological pH, GSH cannot freely diffuse through lipid bilayers. Therefore, all membrane-enclosed organelles require a mechanism for GSH import/export. GSH passes the outer mitochondrial membrane through porins to reach the intermembrane space and equilibrate its GSH pool with the cytosol.²² The inner mitochondrial membrane contains dicarboxylate carriers and oxoglutarate carriers, which transport GSH into the mitochondrial matrix. Yet, E_{GSH} of the mitochondrial matrix does not equilibrate but is mainly influenced by resident GRs.^{22,23}

Redox and GSH homeostasis in the endoplasmic reticulum (ER) is an active field of research with some debate about the prevailing redox potential and GSH concentration.^{24,25}

Through Sec61, GSH from the cytosol reaches the ER lumen by facilitated diffusion.²⁶ In the ER lumen, GSH is oxidized by the machinery for oxidative protein folding, more specifically by Ero1, which is reduced and activated as a result. Active Ero1 mediates the oxidation of immunoglobulin heavy-chain binding protein, Kar2 or BiP, leading to a blockage of Sec61 and therefore reciprocally regulates the GSH import to the ER.^{24,26}

The cytosolic and nuclear GSH pools have been postulated to be connected by diffusion through the nuclear pore complex.²⁷ Concomitantly, nuclear GSH was found to fluctuate with cell proliferation, regulated independently from the cytosolic pool.^{28,29} This result aligns with the fact that deoxyribonucleic acid (DNA) replication requires reductive activity with electrons being provided by GSH or thioredoxin reductase in a complementary manner.^{30,31} A specific accumulation of GSH in the nucleus was also observed during overexpression of Bcl-2, an apoptosis regulator, again implicating a distinct nuclear GSH pool.³² But how the cytosolic and nuclear GSH levels are maintained separately is still unclear. In summary, many open questions remain about the transport and regulation mechanisms that lead to GSH compartmentalization.

Besides its function in redox buffering and compartmentalization, GSH also participates in signaling. As mentioned above, the main mechanism of redox signaling is post-translational modification (PTM) of cysteines. GSH contributes to reactive cysteine modification directly by *S*-glutathionylation as well as indirectly through scavenging of nitric oxide.³³⁻³⁵ A great example for signal modulation through glutathionylation was reported in the context of protein kinase A (PKA) activity. PKA is the main intracellular receptor for cyclic adenosine monophosphate (cAMP) and phosphorylates numerous substrates triggering a complex downstream signaling cascade.³⁶ PKA features a reactive cysteine residue (C199), which stabilizes the phosphorylation of a nearby threonine critical for the enzymatic activity. Glutathionylation of C199 renders this threonine residue labile to dephosphorylation, which abolishes kinase activity.^{37,38} The direct glutathionylation of a cysteine residue can only proceed in locations where the GSH/GSSG ratio is low. Otherwise, proteins can be post-translationally glutathionylated by glutathione *S*-transferases or glutaredoxins (Grx).²⁰ But GSH not only is added to proteins as a PTM but also regulates other PTMs such as *S*-nitrosylation. Nitric oxide (NO) is intracellularly produced by nitric oxide synthases and readily oxidizes available thiols like GSH producing GSNO or cysteine residues of proteins to form P-SNO derivatives.³³ GSNO was

demonstrated to promote nitrosylation of glyceraldehyde-3-phosphate dehydrogenase (GAPDH) stimulating apoptosis.³⁹ In addition to the GSH-mediated nitric oxide transfer, GAPDH can also be post-translationally modified with GSH, which protects it from other oxidizing PTMs.⁴⁰ These two examples highlight how GSH pools regulate cellular signaling by integrating redox-based feedback.

Because of its diverse functions and ubiquitous abundance, GSH is a particularly interesting analyte to study in the context of redox biology.⁴¹

1.3 ER stress

As previously described, deviations from the redox homeostasis impact cellular and organismal health. These disruptions can be divided into oxidative stress, defined as excess levels of pro-oxidants over antioxidant capacity, and reductive stress, which is the opposite.⁴¹ Compared to oxidative stress, reductive stress has been studied less (Figure 2) and is therefore not as thoroughly characterized. Yet, this concept could be of particular importance in the secretory pathway (ER and Golgi apparatus) as these organelles were reported to feature comparably oxidizing environments.⁴²⁻⁴⁴

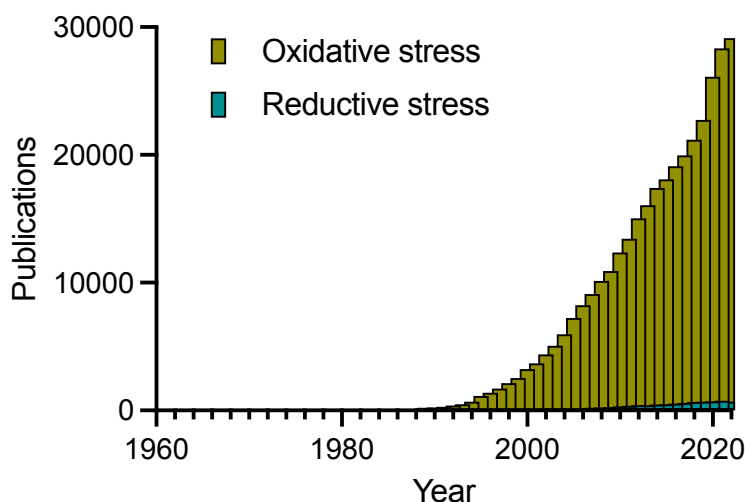
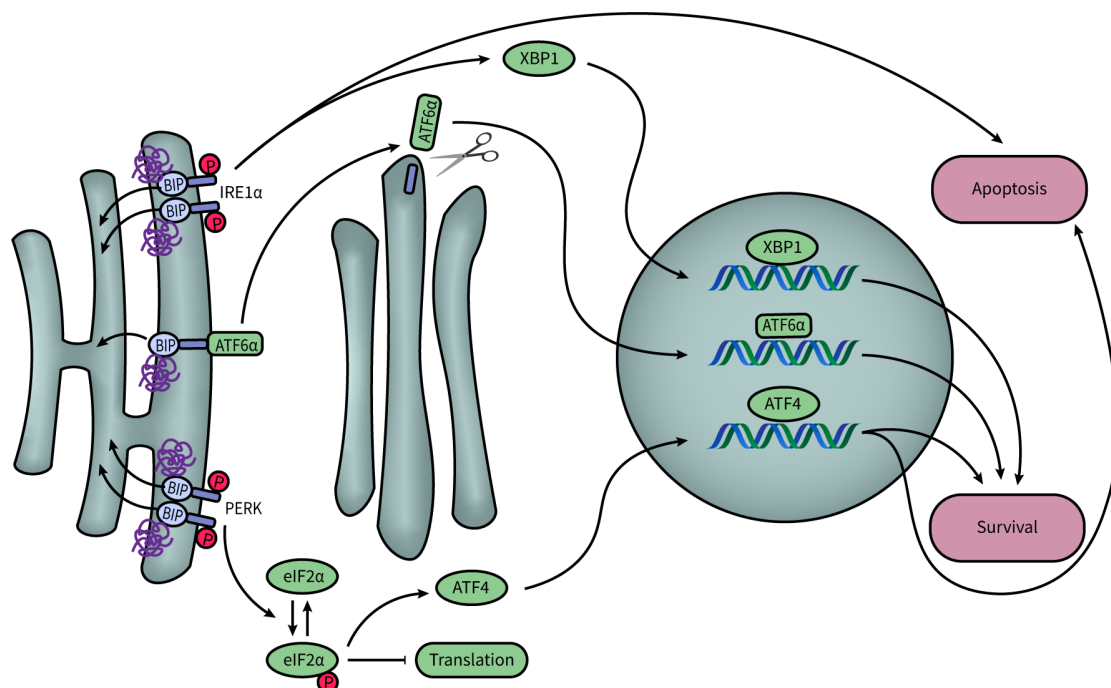


Figure 2. Number of publications on oxidative stress and reductive stress per year according to PubMed.⁴⁵

In the ER, deviations from the physiological redox environment impede the maturation of newly synthesized proteins, which requires formation of disulfide bonds.⁴⁶ This process, which is essential for protein folding, is favored in the oxidizing environment of the ER.^{42,47}

If this redox state cannot be sustained, misfolded or unfolded proteins start to accumulate and form harmful aggregates.⁴⁸ The cell then reacts by triggering a mechanism called the ER unfolded protein response (UPR^{ER}). This signaling pathway is a highly conserved, adaptive response to compensate for external stress factors that would lead to conditions, in which unfolded proteins accumulate.⁴⁹ Activation of the UPR^{ER} starts with the chaperone BiP. Under regular conditions, BiP is bound to the three ER-resident trans-membrane proteins inositol requiring enzyme 1 α (IRE1 α), activating transcription factor 6 α (ATF6 α) and protein kinase R-like ER kinase (PERK), the three main regulators of the UPR^{ER}.⁵⁰ BiP senses ER stress through its preferential interaction with misfolded and unfolded proteins, which releases these three regulators.⁵¹ Each of them, as a consequence, initiates distinct signaling cascades (Scheme 3).⁵² Auto-phosphorylation of IRE1 α results in splicing of X-box binding protein 1 (XBP1) messenger ribonucleic acid (mRNA) to XBP1s, which induces a specific transcriptional program.⁵³ ATF6 α translocates to the Golgi apparatus, where it is cleaved. The activated fragment can further travel into the nucleus to initiate a transcriptional response.⁵⁴ Activated PERK phosphorylates eukaryotic initiation factor 2 α (eIF2 α), which leads to translational attenuation but increases ATF4 activity.⁵⁵ Further downstream events of the UPR^{ER} include upregulation of ER chaperones and eventually apoptosis as a reaction to unresolvable stress.^{53,56–58}



Scheme 3. BiP triggers the UPR^{ER} by binding to misfolded proteins and initiating three signaling cascades by activating the three main regulators IRE1 α , ATF6 α and PERK.

Other compartments besides the ER have defined stress responses too, with mechanisms distinctive from the UPR^{ER}. Examples include the UPR in mitochondria or the Golgi stress response.^{59,60} Nevertheless, the organellar homeostasis is not secluded but there is crosstalk connecting and coordinating the subcellular compartments. In the context of interorganellar stress communication, membrane contact sites are frequently discussed. The contacts between ER and mitochondria, mitochondria-associated membranes (MAM), are probably best understood.⁶¹ At these contact sites, Ca²⁺ channels and transporters can be modulated by ROS and enhance Ca²⁺ flux from the ER to mitochondria.^{62,63} Elevated Ca²⁺ levels in mitochondria stimulate oxidative phosphorylation, which produces additional ROS.⁶⁴ Therefore, there is a mutually reinforcing effect between mitochondrial ROS production and ER stress. Furthermore, many ER-resident oxidoreductases localize near MAMs, forming a “redoxosome”, which could contribute to redox signaling between the ER and mitochondria.^{61,65–67} Redox cues at the MAM are likely also involved in mitochondrial dynamics. Mitochondrial fusion is promoted by glutathionylation of mitofusins.⁶⁸ MAM-localized oxidative signals from the ER influence this PTM and thus connect ER redox homeostasis with mitochondrial dynamics.^{69,70}

The ER and the Golgi apparatus are closely connected through their complementary function in the secretory pathway. Many proteins are transported from the ER through the Golgi apparatus just like ATF6 α , which is processed in the Golgi apparatus as part of the UPR^{ER}.^{71,72} Experimental findings also point toward crosstalk between Golgi stress and the UPR^{ER} although the stress communication has not been studied in detail.⁷³

Not only cellular organelles are interconnected but also individual cells within a population communicate stress. Transmissible ER stress (TERS) has attracted attention in the research community because it has been hypothesized to facilitate resistance of cancer cells to chemotherapy and to spread inflammatory signaling.^{74–77} The most commonly used technique to study TERS is the conditioning of cell culture medium. ER stress is induced in a cell population, usually chemically, and the conditioned culture medium is transferred to a naïve culture. In this second population, induction of the UPR^{ER} could be observed in many cases even though cells had not been exposed to the stressor itself.^{74,75,78–80} However, a recent publication questioned the reliability of those results as carry-over of the used stimulators in the transferred medium cannot be completely excluded.^{74,75,78–81} So far, investigation of this cell-to-cell signaling pathway mostly relied on bulk methods like

quantitative reverse transcriptase polymerase chain reaction (qRT-PCR) or Western blot. However, these techniques are not perfectly suited as the intercellular communication is a process between single cells, which might involve heterogeneity. The development of methods allowing for the observation of TERS with that level of detail could help reveal interesting mechanistic insights.

1.4 Fluorescence microscopy

Fluorescence microscopy has become an indispensable tool to study dynamics of morphology, metabolism and signaling in living cells. This technique features low invasiveness as well as high spatial and temporal resolution. Cellular processes can be visualized in live specimens over time and in excellent detail. A variety of modalities enable imaging across multiple scales and the use of different properties of fluorescence light beyond intensity. While super-resolution imaging reveals details of fine structures⁸² or quantifies minuscule movements,^{83,84} light-sheet imaging routinely allows for samples up to the size of invertebrate and vertebrate embryos.⁸⁵ Adaptations of instrumentation enabled to record the spectrum of fluorescence light in hyperspectral imaging,⁸⁶ the lifetime of emitted photons in fluorescence lifetime imaging microscopy (FLIM)⁸⁷ and the combination of both in sFLIM.⁸⁸

Yet, the informative value of an imaging experiment largely depends on the performance of the fluorescent labels and the reliability of the labeling strategy. The field has developed a huge variety of methods ranging from fluorescent protein (FP) labels to small molecules and hybrid versions of these. The first fluorescent molecules were synthesized in the 19th century including xanthene and cyanine dyes, which are still among the most popular scaffolds today.^{89,90} With the invention of the fluorescence microscope in the early 20th century, researchers started to label biological samples with these fluorophores.⁹¹ Since then, a lot of research has been directed toward the optimization of the photophysical properties of dyes, which now cover the entire visible spectrum and continuously become brighter and more photostable.⁹² Strategies have been developed to selectively target the fluorophores to a subcellular compartment of interest although molecular targeting moieties are never fully generalizable.⁹³ To achieve maximal labeling specificity, fluorescent dyes have been conjugated to antibodies or attached to proteins of interest (POI)

through bioorthogonal chemistry.⁹⁴ However, these methods also have disadvantages as immunostaining is mostly incompatible with live-cell imaging and the introduction of unnatural amino acids for biorthogonal ligation reactions is not yet a routine technique. Alternatively, POIs can be labeled with FPs, an approach that is compatible with living cells and yields perfectly specific targeting. The significance of the discovery of the green fluorescent protein (GFP) and especially its application in bioimaging through construction of fusion proteins can therefore hardly be overestimated.⁹⁵ Engineering the spectral range and photophysical properties of FPs has been a major field of research, yet their tunability, brightness, and photostability generally lags behind synthetic fluorophores.^{96,97}

To visualize smaller metabolites than proteins in fluorescence imaging direct labeling is not applicable. The size of the label generally should not exceed or be too close to the size of the analyte to avoid interference. Both small-molecule fluorophores and FPs have been used to create biosensors to visualize various analytes that cannot be labeled. Metal ion sensors have been developed for Ca^{2+} , Zn^{2+} , $\text{Cu}^+/\text{Cu}^{2+}$ and many others.^{98,99} Sensors for the cellular environment allow monitoring of pH, polarity, viscosity, and transmembrane potential.^{100,101} All kinds of small molecule metabolites, like nucleotides, sugars, or neurotransmitters have been visualized in fluorescence imaging.^{102,103} Typically, the sensing mechanisms are based on supramolecular binding, enzymatic conversions, or covalent bond formation.^{104–106} These events can lead to alteration of the conjugated π -electron system but also to modulation of photo-induced electron transfer (PeT), excited-state intramolecular proton transfer (ESIPT), charge-transfer excited states or Förster resonance energy transfer (FRET).^{105,107,108} As a result, changes in fluorescence intensity, ratio between signal intensities at different wavelengths or fluorescence lifetime can be detected.

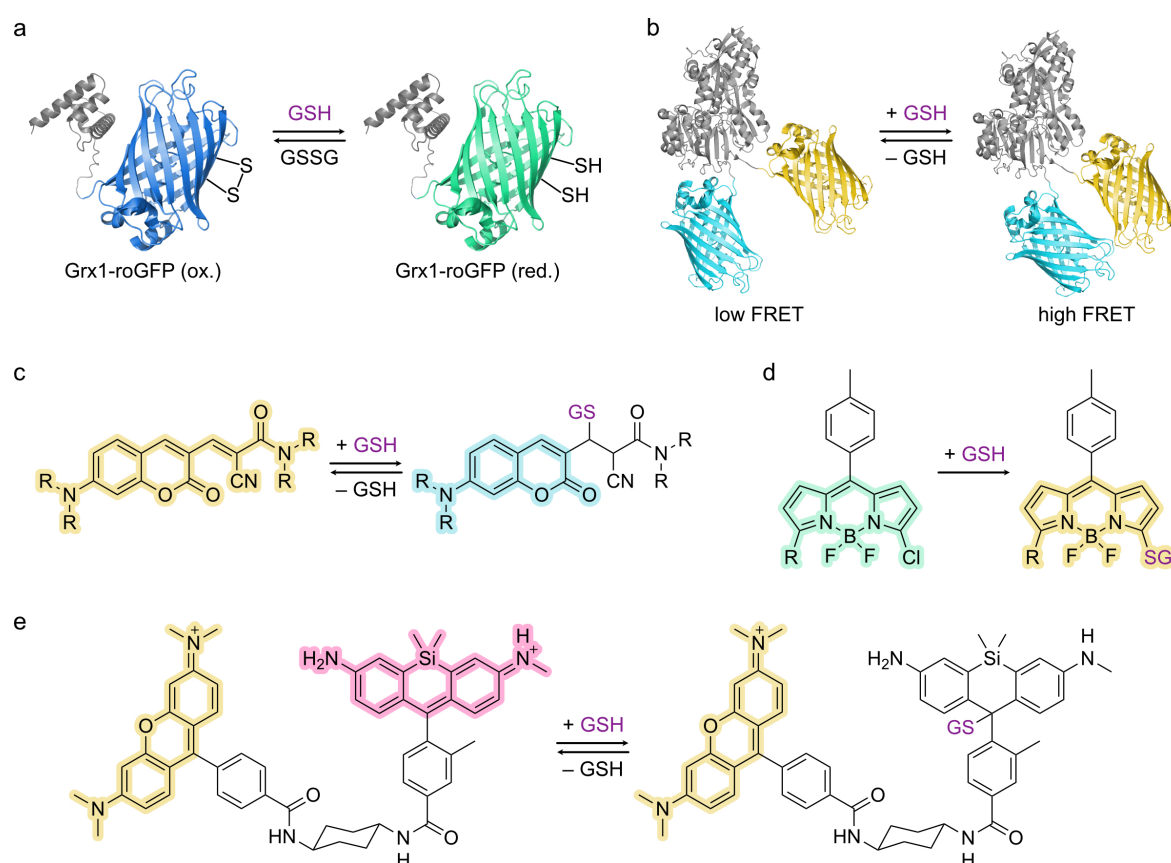
Fluorescence microscopy has also been applied to study cellular redox biology. The redox potential can be measured with redox-sensitive yellow fluorescent proteins (rxYFP) or redox-sensitive GFPs (roGFP).^{109,110} Introduction of a cysteine pair close to the fluorophore, capable of forming a disulfide bond, renders the FPs susceptible to changes in the redox environment (Scheme 4a). Variations of the roGFP sensor have been especially useful as they provide a ratiometric readout. Naturally, GFP possesses two absorption bands corresponding to the protonated and deprotonated form of the fluorophore but a single emission peak due to an ESIPT mechanism. Oxidation results in strengthening of

the blue-shifted band and weakening of the red-shifted band whereas under reducing conditions the opposite is observed.¹⁹ Fusion of Grx1 to roGFP provides selectivity for E_{GSH} through favorable kinetics (Scheme 4a).¹¹¹ Exploiting the merits of genetically encoded sensors, roGFPs have been applied to quantify the GSH/GSSG redox potential in multiple organelles.^{42,112} Similarly, a fusion of roGFP to NADPH-dependent thioredoxin reductase C was used to measure cytosolic and mitochondrial E_{NADPH} .¹¹³ A variety of sensors for studying the cellular redox environment was also created based on different organic fluorophores. Some of them also utilize disulfide bonds in their sensing mechanism but flexible subcellular targeting has so far not been shown.¹¹⁴

A full picture of the cellular redox homeostasis does not only include the redox potential but also the concentration of redox active molecules. A genetically encoded sensor based on a FRET pair fused to the GSH binding protein Ylib, FLIP-G, was able to measure changes in GSH concentration in *E. coli* and yeast (Scheme 4b).¹¹⁵ An absolute quantification was not performed though and kinetics were rather slow. Fusions of circularly permuted FPs and the regulatory domain of the OxyR protein were reported for H_2O_2 sensing. A red-shifted version of this sensor, HyperRed, featured an emission maximum at 605 nm. However, a later derivative based on YFP equilibrated faster and enabled ratiometric measurements in a similar manner as roGFP.^{116,117}

Small-molecule sensors can usually be better fine-tuned. Particularly the red spectral region (~600–700 nm) is easier to reach with synthetic fluorophores, which is desirable for imaging because of decreased autofluorescence and deeper tissue penetration.^{118,119} Many small molecule probes have been reported for measuring GSH in living cells. Recent examples are based on coumarin^{120–123}, boron dipyrrolomethene (BODIPY)^{124,125} and silicon rhodamine (SiR)¹²⁶ scaffolds (Scheme 4c–e). The latter, QG3.0, is especially interesting because of its red fluorescence and fast kinetics. The mentioned examples all exploit the nucleophilicity of the free thiol in GSH to achieve a GSH-responsive fluorescence signal. In contrast to the described genetically encoded sensors that rely on binding affinity, a covalent thioether bond is reversibly formed. However, none of these sensors was able to highlight subcellular differences in GSH. Other redox active molecules were also successfully measured by synthetic fluorescent sensors including several ROS species as well as NAD(P)H.^{127,128}

In summary, fluorescence microscopy constitutes a great tool for studying the dynamics of subcellular redox biology. Tools are constantly developed to visualize the redox potential and concentration of relevant species in living cells with good selectivity and high spatiotemporal resolution. However, full flexibility in terms of targeting and spectral range is still not available for most analytes including GSH.



Scheme 4. Genetically encoded and small-molecule GSH sensors. a) Grx1-roGFP shifts its absorbance maximum between the oxidized and the reduced state. b) FLIP-G undergoes a conformational change upon GSH binding which leads to modulation of FRET. c) Nucleophilic attack of coumarin sensors by GSH leads to a shift in absorbance/emission wavelength. d) Nucleophilic substitution by GSH on a BODIPY core causes a red-shift in absorbance/emission. e) GSH binding to QG3.0 turns off the GSH-sensitive SiR but does not influence signal intensity from the reference fluorophore.

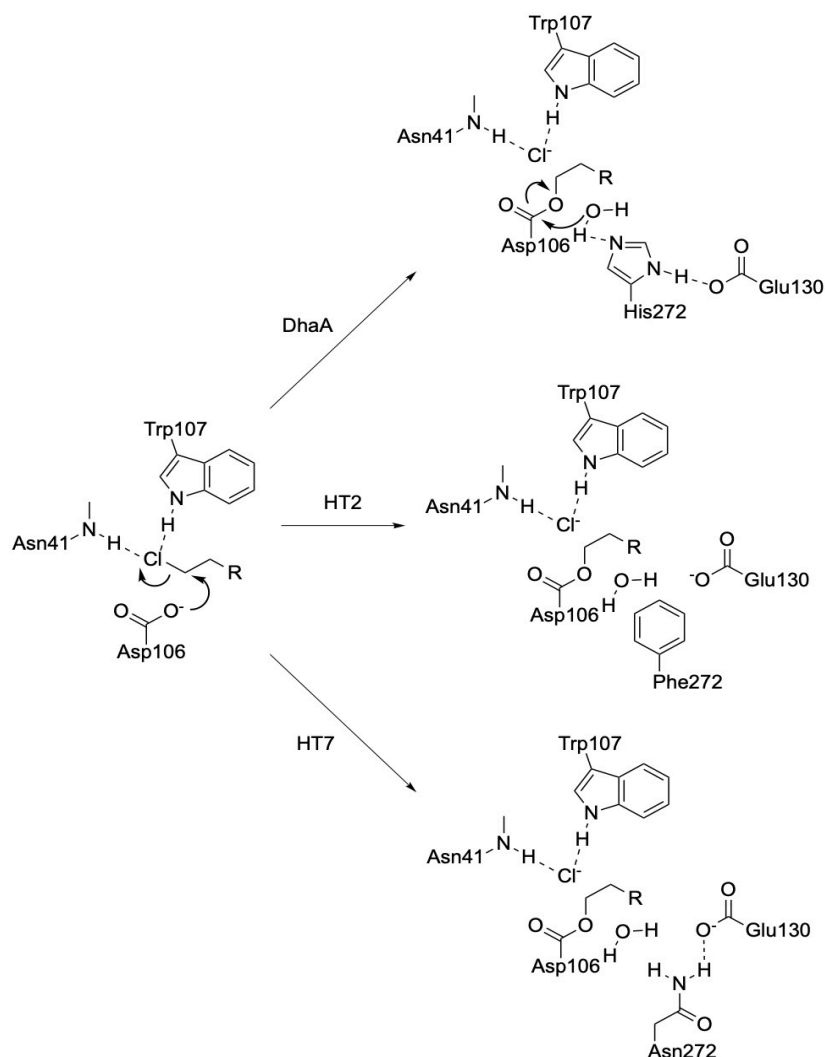
1.5 HaloTag

With the experimental demands for live-cell imaging in mind, self-labeling tags were developed to combine the advantages of genetically encoded and small-molecule labels or sensors. The most important examples are HaloTag (HT),^{129,130} SNAP-tag,^{131,132} CLIP-tag,¹³³ TMP-tag¹³⁴ and PYP-tag.¹³⁵ Fused to a POI these tags covalently bind ligands with

a specific recognition moiety that is orthogonal in cells. The hybrid nature of such systems combines the reliable subcellular targeting of genetically encoded labels with the tunability of small molecules, creating a powerful "chemigenetic" toolbox.

The HT system is of particular interest because of its fast labeling kinetics.¹³⁶ This self-labeling protein emerged from mutagenesis of the *Rhodococcus* dehalogenase (DhaA). This enzyme binds chloroalkanes (CA), cleaves the chloride and releases a corresponding alcohol.¹³⁷ The substitution H272F in the catalytic triad of the enzyme prevents regeneration of the active site and allows for covalent binding of the substrate (Scheme 5). Further screenings revealed a variant, HT2, which accelerated binding kinetics by five orders of magnitude.¹²⁹ In a follow-up study, a more extensive screening effort with random mutations across the entire sequence was conducted for additional improvements of HT. Replacing F272 of HT2 by asparagine was a critical step as it restores hydrogen bonding to the proximal E130 residue from the original enzyme. This adjustment together with many additional mutations improving expression, stability, and binding kinetics yielded the now most commonly used HT7 (Scheme 5).¹³⁰

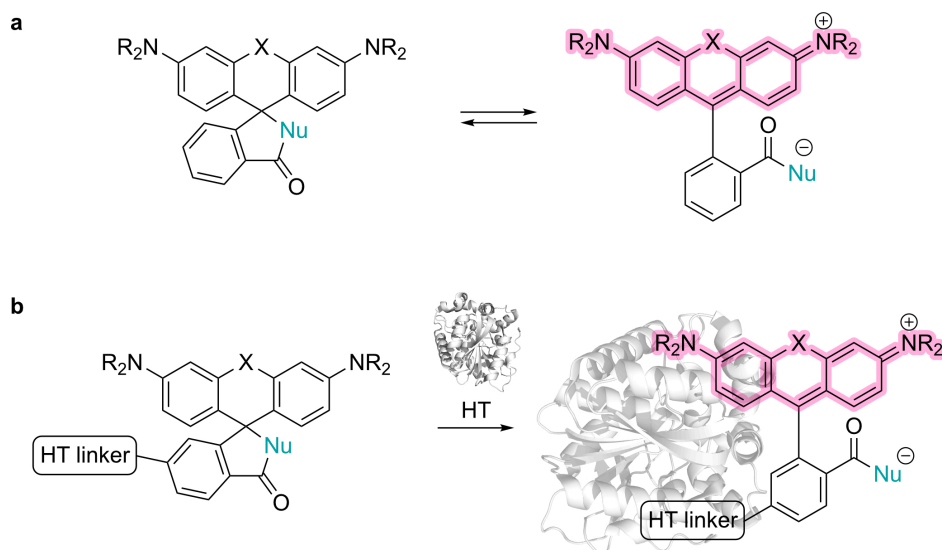
A concern about self-labeling proteins in general was the background signal originating from unbound fluorophores. To avoid a low signal-to-noise ratio (S/N), sample preparation protocols include several washing steps, which can be time-consuming.¹³⁸ Therefore, fluorogenic systems characterized by an unbound non-fluorescent probe that only becomes fluorescent upon binding to its target became very popular. SNAP-tag cleaves a guanine group from its substrates, which was utilized to design fluorogenic probes. Installation of a FRET-based quencher on the leaving group rendered them non-fluorescent until binding to SNAP-tag.^{139–141} The fluorogenicity of PYP-tag relies on a coumarin-fluorescein probe, which forms a non-fluorescent ground-state complex.¹⁴² Binding to the protein impedes complex formation and recovers fluorescence.¹³⁵ However, both systems require a rather large quenching moiety on the substrate, which can hamper compatibility of the probes with live-cell imaging.



Scheme 5. Modifying the active site of the bacterial dehalogenase DhaA to HT2 and HT7 leads to the irreversible and fast binding of chloroalkane substrates.

Rhodamine dyes that are decorated with a nucleophilic group on the bottom phenyl ring exhibit an inherent equilibrium between a spirocyclic non-fluorescent and a zwitterionic fluorescent form (Scheme 6a). This equilibrium between a closed lactone/lactam and an open zwitterion (K_{L-Z}) can shift upon binding to a target.^{143,144} Fine-tuning of K_{L-Z} achieves that the spirocyclic isomer is predominating when the probe is unbound. If binding to the target favors the open form, these probes are fluorogenic. Respective modifications include variation of the nucleophilic group but also different substitution patterns on the aromatic rings. The fluorescence turn-on can for example be triggered by binding to self-labeling tags with HT usually providing the highest turn-on ratio (Scheme 6b).^{145,146} Compared to the attachment of fluorescence quenchers, the chemical modifications to introduce such an open/closed equilibrium are minimal. Moreover, these probes often have many desirable characteristics for live-cell imaging. The unbound spirocyclic form is usually uncharged,

therefore cell-permeable and non-fluorescent, creating virtually no background signal. The open fluorophores are bright and photostable providing excellent contrast. Even though HT was originally optimized for tetramethyl rhodamine (TMR), fluorogenic HT conjugates are not limited to rhodamine dyes. Adaptations of the protein and the CA linkers achieved fluorogenic behavior with styryl pyridinium, benzothiadiazole and cyanine dyes.^{147–149}



Scheme 6. a) Equilibrium of rhodamines between a spirocyclic non-fluorescent and a zwitterionic fluorescent form. b) Binding to HT can favor the open, fluorescent form of rhodamines.

Because of their flexibility, chemigenetic tools for fluorescence microscopy are not only developed and optimized for labeling but also for sensing. The sensing mechanism can either be introduced with a functional small molecule or *via* protein-based recognition.¹⁵⁰ A variety of functional fluorophores have been targeted with HT to sense for example metal ions, transmembrane potential, membrane tension but also GSH with organelle or cell-type specificity.^{121,151–154} Linker design is a critical aspect for these studies to maintain responsiveness of the small molecules.¹⁵⁵ But the HT protein can also be an active player in the sensing mechanism. FRET is a very classical principle used in sensor design. Donor and acceptor can be linked by a recognition unit that undergoes a large conformational change in the presence of the analyte. FRET pairs involving self-labeling tags were optimized to reach almost quantitative FRET efficiency and generate sensors for Ca^{2+} , ATP and NAD(P)^+ with superior dynamic range.^{156,157} Protein-protein interactions can be detected with a tag-assisted splitHaloTag strategy. In this method, the HT protein is split

into two fragments and the fluorescent HT conjugate is only formed when these parts are in proximity to form the full protein. An orthogonal binder is fused to each fragment, which recognizes a tag that can be installed on the POIs. The protein-protein interaction brings the HT fragments close and evokes the fluorescent signal.¹⁵⁸ Protein engineering can also be combined with functional fluorophores to develop new sensing strategies. With an environment-sensitive dye, circularly permuted or aggregation-prone HT variants can be applied in sensing without the need for a second fluorophore as required in FRET-based sensors.^{159,160}

The number of available channels in conventional fluorescence microscopy is usually defined by the spectral overlap between the utilized fluorophores and therefore limited to around four, depending on the instrumentation. Available multiplexing capabilities are critical for the amount of information that can be gathered in a single experiment and influence the ability to directly observe correlations between signals. Hence, additional strategies for multiplexing independent from the spectrum of the emitted light are of great interest. The time dimension that is added in FLIM offers such an opportunity.^{88,161} Recently, HT has been adapted for application in FLIM multiplexing. With a site-saturation mutagenesis approach, the variants HT9–11 were identified, which allowed signal unmixing based on fluorescence lifetime when labeled with the same ligand. In that study, a cell cycle sensor was generated with these mutants requiring a single spectral channel instead of two in previously reported methods.¹⁶²

In conclusion, HT has been a vital part of new developments in fluorescence microscopy tools. With this chemigenetic platform, small-molecule and protein engineering offer infinite opportunities for the optimization of labeling and sensing strategies but also the conception of completely new approaches.

1.6 Outline

Redox biology is an important part of cellular homeostasis. The dynamic and compartmentalized nature of the involved metabolic processes require investigation at high spatiotemporal resolution and with low invasiveness to capture their complexity. Hence, fluorescence microscopy has been an indispensable platform to study the cellular redox state. In this thesis, we aim to expand the fluorescence microscopy toolbox for exploring

redox biology with a particular emphasis on compartmentalization. Thereby, we wanted to demonstrate the versatility of hybrid tools incorporating the advantages of genetically encoded systems and small molecules.

In chapter 2, we describe the design of a targetable GSH sensor (TRaQ-G) based on a GSH-sensitive SiR moiety and the self-labeling protein HT. The distinctive feature of this system is a fluorescence and reactivity turn-on avoiding background fluorescence and interference with cellular GSH homeostasis. Comprehensive structural characterization revealed interesting mechanistic details about the sensor.

Chapter 3 explains how this sensor can be used for GSH quantification in live cells. A robust ratiometric readout was achieved by a fluorescent HT fusion. GSH concentrations of several subcellular compartments were determined, and in a long-term experiment GSH could be monitored during a whole cell cycle.

TRaQ-G has rather slow kinetics and for some organelles the dynamic range might need an adjustment. In chapter 4, a site-saturation mutagenesis pipeline was established to finetune the sensor by means of protein engineering.

In a next step, we wanted to move from observing cellular redox homeostasis to precisely manipulating it. Chapter 5 outlines our attempts to create an inducer of reductive stress that can be triggered in a defined cell population and with subcellular selectivity. Such a tool would be particularly interesting to study the intercellular communication of redox stress.

Finally, chapter 6 covers a brief digression into FLIM with self-labeling proteins. Employing an environment-sensitive fluorophore, we were able to achieve deconvolution of three channels using the same dye, unbound and bound to different HT mutants with minimal screening effort.

2 Design, characterization and structural analysis of TRaQ-G

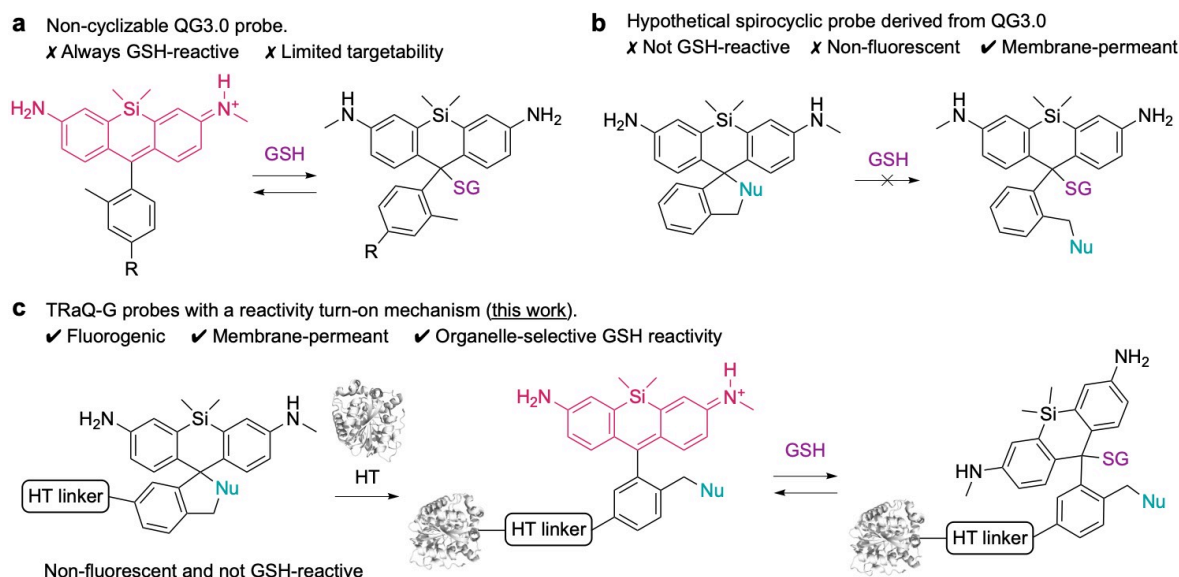
The work discussed in this chapter was conducted in collaboration with Gianluca Quargnali, Sebastian Thallmair, and the Protein Production and Structure Core Facility (PTPSP) at EPFL and was published in *Nature Chemistry*.¹⁶³ Gianluca Quargnali synthesized the TRaQ-G-ctrl ligand under my supervision. We thank Sebastian Thallmair for the molecular dynamics (MD) simulations and the PTPSP, especially Florence Pojer, Kelvin Lau and Amédé Larabi, for their advise on protein purification, for their help with setting up crystallization screens, for performing X-ray diffraction measurements, for their guidance through data analysis and for the verification of the final structures.

2.1 Objective

To study redox compartmentalization, we wanted to create a GSH sensor with subcellular specificity. From the reported GSH sensors, QG3.0, which is based on an electrophilic SiR moiety, is of particular interest because of its red-shifted excitation, reversibility, and fast kinetics.¹²⁶ Since QG3.0 carries two positive charges, it accumulates in mitochondria. We expected targeting moieties to be difficult to introduce and unlikely to override the intrinsic bias for mitochondrial localization. But to investigate GSH compartmentalization, straightforward targeting of the sensor is a desirable feature. We envisioned that a chemigenetic approach attaching the GSH-sensitive small-molecule fluorophore to a self-labeling tag would facilitate targeting. Furthermore, we wanted to avoid reactivity of the sensor toward GSH before it reaches the target localization, which could lead to shuttling of GSH from the cytosol to the compartment of interest. The issue of unintentional alterations of subcellular GSH pools was already raised for an early small-molecule GSH sensor when its GSH conjugate was shown to diffuse from the cytosol into the nucleus.¹⁶⁴ The GSH concentration in the cytosol was reported to be in the mM range¹²¹ and it is difficult to assess how much the sensor itself would influence the GSH distribution. Therefore, we wanted to develop a system with locally activated reactivity toward GSH. We hypothesized that the fluorescence turn-on behavior of dyes binding to self-labeling tags could also lead to a reactivity turn-on.

2.2 Design

Because of its favorable photophysical properties we decided to adapt the previously reported GSH-sensitive SiR for our locally activatable sensor (Scheme 7a).¹²⁶ The SiR scaffold has the additional advantage that a spirocyclizing nucleophile can be introduced to the bottom ring.^{144,145} This modification would keep the unbound molecule in a non-charged and non-fluorescent state. The spirocyclic form would further be unlikely to react with GSH (Scheme 7b). Upon binding to HT, the open fluorescent form should become more favorable and also reactive against GSH (Scheme 7c). By using a HT-based strategy, the advantages of genetically encoded sensors like flexible targeting can be merged with the tunability of small molecules. This design was named Targetable Ratiometric Quantitative GSH (TRaQ-G) sensor.

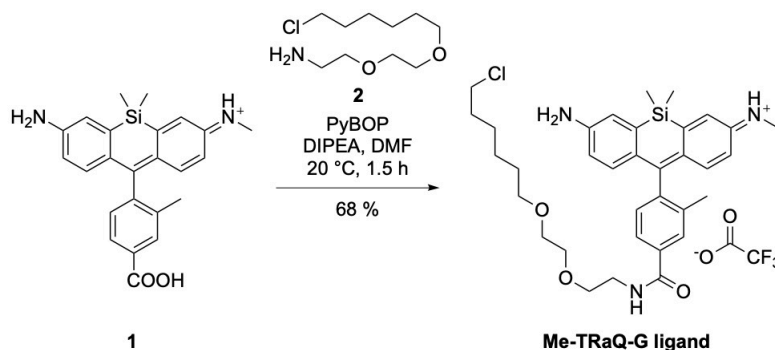


Scheme 7. Graphic from Emmert et al., *Nat. Chem.* 2023 (CC BY 4.0 DEED license).¹⁶³ Comparison of a previously reported SiR-based GSH sensor¹²⁶ and the TRaQ-G design. a) Turn-off mechanism of QG3.0 in the presence of GSH. b) Hypothetical, spirocyclic SiR derivatives based on QG3.0 are non-fluorescent and do not react with GSH. c) Fluorescence and reactivity turn-on of TRaQ-G in the presence of HT. R = cyclohexyl linker attached to a green small-molecule fluorophore for ratiometric measurements. HT linker = chloroalkane moiety optimized for HT binding.

2.3 Glutathione sensitivity of an HT-bound QG3.0 derivative

We first wanted to test if the GSH-sensitive SiR moiety of QG3.0¹²⁶ was still reactive toward GSH when bound to HT. Instead of the green reference fluorophore from the original QG3.0, we attached a CA linker that is optimized for HT binding. The SiR

fluorophore **1** was synthesized according to the reported procedure¹²⁶ and the CA moiety was introduced in the last step *via* amide coupling to yield the Me-TRaQ-G ligand (Scheme 8).



Scheme 8. Graphic from Emmert et al., *Nat. Chem.* 2023.¹⁶³ Synthesis of the Me-TRaQ-G ligand. DIPEA=*N,N*-diisopropylethylamine, DMF=*N,N*-dimethyl formamide, PyBOP= benzotriazole-1-yl-oxy-tris-pyrrolidino-phosphonium hexafluorophosphate.

We expressed HT protein in *E. coli* and the Me-TRaQ-G adduct was prepared, purified, and titrated with 0–20 mM GSH (see section 8.3). The GSH-sensitivity of the Me-TRaQ-G ligand remained almost unchanged compared to QG3.0.¹²⁶ Furthermore, GSH titration of the Me-TRaQ-G ligand and the Me-TRaQ-G HT conjugate (from here on referred to as Me-TRaQ-G) gave almost identical results (Figure 3a,b). Kinetic measurements showed fast binding upon GSH addition ($\tau_{1/2}$ =1.17 s, 95% confidence interval (CI) [1.01–1.30]) as well as fast release of GSH ($\tau_{1/2}$ =5.01 s, 95% CI [4.62–5.60]) when *N*-ethylmaleimide (NEM) was added as a scavenger (Figure 3c). From a structural point of view, these findings suggested that the nucleophilic attack of the fluorophore by GSH is not sterically hindered by the protein and the ligand must be exposed to the solvent to some extent. Indeed, crystallization and X-ray diffraction of the adduct revealed that the xanthene core is positioned flat on the protein surface exposing the electrophilic carbon center on one face. A hydrophobic pocket formed by the residues F152, V167, and T172 accommodates the methyl group of the bottom ring, leaving room for a nucleophilic attack (Figure 3d). MD simulations based on the obtained crystal structure showed that this conformation is preferred (Figure 3e). A second binding mode was predicted, in which the methyl group points toward the solvent and the SiR populates an alternative binding pocket (Figure 3f). This conformation occurred as a rare and short-lived event and is therefore not considered representative.

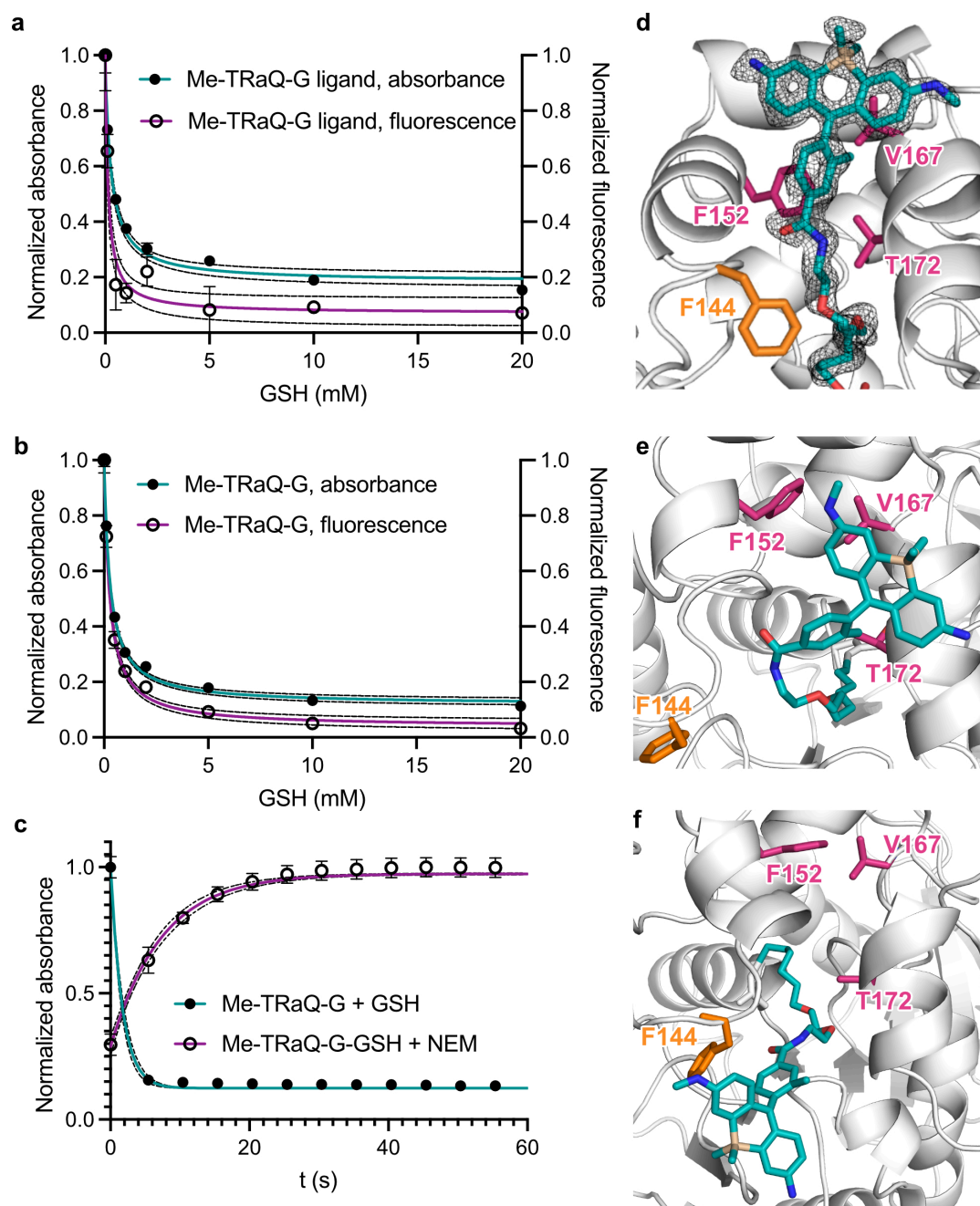
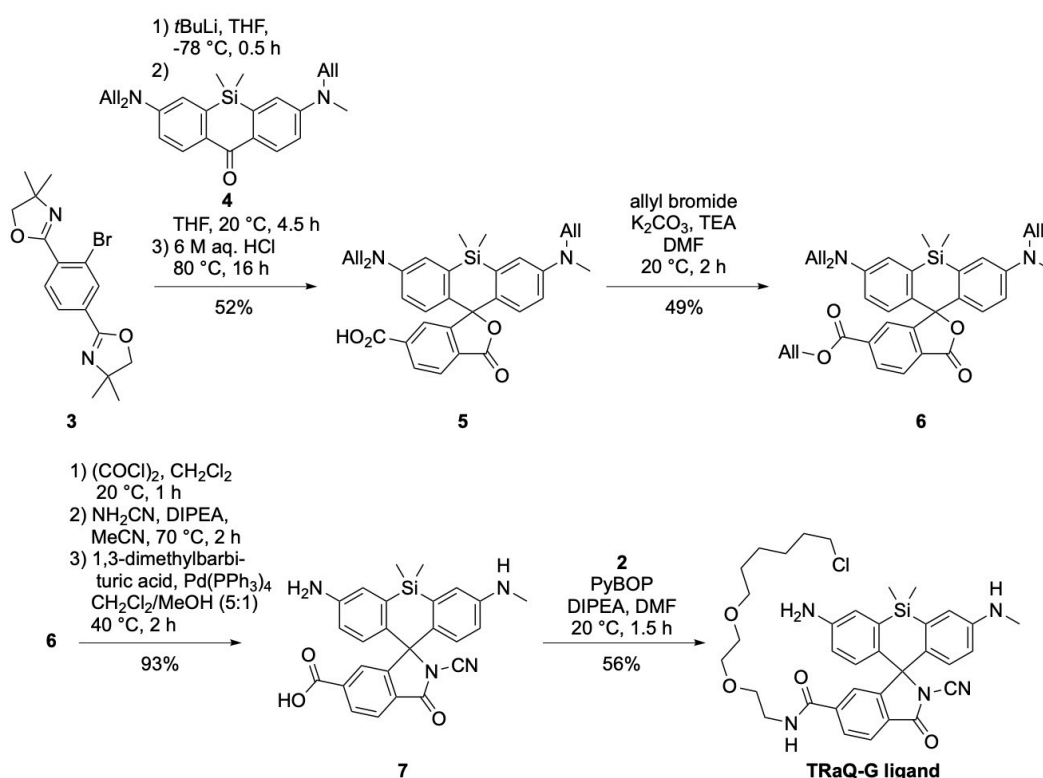


Figure 3. Adapted graphic from Emmert et al., *Nat. Chem.* 2023 (CC BY 4.0 DEED license).¹⁶³ Characterization and structural analysis of Me-TRaQ. a) GSH-sensitivity of the Me-TRaQ-G ligand. b) GSH-sensitivity of the Me-TRaQ-G conjugate. c) Kinetics of GSH binding to and release from Me-TRaQ-G. d) X-ray crystal structure of Me-TRaQ-G (PDB 7ZBA). e) Snapshot (322 ns) during MD simulation of Me-TRaQ-G with the ligand in its preferred conformation. f) Snapshot (457 ns) during MD simulation with the ligand in a short-lived conformation exposing the methyl group to the solvent. Data are presented as mean values and error bars indicate the standard deviation (SD) from $n=3$ technical replicates. Data were fitted with a monoexponential decay. Dotted lines represent 95% CI.

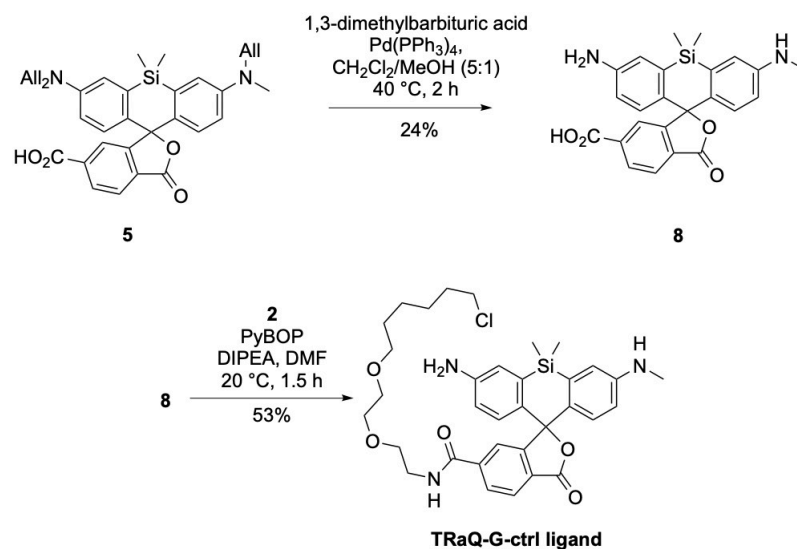
2.4 Synthesis of spirocyclic SiR-based HT ligands for GSH sensing

Next, we asked whether spirocyclization would abolish reactivity toward GSH in respective SiR derivatives and if GSH-sensitivity could be restored by HT binding. Two different derivatives were prepared, with a spirocyclizing cyanamide (Scheme 9) and carboxylic acid (Scheme 10) nucleophile, respectively.^{144,145} The regiochemistry for the substitution with ligand moieties on fluorogenic rhodamines has been reported to play an important role in imaging performance.^{152,165,166} Since the CA linker in the 6'-position has been successfully implemented in several HT-binding SiR-based fluorophores, we decided to synthesize the 6'-isomers.^{144,145} For the preparation of the cyanamide derivative, intermediates **3** and **4** were prepared according to reported procedures.^{126,144} Addition of the protected bottom ring **3** to ketone **4** was mediated by lithium-halogen exchange and subsequent nucleophilic substitution. Acidic deprotection yielded compound **5**. Protection with allyl bromide gave intermediate **6** and installation of the cyanamide followed by deprotection resulted in SiR **7**. Finally, the target compound was obtained by amide coupling with the CA linker **2**.



Scheme 9. Graphic from Emmert et al., *Nat. Chem.* 2023 (CC BY 4.0 DEED license).¹⁶³ Synthesis of the TRaQ-G ligand. TEA=triethylamine, *t*BuLi=*tert*-butyl lithium, THF=tetrahydrofuran.

The corresponding carboxylic acid derivative was synthesized from intermediate **5** in two steps. Deprotection yielded intermediate **8** and amide coupling with CA ligand **2** resulted in the TRaQ-G-ctrl ligand. Both ligands were obtained as pale green/blue solids in accordance with a spirocyclic conformation.



Scheme 10. Graphic from Emmert et al., *Nat. Chem.* 2023 (CC BY 4.0 DEED license).¹⁶³ Synthesis of the TRaQ-G-ctrl ligand.

2.5 *In vitro* characterization

Upon exposure to 10 mM GSH, we found that the cyanamide derivative reacted slowly, whereas the carboxylic acid derivative did not react at all, as determined by liquid chromatography-mass spectrometry (LC-MS). In comparison, the Me-TRaQ-G ligand readily formed its GSH adduct under the same conditions (Figure 4a). Addition of both the TRaQ-G and the TRaQ-G-ctrl ligands to purified HT leads to the appearance of blue color, implying the formation of the zwitterion forms upon binding. When titrated with 0–20 mM GSH, the HT adduct of the carboxylic acid derivative (from here on referred to as TRaQ-G-ctrl) showed no change in fluorescence intensity whereas the HT-bound cyanamide ligand (from here on referred to as TRaQ-G) was responsive in the whole physiologically relevant range. The ligand alone was non-fluorescent and therefore non-responsive to GSH (Figure 4b). Because the carboxylic acid derivative was so similar to the cyanamide compound yet insensitive to GSH, we envisioned it could be used in control experiments.

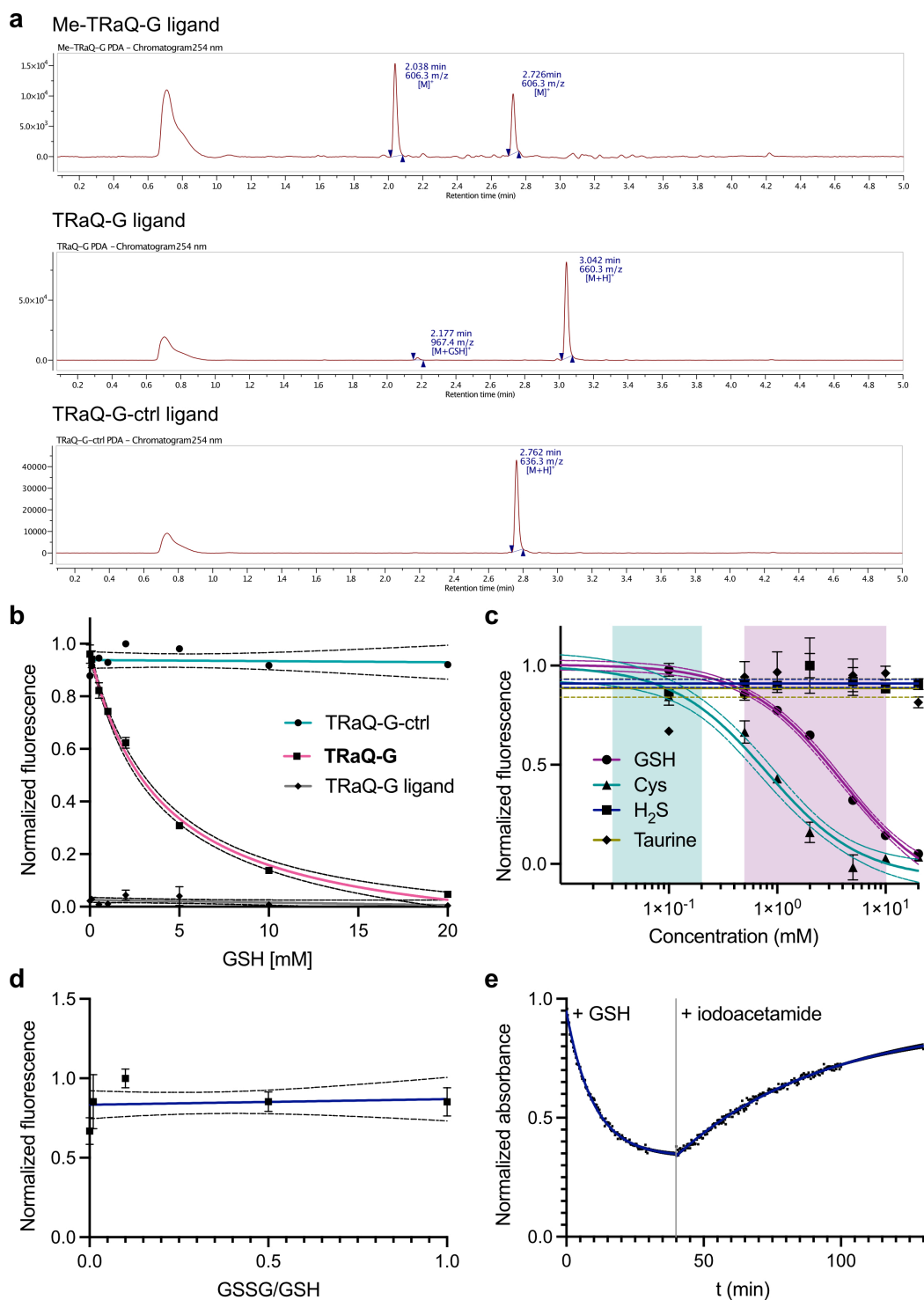


Figure 4. Adapted graphic from Emmert et al., *Nat. Chem.* 2023 (CC BY 4.0 DEED license).¹⁶³ a) LC-MS traces of the Me-TRaQ-G, TRaQ-G and TRaQ-G-ctrl ligands incubated with 10 mM GSH for 10 min. b) GSH titration of the TRaQ-G and TRaQ-G-ctrl adducts as well as the TRaQ-G ligand. c) Response of TRaQ-G to GSH compared to cysteine, H₂S and taurine. Physiological range of concentration is depicted in magenta for GSH¹⁸ and cyan for cysteine.¹²⁶ d) Sensitivity of TRaQ-G to the GSSG/GSH ratio. e) Kinetics of GSH binding to and release from TRaQ-G after addition of GSH and the scavenger iodoacetamide, respectively. Data are presented as mean values and error bars indicate the SD from $n=3$ technical replicates. Data were fitted with monoexponential decay (b,e), linear regression (b-d) or sigmoidal dose-response (c). Dotted lines represent 95% CI.

We further confirmed that no other common intracellular nucleophile reacted with TRaQ-G (Figure 4c) and that only the absolute GSH concentration but not the GSH/GSSG ratio was reported by our probe (Figure 4d). GSH binding to TRaQ-G was found to be reversible, but kinetics were 2–3 orders of magnitude slower than observed for Me-TRaQ-G (Figure 4e). Nevertheless, this measurement demonstrates the full reversibility of the sensor.

Photophysical characterization revealed that quantum yields (QY), and extinction coefficients (ϵ) increased upon HT binding for the TRaQ-G and TRaQ-G-ctrl ligands as the open form becomes favored. Interestingly, even the Me-TRaQ-G ligand experienced a dramatic increase in QY when bound to HT, which potentially originates in added conformational restraints (Table 1).¹⁴⁵ Comparing ϵ of the ligands, TRaQ-G seemed to open to a much less extent than TRaQ-G-ctrl. Further, the TRaQ-G-ctrl ligand could be partially converted to the open form at low pH whereas the TRaQ-G ligand remained completely closed and non-fluorescent. The cyanamide nucleophile was reported to shift the open-close equilibrium more toward the closed form than the carboxylic acid, which could explain the different degree of opening in the bound state.

Table 1. From Emmert et al., *Nat. Chem.* 2023 (CC BY 4.0 DEED license).¹⁶³ Photophysical properties of Me-TRaQ-G, TRaQ-G and TRaQ-G-ctrl ligands and their respective HT adducts. Data are presented as mean from $n=3$ technical replicates.

	QY (%)	ϵ (cm ⁻¹ M ⁻¹)	Brightness (cm ⁻¹ M ⁻¹)
Me-TRaQ-G ligand ^a	14.3	49210	7037
TRaQ-G ligand ^b	--	--	--
TRaQ-G-ctrl ligand ^b	32.6	7869	2565
Me-TRaQ-G ^a	49.5	47650	23586
TRaQ-G ^a	54.2	21450	11625
TRaQ-G-ctrl ^a	56.9	90510	51500

^a Phosphate-buffered saline (PBS); ^b 0.1 M citric acid, pH=2.

2.6 Structural analysis

Since there was no obvious reason for the difference in GSH sensitivity of TRaQ-G and TRaQ-G-ctrl, we thought that structural biology could provide an explanation. We reacted both ligands with HT protein and purified the adducts. Crystallization and X-ray diffraction experiments resulted in structural models of both conjugates. Similarly to Me-TRaQ-G and other reported HT-rhodamine conjugate structures,¹⁵⁹ the xanthene core of the TRaQ-G-ctrl ligand rests on top of an alpha helix (V167–G176) (Figure 5a). MD simulation based on the obtained crystal structure confirmed that the model represents the preferred binding mode (Figure 5b). The solvation of the ligand carboxylate group and an additional hydrogen bond between the amine of the fluorophore and residue E170 seemed to stabilize this conformation. In this model, one face of the molecule is covered by the protein, and the other is blocked by the carboxylate group of the ligand and its solvation sphere. This observation provided a plausible explanation for the lack of reactivity toward GSH.

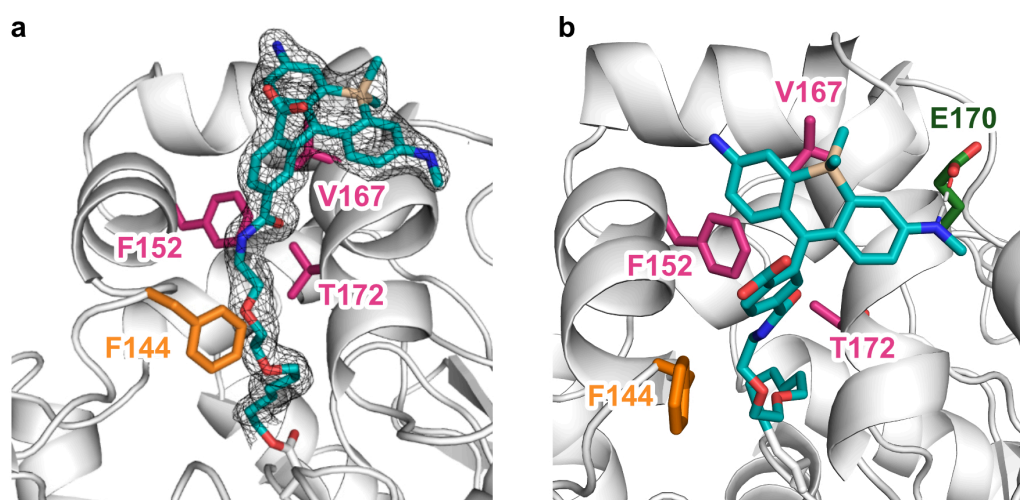


Figure 5. Adapted graphic from Emmert et al., *Nat. Chem.* 2023 (CC BY 4.0 DEED license).¹⁶³ a) X-ray crystal structure of TRaQ-G-ctrl (7ZBB) with highlighted residues forming the hydrophobic binding surface. b) Snapshot from MD simulation (444 ns) with a hydrogen bond between the ligand and the carboxylate group of residue E170.

The X-ray crystal structure of TRaQ-G had a unit cell with two distinct monomers, one with the small molecule in its spirocyclic form (Figure 6a) and another with the open, fluorescent form (Figure 6b). Notably, the ligand binds two different pockets in the closed and open conformation, respectively. The spirocyclic form remains in a similar position to Me-TRaQ-G and TRaQ-G-ctrl whereas the open fluorophore is rotated around the CA chain. Binding to this alternative pocket moreover requires F144 to flip over and

accommodate the ligand (Figure 6c). This behavior was observable in MD simulations, in which rotation of the closed ligand toward the other binding pocket was accompanied by a conformational change of F144 (Figure 6d,e). This residue could be an interesting target for mutagenesis to create HT variants inducing a higher fluorescence turn-on. MD simulations based on the open fluorescent ligand revealed rapid relaxation to a slightly twisted conformation. There, the cyanamide proton forms a hydrogen bond with the backbone carbonyl of P243 (Figure 6f). This hydrogen bond was stable throughout the simulation (Figure 6g) and exposed the electrophilic carbon of the xanthene core to the solvent, providing a mechanistic explanation for the GSH sensitivity of TRaQ-G. This

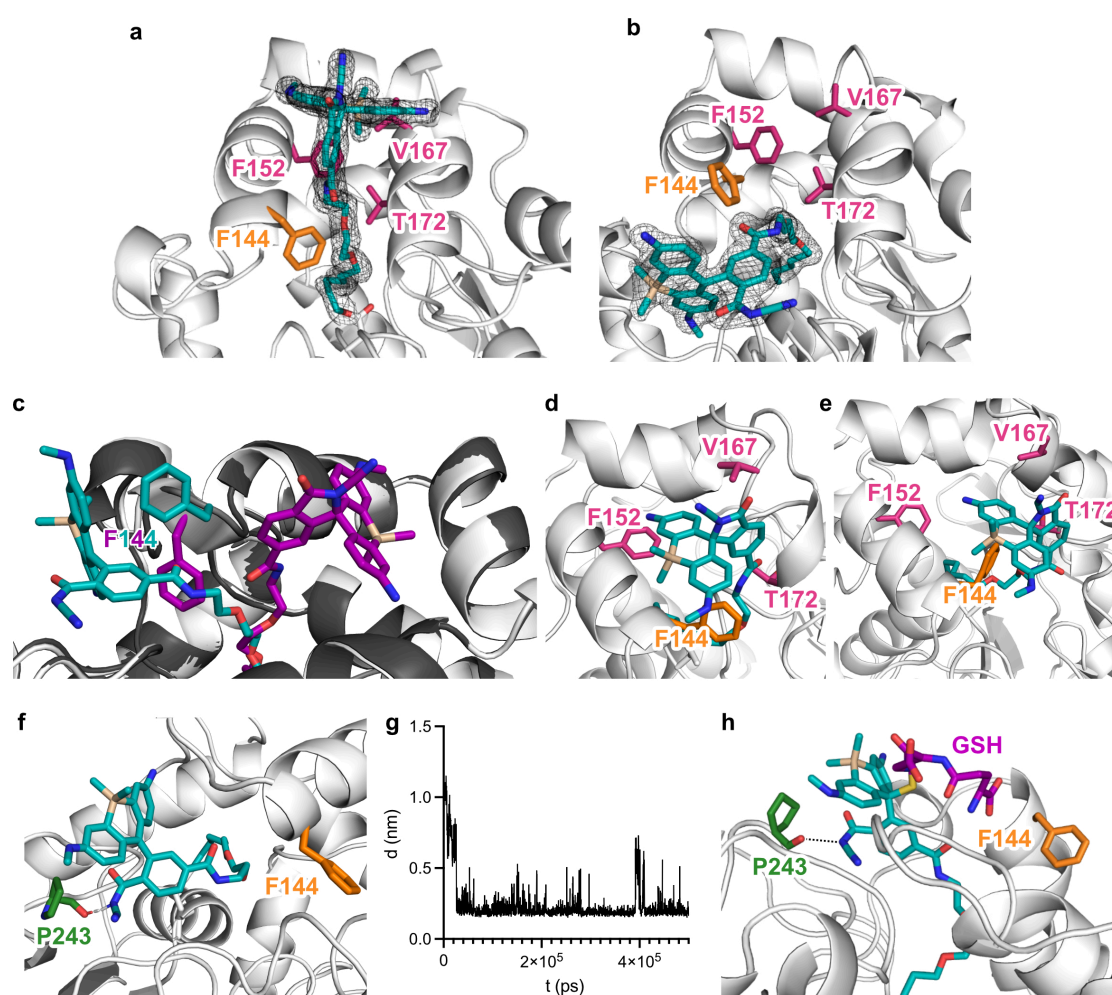


Figure 6. Adapted graphic from Emmert et al., *Nat. Chem.* 2023 (CC BY 4.0 DEED license).¹⁶³ X-ray crystal structure of TRaQ-G (7ZBD) with ligand in spirocyclic form (a), open form (b) and overlay of both monomers (c) highlighting the F144 flip. d–e) MD simulations show the attempt of the spirocyclic ligand to cross F144 and reach the binding pocket of the open form (snapshots at 167 ns and 216 ns, respectively). f) The open fluorophore forms a hydrogen bond with residue P243 in a MD simulation. g) Distance between the backbone carbonyl of P243 and the amide proton of the ligand during the simulation. h) The hydrogen bond is also formed in a MD simulation with the GSH adduct.

hypothesis was further supported by MD simulations with the GSH adduct, in which the same hydrogen bond was observed (Figure 6h).

2.7 Conclusion and outlook

In summary, we built a new GSH sensor with a reactivity turn-on based on a reported GSH-sensitive SiR.¹²⁶ This SiR retained GSH sensitivity when a CA chain was attached and the molecule was bound to HT (Me-TRaQ-G). Synthesis of derivatives with two different spirocyclizing nucleophiles yielded two HT ligands, which were non-fluorescent and non-reactive to GSH in solution. Both ligands became fluorescent upon HT binding but only one of them, the TRaQ-G ligand, also restored GSH-sensitivity. Equilibration with GSH was, however, significantly slower than for Me-TRaQ-G. TRaQ-G-ctrl can serve as a useful control for live-cell experiments. The sensor did not react to other nucleophiles at physiological concentrations and was not sensitive to the GSH/GSSG ratio. Structural biology experiments including X-ray diffraction and MD simulations provided a hypothesis for the mechanism enabling GSH sensitivity of TRaQ-G. A twist of the bottom ring, stabilized by a hydrogen bond to the protein backbone, exposes the electrophilic carbon of the xanthene core to the solvent. In this conformation, TRaQ-G is susceptible to the nucleophilic attack of GSH unlike TRaQ-G-ctrl, in which the reactive carbon is always blocked by the solvent-facing carboxylate group. Based on these data, future studies could aim for the optimization of the interactions between the fluorophore and the protein. Our structural models and the *in vitro* extinction coefficients suggested that the cyanamide-modified SiR only partially opens when bound to HT. The binding pocket could be modified to improve brightness and aid faster equilibration with GSH. Even though the TRaQ-G-GSH adduct was simulated, a successful co-crystallization or soaking experiment followed by X-ray diffraction could provide additional information about GSH binding. Such measurements might be a more robust basis for optimizing the interaction of the sensor with GSH. More generally, our structural data could be used to fine-tune fluorogenicity for similar dye and sensor molecules.

3 Live-cell GSH imaging with TRaQ-G

The work discussed in this chapter was conducted in collaboration with Gianluca Quargnali and was published in *Nature Chemistry*.¹⁶³ Gianluca Quargnali contributed to plasmid generation as well as microscopy data collection and analysis under my supervision.

3.1 Objective

The TRaQ-G sensor described in chapter 2 is a promising design for the measurement of subcellular GSH pools with fluorescence microscopy. In the next step, we wanted to use our sensor in live-cell imaging. As protein expression levels in living systems may vary, a ratiometric read-out with a reference signal is generally more robust for genetically encoded sensors. With a fluorescent protein fused to HT, such an internal standard could be integrated into the TRaQ-G system similarly to the reference fluorophore of QG3.0.¹²⁶ By encoding the protein part of the sensor a plasmid, the construct could be delivered by transient transfection or genetic engineering. As we envisioned a sensor with subcellular precision, we aimed to generate multiple constructs targeted to several organelles. A calibration strategy is needed to measure absolute GSH concentrations. The compatibility of the sensor with the conditions in living cells must be evaluated carefully and validation experiments are required to verify that the output signal indeed reflects changes in GSH concentration. We wanted to demonstrate that our sensor can be used for long-term monitoring by measuring GSH during cell division. Measuring [GSH] and GSH/GSSG simultaneously with TRaQ-G and roGFP, respectively should highlight the versatility of the system. Moreover, if the FP can be freely exchanged, spectral flexibility for different applications could be gained.

3.2 Construct for live-cell imaging

To achieve a ratiometric read-out we fused a bright and photostable FP, mGold,¹⁶⁷ to HT introducing a reliable internal standard. We expected the TRaQ-G ligand to become strongly fluorescent when binding to this construct, but to exhibit decreased emission upon reaction with GSH. The redox-insensitive reference signal of mGold can be used to correct the measurement for varying expression levels of the sensor. We expressed the HT-mGold

fusion protein in *E. coli* and synthesized the adducts with Me-TRaQ-G and TRaQ-G. Figure 7 displays the spectra of the Me-TRaQ-G and TRaQ-G ligands, HT adducts and the HT-mGold conjugates. Comparing the fusion conjugate spectra confirmed that the TRaQ-G ligand is not fully open when bound to HT as the relation between the absorbance bands at 515 nm and 620 nm suggested (Figure 7a,c). Prerequisite for this comparison is quantitative labeling, which we could demonstrate by mass spectrometry (MS). Under our adduct formation conditions, a single peak corresponding to the labeled fusion construct was observed (Figure 7e). These findings match the results of the photophysical characterization (Table 1). With a wide range GSH titration, the K_d of Me-TRaQ-G and TRaQ-G with GSH was estimated (Figure 7b,d). The curves were fitted according to the following equation as proposed in literature:¹²⁶

$$R = R_{bound} + \frac{R_{free} - R_{bound}}{1 + \frac{[GSH]}{K_d}}$$

with the mGold/TRaQ-G ratio R , the ratio when fully bound by GSH R_{bound} , the ratio in the absence of GSH R_{free} and the dissociation constant K_d (M).

From this fit the dynamic range (DR) can be derived as follows:

$$DR = (R_{bound} - R_{free})/R_{free}$$

As the upper plateau (R_{bound}) for TRaQ-G was out of the measurement range the lower limit (95% CI) was chosen to estimate the DR . Notably, TRaQ-G exhibits a higher K_d and a larger DR compared to Me-TRaQ-G (Table 2). The spirocyclization moiety of the ligand seemed to render the sensor less accessible to GSH since it cannot be accommodated as perfectly in the hydrophobic pocket as the Me-TRaQ-G ligand (see section 2.6). Both ligands are able to cover the physiological GSH range.

Table 2. Adapted from Emmert et al., *Nat. Chem.* 2023 (CC BY 4.0 DEED license).¹⁶³ Sensor characterization of Me-TRaQ-G and TRaQ-G.

	$\lambda_{ex}/\lambda_{em}$ (nm)	Brightness	K_d (mM)	DR
Me-TRaQ-G	620/630	23586	8.7 ± 0.8	27
TRaQ-G	620/630	11625	> 56	> 43
mGold	515/530	68480 ¹⁶⁷	--	--

As the intracellular pH can vary between 4.7–8.0 depending on the subcellular compartment,¹⁶⁸ we also evaluated the pH stability of TRaQ-G-mGold *in vitro*. The mGold/TRaQ-G ratio changed only marginally in the range between pH 6–9 (Figure 7f).

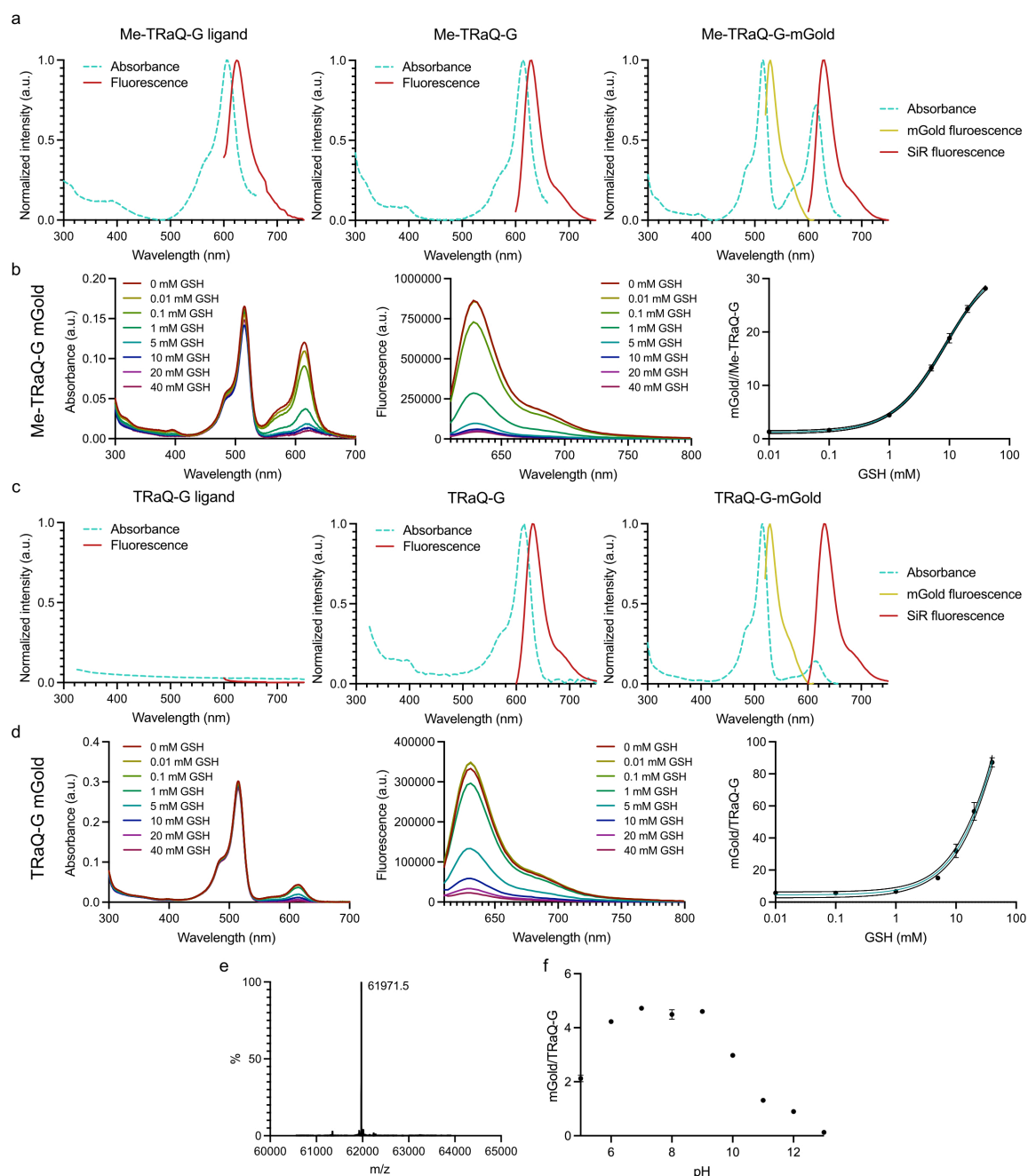


Figure 7. Adapted graphic from Emmert et al., *Nat. Chem.* 2023 (CC BY 4.0 DEED license).¹⁶³ Absorbance and fluorescence spectra of the Me-TRaQ-G (a) and TRaQ-G ligands (c) in comparison to the corresponding HT conjugates and fluorescent fusion conjugates. GSH titration of Me-TRaQ-G-mGold (b) and TRaQ-G-mGold (d) with corresponding curve fit. Deconvoluted mass spectrum gave an experimental value in good accordance with theory (calculated MW=61971.7 g mol⁻¹) (e). pH titration of TRaQ-G-mGold (f). Data are presented as means and error bars indicate the SD from $n=3$ technical replicates. Data were fitted according to the stated equation, dotted lines represent 95% CI.

At lower pH, the protein visibly precipitated, indicating that TRaQ-G is not applicable in acidic organelles such as lysosomes.

3.3 Compatibility of the sensor with live cells

Although Me-TRaQ-G exhibits good *in vitro* properties, we predicted that its applicability in live cells would be limited due to its constant fluorescence and reactivity toward GSH. Imaging of live HeLa cells expressing HT in the nucleus revealed high levels of off-target fluorescence in vesicular structures (Figure 8), confirming our prediction.

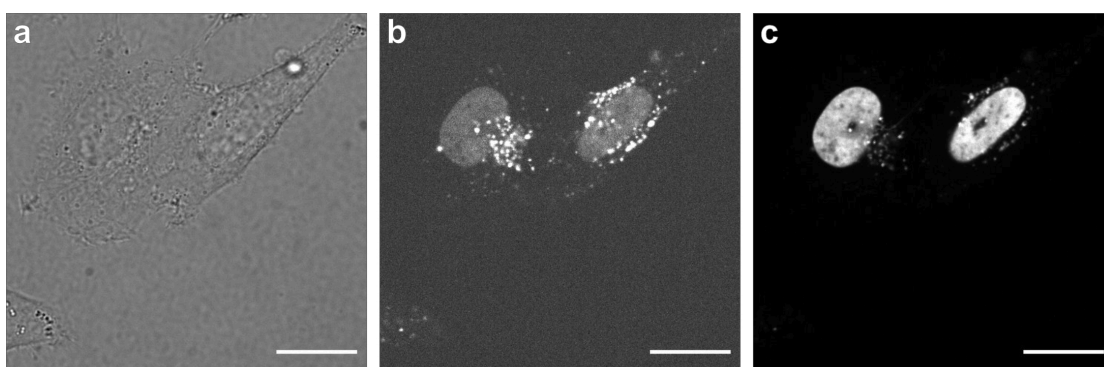


Figure 8. Adapted graphic from Emmert et al., *Nat. Chem.* 2023 (CC BY 4.0 DEED license).¹⁶³ HeLa cells transfected with H2B-HT-emiRFP703 and incubated with the Me-TRaQ-G ligand. Representative images of spinning disk confocal microscopy with brightfield (a), Me-TRaQ-G (b) and FP reference channel (c). Scale bars=20 μm .

The TRaQ-G ligand was designed to minimize off-target signal, therefore we expected it to perform better in live-cell imaging experiments. By Gibson assembly, we generated several plasmids to deliver our HT-mGold fusion protein to specific organelles using established peptide localization sequences. HT-mGold leads to expression in the whole cell, ER targeting was achieved fusing Calnexin to HT-mGold, H2B-HT-mGold is expressed in the nucleus, and the signal sequence of ATP9¹⁶⁹ yields expression in mitochondria. Transiently transfected HeLa cells expressed the fusion protein in the correct localization and incubation with the TRaQ-G ligand led to perfect overlap between the respective FP and ligand channels (Figure 9). The mitochondrial plasmid unfortunately leaked into the cytosol and the nucleus of some cells. Localization could not be improved by incorporation of two consecutive targeting sequences or using the alternative targeting sequence COX8.

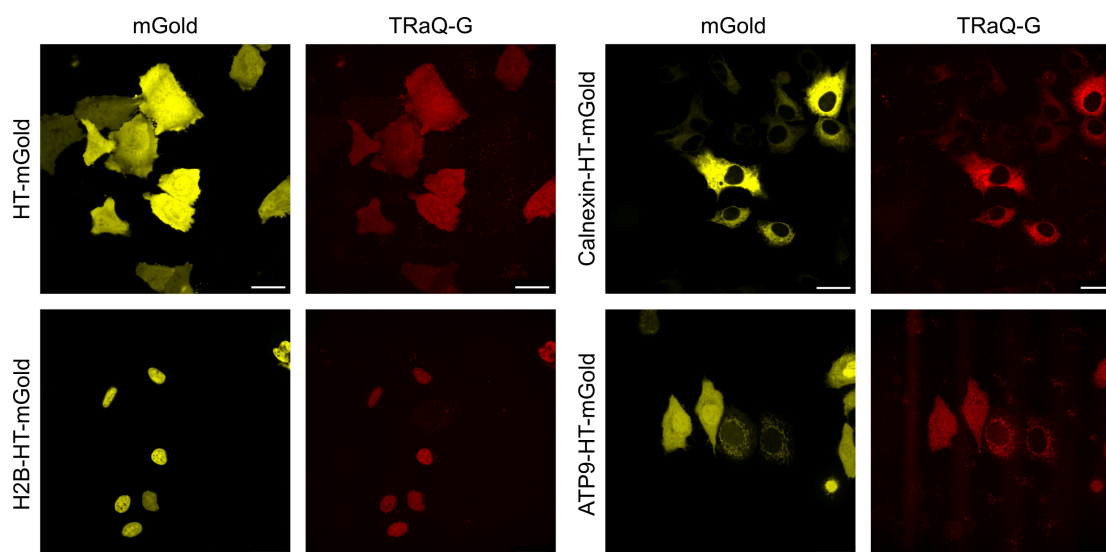


Figure 9. Adapted graphic from Emmert et al., *Nat. Chem.* 2023 (CC BY 4.0 DEED license).¹⁶³ HeLa cells expressing HT-mGold fusion protein in various subcellular localizations and incubated with TRaQ-G ligand. Representative images from three independent measurements, scale bars=30 μm .

Using TRaQ-G-ctrl, we established that intracellular labeling of HT is fast and reaches saturation in less than 30 min (Figure 10). These data suggested that HT is stably labeled to its maximum extent under the experimental conditions.

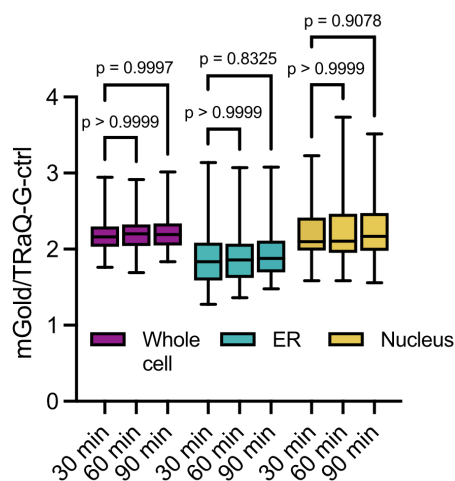


Figure 10. Adapted graphic from Emmert et al., *Nat. Chem.* 2023 (CC BY 4.0 DEED license).¹⁶³ Saturation of the HT-mGold fusion protein with TRaQ-G-ctrl in living HeLa cells. $N=90, 91, 91, 142, 131, 101, 116, 115, 111$ (from left to right) cells from three biological replicates. Boxes represent 25th–75th percentiles, line represents median and whiskers go from minimum to maximum, statistical significance was assessed by one-way ANOVA (Tukey's multiple comparison test).

Before performing GSH measurements in live cells, we wanted to further establish the robustness of TRaQ-G. While the fully assembled sensor should reveal changes in [GSH], neither HT7 alone nor mGold should be sensitive to changes in the redox environment. The

pH stability of TRaQ-G was already investigated *in vitro* with stable mGold/TRaQ-G ratios between pH 6–9 (Figure 7f). A recent publication pointed out that HT labeling kinetics can be sensitive to disulfide bond formation in the protein.¹⁷⁰ As some organelles like the ER are characterized by an oxidizing environment, altered binding behavior could affect the comparability of TRaQ-G measurements between subcellular compartments.⁴² When comparing the proposed redox-insensitive variant HT8¹⁷⁰ with HT7 in the ER, no measurable differences in labeling were observed (Figure 11a). Thus, we continued using the HT7 constructs. mGold should ideally also be insensitive to changes in the redox environment or the GSH homeostasis to ensure that the mGold/TRaQ-G ratio solely reflects the reaction of GSH with the ligand. Treatment of HeLa cells with H₂O₂, buthionine sulfoximine (BSO, an inhibitor of GSH synthesis) or the cell-permeable glutathione ethyl ester (EtGSH) did not alter mGold fluorescence intensity (Figure 11b).

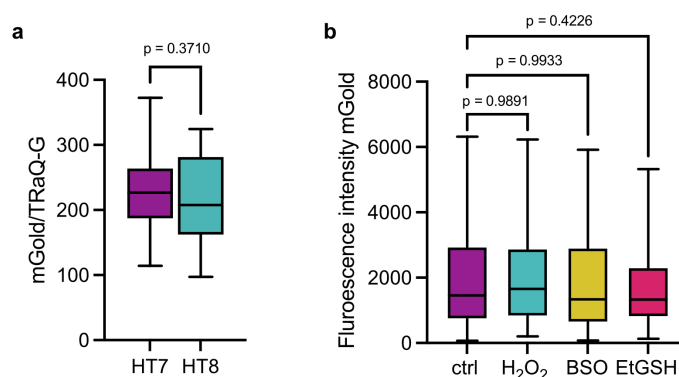


Figure 11. Adapted graphic from Emmert et al., *Nat. Chem.* 2023 (CC BY 4.0 DEED license).¹⁶³ a) Comparison of HT7 to redox-insensitive HT8 displaying similar labeling efficiency with TRaQ-G. $N=37$ (HT7) and 30 (HT8) cells from one biological replicate, statistical significance was assessed by unpaired t-test. b) Stability of mGold to treatments altering the intracellular GSH levels. HeLa cells were transfected with HT-mGold, H2B-HT-mGold or Calnexin-HT-mGold > 24 h prior to imaging. $N=263, 446, 293, 372$ (from left to right) cells from three biological replicates. Boxes represent 25th–75th percentiles, line represents median and whiskers go from minimum to maximum, statistical significance was assessed by one-way ANOVA (Dunnett’s multiple comparison test).

Moreover, the presence of the sensor should change the cellular homeostasis as little as possible in order to enable observation of physiologically relevant behavior. Quantification of cellular GSH with a commercial colorimetric assay indicated that the transfection procedure induced an increase in [GSH]. However, the overexpression of the fusion protein itself did not have an effect compared to mock transfection (Figure 12).

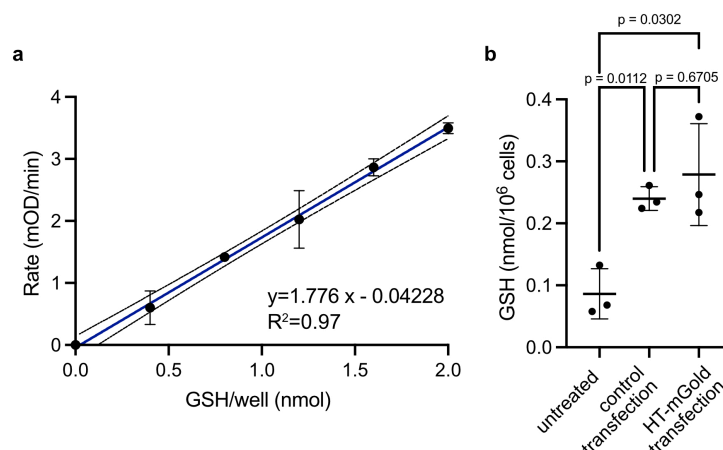


Figure 12. Graphic from Emmert et al., *Nat. Chem.* 2023 (CC BY 4.0 DEED license).¹⁶³ a) Calibration curve to determine absolute amount of GSH in lysate samples with a commercial reduced GSH assay kit. Data are presented as means and error bars indicate the SD from $n=3$ technical replicates and were fitted by linear regression, dotted lines represent 95% CI. b) Measured amounts of reduced GSH in HeLa cells that were untreated, transfected with a control plasmid or with HT-mGold normalized to the number of cells used for the assay. Lines represent means and error bars indicate the SD from $n=3$ biological replicates. Statistical significance was assessed by one-way ANOVA (Tukey's multiple comparison test).

Flow cytometry experiments confirmed that transfection and overexpression did not affect ROS levels or cause cytotoxicity (Table 3 and Figure 13). In summary, TRaQ-G was found to be suitable for live-cell GSH quantification due its robustness and little disruptive behavior in cells.

Table 3. From Emmert et al., *Nat. Chem.* 2023 (CC BY 4.0 DEED license).¹⁶³ Fractions of cells in flow cytometry experiments positive for mGold expression, increased ROS levels indicated by CellROX DeepRed fluorescence or apoptosis indicated by AnnexinV-Pacific Blue fluorescence. Cells were either transfected with HT-mGold, left untreated (negative control) or treated with *tert*-butyl hydrogenperoxide (TBHP, positive control). The gating strategy is described in Figure 13. Presented data are combined from three biological replicates. For each sample at least 25000 events were processed.

	mGold+	ROS+	Apoptosis+
mGold-transfected	40%	21%	15%
untreated	0%	21%	11%
TBHP	0%	35%	38%

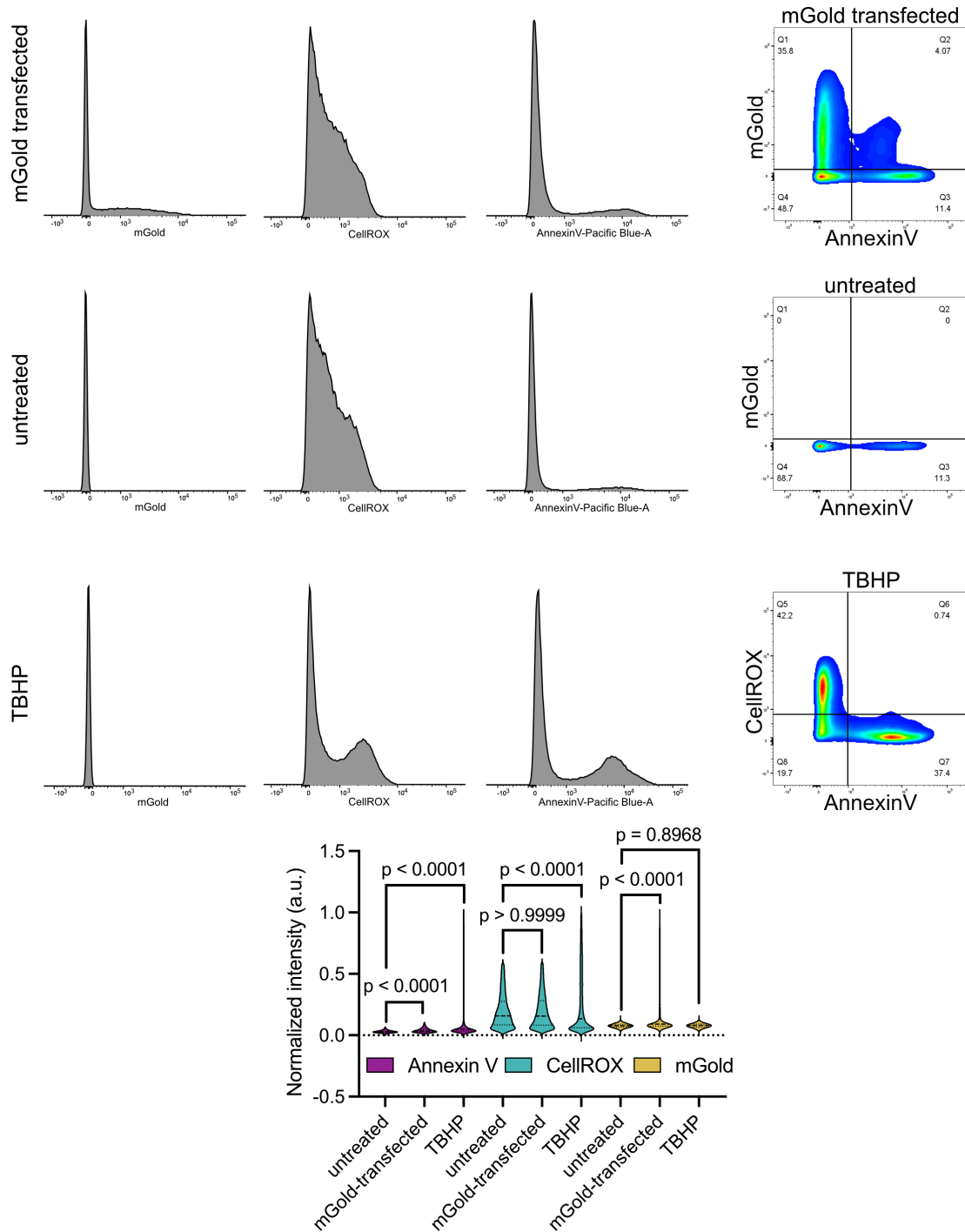


Figure 13. Graphic from Emmert et al., *Nat. Chem.* 2023 (CC BY 4.0 DEED license).¹⁶³ Histograms of cells positive for mGold expression, increased ROS levels indicated by CellROX DeepRed fluorescence, or apoptosis indicated by AnnexinV-Pacific Blue fluorescence in flow cytometry experiments. Cells were either transfected with HT-mGold, left untreated (negative control) or treated with TBHP (positive control). Presented data are combined from three biological replicates. For each sample at least 25000 events were processed. Single-cell data of all replicates were merged and gates were set in FlowJo. Gating strategies are displayed on the right. $N=63526, 61044, 107122, 68867, 69249, 118398, 73953, 61400, 126343$ (from left to right), statistical significance was assessed with a Kruskal-Wallis test except for P(mGold untreated vs. TBHP) as the populations are normally distributed (D'Agostino & Pearson test) and therefore one-way ANOVA was applied.

3.4 Calibration

After confirming the compatibility of TRaQ-G with live-cell imaging, the sensor had to be calibrated for absolute GSH quantification to relate mGold/TRaQ-G ratios to [GSH]. First, we calibrated the sensor with fixed cells to have a very similar environment to the intended measurements. HT-mGold was expressed in the nucleus of HeLa cells, the cells were incubated with the TRaQ-G ligand, fixed, permeabilized and exposed to varying concentrations of GSH. The mGold/TRaQ-G ratio was determined by fluorescence microscopy but the results gave large SDs and the linear regression was unsatisfactory (Figure 14a). It was unclear how much the fixation and permeabilization protocol interfered with the fluorescence signal. Therefore, we considered a more controlled environment for the calibration and used purified HT-mGold conjugates with the TRaQ-G ligand. As discussed above, we could assume full labeling *in vitro* (Figure 7e) and fast saturation in cells (Figure 10), which is crucial for the extrapolation from purified conjugate to live-cell measurements. The sensor was again exposed to varying concentrations of GSH and the mGold/TRaQ-G ratio was measured by fluorescence microscopy. A linear correlation was observed over 1–20 mM GSH with excellent goodness of fit (Figure 14b). This range is

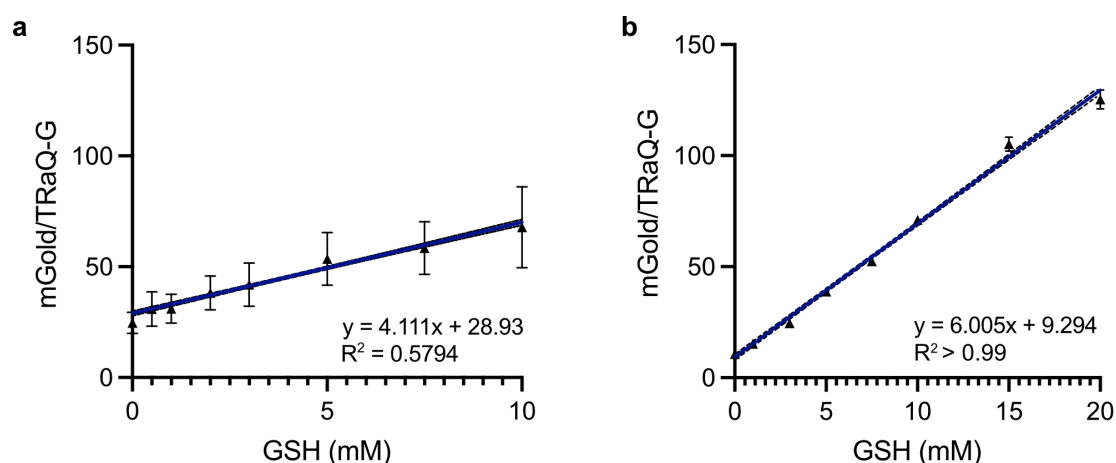


Figure 14. Adapted graphic from Emmert et al., *Nat. Chem.* 2023 (CC BY 4.0 DEED license).¹⁶³ a) Calibration curve with H2B-TRaQ-G-mGold expressed in HeLa cells measured by fluorescence microscopy. After incubation with the TRaQ-G ligand, cells were fixed and incubated in buffer (0.5 M sodium phosphate, pH=7.4) containing GSH at various concentrations (three independent measurements). b) Calibration curve of TRaQ-G with adduct formed by *in vitro* reaction of purified fusion protein with ligand and measured by fluorescence microscopy (three technical replicates). The conjugate was exposed buffer (0.5 M sodium phosphate, pH=7.4) containing GSH at various concentrations. Data are presented as mean values and error bars indicate the SD from $n=3$ biological (a) or technical (b) replicates. Data were fitted by linear regression, dotted line represents 95% CI.

suitable for GSH measurements in the physiological range. Importantly, the calibration curve should be performed at the pH of the subcellular localization of interest since the degree of protonation impacts the nucleophilicity of GSH.

3.5 Validation of the sensor in mammalian cells

After thorough characterization of the sensor, we moved to measuring [GSH] with TRaQ-G in several subcellular localizations. For validation, the results were compared to other reported sensors and methods. In this experiment, HeLa cells were transiently transfected with the respective plasmid and incubated with the TRaQ-G ligand. The mGold/TRaQ-G ratio was measured by fluorescence microscopy and the ratio was converted to absolute [GSH] values using the calibration curve. Expression of the sensor in the whole cell gave an approximate overall GSH concentration of 18.9 ± 9.4 mM. This result is similar to what was obtained with the commercial GSH assay for cell lysates, which estimated 7.7–15.5 mM intracellular GSH depending on the volume assumed for a HeLa cell ($1800\text{--}3600 \mu\text{m}^3$)¹⁷¹ (Figure 12). It is not very surprising that the assay based on cell lysate yields a slightly lower concentration as GSH is prone to oxidation when exposed to air. In the ER, we measured 9.2 ± 5.3 mM GSH with TRaQ-G. This matches investigations relying on roGFP, which reported $[\text{GSX}]_{\text{ER}} = 19 \pm 6$ mM converting to $[\text{GSH}]_{\text{ER}} = 14.3 \pm 4.5$ mM with respect to a GSH/GSSG ratio of 6:1.⁴² The mitochondrial GSH concentration measured with TRaQ-G was 4.8 ± 0.7 mM, which is in very good agreement with results obtained with the parent sensor QG3.0 (4.4 ± 1.3 mM).¹²⁶ It should again be noted that the mitochondrial targeting was far from perfect (Figure 9). Although cells displaying off-target fluorescence could be excluded from the analysis, we decided to refrain from further experiments with this construct. Finally, TRaQ-G revealed a nuclear GSH concentration of 14.0 ± 6.7 mM.

For further verification of our system, we tested whether we could observe the expected changes when the cells were exposed to reagents modifying intracellular GSH. HeLa cells were transfected with the respective construct and exposed to EtGSH, BSO, or H₂O₂. In all localizations, EtGSH increased the measured GSH concentration. When GSH synthesis was inhibited with BSO, lower [GSH] values were observed after 3–4 h in the whole cell and the nucleus. In the ER the effect was not significant. As GSH is synthesized in the cytosol, it is expected that the largest difference is observed there. Oxidation of GSH with

H₂O₂ significantly lowered [GSH] in all observed localizations (Figure 15). These results confirmed that TRaQ-G enables measurement of the absolute GSH concentration in living cells and is furthermore able to detect changes in subcellular GSH pools.

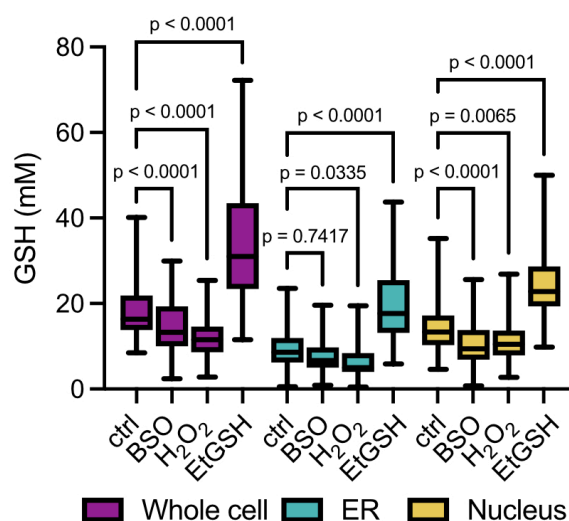


Figure 15. Adapted graphic from Emmert et al., *Nat. Chem.* 2023 (CC BY 4.0 DEED license).¹⁶³ Quantification of GSH concentration in whole cells, the ER or untreated nuclei (ctrl) after the addition of 10 mM EtGSH, 1 mM BSO or 1 mM H₂O₂. Boxes represent 25th to 75th percentiles, the horizontal line represents the median, and whiskers extend from the minimum to the maximum. $N=130, 132, 142, 111, 103, 118, 116, 131, 93, 90, 122, 149, 176, 143, 137$ (from left to right) cells from three biological replicates, statistical significance was evaluated by one-way analysis of variance (ANOVA, Šídák's multiple comparisons test).

3.6 Long-term GSH monitoring with TRaQ-G

The high cell-to-cell variability, which was obtained while quantifying organellar GSH, suggested that there are natural fluctuations. There are contradictory reports on whether the nuclear and cytosolic GSH pools are independent but variations in nuclear GSH have been associated with cell proliferation.^{29,121,172} Considering our experimental observations and literature research, we suspected that we might observe changes in GSH in the course of the cell cycle with TRaQ-G. As outlined in section 1.2, DNA replication requires GSH, which suggests that high GSH levels are expected in the nucleus during the S and G₂ phases.^{29–31} To test this hypothesis, HeLa cells were transfected with HT-mGold or H2B-HT-mGold, synchronized in the early S phase by double thymidine block,¹⁷³ incubated with the TRaQ-G ligand and imaged for 24 h. As a control, we performed the same experiment with the TRaQ-G-ctrl ligand, which is insensitive to GSH (Figure 4b), to exclude artifacts

from changing expression levels, sensor degradation or photobleaching. In the nucleus, a slight increase in GSH was observed 1–2 h after release from the thymidine block corresponding to early S phase. Afterwards, the nuclear GSH concentration dropped, stabilizing through G2 phase and mitosis (Figure 16a,c). TRaQ-G-ctrl on the other hand gave a stable ratiometric signal throughout the measurement (Figure 16b,c), suggesting that the observed changes are indeed due to GSH fluctuations. Interestingly, only subtle fluctuations were detected during the measurement in the whole cell (Figure 16c) and a clear difference in [GSH] between the cytosol and the nucleus was visible in some cells (Figure 16d). However, these fluctuations were heterogenous between biological replicates, possibly due to varying passage number or culture density of the cells.^{29,111} With TRaQ-G-ctrl the mGold/SiR ratio remained stable (Figure 16c) and comparison between the nuclear and whole cell measurements did not reveal notable differences.

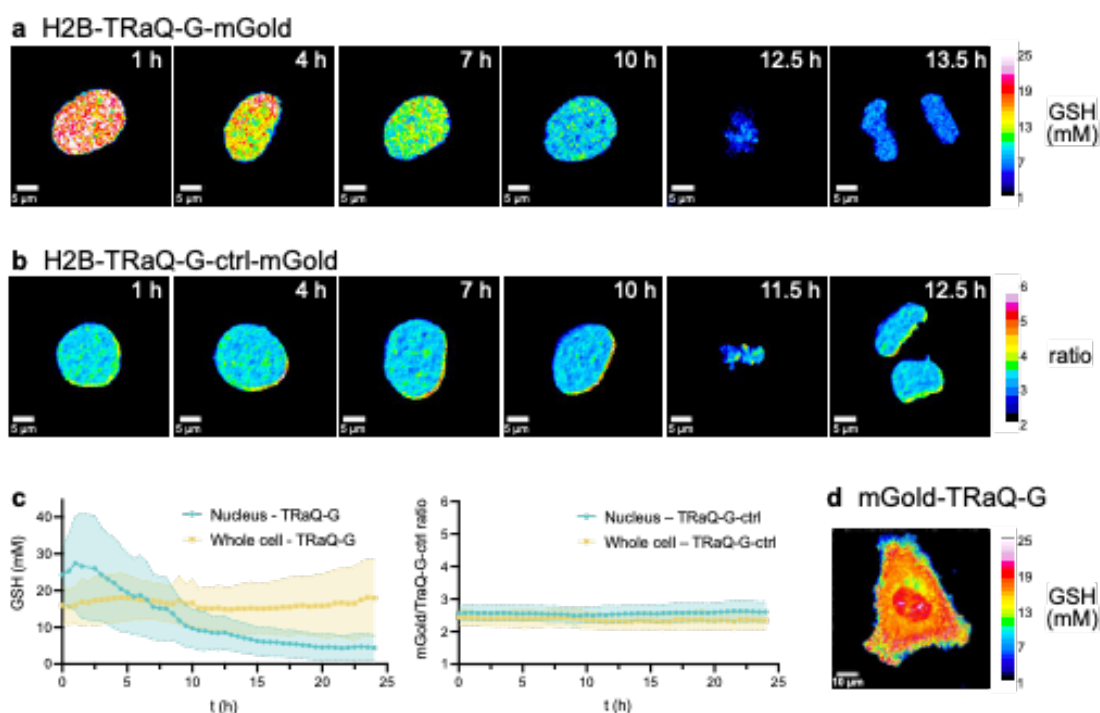


Figure 16. Graphic from Emmert et al., *Nat. Chem.* 2023 (CC BY 4.0 DEED license).¹⁶³ TRaQ-G imaging during the cell cycle with HeLa cells synchronized by double thymidine block. a) H2B-TRaQ-G-mGold ratiometric imaging of a single nucleus from S phase to mitosis, revealing a steady decrease in GSH concentration. b) The control probe TRaQ-G-ctrl-mGold shows a stable mGold/SiR ratio throughout the experiment. c) Quantification of GSH concentrations or the variation of the ratio with the control probe for 24 h after release of cells from thymidine block (early S phase). Lines represent average values, and the shaded areas represent the SD. $N \geq 19$, 50, 42, 19 cells per timepoint from three biological replicates. d) TRaQ-G-mGold ratiometric imaging of a single cell ($t=2$ h) displaying different concentrations in the nucleus and the rest of the cell.

These results indicate an independently regulated nuclear GSH pool, which fluctuates during the cell cycle. Peak GSH concentrations were observed during early S phase matching results from previous reports.²⁹ Why GSH cannot freely diffuse through nuclear pores and how transport between the cytosol and the nucleus is regulated otherwise is beyond the scope of this study but remains an intriguing question. Further investigations are needed to confirm these findings and discover the underlying mechanism. However, this experiment highlighted the strengths of our sensor well. The covalent anchoring allows for long-term measurements and we were able to showcase GSH compartmentalization with separate cytosolic and nuclear GSH pools, which was not detectable with other targetable sensors.¹²¹

3.7 Compatibility with roGFP

Many redox sensors, as well as the widely used roGFP, which reports on E_{GSH} , absorb and emit photons of the blue/green spectral region. TRaQ-G was designed to use the more red-shifted part of the spectrum, which thus allows for multiplexing with roGFP. Simultaneous measurement of the GSH concentration and redox potential in a subcellular region of choice is therefore possible. We planned a 4-color experiment with an optical configuration according to Figure 17a. HeLa cells were transfected with Calnexin-HT-mGold and roGFP-iE-ER, which was specifically engineered for the oxidizing environment in the ER.⁴² The cells were imaged untreated or after exposure to EtGSH. The GSH concentration strongly increased as expected whereas the roGFP signal suggested a slight but non-significant shift toward a more reducing environment (Figure 17b–d). The cells appeared to maintain GSH/GSSG even under GSH accumulation presumably through oxidation to GSSG. These findings showcase that concurrent analysis of [GSH] and GSH/GSSG can be beneficial to obtain a full picture of intracellular GSH and redox homeostasis.

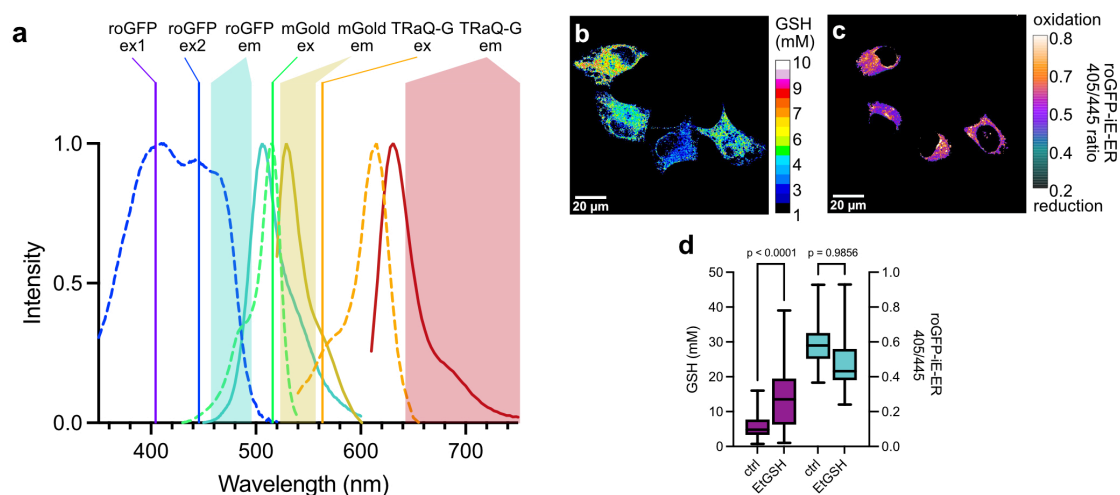


Figure 17. Adapted graphic from Emmert et al., *Nat. Chem.* 2023 (CC BY 4.0 DEED license).¹⁶³ a) Schematic representation of a four-color experiment multiplexing roGFP-iE-ER and Calnexin-TRaQ-G-mGold. Colored lines represent the excitation wavelengths of the chromophores. Absorption (dashed lines) and emission spectra (solid lines) of the different fluorophores are displayed in corresponding colors, and shaded areas indicate the emission filters used to collect photons at different wavelengths. b,c) Ratiometric imaging of total GSH concentration using Calnexin-TRaQ-G-mGold (b) and of redox potential using roGFP-iE-ER (c). The image in c is not calibrated, and only the ratio of emission at 475 nm upon excitation at either 405 or 445 nm is displayed. d) Comparison of GSH concentrations and 405/445 ratios of roGFP-iE-ER in cells either untreated (ctrl) or after incubation with 10 mM EtGSH for 3 h. Boxes represent 25th to 75th percentiles, the center line represents the median, and whiskers extend from minimum to maximum. $N=119, 115, 86, 103$ (from left to right) cells from three biological replicates, statistical significance was evaluated by one-way ANOVA (Šídák's multiple comparisons test).

3.8 Spectral flexibility

The design of TRaQ-G enables the use of a FP of choice providing spectral flexibility. A near-infrared (NIR) version of the sensor was created by replacing mGold with emiRFP703.¹⁷⁴ HeLa cells were transfected with the resulting H2B-HT-emiRFP703 construct, incubated with the TRaQ-G ligand and treated with 1 mM H₂O₂. Over time the emiRFP703/TRaQ-G ratio decreased corresponding to a declining GSH concentration (Figure 18). Cells that displayed high [GSH] at the start of the experiment seemed to experience a more pronounced change. This behavior might reflect the kinetics of GPx-mediated oxidation of GSH, which are linearly dependent on GSH molarity.^{175,176} Our experiments, however, do not allow for definite conclusions. It is noteworthy that emiRFP703 relies on biliverdin as a cofactor forming the fluorophore. Biliverdin is

naturally available in mammalian cells but the sensor version with this FP should be considered less reliable as an added parameter impacts the fluorescence signal.

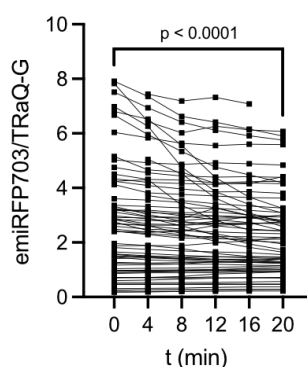


Figure 18. Adapted graphic from Emmert et al., *Nat. Chem.* 2023 (CC BY 4.0 DEED license).¹⁶³ Qualitative monitoring of the decrease in GSH concentration using the NIR sensor H2B-TRaQ-G-emiRFP703 (uncalibrated) in cells treated with 1 mM H₂O₂ during a period of 20 min. $N=67$ single cell values per timepoint from three biological replicates are depicted with connecting lines, statistical significance was evaluated by paired t-test.

3.9 Conclusion and outlook

Fusing the bright and photostable FP mGold to HT, several targeted constructs for live-cell GSH imaging with ratiometric read-out were generated. The spirocyclizing TRaQ-G ligand indeed proved to be better suited for live-cell imaging than Me-TRaQ-G due to its cell permeability and high S/N even though slower kinetics must be accepted. In a series of control experiments the compatibility of TRaQ-G with live-cell imaging was confirmed. The sensor was robust under physiological conditions and showed little interference with cellular homeostasis. A calibration curve with purified fusion protein enabled the determination of the absolute GSH concentration in the whole cell, the ER, mitochondria, and the nucleus. These measurements provide maximum comparability among organelles as the exact same sensor can be used for all localizations. As the transfection reagents seemed to affect the cellular GSH concentration, the generation of cell lines stably expressing the sensor are preferred over transient transfection when accurate absolute quantification is required. Artificial manipulation of [GSH] was detected with TRaQ-G as expected, demonstrating reversibility also in living cells. Because of the covalent anchorage of the sensor, long-term measurements can be performed. GSH levels were monitored in synchronized HeLa cells over a whole cell cycle. Comparison of the results in the nucleus and the whole cell suggested an independent nuclear GSH pool, which

fluctuates with cell proliferation. These findings open up exciting new questions about the mechanisms of GSH homeostasis, transport, and regulation. TRaQ-G could be an important tool to unravel the relevant metabolic pathways and regulatory mechanisms. The TRaQ-G-ctrl ligand offers a convenient control for such studies.

Furthermore, using a red-fluorescent small-molecule sensing unit, TRaQ-G permits multiplexing with roGFP. In a 4-color experiment organellar GSH concentration and GSH/GSSG ratio could be determined in the same cell. The FP of the sensor can in principle be exchanged for any other color complementary to the SiR giving additional flexibility for the planning of multiplexed experiments. Even another self-labeling protein like SNAP-tag could be incorporated. This strategy could be particularly useful to reach the NIR channel as synthetic fluorophores provide better photophysical properties especially in this spectral region. In summary, TRaQ-G is a robust and flexible tool, with which subcellular GSH levels can be investigated in a dynamic and non-invasive manner by fluorescence microscopy. The general concept of a reactivity turn-on could also be used to improve sensors for other analytes beyond GSH.

4 Toward improving TRaQ-G by protein engineering

The work discussed in this chapter was conducted in collaboration with Tatjana Hofmann and Carla Miró Vinyals. Tatjana Hofmann performed mutagenesis experiments and screening assays under my supervision. Carla Miró Vinyals supported us during experimental design and data interpretation.

4.1 Objective

The TRaQ-G sensor is inherently dim as only part of the bound ligand molecules are in the open form. Additionally, a large proportion of the molecules in the open form are attacked by GSH in cells and are therefore also non-fluorescent. We envisioned that the HT protein could be engineered to make the open form of the TRaQ-G ligand more favorable, which corresponds to a higher K_{L-Z} , and render the sensor brighter. A stronger fluorescence signal should improve S/N and therefore allow for more reliable measurements. The cyanamide spirocyclizing moiety shifted the K_d of the sensor toward higher GSH concentrations compared to the parent Me-TRaQ-G. Protein engineering might also enable tuning the K_d of the sensor for organelles with low millimolar GSH concentrations. The Golgi apparatus is an interesting example in this context as preliminary results from Carla Miró Vinyals suggest. Lastly, this approach is also an opportunity to improve the slow equilibration kinetics of TRaQ-G with GSH.

Since we had collected extensive structural data for TRaQ-G, a structurally informed approach for our protein engineering efforts seemed beneficial. With the structural model of our TRaQ-G construct, amino acid residues could be identified that might influence the equilibrium between spirocyclic and open form or GSH binding. Site-saturation mutagenesis of these residues would provide a library of mutants, which can then be screened for the desired properties. Mutations leading to an improvement could be mixed in a combinatorial library to find potential synergistic effects. The goal of this work was to establish an efficient pipeline for site-saturation mutagenesis and subsequent screening assays for brightness, K_d and equilibration kinetics.

4.2 Identification of mutation sites

The first obvious mutation site was F144. This phenylalanine residue has to flip over during the transition of the TRaQ-G ligand between the two binding pockets for the spirocyclized and the open form, respectively (Figure 6a–c). A smaller residue in this position might facilitate opening of the ligand and generate a brighter version of the sensor. For the selection of other target sites, the amino acids surrounding the binding pocket of the open ligand were examined. We hypothesized that additional interactions between the protein and the open TRaQ-G ligand could stabilize this conformation. Furthermore, some mutations might even elicit interactions of the protein with GSH lowering the K_d and improving kinetics. In addition to F144, we chose E143 and G244 for the generation of a first library (Figure 19).

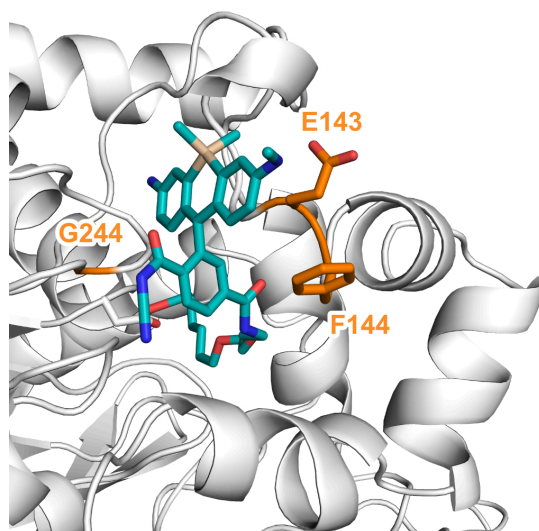


Figure 19. Structural basis for protein engineering of HT to tune brightness, K_d and equilibration kinetics of TRaQ-G. Selected mutation sites are highlighted in orange.

4.3 Initial screening with site-saturation mutagenesis and protein expression

In our site-saturation mutagenesis experiments, we wanted to compare two strategies. For mutation of G244, we designed 19 individual primer pairs to substitute the glycine residue by any other canonical amino acid. Primers for mutation of E143 and F144 were designed according to the "22c trick".¹⁷⁷ This method is based on a mixture of oligonucleotides optimized for minimal codon redundancy. The three forward primers contain the codons NDT, VHG and TGG for the mutation site and are mixed in a 12:9:1 ratio. The ratio of codons to encoded amino acids is significantly improved for this method (22:20) compared

to fully randomized (64:20) or NNK (32:20) libraries. Thus, the screening effort to obtain good coverage of all possible mutants is decreased.

For G244, site-directed mutagenesis with individual primer pairs was successful for 18 out of 19 mutations. However, every mutation required a separate amplification by polymerase chain reaction (PCR) with the mutagenic primers and transformation into *E. coli*. With the 22c mutagenesis design, only one pooled PCR amplification with the primer mix and a single transformation were required but the resulting coverage was much lower. Several rounds of picking single-cell clones yielded 11 and 10 out of 19 possible mutations for E143 and F144, respectively. In both cases we observed high percentages of unmutated clones (Figure 20), which could possibly be alleviated by longer reaction times for the digestion of the template. Additionally, a bias for certain mutations was apparent, which was persistent at different annealing temperatures (Figure 20). Further optimization of the annealing temperature might be beneficial but is laborious.¹⁷⁷ Potential other reasons for

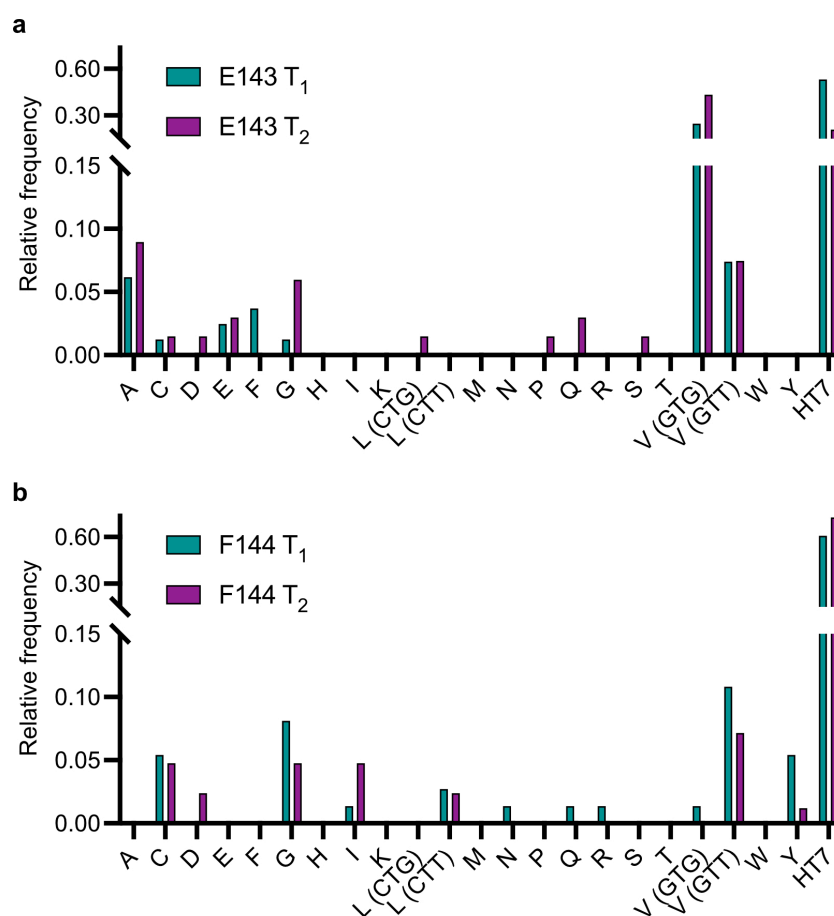


Figure 20. Relative frequency of observed mutations in 22c libraries for E143 (a) and F144 (b). Per mutation site and temperature 96 clones were analyzed. Clones with unintentional mutations were excluded from this analysis.

the unsatisfactory coverage include bias during primer synthesis by the manufacturer or preferential matching with the reverse primer.

4.4 *In vitro* characterization of mutants

For an initial screening, we expressed and purified the variants generated in all mutagenesis experiments on a small scale (5 mL culture volume). The GSH responsiveness in the low millimolar range as well as the equilibration kinetics were measured for all proteins with sufficient expression yield. The fluorescence signals in the absence of GSH suggest that there is no obviously brighter mutant than HT7. Yet, several mutants show a steeper GSH response in the range of 0–1 mM (Figure 21a–c). The influence of the mutations on the equilibration kinetics was very subtle. Even the most favorable mutants were hardly any faster than HT7 (Figure 21d).

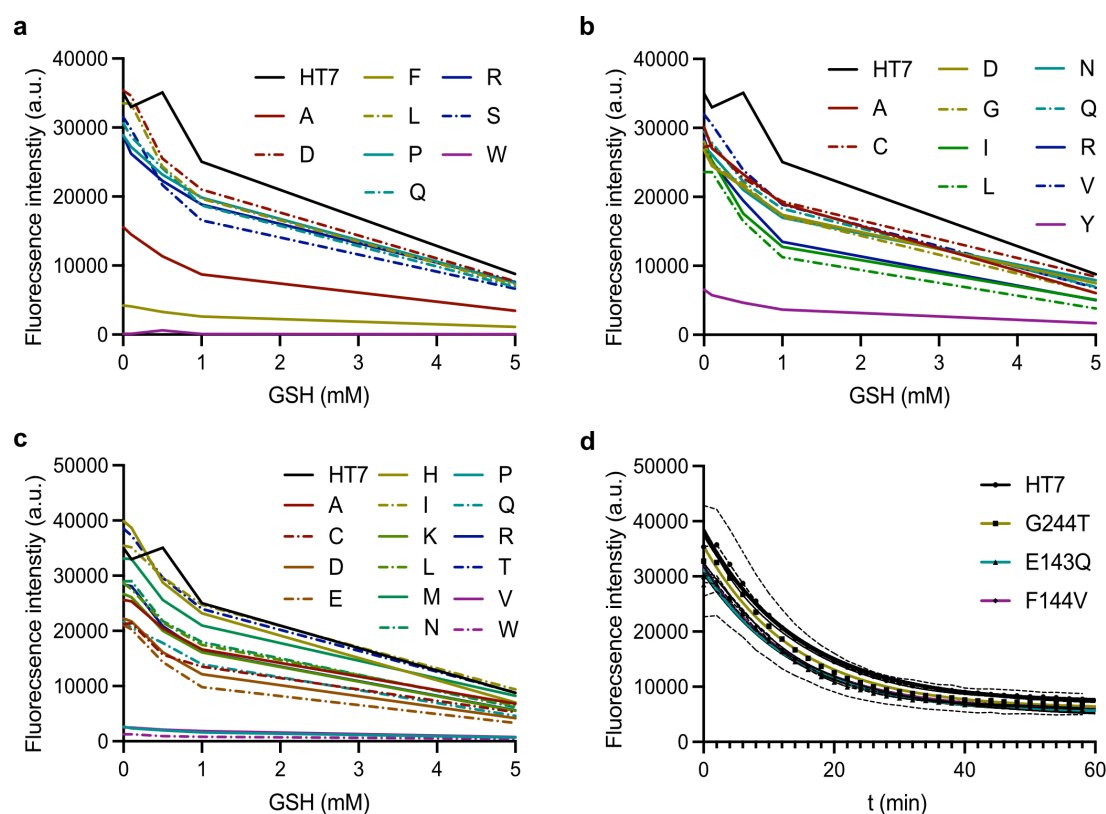


Figure 21. Characterization of the mutants from the site-saturation mutagenesis library. GSH titration of mutant conjugates (3 μ M) from E143 (a), F144 (b) and G244 (c). Data are presented as means with connecting lines from technical duplicates. d) GSH equilibration kinetics (5 mM) of the most favorable mutants for every mutation site. Data are presented as means from technical triplicates. Data were fitted with a one-phase decay, dotted lines represent 95% CI.

4.5 Conclusion and outlook

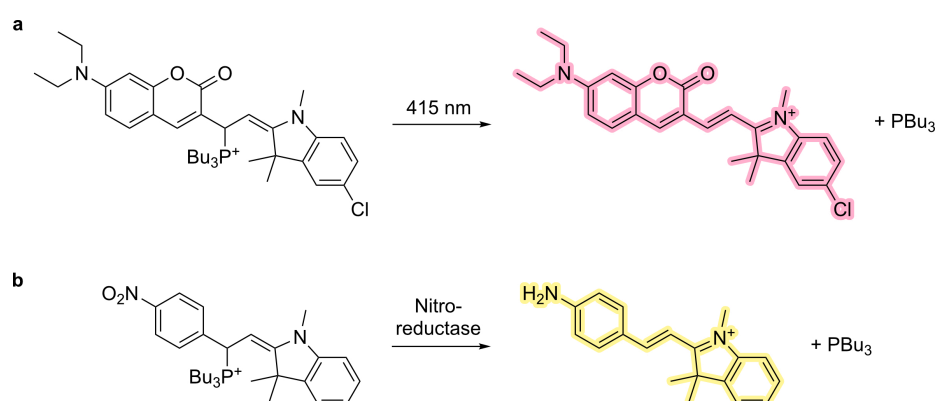
We tested two approaches for structurally informed library generation of HT mutants to fine-tune TRaQ-G. Three mutation sites were selected based on the available structural data for TRaQ-G and site-saturation mutagenesis was performed either by mutating single amino acids or with the 22c method. In our hands, the 22c-based experimental design led to significantly lower diversity but required less laborious library preparation. The resulting variants were expressed and purified in *E. coli*, resulting in a library of 37 mutants, which could be screened for the desired properties. No significantly brighter or faster equilibrating mutants were found in this screening even though several mutants seemed to feature a stronger GSH response at low concentrations, which is beneficial in some target localizations.

Based on these results, generation of combinatorial mutants could reveal synergistic behavior and improve properties beyond the cumulative effect of the single mutations. If needed, more mutation sites could be identified by alanine scanning.¹⁷⁸ Extending the screening is especially interesting with respect to the properties that could not be significantly improved so far. Further optimization of our site-saturation pipeline could reduce the hands-on time and enable larger follow-up screenings. A significant improvement could be the use of an *E. coli* strain suitable for both DNA amplification and protein expression. With this adjustment, the DNA purification step and one transformation step could be eliminated. DH10 β have been used for DNA amplification and efficient arabinose-inducible protein expression, which would make them a suitable host.¹⁷⁹ The best HT variants should be tested in living cells for a more comprehensive characterization.

5 Subcellularly probing reductive stress with HT-releasable phosphines

5.1 Objective

Beyond the characterization of the redox environment, we also envisioned the directed and organelle-specific manipulation of the same to study related cellular stress responses. Our group has already reported activatable tools to induce reductive stress, which enable spatial and temporal control. The release of PBu_3 from a fluorogenic scaffold can be triggered either by irradiation with light¹⁸⁰ or by an enzymatic reaction (Scheme 11).¹⁸¹ Successful activation can be visualized by fluorescence microscopy as cleavage of the phosphine moiety results in restoration of the conjugated π -electron system. The released phosphine is a reducing agent and shifts the GSH/GSSG equilibrium toward reduced GSH.¹⁸² The ubiquitous GSSG ensures immediate scavenging of the phosphine and its oxidation to phosphineoxide is irreversible. Therefore re-addition of the phosphine to the fluorophore is improbable.



Scheme 11. Previously reported probes that release tributyl phosphine to intracellularly induce reductive stress. a) Photoactivatable probe, which releases phosphine upon irradiation at 415 nm following a PeT-based mechanism. b) Phosphine-releasing probe triggered by nitroreductase activity.

The described photo-activatable probe offers great potential since the release of the phosphine can be temporally and spatially controlled by laser irradiation during fluorescence microscopy.¹⁸⁰ However, numerous attempts derivatizing the compound to achieve selective subcellular localization through targeting moieties were unsuccessful. By including multiple functionalities, the molecule becomes large and loses compatibility with live-cell imaging.¹⁸³ Since nitroreductase activity is limited to mitochondria in mammalian cells, the enzymatically activated probe features specificity for this compartment¹⁸¹ but a

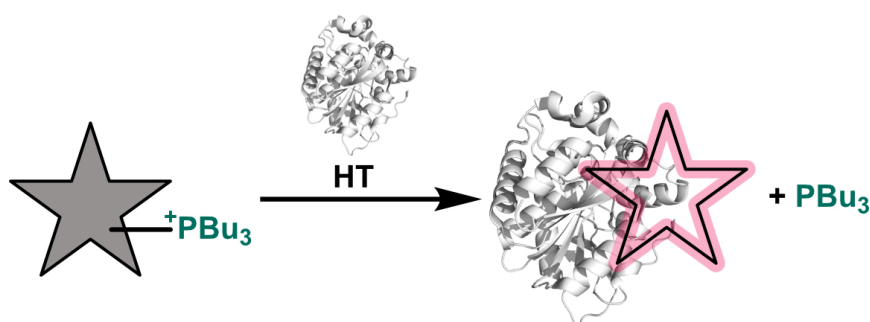
generalization of the approach to other organelles with similar specificity is not immediately apparent.

We therefore wanted to modify the phosphine-releasing probes to use HT binding for activation. Such a system would provide a general tool for the controlled induction of reductive stress in any subcellular localization. Beyond specificity for a subcellular compartment, it would allow the targeting of a certain cell population that expresses the HT construct. By mixing cells with and without the construct intercellular communication due to the evoked stress could be studied in detail. Such investigations are especially interesting in the ER where the physiological environment is comparably oxidizing and reductive stress could trigger the UPR^{ER}.^{42,47,49} Intercellular communication of ER stress (TERS) was previously described but due to the lack of specific stress inducers the available studies are limited and debated.^{74,75,81} We therefore believe that a HT-activatable inducer of reductive stress could offer a great opportunity to learn more about stress responses and connected signaling pathways.

5.2 General principle

As outlined in section 1.5, many rhodamine derivatives exist in an equilibrium between a neutral non-fluorescent and a zwitterionic fluorescent form (Scheme 6). In this equilibrium, the non-fluorescent form arises from intra-¹⁴⁵ or intermolecular^{126,184} nucleophilic attack interrupting the conjugated π -electron system. Phosphines as well are able to attack electrophilic fluorophores and disrupt π -conjugation.^{180,181,185} Binding to HT often leads to a preference for the fluorescent form resulting in fluorescence turn-on. We therefore hypothesized that HT binding could also release a phosphine nucleophile from a fluorogenic scaffold and consequently induce reductive stress (Scheme 12). The fluorophore must be electrophilic enough to form a stable phosphonium compound with minimal off-target release of phosphine. If necessary, the interactions between small molecule and HT could be adjusted by protein engineering to ensure fast binding and release. Moreover, the HT protein or the small molecule could be altered to transiently bind instead of forming a covalent linkage as reported in literature.^{186,187} This adaption would

allow many equivalents of phosphine to be released by one protein ensuring efficient release of phosphine even with lower HT expression levels.



Scheme 12. General principle of probes releasing tributyl phosphine from a fluorogenic scaffold upon binding to HT.

5.3 Rhodamine-based scaffolds

The first choice for an electrophilic fluorophore for our system were rhodamine-based dyes since HT was evolved to bind them efficiently.¹²⁹ SiRs are generally more electrophilic (lower K_{L-Z}) than the respective rhodamine derivatives and their intermolecular reaction with nucleophiles is reported.^{126,146,184} Electron-withdrawing substituents increase the electrophilicity of the SiR core, which can be used to stabilize a phosphine adduct. We supported this assumption by computational modeling with density functional theory (DFT). The transition states of phosphine dissociation with the corresponding energy barriers were calculated for several hypothetical SiR-based phosphonium compounds.

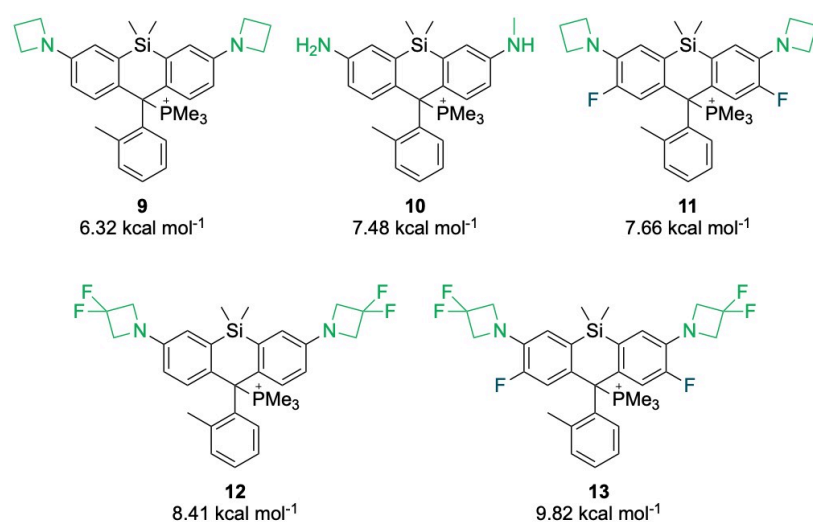
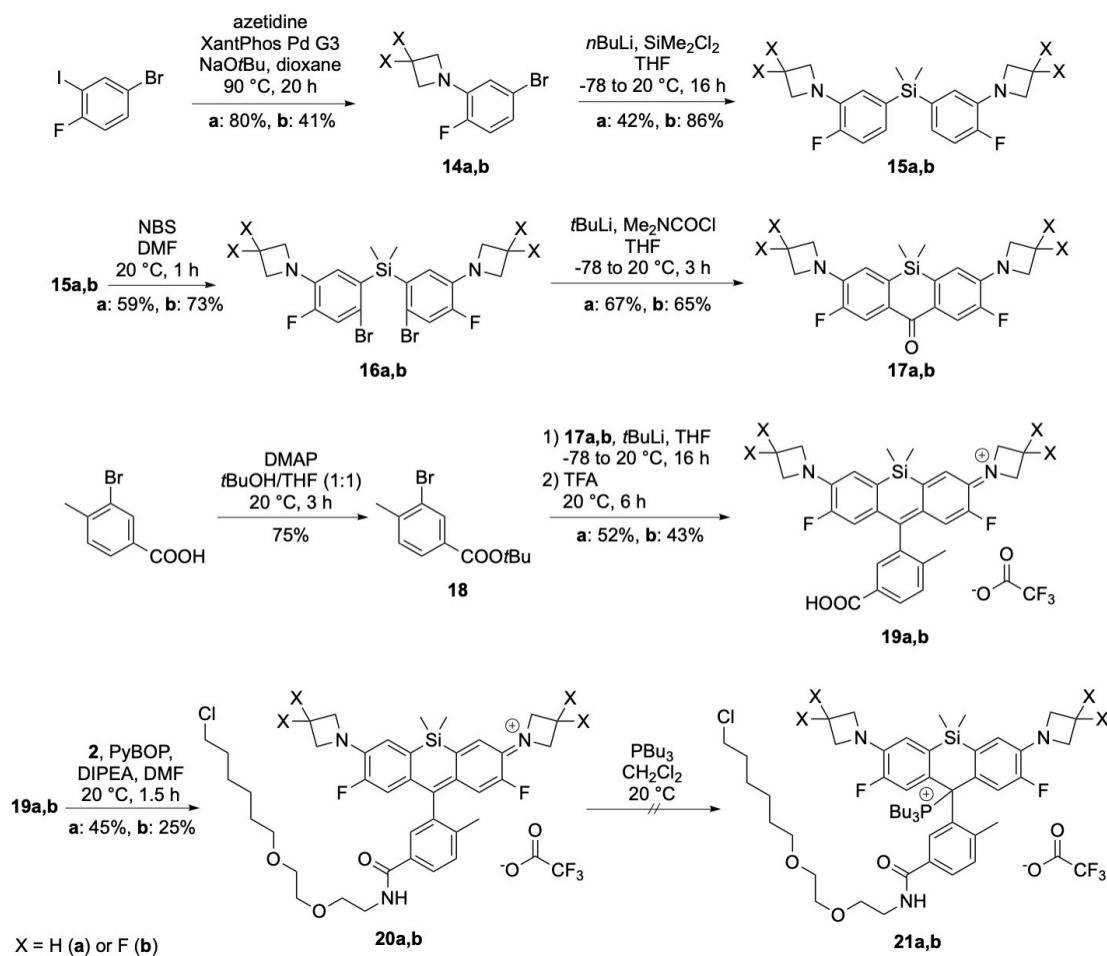


Figure 22. Computational modeling of SiR phosphonium compounds. Molecules with increasingly electron-withdrawing substituents are depicted with their calculated transition state energy barriers for phosphine cleavage. To facilitate calculations PMe_3 -adducts were modeled.

Fluorine substituents were added to obtain increasingly electron-poor SiR cores from compound **9** to **13**, which led to higher energy barriers for phosphine cleavage (Figure 22).

For a first experimental approximation of the stability of compounds **9–13**, the MeTRaQ-G ligand, which bears the same SiR core as phosphonium **10** was treated with PBU_3 . Unfortunately, no loss of color was observed, even in the presence of excess PBU_3 , indicating that phosphine addition was not possible under the reaction conditions. Therefore, the SiR-HT ligands corresponding to **11** and **13** were synthesized, to test if the fluorine substituents could promote formation of stable phosphine adducts (Scheme 13). Starting from 5-bromo-2-fluoroiodobenzene a Buchwald-Hartwig coupling gave **14a,b**. Lithium-halogen exchange with *n*-butyl lithium (*n*BuLi) and nucleophilic substitution of SiMe_2Cl_2 yielded silane intermediates **15a,b**. Treatment with *N*-bromosuccinimide (NBS) led to the dibromo compounds **16a,b** and after subsequent reaction with *t*BuLi and dimethylcarbamoyl chloride the corresponding ketone intermediates **17a,b** was obtained.



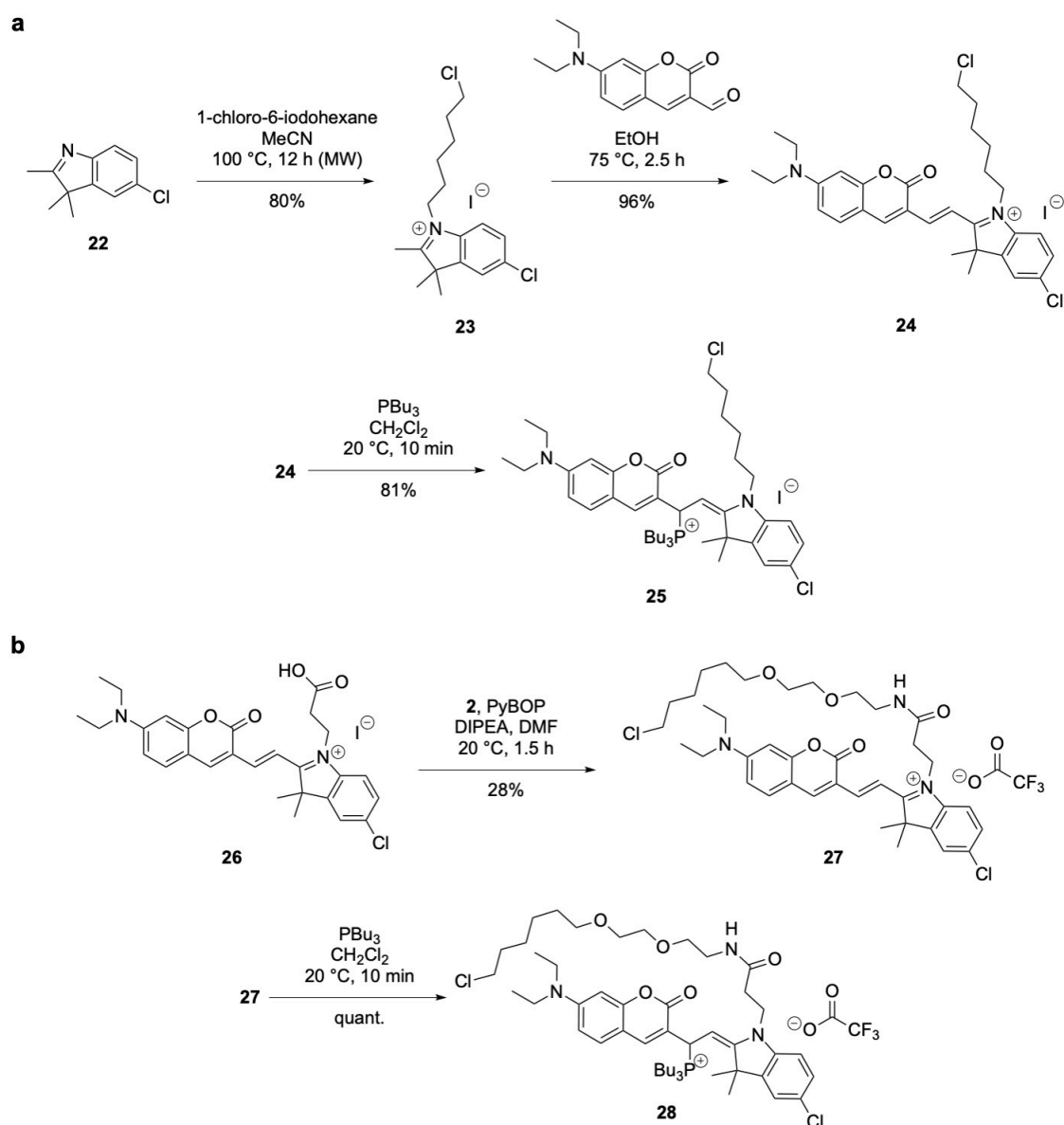
Scheme 13. Synthesis of electron-deficient SiR-HT ligands to test stability of phosphine adducts. DMAP=4-(dimethylamino)pyridine, TFA=trifluoro-acetic acid.

The addition of compound **18** to the ketones **17a,b** followed by deprotection gave dye **19a,b**. Afterwards, the HT-ligand moiety could be installed by amide coupling yielding SiR-HT ligands **20a,b**. Unfortunately, when trying to react either SiR with PBu₃, the phosphoniums **21a,b** could not be isolated. However, addition of PBu₃ (5 equiv.) to **21b** caused the immediate decoloration of the reaction mixture, a strong indication for the formation of the respective phosphonium. Yet, since the phosphonium was too labile, we concluded that SiR-based phosphonium compounds might not be feasible for application in live cells.

5.4 Hybrid coumarin-based scaffolds

Since SiRs **20a,b** did not form stable phosphoniums and the synthetic effort for creating a larger library is very high, we started to reconsider our choice of scaffold. The hybrid coumarin dyes used in the original phosphine-releasing probe (Scheme 11a), are prepared in much shorter synthetic routes and can also easily be tuned *via* the substituent of the indoleninium moiety.¹⁸⁰ If these compounds are decorated with a CA linker, HT binding might weaken the C-P bond enough to create an alternative release mechanism to photoactivation. Nevertheless, attachment point and length of the linker are not obvious as nothing is known about the binding geometry of hybrid coumarin ligands to HT. Synthetically, the nitrogen atom of the indoleninium moiety offers an easy way to attach a CA chain. The length of the chain likely influences the interactions of the ligand with the protein, hence we planned to test different derivatives to find the most suitable linker.

For a first candidate molecule, chlorohexane was directly attached to the nitrogen atom of precursor **22** to give indoleninium **23**. Condensation with dimethylaminocoumarin-3-aldehyde yielded the hybrid dye **24** and addition of PBu₃ resulted in phosphonium **25** (Scheme 14a). This short linker has previously been reported to be beneficial for styryl pyridinium dyes (also called “channel dyes”).¹⁸⁸ For more flexibility, we also prepared a derivative with a propionic acid substituent on the indoleninium moiety, to which any linker could be attached *via* amide coupling (Scheme 14b). The respective condensation product with the coumarin moiety **26** was provided by Alina Tirla. Coupling with the most widely used HT linker **2** containing two ethylene glycol moieties yielded compound **27**. Subsequent phosphine addition gave phosphonium **28**.



Scheme 14. Synthesis of hybrid coumarin-based phosphonium compounds with CA linkers for HT binding.

Incubation of compound **25** with HT did not result in the expected increase in absorbance around 600 nm (Figure 23). This absorbance band corresponds to dye **24** and thus strengthening of this band would indicate release of the phosphine and restoration of the conjugated π -electron system. Consequently, the probe either did not bind HT or despite binding, the phosphine was not released. The former seemed likely, considering the short CA chain compared to the most frequently used linker **2** in combination with the bulky phosphonium. Indeed, the phosphonium compound **28** with the longer HT linker showed a clear change in the absorbance spectrum upon incubation with HT in an initial experiment (Figure 23). However, in the absence of HT absorbance at 600 nm was also observed, even

though to a much less extent, indicating spontaneous decomposition of the adduct. For live cell experiments a more stable phosphonium is likely required. Instead of the chloride, CF₃-substitution on the indoleninium was reported to form a more stable phosphonium, which cannot be activated by light and could therefore be an interesting modification for our probe.¹⁸⁰

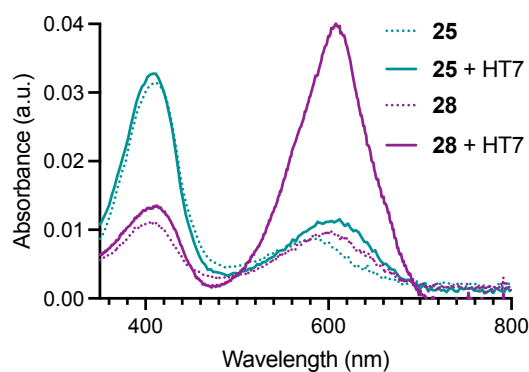
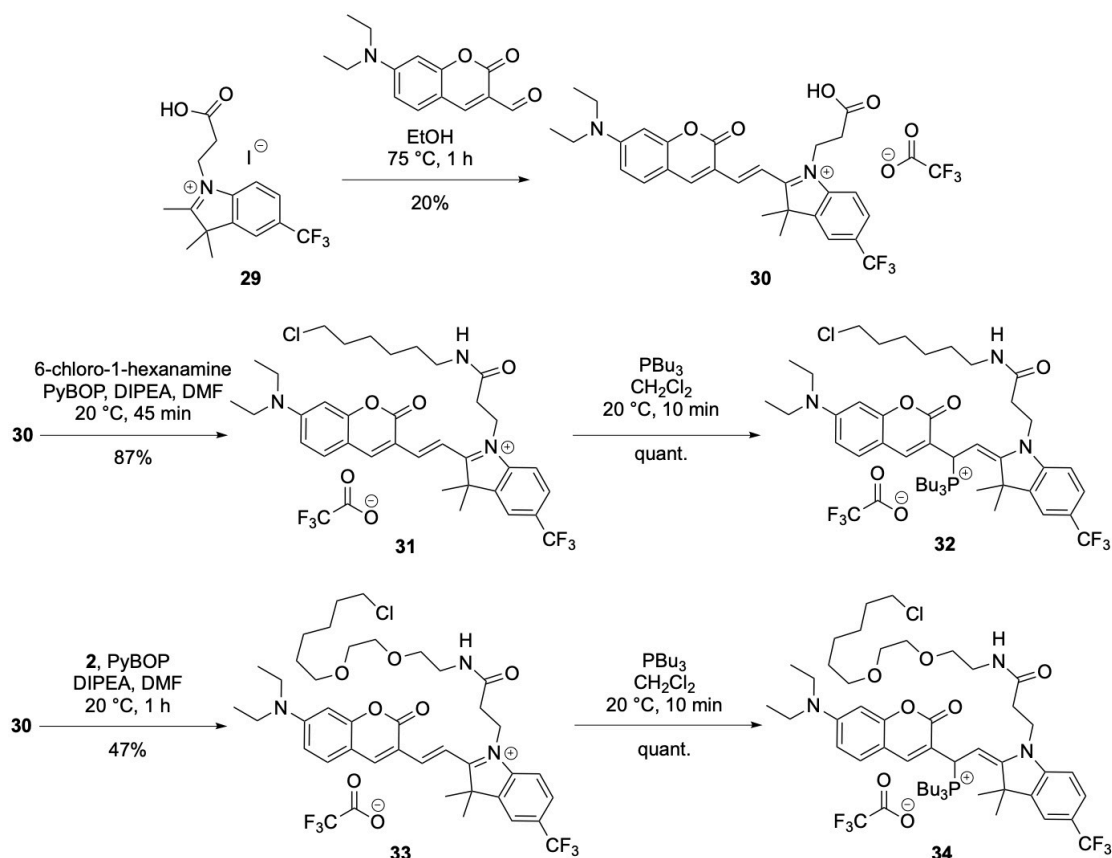


Figure 23. Absorbance spectra of compounds **25** and **28** (5 μM) in the absence and presence of HT7 (10 μM). GSSG (10 μM) was added to scavenge released phosphine. Samples were incubated for 1–2 h at 37 $^{\circ}\text{C}$.

For a CF₃-substituted derivative of probe **28**, 2,3,3-trimethyl-5-(trifluoromethyl)-3*H*-indole and the corresponding indoleninium **29** were synthesized according to reported procedures.^{189,190} Analogously to the synthetic strategies discussed before, the preparation started with condensation between dimethylaminocoumarin-3-aldehyde and the propionic acid indoleninium **29** resulting in compound **30**. For comparison, we used two different linkers again. A short chloroalkane was coupled to precursor **30** to yield dye **31** and addition of PBu₃ gave the respective phosphonium **32**. Amide coupling of **30** with CA **2** gave dye **33**. The amount of added base (2 equiv.) and the reaction time (< 1 h) were crucial in this step as otherwise decomposition of the product was observed. Addition of PBu₃ yielded phosphonium **34** (Scheme 15).



Scheme 15. Synthesis of a CF_3 -substituted hybrid coumarin-based phosphonium compounds with CA linkers for HT binding.

We tested the new compounds by subjecting them to HT and GSSG. Whereas compound **34** exhibits a clear turn-on with a half-life of $\tau_{1/2}=35$ min, compound **32** appears stable in the presence of HT (Figure 24a). Interestingly, HT binding is able to cleave the C–P bond in the CF_3 -substituted molecule even though photoactivation was shown to be impeded

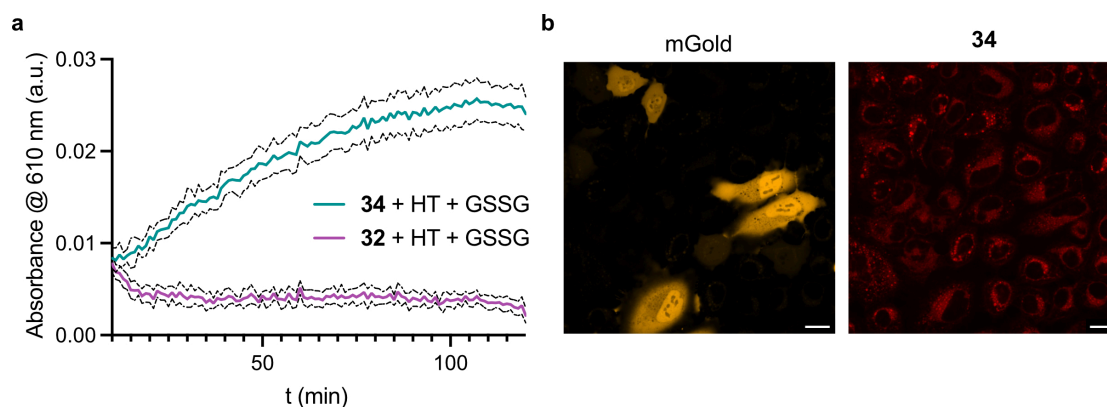
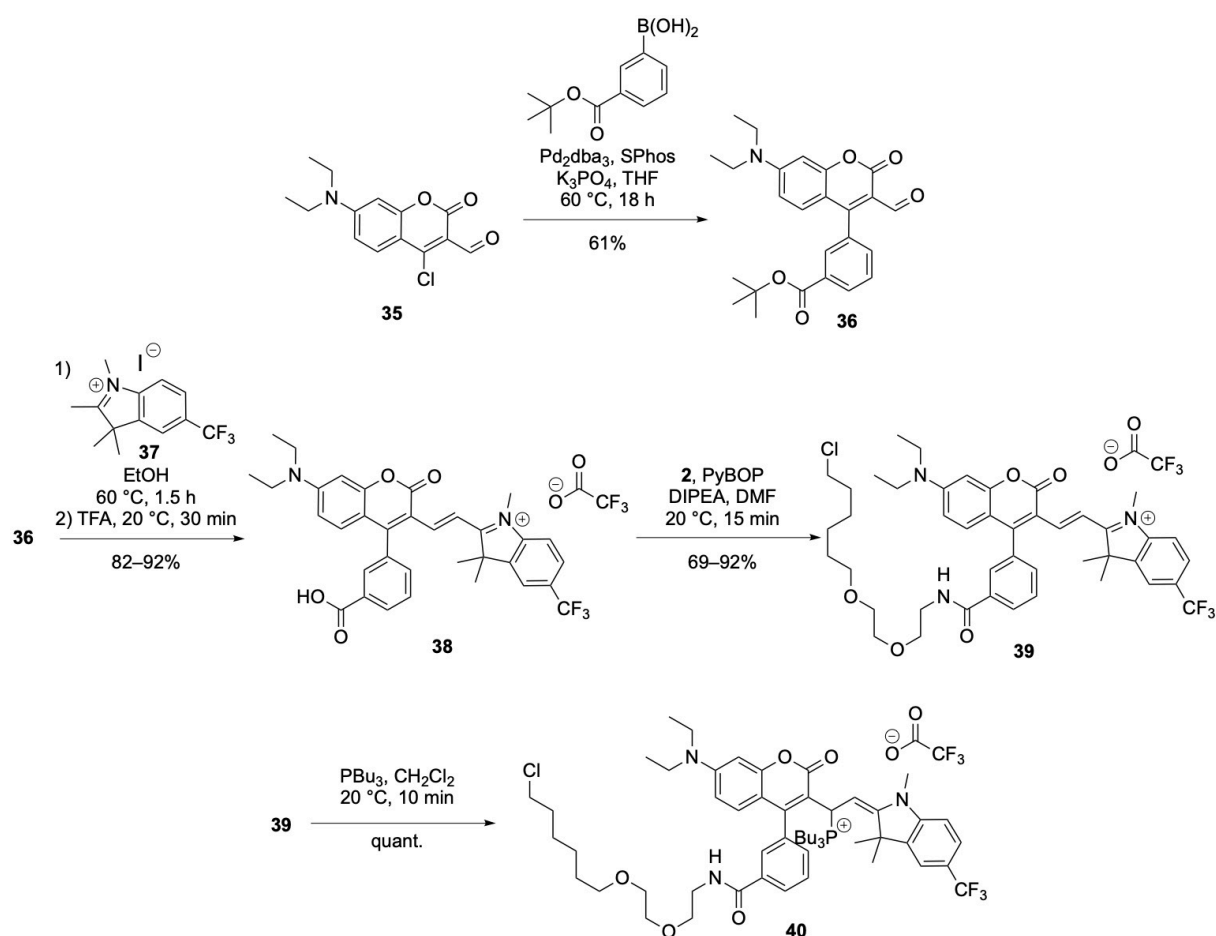


Figure 24. a) Absorbance at 610 nm of compounds **32** and **34** ($10 \mu\text{M}$) in the presence of HT ($20 \mu\text{M}$) and GSSG ($20 \mu\text{M}$) in PBS at 37°C . Data are presented as means with connecting lines and dashed lines indicate SD from $n=3$ technical replicates. b) Fluorescence microscopy of HeLa cells transfected with HT-mGold and incubated with compound **34** for 2–3 h. Scale bars= $20 \mu\text{m}$.

for a similar molecule.¹⁸⁰ Our experiments also highlighted the importance of the linker design as the shorter linker prevented HT binding on the observed timescale. To test if the targeted release of tributyl phosphine also works in living cells, HeLa cells were transfected with HT-mGold and incubated with **34**. Unfortunately, there was no correlation between the signal from expressed HT-mGold fusion protein and the cleaved reporter fluorophore. Instead, **34** seemed to be subject to unspecific binding and activation in the ER and vesicles (Figure 24b).

The slow kinetics and lack of HT-binding in live cells of compound **34** made clear that our molecular design needed a more substantial change. As the HT protein was heavily optimized for rhodamine dyes, we envisioned that adapting our scaffold to mimic rhodamines might be beneficial. A molecule that has the CA linker connected *via* an additional aromatic ring on the coumarin similar to the bottom ring of a rhodamine would better resemble the binding geometry that HT7 was engineered for. We designed and



Scheme 16. Synthesis of rhodamine-like coumarin hybrid dyes for HT-activatable phosphine release.

synthesized such a molecule with the CF₃-substituent on the indoleninium (Scheme 16). Coumarin **35** was synthesized as reported in literature¹⁹¹ and transformed *via* Suzuki coupling¹⁹² with a (3-(*tert*-butoxycarbonyl)phenyl)boronic acid building block to intermediate **36**. Condensation with indoleninium **37** and subsequent deprotection resulted in **38**, which was coupled to CA **2** yielding dye **39**. Finally, addition of PBu₃ led to compound **40** although the reaction yielded an inseparable mixture of products. The phosphine addition might result in rotationally restricted isomers due to the bulkiness of the tributyl phosphine in proximity to the newly introduced phenyl ring.

Yet, compound **40** was still worthy of being characterized *in vitro* and in living cells to evaluate if the molecular design is promising. Measuring the absorbance at 605 nm of **40** in the presence of HT and GSSG over time, we observed a fast and clear turn-on, indicating PBu₃ cleavage by HT binding (Figure 25a). Incubating HeLa cells expressing HT-mGold in various subcellular locations with **40**, showed good colocalization between the fluorescent fusion protein and the small molecule (Figure 25b). Nevertheless, some unspecific signal was displayed in vesicles. Lysosomal vesicles are known to feature acidic pH, therefore we measured a pH profile of phosphonium **40** and the corresponding precursor dye **39**. Indeed, when compound **40** was subjected to buffers with pH values ranging from 2 to 13 a clear dependence of the absorbance around 600 nm on the pH was observed suggesting cleavage of the phosphonium (Figure 25c). Notably, dye **39** also exhibited pH-dependent absorbance and did not display absorbance at 600 nm at physiological pH (Figure 25c). However, we observed well colocalized fluorescence signal in live cells expressing HT when incubating them with **40**, which is transformed to **39** upon binding. Consequently, **39** displays sort of a turn-on behavior without any intramolecular nucleophiles nor additives in the buffer. We suspect that hydroxide ions can attack the molecule at the indoleninium moiety, which was reported for similar compounds.¹⁹³ HO⁻ likely attacks a different carbon atom in the conjugation system compared to PBu₃ as it is a much harder nucleophile. The equilibrium with HO⁻ leads to a pH-dependent turn-on behavior as previously observed for certain SiR derivatives (Figure 26a).¹⁸⁴ Considering these results, phosphonium **40** is potentially not stable in aqueous buffer but off-target activation is easily overlooked as **39** is non-fluorescent itself until binding to HT.

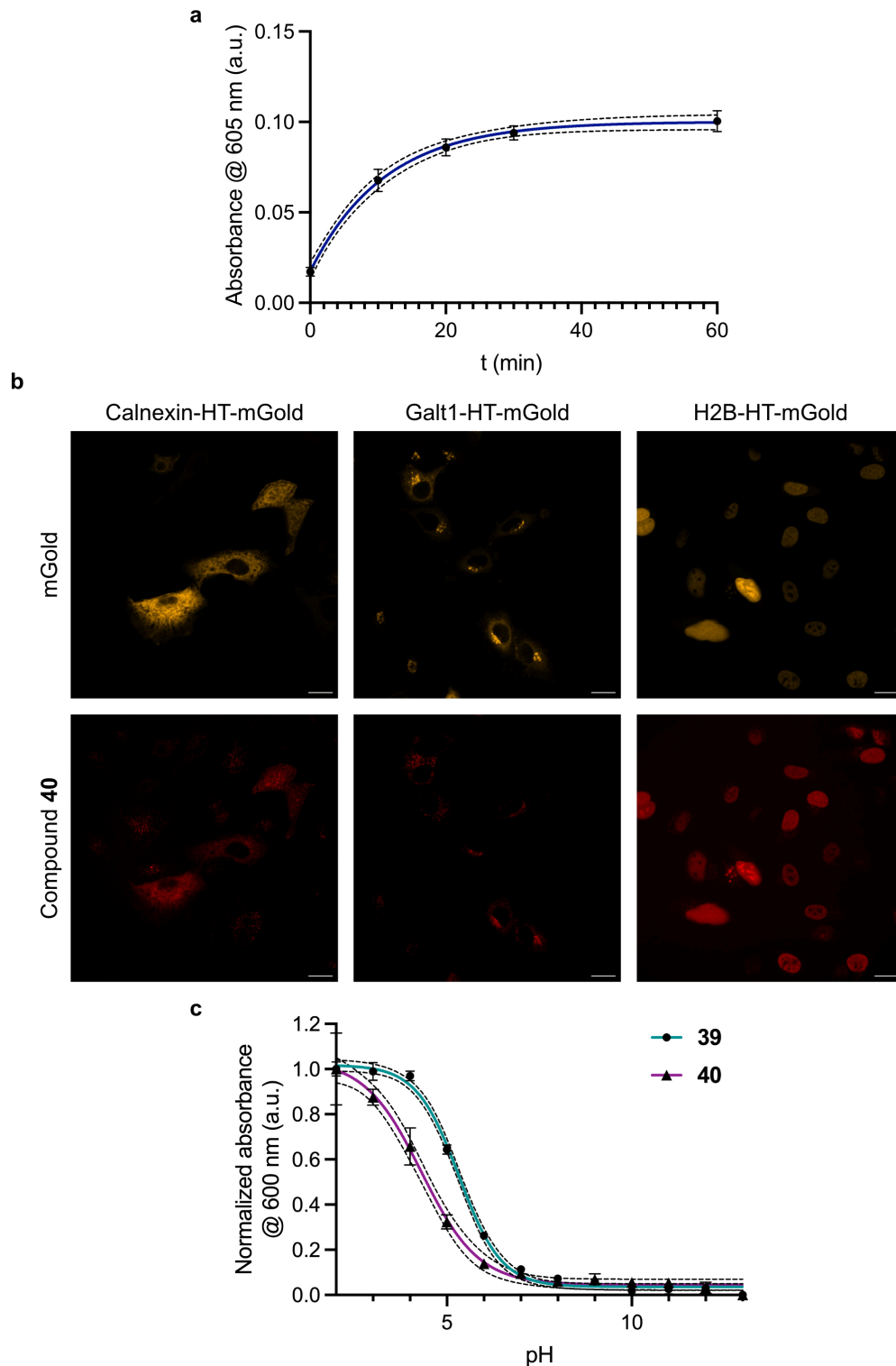


Figure 25. a) Absorbance of **40** at 605 nm in the presence of HT (1.5x excess) and GSSG (1 mM) at 37 °C over time. b) HeLa cells transfected with Calnexin-HT-mGold (ER targeting), Galt1-HT-mGold (Golgi targeting) and H2B-HT-mGold (nuclear targeting) respectively and incubated with **40** (100 nM) for 1 h. Scale bars=20μm. c) pH profile of **39** and **40**. Data are presented as means and error bars indicate SD from $n=3$ technical replicates. Data were fitted with a one-phase decay (a) or sigmoidal dose-response (c), dotted lines represent 95% CI.

The unusual turn-off in aqueous solution originating from its electrophilicity leads to a more amphiphilic character of compound **39** compared to most fluorogenic rhodamine dyes. Since the amphiphilic moment was determined a key factor for uptake in Gram-negative bacteria, we were curious if compound **39** was suitable for bacterial imaging.¹⁹⁴

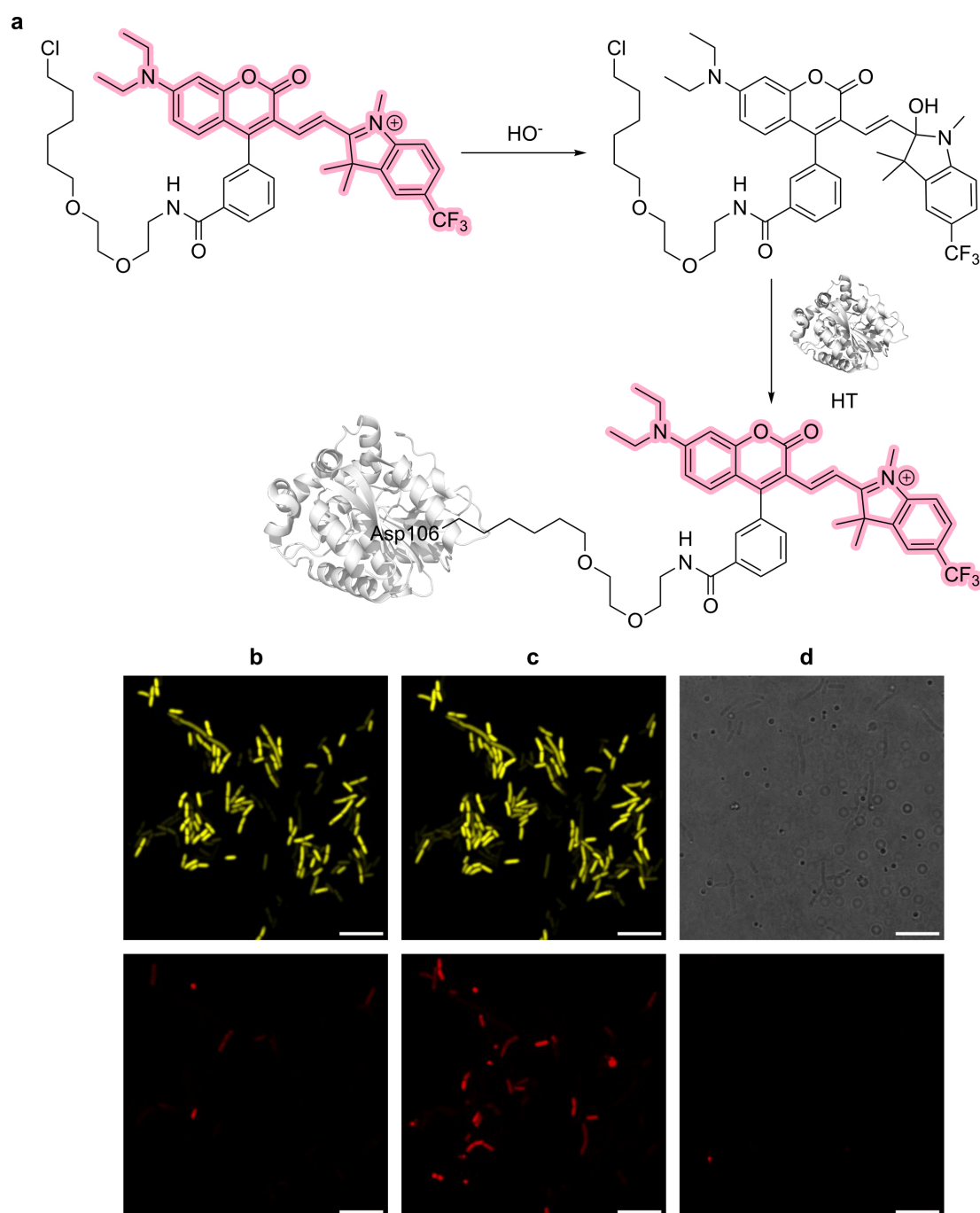


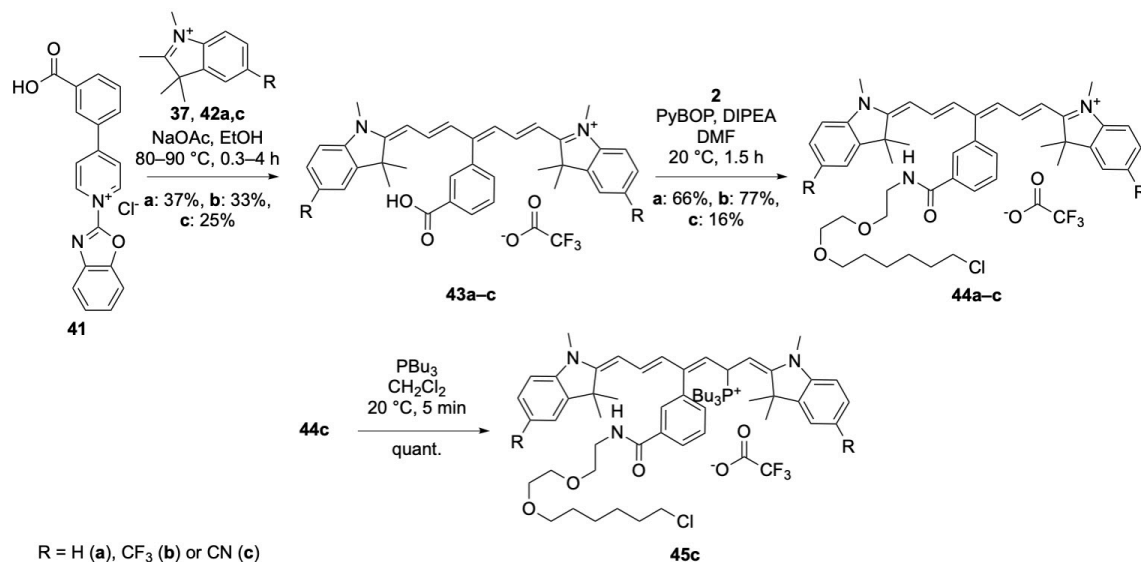
Figure 26. a) Proposed mechanism of fluorogenicity for compound **39**. b–d) *E. coli* imaging. *E. coli* BL21(DE3) expressing HT-mGold and incubated with **39** (5 μ M) for 30 min (b) or 60 min (c) and cells were imaged without washing. As a control *E. coli* without the construct were incubated with **39** for 60 min (d). Left panel mGold/transmission, right panel coumarin hybrid dye. Contrast settings are for all images. Scale bar=10 μ m.

The probe might further be better suited for imaging bacteria compared to mammalian cells since the former do not contain acidic vesicles, which induce background signal due to the pH-sensitive fluorogenicity. To test labeling of HT with compound **39** in bacteria, HT-mGold expression was induced in the *E. coli* strain BL21(DE3) and the cells were incubated with **39** for 30–60 min. As a control *E. coli* not containing the vector were imaged. The probe was taken up by some cells, however not uniformly, and labeling did not correlate with expression levels. Uptake, binding and/or turn-on increased over time but at this point it is not clear, which was the rate-limiting factor (Figure 26b,c). *E. coli* that are not expressing the construct exhibited virtually no background (Figure 26d). Follow-up studies could aim to improve the bacterial uptake of these molecules to create highly fluorogenic labels compatible with Gram-negative bacteria.

5.5 Cy7-based scaffolds

Circling back to identifying a HT-releasable phosphine probe, we were able to take advantage of very recent developments in fluorophore engineering. Polymethine or cyanine dyes are an appealing scaffold for our probe design since they have been used with phosphine-containing buffers for superresolution imaging. Hence, the reversible formation of phosphonium products is already reported for this class of fluorophores.¹⁸⁵ However, systems with optimized interactions between cyanine dyes and self-labeling proteins have only recently been described.^{149,195} On that basis, we decided to investigate if we could form stable phosphine adducts with Cy7 dyes, cyanine derivatives that feature a C7-bridge. Synthetic strategies based on pyridinium ring opening allow easy diversification of Cy7 dyes and the long absorption and emission wavelengths ensure compatibility with other sensors and probes like roGFP and TRaQ-G.^{19,149,163,196} Similar to the coumarin hybrid dyes, electron-withdrawing substituents should stabilize potential phosphine adducts. Following the reported synthetic approach for Cy7-HT ligands,¹⁴⁹ two derivatives with either -CF₃ or -CN substituted indoleninium moieties were synthesized (Scheme 17). The pyridinium benzoxazole precursor **41** was treated with the respective indoleniniums **37** or **42a,c** to yield intermediates **43a–c**. Amide coupling with CA **2** resulted in dyes **44a–c**. Phosphine addition (1.5 equiv.) was not observed with the unsubstituted derivative **44a**. Decoloration of the reaction mixture was observed with **44b,c** indicating formation of phosphoniums **45b,c**. However, **45b** was not stable when being triturated and re-dissolved

for characterization. Probe **45c** was stable enough to be characterized by ^{31}P -nuclear magnetic resonance (NMR) and MS. Stock solutions of the compound in dimethylsulfoxide (DMSO) were stable at $-80\text{ }^\circ\text{C}$ for several weeks. The trend shows again clearly that more electron-withdrawing substituents stabilize the phosphonium.



Scheme 17. Synthesis of Cy7-based HT-releasable phosphine probes.

We tested **45c** *in vitro* to check if it had the desired properties to function as an HT-activatable inducer of reductive stress. Increasing absorbance at 780 nm after addition of HT suggested successful phosphine release upon binding with $\tau_{1/2}=11.0$ min, 95% CI [10.9–11.1 min] (Figure 27a). Due to aggregation in aqueous buffer, the stability of **45c** could not be determined by a control experiment without the addition of HT. Supplementing the buffer with SDS to solubilize the compound also lead to cleavage of the phosphine (Figure 27a). We further wanted to establish if the released phosphine is able to reduce GSSG. For this purpose, the GSH and GS_{tot} contents of samples containing GSSG incubated with **45c** in the presence and absence of HT were determined using a commercial fluorimetric GSH assay (Figure 27b). As a control, we used **44c**, which binds to HT but does not release a reducing agent. Indeed, an increase in formed GSH was measured in samples containing HT-**45c**. But also compound **45c** itself seems to generate some GSH even if less so. The effect was more obvious when the GSH/GSSG ratio is calculated. As expected, the Cy7 precursor **44c** did not lead to GSH formation. It is however not clear, why the sample with HT-**44c** showed a slight increase in GSH. The protein contents were removed from the samples before performing the assay and should therefore not interfere

with the measurement. Potentially, the cysteine pair in HT can be directly oxidized by GSSG to some extent, generating GSH.¹⁷⁰

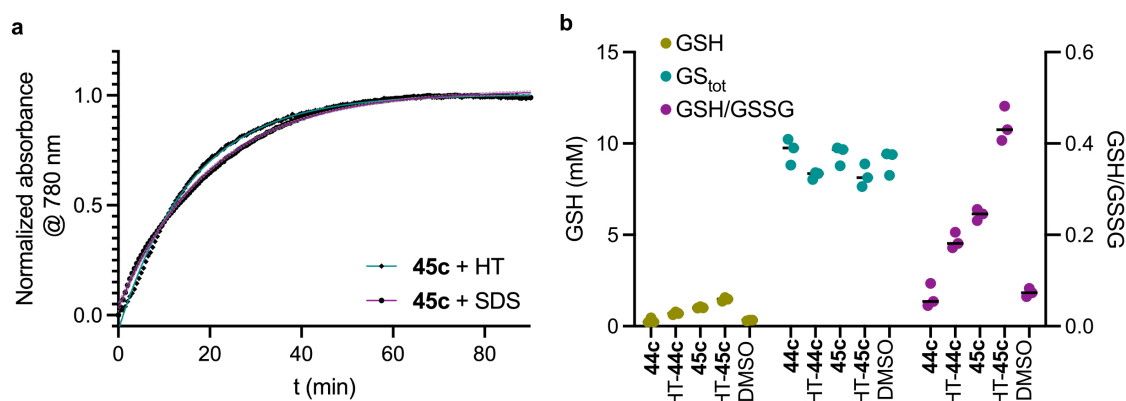


Figure 27. a) Kinetics of phosphine release determined by absorbance intensity at 780 nm for **45c** (10 μ M) in PBS in the presence of HT (15 μ M) or SDS (0.1%) at 37 $^{\circ}$ C. GSSG was added to scavenge released phosphine. Data are represented as means from $n=3$ technical replicates and were fitted with a one-phase decay and dotted lines represent 95% CI. b) Fluorimetric GSH assay to probe reduction of GSSG to GSH by released phosphine from HT-**45c**. Single values from $n=3$ technical replicates are depicted and the bar indicates their corresponding mean.

Even though the *in vitro* experiments gave somewhat ambiguous results, we wanted to test **45c** in cells. A cell viability assay based on 3-[4,5-dimethylthiazol-2-yl]-2,5-diphenyl tetrazolium bromide (MTT) was performed to assess the toxicity of compounds **44c** and **45c** in the absence of HT (Figure 28a). The compounds exhibited very similar but low toxicity, which was not concerning for subsequent live cell experiments. The turn-on kinetics in live cells revealed reasonably quick saturation at 500 nM **45c** with $\tau_{1/2}=18.6$ min, 95% CI [14.7–24.4 min] (Figure 28b). Good colocalization was observed in HeLa cells expressing a fluorescent HT fusion targeted to various subcellular compartments and incubated with **45c** (Figure 28c). Yet, unspecific background signal from vesicular structures was clearly visible. Next, we wanted to assess if **45c** would also reduce GSSG in live cells leading to a shift in the GSH/GSSG ratio. We decided to test the probe in the ER first as its oxidative environment should react very sensitive to reductive stress. Therefore, the effect of the probe was expected to be more distinct than in organelles that have a more reducing environment to begin with. A large shift in E_{GSH} toward a more reducing potential and a clear stress response would validate the effectiveness of our probe. For this validation experiment, a fluorescent fusion of HT with mScarlet3¹⁹⁷ targeted to the ER and roGFP-iE-ER⁴² were co-expressed in HeLa cells. The ratio of roGFP fluorescence intensity with excitation at 405 nm/445 nm was measured before and after addition of **45c**.

As a control, we used **44c**, which does not bear the phosphonium to be released. Surprisingly, addition of **44c** and **45c** likewise resulted in a higher 405 nm/445 nm ratio, which corresponds to a more oxidizing E_{GSH} . Moreover, this shift to lower GSH/GSSG ratios was observed in the presence and absence of HT (Figure 28d). Additionally, the same experiment was conducted with reHT,¹⁸⁷ a retro-engineered version of HT7 that binds its ligands transiently. Once the CA substrate has bound, the chloride is substituted by a hydroxyl group and the affinity of the ligand should decrease. Therefore, rebinding of already activated probe would be unlikely. We envisioned that reHT could achieve a higher phosphine release than HT7 since a single enzyme can activate multiple equivalents of the probe. But even with reHT, the expected shift of E_{GSH} toward more reducing conditions could not be measured (Figure 28d). Induced reductive stress may trigger a compensation reaction in the cell, which results in a more oxidative environment than the observed basal state.¹⁸¹ However, more detailed experiments such as timelapse imaging would have to be conducted to test this hypothesis. The lability of **45c** could also result in phosphine release already in the medium so that the reducing agent never reaches the cell. The oxidative shift might then just be an experimental artifact from the incubation time with the probe. Clearly, the molecular design must be further optimized to achieve a robust and easy to handle tool for the targeted induction of reductive stress.

In a recent report, an open-closed equilibrium was introduced to Cy7-dyes, which was tuned by changing the *N*-substitution of the indoleninium moiety.¹⁴⁹ Inspired by this approach, we also intended to synthesize a derivative of our Cy7-based probes with the reported trifluoroethyl substituent. To estimate the impact of this modification on the phosphonium's stability, we performed computational modeling with DFT of the transition states for phosphine release of compounds **46–51** (Figure 29). The results suggested that this modification should yield more stable phosphine adducts than the reported hybrid coumarin probe¹⁸⁰ or the proposed Cy7 probes without the trifluoroethyl substituent.

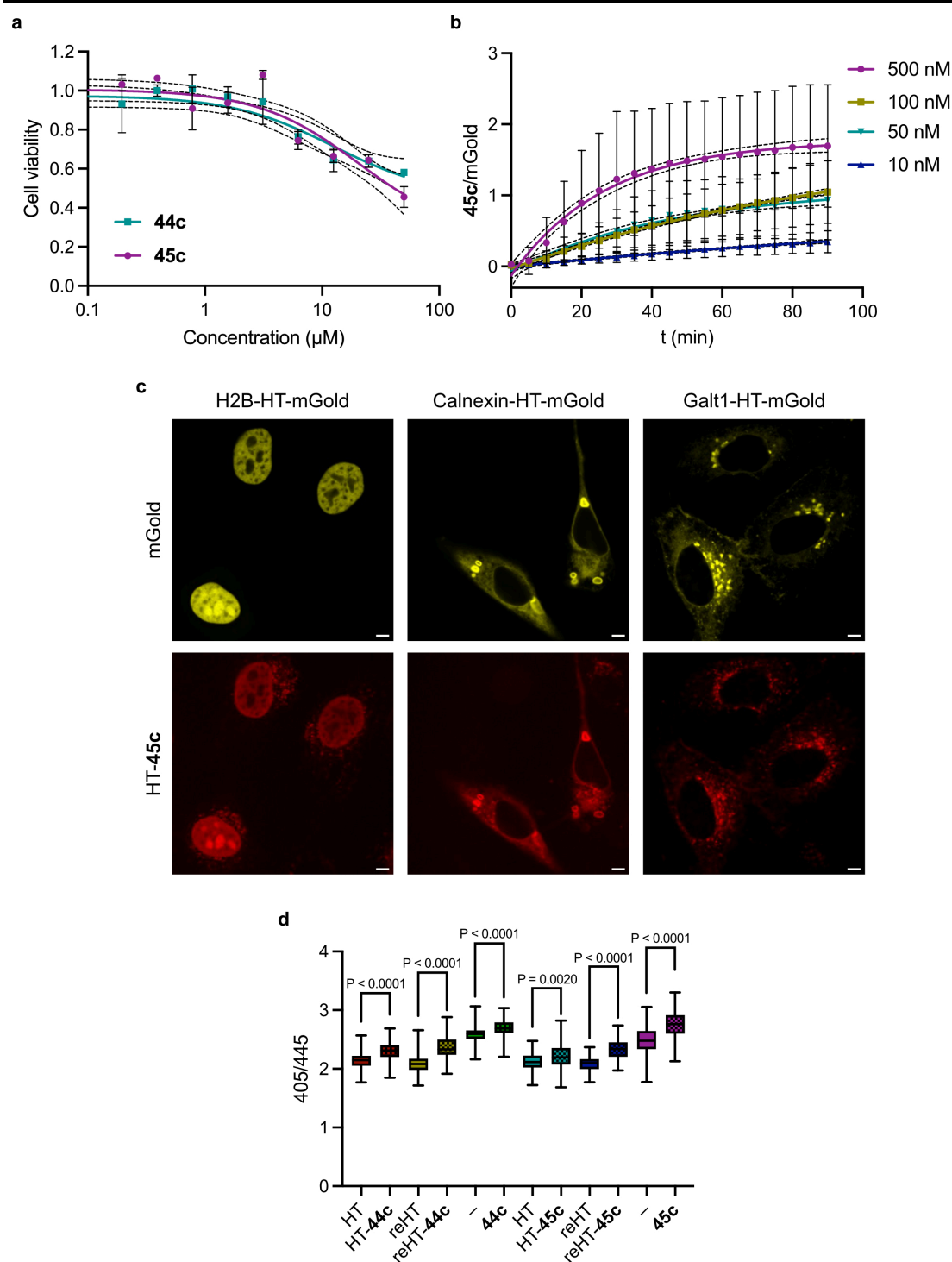


Figure 28. a) MTT cell viability assay in HeLa cells incubated with **44c** and **45c** for 24 h. Data are presented as means with error bars indicating the SD from $n=3$ technical replicates and were fitted with a sigmoidal dose-response, dotted lines represent 95% CI. b) Kinetics of HT binding for **45c** in living HeLa cells. Data are presented as means with error bars indicating the SD from $N \geq 48, 58, 19, 25$ cells per timepoint (from top to bottom). Data were fit with a one-phase decay, dotted lines represent 95% CI. c) Colocalization of HT-mGold targeted to various subcellular compartments and **45c**. Scale bars=5 μm . d) E_{GSH} measurement in the ER with roGFP in cells before and after incubation with **45c** (500 nM for 30 min). $N=91, 97, 91, 86, 72, 71, 92, 89, 83, 77, 111, 108$ (from left to right) cells from a single biological replicate. Boxes represent 25th–75th percentiles, line represents median and whiskers go from minimum to maximum, statistical significance was assessed by one-way ANOVA (Šidák multiple comparison test).

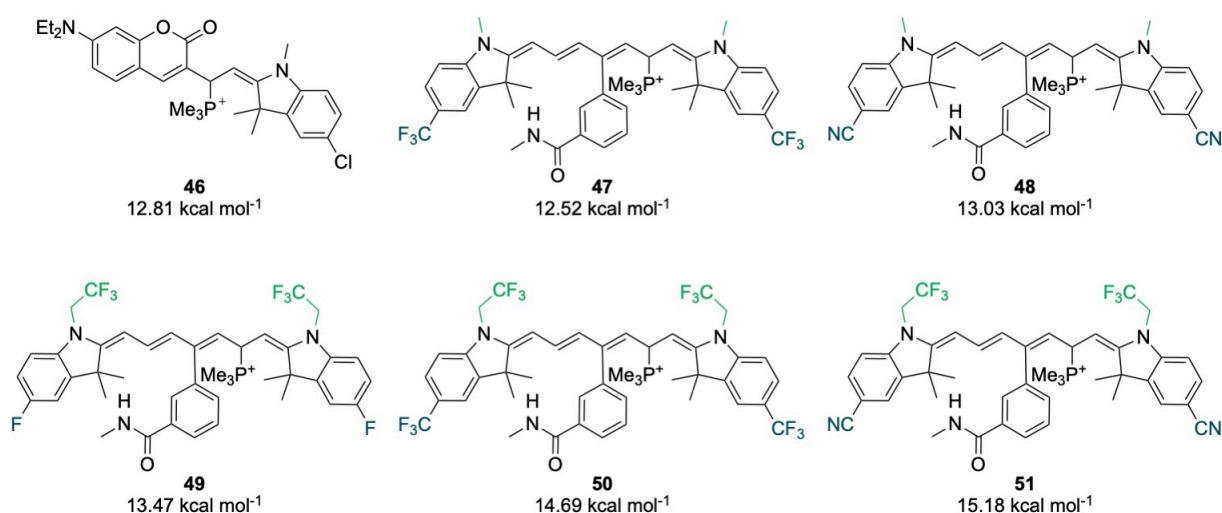
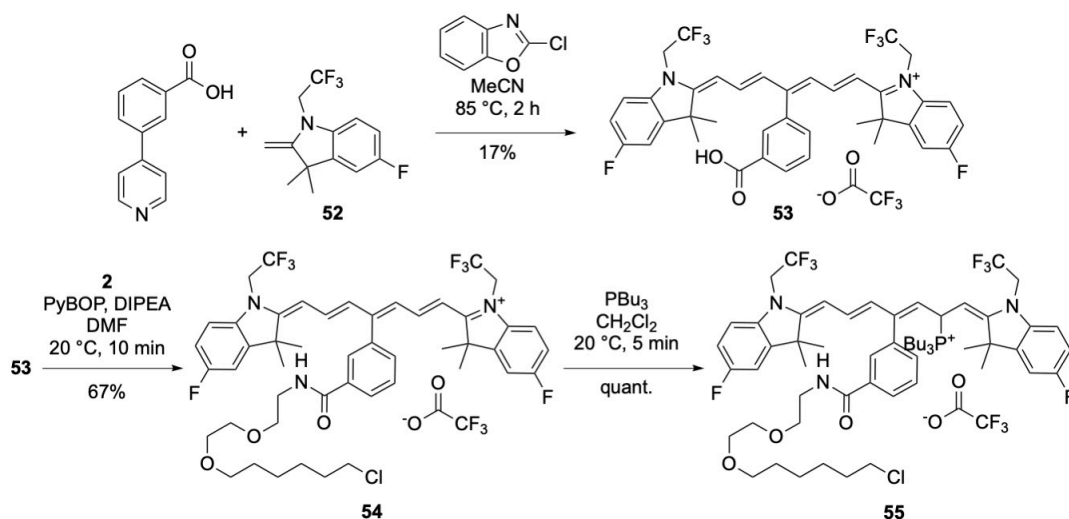


Figure 29. Computational modeling of Cy7 phosphonium compounds. Molecules with various electron-withdrawing substituents are depicted with their calculated transition state energy barriers for phosphine cleavage. As a comparison the transition state for the reported photoactivatable phosphine probe was calculated with the same level of theory. To facilitate calculations PMe_3 -adducts were modeled.

We prepared a probe, which bore a fluoride substituent on the aromatic ring of the indoleninium, as synthesis with CF_3 - or CN -substituents did not proceed under the tested conditions (Scheme 18). Reaction of the respective indolenine **52** with 3-(pyridin-4-yl)benzoic acid in the presence of 2-chlorobenzoxazole yielded fluorophore **53**. Amide coupling with CA **2** gave HT ligand **54**, which was transformed to probe **55** by phosphine addition.



Scheme 18. Synthesis of a Cy7-based HT-releasable phosphine probe with altered *N*-substitution on the indoleninium building block.

When incubated with HT in the presence of GSSG, **55** exhibited a clear turn-on manifesting in the appearance of an absorbance band around 760 nm (Figure 30a) although kinetics were slower compared to **45c** ($\tau_{1/2}$ =61.3 min, 95% CI [38.5–131 min]). Unfortunately, no

signal in the far-red channel was observed in HeLa cells expressing HT after incubation with **55** (Figure 30b). The compound might suffer from poor cell permeability or could be quenched by intracellular nucleophiles. We conclude that the probe design requires

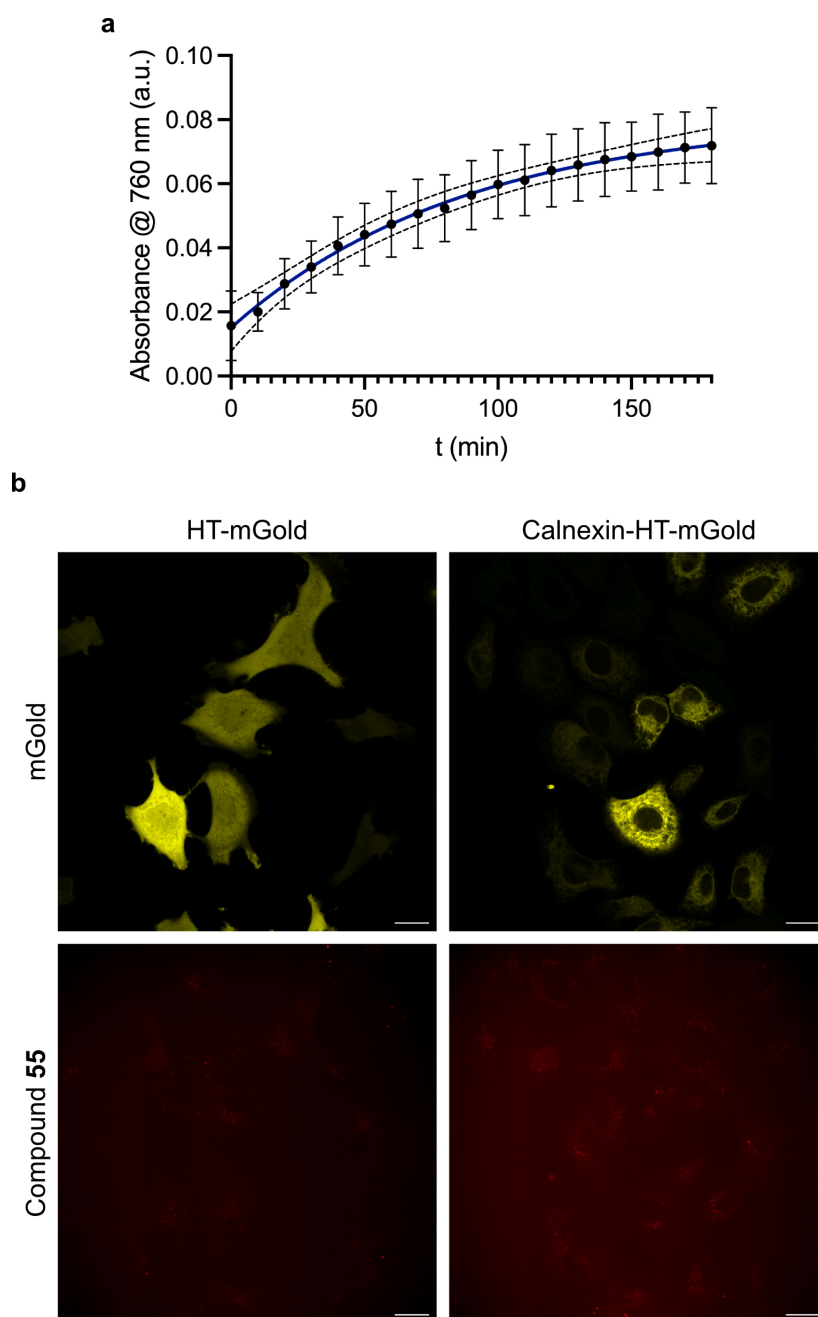


Figure 30. a) Absorbance at 760 nm of compound **55** ($15 \mu\text{M}$) upon addition of HT ($20 \mu\text{M}$) in the presence of GSSG ($20 \mu\text{M}$) as a phosphine scavenger. Data are presented as means with error bars indicating SD from $n=3$ technical replicates. Data were fitted with a one-phase decay, dotted lines represent 95% CI. b) Live cell imaging of HeLa cells transfected with HT-mGold or Calnexin-HT-mGold and incubated with **55** ($1 \mu\text{M}$) for 30 min. Scale bars= $20 \mu\text{m}$.

additional adjustments to achieve the desired characteristics for HT-activatable phosphine release while maintaining compatibility with live cells.

5.6 Conclusion and outlook

In order to create a chemigenetic system for the controlled and targeted induction of reductive stress in live cells, we explored several molecular scaffolds to find a HT-releasable phosphine. Since HT was optimized for binding rhodamine dyes, a rhodamine-based design was the obvious starting point. However, the tested modifications with electron-withdrawing substituents did not yield stable adducts with tributyl phosphine. Future efforts could be directed toward P-rhodamines with phosphine oxides as the central atom of the xanthene core. These dyes were reported to have considerably lower K_{L-Z} values than the corresponding SiR compounds, implicating a more electron-poor fluorophore, which should stabilize the phosphonium better.¹⁴⁶ Another advantage of these compounds would be their spectral properties, which reach into the NIR and prevent spectral overlap with other tools like TRaQ-G.¹⁶³

Next, we aimed to adapt the reported photoactivatable hybrid coumarin phosphonium compounds for HT binding.¹⁸⁰ Optimization of CA linker length and position led us to a “rhodamine-like” coumarin hybrid dye, which bound HT efficiently. Even though the phosphonium derived from this compound was not stable in aqueous solution, we observed interesting behavior with the precursor **39**. Presumably, hydroxide ions attack the electrophilic fluorophore in aqueous solution and interrupt the conjugated pathway preventing fluorescence in the red channel. Upon binding to HT, this reaction is reversed and fluorescence is restored. We used this effect for HT labeling in *E. coli* but labeling was slow and not consistent, which might be due to limited uptake or efflux of the compound. Further tuning of the compound is necessary to enable robust application. One possibility could be to further increase the amphiphilic moment or the rigidity of the molecule, which should improve bacterial uptake.¹⁹⁴

Lastly, we turned to Cy7-based scaffolds, which feature NIR fluorescence and are easily tunable. Exploiting different substitution patterns, two stable phosphonium compounds **45c** and **49** were prepared. However, none of them exhibited the desired characteristics in live cells. Problems with solubility and stability in different environments led to unsatisfactory

results. Thus, future development of these probes should include the introduction of solubilizing substituents. Placing electron-withdrawing groups into the bridge of the Cy7 scaffold rather than onto the indoleninium moiety might stabilize the phosphonium without impeding indoleninium addition to the pyridinium precursor.

A system for the targeted induction of reductive stress does not necessarily require a small molecule reducing agent. An alternative strategy could for example include inducible gene expression of GR. There is a number of reported systems available allowing controlled gene expression induced chemically or with light.^{198,199} However, the response time might be slow especially for switching the system off. A chemigenetic system would likely provide more control over the dose and timing. As mentioned at the beginning of this chapter, such a tool could be of great interest to study intra- and intercellular stress responses and communication.

6 FLIM multiplexing with COUPY dyes

The work discussed in this chapter was conducted in collaboration with Anna Rovira Vidal who synthesized the dyes and contributed to plasmid generation, *in vitro* characterization, and microscopy.

6.1 Objective

As discussed in chapter 1, increasing the number of available channels in fluorescence microscopy experiments allows to collect more information in a single experiment and facilitates the visualization of co-dependent signals. The extra temporal dimension in FLIM enables to distinguish signals with a combination of spectral separation and lifetime unmixing.^{88,161} A valuable expansion of this technique was the recent adaptation of the self-labeling protein HT for FLIM multiplexing. With a site-saturation mutagenesis screening, several HT variants were discovered that featured distinct fluorescence lifetimes bound to the same fluorophore. Up to three targets could be labeled with one dye and the corresponding structures could be reconstructed by lifetime unmixing.¹⁶² Different dyes displayed smaller or larger shifts in lifetime when bound to those variants, suggesting that the dyes have varying sensitivity to the environment created by the HT mutants. This observation indicated that dyes that are particularly sensitive to their environment might facilitate FLIM with self-labeling proteins. This hypothesis is backed by many studies using specialized fluorophores in FLIM to sense different parameters in their environment like pH or viscosity.^{200–202} COUPY dyes show remarkable environment-dependent changes in their photophysical properties (Figure 31). They are straightforward to synthesize and possess many desirable characteristics for bioimaging such as emission reaching into the far-red spectral region and large Stokes' shifts.²⁰³ We envisioned that binding to a self-labeling protein like HT would shift the fluorescence lifetime of COUPY dyes significantly since the protein would provide a different environment for the dyes than the solvent. Also, small changes on the protein surface close to the binding site might change the lifetime measurably. Considering the environment-sensitivity of the fluorophore, we expected a small library of HT variants to be sufficient for the identification of appropriate mutants for multiplexing. Taken together, the application of COUPY dyes in HT-based FLIM

multiplexing appeared to be an interesting case study for efficiently designing and optimizing such systems.

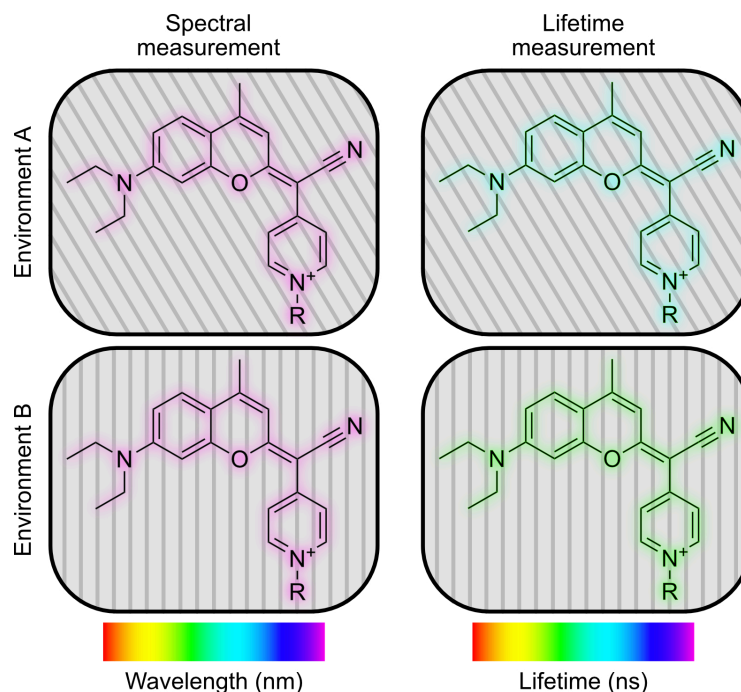


Figure 31. Environment-sensitive COUPY dyes exhibit similar spectral properties but varying fluorescence lifetime in different environments.

6.2 Synthesis and characterization of COUPY-based HT ligands

A HT-binding CA chain can easily be introduced to the COUPY scaffold by *N*-alkylation of the pyridinium moiety. The length of this chain was reported to influence binding efficiency,¹⁸⁸ thus two derivatives were synthesized bearing a C6 (COUPY-CA6) or a C7 (COUPY-CA7) linker (Figure 32a). Absorbance and emission spectra of these fluorophores are nearly identical, and environment-sensitive behavior is readily observed in different solvents (Figure 32b and Table 4). Since the compounds are non-fluorogenic, we needed to determine their background signal in live cells. We incubated HeLa cells (not expressing HT) with both compounds and measured the signal of the unbound dye by confocal microscopy. COUPY-CA6 and COUPY-CA7 showed accumulation in mitochondria most likely because they are positively charged. However, COUPY-CA7 also produced some signal in other parts of the cell resembling the ER (Figure 32c). Clearly localized signals with minimal overlap facilitate lifetime unmixing therefore COUPY-CA6 was selected for all subsequent experiments.

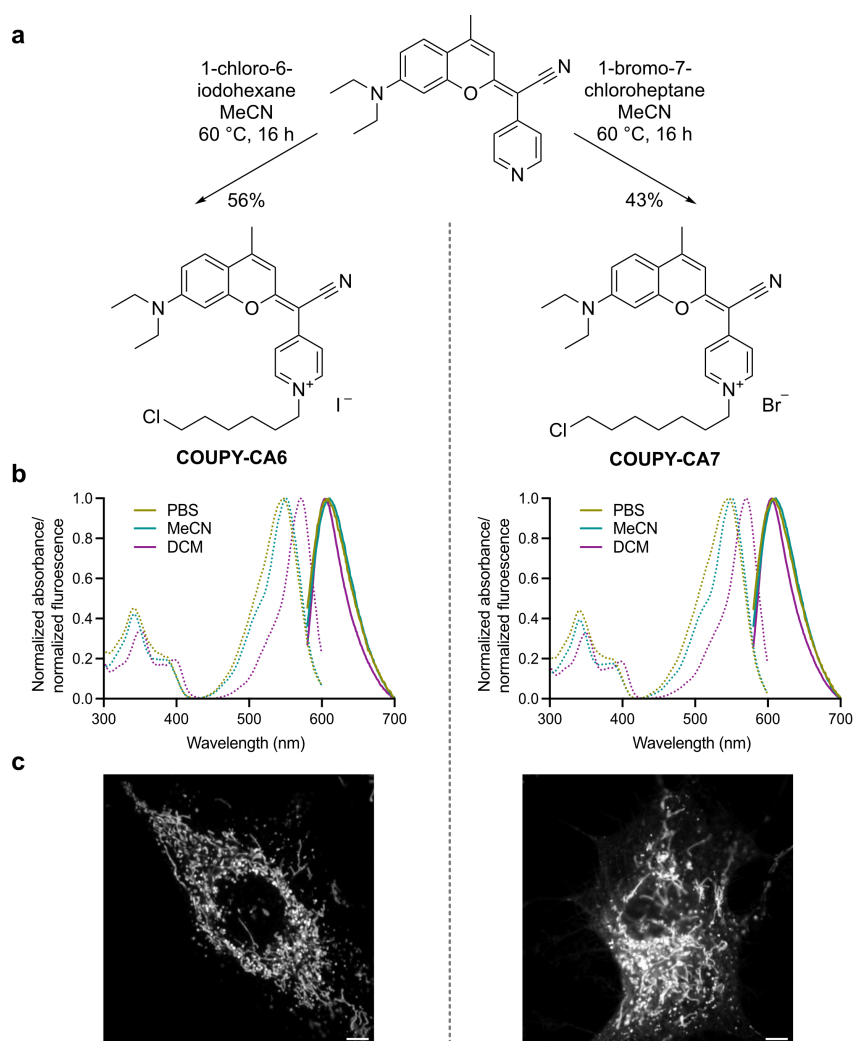


Figure 32. Synthesis of COUPY-based HT ligands (a), their absorbance and emission spectra (b) and their respective localization in living HeLa cells (c). Cells were incubated with 100 nM of the respective dye for 4 h. Scale bars = 5 μ m.

Table 4. Photophysical properties of COUPY CA-6 in different solvents.

Environment	$\lambda_{ex,max}$ (nm)	$\lambda_{em,max}$ (nm)	QY	τ (ns)
CH ₂ Cl ₂	572	604	0.70	5.2
MeCN	550	610	0.19	1.8
PBS	547	609	0.11	1.4

6.3 HT mutants suitable for COUPY dyes

Originally, HT was optimized for binding rhodamines.¹²⁹ Other types of compounds are therefore usually bound less efficiently¹³⁶ or with weaker fluorescence turn-on.^{145,188} Often, protein engineering is required to achieve optimal interaction between HT and non-rhodamine ligands. For styryl pyridinium dyes, such an optimization process yielded HT variants with 42-fold faster binding kinetics and more than 3-fold improved fluorescence enhancement.¹⁴⁷ Given the geometric similarity between COUPY and styryl pyridinium scaffolds, we hypothesized that the reported mutants might also be beneficial for COUPY dyes. Lifetime unmixing results generally improve with increasing photon count.²⁰⁴ Thus, we first screened for bright conjugates between HT mutants and COUPY-CA6. For this purpose, the most widely used HT7 and 9 mutants from the combinatorial library for the styryl pyridinium dye were selected (Table 5).¹⁴⁷ The selection included the 5 top hits for the styryl pyridinium dye and variants that introduced additional charge, as polarity strongly influenced the lifetime of COUPY dyes (Table 4).

Table 5. Screening HT mutant proteins conjugated to COUPY-CA6 for brightness and fluorescence lifetime. In a 96-well plate, solutions of the HT variants (4 μ M) and COUPY-CA6 (2 μ M) in PBS were prepared and FLIM was performed. For the whole field of view (FOV) the lifetimes were analyzed (2 components fit). The intensity sum was used to compare the brightness of mutants and τ_2 to compare the fluorescence lifetime (the longer of the two lifetimes always had a higher contribution and likely corresponds to the bound species). Three technical replicates were measured.

Variant	Mutations	Brightness (relative)	τ (ns)
HT7		1.0	5.58
HT-CDD	R133C, F144D, L271D	0.5	5.28
HT-CMHYA	R133C, E143M, F144H, M175Y, V245A	2.6	5.92
HT-CYA	R133C, M175Y, V245A	3.4	5.78
HT-CYAD	R133C, M175Y, V245A, L271D	0.8	5.58
HT-MHD	E143M, F144H, L271D	0.3	4.85
HT-MHYAD	E143M, F144H, M175Y, V245A, L271D	1.9	5.52
HT-NCDD	R133N, F144D, M175C, L271D	0.7	5.55

HT-YAD	M175Y, V245A, L271D	4.6	5.57
HT-YD	M175Y, L271D	2.1	5.66

Adducts of all variants and COUPY-CA6 were prepared *in vitro* and assessed with respect to brightness and fluorescence (Table 5). HT-CMHYA, HT-CYA, HT-MHYAD, HT-YAD and HT-YD stood out with 2–5-fold increased brightness compared to HT7. The observed lifetimes ranged from 4.9–5.9 ns, which provides a large range especially when considering the unbound dye with 1.4 ns.

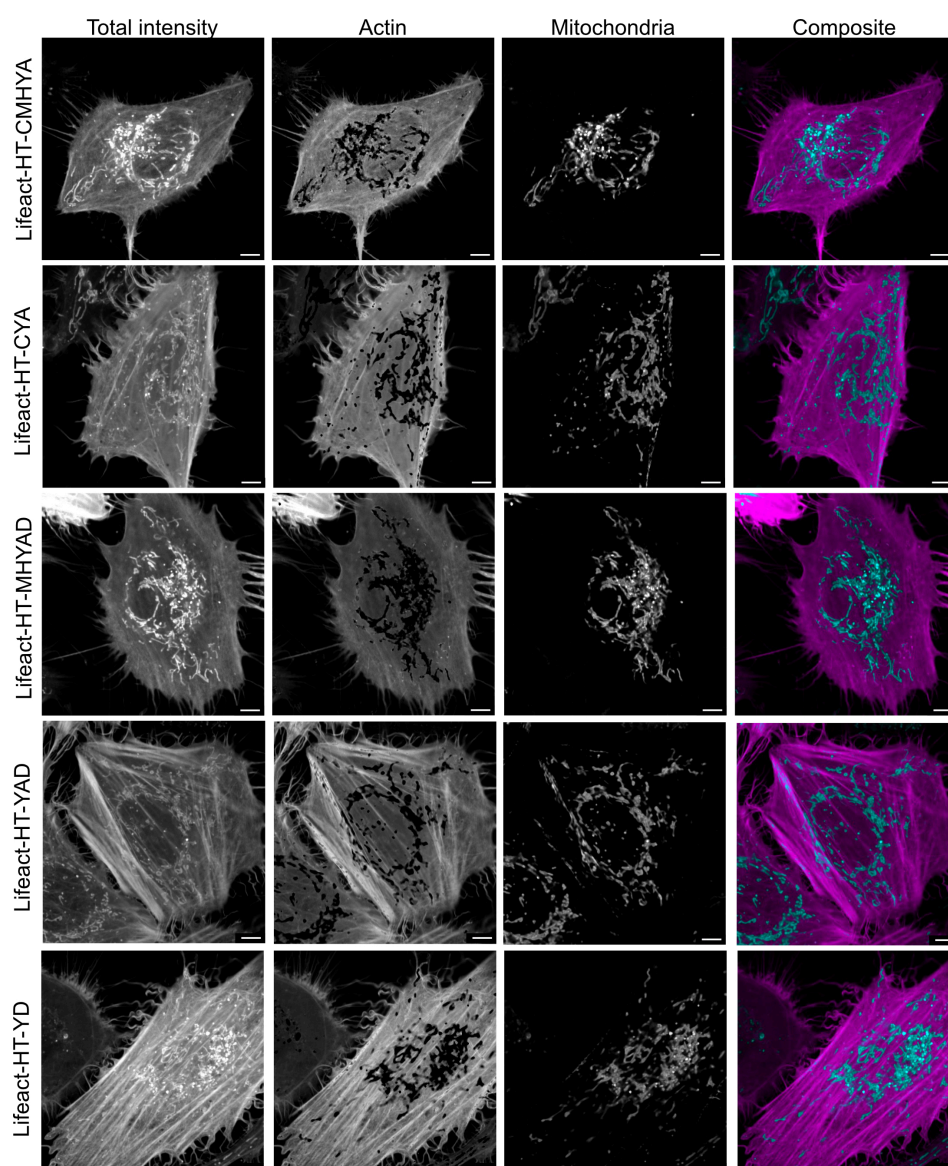


Figure 33. FLIM of HeLa cells expressing various HT mutants fused to actin and incubated with 500 nM COUPY-CA6 for 16 h. For each transfection condition the total intensity, the separated species and a composite image are depicted. Lifetime unmixing was performed applying a wavelet filter and the phasor method. Scale bars=5 μ m.

6.4 Lifetime multiplexing with free and HT-bound COUPY dye

To evaluate their performance in live-cell FLIM, plasmid constructs of the brightest mutants fused to actin were generated. HeLa cells were transfected with these plasmids and labeled with COUPY-CA6. All HT variants gave sufficient signal for imaging and the contributions from unbound and bound dye were well separated in all cases by lifetime unmixing using a wavelet filter and the phasor method (Figure 33).^{204,205} The actin filaments were clearly reproduced in the corresponding channel even though COUPY-CA6 is non-fluorogenic. Signal originating from the unbound dye can either be removed or provide information about mitochondrial morphology, a marker for cell health.²⁰⁶

6.5 Lifetime multiplexing with different HT mutants

Even when bound to HT, the specific cellular surroundings might still contribute to the close environment of the COUPY dye, thereby affecting its fluorescence lifetime. The proportionate influence of these two factors is an important parameter for evaluating the multiplexing capabilities of the HT-COUPY system. To this end, HeLa cells were co-transfected with plasmids encoding for either the same or different HT variants, targeted to the Golgi apparatus and the nucleus. We chose these compartments since their structures barely overlap but can be captured in the same z-plane, which produced well comparable unmixing results. From the screened mutants, HT-CMHYA and HT-MHYAD provided a good combination of brightness and lifetime separation *in vitro* (Table 5) and were therefore used in subsequent live-cell experiments. When HT-CMHYA was expressed simultaneously in the Golgi and the nucleus, lifetimes were already different enough to achieve some separation (Figure 34a). However, better unmixing results were achieved with HT-CMHYA targeted to the Golgi and HT-MHYAD localized in the nucleus (Figure 34b). The HT variant clearly seemed to be the dominating factor in the environment of the dye although the subcellular surroundings also played a role. These findings imply that the employed mutants should be optimized for each given combination of subcellular localizations. Additionally, the plasmid ratios for co-transfection and incubation with COUPY-CA6 must be well adjusted (see section 8.7) to balance signal intensities, which leads to fewer visible artifacts after unmixing.

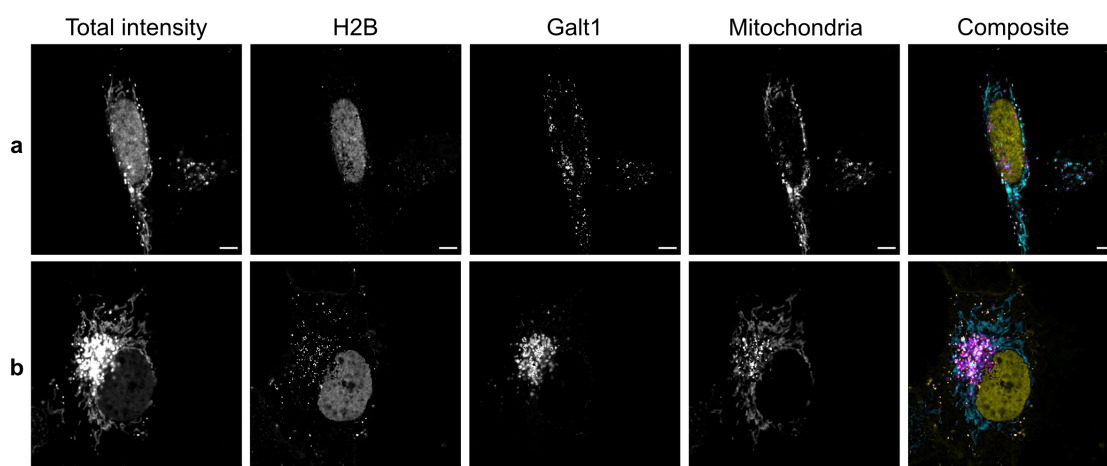


Figure 34. FLIM of HeLa cells expressing Galt1-HT-CMHYA + H2B-HT-CMHYA (a) or Galt1-HT-CMHYA + H2B-HT-MHYAD (b) and incubated with COUPY-CA6. For each transfection condition the total intensity, the separated species and a composite image are depicted. Lifetime unmixing was performed applying a wavelet filter and the phasor method. Scale bars=5 μ m.

6.6 Lifetime multiplexing with different dehalogenases

The potential of other dehalogenase enzymes for HT labeling was recently pointed out as an opportunity for optimization especially for non-rhodamine ligands.²⁰⁷ We were inspired by this work to investigate if combining different dehalogenases would lead to better unmixing results than mutants of the same protein. We designed plasmid constructs for the expression of 6 different dehalogenases in mammalian cells: DbeA, DbjA, DhlA-W175Y, DmmaA, DppA, and LinB. All genes were modified with a H→F mutation in the catalytic site, which was reported to achieve covalent labeling for DmmaA and LinB.²⁰⁷ When HeLa cells were transfected with these constructs, only DppA yielded a measurable fluorescence signal after incubation with COUPY-CA6 (Figure 35).

To test if DppA could be applied for FLIM multiplexing, a plasmid construct with the protein targeted to the nucleus was prepared. The gene further contained a FP in order to find transfected cells easily albeit the signal of the DppA-COUPY conjugate was dim. This fusion protein was expressed together with Galt1-HT-CMHYA in HeLa cells and labeled with COUPY-CA6. With unmixing the labeled structures were reconstructed even though the channel of the nucleus exhibited artifacts in the form of bright spots (Figure 36). This problem could likely be solved by increasing the brightness of the nuclear signal.

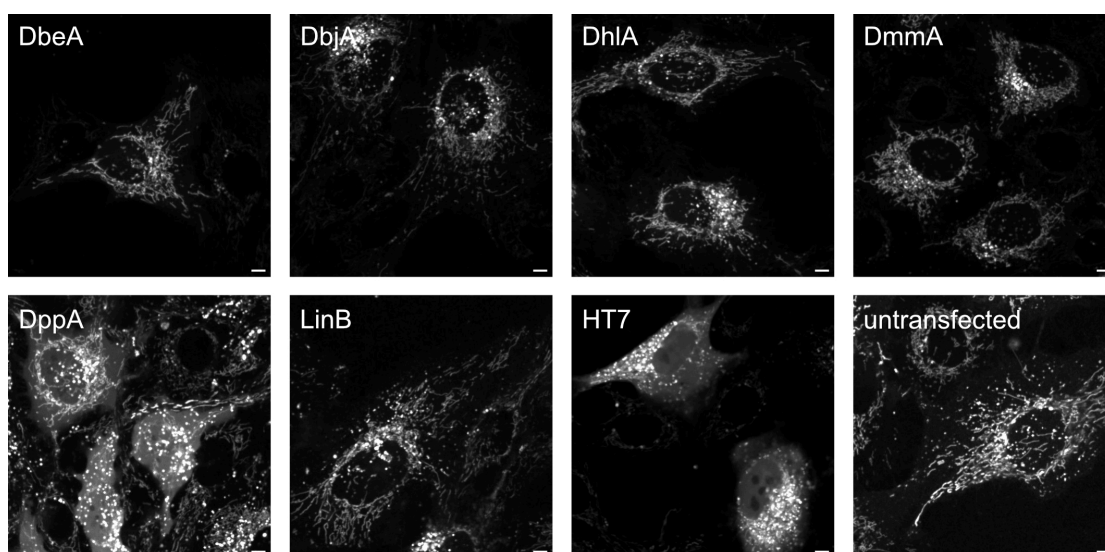


Figure 35. HeLa cells transfected with various dehalogenase constructs, stained with 0.5 μM COUPY-CA6 for 16 h (washed 3x 1 h with fresh growth medium) and analyzed by confocal spinning disk microscopy. Scale bars=5 μm .

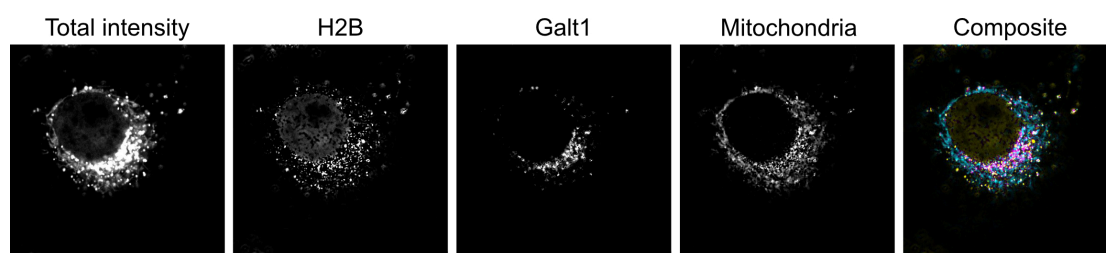


Figure 36. FLIM of HeLa cells expressing Galt1-HT-CMHYA + H2B-DppA-mGold and incubated with COUPY-CA6. For each transfection condition the total intensity, the separated species and a composite image are depicted. Lifetime unmixing was performed applying a wavelet filter and the phasor method. Scale bars=5 μm .

6.7 Conclusion and outlook

COUPY dyes are environment-sensitive and therefore exhibit shifts in fluorescence lifetime depending on their close surroundings. As a result, the lifetime changes significantly when COUPY-CA6 binds the self-labeling protein HT. This behavior is beneficial for FLIM multiplexing applications. The signals of unbound fluorophore, accumulating in mitochondria, and HT conjugate were separable using the phasor method and represented the labeled structures in pseudo-multicolor images effectively. Different mutants of the HT protein already changed the environment enough to enable lifetime unmixing. Screening a small library comprising only 10 HT variants, led to the identification of a pair of mutants that enabled FLIM multiplexing and visualization of the

Golgi apparatus, the nucleus and mitochondria with the same dye. We further investigated if pairing different dehalogenase proteins could yield better unmixing results. DppA, modified for covalent binding of CA substrates, was able to bind COUPY-CA6. Labeling of the Golgi and the nucleus with COUPY-CA6 bound to HT and DppA respectively also led to good unmixing results. However, bright spots in the lifetime channel representing the nucleus could not be avoided. A possible reason is the comparably weak fluorescence signal of the DppA conjugate. With other tested dehalogenases no labeling with COUPY-CA6 was observed at all. Compared to these other proteins, DppA features a relatively short tunnel for substrate binding, which potentially accommodates the short CA linker of COUPY-CA6 better.²⁰⁷ Nevertheless, with more extensive protein engineering of other dehalogenases, the brightness of the corresponding fluorescent adducts could be improved. Such efforts would generally broaden the toolbox for optimizing FLIM multiplexing with HT. Moreover, we also noticed spectral shifts for COUPY-CA6 in different solvents. It is thus likely that more complex imaging modalities like sFLIM further improve unmixing.⁸⁸

7 General conclusion and outlook

The cellular redox homeostasis is comprised of a complex network of pro-oxidants and antioxidants and is an integral part of cellular function. To capture redox biology in detail, methods with molecular specificity, low invasiveness and subcellular precision are needed. In this thesis, we developed chemigenetic tools for fluorescence microscopy to study aspects of redox biology and to visualize compartmentalization. The combination of functional small-molecule fluorophores with the self-labeling protein HT provided a versatile platform for our systems.

We reported the development of TRaQ-G, a targetable GSH sensor with robust ratiometric read-out and a reactivity turn-on (Figure 37). X-ray crystal structures and MD simulations reported on the molecular interactions between the small molecule sensing moiety and the HT protein. These insights provide a valuable basis for further improving TRaQ-G and have general relevance for chemigenetic tools with similar HT ligands. In live-cell imaging, the sensor reacted to induced changes of the GSH concentration as expected and was also used to monitor GSH in long-term experiments. Compartmentalization of GSH was clearly demonstrated, which highlights an important advantage of TRaQ-G, its targetability. We aimed to tune kinetics and dynamic range of the sensor by protein engineering and set up a site-saturation mutagenesis pipeline including the respective screening assays.

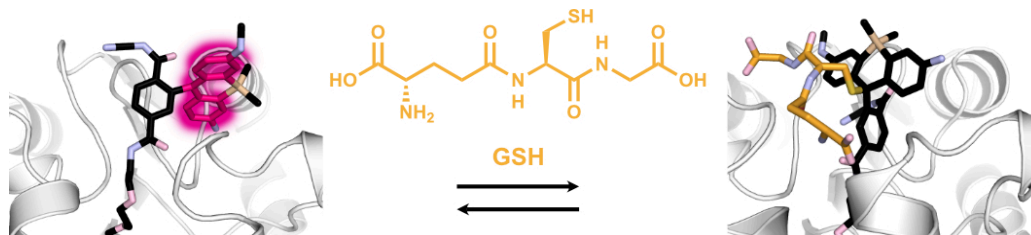


Figure 37. Adapted graphic from Emmert et al., *Nat. Chem.* 2023 (CC BY 4.0 DEED license).¹⁶³ GSH-sensing with TRaQ-G through an HT-bound electrophilic SiR, which is prone to nucleophilic attack by GSH.

With TRaQ-G, we not only added to the toolbox for studying redox biology but also introduced a useful new design principle. The reactivity turn-on mechanism described for TRaQ-G could also benefit other sensors for small metabolites, eradicating the concern of inadvertently manipulating the local concentration through shuttling. Even though there are ongoing efforts in our laboratory to optimize this system for different applications, the sensor as is can be used to explore little understood aspects of GSH homeostasis such as GSH transport mechanisms and their regulation. TRaQ-G could for example be used to

detect changes of GSH distribution in knock-down screens for potential transporter proteins, which could then point to regulatory mechanisms. Such revelations could be medically relevant as, for example, many cancer types exhibit elevated GSH levels as part of metabolic reprogramming to protect them from biological challenges in the tumor environment.²⁰⁸

From sensing GSH, we moved on to manipulating the GSH/GSSG equilibrium in a compartment-specific manner. We explored various molecular designs to find a probe that releases the reducing agent PBU_3 from a fluorogenic scaffold upon binding to HT. This led us to the serendipitous discovery of fluorogenic hybrid coumarin dyes. Due to their electrophilicity, neither intramolecular nucleophiles nor additives in the buffer were required to interrupt the π -electron system of these dyes. In an aqueous environment, hydroxide ions reacted with these fluorophores, which created an equilibrium between the fluorescent form and the non-fluorescent hydroxide adduct. The most promising molecular design for targeted phosphine-release was, however, Cy7-based (Figure 38). We were able to isolate several phosphonium compounds which showed a fluorescent turn-on upon binding to HT.

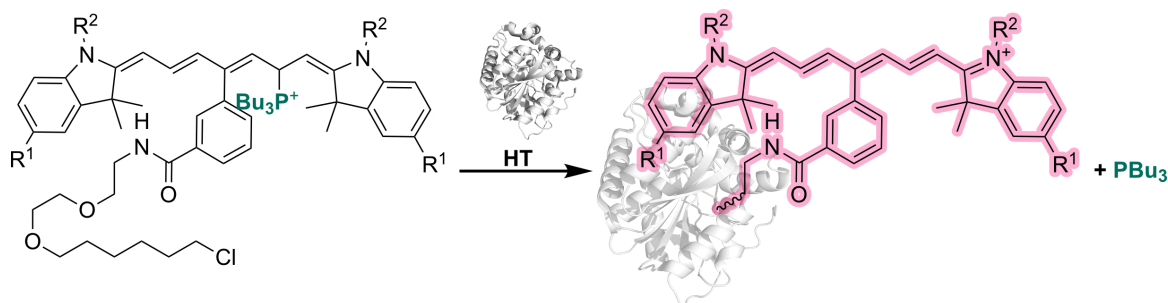


Figure 38. Cy7-based probes for the targeted release of tributyl phosphine with HT.

With improvements to the stability and live-cell compatibility of these Cy7 probes, they could become a valuable tool to study reductive stress in the future. Modifications such as using HT variants that exhibit transient binding, would create a probe where phosphine release is less dependent on expression levels of the protein construct and could be controlled by the dosage of the phosphine carrier. As Cy7 dyes absorb and emit in the NIR spectral range, other sensors like roGFP or TRaQ-G can be used to validate the evoked changes in GSH homeostasis. An interesting first target for testing the organellar response to reductive stress would be the ER with its oxidizing environment. A potential experiment would be to check for upregulation of UPR^{ER} markers by transcriptomics after inducing

stress in the ER. The probe could also be used to characterize the stress response in other organelles in a similar manner. Furthermore, experiments with mixed cell populations of HT-expressing cells and cells without the construct could be conducted to observe and study TERS or other types of intercellular stress communication.

Finally, we performed some FLIM experiments with self-labeling proteins. We used an environment sensitive COUPY dye to screen for HT mutants that would allow lifetime unmixing. With this dye, we were able to visualize up to three different cellular structures simultaneously in one spectral channel. Additionally, we tested if different dehalogenase enzymes yielded better unmixing results than mutants of the same protein. Preliminary results indicated that with some protein engineering other dehalogenase enzymes could be a valuable option for optimizing HT-based systems especially for non-rhodamine compounds.

In summary, the combination of the tools described in this thesis is a step toward enabling the detailed investigation of redox compartmentalization. Mapping localization and trafficking of GSH and other redox-active molecules is certainly part of the overall goal to gain a complete picture of cellular redox biology. Future studies might aim toward understanding how changes in the subcellular redox environments influence different metabolic pathways and signaling between subcellular compartments or single cells.

8 Experimental

8.1 General remarks

Unless stated otherwise, all reagents and solvents were purchased from commercial sources and used as received. NMR spectra were acquired on Bruker AVANCE NEO-400, Bruker AVANCE II-400, Bruker AVANCE III-400, Bruker AVANCE III HD-600, and Bruker AVANCE II-800 instruments. ^1H NMR chemical shifts are reported in ppm relative to SiMe_4 ($\delta = 0$) and were referenced internally with respect to residual protons in the solvent ($\delta = 1.94$ CD_3CN , $\delta = 7.26$ for CDCl_3 , $\delta = 2.50$ for $\text{DMSO-}d_6$ and $\delta = 3.31$ for CD_3OD)²⁰⁹. Coupling constants are reported in Hz. ^{13}C NMR chemical shifts are reported in ppm relative to SiMe_4 ($\delta = 0$) and were referenced internally with respect to solvent signal ($\delta = 1.32$ for CD_3CN , $\delta = 77.16$ for CDCl_3 , $\delta = 39.52$ for $\text{DMSO-}d_6$ and $\delta = 49.00$ for CD_3OD)²⁰⁹. Preliminary peak assignments are based on calculated chemical shift and multiplicity. High-resolution mass spectrometry (HRMS) with electrospray ionization (ESI), electron ionization (EI) or matrix-assisted laser desorption/ionization (MALDI) was performed by the MS facilities of EPFL and University of Zurich. Reaction progress was followed by thin-layer chromatography (TLC), TLC-MS on an Advion expression system and UHPLC-MS on a Shimadzu LC-MS 2020 system or a Waters system with an ACQUITY ultra-high performance liquid chromatography (UHPLC) system and a SYNAPT-G2 mass spectrometer using ESI. Purification by flash column chromatography was performed using a Büchi Pure-Chromatography-System or a Biotage Selekt instrument and Büchi FlashPure columns. Preparative high-performance liquid chromatography (HPLC) was conducted on a Büchi Pure-Chromatography-System or an Agilent 1290 Infinity II system using a Phenomenex C18 column with $\text{ddH}_2\text{O} + 0.1\%$ TFA (eluent A) and $\text{MeCN} + 0.1\%$ TFA (eluent B). IUPAC names of all compounds are provided and were determined using CS ChemDraw.

8.2 General methods

Optical spectroscopic methods

Stock solutions were prepared in DMSO (spectrophotometric grade >99.9%) at concentrations of 50 mM and stored at -20 °C. UV-Vis spectra were acquired using a Multiskan SkyHigh Microplate Spectrophotometer (ThermoFisher Scientific) with SkanIt

Software and quartz cuvettes or 96-well plates (Corning). Fluorescence measurements were conducted with an FS5 Spectrofluorometer (Edinburgh Instruments) and Fluoracle software or an Infinite® M Nano+ (Tecan) using quartz cuvettes or 96-well plates (Corning). The obtained spectra were background corrected. All measurements were carried out as three technical replicates.

Cloning

Primers for Gibson assembly were designed using SnapGene. Reagents and general procedures from the Gibson Assembly Cloning Kit from New England Biolabs (NEB) were used. Vector and insert fragments were linearized by PCR and template DNA was digested with DpnI. PCR fragments were purified with the QIAquick PCR Purification Kit from Qiagen. Backbone and insert fragment were ligated and transformed by heat shock into NEB 5 α competent cells following the provided standard procedure of the vendor. Plasmids were amplified by incubation of lysogeny broth (LB) cultures containing the appropriate antibiotics overnight at 37 °C. DNA was isolated using the Qiagen Plasmid Mini Kit or the Qiagen Plasmid Plus Midi Kit. The correct sequence of the gene of interest (GOI) was confirmed by the Sanger sequencing service of Microsynth.

Site-directed mutagenesis

Primers for site-directed mutagenesis were designed with NEBaseChanger. The standard procedure and reagents from the Q5 Site-Directed Mutagenesis Kit (NEB) were used to insert mutations, ligate plasmids and transform them into NEB 5 α competent cells by heat shock. The correct sequence of the GOI was confirmed by the Sanger sequencing service of Microsynth.

Protein expression

BL21(DE3) competent cells from NEB were transformed with the respective plasmid by heat shock following the provided standard procedure of the vendor. LB was prepared with the appropriate antibiotic. A single colony was inoculated into 20–100 mL LB and incubated at 37 °C overnight. The appropriate amount of LB for the protein expression

scale was inoculated from the starter culture and incubated at 37 °C until the optical density $OD=0.4-0.8$ was reached. Isopropyl β -D-1-thiogalactopyranoside (IPTG) was added to a final concentration of 1 mM and the culture was further incubated at 18 °C overnight. *E. coli* were harvested by centrifugation and resuspended in HEPES buffer (20 mM HEPES, 300 mM NaCl, pH=7.4). Glycerol was added to a final concentration of 10% as well as Turbonuclease (5 μ L) and a protease inhibitor cocktail tablet (Roche). The cells were lysed by sonication (70% amplitude, 10 s pulse/10 s pulse off for 2.5 min). The lysate was cleared by centrifugation and the protein was purified by Ni-His-affinity chromatography in batch-mode. Fractions were analyzed by gel electrophoresis and pure fractions were pooled and dialyzed against PBS.

Cell culture

HeLa cells were grown in Dulbecco's modified Eagle medium (DMEM) supplemented with fetal bovine serum (FBS, 10%) and penicillin (100 U mL⁻¹)/streptomycin (100 μ g mL⁻¹)/fungizone (0.25 μ g mL⁻¹) at 37 °C in 5% CO₂ environment. For imaging, 15'000–20'000 cells were seeded per well of an 8-well Ibidi chambered cover glass 2–3 days prior to imaging. If required, cells were transfected with plasmid DNA using jetPRIME according to the recommended protocol of the supplier 1–2 days prior to imaging. The cells were incubated with the respective probes in growth medium for the indicated time. Before imaging, the growth medium was removed, the cells were washed with PBS (2x) and imaged in FluoroBrite DMEM.

Spinning disk confocal microscopy

Confocal imaging was performed with a dual-camera Nikon W1 spinning disc microscope equipped with an sCMOS camera (Photometrix). Brightfield imaging was performed with a white LED. Laser lines and filters were set up for the appropriate channels as described. Images were collected using a CFI Plan Apochromat Lambda D oil immersion objective (60x, numerical aperture (NA)=1.4) or a CFI Plan Apo VC water immersion objective (60x, NA=1.2). Channels were imaged sequentially. The microscope was operated using the NIS elements software. Imaging was performed at 37 °C in a 5% CO₂ environment.

FLIM

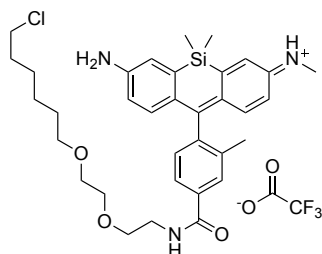
Fluorescence lifetime imaging was carried out on a Leica SP8 Falcon system equipped with a white laser and PMT/HyD detectors. For FLIM acquisition the HyD detector in photon counting mode and an HC PLAPO corr CS2 oil immersion objective (63x, $NA=1.4$) were used. Data were acquired and analyzed using the LAS X 4 software.

8.3 Experimental procedures for chapter 2

The experimental procedures for chapter 2 are also published in Emmert et al., *Nat. Chem.* 2023.¹⁶³

Synthetic procedures

(E)-N-(7-Amino-10-(4-((2-(2-((6-chlorohexyl)oxy)ethoxy)ethyl)carbamoyl)-2-methylphenyl)-5,5-dimethyldibenzo[*b,e*]silin-3(5*H*)-ylidene)methanaminium trifluoroacetate (Me-TRaQ-G ligand)



Boc-protected CA **2** (48.6 mg, 146 μmol , 5 equiv.) was dissolved in HCl (4 M in dioxane, 750 μL) in a round bottom flask, cooled with ice. The mixture was stirred at 20 $^{\circ}\text{C}$ for 45 min. Saturated aqueous Na_2CO_3 was added and the aqueous layer was extracted with CH_2Cl_2 (3x). The combined organic

layers were dried over Na_2SO_4 and the solvent was evaporated.

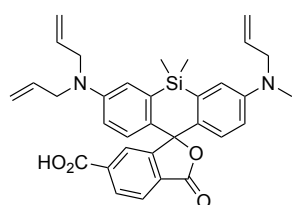
Intermediate **1** (15.0 mg, 29.2 μmol , 1 equiv.), deprotected CA **2** and PyBOP (30.3 mg, 58.3 μmol , 2 equiv.) were added to a pre-dried flask under an N_2 atmosphere. The solids were dissolved in DMF (1.5 mL) and treated with DIPEA (72 μL , 0.44 μmol , 15 equiv.). The resulting solution was stirred at 20 $^{\circ}\text{C}$ for 1.5 h. All volatile material was evaporated under reduced pressure, and the residue was purified by preparative HPLC ($\text{C}_{18}\text{-SiO}_2$, 10 \rightarrow 90 % MeCN in ddH₂O + 0.1% TFA) to yield a blue solid (13.9 mg, 19.7 μmol , 68%).

^1H NMR (400 MHz, CD_3OD) δ 7.54 (d, $J = 7.7$ Hz, 1H), 7.22 – 7.12 (m, 5H), 7.08 (d, $J = 9.3$ Hz, 1H), 6.63 – 6.58 (m, 1H), 6.56 (dd, $J = 9.3, 2.5$ Hz, 1H), 3.73 – 3.66 (m, 4H), 3.64 – 3.60 (m, 4H), 3.52 – 3.48 (m, 4H), 3.07 (s, 3H), 2.49 (s, 3H), 1.72 (dt, $J = 8.0, 6.5$ Hz, 2H), 1.60 – 1.57 (m, 2H), 1.48 – 1.34 (m, 2H), 0.55 (s, 6H).

^{13}C NMR (201 MHz, CD_3OD) δ 172.4, 170.6, 162.5, 158.2, 157.4, 150.2, 144.3, 142.1, 138.4, 137.2, 133.5, 132.4, 130.2, 128.8, 128.8, 128.0, 128.0, 127.8, 124.4, 116.5, 72.3, 71.3, 71.3, 70.5, 45.7, 45.7, 40.8, 33.7, 30.6, 27.8, 26.5, 19.7, -1.4, -1.5.

HRMS (ESI/LTQ-Orbitrap) $[\text{M}+\text{H}]^+$ calculated for $\text{C}_{34}\text{H}_{45}\text{ClN}_3\text{O}_3\text{Si}^+$ 606.2913; found 606.2927.

3-(Allyl(methyl)amino)-7-(diallylamino)-5,5-dimethyl-3'-oxo-3'*H*,5*H*-spiro[dibenzo-*b,e*]siline-10,1'-isobenzofuran]-6'-carboxylic acid (5)



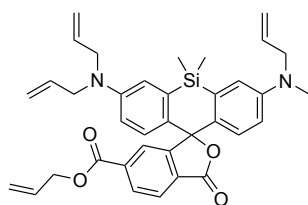
Compound **3** (650 mg, 1.85 mmol, 3 equiv.) was added to a pre-dried flask under an N_2 atmosphere, dissolved in dry THF (31 mL), and cooled to -78°C . *t*BuLi (1.7 M, 1.1 mL, 1.9 mmol, 3 equiv.) was slowly added dropwise and the solution was stirred at the same temperature for 30 min. Ketone **4** (249 mg, 617 μmol , 1 equiv.) in dry tetrahydrofuran (15 mL) was added dropwise via a syringe, and the solution was warmed to ambient temperature and stirred for 4.5 h. Acetic acid (3.5 mL, 62 mmol, 100 equiv.) was added to the mixture and the resulting intensely blue solution was evaporated under reduced pressure. The crude product was dissolved in hydrochloric acid (6 M, 51 mL, 500 equiv.) and stirred at 80°C for 16 h. After cooling to ambient temperature, the solution was added to saturated aqueous Na_2CO_3 (50 mL), the pH was adjusted to ~ 2 and the mixture was extracted with CH_2Cl_2 (3x). The combined organic phases were dried over Na_2SO_4 and evaporated under reduced pressure. The residue was purified by flash column chromatography (SiO_2 , 0 \rightarrow 5% MeOH in CH_2Cl_2) to yield a green solid (178 mg, 322 μmol , 52%).

^1H NMR (800 MHz, CD_3OD) δ 8.27 (dd, $J = 8.1, 1.5$ Hz, 1H), 8.18 (d, $J = 8.1$ Hz, 1H), 7.84 (s, 1H), 7.20 – 7.16 (m, 2H), 6.86 – 6.82 (m, 2H), 6.72 – 6.68 (m, 2H), 5.93 – 5.84 (m, 3H), 5.24 – 5.13 (m, 6H), 4.16 – 4.13 (m, 6H), 3.15 (s, 3H), 0.61 (s, 3H), 0.53 (s, 3H).

^{13}C NMR (201 MHz, CD_3OD) δ 172.4, 168.0, 162.7, 150.5, 149.5, 136.5, 136.5, 136.4, 133.9, 133.4, 131.3, 131.2, 130.9, 129.8, 129.6, 126.3, 120.3, 120.2, 117.4, 117.3, 116.5, 115.2, 115.2, 100.0, 56.0, 54.2, 39.0, -0.4, -1.7.

HRMS (ESI/QTOF) $[\text{M}+\text{H}]^+$ calculated for $[\text{C}_{33}\text{H}_{35}\text{N}_2\text{O}_4\text{Si}]^+$ 551.2361; found 551.2373.

Allyl 3-(allyl(methyl)amino)-7-(diallylamino)-5,5-dimethyl-3'-oxo-3'H,5H-spiro-[dibenzo[b,e]siline-10,1'-isobenzofuran]-6'-carboxylate (6)



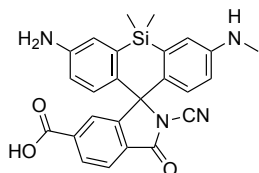
Compound **5** (150 mg, 272 μmol , 1 equiv.) was added to a pre-dried flask under an N_2 atmosphere, dissolved in DMF (3.9 mL) and treated with K_2CO_3 (75.1 mg, 544 μmol , 2 equiv.) and TEA (75.6 μL , 544 μmol , 2 equiv.). The mixture was cooled to 0 $^\circ\text{C}$ with an ice bath, treated with allyl bromide (35.5 μL , 408 μmol , 1.5 equiv.) and stirred at 20 $^\circ\text{C}$ for 2 h. The resulting solution was diluted with water and extracted with CH_2Cl_2 (3x). The combined organic layers were dried over Na_2SO_4 and concentrated under reduced pressure. The crude product was purified by flash column chromatography (SiO_2 , 0 \rightarrow 25 % ethyl acetate (EtOAc) in hexane) to yield a yellow solid (78 .0 mg, 132 μmol , 49%).

^1H NMR (600 MHz, CD_3CN) δ 8.19 (dd, $J = 8.1, 1.4$ Hz, 1H), 8.01 (d, $J = 8.0$ Hz, 1H), 7.79 – 7.76 (m, 1H), 7.05 (2x d, $J = 2.9$ Hz, 2H), 6.73 (2x d, $J = 9.0$ Hz, 2H), 6.59 (2x dd, $J = 9.0, 2.9$ Hz, 2H), 6.01 (ddt, $J = 17.2, 10.4, 5.7$ Hz, 1H), 5.90 – 5.78 (m, 3H), 5.37 – 5.34 (m, 1H), 5.25 (m, 1H), 5.17 – 5.07 (m, 6H), 4.76 (dt, $J = 5.8, 1.4$ Hz, 2H), 4.00 – 3.95 (m, 6H), 2.97 (s, 3H), 0.60 (s, 3H), 0.51 (s, 3H).

^{13}C NMR (151 MHz, CD_3CN) δ 170.1, 165.6, 155.2, 149.7, 148.9, 138.0, 137.8, 136.5, 134.8, 134.3, 133.1, 131.5, 131.4, 130.9, 130.7, 129.8, 129.7, 127.2, 126.0, 119.1, 118.1, 118.1, 116.8, 116.5, 114.8, 114.7, 67.1, 55.3, 53.5, 38.6, -0.1, -1.2. (One carbon is likely hidden under the solvent peak.)

HRMS (ESI/QTOF) $[\text{M}+\text{H}]^+$ calculated for $\text{C}_{36}\text{H}_{39}\text{N}_2\text{O}_4\text{Si}^+$ 591.2674; found 591.2687.

3-Amino-2'-cyano-5,5-dimethyl-7-(methylamino)-3'-oxo-5H-spiro[dibenzo[b,e]siline-10,1'-isoindoline]-6'-carboxylic acid (7)



Compound **6** (70.0 mg, 118 μmol , 1 equiv.) was added to a pre-dried flask under an N_2 atmosphere, dissolved in dry CH_2Cl_2 (5.9 mL) and treated with oxalyl chloride (0.50 M, 0.36 mL, 1.5 equiv.) at 0 $^\circ\text{C}$. The resulting solution was stirred at 20 $^\circ\text{C}$ for 2 h. The solvent was evaporated under reduced pressure and the product was used without further purification for the next step.

The crude acyl chloride was dissolved in dry MeCN (5.9 mL) under an N₂ atmosphere and treated with a solution of cyanamide (49.8 mg, 1.18 mmol, 10 equiv.) and DIPEA (294 μL, 1.78 mmol, 15 equiv.) in dry MeCN (3.0 mL). The resulting solution was stirred at 70 °C for 3 h. The solvent was evaporated under reduced pressure and the product was used without further purification in the next step.

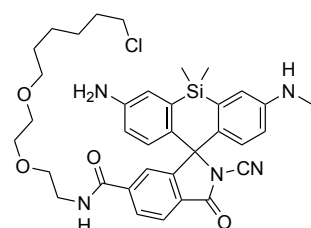
The crude cyanamide, 1,3-dimethyl-1,3-diazinane-2,4,6-trione (370 mg, 2.37 mmol, 20 equiv.) and tetrakis(triphenylphosphine)-palladium(0) (68.5 mg, 59.2 μmol, 0.5 equiv.) were dissolved in a degassed mixture (5:1) of CH₂Cl₂ (5.9 mL) and MeOH (1.2 mL) under an N₂ atmosphere. The resulting mixture was stirred at 40 °C for 2 h. The solution was diluted with CH₂Cl₂ and washed with saturated aqueous Na₂CO₃ solution. The aqueous phase was re-extracted with CH₂Cl₂ (2x). The combined organic phases were dried over Na₂SO₄ and the solvent was evaporated under reduced pressure. The crude product was purified by flash column chromatography (SiO₂, 0 → 10 % MeOH in CH₂Cl₂) to yield a yellowish solid (50.2 mg, 110 μmol, 93%).

¹H NMR (600 MHz, CD₃OD) δ 8.18 (dd, *J* = 8.1, 1.3 Hz, 1H), 8.08 (d, *J* = 8.0 Hz, 1H), 7.55 (s, 1H), 7.37 (d, *J* = 2.6 Hz, 1H), 7.00 (d, *J* = 4.9 Hz, 2H), 6.89 (d, *J* = 8.7 Hz, 1H), 6.75 (d, *J* = 8.8 Hz, 1H), 6.70 (dd, *J* = 8.9, 2.6 Hz, 1H), 2.83 (s, 3H), 0.65 (s, 3H), 0.59 (s, 3H).

¹³C NMR (151 MHz, CD₃OD) δ 168.3, 167.5, 162.5, 156.3, 149.8, 141.9, 139.0, 138.3, 136.5, 131.3, 130.2, 130.1, 129.8, 129.3, 126.3, 126.1, 124.3, 122.2, 118.1, 117.3, 107.5, 75.8, 30.4, 0.0, -0.1.

HRMS (ESI/QTOF) [M+H]⁺ calculated for C₂₅H₂₃N₄O₃Si⁺ 455.1534; found 455.1542.

3-Amino-*N*-(2-(2-((6-chlorohexyl)oxy)ethoxy)ethyl)-2'-cyano-5,5-dimethyl-7-(methylamino)-3'-oxo-5*H*-spiro[dibenzo[*b,e*]siline-10,1'-isoindoline]-6'-carboxamide (TraQ-G ligand)



Boc-protected CA **2** (42.7 mg, 132 μmol, 3 equiv.) was dissolved in HCl (4 M in dioxane, 660 μL) in a round bottom flask, cooled with an ice bath. The mixture was stirred at 20 °C for 45 min. Saturated aqueous Na₂HCO₃ was added and the aqueous layer

was extracted with CH₂Cl₂ (3x). The combined organic layers were dried over Na₂SO₄ and the solvent was evaporated.

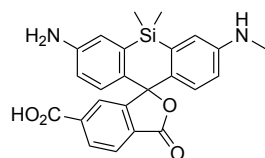
The deprotected CA **2**, compound **7** (20.0 mg, 44.0 μmol, 1 equiv.) and PyBOP (45.8 mg, 88.0 μmol, 2 equiv.) were added to a pre-dried flask under an N₂ atmosphere, dissolved in DMF (2.2 mL) and treated with DIPEA (72.7 μL, 440 μmol, 10 equiv.). The resulting solution was stirred at 20 °C for 2.5 h. All volatiles were removed under reduced pressure and the residue was purified by preparative HPLC (C18-SiO₂, 10 → 95 % MeCN in ddH₂O + 0.1% TFA) to yield a light green solid (16.3 mg, 24.5 μmol, 56%).

¹H NMR (600 MHz, CD₃CN) δ 8.01 (d, *J* = 8.0 Hz, 1H), 7.89 (dd, *J* = 8.0, 1.4 Hz, 1H), 7.29 – 7.27 (m, 1H), 7.19 (s, 1H), 7.06 – 7.05 (m, 1H), 7.00 – 6.99 (m, 1H), 6.76 – 6.73 (m, 1H), 6.72 – 6.65 (m, 3H), 3.53 (t, *J* = 6.7 Hz, 2H), 3.51 – 3.48 (m, 4H), 3.45 – 3.37 (m, 4H), 3.30 (t, *J* = 6.5 Hz, 2H), 2.81 (s, 3H), 1.69 – 1.66 (m, 2H), 1.43 – 1.37 (m, 2H), 1.36 – 1.30 (m, 2H), 1.26 – 1.19 (m, 2H), 0.58 (s, 3H), 0.52 (s, 3H).

¹³C NMR (151 MHz, CD₃CN) δ 168.0, 166.3, 159.6, 156.2, 148.7, 147.1, 142.9, 137.1, 131.2, 130.8, 130.2, 130.1, 128.72, 127.7, 126.1, 123.6, 120.2, 119.1, 117.9, 117.3, 107.85, 75.5, 71.5, 70.8, 70.7, 69.8, 46.2, 40.5, 33.3, 31.2, 30.2, 27.3, 26.1, -0.04. (Two carbons adjacent to silicon carbons are likely overlapping.)

HRMS (ESI/QTOF) [M+H]⁺ calculated for C₃₅H₄₃ClN₅O₄Si⁺ 660.2767; found 660.2787.

3-Amino-5,5-dimethyl-7-(methylamino)-3'-oxo-3'*H*,5*H*-spiro[dibenzo[*b,e*]siline-10,1'-isobenzofuran]-6'-carboxylic acid (**8**)



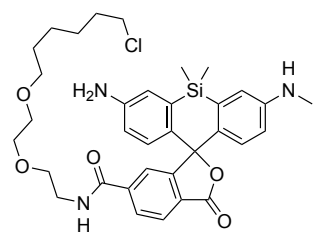
Compound **5**, 1,3-dimethylbarbituric acid (370 mg, 2.37 mmol, 20 equiv.) and tetrakis(triphenylphosphine)palladium(0) (68.5 mg, 59.2 μmol, 0.5 equiv.) were dissolved in a degassed mixture (5:1) of CH₂Cl₂ (0.42 mL) and MeOH (0.86 mL) under an Ar atmosphere. The resulting mixture was stirred at 40 °C for 2 h. The solution was diluted with CH₂Cl₂ and washed with saturated aqueous Na₂CO₃ solution. The aqueous phase was re-extracted with CH₂Cl₂ (2x). The combined organic phases were dried over Na₂SO₄ and the solvent was evaporated under reduced pressure. The crude product was purified by preparative HPLC (C18-SiO₂, 10 → 95% MeCN in ddH₂O with 0.1% TFA) to yield a blue solid (9.3 mg, 21 μmol, 24%).

^1H NMR (800 MHz, CD_3OD) δ 8.30 (dd, $J = 8.1, 1.5$ Hz, 1H), 8.24 (s, 1H), 7.86 (d, $J = 1.5$ Hz, 1H), 7.26 (s, 1H), 7.14 (s, 1H), 6.89 (d, $J = 9.1$ Hz, 1H), 6.69 (s, 2H), 6.61 (dd, $J = 9.2, 2.6$ Hz, 1H), 2.98 (s, 3H), 0.64 (s, 3H), 0.56 (s, 3H).

^{13}C NMR (201 MHz, CD_3OD) δ 172.4, 168.0, 162.7, 150.5, 149.5, 136.5, 136.5, 136.4, 133.9, 133.4, 131.3, 131.2, 130.9, 129.8, 129.6, 126.3, 120.3, 120.2, 117.4, 117.3, 116.5, 115.2, 115.2, 100.0, 56.0, 54.2, 40.4, 39.0, -0.4, -1.7.

HRMS (ESI/QTOF) $[\text{M}+\text{H}]^+$ calculated for $\text{C}_{24}\text{H}_{23}\text{N}_2\text{O}_4\text{Si}^+$ 431.1422; found 431.1424.

3-Amino-*N*-(2-(2-((6-chlorohexyl)oxy)ethoxy)ethyl)-5,5-dimethyl-7-(methylamino)-3'-oxo-3'*H*,5*H*-spiro[dibenzo[*b,e*]siline-10,1'-isobenzofuran]-6'-carboxamide (TraQ-G-ctrl ligand)



Boc-protected CA **2** (42.7 mg, 132 μmol , 3 equiv.) was dissolved in HCl (4 M in dioxane, 660 μL) in a round bottom flask, cooled with an ice bath. The solution was stirred at 20 $^\circ\text{C}$ for 45 min. Saturated aqueous Na_2HCO_3 was added and the aqueous layer was extracted with CH_2Cl_2 (3x). The combined organic layers were dried over Na_2SO_4 and the solvent was evaporated.

Deprotected CA **2**, compound **8** (7.0 mg, 16 μmol , 1 equiv.) and PyBOP (17 mg, 32 μmol , 2 equiv.) were added to a pre-dried flask under an N_2 atmosphere, dissolved in DMF (0.8 mL) and treated with DIPEA (27 μL , 0.16 mmol, 10 equiv.). The resulting solution was stirred at 20 $^\circ\text{C}$ for 2.5 h. All volatiles were removed, and the residue was purified by preparative HPLC (C18- SiO_2 , 10 \rightarrow 95% MeCN in ddH $_2\text{O}$ with 0.1% TFA) to yield a blue solid (5.7 mg, 8.6 μmol , 53%).

^1H NMR (600 MHz, CD_3OD) δ 8.75–8.74 (m, 1H), 8.07 (s, 2H), 7.72 (d, $J = 1.1$ Hz, 1H), 7.10 (d, $J = 2.5$ Hz, 1H), 6.98 (d, $J = 2.6$ Hz, 1H), 6.69 (2x d, $J = 8.8$ Hz, 2H), 6.59 (dd, $J = 8.7, 2.6$ Hz, 1H), 6.51 (dd, $J = 8.9, 2.7$ Hz, 1H), 3.65 (t, $J = 5.3$ Hz, 2H), 3.63 – 3.60 (m, 2H), 3.59 – 3.54 (m, 4H), 3.51 (t, $J = 6.7$ Hz, 2H), 3.41 (t, $J = 6.5$ Hz, 2H), 2.83 (s, 3H), 1.73 – 1.66 (m, 2H), 1.49 – 1.44 (m, 2H), 1.42 – 1.34 (m, 2H), 1.30 – 1.25 (m, 2H), 0.63 (s, 3H), 0.54 (s, 3H).

^{13}C NMR (151 MHz, CD_3OD) δ 171.2, 168.7, 151.8, 149.8, 141.0, 140.2, 133.5, 133.2, 131.7, 130.8, 130.2, 129.3, 128.0, 127.6, 125.6, 121.6, 118.9, 117.4, 116.0, 114.3, 72.1, 71.2, 71.1, 70.3, 45.7, 41.1, 40.4, 33.7, 30.4, 30.3, 27.7, 26.4, -0.0, -1.5.

HRMS (ESI/QTOF) $[\text{M}+\text{H}]^+$ calculated for $[\text{C}_{34}\text{H}_{43}\text{ClN}_3\text{O}_5\text{Si}]^+$ 636.2655; found 636.2667.

Optical spectroscopic methods

Quantum yields were measured at concentrations of 1–10 μM depending on the brightness of the respective molecule using an integrating sphere and quartz cuvettes. Extinction coefficients were measured by creating a dilution series (1–15 μM), measuring the absorbance at λ_{max} , and applying a linear regression. Measurements for the turn-on ligands were performed at $\text{pH}=2$ to enhance the zwitterionic form as much as possible. Extinction coefficients of HT adducts were measured in the presence of a two-fold excess of HT protein to ensure quantitative reaction of the ligand. All measurements were carried out as technical triplicates and at 20 $^\circ\text{C}$.

Protein expression of HT

The HT7-His6 plasmid was a gift from Thomas Ward (University of Basel). The general protocol for protein expression (section 8.2) was followed.

Protein crystallization and structural analysis

HT protein ($\sim 1 \text{ mg mL}^{-1}$) was reacted with the respective ligand (1.5x excess) in PBS at 20 $^\circ\text{C}$ for 1 h. The adduct was purified by size-exclusion chromatography and concentrated to $\sim 10 \text{ mg mL}^{-1}$. The adducts were screened by the sitting-drop vapor diffusion method using commercially available screens from Molecular Dimensions and Qiagen, dispensed by the Mosquito robot (TTP Labtech). Crystals of HT adducts formed in a couple of days in 25% v/v polyethylene glycol (PEG) smear medium and 0.1 M tris(hydroxymethyl)aminomethane (Tris) pH 8.5 (Me-TRaQ-G), in 20% v/v PEG 6000, 10% ethylene glycol, 0.1 M $\text{MgCl}_2 \cdot 6 \text{ H}_2\text{O}$ and 0.1 M 2-(*N*-morpholino)ethane-sulfonic acid (MES) pH 6 (TRaQ-G) and in 20% v/v PEG 6000, 0.1 M LiCl and 0.1 M sodium citrate pH 4 (TRaQ-G-ctrl). The crystals were cryoprotected with 25% glycerol. Diffraction

data were collected at the Paul Scherrer Institute (Swiss light source, Villigen) at the PXIII beamline. Data were processed with the XDS program package.²¹⁰ Structures were solved by molecular replacement using Phaser-MR and chain A of PDB entry 6U32 as the model. Manual model building and structure refinement were carried out with PHENIX (version 1.20.1-4487),²¹¹ Coot (version 0.9.6)²¹² and phenix-refine, respectively. After validation, the structures of the HaloTag adducts were deposited in the PDB database under PDB codes 7ZBA (Me-TRaQ-G), 7ZBB (TRaQ-G-ctrl), and 7ZBD (TRaQ-G). Data collection and refinement statistics are summarized in Table 6. Depictions of adduct structures were generated using PyMOL (version 2.4.0).²¹³

Table 6. Data collection and refinement statistics.

	Me-TRaQ-G	TRaQ-G	TRaQ-G-ctrl
Data collection			
Space group	P 21 21 21	C 1 2 1	P 61
Cell dimensions			
<i>a</i> , <i>b</i> , <i>c</i> (Å)	44.36, 81.50, 159.65	166.91, 50.46, 79.48	94.01, 94.01, 132.56
α , β , γ (°)	90, 90, 90	90, 117.737, 90	90, 90, 120
Resolution (Å)	1.23–50 (1.23–1.3)	1.68–50 (1.68–1.79)	1.95–44.3 (1.95–2.06)
<i>R</i> _{meas} (%)	8.8 (153.6)	11.1 (109.2)	20.7 (114.6)
<i>I</i> / σ <i>I</i>	14.16 (1.15)	7.24 (0.98)	6.42 (1.55)
Completeness (%)	99.8 (98.7)	98.4 (96.2)	99.8 (99.2)
Redundancy	10.5 (8.2)	3.0 (2.6)	4.6 (4.4)
Refinement			
Resolution (Å)	1.23	1.68	1.95
No. reflections	168606	65995	94488
<i>R</i> _{work} / <i>R</i> _{free}	0.23 / 0.25	0.19 / 0.22	0.18 / 0.22
No. atoms			
Protein	4699	4694	4730
Ligand/ion	294	205	216
Water	478	434	436
<i>B</i> -factors			
Protein	16.94	26.40	22.61
Ligand/ion	33.29	29.84	30.34
Water	26.60	33.94	29.81
R.m.s. deviations			
Bond lengths (Å)	0.005	0.012	0.008
Bond angles (°)	0.865	1.173	1.004

MD simulations (performed by Sebastian Thallmair)

Atomistic MD simulations were performed starting from the crystal structures of HT with the closed and open form of TRaQ-G probe, as well as with Me-TRaQ-G and TRaQ-G-ctrl probe. All MD simulations were performed with the program package GROMACS (version 2020.4)²¹⁴ using the GROMOS 54a7 force field.²¹⁵ The ligand parameters were obtained from the Automated Topology Builder.^{216,217}

The ligands were bound to D106 according to the crystal structures using the [intermolecular_interactions] block of GROMACS with a bond length of 0.185 nm, a force constant of 10^5 kJ mol⁻¹ nm⁻², and bond type 6. The proteins were neutralized and solvated in 0.15 M NaCl solution using the SPC water model and a box size of $7.0 \times 7.0 \times 7.0$ nm³. After a steepest decent minimization (5,000 steps), the systems were equilibrated in several steps (1. 500 ps NVT simulation with time step of $\Delta t = 0.5$ fs time step; 2. 1 ns NPT simulation with $\Delta t = 1$ fs; 3. 1 ns NPT simulation with $\Delta t = 1$ fs; 4. 1 ns NPT simulation $\Delta t = 2$ fs). During the first two equilibration steps, position restraints were applied to the protein. The production simulations were performed for 500 ns using a time step of $\Delta t = 2$ fs. The temperature was kept at 300 K in all simulations using a velocity rescaling thermostat²¹⁸ and the pressure was kept at 1 bar (using a Berendsen barostat²¹⁹ for the equilibration steps and a Parrinello-Rahman barostat²²⁰ for the production). All bond lengths were constraint using the LINCS algorithm.²²¹ Van der Waals interactions were treated with a cutoff scheme; Coulomb interactions were calculated using PME. The analyses were performed using GROMACS tools.

In addition, simulations of the GSH adducts of TRaQ-G and Me-TRaQ-G were performed following the protocol described above. The starting conformations were obtained by manually binding GS(H) to a snapshot of the MD simulation of TRaQ-G and the crystal structure of Me-TRaQ-G, respectively.

In vitro GSH sensitivity and selectivity experiments

The HT adducts were prepared by combining the HT protein (~ 50 μ M in PBS) with the respective TRaQ-G ligand (1.5–2x excess, stock solution 50 mM in DMSO) and rotating the resulting solution for 1 h at 20 °C. The adduct was further concentrated and excess TRaQ-G ligand was removed by desalting with Zeba spin desalting columns (7 kDa

molecular weight cut-off (MWCO), 0.5 mL). The product was diluted with 0.5 M sodium phosphate buffer to a final concentration of ~5–15 μM . In a 96-well plate, the adduct solution was treated with the appropriate amount of an aqueous stock solution of GSH, GSSG, cysteine, H_2S , or taurine and the solutions were incubated at 20 °C for 30–60 min. Absorbance at 615 nm and/or fluorescence at 630 nm was measured in triplicates and including separate blanks for every concentration of the reagents.

Kinetics measurements

HT adducts were prepared as described before. A final concentration of ~15 μM adduct was used for the measurements. In a 96-well plate, GSH was added (final concentration 5 mM) to the adduct solution and the measurement loop was started. Absorbance was measured in triplicates including a blank measurement without adduct present. After equilibration was reached, NEM (final concentration 40 mM) or iodoacetamide (final concentration 50 mM) were added and a second measurement loop was started. For Me-TRaQ-G the measurement was carried out at 20 °C, for TRaQ-G the measurement was carried out at 37 °C.

8.4 Experimental procedures for chapter 3

The experimental procedures for chapter 3 were also published in Emmert et al., *Nat. Chem.* 2023.¹⁶³

Cloning

Plasmid sources and primers for cloning are listed in Table 7 and Table 8. The reported constructs were deposited on Addgene: H2B-HT-emiRFP703 (183985), HT-mGold (183986), Calnexin-HT-mGold (183987), H2B-HT-mGold (183988), and Calnexin-HT8-mGold (183989).

Table 7. Plasmid sources.

Plasmid	Source	Vector precursor	Insert precursor
Calnexin-mGold	Addgene 158004 ¹⁶⁷		
TUBB5-Halo	Addgene 64691 ²²²		

H2B-emiRFP703	Addgene 136567 ¹⁷⁴		
H2B-HT-emiRFP703	Gibson assembly	H2B-emiRFP703	TUBB5-Halo
HT-mGold	Gibson assembly	Calnexin-mGold	TUBB5-Halo
ER-HT-mGold	Gibson assembly	Calnexin-mGold	TUBB5-Halo
H2B-HT-mGold	Gibson assembly	H2B-HT-emiRFP703	ER-HT-mGold
ER-HT8-mGold	Site-directed mutagenesis	ER-HT-mGold	
HT-mGold-His6	Twist Bioscience		
roGFP-iE-ER	Gift from Christian Appenzeller-Herzog (University of Basel).		

Table 8. Primers for plasmid generation.

Plasmid	Vector forward	Vector reverse	Insert forward	Insert reverse
H2B-HT-emiRFP703	atttccggcgatccacc	gtcgactgcttagcgct	agcgctaagcagtcga	ggtggatgccggaaa
	ggt	ggt	cgc	tctcg
HT-mGold	atttccggcgtgagcaa	ccgatttccatggcggt	cgccatggaatcggt	tgctcacgccggaat
	gggc	ctc	actgg	ctc
ER-HT-mGold	atttccggcgtgagcaa	tcgactgcatggtggc	accatgcagtcgaccg	ttgctcacgccggaat
	ggg	ga	gca	ctcg
H2B-HT-mGold	gtacaagtaagagagc	tggccattcgtcccagg	gacctgggacgaatgg	ccgcttagctctcttactt
	taagcggc	t	cca	gtacagctc
ER-HT8-mGold	gaccatcgcagcatt	ggtgcaacatcgggga		
C61S	gctcc	tg		
ER-HT8-mGold	cctgcctaacagcaag	cttttggccaggcgagc		
C262S	gctgtg	g		

Protein expression of HT-mGold

The general protocol for protein expression (section 8.2) was followed.

pH profile

Adduct of purified HT-mGold fusion protein with TRaQ-G ligand (20 μ M) was added to buffers of pH 2–13 (pH 2: citric acid, pH 3–7: citric acid/ Na_2HPO_4 , pH 8: Na_2HPO_4 , pH 9–11: $\text{NaHCO}_3/\text{Na}_2\text{CO}_3$, pH 12–13: KCl/NaOH) and fluorescence spectra were measured. The ratio between mGold and the SiR fluorescence at λ_{max} was calculated. At pH < 5, the protein precipitated and at pH > 9, the mGold fluorescence dropped dramatically. The ratio

is stable between pH 6–9, but separate calibration curves for every specific pH are recommended as the protonation state of GSH changes.

Calibration curve

The TRaQ-G sensor was assembled *in vitro* as described before using the purified HT-mGold fusion protein. The adduct was used in a final concentration of 10 μ M. In a 96-well plate, the adduct was treated with the appropriate amount of GSH. The mGold/SiR ratio was measured by fluorescence microscopy. The ratiometric measurement was carried out with the same instrument using the same settings as for all other measurements. The measurement was performed in three technical replicates and the blank averaged over all concentrations. Three FOVss) were measured per well. Image analysis was performed with Fiji (ImageJ). The background was determined from the blank measurements calculating the mean of all the pixels in the FOV per channel excluding the edges. The background was subtracted for the sample measurements and each channel. The mGold channel was divided by the SiR channel in a pixel-by-pixel manner and the mean of all pixels in the FOV excluding the edges was calculated. Every FOV gave one data point.

Flow cytometry

HeLa cells were transfected >24 h before the measurement with HT-mGold, if applicable. Cells were detached by trypsination. The positive control was treated with 1 mM TBHP) at 37 °C for 1 h and incubated with 1 μ M CellROX DeepRed at 37 °C for 1 h. The cells were then harvested by centrifugation, washed with cold PBS, and incubated with AnnexinV-Pacific Blue in annexin-binding buffer at 20 °C for 15 min. Samples were filtered through cell strainer tubes and analyzed by a FACS Canto II equipped with 405 nm, 448 nm, and 633 laser lines. Data were analyzed using the FlowJo (v9) software.

Confocal microscopy

The optical settings for all microscopy experiments are summarized in Table 9.

Table 9. Optical configurations for microscopy experiments.

Channel	λ excitation	Emission filter
roGFP blue	405 nm	472/30
roGFP green	445 nm	472/30
mGold	515 nm	542/27
SiR with mGold	561 nm	642 LP
SiR with emiRFP703	561 nm	600/52
emiRFP703	638 nm	708/75

Image analysis

The background was determined by manually picking regions without cells or with untransfected cells. The mean background value for each channel was further used in automated image analysis. Ratiometric image analysis was conducted using a Python script (available under <https://gitlab.uzh.ch/locbp/public/ratiometric-image-analysis>). The background was subtracted for each channel and the regions of interest (ROIs, =transfected cells) were determined by thresholding or with the Cellpose²²³ algorithm in the channel of the FP. To obtain ratiometric images, the masks were applied to the background-subtracted images and the FP channel was divided by the SiR channel in a pixel-by-pixel manner within the ROI. Single cells were either identified by selecting coherent regions in a certain range of size or by using the ROIs earlier defined by Cellpose. For measurements with ATP9-HT-mGold, cells with appropriate localization of the sensor and segmentation of mitochondria were selected manually from the ratiometric images. The mean of all ratiometric pixels per cell was calculated and represents one data point. Cells from all replicates were combined for further analyses. The statistical analyses were performed using Prism9 GraphPad and generally included a ROUT outlier analysis. Calculated values are always given as mean \pm SD. Additionally, our linear calibration equation was applied to the ratiometric images and saved for each FOV. For display only, images were despeckled with Fiji (ImageJ).

GSH measurement in living HeLa cells

HeLa cells were plated and transfected with the respective HT-mGold plasmid. After 24–48 h, the cells were incubated with 100 nM TRaQ-G ligand for 1 h. The cells were treated with 10 mM EtGSH in FluoroBrite DMEM for 3–4 h, 1 mM BSO in FluoroBrite DMEM for 3–4 h, 1 mM H₂O₂ for 20 min in FluoroBrite or vehicle (FluoroBrite DMEM). GSH concentration was measured by fluorescence microscopy using the calibration curve. The experiment was carried out in three biological replicates on different days with cells from different passages. The data sets were combined for analysis. In total, 90–176 cells were analyzed per condition. The calibration curve was used to interpolate/extrapolate means as well as upper and lower bounds expressed in GSH concentration for single cells.

GSH measurement during cell proliferation

HeLa cells were plated and transfected with the HT-mGold or H2B-HT-mGold plasmid. About 8 h after transfection, thymidine (100 mM aqueous stock solution, final concentration 2 mM) was added to the cells and incubated for 16 h. The cells were washed with PBS and incubated in fresh medium for 9 h. Thymidine was added again (final concentration 2 mM) and incubated for 18 h. Before imaging, the cells were incubated with 100 nM TRaQ-G or TRaQ-G-ctrl ligand for 1 h in culture medium still containing thymidine. Cells were imaged in fresh FluoroBrite DMEM supplemented with 4 mM glutamine, 1 mM sodium pyruvate, 10% FBS and penicillin (100 U mL⁻¹)/streptomycin (100 µg mL⁻¹)/fungizone (0.25 µg mL⁻¹). Frames were taken every 30 min over 24 h. For analysis, ratiometric images of the whole FOV were generated with the method described before. From each FOV the dividing cells were segmented and followed over time by hand. The mean of all pixels within one cell represents one data point. The experiment was carried out in three biological replicates on different days with cells from different passages. The data sets were combined for analysis. In total, a minimum of 19 cells were analyzed per condition and frame. The calibration curve was used to interpolate/extrapolate means as well as upper and lower bounds expressed in GSH concentration per timepoint.

Four-color imaging with TRaQ-G and roGFP

HeLa cells were plated and co-transfected with ER-Halo-mGold and roGFP-iE-ER (3:1). After 24–48 h, cells were incubated with the TRaQ-G ligand for 1 h. Cells were treated with 10 mM EtGSH in FluoroBrite DMEM for 3–4 h or vehicle (FluoroBrite DMEM). The same cells were imaged with the 60x oil immersion objective for the GSH concentration and the 60x water immersion objective for the redox potential. The experiment was carried out in three biological replicates on different days with cells from different passages. The data sets were combined for analysis. In total, 86–119 cells were imaged per condition. The calibration curve was used to interpolate/extrapolate means as well as upper and lower bounds expressed in GSH concentration for single cells.

8.5 Experimental procedures for chapter 4

Site-directed mutagenesis

Primers for site-directed mutagenesis are listed in Table 10. The codon for residue G244 is marked in blue within the primer sequence. The sequences of the respective reverse primers are CAGAACAGCAGCTTCGGA (1), CAGAACAGCAGCTTCGGAAC (2), CAGAACAGCAGCTTCGGAACAGG (3) and CAGAACAGCAGCTTCGGA (4).

Table 10. Primers for site-directed mutagenesis.

Mutation	Forward	Reverse	T _a
G244A	GGGCACCCCAGCGGTTCTGATCC	1	63
G244C	GGGCACCCCATGCGTTCTGATCC	2	67
G244D	GGGCACCCCAGATGTTCTGATCC	1	64
G244E	GGGCACCCCAGAAGTTCTGATCC	1	64
G244F	GGGCACCCCATTTGTTCTGATCCCAC	1	62
G244H	GGGCACCCCACATGTTCTGATCCCACC	1	62
G244I	GGGCACCCCAATTGTTCTGATCCC	1	61
G244K	GGGCACCCCAAAAGTTCTGATCCC	1	61

G244L	GGGCACCCCACTGGTTCTGATCCCACC	1	63
G244M	GGGCACCCCAATGGTTCTGATCCC	1	61
G244N	GGGCACCCCAAACGTTCTGATCC	1	65
G244P	GGGCACCCCACCGGTTCTGATCCCAC	1	61
G244Q	GGGCACCCCA CAGGTTCTGATCCCACC	1	63
G244R	GGGCACCCCA CGCGTTCTGATCC	2	67
G244S	GGGCACCCCAAGCGTTCTGATCC	3	71
G244T	GGGCACCCCAACCGTTCTGATCC	1	64
G244V	GGGCACCCCA GTGGTTCTGATCC	1	63
G244W	GGGCACCCCA TGGGTTCTGATCC	4	66
G244Y	GGGCACCCCA TATGTTCTGATCCCAC	1	62

Site-saturation mutagenesis

Primers for the site-saturation mutagenesis of E143 and F144 (Table 11) were designed with NEBaseChanger. The forward primers were mixed in a ratio of 12:9:1 (for1:for2:for3). For each mutation site the PCR was conducted at three different temperatures ($T_1 = 67^\circ\text{C}$, $T_2 = 70^\circ\text{C}$, $T_3 = 72^\circ\text{C}$). The standard procedure and reagents from the Q5 Site-Directed Mutagenesis Kit (NEB) were used to insert mutations, ligate plasmids and transform them into DH10 β competent cells by heat shock. The correct sequence of the GOI was confirmed by the Sanger sequencing service of Microsynth. Plasmid DNA was purified with the QIAGEN Miniprep Kit.

Table 11. Primers for site-saturation mutagenesis.

Primer	Sequence
E143_for1	CGA ATG GCC AND TTT TGC CCG TGA AAC C
E143_for2	CGA ATG GCC AVH GTT TGC CCG TGA AAC C
E143_for3	CGA ATG GCC ATG GTT TGC CCG TGA AAC C
E143_rev	TCC CAG GTC GGA ATA GGG
F144_for1	ATG GCC AGA AND TGC CCG TGA AA

F144_for2 ATG GCC AGA AVH GGC CCG TGA AA
F144_for3 ATG GCC AGA ATG GGC CCG TGA AA
F144_rev TCG TCC CAG GTC GGA ATA G

Protein expression on screening scale

BL21(DE3) competent cells were transformed with the respective plasmid by heat shock following the provided standard procedure. LB medium was prepared with the appropriate antibiotic. A single colony was inoculated into 1 mL LB and incubated at 37 °C overnight. 250 µL of the starter culture were inoculated into 5 mL medium and incubated at 37 °C for 4 h. IPTG was added to a final concentration of 0.5 mM and the culture was further incubated at 18 °C overnight. *E. coli* were harvested by centrifugation and the bacterial pellets were frozen to -80 °C and thawed twice. The pellets were resuspended and lysed in 50 mM NaH₂PO₄ buffer (400 µL, pH=7.4) containing 300 mM NaCl, lysozyme (10 mg mL⁻¹) and benzonase (15 units). The lysate was cleared by centrifugation and the protein was purified by using the QIAGEN Ni-NTA Spin Kit or the HisPur™ Ni-NTA Spin Plate. Fractions were analyzed by SDS page gel electrophoresis and pure fractions were combined and dialyzed in PBS. Proteins were concentrated by Amicon Ultra-0.5 Centrifugal Filters (3 kDa or 30 kDa).

Sensitivity to GSH

In a black 96-well plate, the mutant HT proteins (final concentration 3 µM) were added to the TRaQ-G ligand (4.5 µM) in 0.5 M sodium phosphate buffer (pH=7.4). The resulting solution was incubated while rotating for 1 h at 20 °C. Fluorescence (ex. 580 nm, em. 630 nm) was measured by Tecan M Nano+ in technical duplicates. GSH was successively added to increase the concentration to 0.1 mM, 0.5 mM, 1 mM and 5 mM, respectively. Fluorescence was re-measured after each addition.

Kinetic measurements

In a black 96-well plate, the mutant HT proteins (final concentration 3 µM) were added to the TRaQ-G ligand (4.5 µM) in 0.5 M sodium phosphate buffer (pH=7.4). The resulting

solution was incubated while rotating for 1 h at 20 °C. GSH (final concentration 5 mM) was added to the conjugate and fluorescence (ex. 580 nm, em. 630 nm) was measured at 37 °C with a Tecan M Nano+ in technical triplicates.

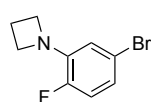
8.6 Experimental procedures for chapter 5

Synthetic procedures

General procedure to synthesize bromophenylazetidines (14a,b)

3-Bromiodobenzene (1.1 equiv.) or 5-bromo-2-fluoriodobenzene, the respective azetidine or azetidine hydrochloride (1 equiv.) and XantPhos Pd G3 (0.01 equiv.) were added to a pre-dried flask under an Ar atmosphere and dissolved in dry dioxane. Ar was bubbled through for 10 min, then NaOtBu (3 equiv.) was added and Ar was bubbled through the solution for another 1 min. The mixture was stirred at 90 °C for 20 h. The resulting solution was diluted with EtOAc and washed with water (2x) and brine. The organic layer was dried over Na₂SO₄ and concentrated under reduced pressure. The residue was purified by flash column chromatography (SiO₂, 0 → 5% EtOAc in hexane).

1-(5-Bromo-2-fluorophenyl)azetidine (14a)



Colorless oil (553 mg, 2.40 mmol, 80%).

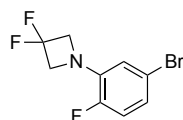
¹H NMR (400 MHz, CDCl₃) δ 6.83 – 6.70 (m, 2H), 6.53 (dd, J = 8.1, 2.2 Hz, 1H), 3.97 (t, J = 7.4 Hz, 4H), 2.41 – 2.29 (m, 2H).

¹³C NMR (101 MHz, CDCl₃) δ 151.5 (d, J = 241.7 Hz), 141.3 (d, J = 11.5 Hz), 120.7 (d, J = 6.8 Hz), 117.2, 117.0, 116.9 (d, J = 4.6 Hz), 54.0 (d, J = 2.3 Hz), 18.0 (d, J = 2.4 Hz).

¹⁹F NMR (377 MHz, CDCl₃) δ -135.16 (ddd, J = 12.5, 8.7, 4.5 Hz).

HRMS (ESI) calculated for [C₉H₁₀BrFN]⁺: 229.99752, found 229.99771.

1-(5-Bromo-2-fluorophenyl)-3,3-difluoroazetidine (14b)



Colorless oil (326 mg, 1.23 mmol, 41%).

^1H NMR (400 MHz, CDCl_3) δ 6.91 – 6.82 (m, 2H), 6.59 (dd, $J = 7.9, 2.2$ Hz, 1H), 4.31 (t, $J = 11.8$ Hz, 4H).

^{13}C NMR (101 MHz, CDCl_3) δ 151.6 (d, $J = 241.7$ Hz), 142.5, 138.8, 122.6 (d, $J = 6.9$ Hz), 117.7 (d, $J = 4.0$ Hz), 117.5 (d, $J = 20.2$ Hz), 117.1 (td, $J = 87.0, 3.0$ Hz), 64.5 (td, $J = 26.2, 2.7$ Hz).

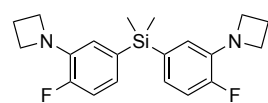
^{19}F NMR (376 MHz, CDCl_3) δ -100.16 (p, $J = 11.8$ Hz), -134.72 (ddd, $J = 7.5, 5.4, 2.9$ Hz).

HRMS (EI) calculated for $[\text{C}_9\text{H}_7\text{BrF}_3\text{N}]^+$: 264.97085, found 264.97094.

General procedure to synthesize silane intermediates (15a,b)

Bromophenylazetidines (2 equiv.) were added to a pre-dried flask under an N_2 atmosphere and dissolved in dry THF and the solution was cooled to -78 °C. $n\text{BuLi}$ solution (2.1 equiv., 2.5 M in hexane) was added dropwise, and the solution was stirred at the same temperature for 30 min. Then, dichlorodimethylsilane (1 equiv.) was added and the mixture was warmed to 20 °C and stirred for 16 h. The resulting solution was diluted with saturated aqueous NH_4Cl solution and extracted with CH_2Cl_2 (3x). The organic layer was dried over Na_2SO_4 and concentrated under reduced pressure. The residue was purified by flash column chromatography (SiO_2 , $0 \rightarrow 5\%$ EtOAc in hexane).

bis(3-(Azetidino-1-yl)-4-fluorophenyl)dimethylsilane (15a)



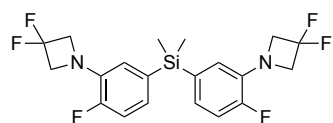
Colorless oil (164 mg, 0.457 mmol, 42%).

^1H NMR (400 MHz, CDCl_3) δ 6.92 (dd, $J = 12.8, 7.9$ Hz, 2H), 6.81 (ddd, $J = 7.8, 4.9, 1.5$ Hz, 2H), 6.56 (dd, $J = 9.8, 1.5$ Hz, 2H), 3.94 (t, $J = 7.2$ Hz, 8H), 2.32 (p, $J = 7.2$ Hz, 4H), 0.48 (s, 6H).

^{13}C NMR (101 MHz, CDCl_3) δ 153.5 (d, $J = 244.1$ Hz), 139.7 (d, $J = 10.0$ Hz), 133.8 (d, $J = 4.1$ Hz), 124.9 (d, $J = 6.3$ Hz), 119.8 (d, $J = 4.7$ Hz), 115.4 (d, $J = 17.5$ Hz), 54.1 (d, $J = 2.4$ Hz), 18.2 (d, $J = 2.3$ Hz), -1.9.

^{19}F NMR (377 MHz, CDCl_3) δ -130.91 – -131.02 (m).

HRMS (ESI) calculated for $[\text{C}_{20}\text{H}_{25}\text{F}_2\text{N}_2\text{Si}]^+$: 359.17496, found 359.17530.

bis(3-(3,3-Difluoroazetid-1-yl)-4-fluorophenyl)dimethylsilane (15b)

Colorless oil (195 mg, 0.453 mmol, 86%).

^1H NMR (400 MHz, CDCl_3) δ 6.99 (dd, $J = 12.5, 8.0$ Hz, 2H), 6.91 (ddd, $J = 8.0, 5.0, 1.5$ Hz, 2H), 6.54 (dd, $J = 9.6, 1.5$ Hz, 2H), 4.28 (td, $J = 11.9, 2.2$ Hz, 8H), 0.50 (s, 6H).

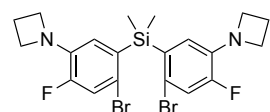
^{13}C NMR (101 MHz, CDCl_3) δ 153.6 (d, $J = 244.3$ Hz), 137.2 (d, $J = 10.7$ Hz), 134.1 (d, $J = 4.2$ Hz), 126.4 (d, $J = 6.5$ Hz), 120.1 (d, $J = 3.5$ Hz), 116.5 (td, $J = 300.8, 3.1$ Hz), 115.8 (d, $J = 17.7$ Hz), 64.5 (td, $J = 25.7, 2.5$ Hz), -2.0.

^{19}F NMR (377 MHz, CDCl_3) δ -100.15 (p, $J = 12.0$ Hz), -129.46 – -135.24 (m).

HRMS (ESI) calculated for $[\text{C}_{20}\text{H}_{21}\text{F}_6\text{N}_2\text{Si}]^+$: 431.13727, found 431.13717.

General procedure to synthesize dibromo intermediates (16a,b)

Silane intermediate (1 equiv.) was dissolved in DMF and NBS (2 equiv.) was added slowly over the course of 1 min. The solution was stirred at 20 °C for 1 h. Then, water was added, and the aqueous phase was extracted with CH_2Cl_2 (3x). The organic layer was dried over Na_2SO_4 and the solvent was evaporated. The crude product was purified by flash column chromatography (SiO_2 , 0 → 5 % EtOAc in hexane).

bis(5-(Azetid-1-yl)-2-bromo-4-fluorophenyl)dimethylsilane (16a)

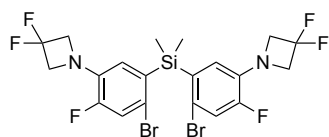
Colorless oil (122 mg, 235 μmol , 59%).

^1H NMR (400 MHz, CDCl_3) δ 7.11 (d, $J = 11.9$ Hz, 2H), 6.48 (d, $J = 10.3$ Hz, 2H), 3.91 (t, $J = 7.3$ Hz, 8H), 2.33 (p, $J = 7.3$ Hz, 4H), 0.69 (s, 6H).

^{13}C NMR (101 MHz, CDCl_3) δ 152.9 (d, $J = 248.8$ Hz), 138.8 (d, $J = 9.9$ Hz), 134.0 (d, $J = 3.9$ Hz), 122.6 (d, $J = 5.2$ Hz), 120.3 (d, $J = 21.0$ Hz), 116.8 (d, $J = 7.9$ Hz), 54.0 (d, $J = 2.1$ Hz), 18.2 (d, $J = 2.2$ Hz), -0.8.

^{19}F NMR (377 MHz, CDCl_3) δ -128.83 (dd, $J = 12.2, 10.1$ Hz).

HRMS (ESI) calculated for $[\text{C}_{20}\text{H}_{23}\text{Br}_2\text{F}_2\text{N}_2\text{Si}]^+$: 514.99598, found 514.99639.

bis(2-Bromo-5-(3,3-difluoroazetid-1-yl)-4-fluorophenyl)dimethylsilane (16b)

Beige solid (171 mg, 0.291 mmol, 73%).

^1H NMR (400 MHz, CDCl_3) δ 7.20 (d, $J = 11.7$ Hz, 2H), 6.51 (d, $J = 10.2$ Hz, 2H), 4.26 (t, $J = 11.9$ Hz, 8H), 0.70 (s, 6H).

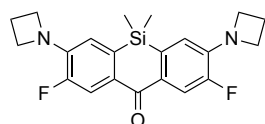
^{13}C NMR (101 MHz, CDCl_3) δ 153.0 (d, $J = 249.1$ Hz), 136.3 (d, $J = 7.9$ Hz), 134.4 (d, $J = 4.0$ Hz), 122.8 (d, $J = 4.2$ Hz), 120.8 (d, $J = 21.0$ Hz), 118.5 (d, $J = 7.9$ Hz), 116.6 – 116.1 (m), 64.3 (td, $J = 25.9, 2.4$ Hz), -1.0.

^{19}F NMR (377 MHz, CDCl_3) δ -100.08 (p, $J = 11.8$ Hz), -127.26 – -130.15 (m).

HRMS (ESI) calculated for $[\text{C}_{20}\text{H}_{19}\text{Br}_2\text{F}_6\text{N}_2\text{Si}]^+$: 586.95830, found 586.95884.

General procedure to synthesize ketone intermediates (17a,b)

Dibromo intermediate (1 equiv.) was added to a pre-dried flask under an N_2 atmosphere and dissolved in dry THF. The solution was cooled to -78 °C, $t\text{BuLi}$ solution (2.2 equiv., 1.7 M in pentane) was added dropwise and the mixture was stirred for 30 min at the same temperature. Then, dimethylcarbamoyl chloride (1.1 equiv.) was added, the solution was warmed to 20 °C and stirred for 3 h. The mixture was diluted with saturated aqueous NH_4Cl solution and extracted with CH_2Cl_2 (3x). The organic layer was dried over Na_2SO_4 and concentrated under reduced pressure. The residue was purified by flash column chromatography (SiO_2 , 0 \rightarrow 20% EtOAc in hexane).

3,7-Di(azetid-1-yl)-2,8-difluoro-5,5-dimethyldibenzo[*b,e*]silin-10(5*H*)-one (17a)

Yellow solid (57.0 mg, 0.148 mmol, 67%).

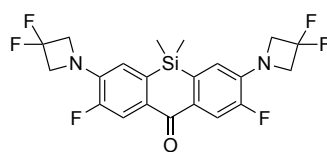
^1H NMR (400 MHz, CDCl_3) δ 8.03 (d, $J = 15.0$ Hz, 2H), 6.45 (d, $J = 9.5$ Hz, 2H), 4.16 (t, $J = 7.4$ Hz, 8H), 2.43 (p, $J = 7.4$ Hz, 4H), 0.41 (s, 6H).

^{13}C NMR (101 MHz, CDCl_3) δ 153.2 (d, $J = 244.1$ Hz), 142.3 (d, $J = 10.9$ Hz), 136.0 (d, $J = 3.3$ Hz), 131.7, 117.0 (d, $J = 18.6$ Hz), 116.3 (d, $J = 4.5$ Hz), 53.8 (d, $J = 2.5$ Hz), 17.9 (d, $J = 2.6$ Hz), -0.9.

^{19}F NMR (376 MHz, CDCl_3) δ -131.29 – -132.51 (m).

HRMS (ESI) calculated for $[C_{21}H_{23}F_2N_2OSi]^+$: 385.15422, found 385.15460.

3,7-bis(3,3-Difluoroazetid-1-yl)-2,8-difluoro-5,5-dimethyldibenzo[*b,e*]silin-10(5*H*)-one (17b)



Brown solid (67.8 mg, 0.149 mmol, 65%).

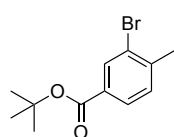
1H NMR (400 MHz, $CDCl_3$) δ 8.09 (d, $J = 14.6$ Hz, 2H), 6.53 (d, $J = 9.3$ Hz, 2H), 4.48 (t, $J = 11.8$ Hz, 8H), 0.44 (s, 6H).

^{13}C NMR (101 MHz, $CDCl_3$) δ 153.4 (d, $J = 244.5$ Hz), 139.9 (d, $J = 40.3$ Hz), 136.1 (d, $J = 4.0$ Hz), 133.4 (d, $J = 4.4$ Hz), 117.5 (d, $J = 13.8$ Hz), 117.3 (d, $J = 1.4$ Hz), 116.2, 64.6 (td, $J = 26.9, 2.3$ Hz), -1.0.

^{19}F NMR (377 MHz, $CDCl_3$) δ -100.17 (p, $J = 11.9$ Hz), -129.99 – -131.82 (m).

HRMS (ESI) calculated for $[C_{21}H_{19}F_6N_2OSi]^+$: 457.11654, found 457.11594.

***tert*-Butyl 3-bromo-4-methylbenzoate (18)²²⁴**



3-Bromo-4-methylbenzoic acid (1.08 g, 5.00 mmol, 1 equiv.) and DMAP (916 mg, 7.50 mmol, 1.5 equiv.) were suspended in a mixture of *t*BuOH and THF (1:1, 11 mL). Di-*tert*-butyl dicarbonate (2.18 g, 10.0 mmol, 2 equiv.) was slowly added and after no more gas evolved, the solution was warmed to

70 °C and stirred for 15 h. The mixture was concentrated under reduced pressure. The residue was taken up in EtOAc, washed with saturated aqueous $NaHCO_3$ solution (2x) and brine, and dried over Na_2SO_4 . The crude product was purified by flash column chromatography (SiO_2 , 0 \rightarrow 15% EtOAc in hexane). Residual impurities were removed by Kugelrohr distillation (1.5 mbar, 60 °C) to yield a colorless oil (1.02 g, 3.76 mmol, 75%).

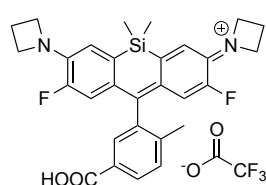
1H NMR (400 MHz, $CDCl_3$) δ 8.12 (d, $J = 1.7$ Hz, 1H), 7.81 (dd, $J = 7.9, 1.8$ Hz, 1H), 7.27 (d, $J = 7.6$ Hz, 1H), 2.44 (s, 3H), 1.58 (s, 9H).

HRMS (EI) calculated for $[C_{12}H_{15}BrO_2]^+$: 270.02499, found 270.02476.

General procedure to synthesize SiR dyes (19a,b)

Compound **5** (5.5 equiv.) was dissolved in dry THF under an N₂ atmosphere in a pre-dried flask and cooled to -78 °C. Then, *t*BuLi solution (1.7 M in pentane, 5 equiv.) was added and the mixture was stirred at the same temperature for 10 min. Ketone intermediate (1 equiv.), dissolved in dry THF, was slowly added and the resulting solution was warmed to ambient temperature and stirred for 16 h. 1 M HCl was added, the mixture was diluted with saturated aqueous NH₄Cl solution and extracted with CH₂Cl₂ (3x). The combined organic phases were dried over Na₂SO₄ and the solvent was evaporated.

The resulting *tert*-butyl ester was dissolved in TFA (100 equiv.) and the solution was stirred at 20 °C for 6 h. After evaporation of all volatiles, the residue was purified by preparative HPLC (C18-SiO₂, 10 → 95 % MeCN in ddH₂O + 0.1% TFA).

1-(7-(Azetidin-1-yl)-10-(5-carboxy-2-methylphenyl)-2,8-difluoro-5,5-dimethyl-di-benzo[*b,e*]silin-3(*5H*)-ylidene)azetidin-1-ium trifluoroacetate (19a)

Blue solid (42.0 mg, 68.0 μmol, 52%).

¹H NMR (400 MHz, CD₃OD) δ 8.18 – 8.10 (m, 1H), 7.73 (d, *J* = 1.8 Hz, 1H), 7.57 (d, *J* = 8.1 Hz, 1H), 6.98 (d, *J* = 9.5 Hz, 2H), 6.55 (d, *J* = 16.0 Hz, 2H), 4.59 (t, *J* = 7.8 Hz, 8H), 2.58 (p, *J* = 7.8 Hz,

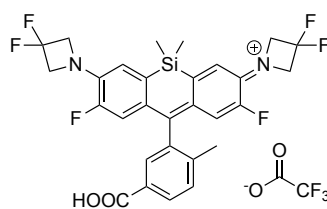
4H), 2.12 (s, 3H), 0.59 (s, 2H), 0.56 (s, 3H).

¹³C NMR (101 MHz, CD₃OD) δ 168.9, 167.6, 152.0 (d, *J* = 247.0 Hz), 146.6, 145.9 (d, *J* = 11.8 Hz), 142.4, 139.9, 132.1, 131.621, 131.041, 130.141, 129.201 (d, *J* = 5.6 Hz), 123.9 (d, *J* = 17.9 Hz), 122.5 (d, *J* = 4.4 Hz), 19.5, 18.0, 18.0, -1.3, -1.5.

¹⁹F NMR (377 MHz, CD₃OD) δ -77.22, -133.50 (dd, *J* = 16.0, 9.6 Hz).

HRMS (ESI) calculated for [C₂₉H₂₉F₂N₂O₂Si]⁺: 503.19609, found 503.19621.

1-(10-(5-Carboxy-2-methylphenyl)-7-(3,3-difluoroazetid-1-yl)-2,8-difluoro-5,5-dimethyldibenzo[*b,e*]silin-3(*5H*)-ylidene)-3,3-difluoroazetid-1-ium trifluoroacetate (19b)



Blue solid (34.1 mg, 49.5 μmol , 43%). Used in the next step still containing $\sim 30\%$ impurities.

^1H NMR (400 MHz, CD_3OD) δ 8.99 (d, $J = 1.9$ Hz, 1H), 7.86 (dd, $J = 7.8, 1.9$ Hz, 1H), 7.05 (d, $J = 7.9$ Hz, 1H), 6.79 (d, $J = 10.0$ Hz, 2H), 6.61 (d, $J = 15.0$ Hz, 2H), 4.33 (t, $J = 12.0$ Hz, 8H), 1.57 (s, 3H), 0.53 (s, 3H), 0.47 (s, 3H).

^{13}C NMR was not recorded due to remaining impurities.

^{19}F NMR (377 MHz, CD_3OD) δ -76.97, -102.15 (p, $J = 12.0$ Hz), -129.46 – -134.03 (m).

HRMS (ESI) calculated for $[\text{C}_{29}\text{H}_{25}\text{F}_6\text{N}_2\text{O}_2\text{Si}]^+$: 575.15840, found 575.15784.

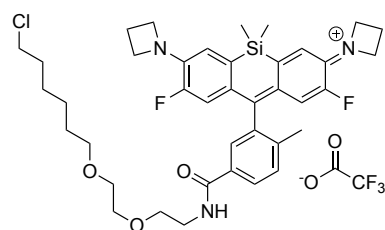
General procedure to synthesize SiR-HaloTag ligands (20a,b)

Boc-protected CA **2** (5 equiv.) was dissolved in HCl (4 M in dioxane) in a round bottom flask, cooled with ice. The mixture was stirred at 20 $^\circ\text{C}$ for 45 min. Saturated aqueous Na_2CO_3 was added and the aqueous layer was extracted with CH_2Cl_2 (3x). The combined organic layers were dried over Na_2SO_4 and the solvent was evaporated.

SiR dye (1 equiv.), CA **2** (5 equiv.) and PyBOP (2 equiv.) were dissolved in dry DMF in a pre-dried flask under an N_2 atmosphere and treated with DIPEA (15 equiv.). The resulting solution was stirred at 20 $^\circ\text{C}$ for 1.5 h. All volatiles were removed and the residue was purified by preparative HPLC (C18- SiO_2 , 10 \rightarrow 95 % MeCN in dd H_2O + 0.1% TFA).

1-(7-(Azetid-1-yl)-10-(5-((2-(2-((6-chlorohexyl)oxy)ethoxy)ethyl)carbamoyl)-2-methylphenyl)-2,8-difluoro-5,5-dimethyldibenzo[*b,e*]silin-3(*5H*)-ylidene)azetid-1-ium trifluoroacetate (20a)

Blue solid (12.9 mg, 16.0 μmol , 45%).



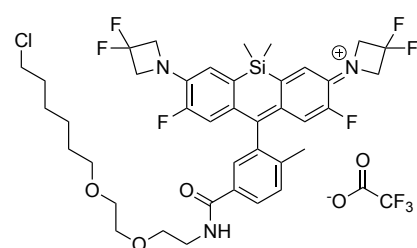
$^1\text{H NMR}$ (400 MHz, CD_3OD) δ 7.97 (dd, $J = 8.0, 2.0$ Hz, 1H), 7.60 (d, $J = 1.9$ Hz, 1H), 7.56 (d, $J = 8.1$ Hz, 1H), 6.98 (d, $J = 9.5$ Hz, 2H), 6.58 (d, $J = 15.9$ Hz, 2H), 4.59 (t, $J = 7.8$ Hz, 8H), 3.69 – 3.61 (m, 4H), 3.59 – 3.57 (m, 4H), 3.53 (t, $J = 6.6$ Hz, 2H), 3.45 (t, $J = 6.5$ Hz, 2H), 2.62 – 2.54 (m, 4H), 2.10 (s, 3H), 1.72 (d, $J = 6.8$ Hz, 2H), 1.56 – 1.49 (m, 2H), 1.46 – 1.28 (m, 4H), 0.58 (s, 3H), 0.57 (s, 3H).

$^{13}\text{C NMR}$ (101 MHz, CD_3OD) δ 167.8, 166.4, 160.3, 150.6 (d, $J = 246.9$ Hz), 145.2, 144.5 (d, $J = 11.6$ Hz), 139.5, 138.5, 132.2, 130.6, 127.8, 127.7 (d, $J = 36.7$ Hz), 122.7 (d, $J = 17.8$ Hz), 121.1 (d, $J = 4.4$ Hz), 70.7, 69.8, 69.7, 69.1, 44.3, 39.6, 32.3, 29.1, 26.3, 25.0, 18.0, 16.6, 16.6, -2.7, -2.8.

$^{19}\text{F NMR}$ (376 MHz, CD_3OD) δ -77.14, -133.56 (dd, $J = 15.6, 9.9$ Hz).

HRMS (ESI) calculated for $[\text{C}_{39}\text{H}_{49}\text{ClF}_2\text{N}_3\text{O}_3\text{Si}]^+$: 708.31943, found 708.31844.

1-(10-(5-((2-(2-((6-Chlorohexyl)oxy)ethoxy)ethyl)carbamoyl)-2-methylphenyl)-7-(3,3-difluoroazetidini-1-yl)-2,8-difluoro-5,5-dimethyldibenzo[*b,e*]silin-3(5*H*)-ylidene)-3,3-difluoroazetidini-1-ium trifluoroacetate (20b)



Blue solid (3.4 mg, 3.8 μmol , 25%).

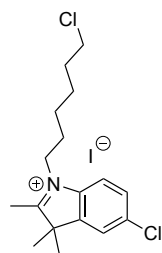
$^1\text{H NMR}$ (400 MHz, CDCl_3) δ 7.92 (dd, $J = 8.0, 1.7$ Hz, 1H), 7.65 (d, $J = 1.7$ Hz, 1H), 7.46 (d, $J = 8.0$ Hz, 1H), 7.02 (d, $J = 9.2$ Hz, 2H), 6.75 (d, $J = 15.1$ Hz, 2H), 4.93 (t, $J = 11.4$ Hz, 8H), 3.70 – 3.63 (m, 6H), 3.60 – 3.57 (m, 2H), 3.52 (t, $J = 6.6$ Hz, 2H), 3.45 (t, $J = 6.7$ Hz, 2H), 2.08 (s, 3H), 1.78 – 1.71 (m, 2H), 1.58 – 1.54 (m, 2H), 1.48 – 1.32 (m, 4H), 0.59 (s, 3H), 0.57 (s, 3H).

$^{13}\text{C NMR}$ was not measured due to limited amount of available sample.

$^{19}\text{F NMR}$ (377 MHz, CDCl_3) δ -75.70, -100.28 – -100.48 (m), -131.06 (m).

HRMS (ESI) calculated for $[\text{C}_{39}\text{H}_{45}\text{ClF}_6\text{N}_3\text{O}_3\text{Si}]^+$: 780.28174, found 780.28138.

5-Chloro-2,3,3-trimethyl-3*H*-indole (22) was synthesized by Alina Tirla.

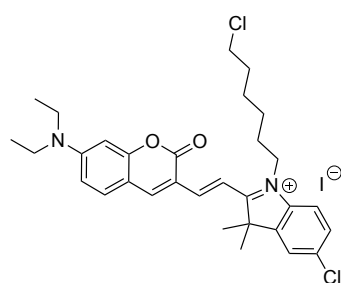
5-Chloro-1-(6-chlorohexyl)-2,3,3-trimethyl-3H-indol-1-ium iodide (23)

A microwave vessel was charged with compound **22** (116 mg, 600 μ mol, 1 equiv.), 1-chloro-6-iodohexane (740 mg, 3.00 mmol, 5 equiv.) and MeCN (1 mL). The mixture was stirred at 100 $^{\circ}$ C for 12 h, concentrated under reduced pressure, and the residue was purified by flash column chromatography (SiO₂, 0 \rightarrow 10% MeOH in CH₂Cl₂) to yield a brown solid (212 mg, 0.482 mmol, 80%).

¹H NMR (400 MHz, CDCl₃) δ 7.71 (d, J = 8.5 Hz, 1H), 7.54 (m, 2H), 4.72 (s, 2H), 3.54 (t, J = 6.4 Hz, 2H), 3.18 (t, J = 6.8 Hz, 2H), 3.13 (s, 3H), 1.95 (s, 2H), 1.84 – 1.79 (m, 2H), 1.67 (s, 6H), 1.60 (s, 2H).

¹³C NMR (101 MHz, CD₃OD) δ 198.3, 145.3, 141.2, 137.5, 130.7, 125.3, 118.0, 56.1, 45.6, 33.4, 31.0, 28.7, 27.5, 26.6, 22.7, 6.6.

HRMS (ESI) calculated for [C₁₇H₂₄Cl₂N]⁺ 312.12803, found 312.12829.

(E)-5-Chloro-1-(6-chlorohexyl)-2-(2-(7-(diethylamino)-2-oxo-2H-chromen-3-yl)-vinyl)-3,3-dimethyl-3H-indol-1-ium iodide (24)

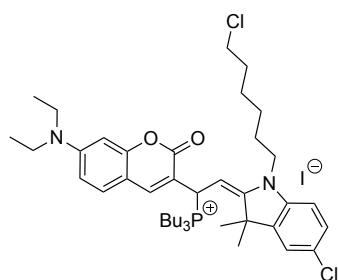
Intermediate **23** (52.8 mg, 0.120 mmol, 1.2 equiv.) and dimethylaminocoumarin-3-aldehyde (24.6 mg, 100 μ mol, 1 equiv.) were dissolved in EtOH (2.5 mL) in a pre-dried flask under an N₂ atmosphere. The solution was stirred at 75 $^{\circ}$ C for 2.5 h. The color changed from red to blue. The solvent was evaporated, and the residue was re-dissolved in CH₂Cl₂. The organic layer was washed with water and the aqueous phase was re-extracted with CH₂Cl₂ (3x). The combined organic layers were dried over Na₂SO₄ and the solvent was evaporated. The crude product was purified by flash column chromatography (SiO₂, 0 \rightarrow 5 % MeOH in CH₂Cl₂) to yield a blue solid (63.8 mg, 95.6 μ mol, 96%).

¹H NMR (400 MHz, CDCl₃) δ 10.19 (s, 1H), 8.61 (d, J = 15.8 Hz, 1H), 8.20 – 8.12 (m, 1H), 8.02 (dd, J = 15.8, 1.5 Hz, 1H), 7.53 – 7.46 (m, 2H), 7.32 (dd, J = 8.5, 1.6 Hz, 1H), 6.70 (dd, J = 9.2, 2.4 Hz, 1H), 6.45 (d, J = 2.4 Hz, 1H), 4.78 (t, J = 7.5 Hz, 2H), 3.52 (q, J = 7.3 Hz, 4H), 1.98 – 1.94 (m, 2H), 1.85 (s, 6H), 1.83 – 1.75 (m, 2H), 1.69 – 1.59 (m, 2H), 1.59 – 1.48 (m, 4H), 1.29 (t, J = 7.1 Hz, 6H).

^{13}C NMR (101 MHz, CDCl_3) δ 180.6, 161.3, 159.3, 159.2, 155.1, 144.8, 139.6, 135.1, 134.8, 129.7, 123.6, 114.4, 112.8, 111.6, 111.3, 111.2, 108.6, 97.1, 53.6, 51.8, 45.88, 33.1, 32.3, 30.3, 28.0, 26.7, 25.8, 12.8.

HRMS (ESI) calculated for $[\text{C}_{31}\text{H}_{37}\text{Cl}_2\text{N}_2\text{O}_2]^+$ 539.22266, found 539.22268.

(E)-Tributyl(2-(5-chloro-1-(6-chlorohexyl)-3,3-dimethylindolin-2-ylidene)-1-(7-(diethylamino)-2-oxo-2H-chromen-3-yl)ethyl)phosphonium iodide (25)



Compound **24** (20.0 mg, 30.0 μmol , 1 equiv.) was dissolved in CH_2Cl_2 (2 mL) in a pre-dried flask under an N_2 atmosphere and treated with tri-*n*-butylphosphine (30.3 mg, 150 μmol , 5 equiv.). The mixture was stirred at 20 $^\circ\text{C}$ for 15 min. The solvent was evaporated, and the crude product was washed with pentane to yield an orange solid (21.1 mg, 24.3 μmol ,

81%).

^1H NMR (400 MHz, $\text{DMSO-}d_6$) δ 8.18 (d, $J = 3.4$ Hz, 1H), 7.45 (d, $J = 9.2$ Hz, 1H), 7.29 (d, $J = 2.2$ Hz, 1H), 7.12 (dd, $J = 8.4, 2.2$ Hz, 1H), 6.77 (dd, $J = 9.0, 2.5$ Hz, 1H), 6.70 (d, $J = 8.4$ Hz, 1H), 6.58 (d, $J = 2.6$ Hz, 1H), 5.02 – 4.83 (m, 2H), 3.66 – 3.56 (m, 2H), 3.45 (q, $J = 7.0$ Hz, 4H), 3.39 – 3.31 (m, 2H), 2.33 – 2.23 (m, 6H), 1.72 – 1.65 (m, 2H), 1.57 (s, 6H), 1.54 – 1.47 (m, 4H), 1.45 – 1.33 (m, 12H), 1.24 (s, 2H), 1.12 (t, $J = 7.0$ Hz, 6H), 0.87 (t, $J = 7.2$ Hz, 9H).

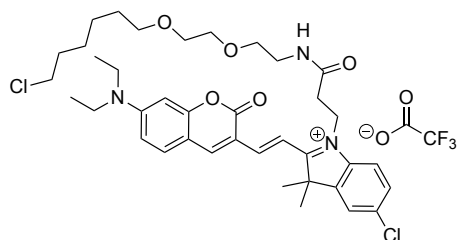
^{31}P NMR (162 MHz, $\text{DMSO-}d_6$) δ 36.56.

^{13}C NMR not measured due to low stability of the compound.

HRMS (ESI) calculated for $[\text{C}_{43}\text{H}_{64}\text{Cl}_2\text{N}_2\text{O}_2\text{P}]^+$ 741.40770, found 741.40701.

(E)-1-(2-Carboxyethyl)-5-chloro-2-(2-(7-(diethylamino)-2-oxo-2H-chromen-3-yl)-vinyl)-3,3-dimethyl-3H-indol-1-ium iodide (26) was synthesized by Alina Tirla.

(*E*)-5-Chloro-1-(3-((2-(2-((6-chlorohexyl)oxy)ethoxy)ethyl)amino)-3-oxopropyl)-2-(2-(7-(diethylamino)-2-oxo-2*H*-chromen-3-yl)vinyl)-3,3-dimethyl-3*H*-indol-1-ium trifluoroacetate (27**)**



Boc-protected CA **2** (25.9 mg, 80.0 μmol , 5 equiv.) was dissolved in hydrochloric acid (4 M in dioxane, 0.30 mL, 1.3 mmol, 80 equiv.) and stirred at 20 $^{\circ}\text{C}$ for 30 min. Saturated aqueous Na_2CO_3 was added and the aqueous layer was extracted with CH_2Cl_2

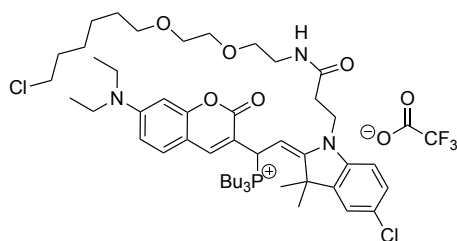
(3x). The combined organic layers were dried over Na_2SO_4 and the solvent was evaporated. Compound **26** (9.93 mg, 0.0160 mmol, 1 equiv.), deprotected CA **2** and PyBOP (16.7 mg, 0.0320 mmol, 2 equiv.) were dissolved in DMF (1 mL) in a pre-dried flask under an N_2 atmosphere and treated with DIPEA (40 μL , 0.24 mmol, 15 equiv.). The resulting solution was stirred at 20 $^{\circ}\text{C}$ for 1.5 h. All volatiles were removed and the residue was purified by preparative HPLC ($\text{C}_{18}\text{-SiO}_2$, 10 \rightarrow 95 % MeCN in dd H_2O + 0.1% TFA) to yield a blue solid (3.6 mg, 4.4 μmol , 28%).

^1H NMR (400 MHz, CD_3CN) δ 8.40 (s, 1H), 8.17 (d, $J = 15.6$ Hz, 1H), 7.85 (d, $J = 15.5$ Hz, 1H), 7.71 (d, $J = 2.0$ Hz, 1H), 7.62 (d, $J = 8.6$ Hz, 1H), 7.57 (dd, $J = 8.6, 2.0$ Hz, 1H), 7.53 (d, $J = 9.1$ Hz, 1H), 6.85 (dd, $J = 9.2, 2.5$ Hz, 1H), 6.71 (s, 1H), 6.61 (d, $J = 2.4$ Hz, 1H), 4.59 (t, $J = 6.5$ Hz, 2H), 3.64 – 3.52 (m, 6H), 3.41 (s, 4H), 3.38 – 3.29 (m, 4H), 3.19 – 3.16 (m, 2H), 2.77 (t, $J = 6.5$ Hz, 2H), 1.76 (s, 6H), 1.75 – 1.66 (m, 2H), 1.50 – 1.47 (m, 2H), 1.44 – 1.35 (m, 2H), 1.34 – 1.27 (m, 2H), 1.24 (t, $J = 7.1$ Hz, 6H).

^{13}C NMR (151 MHz, CD_3CN) δ 182.6, 169.5, 160.6, 159.4, 155.9, 152.1, 145.8, 140.9, 134.9, 133.6, 130.0, 124.2, 116.7, 113.5, 112.5, 111.1, 110.4, 97.7, 71.5, 70.8, 70.6, 69.8, 52.7, 46.3, 46.2, 44.1, 40.0, 34.3, 33.2, 30.2, 27.3, 27.0, 26.1, 12.8.

HRMS (ESI) calculated for $[\text{C}_{38}\text{H}_{50}\text{Cl}_2\text{N}_3\text{O}_5]^+$ 698.31220, found 698.31247.

(E)-Tributyl(2-(5-chloro-1-(3-((2-(2-((6-chlorohexyl)oxy)ethoxy)ethyl)amino)-3-oxopropyl)-3,3-dimethylindolin-2-ylidene)-1-(7-(diethylamino)-2-oxo-2H-chromen-3-yl)ethyl)phosphonium triflate (28)



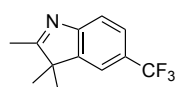
Compound **27** (2.84 mg, 3.50 μmol , 1.0 equiv.) was dissolved in CH_2Cl_2 (1 mL) in a pre-dried flask under an N_2 atmosphere and treated with tri-*n*-butylphosphine (1 drop). The mixture was stirred at 20 $^\circ\text{C}$ for 15 min. The solvent was evaporated and the crude

product was washed with pentane to yield a yellow oil (quant.).

NMR analysis was performed due to low stability of the compound.

HRMS (ESI) calculated for $[\text{C}_{50}\text{H}_{77}\text{Cl}_2\text{N}_3\text{O}_5\text{P}]^+$ 900.49724, found 900.49653.

2,3,3-Trimethyl-5-(trifluoromethyl)-3H-indole (28)¹⁸⁹



Under N_2 atmosphere in a pre-dried flask, 1-[4-(trifluoromethyl)phenyl]hydrazine (2.00 g, 11.4 mmol, 1 equiv.) was dissolved in dry MeOH (2.3 mL) and 3-methyl-2-butanone (3.67 mL, 34.1 mmol, 3 equiv.) was added. The resulting mixture was stirred at 70 $^\circ\text{C}$ for 4 h. The solution was concentrated under reduced pressure and taken up in CH_2Cl_2 . The organic layer was washed with water and the aqueous phase was re-extracted with CH_2Cl_2 (3x). The combined organic phases were dried over Na_2SO_4 and concentrated under reduced pressure.

Under N_2 atmosphere in a pre-dried flask, the intermediate was dissolved in acetic acid (0.40 M, 28 mL) and boron trifluoride etherate (1.40 mL, 11.4 mmol, 1 equiv.) was added to the solution. The mixture was stirred at 120 $^\circ\text{C}$ for 15 h and, after cooling to ambient temperature, concentrated under reduced pressure. The residue was dissolved in CH_2Cl_2 and washed with water, saturated aqueous Na_2CO_3 solution and brine. The combined aqueous layers were re-extracted with CH_2Cl_2 (3x). The combined organic layers were dried over Na_2SO_4 and the solvent was evaporated. The crude product was purified by flash column chromatography (SiO_2 , 10 \rightarrow 40 % EtOAc in hexane) to yield a brown oil (1.65 g, 7.25 mmol, 64%).

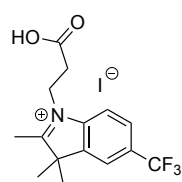
^1H NMR (400 MHz, CDCl_3) δ 7.66 – 7.55 (m, 2H), 7.51 (s, 1H), 2.32 (s, 3H), 1.33 (s, 6H).

^{13}C NMR (101 MHz, CDCl_3) δ = 191.2, 156.7, 146.3, 127.6, 127.2, 125.5 (q, J = 4.0 Hz), 123.4, 120.1, 118.6 (q, J = 3.7 Hz), 54.2, 23.0, 15.8.

^{19}F NMR (376 MHz, CDCl_3) δ -61.33.

HRMS (ESI) calculated for $[\text{C}_{12}\text{H}_{13}\text{F}_3\text{N}]^+$: 228.09891, found 228.09995.

1-(2-Carboxyethyl)-2,3,3-trimethyl-5-(trifluoromethyl)-3H-indol-1-ium iodide (**29**)¹⁹⁰



Compound **29** (420 mg, 1.85 mmol, 1 equiv.) was dissolved in MeCN (1.0 mL) and 3-iodopropionic acid (554 mg, 2.77 mmol, 1.5 equiv.) was added.

The resulting mixture was stirred at 110 °C for 3 h in a microwave reactor.

The solvent was evaporated and the residue was taken up in a small amount of EtOAc. Dropwise addition of hexane led to precipitation and the mixture was cooled to -20 °C to further assist precipitation. The precipitate was centrifuged and washed with EtOAc to yield a beige solid (329 mg, 770 μmol , 42%).

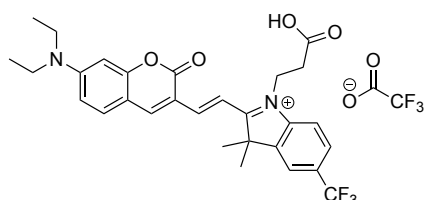
^1H NMR (400 MHz, CD_3OD) δ 8.20 (s, 1H), 8.13 (d, J = 8.5 Hz, 1H), 7.99 (d, J = 8.5 Hz, 1H), 4.82 (t, J = 6.4 Hz, 2H), 3.12 (t, J = 6.5 Hz, 2H), 1.66 (s, 6H). Protons of the single methyl group are not visible because of deuterium exchange with the NMR solvent.

^{13}C NMR (101 MHz, CD_3OD) δ 203.2, 173.0, 145.0, 144.3, 132.8, 128.0, 126.5, 123.8, 122.1, 117.8, 56.7, 45.6, 31.7, 22.5.

^{19}F NMR (376 MHz, CD_3OD) δ -63.57.

HRMS (ESI) calculated for $[\text{C}_{15}\text{H}_{17}\text{F}_3\text{NO}_2]^+$: 300.12059, found 300.11995.

(*E*)-1-(2-carboxyethyl)-2-(2-(7-(diethylamino)-2-oxo-2H-chromen-3-yl)vinyl)-3,3-dimethyl-5-(trifluoromethyl)-3H-indol-1-ium trifluoroacetate (**30**)



Intermediate **29** (205 mg, 0.480 mmol, 1.2 equiv.) and dimethylaminocoumarin-3-aldehyde (98.5 mg,

0.400 mmol, 1 equiv.) were dissolved in EtOH (20 mL) in a pre-dried flask under an N_2 atmosphere. The

solution was stirred at 75 °C for 1 h. The color changed from red to blue. The solvent was evaporated and the residue was re-dissolved in CH_2Cl_2 . The organic layer was washed with water and the aqueous phase was re-extracted with CH_2Cl_2 (3x). The combined organic layers were dried over Na_2SO_4 and the solvent was evaporated. The crude product was

purified by preparative HPLC (C18-SiO₂, 10 → 95% MeCN in ddH₂O + 0.1% TFA) to yield a blue solid (50.0 mg, 78.1 μmol, 20%).

¹H NMR (400 MHz, CD₃OD) δ 8.58 (s, 1H), 8.44 (d, *J* = 15.5 Hz, 1H), 8.10 – 8.01 (m, 2H), 7.96 – 7.87 (m, 2H), 7.61 (d, *J* = 9.2 Hz, 1H), 6.95 (dd, *J* = 9.2, 2.4 Hz, 1H), 6.68 (d, *J* = 2.4 Hz, 1H), 4.78 (t, *J* = 6.9 Hz, 2H), 3.65 (q, *J* = 7.1 Hz, 4H), 3.03 (t, *J* = 6.9 Hz, 2H), 1.87 (s, 6H), 1.29 (t, *J* = 7.1 Hz, 6H).

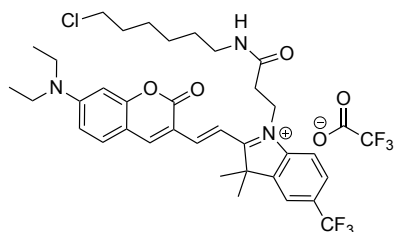
¹³C NMR (101 MHz, CD₃OD) δ 184.8, 173.1, 161.4, 160.0, 156.9, 154.4, 152.2, 145.3, 145.1, 134.3, 131.4, 131.1, 127.8, 121.3, 116.0, 113.9, 113.1, 112.1, 110.5, 98.1, 53.2, 46.7, 43.5, 32.6, 27.1, 12.9.

¹⁹F NMR (376 MHz, CD₃OD) δ -63.31, -77.36.

HRMS (ESI) calculated for [C₂₉H₃₀F₃N₂O₄]⁺ 527.21522, found 527.21516.

6-Chlorohexan-1-amine was synthesized according to reported procedures.²²⁵

(*E*)-1-(3-(((6-Chlorohexyl)amino)-3-oxopropyl)-2-(2-(7-(diethylamino)-2-oxo-2*H*-chromen-3-yl)vinyl)-3,3-dimethyl-5-(trifluoromethyl)-3*H*-indol-1-ium trifluoroacetate (31)



Compound **30** (9.61 mg, 15.0 μmol, 1 equiv.), PyBOP (15.6 mg, 30.0 μmol, 2 equiv.) and 6-chlorohexan-1-amine (10.2 mg, 75.0 μmol, 5 equiv.) were dissolved in DMF (1 mL) in a pre-dried flask under an N₂ atmosphere and treated with DIPEA (12.5 μL, 75.0 μmol, 5 equiv.).

The resulting solution was stirred at 20 °C for 45 min. A drop of 1 M HCl was added, all volatiles were removed and the residue was purified by preparative HPLC (C18-SiO₂, 10 → 95% MeCN in ddH₂O + 0.1% TFA) to yield a blue solid (9.9 mg, 13 μmol, 87%).

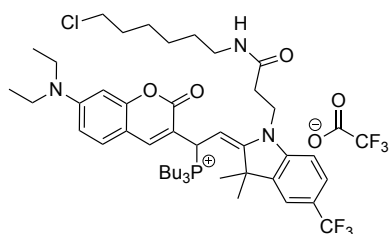
¹H NMR (400 MHz, CDCl₃) δ 9.05 (s, 1H), 8.56 (d, *J* = 15.8 Hz, 1H), 8.15 (s, 1H), 7.84 – 7.62 (m, 5H), 6.75 (dd, *J* = 9.2, 2.4 Hz, 1H), 6.50 (d, *J* = 2.4 Hz, 1H), 4.86 (t, *J* = 6.7 Hz, 2H), 3.56 (q, *J* = 7.2 Hz, 4H), 3.43 (t, *J* = 6.7 Hz, 2H), 3.10 – 3.05 (m, 2H), 2.95 (t, *J* = 6.7 Hz, 2H), 1.83 (s, 6H), 1.67 – 1.63 (m, 2H), 1.42 – 1.39 (m, 2H), 1.31 (t, *J* = 7.1 Hz, 6H), 1.27 – 1.14 (m, 4H).

^{13}C NMR (101 MHz, CDCl_3) δ 182.3, 168.9, 161.3, 160.9, 159.3, 155.5, 152.2, 147.6, 143.6, 143.1, 134.4, 130.8, 127.3, 119.8, 114.5, 113.0, 111.9, 111.6, 107.7, 97.5, 51.9, 46.1, 45.1, 43.6, 39.9, 34.5, 32.5, 29.0, 27.9, 26.6, 26.3, 12.8.

^{19}F NMR (376 MHz, CDCl_3) δ -61.94, -75.67.

HRMS (ESI) calculated for $[\text{C}_{35}\text{H}_{42}\text{ClF}_3\text{N}_3\text{O}_3]^+$ 644.28613, found 644.28577.

(*E*)-Tributyl(2-(1-(3-((6-chlorohexyl)amino)-3-oxopropyl)-3,3-dimethyl-5-(trifluoromethyl)indolin-2-ylidene)-1-(7-(diethylamino)-2-oxo-2*H*-chromen-3-yl)ethyl)-phosphonium trifluoroacetate (32)



Compound **31** (3.0 mg, 4.0 μmol , 1 equiv.) was dissolved in CH_2Cl_2 (1 mL) in a pre-dried flask under an N_2 atmosphere and treated with tri-*n*-butylphosphine (5.0 μL , 20 μmol , 5 equiv.). The mixture was stirred at 20 $^\circ\text{C}$ for 5 min. The solvent was evaporated and the crude product

was washed with pentane to yield a yellow solid (quant.).

^1H NMR (400 MHz, CDCl_3) δ 8.51 (s, 1H), 7.58 (d, J = 8.9 Hz, 1H), 7.45 – 7.39 (m, 1H), 7.20 (d, J = 1.8 Hz, 1H), 6.89 (d, J = 8.3 Hz, 1H), 6.65 (dd, J = 9.0, 2.5 Hz, 1H), 6.47 (d, J = 2.5 Hz, 1H), 5.59 – 5.46 (m, 1H), 5.14 (dd, J = 16.0, 12.3 Hz, 1H), 4.15 – 3.92 (m, 2H), 3.52 (t, J = 6.8 Hz, 2H), 3.43 (q, J = 7.1 Hz, 4H), 3.24 (s, 2H), 2.83 – 2.55 (m, 2H), 2.40 – 2.23 (m, 6H), 1.81 – 1.67 (m, 4H), 1.61 (s, 3H), 1.59 – 1.32 (m, 10H), 1.31 (s, 3H), 1.21 (t, J = 7.1 Hz, 6H), 1.00 – 0.85 (m, 15H).

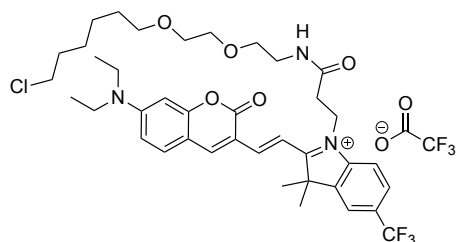
^{13}C NMR (101 MHz, CDCl_3) δ 170.9, 162.8, 157.5, 156.2, 151.8, 147.2, 146.7, 137.5, 130.8, 126.5, 121.7, 118.3, 115.7, 113.7, 110.0, 108.8, 106.5, 96.7, 83.9, 45.3, 45.1, 45.0, 40.5, 39.7, 33.8, 32.7, 29.3, 28.0, 27.7, 27.5, 27.1, 26.7, 26.4, 24.4, 24.3, 24.3, 24.3, 24.2, 24.1, 23.8, 23.8, 18.9, 18.5, 13.7, 13.5, 12.6. (Multiplets were not analyzed.)

^{19}F NMR (377 MHz, CDCl_3) δ -60.84, -75.27.

^{31}P NMR (162 MHz, CDCl_3) δ 35.90.

HRMS (ESI) calculated for $[\text{C}_{47}\text{H}_{69}\text{ClF}_3\text{N}_3\text{O}_3\text{P}]^+$ 846.47117, found 846.47078.

(*E*)-1-(3-((2-(2-((6-Chlorohexyl)oxy)ethoxy)ethyl)amino)-3-oxopropyl)-2-(2-(7-(diethylamino)-2-oxo-2*H*-chromen-3-yl)vinyl)-3,3-dimethyl-5-(trifluoromethyl)-3*H*-indol-1-ium trifluoroacetate (33)



Boc-protected CA **2** (24.3 mg, 75.0 μmol , 5 equiv.) was dissolved in hydrochloric acid (4 M in dioxane, 0.30 mL, 1.2 mmol, 80 equiv.) and stirred at 20 $^{\circ}\text{C}$ for 30 min. Saturated aqueous Na_2CO_3 was added and the aqueous layer was extracted with CH_2Cl_2 (3x).

The combined organic layers were dried over Na_2SO_4 and the solvent was evaporated.

Compound **30** (9.61 mg, 15.0 μmol , 1 equiv.), deprotected CA **2**, PYBOP (15.6 mg, 30.0 μmol , 2 equiv.) and the deprotected chloroalkane linker were dissolved in DMF (1 mL) in a pre-dried flask under an N_2 atmosphere and treated with DIPEA (5.0 μL , 30 μmol , 2 equiv.). The resulting solution was stirred at 20 $^{\circ}\text{C}$ for 1 h. Two drops of 1 M HCl were added, all volatiles were removed and the residue was purified by preparative HPLC ($\text{C}_{18}\text{-SiO}_2$, 10 \rightarrow 95 % MeCN in ddH $_2\text{O}$ + 0.1% TFA) to yield a blue solid (5.9 mg, 7.0 μmol , 47%).

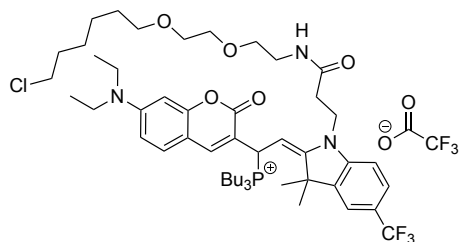
^1H NMR (400 MHz, CDCl_3) δ 8.93 (s, 1H), 8.55 (d, $J = 15.7$ Hz, 1H), 7.83 – 7.62 (m, 5H), 6.74 (dd, $J = 9.2, 2.4$ Hz, 1H), 6.49 (d, $J = 2.3$ Hz, 1H), 5.53 (br s, 1H), 4.82 (t, $J = 6.6$ Hz, 2H), 3.56 (q, $J = 7.0$ Hz, 4H), 3.52 – 3.48 (m, 6H), 3.46 (t, $J = 5.6$ Hz, 2H), 3.42 (t, $J = 6.7$ Hz, 2H), 3.35 – 3.32 (m, 2H), 2.95 (t, $J = 6.5$ Hz, 2H), 1.82 (s, 6H), 1.78 – 1.71 (m, 2H), 1.59 – 1.54 (m, 2H), 1.46 – 1.37 (m, 4H), 1.31 (t, $J = 7.1$ Hz, 6H).

^{13}C NMR (101 MHz, CDCl_3) δ 182.2, 169.2, 160.8, 159.3, 155.5, 152.6, 143.7, 143.1, 134.5, 130.7, 130.4, 127.2, 123.8 (q, $J = 271.6$ Hz), 119.8, 114.6, 113.0, 111.9, 111.6, 107.6, 97.4, 71.4, 70.3, 70.0, 69.3, 51.8, 46.1, 45.2, 43.3, 39.6, 34.3, 32.7, 29.5, 27.8, 26.8, 25.5, 12.8.

^{19}F NMR (376 MHz, CDCl_3) δ -61.94, -75.70.

HRMS (ESI) calculated for $[\text{C}_{39}\text{H}_{50}\text{ClF}_3\text{N}_3\text{O}_5]^+$ 732.33856, found 732.33858.

(*E*)-Tributyl(2-(1-(3-((2-(2-((6-chlorohexyl)oxy)ethoxy)ethyl)amino)-3-oxopro-pyl)-3,3-dimethyl-5-(trifluoromethyl)indolin-2-ylidene)-1-(7-(diethylamino)-2-oxo-2*H*-chromen-3-yl)ethyl)phosphonium trifluoroacetate (34)



Compound **33** (2.96 mg, 3.50 μmol , 1 equiv.) was dissolved in CH_2Cl_2 (1 mL) in a pre-dried flask under an N_2 atmosphere and treated with tri-*n*-butylphosphine (4.3 μL , 18 μmol , 5 equiv.). The mixture was stirred at 20 $^\circ\text{C}$ for 5 min. The solvent was evaporated and the crude product was washed with pentane to yield a yellow film (quant.).

^1H NMR (400 MHz, CD_3CN) δ 8.04 (s, 1H), 7.50 – 7.37 (m, 3H), 6.79 (d, $J = 8.3$ Hz, 1H), 6.73 (dd, $J = 8.9, 2.5$ Hz, 1H), 6.56 (d, $J = 2.5$ Hz, 1H), 5.11 – 4.95 (m, 2H), 4.00 – 3.99 (m, 2H), 3.55 (t, $J = 6.7$ Hz, 2H), 3.45 (q, $J = 7.0$ Hz, 4H), 3.40 (s, 2H), 3.35 (t, $J = 6.5$ Hz, 2H), 3.30 (t, $J = 5.2$ Hz, 2H), 3.23 – 3.21 (m, 2H), 2.56 – 2.43 (m, 2H), 2.24 – 2.14 (m, 6H), 1.76 – 1.67 (m, 2H), 1.65 – 1.63 (m, 2H), 1.60 (s, 3H), 1.59 – 1.36 (m, 18H), 1.28 (s, 3H), 1.17 (t, $J = 7.0$ Hz, 6H), 0.92 (t, $J = 7.2$ Hz, 9H).

^{13}C NMR (101 MHz, CD_3CN) δ 171.5, 168.5, 163.0, 157.7, 157.2, 153.6, 152.6, 148.6, 145.9, 139.1, 130.7, 118.3, 115.3, 110.6, 109.2, 107.0, 97.4, 85.4, 79.7, 79.6, 71.5, 70.9, 70.6, 70.0, 46.1, 45.7, 45.5, 40.0, 39.7, 33.8, 33.3, 32.5, 30.2, 28.0, 27.7, 27.3, 26.1, 24.8, 24.7, 24.6, 24.5, 24.5, 18.8, 18.3, 13.9, 13.5, 12.6. (Multiplets were not analyzed.)

^{19}F NMR (376 MHz, CD_3CN) δ -61.20, -75.69.

^{31}P NMR (162 MHz, CD_3CN) δ 36.84.

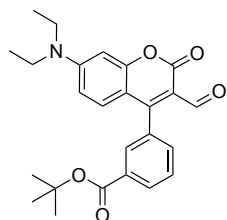
HRMS (ESI) calculated for $[\text{C}_{51}\text{H}_{77}\text{ClF}_3\text{N}_3\text{O}_5\text{P}]^+$ 934.52360, found 934.52345.

4-Chloro-7-(diethylamino)-2-oxo-2*H*-chromene-3-carbaldehyde (35)

Compound **35** was prepared according to reported procedures.¹⁹¹

^1H NMR (400 MHz, CDCl_3) δ 10.31 (s, 1H), 7.85 (d, $J = 9.3$ Hz, 1H), 6.69 (dd, $J = 9.3, 2.5$ Hz, 1H), 6.45 (d, $J = 2.5$ Hz, 1H), 3.48 (q, $J = 7.2$ Hz, 4H), 1.26 (t, $J = 7.2$ Hz, 6H).

HRMS (ESI) calculated for $[\text{C}_{14}\text{H}_{15}\text{ClNO}_3]^+$ 280.07350, found 280.07358.

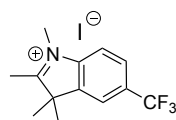
***tert*-Butyl 3-(7-(diethylamino)-3-formyl-2-oxo-2*H*-chromen-4-yl)benzoate (36)**

Compound **35** (42 mg, 0.15 mmol, 1 equiv.), 3-(*tert*-butoxycarbonyl)phenylboronic acid (36.6 mg, 0.165 mmol, 1.1 equiv.), tris(dibenzylideneacetone)dipalladium(0) (6.9 mg, 7.0 μ mol, 0.05 equiv.) and SPhos (9.2 mg, 0.022 mmol, 0.15 equiv.) were dissolved in THF (3 mL) in a pre-dried flask under an Ar atmosphere. Ar was bubbled through the solution for 10 min, then K_3PO_4 (63.7 mg, 0.300 mmol, 2 equiv.) was added and Ar was bubbled through the solution for another 5 min. The resulting mixture was stirred at 60 °C for 18 h. After cooling to ambient temperature, the mixture was filtered over a thin pad of Celite, washed with MeOH and the solvent was evaporated. The crude product was purified by flash column chromatography (SiO_2 , 0 \rightarrow 5% MeOH in CH_2Cl_2) followed by a 2nd column (SiO_2 , CH_2Cl_2) to yield an orange foam (38.7 mg, 91.8 μ mol, 61%).

1H NMR (400 MHz, $CDCl_3$) δ 9.91 (s, 1H), 8.13 (d, $J = 7.9$ Hz, 1H), 7.86 – 7.84 (m, 1H), 7.58 – 7.54 (m, 1H), 7.41 (d, $J = 7.6$ Hz, 1H), 1H), 6.87 (d, $J = 9.1$ Hz, 1H), 6.53 (d, $J = 2.5$ Hz, 1H), 6.50 (dd, $J = 9.2, 2.6$ Hz, 1H), 3.45 (q, $J = 7.1$ Hz, 4H), 1.59 (s, 9H), 1.23 (t, $J = 7.1$ Hz, 6H).

^{13}C NMR (101 MHz, $CDCl_3$) δ 188.3, 165.1, 160.4, 158.0, 153.3, 133.7, 132.5, 132.2, 131.1, 130.1, 129.0, 128.5, 112.3, 110.0, 109.2, 97.3, 81.8, 53.6, 45.4, 28.3, 12.6.

HRMS (ESI) calculated for $[C_{25}H_{28}NO_5]^+$ 422.19620, found 422.19632.

1,2,3,3-Tetramethyl-5-(trifluoromethyl)-3*H*-indol-1-ium iodide (37)

Compound **28** (500 mg, 2.2 mmol, 1 equiv.) was combined with iodomethane (411 μ L, 6.6 mmol, 3 equiv.). The resulting mixture was stirred at 120 °C for 30 min in a microwave reactor. The crude product was washed with Et_2O and the precipitate was filtered to yield a beige solid (637 mg, 1.73 mmol, 78%).

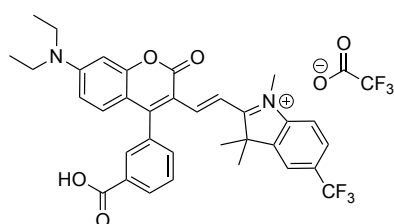
1H NMR (400 MHz, CD_3OD) δ 8.19 (s, 1H), 8.06 (d, $J = 8.5$ Hz, 1H), 7.99 (d, $J = 8.7$ Hz, 1H), 4.11 (s, 3H), 1.67 (s, 6H). Protons of the single methyl group are not visible because of deuterium exchange with the NMR solvent.

^{13}C NMR (101 MHz, CD_3OD) δ 199.6, 144.9, 142.7, 131.5, 126.6, 125.1, 120.5, 115.8, 55.0, 34.4, 20.9.

^{19}F NMR (376 MHz, CD_3OD) δ -63.50.

HRMS (ESI) calculated for $[\text{C}_{13}\text{H}_{15}\text{F}_3\text{N}]^+$: 242.11511, found 242.11565.

(*E*)-2-(2-(4-(3-Carboxyphenyl)-7-(diethylamino)-2-oxo-2*H*-chromen-3-yl)vinyl)-1,3,3-trimethyl-5-(trifluoromethyl)-3*H*-indol-1-ium trifluoroacetate (38)



Compound **37** (37.3 mg, 0.101 mmol, 1.1 equiv.) and compound **36** (38.7 mg, 92.0 μmol , 1 equiv.) were dissolved in EtOH (5 mL) in a pre-dried flask under an N_2 atmosphere. The solution was stirred at 60 $^\circ\text{C}$ for 1.5 h.

The color changed from red to blue. The solvent was evaporated and the residue was re-dissolved in TFA (0.5 mL) and stirred at 20 $^\circ\text{C}$ for 30 min. The mixture was diluted with CH_2Cl_2 , the organic layer was washed with saturated brine and the aqueous phase was re-extracted with CH_2Cl_2 (2x). The combined organic layers were dried over Na_2SO_4 and the solvent was evaporated. The crude product was purified by preparative HPLC (C18- SiO_2 , 10 \rightarrow 95% MeCN in H_2O + 0.1% TFA) to yield a blue solid (53 mg, 75 μmol , 82%).

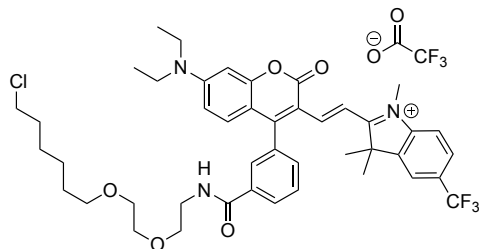
^1H NMR (400 MHz, CD_3CN) δ 8.30 (d, $J = 7.9$, 1H), 8.02 (s, 1H), 7.98 (d, $J = 15.3$ Hz, 1H), 7.96 – 7.86 (m, 2H), 7.84 – 7.79 (m, 1H), 7.70 – 7.65 (m, 2H), 7.62 (d, $J = 7.7$ Hz, 1H), 6.99 (d, $J = 9.4$ Hz, 1H), 6.75 (dd, $J = 9.4, 2.5$ Hz, 1H), 6.68 (d, $J = 2.5$ Hz, 1H), 3.80 (s, 3H), 3.57 (q, $J = 7.1$ Hz, 4H), 1.26 (2x s, 6H), 1.23 (t, $J = 7.1$ Hz, 6H).

^{13}C NMR (101 MHz, CD_3CN) δ 201.2, 184.5, 167.2, 163.0, 160.2, 159.0, 156.0, 152.2, 144.2, 135.1, 133.7, 133.1, 132.9, 131.8, 130.7, 130.6, 127.7, 127.1, 126.4, 121.1, 115.4, 112.8, 112.6, 111.6, 110.9, 97.9, 52.2, 46.4, 34.5, 26.7, 12.9.

^{19}F NMR (377 MHz, CD_3CN) δ -62.41, -76.10.

HRMS (ESI) calculated for $[\text{C}_{34}\text{H}_{32}\text{F}_3\text{N}_2\text{O}_4]^+$ 589.23087, found 589.23072.

(*E*)-2-(2-(4-(3-((2-(2-((6-Chlorohexyl)oxy)ethoxy)ethyl)carbamoyl)phenyl)-7-(diethylamino)-2-oxo-2*H*-chromen-3-yl)vinyl)-1,3,3-trimethyl-5-(trifluoromethyl)-3*H*-indol-1-ium trifluoroacetate (39**)**



Boc-protected CA **2** (48.6 mg, 150 μmol , 5 equiv.) was dissolved in hydrochloric acid (4 M in dioxane, 0.60 mL, 2.40 mmol, 80 equiv.) and stirred at 20 $^{\circ}\text{C}$ for 30 min. Saturated aqueous NaHCO_3 was added and the aqueous layer was extracted with

CH_2Cl_2 (3x). The combined organic layers were dried over Na_2SO_4 and the solvent was evaporated.

Compound **38** (21.1 mg, 30.0 μmol , 1 equiv.), PyBOP (31.2 mg, 60.0 μmol , 2 equiv.) and deprotected CA **2** were dissolved in DMF (3 mL) in a pre-dried flask under an N_2 atmosphere and treated with DIPEA (9.9 μL , 60.0 μmol , 2 equiv.). The resulting solution was stirred at 20 $^{\circ}\text{C}$ for 15 min. 5 drops of 1 M HCl were added, all volatiles were removed and the residue was purified by preparative HPLC (C18-SiO₂, 10 \rightarrow 95 % MeCN in ddH₂O + 0.1% TFA) to yield a blue solid (27 mg, 30 μmol , 99%).

^1H NMR (400 MHz, CDCl_3) δ 8.16 (d, $J = 8.0$ Hz, 1H), 8.01 – 7.94 (m, 2H), 7.79 – 7.70 (m, 3H), 7.62 (d, $J = 1.6$ Hz, 1H), 7.53 (d, $J = 8.4$ Hz, 1H), 7.45 (d, $J = 7.7$ Hz, 1H), 7.03 (d, $J = 9.3$ Hz, 1H), 6.64 (dd, $J = 9.4, 2.5$ Hz, 1H), 6.58 (d, $J = 2.4$ Hz, 1H), 3.87 (s, 3H), 3.70 – 3.65 (m, 4H), 3.65 – 3.61 (m, 2H), 3.58 – 3.54 (m, 6H), 3.51 (t, $J = 6.7$ Hz, 2H), 3.44 (t, $J = 6.8$ Hz, 2H), 1.80 – 1.69 (m, 2H), 1.58 – 1.54 (m, 2H), 1.46 – 1.37 (m, 4H), 1.36 (s, 3H), 1.34 (s, 3H), 1.30 (t, $J = 7.1$ Hz, 6H).

^{13}C NMR (101 MHz, CDCl_3) δ 183.6, 167.1, 162.5, 159.3, 158.2, 155.2, 152.2, 144.2, 142.8, 136.0, 133.6, 132.6, 131.1, 131.0, 129.8, 129.4, 128.1, 127.2, 119.9, 114.3, 113.8, 111.9, 111.8, 110.9, 110.1, 97.5, 71.3, 70.2, 70.1, 69.4, 51.5, 46.0, 45.2, 40.1, 33.9, 32.7, 29.5, 27.1, 26.8, 25.5, 12.8.

^{19}F NMR (376 MHz, CDCl_3) δ -62.09, -75.84.

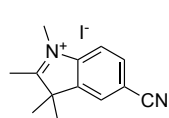
HRMS (ESI) calculated for $[\text{C}_{44}\text{H}_{52}\text{ClF}_3\text{N}_3\text{O}_5]^+$ 794.35421, found 794.35411.

1-(Benzo[*d*]oxazol-2-yl)-4-(3-carboxyphenyl)pyridin-1-ium (41)

Compound **41** was synthesized *via* 3-(pyridin-4-yl)benzoic acid according to reported procedures.^{149,226}

1,2,3,3-Tetramethyl-3*H*-indol-1-ium iodide (42a)

Compound **42a** was synthesized according to a reported procedure.²²⁷

5-Cyano-1,2,3,3-tetramethyl-3*H*-indol-1-ium iodide (42c)

2,3,3-Trimethyl-3*H*-indole-5-carbonitrile²²⁸ (300 mg, 1.63 mmol, 1 equiv.) was combined with iodomethane (507 μ L, 8.14 mmol, 5 equiv.). The resulting mixture was stirred at 120 °C for 1 h in the microwave. The crude product was washed with Et₂O and the precipitate was centrifuged to yield a beige solid (377 mg, 1.16 mmol, 71%).

¹H NMR (400 MHz, CD₃OD) δ 8.24 (s, 1H), 8.07 – 8.02 (m, 2H), 4.09 (s, 3H), 1.65 (s, 6H). Protons of the single methyl group are not visible because of deuterium exchange with the NMR solvent.

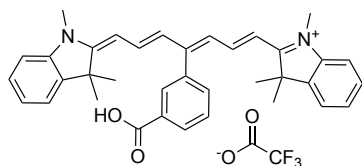
¹³C NMR (101 MHz, CD₃OD) δ 158.2, 142.7, 142.1, 133.7, 127.2, 117.2, 116.2, 113.4, 95.6, 55.0, 34.5, 20.8.

HRMS (ESI) calculated for [C₁₃H₁₅N₂]⁺: 199.12297, found 199.12305.

General procedure to synthesize Cy7 intermediates (43a–c)

Compound **41** (1 equiv.), indoleninium **37**, **42a** or **42c** (2.2 equiv.) and sodium acetate (4 equiv.) were added to EtOH in a microwave vessel. The mixture was stirred at the indicated temperature for the indicated time in the microwave. The solvent was evaporated and the residue was purified by preparative HPLC (C18-SiO₂, 10 \rightarrow 95% MeCN in ddH₂O + 0.1% TFA).

2-(4-(3-Carboxyphenyl)-7-(1,3,3-trimethylindolin-2-ylidene)hepta-1,3,5-trien-1-yl)-1,3,3-trimethyl-3*H*-indol-1-ium trifluoroacetate (43a)¹⁴⁹

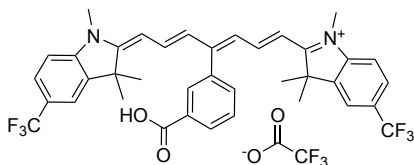


Reaction mixture was stirred at 80 °C for 15 min. Green solid (23.6 mg, 36.7 μmol, 37%).

¹H NMR (400 MHz, CD₃OD) δ 8.26 (d, *J* = 7.8 Hz, 1H), 7.99 (t, *J* = 1.7 Hz, 1H), 7.79 – 7.75 (m, 1H), 7.61 (d, *J* = 7.6 Hz, 1H), 7.48 – 7.35 (m, 6H), 7.28 – 7.17 (m, 4H), 6.77 (d, *J* = 13.1 Hz, 2H), 6.34 (d, *J* = 13.6 Hz, 2H), 3.58 (s, 6H), 1.33 (s, 12H).

HRMS (ESI) calculated for [C₃₆H₃₇N₂O₂]⁺: 529.28495, found 529.28462.

2-(4-(3-Carboxyphenyl)-7-(1,3,3-trimethyl-5-(trifluoromethyl)indolin-2-ylidene)hepta-1,3,5-trien-1-yl)-1,3,3-trimethyl-5-(trifluoromethyl)-3*H*-indol-1-ium trifluoroacetate (43b)



Reaction mixture was stirred at 90 °C for 20 min. Green solid (25.4 mg, 32.6 μmol, 33%).

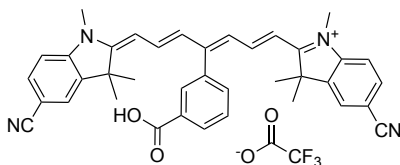
¹H NMR (400 MHz, CD₃OD) δ 8.28 (d, *J* = 7.8 Hz, 1H), 8.03 – 8.00 (t, *J* = 1.7 Hz, 1H), 7.82 – 7.76 (m, 1H), 7.73 – 7.67 (m, 4H), 7.63 (d, *J* = 7.5 Hz, 1H), 7.55 – 7.45 (m, 2H), 7.40 (d, *J* = 8.2 Hz, 2H), 6.88 (d, *J* = 13.2 Hz, 2H), 6.44 (d, *J* = 13.6 Hz, 2H), 3.62 (s, 6H), 1.38 (s, 12H).

¹³C NMR (101 MHz, CD₃OD) δ 174.8, 168.7, 151.2, 147.3, 142.9, 135.0, 132.9, 131.7, 131.6, 130.4, 128.5, 127.9, 127.6, 127.5, 120.5, 112.0, 106.3, 50.1, 31.8, 27.7.

¹⁹F NMR (377 MHz, CD₃OD) δ -62.93, -77.17.

HRMS (ESI) calculated for [C₃₈H₃₅F₆N₂O₂]⁺: 665.25972, found 665.25895.

2-(4-(3-Carboxyphenyl)-7-(5-cyano-1,3,3-trimethylindolin-2-ylidene)hepta-1,3,5-trien-1-yl)-5-cyano-1,3,3-trimethyl-3*H*-indol-1-ium trifluoroacetate (43c)



Reaction was stirred at 80 °C for 4 h. Green solid (86.5 mg, 0.125 mmol, 25%).

^1H NMR (400 MHz, CD_3OD) δ 8.28 (d, $J = 7.8$ Hz, 1H), 8.01 – 8.00 (m, 1H), 7.82 – 7.73 (m, 5H), 7.63 (d, $J = 7.6$ Hz, 1H), 7.54 – 7.47 (m, 2H), 7.39 (d, $J = 8.2$ Hz, 2H), 6.91 (d, $J = 13.2$ Hz, 2H), 6.47 (d, $J = 13.6$ Hz, 2H), 3.61 (s, 6H), 1.36 (s, 12H).

^{13}C NMR (101 MHz, CD_3OD) δ 174.6, 168.6, 166.7, 151.5, 147.9, 143.1, 134.9, 134.9, 134.4, 132.9, 131.7, 130.4, 129.1, 127.1, 119.8, 112.6, 108.6, 106.8, 49.9, 31.8, 27.7.

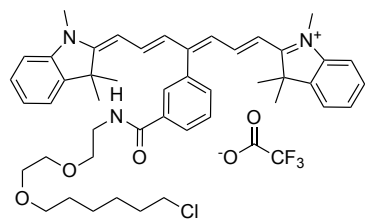
HRMS (ESI) calculated for $[\text{C}_{46}\text{H}_{57}\text{ClN}_3\text{O}_3]^+$: 734.30830, found 579.27521.

General procedure to synthesize HT ligands (44a–c)

Boc-protected CA **2** (3 equiv.) was dissolved in hydrochloric acid (4 M in dioxane, 80 equiv.) and stirred at 20 °C for 30 min. Saturated aqueous NaHCO_3 was added and the aqueous layer was extracted with CH_2Cl_2 (3x). The combined organic layers were dried over Na_2SO_4 and the solvent was evaporated.

Compound **43a–c** (1 equiv.), PyBOP (2 equiv.) and the deprotected CA linker were dissolved in DMF in a pre-dried flask under an N_2 atmosphere and treated with DIPEA (2 equiv.). The resulting solution was stirred at 20 °C for 1.5 h. 1 M HCl (3 drops) were added. All volatiles were removed and the residue was purified by prep-HPLC (10 → 95 % MeCN in ddH₂O + 0.1% TFA).

2-(4-(3-((2-(2-((6-Chlorohexyl)oxy)ethoxy)ethyl)carbamoyl)phenyl)-7-(1,3,3-trimethylindolin-2-ylidene)hepta-1,3,5-trien-1-yl)-1,3,3-trimethyl-3H-indol-1-ium trifluoroacetate (44a)



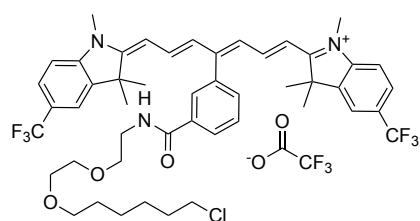
Green solid (11.2 mg, 13.2 μmol , 66%).

^1H NMR (400 MHz, CDCl_3) δ 8.12 (d, $J = 7.8$ Hz, 1H), 7.89 (d, $J = 1.8$ Hz, 1H), 7.68 – 7.61 (m, 1H), 7.56 (s, 1H), 7.43 (d, $J = 7.5$ Hz, 1H), 7.37 – 7.30 (m, 4H), 7.23 (dd, $J = 7.5$, 1.3 Hz, 2H), 7.20 – 7.14 (m, 2H), 7.05 (d, $J = 7.9$ Hz, 2H), 6.75 (d, $J = 13.1$ Hz, 2H), 6.25 (d, $J = 13.5$ Hz, 2H), 3.70 (d, $J = 2.4$ Hz, 4H), 3.65 (dd, $J = 5.8$, 3.4 Hz, 2H), 3.57 (d, $J = 3.1$ Hz, 2H), 3.56 (s, 6H), 3.51 (t, $J = 6.6$ Hz, 2H), 3.44 (t, $J = 6.7$ Hz, 2H), 1.82 – 1.69 (m, 2H), 1.58 – 1.55 (m, 2H), 1.47 – 1.35 (m, 2H), 1.33 (s, 12H).

^{13}C NMR (101 MHz, CDCl_3) δ 172.4, 166.9, 159.9, 159.5, 149.09, 142.9, 140.7, 135.0, 132.2, 128.9, 128.8, 128.5, 128.4, 125.1, 122.2, 110.3, 104.5, 71.4, 70.3, 70.1, 69.6, 48.9, 45.2, 40.0, 32.6, 31.4, 29.5, 27.9, 26.8, 25.5.

HRMS (ESI) calculated for $[\text{C}_{46}\text{H}_{57}\text{ClN}_3\text{O}_3]^+$: 734.30830, found 734.40792.

2-(4-(3-((2-(2-((6-Chlorohexyl)oxy)ethoxy)ethyl)carbamoyl)phenyl)-7-(1,3,3-trimethyl-5-(trifluoromethyl)indolin-2-ylidene)hepta-1,3,5-trien-1-yl)-1,3,3-trimethyl-5-(trifluoromethyl)-3H-indol-1-ium trifluoroacetate (44b)



Blue solid (15.2 mg, 154 μmol , 77%).

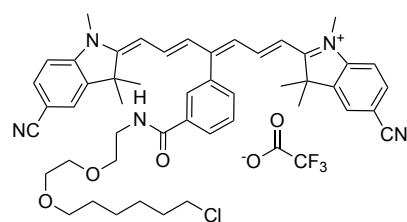
^1H NMR (400 MHz, CDCl_3) δ 8.08 (d, $J = 7.8$ Hz, 1H), 7.93 (d, $J = 1.8$ Hz, 1H), 7.68 – 7.66 (m, 1H), 7.64 – 7.60 (m, 2H), 7.51 – 7.41 (m, 6H), 7.13 (d, $J = 8.4$ Hz, 2H), 6.93 (d, $J = 13.1$ Hz, 2H), 6.42 (d, $J = 13.4$ Hz, 2H), 3.70 (d, $J = 2.3$ Hz, 4H), 3.66 (dd, $J = 5.9, 3.3$ Hz, 2H), 3.62 (s, 6H), 3.60 – 3.56 (m, 2H), 3.51 (t, $J = 6.7$ Hz, 2H), 3.45 (t, $J = 6.7$ Hz, 2H), 1.9 – 1.72 (m, 2H), 1.62 – 1.52 (m, 2H), 1.51 – 1.30 (m, 4H), 1.38 (s, 12H).

^{13}C NMR (101 MHz, CDCl_3) δ 172.8, 167.1, 145.7, 141.2, 135.1, 132.3, 129.0, 128.7, 128.6, 126.7, 126.6, 125.5, 119.4, 110.3, 106.0, 71.4, 70.3, 70.1, 69.6, 48.8, 45.2, 40.1, 32.6, 31.9, 29.5, 27.9, 26.8, 25.5.

^{19}F NMR (377 MHz, CDCl_3) δ -61.55, -75.81.

HRMS (ESI) calculated for $[\text{C}_{48}\text{H}_{55}\text{ClF}_6\text{N}_3\text{O}_3]^+$: 870.38307, found 870.38297.

2-(4-(3-((2-(2-((6-Chlorohexyl)oxy)ethoxy)ethyl)carbamoyl)phenyl)-7-(5-cyano-1,3,3-trimethylindolin-2-ylidene)hepta-1,3,5-trien-1-yl)-5-cyano-1,3,3-trimethyl-3H-indol-1-ium trifluoroacetate (44c)



Green solid (4.4 mg, 4.9 μmol , 16%).

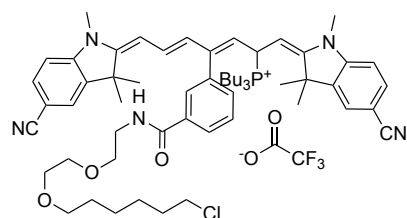
^1H NMR (400 MHz, CDCl_3) δ 8.06 (d, $J = 7.8$ Hz, 1H), 7.95 (s, 1H), 7.70 – 7.61 (m, 3H), 7.48 – 7.40 (m, 6H), 7.13 (d, $J = 8.3$ Hz, 2H), 7.05 (d, $J = 13.0$ Hz, 2H), 6.55 (d, $J = 13.4$ Hz, 2H), 3.71 (s, 4H), 3.68 – 3.63 (m, 8H), 3.61 – 3.57 (m, 2H), 3.52 (t, $J =$

6.6 Hz, 2H), 3.46 (t, $J = 6.7$ Hz, 2H), 1.79 – 1.72 (m, 2H), 1.62 – 1.55 (m, 2H), 1.45 (dd, $J = 15.5, 7.3$ Hz, 2H), 1.38 (s, 12H), 1.34 – 1.22 (m, 2H).

^{13}C NMR not measured due to low amount of available sample.

HRMS (ESI) calculated for $[\text{C}_{48}\text{H}_{55}\text{ClN}_5\text{O}_3]^+$: 784.39879, found 784.39838.

Tributyl(4-(3-((2-(2-((6-chlorohexyl)oxy)ethoxy)ethyl)carbamoyl)phenyl)-1,7-bis(5-cyano-1,3,3-trimethylindolin-2-ylidene)hepta-3,5-dien-2-yl)phosphonium trifluoroacetate (45c)



Compound **44c** (3.14 mg, 4.00 μmol , 1 equiv.) was dissolved in dry CH_2Cl_2 (1 mL) in a pre-dried flask under a N_2 atmosphere and treated with tri-*n*-butylphosphine (0.1 M solution in CH_2Cl_2 , 17.5 μmol , 175 μL , 5 equiv.).

The mixture was stirred at 20 $^\circ\text{C}$ for 5 min while the color turns from green to yellow/brown. The solvent was evaporated, the residue was washed with pentane (3x) and dried to yield a yellow film (quant.).

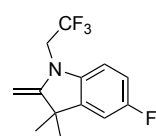
^1H NMR and ^{13}C NMR are not reported as the instability of the compound hampered interpretation of spectra.

^{31}P NMR (162 MHz, CD_3CN) δ 36.29.

HRMS (ESI) calculated for $[\text{C}_{60}\text{H}_{82}\text{ClN}_5\text{O}_3\text{P}]^+$: 986.58383, found 986.58459.

5-Fluoro-2,3,3-trimethyl-3*H*-indole was synthesized as previously reported.²²⁹

5-Fluoro-3,3-dimethyl-2-methylene-1-(2,2,2-trifluoroethyl)indoline (52)



Synthetic procedure was modified from previous report.¹⁴⁹

5-Fluoro-2,3,3-trimethyl-3*H*-indole (532 mg, 3.00 mmol, 1 equiv.), 2,2,2-trifluoroethyl trifluoromethanesulfonate (2.09 g, 9.00 mmol, 3 equiv.) and K_2CO_3 (1451 mg, 10.5 mmol, 3.5 equiv.) were suspended in MeCN (10 mL) and stirred in the microwave at 120 $^\circ\text{C}$ for 5 h. The suspension was filtered, washed with CH_2Cl_2 and the filtrate was evaporated. The residue was taken up in CH_2Cl_2 and washed with dH_2O and

brine. The organic layer was dried over Na_2SO_4 and the solvent was evaporated. The residue was purified by flash column chromatography (SiO_2 , 5 \rightarrow 25% EtOAc in hexane) to yield a red oil (416 mg, 1.60 mmol, 53%).

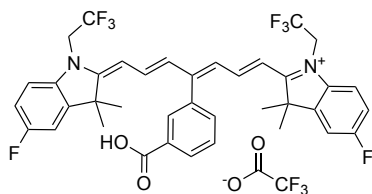
^1H NMR (400 MHz, CD_3CN) δ 6.99 (dd, $J = 8.5, 2.7$ Hz, 1H), 6.92 – 6.87 (m, 1H), 6.68 (dd, $J = 8.6, 4.1$ Hz, 1H), 4.23 – 4.14 (m, 3H), 4.04 (s, 1H), 1.34 (s, 6H).

^{13}C NMR (101 MHz, CD_3CN) δ 162.4, 160.0, 157.7, 140.1, 128.0, 114.3 (d, $J = 23.6$ Hz), 111.0 (d, $J = 24.8$ Hz), 107.5 (d, $J = 7.4$ Hz), 77.2, 46.4 (q, $J = 34.6$ Hz), 45.4, 30.3.

^{19}F NMR (376 MHz, CD_3CN) δ -70.24 (t, $J = 9.4$ Hz), -126.76 (td, $J = 9.0, 4.1$ Hz).

HRMS (ESI) calculated for $[\text{C}_{13}\text{H}_{14}\text{F}_4\text{N}]^+$: 260.10569, found 260.10582.

2-(4-(3-Carboxyphenyl)-7-(5-fluoro-3,3-dimethyl-1-(2,2,2-trifluoroethyl)indolin-2-ylidene)hepta-1,3,5-trien-1-yl)-5-fluoro-3,3-dimethyl-1-(2,2,2-trifluoroethyl)-3H-indol-1-ium trifluoroacetate (53)



3-(Pyridin-4-yl)benzoic acid (99.6 mg, 0.500 mmol, 1 equiv.), compound **52** (389 mg, 1.50 mmol, 3 equiv.) and 2-chlorobenzoxazole (230 mg, 1.50 mmol, 3 equiv.) were added to dry MeCN (10 mL) in a pre-dried microwave

vessel under an Ar atmosphere. The mixture was degassed for a couple of minutes by bubbling Ar through it. The mixture was stirred at 85 °C for 2 h in the microwave. The solvent was evaporated and the residue was purified by preparative HPLC ($\text{C}_{18}\text{-SiO}_2$, 10 \rightarrow 95% MeCN in ddH₂O + 0.1% TFA) to yield a green solid (70.9 mg, 87.0 μmol , 17%).

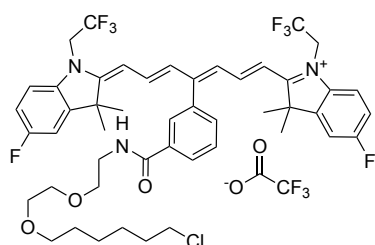
^1H NMR (400 MHz, CD_3OD) δ 8.29 (d, $J = 7.9$ Hz, 1H), 8.03 (d, $J = 1.9$ Hz, 1H), 7.83 – 7.76 (m, 1H), 7.65 (d, $J = 7.6$ Hz, 1H), 7.61 – 7.52 (m, 2H), 7.33 (dd, $J = 8.8, 4.0$ Hz, 2H), 7.27 (dd, $J = 8.1, 2.6$ Hz, 2H), 7.18 – 7.10 (m, 2H), 6.91 (d, $J = 13.2$ Hz, 2H), 6.57 (d, $J = 13.4$ Hz, 2H), 5.02 (q, $J = 8.6$ Hz, 4H), 1.38 (s, 12H).

^{13}C NMR (101 MHz, CD_3OD) δ 175.5, 168.6, 163.7, 161.3, 153.9, 152.2, 143.7, 143.6, 139.4, 134.9, 133.0, 131.8, 131.7, 130.5, 116.5, 116.3, 113.4, 111.6, 111.3, 106.7, 50.5, 49.7, 28.3. Multiplet analysis was not performed.

^{19}F NMR (376 MHz, CD_3OD) δ -69.78 (t, $J = 8.5$ Hz), -77.22, -118.16 (td, $J = 8.4, 3.9$ Hz).

HRMS (ESI) calculated for $[\text{C}_{38}\text{H}_{33}\text{F}_8\text{N}_2\text{O}_2]^+$: 701.24088, found 701.24070.

2-(4-(3-((2-(2-((6-Chlorohexyl)oxy)ethoxy)ethyl)carbamoyl)phenyl)-7-(5-fluoro-3,3-dimethyl-1-(2,2,2-trifluoroethyl)indolin-2-ylidene)hepta-1,3,5-trien-1-yl)-5-fluoro-3,3-dimethyl-1-(2,2,2-trifluoroethyl)-3*H*-indol-1-ium trifluoroacetate (54)



Boc-protected CA **2** (48.6 mg, 0.150 mmol, 5 equiv.) was dissolved in hydrochloric acid (4 M in dioxane, 0.60 mL, 2.4 mmol, 80 equiv.) and stirred at 20 °C for 30 min. Saturated aqueous NaHCO₃ was added and the aqueous layer was extracted with CH₂Cl₂ (3x). The combined organic layers were dried over Na₂SO₄ and the solvent was evaporated.

Compound **53** (24.4 mg, 30.0 μmol, 1 equiv.), PyBOP (31.2 mg, 60.0 μmol, 2 equiv.) and deprotected CA **2** were dissolved in DMF (2 mL) in a pre-dried flask under a N₂ atmosphere and treated with DIPEA (7.75 mg, 60.0 μmol, 2 equiv.). The resulting solution was stirred at 20 °C for 10 min. 1 M HCl (3 drops) was added, all volatiles were removed and the residue was purified by preparative HPLC (C18-SiO₂, 10 → 95 % MeCN in ddH₂O + 0.1% TFA) to yield a green solid (20.5 mg, 20.1 μmol, 67%).

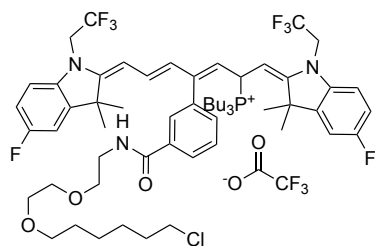
¹H NMR (400 MHz, CDCl₃) δ 8.11 (d, *J* = 7.7 Hz, 1H), 7.96 (s, 1H), 7.67 – 7.63 (m, 1H), 7.51 – 7.40 (m, 3H), 7.09 – 7.03 (m, 4H), 6.98 – 6.91 (m, 4H), 6.58 (d, *J* = 13.3 Hz, 2H), 4.86 (q, *J* = 8.6 Hz, 4H), 3.70 (s, 4H), 3.66 – 3.64 (m, 2H), 3.58 – 3.56 (m, 2H), 3.52 (t, *J* = 6.7 Hz, 2H), 3.44 (t, *J* = 6.7 Hz, 2H), 1.81 – 1.70 (m, 2H), 1.59 – 1.55 (m, 2H), 1.48 – 1.41 (m, 2H), 1.39 (s, 12H), 1.37 – 1.31 (m, 2H).

¹³C NMR (101 MHz, CDCl₃) δ 173.3, 162.3, 150.2, 142.1, 138.0, 132.2, 129.0, 128.9, 128.6, 115.8, 115.6, 111.7, 110.5, 110.3, 106.5, 77.4, 71.4, 70.3, 70.1, 69.6, 49.3, 45.2, 40.0, 32.6, 29.5, 28.4, 26.8, 25.5. Not all carbon signals were detected.

¹⁹F NMR (377 MHz, CDCl₃) δ -67.80 (t, *J* = 8.2 Hz), -75.96, -115.52 – -115.60 (m).

HRMS (ESI) calculated for [C₄₈H₅₃ClF₈N₃O₃]⁺: 906.36422, found 906.36492.

Tributyl(4-(3-((2-(2-((6-chlorohexyl)oxy)ethoxy)ethyl)carbamoyl)phenyl)-1,7-bis(5-fluoro-3,3-dimethyl-1-(2,2,2-trifluoroethyl)indolin-2-ylidene)hepta-3,5-dien-2-yl)phosphonium trifluoroacetate (55)



Compound **54** (3.06 mg, 3.00 μmol , 1 equiv.) was dissolved in dry CH_2Cl_2 in a pre-dried flask under a N_2 atmosphere and treated with tri-*n*-butylphosphine (0.1 M solution in CH_2Cl_2 , 90 μL , 9.0 μmol , 3 equiv.). The mixture was stirred at 20 $^\circ\text{C}$ for 5 min while the color turned from green to

colorless. The solvent was evaporated and the residue was washed with pentane (3x) and lyophilized to yield a slightly greenish solid (quant.).

^1H NMR (400 MHz, CD_3CN) δ 7.84 (d, $J = 7.9$ Hz, 1H), 7.78 (d, $J = 2.8$ Hz, 1H), 7.53 – 7.47 (m, 2H), 7.41 (d, $J = 7.7$ Hz, 1H), 7.06 (dd, $J = 8.5, 2.6$ Hz, 1H), 6.98 – 6.89 (m, 3H), 6.77 (dd, $J = 8.6, 4.0$ Hz, 1H), 6.71 (dd, $J = 8.6, 4.0$ Hz, 1H), 6.65 – 6.60 (m, 2H), 5.92 – 5.84 (m, 1H), 5.16 (dd, $J = 10.0, 4.1$ Hz, 1H), 4.81 – 4.69 (m, 1H), 4.62 – 4.51 (m, 1H), 4.44 – 4.23 (m, 4H), 3.60 – 3.53 (m, 6H), 3.52 – 3.46 (m, 4H), 3.36 (t, $J = 6.5$ Hz, 2H), 2.23 – 2.18 (m, 12H), 1.69 – 1.60 (m, 6H), 1.49 – 1.41 (m, 20H), 0.95 – 0.90 (m, 9H).

^{13}C NMR was not measured.

^{19}F NMR (377 MHz, CD_3CN) δ -69.39 (t, $J = 9.1$ Hz), -69.58 (t, $J = 9.0$ Hz), -75.50, -125.08 (td, $J = 9.0, 4.1$ Hz), -125.56 (td, $J = 8.9, 4.0$ Hz).

^{31}P NMR (162 MHz, CD_3CN) δ 36.53.

HRMS (ESI) calculated for $[\text{C}_{60}\text{H}_{80}\text{ClF}_8\text{N}_3\text{O}_3\text{P}]^+$: 1108.54926, found 1108.54832.

DFT

Computational modeling was carried out using Gaussian 09 at the B3LYP/6-311G+(d,p) level of theory. An implicit solvation model (IEFPCM) was used to simulate the effect of an aqueous environment. The calculations were carried out on the ScienceCluster of UZH with 32 cores per task and 48 GB memory. All stationary states were characterized by harmonic analysis at the same level of theory. All minima displayed zero imaginary frequencies and all transition states gave one imaginary frequency along the C–P bond elongation coordinate. Energies were corrected by zero-point energy. Cartesian coordinates for all compounds modeled are provided in the appendix.

Cloning

Plasmid sources and primers for cloning are listed in Table 12 and Table 13.

Table 12. Plasmid sources.

Plasmid	Source	Vector precursor	Insert precursor
pmTurquoise2-Golgi	Addgene #36205 ²³⁰		
pmScarlet3	Addgene #189753 ¹⁹⁷		
Galt1-HT-mGold	Gibson assembly	pmTurquoise2-Golgi	Calnexin-HT-mGold
Calnexin-HT-mScarlet3	Gibson assembly	Calnexin-HT-mGold	pmScarlet3
Calnexin-reHT-mScarlet3	Site-directed mutagenesis	Calnexin-HT-mScarlet3	

Table 13. Primers for plasmid generation.

Plasmid	Vector forward	Vector reverse	Insert forward	Insert reverse
Galt1-HT-mGold	aagtaaagcggccg c	attcgggtggcgacc	cgccaccgaaatcg gtact	cggccgctttactgt acag
Calnexin-HT-mScarlet3	ggatctagaaagtaa agcggc	gtgctatcgccgaa atctc	ttccggcgatagcac cgag	cgcttactttctagat ccggtgg
Calnexin-reHT-mScarlet3	cccgggtctgcatct gctgcaag	ccgatgtccacagc cttg		

pH profile

Experimental procedure as outlined in section 8.4.

GSH assay

To measure reduced and total GSH content the GSH/GSSG Ratio Detection Assay Kit II (abcam) was used. Samples were prepared in PBS containing the respective compound (5 μ M), GSSG (5 μ M) and HT (7.5 μ M), if applicable. The prepared samples were rotated at 37 °C for 20 min and filtered through Amicon centrifugal units (10 kDa MWCO). The flow through was analyzed according to the provided procedure of the assay.

Cell viability assay

The cytotoxicity of the probes was determined with an MTT colorimetric assay. HeLa cells were seeded into a 96-well plate (9000 per well) and incubated at 37 °C for 24 h. The compounds were incubated for 24 h at different concentrations ranging from 10 nM to 50 μM. Stock solutions of the compounds were prepared in DMSO, and cells were incubated in growth medium with a final DMSO concentration of 0.5%. DMSO was used as control treatment to obtain a reference for 100% cell viability. After the incubation time, 10% MTT solution (5 mg mL⁻¹ in FluoroBrite DMEM) was added to the cells and incubated for 3 h. The medium was then removed, and 2-propanol (100 μL) was added. The plates were shaken for 30 min, and the absorbance at 550 nm was measured. Technical triplicates were measured for each compound, and Prism (Graph Pad) was used to fit a sigmoidal dose-response regression.

Confocal microscopy

The optical settings for all microscopy experiments are summarized in Table 14.

Table 14. Optical configurations for microscopy experiments.

Channel	λ excitation	Emission filter
roGFP blue	405 nm	525/50
roGFP green	445 nm	525/50
mGold	515 nm	542/27
mScarlet3	561 nm	600/52
Coumarin hybrid dyes	640 nm	708/75
Cy7 dyes	640 nm	647/LP

Bacterial imaging

BL21(DE3) *E. coli* with or without the HT-mGold-His6 plasmid were inoculated into 5 mL LB with the appropriate antibiotic if applicable and incubated at 37 °C overnight. A chambered 8-well ibidi plate was coated with poly-*D*-lysine (50 μg mL⁻¹ in ddH₂O, 250 μL) and incubated at room temperature for 30 min. The poly-*D*-lysine solution was removed, and the chambered slide was washed twice with ddH₂O (400 μL). The excess water was

removed after the final wash and the slides were allowed to air-dry at room temperature overnight. In a new tube the culture was diluted to $OD_{600}=0.4$ in LB (5 mL), 1 mM IPTG was added to the cells carrying the plasmid, and the cells were incubated while shaking for 3 h at 37 °C. The culture (200 μ L) was pelleted and the pellet was suspended in FluoroBrite (1 mL). To each well 200 μ L of the prepared culture was added and the plate was incubated at 37 °C for 20 min. The wells were washed with FluoroBrite (2x 400 μ L, 1x 270 μ L) to remove unattached bacteria and the respective compound (50 μ M in FluoroBrite, 30 μ L) was added on top. The cells were imaged after incubation at 37 °C for the indicated time.

roGFP measurements before and after phosphine release

HeLa cells were plated and transfected with roGFP-iE-ER and Calnexin-HT-mScarlet3 or Calnexin-reHT-mScarlet3 as previously described. The basal roGFP ratio was measured by imaging >24 h after transfection. The cells were incubated with the compound (500 nM) for 30 min and the same positions were imaged again. Data analysis was performed with an adapted Python script as described in section 8.4.

8.7 Experimental procedures for chapter 6

Synthetic procedures

COUPY-CA6 and COUPY-CA7 were provided by Anna Rovira Vidal and detailed synthetic procedures are therefore not reported here.

Cloning

Plasmid sources and primers for cloning are listed in Table 15 and Table 16.

Table 15. Plasmid sources.

Plasmid	Source	Vector precursor	Insert precursor
HT7-His6	a)		
HT-CDD-His6	a)		
HT-CMHYA-His6	a)		
HT-CYA-His6	a)		
HT-CYAD-His6	a)		

Experimental

HT-MHD-His6	a)		
HT-MHYAD-His6	a)		
HT-NCDD-His6	a)		
HT-YAD-His6	a)		
HT-YD-His6	a)		
Lifeact-HT-CMHYA	a)		
Lifeact-HT-CYA	a)		
Lifeact-HT-MHYAD	a)		
Lifeact-YAD	a)		
Lifeact-HT-YD	a)		
Galt1-HT-CMHYA	Gibson assembly	Galt1-HT-mGold	Lifeact-HT-CMHYA
H2B-HT-CMHYA	Gibson assembly	H2B-HT-mGold	Lifeact-HT-CMHYA
H2B-HT-MHYAD	Gibson assembly	H2B-HT-mGold	Lifeact-HT-MHYAD
DbeA-H280F	Gibson assembly	HT-mGold	b)
DbjA-H280F	Gibson assembly	HT-mGold	b)
DhlA-W175Y-H289F	Gibson assembly	HT-mGold	b)
DmmA-H315F	Gibson assembly	HT-mGold	b)
DppA-H278F	Gibson assembly	HT-mGold	b)
LinB-H272F	Gibson assembly	HT-mGold	b)
H2B-DppA-H278F-mGold	Gibson assembly		DppA-H278F

a) Gift from Thomas Ward (University of Basel)

b) Purchased from Twist Bioscience

Table 16. Primers for plasmid generation.

Plasmid	Vector forward	Vector reverse	Insert forward	Insert reverse
Galt1-HT-CMHYA	agatttcctaaagcg gccg	aagccagtaccgatt tcggt	aatcggctactggettt cca	ccgcttaggaaatct ccagag
H2B-HT-CMHYA	accgctcgagagct aagcg	atttcggagccggtc gactg	gaccggctccgaaa tcggt	tagctctcgagcggg tatca
H2B-HT-MHYAD	accgctcgagagct aagcg	atttcggagccggtc gactg	gaccggctccgaaa tcggt	tagctctcgagcggg tatca

DbeA-H280F	ggaatgaggccg actct	tcgccatgagatct gagtccg	agatctc ^{c)}	ggccgcga ^{c)}
DbjA-H280F	cgtagattgacgca ctctaga	ttagacatggcggtc tcgag	gaccgcc ^{c)}	cgcgactc ^{c)}
DhlA-W175Y-H289F	agagtgacgagct ctaga	ttaatcatggcggct cgag	gaccgcc ^{c)}	cgcgactc ^{c)}
DmmA-H315F	cgagtgacgagct ctaga	cttgccatgagatct gagtccg	agatctc ^{c)}	cgcgactc ^{c)}
DppA-H278F	gcagtgacgagct ctaga	aactccatggcggtc tcgag	gaccgcc ^{c)}	cgcgactc ^{c)}
LinB-H272F	ggcgtgacgagct ctaga	agactcatggcggtc tcgag	gaccgcc ^{c)}	cgcgactc ^{c)}
H2B-DppA-H278F- mGold	tgggcaggagatttc cggc	acgaaactgctgcc ggtcga	cggcagcgagttcg ttaggac	gaaatctctgccca aacgc

^{c)} Insert overhangs were included in the design of ordered genes.

Protein expression of HT mutants

The general protocol for protein expression (section 8.2) was followed.

FLIM

The optical settings for all microscopy experiments included excitation at 561 nm and detection with a HyD detector in photon counting mode (580–700 nm). Specific sample preparation is summarized in (Table 17).

Table 17. Transfection and incubation conditions for FLIM multiplexing experiments.

Plasmid 1	Plasmid 2	Incubation with dye	Wash
Galt1-HT-CMHYA (200 ng)	H2B-HT-CMHYA (100 ng)	100 nM for 3 h	overnight
Galt1-HT-CMHYA (200 ng)	H2B-HT-MHYAD (300 ng)	100 nM for 4 h	/
Galt1-HT-CMHYA (100 ng)	H2B-DppA-mGold (400 ng)	100 nM for 4 h	4 h

9 References

1. Romero, M. F. In the beginning, there was the cell: cellular homeostasis. *Adv. Physiol. Educ.* **28**, 135–138 (2004).
2. Le Gal, K., Schmidt, E. E. & Sayin, V. I. Cellular redox homeostasis. *Antioxidants* **10**, 1377 (2021).
3. Ursini, F., Maiorino, M. & Forman, H. J. Redox homeostasis: the golden mean of healthy living. *Redox Biol.* **8**, 205–215 (2016).
4. Wang, K., Zhang, T., Dong, Q., Nice, E. C., Huang, C. & Wei, Y. Redox homeostasis: the linchpin in stem cell self-renewal and differentiation. *Cell Death Dis.* **4**, e537–e537 (2013).
5. Bartosz, G. Reactive oxygen species: destroyers or messengers? *Biochem. Pharmacol.* **77**, 1303–1315 (2009).
6. Nordberg, J. & Arnér, E. S. J. Reactive oxygen species, antioxidants, and the mammalian thioredoxin system. *Free Radic. Biol. Med.* **31**, 1287–1312 (2001).
7. Chandel, N. S. NADPH – the forgotten reducing equivalent. *Cold Spring Harb. Perspect. Biol.* **13**, a040550 (2021).
8. Buettner, G. R., Wagner, B. A. & Rodgers, V. G. J. Quantitative redox biology: an approach to understand the role of reactive species in defining the cellular redox environment. *Cell Biochem. Biophys.* **67**, 477–483 (2013).
9. Holmström, K. M. & Finkel, T. Cellular mechanisms and physiological consequences of redox-dependent signalling. *Nat. Rev. Mol. Cell Biol.* **15**, 411–421 (2014).
10. Lennicke, C. & Cochemé, H. M. Redox metabolism: ROS as specific molecular regulators of cell signaling and function. *Mol. Cell* **81**, 3691–3707 (2021).
11. Chiu, J. & Dawes, I. W. Redox control of cell proliferation. *Trends Cell Biol.* **22**, 592–601 (2012).
12. Denu, J. M. & Tanner, K. G. Specific and reversible inactivation of protein tyrosine phosphatases by hydrogen peroxide: evidence for a sulfenic acid intermediate and implications for redox regulation. *Biochemistry* **37**, 5633–5642 (1998).
13. Paulsen, C. E., Truong, T. H., Garcia, F. J., Homann, A., Gupta, V., Leonard, S. E. & Carroll, K. S. Peroxide-dependent sulfenylation of the EGFR catalytic site enhances kinase activity. *Nat. Chem. Biol.* **8**, 57–64 (2012).

14. Oda, K., Matsuoka, Y., Funahashi, A. & Kitano, H. A comprehensive pathway map of epidermal growth factor receptor signaling. *Mol. Syst. Biol.* **1**, 2005.0010 (2005).
15. Lennicke, C. & Cochemé, H. M. Redox regulation of the insulin signalling pathway. *Redox Biol.* **42**, 101964 (2021).
16. Hornsveld, M. & Dansen, T. B. The hallmarks of cancer from a redox perspective. *Antioxid. Redox Signal.* **25**, 300–325 (2016).
17. Sbodio, J. I., Snyder, S. H. & Paul, B. D. Redox mechanisms in neurodegeneration: from disease outcomes to therapeutic opportunities. *Antioxid. Redox Signal.* **30**, 1450–1499 (2019).
18. Meister, A. & Anderson, M. E. Glutathione. *Ann. Rev. Biochem.* **52**, 711–760 (1983).
19. Meyer, A. J. & Dick, T. P. Fluorescent protein-based redox probes. *Antioxid. Redox Signal.* **13**, 621–650 (2010).
20. Scirè, A., Cianfruglia, L., Minnelli, C., Bartolini, D., Torquato, P., Principato, G., Galli, F. & Armeni, T. Glutathione compartmentalization and its role in glutathionylation and other regulatory processes of cellular pathways. *Biofactors* **45**, 152–168 (2019).
21. Griffith, O. W. Biologic and pharmacologic regulation of mammalian glutathione synthesis. *Free Radic. Biol. Med.* **27**, 922–935 (1999).
22. Kojer, K., Bien, M., Gangel, H., Morgan, B., Dick, T. P. & Riemer, J. Glutathione redox potential in the mitochondrial intermembrane space is linked to the cytosol and impacts the Mia40 redox state. *EMBO J.* **31**, 3169–3182 (2012).
23. Chen, Z. & Lash, L. H. Evidence for mitochondrial uptake of glutathione by dicarboxylate and 2-oxoglutarate carriers. *J. Pharmacol. Exp. Ther.* **285**, 608–618 (1998).
24. Appenzeller-Herzog, C. Glutathione- and non-glutathione-based oxidant control in the endoplasmic reticulum. *J. Cell Sci.* **124**, 847–855 (2011).
25. Oestreicher, J. & Morgan, B. Glutathione: subcellular distribution and membrane transport. *Biochem. Cell Biol.* **97**, 270–289 (2019).
26. Ponsero, A. J., Igarria, A., Darch, M. A., Miled, S., Outten, C. E., Winther, J. R., Palais, G., D’Autréaux, B., Delaunay-Moisan, A. & Toledano, M. B. Endoplasmic reticulum transport of glutathione by Sec61 is regulated by Ero1 and BiP. *Mol. Cell* **67**, 962–973.e5 (2017).

27. Bellomo, G., Palladini, G. & Vairetti, M. Intranuclear distribution, function and fate of glutathione and glutathione-S-conjugate in living rat hepatocytes studied by fluorescence microscopy. *Microsc. Res. Techniq.* **36**, 243–252 (1997).
28. Vivancos, P. D., Dong, Y., Ziegler, K., Markovic, J., Pallardó, F. V., Pellny, T. K., Verrier, P. J. & Foyer, C. H. Recruitment of glutathione into the nucleus during cell proliferation adjusts whole-cell redox homeostasis in *Arabidopsis thaliana* and lowers the oxidative defence shield. *Plant J.* **64**, 825–838 (2010).
29. Markovic, J., Borrás, C., Ortega, Á., Sastre, J., Viña, J. & Pallardó, F. V. Glutathione is recruited into the nucleus in early phases of cell proliferation. *J. Biol. Chem.* **282**, 20416–20424 (2007).
30. Prigge, J. R., Eriksson, S., Iverson, S. V., Meade, T. A., Capecchi, M. R., Arnér, E. S. J. & Schmidt, E. E. Hepatocyte DNA replication in growing liver requires either glutathione or a single allele of *txnrd1*. *Free Radic. Biol. Med.* **52**, 803–810 (2012).
31. Holmgren, A. Hydrogen donor system for *Escherichia coli* ribonucleoside-diphosphate reductase dependent upon glutathione. *Proc. Natl. Acad. Sci. U.S.A.* **73**, 2275–2279 (1976).
32. Voehringer, D. W., McConkey, D. J., McDonnell, T. J., Brisbay, S. & Meyn, R. E. Bcl-2 expression causes redistribution of glutathione to the nucleus. *Proc. Natl. Acad. Sci. U.S.A.* **95**, 2956–2960 (1998).
33. Baldelli, S., Ciccarone, F., Limongi, D., Checconi, P., Palamara, A. T. & Ciriolo, M. R. Glutathione and nitric oxide: key team players in use and disuse of skeletal muscle. *Nutrients* **11**, 2318 (2019).
34. Aquilano, K., Baldelli, S. & Ciriolo, M. R. Glutathione: new roles in redox signaling for an old antioxidant. *Front. Pharmacol.* **5**, (2014).
35. Pastore, A. & Piemonte, F. S-Glutathionylation signaling in cell biology: progress and prospects. *Eur. J. Pharm. Sci.* **46**, 279–292 (2012).
36. Torres-Quesada, O., Mayrhofer, J. E. & Stefan, E. The many faces of compartmentalized PKA signalosomes. *Cell. Signal.* **37**, 1–11 (2017).
37. Humphries, K. M., Deal, M. S. & Taylor, S. S. Enhanced dephosphorylation of cAMP-dependent protein kinase by oxidation and thiol modification. *J. Biol. Chem.* **280**, 2750–2758 (2005).
38. Humphries, K. M., Juliano, C. & Taylor, S. S. Regulation of cAMP-dependent protein kinase activity by glutathionylation. *J. Biol. Chem.* **277**, 43505–43511 (2002).

39. Hara, M. R., Agrawal, N., Kim, S. F., Cascio, M. B., Fujimuro, M., Ozeki, Y., Takahashi, M., Cheah, J. H., Tankou, S. K., Hester, L. D., Ferris, C. D., Hayward, S. D., Snyder, S. H. & Sawa, A. S-nitrosylated GAPDH initiates apoptotic cell death by nuclear translocation following Siah1 binding. *Nat. Cell Biol.* **7**, 665–674 (2005).
40. Newman, S. F., Sultana, R., Perluigi, M., Coccia, R., Cai, J., Pierce, W. M., Klein, J. B., Turner, D. M. & Butterfield, D. A. An increase in S-glutathionylated proteins in the Alzheimer's disease inferior parietal lobule, a proteomics approach. *J. Neurosci. Res.* **85**, 1506–1514 (2007).
41. Xiao, W. & Loscalzo, J. Metabolic responses to reductive stress. *Antioxid. Redox Signal.* **32**, 1330–1347 (2020).
42. Birk, J., Meyer, M., Aller, I., Hansen, H. G., Odermatt, A., Dick, T. P., Meyer, A. J. & Appenzeller-Herzog, C. Endoplasmic reticulum: reduced and oxidized glutathione revisited. *J. Cell Sci.* **126**, 1604–1617 (2013).
43. Hatori, Y., Kubo, T., Sato, Y., Inouye, S., Akagi, R. & Seyama, T. Visualization of the redox status of cytosolic glutathione using the organelle- and cytoskeleton-targeted redox sensors. *Antioxidants* **9**, 129 (2020).
44. Hwang, C., Sinskey, A. J. & Lodish, H. F. Oxidized redox state of glutathione in the endoplasmic reticulum. *Science* **257**, 1496–1502 (1992).
45. PubMed. <https://pubmed.ncbi.nlm.nih.gov/> (2023).
46. Schwarz, D. S. & Blower, M. D. The endoplasmic reticulum: structure, function and response to cellular signaling. *Cell. Mol. Life Sci.* **73**, 79–94 (2016).
47. Braakman, I. & Bulleid, N. J. Protein folding and modification in the mammalian endoplasmic reticulum. *Annu. Rev. Biochem.* **80**, 71–99 (2011).
48. Chipurupalli, S., Kannan, E., Tergaonkar, V., D'andrea, R. & Robinson, N. Hypoxia induced ER stress response as an adaptive mechanism in cancer. *Int. J. Mol. Sci.* **20**, (2019).
49. Schröder, M. & Kaufman, R. J. ER stress and the unfolded protein response. *Mutat. Res.* **569**, 29–63 (2005).
50. Ron, D. & Walter, P. Signal integration in the endoplasmic reticulum unfolded protein response. *Nat. Rev. Mol. Cell Biol.* **8**, 519–529 (2007).
51. Bertolotti, A., Zhang, Y., Hendershot, L. M., Harding, H. P. & Ron, D. Dynamic interaction of BiP and ER stress transducers in the unfolded-protein response. *Nat. Cell Biol.* **2**, 326–332 (2000).

-
52. Walter, P. & Ron, D. The unfolded protein response: From stress pathway to homeostatic regulation. *Science* **334**, 1081–1086 (2011).
 53. Calton, M., Zeng, H., Urano, F., Till, J. H., Hubbard, S. R., Harding, H. P., Clark, S. G. & Ron, D. IRE1 couples endoplasmic reticulum load to secretory capacity by processing the XBP-1 mRNA. *Nature* **415**, 92–96 (2002).
 54. Haze, K., Yoshida, H., Yanagi, H., Yura, T. & Mori, K. Mammalian transcription factor ATF6 is synthesized as a transmembrane protein and activated by proteolysis in response to endoplasmic reticulum stress. *Mol. Biol. Cell* **10**, 3787–3799 (1999).
 55. Harding, H. P., Novoa, I., Zhang, Y., Zeng, H., Wek, R., Schapira, M. & Ron, D. Regulated translation initiation controls stress-induced gene expression in mammalian cells. *Mol. Cell* **6**, 1099–1108 (2000).
 56. Lee, A.-H., Iwakoshi, N. N. & Glimcher, L. H. XBP-1 regulates a subset of endoplasmic reticulum resident chaperone genes in the unfolded protein response. *Mol. Cell Biol.* **23**, 7448–7459 (2003).
 57. Okada, T., Yoshida, H., Akazawa, R., Negishi, M. & Mori, K. Distinct roles of activating transcription factor 6 (ATF6) and double-stranded RNA-activated protein kinase-like endoplasmic reticulum kinase (PERK) in transcription during the mammalian unfolded protein response. *Biochem. J.* **366**, 585–594 (2002).
 58. Rutkowski, D. T. & Kaufman, R. J. A trip to the ER: coping with stress. *Trends Cell Biol.* **14**, 20–28 (2004).
 59. Shpilka, T. & Haynes, C. M. The mitochondrial UPR: mechanisms, physiological functions and implications in ageing. *Nat. Rev. Mol. Cell Biol.* **19**, 109–120 (2018).
 60. Gao, J., Gao, A., Liu, W. & Chen, L. Golgi stress response: a regulatory mechanism of Golgi function. *BioFactors* **47**, 964–974 (2021).
 61. Yoboue, E. D., Sitia, R. & Simmen, T. Redox crosstalk at endoplasmic reticulum (ER) membrane contact sites (MCS) uses toxic waste to deliver messages. *Cell Death Dis.* **9**, 1–14 (2018).
 62. Rizzuto, R., Pinton, P., Carrington, W., Fay, F. S., Fogarty, K. E., Lifshitz, L. M., Tuft, R. A. & Pozzan, T. Close contacts with the endoplasmic reticulum as determinants of mitochondrial Ca²⁺ responses. *Science* **280**, 1763–1766 (1998).
 63. Raturi, A., Ortiz-Sandoval, C. & Simmen, T. Redox dependence of endoplasmic reticulum (ER) Ca²⁺ signaling. *Histol. Histopathol.* **29**, 543–552 (2014).

64. Bravo, R., Vicencio, J. M., Parra, V., Troncoso, R., Munoz, J. P., Bui, M., Quiroga, C., Rodriguez, A. E., Verdejo, H. E., Ferreira, J., Iglewski, M., Chiong, M., Simmen, T., Zorzano, A., Hill, J. A., Rothermel, B. A., Szabadkai, G. & Lavandro, S. Increased ER–mitochondrial coupling promotes mitochondrial respiration and bioenergetics during early phases of ER stress. *J. Cell Sci.* **124**, 2511 (2011).
65. Benson, M. & Simmen, T. Ero1 α requires oxidizing and normoxic conditions to localize to the mitochondria-associated membrane (MAM). *Cell Stress Chaperones* (2010).
66. Yoboue, E. D., Rimessi, A., Anelli, T., Pinton, P. & Sitia, R. Regulation of calcium fluxes by GPX8, a type-II transmembrane peroxidase enriched at the mitochondria-associated endoplasmic reticulum membrane. *Antioxid. Redox Signal.* **27**, 583–595 (2017).
67. Raturi, A., Gutiérrez, T., Ortiz-Sandoval, C., Ruangkittisakul, A., Herrera-Cruz, M. S., Rockley, J. P., Gesson, K., Ourdev, D., Lou, P.-H., Lucchinetti, E., Tahbaz, N., Zaugg, M., Baksh, S., Ballanyi, K. & Simmen, T. TMX1 determines cancer cell metabolism as a thiol-based modulator of ER–mitochondria Ca²⁺ flux. *J. Cell Biol.* **214**, 433–444 (2016).
68. Shutt, T., Geoffrion, M., Milne, R. & McBride, H. M. The intracellular redox state is a core determinant of mitochondrial fusion. *EMBO Rep.* **13**, 909–915 (2012).
69. Redpath, C. J., Khalil, M. B., Drozdal, G., Radisic, M. & McBride, H. M. Mitochondrial hyperfusion during oxidative stress is coupled to a dysregulation in calcium handling within a C2C12 cell model. *PLoS One* **8**, e69165 (2013).
70. Wu, W., Lin, C., Wu, K., Jiang, L., Wang, X., Li, W., Zhuang, H., Zhang, X., Chen, H., Li, S., Yang, Y., Lu, Y., Wang, J., Zhu, R., Zhang, L., Sui, S., Tan, N., Zhao, B., Zhang, J., Li, L. & Feng, D. FUNDC1 regulates mitochondrial dynamics at the ER–mitochondrial contact site under hypoxic conditions. *EMBO J.* **35**, 1368–1384 (2016).
71. Presley, J. F., Cole, N. B., Schroer, T. A., Hirschberg, K., Zaal, K. J. M. & Lippincott-Schwartz, J. ER-to-Golgi transport visualized in living cells. *Nature* **389**, 81–85 (1997).
72. Klumperman, J. Transport between ER and Golgi. *Curr. Opin. Cell Biol.* **12**, 445–449 (2000).

-
73. Serebrenik, Y. V., Hellerschmied, D., Toure, M., López-Giráldez, F., Brookner, D. & Crews, C. M. Targeted protein unfolding uncovers a Golgi-specific transcriptional stress response. *Mol. Biol. Cell* **29**, 1284–1298 (2018).
74. Mahadevan, N. R., Rodvold, J., Sepulveda, H., Rossi, S., Drew, A. F., Zanetti, M. & Rosenfeld, M. G. Transmission of endoplasmic reticulum stress and pro-inflammation from tumor cells to myeloid cells. *Proc. Natl. Acad. Sci. U.S.A.* **108**, 6561–6566 (2011).
75. Rodvold, J. J., Chiu, K. T., Hiramatsu, N., Nussbacher, J. K., Galimberti, V., Mahadevan, N. R., Willert, K., Lin, J. H. & Zanetti, M. Intercellular transmission of the unfolded protein response promotes survival and drug resistance in cancer cells. *Sci. Signal.* **10**, eaah7177 (2017).
76. Rodvold, J. J., Mahadevan, N. R. & Zanetti, M. Immune modulation by ER stress and inflammation in the tumor microenvironment. *Cancer Lett.* **380**, 227–236 (2016).
77. Zanetti, M., Rodvold, J. J. & Mahadevan, N. R. The evolving paradigm of cell-nonautonomous UPR-based regulation of immunity by cancer cells. *Oncogene* **35**, 269–278 (2016).
78. Cullen, S. J., Fatemie, S. & Ladiges, W. Breast tumor cells primed by endoplasmic reticulum stress remodel macrophage phenotype. *Am. J. Cancer Res.* **3**, 196–210 (2013).
79. Meares, G. P., Liu, Y., Rajbhandari, R., Qin, H., Nozell, S. E., Mobley, J. A., Corbett, J. A. & Benveniste, E. N. PERK-dependent activation of JAK1 and STAT3 contributes to endoplasmic reticulum stress-induced inflammation. *Mol. Cell. Biol.* **34**, 3911–3925 (2014).
80. Sprengle, N. T., Lahiri, A., Simpkins, J. W. & Meares, G. P. Endoplasmic reticulum stress is transmissible in vitro between cells of the central nervous system. *J. Neurochem.* **148**, 516–530 (2019).
81. van Ziel, A. M., Wolzak, K., Nölle, A., Hoetjes, P. J., Berenjano-Correa, E., van Anken, E., Struys, E. A. & Scheper, W. No evidence for cell-to-cell transmission of the unfolded protein response in cell culture. *J. Neurochem.* **152**, 208–220 (2020).
82. Huang, B., Babcock, H. & Zhuang, X. Breaking the diffraction barrier: super-resolution imaging of cells. *Cell* **143**, 1047–1058 (2010).

83. Wolff, J. O., Scheiderer, L., Engelhardt, T., Engelhardt, J., Matthias, J. & Hell, S. W. MINFLUX dissects the unimpeded walking of kinesin-1. *Science* **379**, 1004–1010 (2023).
84. Deguchi, T., Iwanski, M. K., Schentarra, E.-M., Heidebrecht, C., Schmidt, L., Heck, J., Weihs, T., Schnorrenberg, S., Hoess, P., Liu, S., Chevyreva, V., Noh, K.-M., Kapitein, L. C. & Ries, J. Direct observation of motor protein stepping in living cells using MINFLUX. *Science* **379**, 1010–1015 (2023).
85. Royer, L. A., Lemon, W. C., Chhetri, R. K., Wan, Y., Coleman, M., Myers, E. W. & Keller, P. J. Adaptive light-sheet microscopy for long-term, high-resolution imaging in living organisms. *Nat. Biotechnol.* **34**, 1267–1278 (2016).
86. Schultz, R. A., Nielsen, T., Zavaleta, J. R., Ruch, R., Wyatt, R. & Garner, H. R. Hyperspectral imaging: a novel approach for microscopic analysis. *Cytometry* **43**, 239–247 (2001).
87. Lakowicz, J. R., Szmajcinski, H., Nowaczyk, K., Berndt, K. W. & Johnson, M. Fluorescence lifetime imaging. *Anal. Biochem.* **202**, 316–330 (1992).
88. Niehörster, T., Löscherger, A., Gregor, I., Krämer, B., Rahn, H.-J., Patting, M., Koberling, F., Enderlein, J. & Sauer, M. Multi-target spectrally resolved fluorescence lifetime imaging microscopy. *Nat. Methods* **13**, 257–262 (2016).
89. Baeyer, A. Ueber eine neue Klasse von Farbstoffen. *Ber. Dt. Chem. Ges.* **4**, 555–558 (1871).
90. Schnermann, M. J. & Lavis, L. D. Rejuvenating old fluorophores with new chemistry. *Curr. Opin. Chem. Biol.* **75**, 102335 (2023).
91. Terai, T. & Nagano, T. Small-molecule fluorophores and fluorescent probes for bioimaging. *Pflügers Arch.* **465**, 347–359 (2013).
92. Grimm, J. B. & Lavis, L. D. Caveat fluorophore: an insiders' guide to small-molecule fluorescent labels. *Nat. Methods* **19**, 149–158 (2022).
93. Lin, J., Yang, K. & J. New, E. Strategies for organelle targeting of fluorescent probes. *Org. Biomol. Chem.* **19**, 9339–9357 (2021).
94. Lang, K. & Chin, J. W. Cellular incorporation of unnatural amino acids and bioorthogonal labeling of proteins. *Chem. Rev.* **114**, 4764–4806 (2014).
95. Chalfie, M., Tu, Y., Euskirchen, G., Ward, W. W. & Prasher, D. C. Green fluorescent protein as a marker for gene expression. *Science* **263**, 802–805 (1994).

96. Tsien, R. Y. Constructing and exploiting the fluorescent protein paintbox (Nobel lecture). *Angew. Chem. Int. Ed.* **48**, 5612–5626 (2009).
97. Xia, T., Li, N. & Fang, X. Single-molecule fluorescence imaging in living cells. *Annu. Rev. Phys. Chem.* **64**, 459–480 (2013).
98. Domaille, D. W., Que, E. L. & Chang, C. J. Synthetic fluorescent sensors for studying the cell biology of metals. *Nat. Chem. Biol.* **4**, 168–175 (2008).
99. Torres-Ocampo, A. P. & Palmer, A. E. Genetically encoded fluorescent sensors for metals in biology. *Curr. Opin. Chem. Biol.* **74**, 102284 (2023).
100. Tan, N. K., Zhu, J. & New, E. J. Fluorescent sensors of the cellular environment. in *Molecular Fluorescent Sensors for Cellular Studies* 173–200 (John Wiley & Sons, Ltd, 2022). doi:10.1002/9781119749844.ch6.
101. St-Pierre, F., Chavarha, M. & Lin, M. Z. Designs and sensing mechanisms of genetically encoded fluorescent voltage indicators. *Curr. Opin. Chem. Biol.* **27**, 31–38 (2015).
102. Hong, S., Pawel, G. T., Pei, R. & Lu, Y. Recent progress in developing fluorescent probes for imaging cell metabolites. *Biomed. Mater.* **16**, 044108 (2021).
103. Liang, R., Broussard, G. J. & Tian, L. Imaging chemical neurotransmission with genetically encoded fluorescent sensors. *ACS Chem. Neurosci.* **6**, 84–93 (2015).
104. Guo, C., Sedgwick, A. C., Hirao, T. & Sessler, J. L. Supramolecular fluorescent sensors: an historical overview and update. *Coord. Chem. Rev.* **427**, 213560 (2021).
105. Jun, M. E., Roy, B. & Ahn, K. H. “Turn-on” fluorescent sensing with “reactive” probes. *Chem. Commun.* **47**, 7583–7601 (2011).
106. Singh, H., Tiwari, K., Tiwari, R., Pramanik, S. K. & Das, A. Small molecule as fluorescent probes for monitoring intracellular enzymatic transformations. *Chem. Rev.* **119**, 11718–11760 (2019).
107. de Silva, A. P., Gunaratne, H. Q. N., Gunlaugsson, T., Huxley, A. J. M., McCoy, C. P., Rademacher, J. T. & Rice, T. E. Signaling recognition events with fluorescent sensors and switches. *Chem. Rev.* **97**, 1515–1566 (1997).
108. Wu, L., Huang, C., P. Emery, B., C. Sedgwick, A., D. Bull, S., He, X.-P., Tian, H., Yoon, J., L. Sessler, J. & D. James, T. Förster resonance energy transfer (FRET)-based small-molecule sensors and imaging agents. *Chem. Soc. Rev.* **49**, 5110–5139 (2020).

109. Østergaard, H., Henriksen, A., Hansen, F. G. & Winther, J. R. Shedding light on disulfide bond formation: engineering a redox switch in green fluorescent protein. *EMBO J.* **20**, 5853–5862 (2001).
110. Dooley, C. T., Dore, T. M., Hanson, G. T., Jackson, W. C., Remington, S. J. & Tsien, R. Y. Imaging dynamic redox changes in mammalian cells with green fluorescent protein indicators. *J. Biol. Chem.* **279**, 22284–22293 (2004).
111. Gutscher, M., Pauleau, A. L., Marty, L., Brach, T., Wabnitz, G. H., Samstag, Y., Meyer, A. J. & Dick, T. P. Real-time imaging of the intracellular glutathione redox potential. *Nat. Methods* **5**, 553–559 (2008).
112. Hanson, G. T., Aggeler, R., Oglesbee, D., Cannon, M., Capaldi, R. A., Tsien, R. Y. & Remington, S. J. Investigating mitochondrial redox potential with redox-sensitive green fluorescent protein indicators. *J. Biol. Chem.* **279**, 13044–13053 (2004).
113. Molinari, P. E., Krapp, A. R., Weiner, A., Beyer, H. M., Kondadi, A. K., Blomeier, T., López, M., Bustos-Sanmamed, P., Tevere, E., Weber, W., Reichert, A. S., Calcaterra, N. B., Beller, M., Carrillo, N. & Zurbriggen, M. D. NERNST: a genetically-encoded ratiometric non-destructive sensing tool to estimate NADP(H) redox status in bacterial, plant and animal systems. *Nat. Commun.* **14**, 3277 (2023).
114. Kaur, A. & New, E. J. Bioinspired small-molecule tools for the imaging of redox biology. *Acc. Chem. Res.* **52**, 623–632 (2019).
115. Ahmad, M., Anjum, N. A., Asif, A. & Ahmad, A. Real-time monitoring of glutathione in living cells using genetically encoded FRET-based ratiometric nanosensor. *Sci. Rep.* **10**, 992 (2020).
116. Pak, V. V., Ezeriņa, D., Lyublinskaya, O. G., Pedre, B., Tyurin-Kuzmin, P. A., Mishina, N. M., Thauvin, M., Young, D., Wahni, K., Gache, S. A. M., Demidovich, A. D., Ermakova, Y. G., Maslova, Y. D., Shokhina, A. G., Eroglu, E., Bilan, D. S., Bogeski, I., Michel, T., Vriza, S., Messens, J. & Belousov, V. V. Ultrasensitive genetically encoded indicator for hydrogen peroxide identifies roles for the oxidant in cell migration and mitochondrial function. *Cell Metab.* **31**, 642-653.e6 (2020).
117. Ermakova, Y. G., Bilan, D. S., Matlashov, M. E., Mishina, N. M., Markvicheva, K. N., Subach, O. M., Subach, F. V., Bogeski, I., Hoth, M., Enikolopov, G. & Belousov, V. V. Red fluorescent genetically encoded indicator for intracellular hydrogen peroxide. *Nat. Commun.* **5**, 5222 (2014).

-
118. Leavesley, S. J., Annamdevula, N., Boni, J., Stocker, S., Grant, K., Troyanovsky, B., Rich, T. C. & Alvarez, D. F. Hyperspectral imaging microscopy for identification and quantitative analysis of fluorescently-labeled cells in highly autofluorescent tissue. *J. Biophotonics* **5**, 67–84 (2012).
119. Ash, C., Dubec, M., Donne, K. & Bashford, T. Effect of wavelength and beam width on penetration in light-tissue interaction using computational methods. *Lasers Med. Sci.* **32**, 1909–1918 (2017).
120. Jiang, X., Chen, J., Bajić, A., Zhang, C., Song, X., Carroll, S. L., Cai, Z.-L., Tang, M., Xue, M., Cheng, N., Schaaf, C. P., Li, F., MacKenzie, K. R., Ferreón, A. C. M., Xia, F., Wang, M. C., Maletić-Savatić, M. & Wang, J. Quantitative real-time imaging of glutathione. *Nat. Commun.* **8**, 16087 (2017).
121. Jiang, X., Zhang, C., Chen, J., Choi, S., Zhou, Y., Zhao, M., Song, X., Chen, X., Maletić-Savatić, M., Palzkill, T., Moore, D., Wang, M. C. & Wang, J. Quantitative real-time imaging of glutathione with subcellular resolution. *Antioxid. Redox Signal.* **30**, 1900–1910 (2019).
122. Jiang, X., Yu, Y., Chen, J., Zhao, M., Chen, H., Song, X., Matzuk, A. J., Carroll, S. L., Tan, X., Sizovs, A., Cheng, N., Wang, M. C. & Wang, J. Quantitative imaging of glutathione in live cells using a reversible reaction-based ratiometric fluorescent probe. *ACS Chem. Biol.* **10**, 864–874 (2015).
123. Jeong, E. M., Yoon, J.-H., Lim, J., Shin, J.-W., Cho, A. Y., Heo, J., Lee, K. B., Lee, J.-H., Lee, W. J., Kim, H.-J., Son, Y. H., Lee, S.-J., Cho, S.-Y., Shin, D.-M., Choi, K. & Kim, I.-G. Real-time monitoring of glutathione in living cells reveals that high glutathione levels are required to maintain stem cell function. *Stem Cell Rep.* **10**, 600–614 (2018).
124. Niu, L.-Y., Guan, Y.-S., Chen, Y.-Z., Wu, L.-Z., Tung, C.-H. & Yang, Q.-Z. BODIPY-based ratiometric fluorescent sensor for highly selective detection of glutathione over cysteine and homocysteine. *J. Am. Chem. Soc.* **134**, 18928–18931 (2012).
125. Wang, F., Zhou, L., Zhao, C., Wang, R., Fei, Q., Luo, S., Guo, Z., Tian, H. & Zhu, W.-H. A dual-response BODIPY-based fluorescent probe for the discrimination of glutathione from cystein and homocystein. *Chem. Sci.* **6**, 2584–2589 (2015).

126. Umezawa, K., Yoshida, M., Kamiya, M., Yamasoba, T. & Urano, Y. Rational design of reversible fluorescent probes for live-cell imaging and quantification of fast glutathione dynamics. *Nat. Chem.* **9**, 279–286 (2017).
127. Bai, X., Ng, K. K.-H., Hu, J. J., Ye, S. & Yang, D. Small-molecule-based fluorescent sensors for selective detection of reactive oxygen species in biological systems. *Annu. Rev. Biochem.* **88**, 605–633 (2019).
128. Sun, P., Zhang, H., Sun, Y. & Liu, J. The recent development of fluorescent probes for the detection of NADH and NADPH in living cells and in vivo. *Spectrochim. Acta A Mol. Biomol. Spectrosc.* **245**, 118919 (2021).
129. Los, G. V., Encell, L. P., McDougall, M. G., Hartzell, D. D., Karassina, N., Zimprich, C., Wood, M. G., Learish, R., Ohana, R. F., Urh, M., Simpson, D., Mendez, J., Zimmerman, K., Otto, P., Vidugiris, G., Zhu, J., Darzins, A., Klaubert, D. H., Bulleit, R. F. & Wood, K. V. HaloTag: a novel protein labeling technology for cell imaging and protein analysis. *ACS Chem. Biol.* **3**, 373–382 (2008).
130. Encell, L. P., Friedman Ohana, R., Zimmerman, K., Otto, P., Vidugiris, G., Wood, M. G., Los, G. V., McDougall, M. G., Zimprich, C., Karassina, N., Learish, R. D., Hurst, R., Hartnett, J., Wheeler, S., Stecha, P., English, J., Zhao, K., Mendez, J., Benink, H. A., Murphy, N., Daniels, D. L., Slater, M. R., Urh, M., Darzins, A., Klaubert, D. H., Bulleit, R. F. & Wood, K. V. Development of a dehalogenase-based protein fusion tag capable of rapid, selective and covalent attachment to customizable ligands. *Curr. Chem. Genomics* **6**, 55–71 (2012).
131. Keppler, A., Gendreizig, S., Gronemeyer, T., Pick, H., Vogel, H. & Johnsson, K. A general method for the covalent labeling of fusion proteins with small molecules in vivo. *Nat. Biotechnol.* **21**, 86–89 (2003).
132. Juillerat, A., Gronemeyer, T., Keppler, A., Gendreizig, S., Pick, H., Vogel, H. & Johnsson, K. Directed evolution of O6-alkylguanine-DNA alkyltransferase for efficient labeling of fusion proteins with small molecules In vivo. *Chem. Biol.* **10**, 313–317 (2003).
133. Gautier, A., Juillerat, A., Heinis, C., Corrêa, I. R., Kindermann, M., Beaufils, F. & Johnsson, K. An engineered protein tag for multiprotein labeling in living cells. *Chem. Biol.* **15**, 128–136 (2008).
134. Gallagher, S. S., Sable, J. E., Sheetz, M. P. & Cornish, V. W. An in vivo covalent TMP-tag based on proximity-induced reactivity. *ACS Chem. Biol.* **4**, 547–556 (2009).

-
135. Hori, Y., Ueno, H., Mizukami, S. & Kikuchi, K. Photoactive yellow protein-based protein labeling system with turn-on fluorescence intensity. *J. Am. Chem. Soc.* **131**, 16610–16611 (2009).
136. Wilhelm, J., Kühn, S., Tarnawski, M., Gotthard, G., Tünnermann, J., Tänzer, T., Karpenko, J., Mertes, N., Xue, L., Uhrig, U., Reinstein, J., Hiblot, J. & Johnsson, K. Kinetic and structural characterization of the self-labeling protein tags HaloTag7, SNAP-tag and CLIP-tag. *Biochemistry* **60**, 2560–2575 (2021).
137. Janssen, D. B. Evolving haloalkane dehalogenases. *Current Opinion in Chemical Biology* **8**, 150–159 (2004).
138. Hori, Y. & Kikuchi, K. Protein labeling with fluorogenic probes for no-wash live-cell imaging of proteins. *Curr. Opin. Chem. Biol.* **17**, 644–650 (2013).
139. Komatsu, T., Johnsson, K., Okuno, H., Bito, H., Inoue, T., Nagano, T. & Urano, Y. Real-time measurements of protein dynamics using fluorescence activation-coupled protein labeling method. *J. Am. Chem. Soc.* **133**, 6745–6751 (2011).
140. Sun, X., Zhang, A., Baker, B., Sun, L., Howard, A., Buswell, J., Maurel, D., Masharina, A., Johnsson, K., Noren, C. J., Xu, M.-Q. & Corrêa Jr., I. R. Development of SNAP-tag fluorogenic probes for wash-free fluorescence imaging. *ChemBioChem* **12**, 2217–2226 (2011).
141. Zhang, C.-J., Li, L., Chen, G. Y. J., Xu, Q.-H. & Yao, S. Q. One- and two-photon live cell imaging using a mutant SNAP-tag protein and its FRET substrate pairs. *Org. Lett.* **13**, 4160–4163 (2011).
142. Takakusa, H., Kikuchi, K., Urano, Y., Higuchi, T. & Nagano, T. Intramolecular fluorescence resonance energy transfer system with coumarin donor included in β -cyclodextrin. *Anal. Chem.* **73**, 939–942 (2001).
143. Lukinavičius, G., Reymond, L., Umezawa, K., Sallin, O., D'Este, E., Göttfert, F., Ta, H., Hell, S. W., Urano, Y. & Johnsson, K. Fluorogenic probes for multicolor imaging in living cells. *J. Am. Chem. Soc.* **138**, 9365–9368 (2016).
144. Lukinavičius, G., Umezawa, K., Olivier, N., Honigmann, A., Yang, G., Plass, T., Mueller, V., Reymond, L., Corrêa Jr, I. R., Luo, Z.-G., Schultz, C., Lemke, E. A., Heppenstall, P., Eggeling, C., Manley, S. & Johnsson, K. A near-infrared fluorophore for live-cell super-resolution microscopy of cellular proteins. *Nat. Chem.* **5**, 132–139 (2013).

145. Wang, L., Tran, M., Roberti, J., Koch, B., Xue, L. & Johnsson, K. A general strategy to develop cell permeable and fluorogenic probes for multicolour nanoscopy. *Nat. Chem.* **12**, 165–172 (2020).
146. Grimm, J. B., Tkachuk, A. N., Xie, L., Choi, H., Mohar, B., Falco, N., Schaefer, K., Patel, R., Zheng, Q., Liu, Z., Lippincott-Schwartz, J., Brown, T. A. & Lavis, L. D. A general method to optimize and functionalize red-shifted rhodamine dyes. *Nat. Methods* **17**, 815–821 (2020).
147. Miró-Vinyals, C., Stein, A., Fischer, S., Ward, T. R. & Deliz Liang, A. HaloTag engineering for enhanced fluorogenicity and kinetics with a styrylpyridium dye. *ChemBioChem* **22**, 3398–3401 (2021).
148. Liu, Y., Miao, K., Dunham, N. P., Liu, H., Fares, M., Boal, A. K., Li, X. & Zhang, X. The Cation– π interaction enables a Halo-Tag fluorogenic probe for fast no-wash live cell imaging and gel-free protein quantification. *Biochemistry* **56**, 1585–1595 (2017).
149. Usama, S. M., Marker, S. C., Li, D.-H., Caldwell, D. R., Stroet, M., Patel, N. L., Tebo, A. G., Hernot, S., Kalen, J. D. & Schnermann, M. Method to diversify cyanine chromophore functionality enables improved biomolecule tracking and intracellular imaging. *J. Am. Chem. Soc.* **145**, 14647–14659 (2023).
150. Gautier, A. & Tebo, A. G. Sensing cellular biochemistry with fluorescent chemical–genetic hybrids. *Curr. Opin. Chem. Biol.* **57**, 58–64 (2020).
151. Zastrow, M. L., Huang, Z. & Lippard, S. J. HaloTag-Based hybrid targetable and ratiometric sensors for intracellular zinc. *ACS Chem. Biol.* **15**, 396–406 (2020).
152. Deo, C., Sheu, S.-H., Seo, J., Clapham, D. E. & Lavis, L. D. Isomeric tuning yields bright and targetable red Ca²⁺ indicators. *J. Am. Chem. Soc.* **141**, 13734–13738 (2019).
153. Ortiz, G., Liu, P., E. Deal, P., K. Nensel, A., N. Martinez, K., Shamardani, K., Adesnik, H. & W. Miller, E. A silicon-rhodamine chemical-genetic hybrid for far red voltage imaging from defined neurons in brain slice. *RCS Chem.Biol.* **2**, 1594–1599 (2021).
154. Straková, K., López-Andarias, J., Jiménez-Rojo, N., Chambers, J. E., Marciniak, S. J., Riezman, H., Sakai, N. & Matile, S. HaloFlippers: a general tool for the fluorescence imaging of precisely localized membrane tension changes in living cells. *ACS Cent. Sci.* **6**, 1376–1385 (2020).

-
155. Cook, A., Walterspiel, F. & Deo, C. HaloTag-based reporters for fluorescence imaging and biosensing. *ChemBioChem* **24**, e202300022 (2023).
156. Hellweg, L., Edenhofer, A., Barck, L., Huppertz, M.-C., Frei, Michelle. S., Tarnawski, M., Bergner, A., Koch, B., Johnsson, K. & Hiblot, J. A general method for the development of multicolor biosensors with large dynamic ranges. *Nat. Chem. Biol.* **19**, 1147–1157 (2023).
157. Sallin, O., Reymond, L., Gondrand, C., Raith, F., Koch, B. & Johnsson, K. Semisynthetic biosensors for mapping cellular concentrations of nicotinamide adenine dinucleotides. *eLife* **7**, e32638 (2018).
158. Makhija, S., Brown, D., Rudlaff, R. M., Doh, J. K., Bourke, S., Wang, Y., Zhou, S., Cheloor-Kovilakam, R. & Huang, B. Versatile labeling and detection of endogenous proteins using tag-assisted split enzyme complementation. *ACS Chem. Biol.* **16**, 671–681 (2021).
159. Deo, C., Abdelfattah, A. S., Bhargava, H. K., Berro, A. J., Falco, N., Farrant, H., Moeyaert, B., Chupanova, M., Lavis, L. D. & Schreiter, E. R. The HaloTag as a general scaffold for far-red tunable chemigenetic indicators. *Nat. Chem. Biol.* **17**, 718–723 (2021).
160. Liu, Y., Fares, M., Dunham, N. P., Gao, Z., Miao, K., Jiang, X., Bollinger, S. S., Boal, A. K. & Zhang, X. AgHalo: a facile fluorogenic sensor to detect drug-induced proteome stress. *Angew. Chem. Int. Ed.* **56**, 8672–8676 (2017).
161. Frei, M. S., Koch, B., Hiblot, J. & Johnsson, K. Live-cell fluorescence lifetime multiplexing using synthetic fluorescent probes. *ACS Chem. Biol.* **17**, 1321–1327 (2022).
162. Frei, M. S., Tarnawski, M., Roberti, M. J., Koch, B., Hiblot, J. & Johnsson, K. Engineered HaloTag variants for fluorescence lifetime multiplexing. *Nat. Methods* **19**, 65–70 (2022).
163. Emmert, S., Quargnali, G., Thallmair, S. & Rivera-Fuentes, P. A locally activatable sensor for robust quantification of organellar glutathione. *Nat. Chem.* **15**, 1415–1421 (2023).
164. Briviba, K., Fraser, G., Sies, H. & Ketterer, B. Distribution of the monochlorobimane-glutathione conjugate between nucleus and cytosol in isolated hepatocytes. *Biochem. J.* **294**, 631–633 (1993).

165. Bucevičius, J., Keller-Findeisen, J., Gilat, T., Hell, S. W. & Lukinavičius, G. Rhodamine–Hoechst positional isomers for highly efficient staining of heterochromatin. *Chem. Sci.* **10**, 1962–1970 (2019).
166. Stagge, F., Mitronova, G. Y., Belov, V. N., Wurm, C. A. & Jakobs, S. Snap-, CLIP- and Halo-tag labelling of budding yeast cells. *PLoS One* **8**, e78745 (2013).
167. Lee, J., Liu, Z., Suzuki, P. H., Ahrens, J. F., Lai, S., Lu, X., Guan, S. & St-Pierre, F. Versatile phenotype-activated cell sorting. *Sci. Adv.* **6**, eabb7438 (2020).
168. Casey, J. R., Grinstein, S. & Orłowski, J. Sensors and regulators of intracellular pH. *Nat. Rev. Mol. Cell Biol.* **11**, 50–61 (2010).
169. Fehrenbacher, K. L., Yang, H.-C., Gay, A. C., Huckaba, T. M. & Pon, L. A. Live cell imaging of mitochondrial movement along actin cables in budding yeast. *Curr. Biol.* **14**, 1996–2004 (2004).
170. Deprey, K. & Kritzer, J. A. HaloTag forms an intramolecular disulfide. *Bioconjugate Chem.* **32**, 964–970 (2021).
171. Cadart, C., Venkova, L., Piel, M. & Cosentino Lagomarsino, M. Volume growth in animal cells is cell cycle dependent and shows additive fluctuations. *eLife* **11**, e70816 (2022).
172. García-Giménez, J. L., Markovic, J., Dasí, F., Queval, G., Schnaubelt, D., Foyer, C. H. & Pallardó, F. V. Nuclear glutathione. *Biochim. Biophys. Acta* **1830**, 3304–3316 (2013).
173. Chen, G. & Deng, X. Cell synchronization by double thymidine block. *Bio Protoc.* **8**, e2994 (2018).
174. Matlashov, M. E., Shcherbakova, D. M., Alvelid, J., Baloban, M., Pennacchietti, F., Shemetov, A. A., Testa, I. & Verkhusha, V. V. A set of monomeric near-infrared fluorescent proteins for multicolor imaging across scales. *Nat. Commun.* **11**, 1–12 (2020).
175. Flohé, L. & Brand, I. Kinetics of glutathione peroxidase. *Biochim. Biophys. Acta* **191**, 541–549 (1969).
176. Lubos, E., Loscalzo, J. & Handy, D. E. Glutathione peroxidase-1 in health and disease: From molecular mechanisms to therapeutic opportunities. *Antioxidants & Redox Signaling* **15**, 1957–1997 (2011).
177. Kille, S., Acevedo-Rocha, C. G., Parra, L. P., Zhang, Z.-G., Opperman, D. J., Reetz, M. T. & Acevedo, J. P. Reducing codon redundancy and screening effort of

- combinatorial protein libraries created by saturation mutagenesis. *ACS Synth. Biol.* **2**, 83–92 (2013).
178. Kristensen, C., Kjeldsen, T., Wiberg, F. C., Schäffer, L., Hach, M., Havelund, S., Bass, J., Steiner, D. F. & Andersen, A. S. Alanine scanning mutagenesis of insulin. *J. Biol. Chem.* **272**, 12978–12983 (1997).
179. Miret, J., Román, R., Benito, M., Casablancas, A., Guillén, M., Álvaro, G. & González, G. Development of a highly efficient production process for recombinant protein expression in *Escherichia coli* NEB10 β . *Biochem. Eng. J.* **159**, 107612 (2020).
180. Tirla, A. & Rivera-Fuentes, P. Development of a photoactivatable phosphine probe for induction of intracellular reductive stress with single-cell precision. *Angew. Chem. Int. Ed.* **128**, 14929–14932 (2016).
181. Nguyen, J., Tirla, A. & Rivera-Fuentes, P. Disruption of mitochondrial redox homeostasis by enzymatic activation of a trialkylphosphine probe. *Org. Biomol. Chem.* **19**, 2681–2687 (2021).
182. Cline, D. J., Redding, S. E., Brohawn, S. G., Psathas, J. N., Schneider, J. P. & Thorpe, C. New water-soluble phosphines as reductants of peptide and protein disulfide bonds: reactivity and membrane permeability. *Biochemistry* **43**, 15195–15203 (2004).
183. Lipinski, C. A., Lombardo, F., Dominy, B. W. & Feeney, P. J. Experimental and computational approaches to estimate solubility and permeability in drug discovery and development settings. *Adv. Drug Deliv. Rev.* **23**, 3–25 (1997).
184. Frei, M. S., Hoess, P., Lampe, M., Nijmeijer, B., Kueblbeck, M., Ellenberg, J., Wadepohl, H., Ries, J., Pitsch, S., Reymond, L. & Johnsson, K. Photoactivation of silicon rhodamines via a light-induced protonation. *Nat. Commun.* **10**, 4580 (2019).
185. Vaughan, J. C., Dempsey, G. T., Sun, E. & Zhuang, X. Phosphine quenching of cyanine dyes as a versatile tool for fluorescence microscopy. *J. Am. Chem. Soc.* **135**, 1197–1200 (2013).
186. Kompa, J., Bruins, J., Glogger, M., Wilhelm, J., Frei, M. S., Tarnawski, M., D’Este, E., Heilemann, M., Hiblot, J. & Johnsson, K. Exchangeable HaloTag ligands for super-resolution fluorescence microscopy. *J. Am. Chem. Soc.* **145**, 3075–3083 (2023).
187. Piehler, J., Holtmannspötter, M., Wienbeucker, E., Dellmann, T., Watrinet, I., Garcia Saez, A. J., Johnsson, K. & Kurre, R. Reversible live-cell labeling with retro-engineered HaloTags enables long-term high- and super-resolution imaging. *Angew. Chem. Int. Ed.* **62**, e202219050 (2023).

188. Clark, S. A., Singh, V., Vega Mendoza, D., Margolin, W. & Kool, E. T. Light-up “channel dyes” for haloalkane-based protein labeling in vitro and in bacterial cells. *Bioconjugate Chem.* **27**, 2839–2843 (2016).
189. Troitskaya, V. I., Oksengendler, I. G., Pazenok, S. V., Lyubich, M. S., Larina, S. M. & Yagupol'skii, L. M. Cyanine dyes from derivatives of 4-, 5-, and 6-trifluoromethylindolenines. *Chem. Heterocycl. Compd.* **18**, 39–43 (1982).
190. Tirla, A. Development of photoactivatable phosphines for the induction of reductive stress and peptides for subcellular targeting. (ETH Zurich, 2019). doi:10.3929/ETHZ-B-000370541.
191. Liu, J., Sun, Y.-Q., Huo, Y., Zhang, H., Wang, L., Zhang, P., Song, D., Shi, Y. & Guo, W. Simultaneous fluorescence sensing of Cys and GSH from different emission channels. *J. Am. Chem. Soc.* **136**, 574–577 (2014).
192. Hettie, K. S. & Glass, T. E. Coumarin-3-aldehyde as a scaffold for the design of tunable PET-modulated fluorescent sensors for neurotransmitters. *Chem. Eur. J.* **20**, 17488–17499 (2014).
193. Zhang, Y., Chen, Y., Fang, H., Wang, Y., Li, S., Yuan, H., Yao, S., Qin, S., He, W. & Guo, Z. A ratiometric pH probe for acidification tracking in dysfunctional mitochondria and tumour tissue in vivo. *J. Mater. Chem. B* **10**, 5422–5429 (2022).
194. Richter, M. F., Drown, B. S., Riley, A. P., Garcia, A., Shirai, T., Svec, R. L. & Hergenrother, P. J. Predictive compound accumulation rules yield a broad-spectrum antibiotic. *Nature* **545**, 299–304 (2017).
195. Martin, A. & Rivera-Fuentes, P. A general strategy to develop fluorogenic polymethine dyes for bioimaging. *Nat. Chem.* **16**, 28–35 (2024).
196. Štacková, L., Štacko, P. & Klán, P. Approach to a substituted heptamethine cyanine chain by the ring opening of Zincke salts. *J. Am. Chem. Soc.* **141**, 7155–7162 (2019).
197. Gadella, T. W. J., van Weeren, L., Stouthamer, J., Hink, M. A., Wolters, A. H. G., Giepmans, B. N. G., Aumonier, S., Dupuy, J. & Royant, A. mScarlet3: a brilliant and fast-maturing red fluorescent protein. *Nat. Methods* **20**, 541–545 (2023).
198. Ma, D., Yuan, Q., Peng, F., Paredes, V., Zeng, H., Osikpa, E. C., Yang, Q., Peddi, A., Patel, A., Liu, M. S., Sun, Z. & Gao, X. Engineered PROTAC-CID systems for mammalian inducible gene regulation. *J. Am. Chem. Soc.* **145**, 1593–1606 (2023).

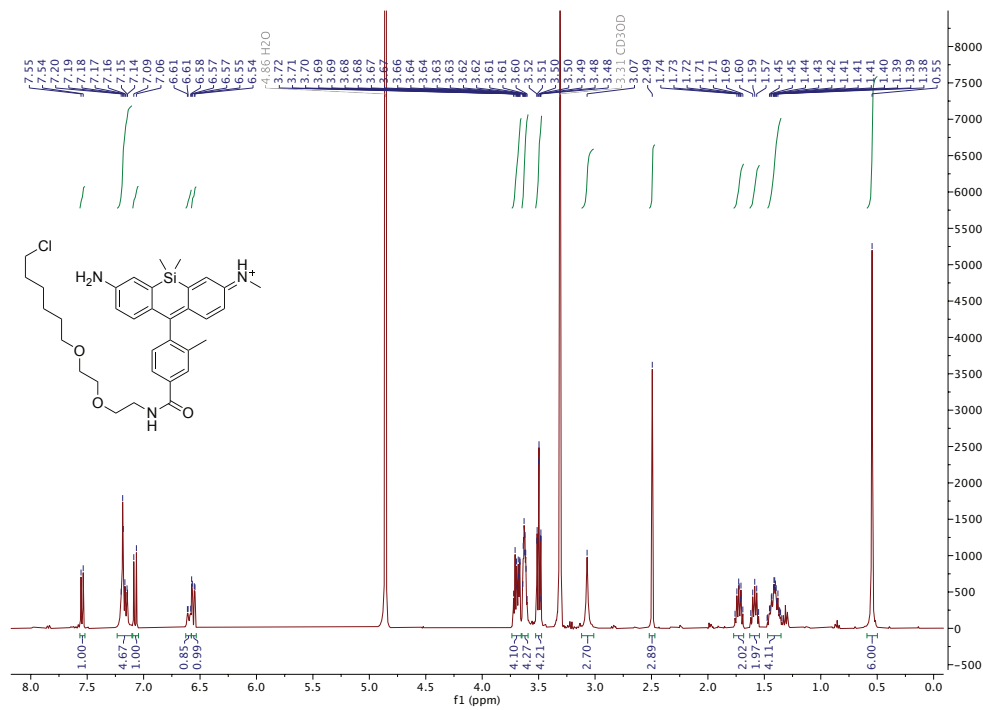
-
199. Polstein, L. R. & Gersbach, C. A. Light-inducible spatiotemporal control of gene activation by customizable zinc finger transcription factors. *J. Am. Chem. Soc.* **134**, 16480–16483 (2012).
200. Klymchenko, A. S. Solvatochromic and fluorogenic dyes as environment-sensitive probes: design and biological applications. *Acc. Chem. Res.* **50**, 366–375 (2017).
201. Colom, A., Derivery, E., Soleimanpour, S., Tomba, C., Molin, M. D., Sakai, N., González-Gaitán, M., Matile, S. & Roux, A. A fluorescent membrane tension probe. *Nat. Chem.* **10**, 1118–1125 (2018).
202. Rennick, J. J., Nowell, C. J., Pouton, C. W. & Johnston, A. P. R. Resolving subcellular pH with a quantitative fluorescent lifetime biosensor. *Nat. Commun.* **13**, 6023 (2022).
203. Gandioso, A., Bresolí-Obach, R., Nin-Hill, A., Bosch, M., Palau, M., Galindo, A., Contreras, S., Rovira, A., Rovira, C., Nonell, S. & Marchán, V. Redesigning the coumarin scaffold into small bright fluorophores with far-red to near-infrared emission and large Stokes shifts useful for cell imaging. *J. Org. Chem.* **83**, 1185–1195 (2018).
204. Wang, P., Hecht, F., Ossato, G., Tille, S., Fraser, S. E. & Junge, J. A. Complex wavelet filter improves FLIM phasors for photon starved imaging experiments. *Biomed. Opt. Express* **12**, 3463–3473 (2021).
205. Digman, M. A., Caiolfa, V. R., Zamai, M. & Gratton, E. The phasor approach to fluorescence lifetime imaging analysis. *Biophys. J.* **94**, L14–L16 (2008).
206. Karbowski, M. & Youle, R. J. Dynamics of mitochondrial morphology in healthy cells and during apoptosis. *Cell Death Differ* **10**, 870–880 (2003).
207. Marques, S. M., Slanska, M., Chmelova, K., Chaloupkova, R., Marek, M., Clark, S., Damborsky, J., Kool, E. T., Bednar, D. & Prokop, Z. Mechanism-based strategy for optimizing HaloTag protein labeling. *JACS Au* **2**, 1324–1337 (2022).
208. Bansal, A. & Simon, M. C. Glutathione metabolism in cancer progression and treatment resistance. *J. Cell Biol.* **217**, 2291–2298 (2018).
209. Fulmer, G. R., Miller, A. J. M., Sherden, N. H., Gottlieb, H. E., Nudelman, A., Stoltz, B. M., Bercaw, J. E. & Goldberg, K. I. NMR chemical shifts of trace impurities: Common laboratory solvents, organics, and gases in deuterated solvents relevant to the organometallic chemist. *Organometallics* **29**, 2176–2179 (2010).
210. Kabsch, W. XDS. *Acta Crystallogr. D* **66**, 125–132 (2010).

211. Liebschner, D., Afonine, P. V., Baker, M. L., Bunkóczi, G., Chen, V. B., Croll, T. I., Hintze, B., Hung, L.-W., Jain, S., McCoy, A. J., Moriarty, N. W., Oeffner, R. D., Poon, B. K., Prisant, M. G., Read, R. J., Richardson, J. S., Richardson, D. C., Sammito, M. D., Sobolev, O. V., Stockwell, D. H., Terwilliger, T. C., Urzhumtsev, A. G., Videau, L. L., Williams, C. J. & Adams, P. D. Macromolecular structure determination using X-rays, neutrons and electrons: recent developments in Phenix. *Acta Crystallogr. D* **75**, 861–877 (2019).
212. Emsley, P., Lohkamp, B., Scott, W. G. & Cowtan, K. Features and development of Coot. *Acta Crystallogr. D* **66**, 486–501 (2010).
213. Schrödinger, LLC. The PyMOL molecular graphics system, Version 1.8. (2015).
214. Abraham, M. J., Murtola, T., Schulz, R., Páll, S., Smith, J. C., Hess, B. & Lindahl, E. GROMACS: High performance molecular simulations through multi-level parallelism from laptops to supercomputers. *SoftwareX* **1–2**, 19–25 (2015).
215. Schmid, N., Eichenberger, A. P., Choutko, A., Riniker, S., Winger, M., Mark, A. E. & van Gunsteren, W. F. Definition and testing of the GROMOS force-field versions 54A7 and 54B7. *Eur. Biophys. J.* **40**, 843–856 (2011).
216. Malde, A. K., Zuo, L., Breeze, M., Stroet, M., Poger, D., Nair, P. C., Oostenbrink, C. & Mark, A. E. An automated force field topology builder (ATB) and repository: Version 1.0. *J. Chem. Theory Comput.* **7**, 4026–4037 (2011).
217. Stroet, M., Caron, B., Visscher, K. M., Geerke, D. P., Malde, A. K. & Mark, A. E. Automated topology builder Version 3.0: Prediction of solvation free enthalpies in water and hexane. *J. Chem. Theory Comput.* **14**, 5834–5845.
218. Bussi, G., Donadio, D. & Parrinello, M. Canonical sampling through velocity rescaling. *J. Chem. Phys.* **126**, 014101 (2007).
219. Berendsen, H. J. C., Postma, J. P. M., van Gunsteren, W. F., DiNola, A. & Haak, J. R. Molecular dynamics with coupling to an external bath. *J. Chem. Phys.* **81**, 3684–3690 (1984).
220. Parrinello, M. & Rahman, A. Polymorphic transitions in single crystals: A new molecular dynamics method. *J. Appl. Phys.* **52**, 7182–7190 (1981).
221. Hess, B. P-LINCS: A parallel linear constraint solver for molecular simulation. *J. Chem. Theory Comput.* 116–122 (2008) doi:10.1021/ct700200b.
222. Uno, S. N., Kamiya, M., Yoshihara, T., Sugawara, K., Okabe, K., Tarhan, M. C., Fujita, H., Funatsu, T., Okada, Y., Tobita, S. & Urano, Y. A spontaneously blinking

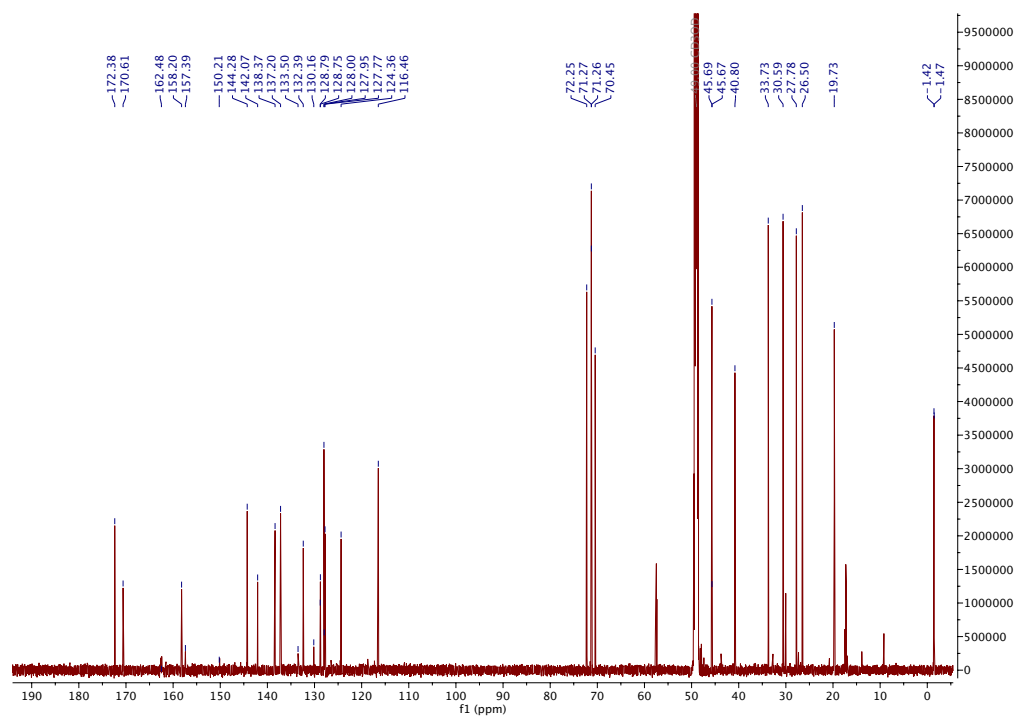
- fluorophore based on intramolecular spirocyclization for live-cell super-resolution imaging. *Nat. Chem.* **6**, 681–689 (2014).
223. Stringer, C., Wang, T., Michaelos, M. & Pachitariu, M. Cellpose: a generalist algorithm for cellular segmentation. *Nat. Methods* **18**, 100–106 (2021).
224. Numasawa, K., Hanaoka, K., Saito, N., Yamaguchi, Y., Ikeno, T., Echizen, H., Yasunaga, M., Komatsu, T., Ueno, T., Miura, M., Nagano, T. & Urano, Y. A fluorescent probe for rapid, high-contrast visualization of folate-receptor-expressing tumors in vivo. *Angew. Chem. Int. Ed.* **59**, 6015–6020 (2020).
225. Hallett, A. J., Christian, P., Jones, J. E. & Pope, S. J. A. Luminescent, water-soluble gold nanoparticles functionalised with 3MLCT emitting rhenium complexes. *Chem. Commun.* 4278–4280 (2009) doi:10.1039/B905692K.
226. Zeng, G., Xing, S., Wang, X., Yang, Y., Ma, D., Liang, H., Gao, L., Hua, J., Li, G., Shi, Z. & Feng, S. 3d–4f Metal–organic framework with dual luminescent centers that efficiently discriminates the isomer and homologues of small organic molecules. *Inorg. Chem.* **55**, 1089–1095 (2016).
227. Owens, E. A., Bruschi, N., Tawney, J. G. & Henary, M. A microwave-assisted and environmentally benign approach to the synthesis of near-infrared fluorescent pentamethine cyanine dyes. *Dyes Pigments* **113**, 27–37 (2015).
228. Shivashimpi, G. M., Pandey, S. S., Watanabe, R., Fujikawa, N., Ogomi, Y., Yamaguchi, Y. & Hayase, S. Novel unsymmetrical squaraine dye bearing cyanoacrylic acid anchoring group and its photosensitization behavior. *Tetrahedron Lett.* **53**, 5437–5440 (2012).
229. Punzi, A., Capozzi, M. a. M., Fino, V., Carlucci, C., Suriano, M., Mesto, E., Schingaro, E., Orgiu, E., Bonacchi, S., Leydecker, T., Samorì, P., Musio, R. & Farinola, G. M. Croconaines as molecular materials for organic electronics: synthesis, solid state structure and use in transistor devices. *J. Mater. Chem. C* **4**, 3138–3142 (2016).
230. Goedhart, J., von Stetten, D., Noirclerc-Savoye, M., Lelimosin, M., Joosen, L., Hink, M. A., van Weeren, L., Gadella, T. W. J. & Royant, A. Structure-guided evolution of cyan fluorescent proteins towards a quantum yield of 93%. *Nat. Commun.* **3**, 751 (2012).

10 Appendix

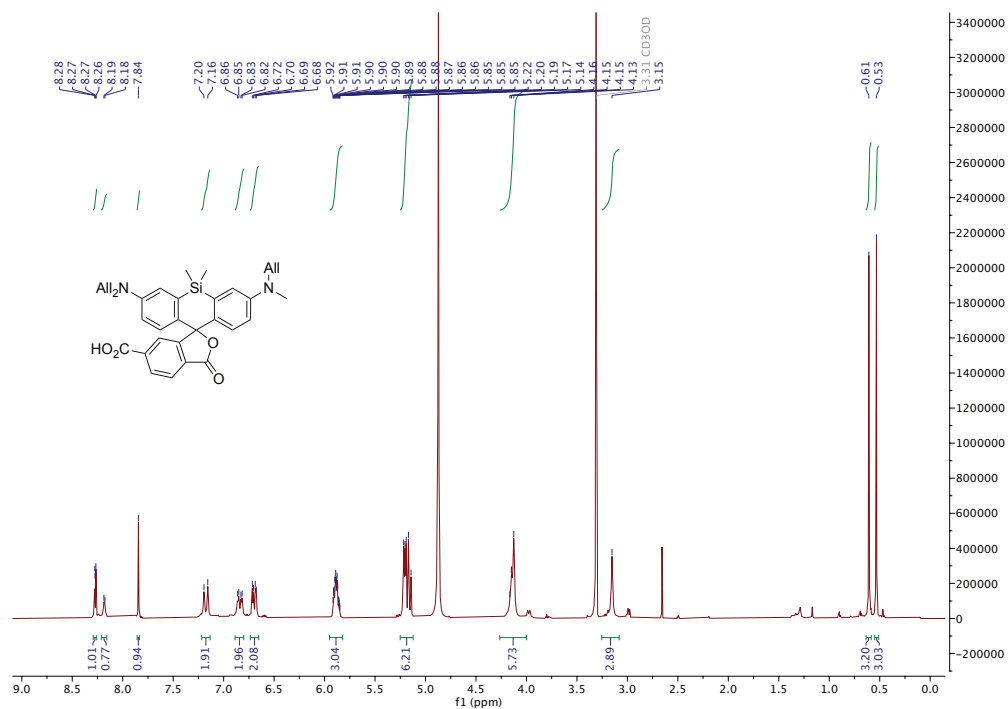
10.1 NMR spectra



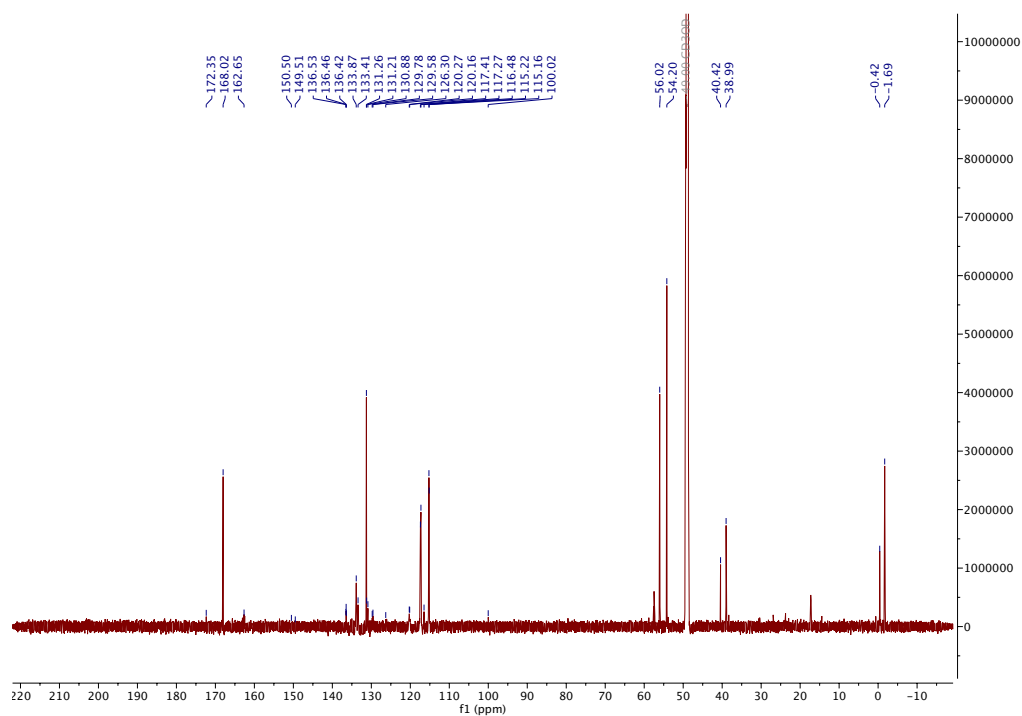
¹H-NMR (400 MHz, CD₃OD) of the Me-TRaQ-G ligand.



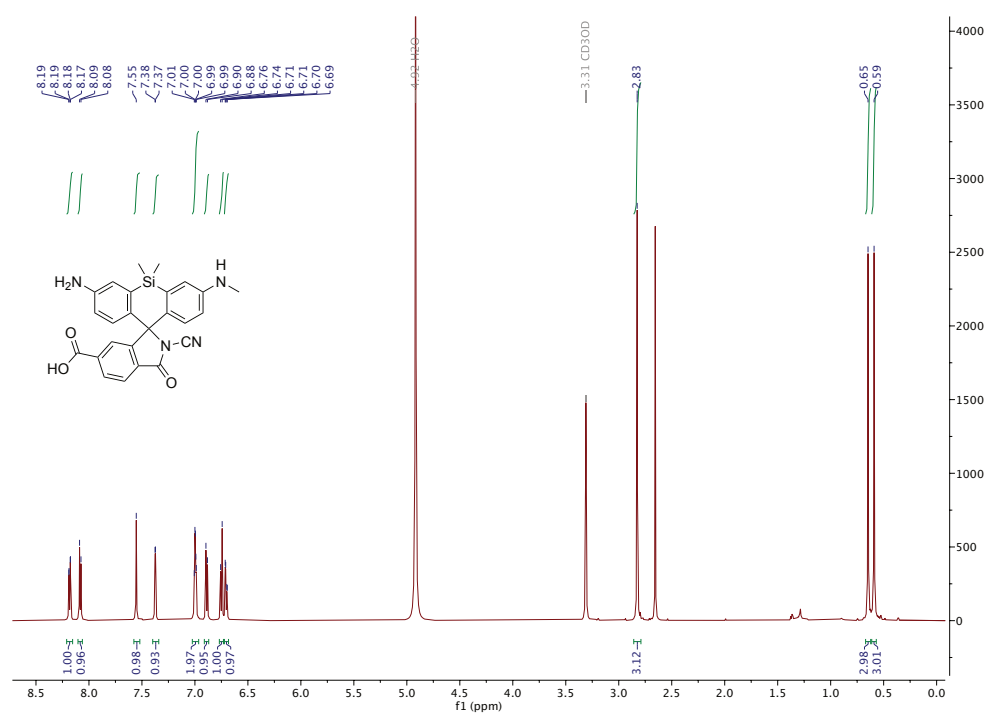
¹³C-NMR (201 MHz, CD₃OD) of the Me-TRaQ-G ligand.



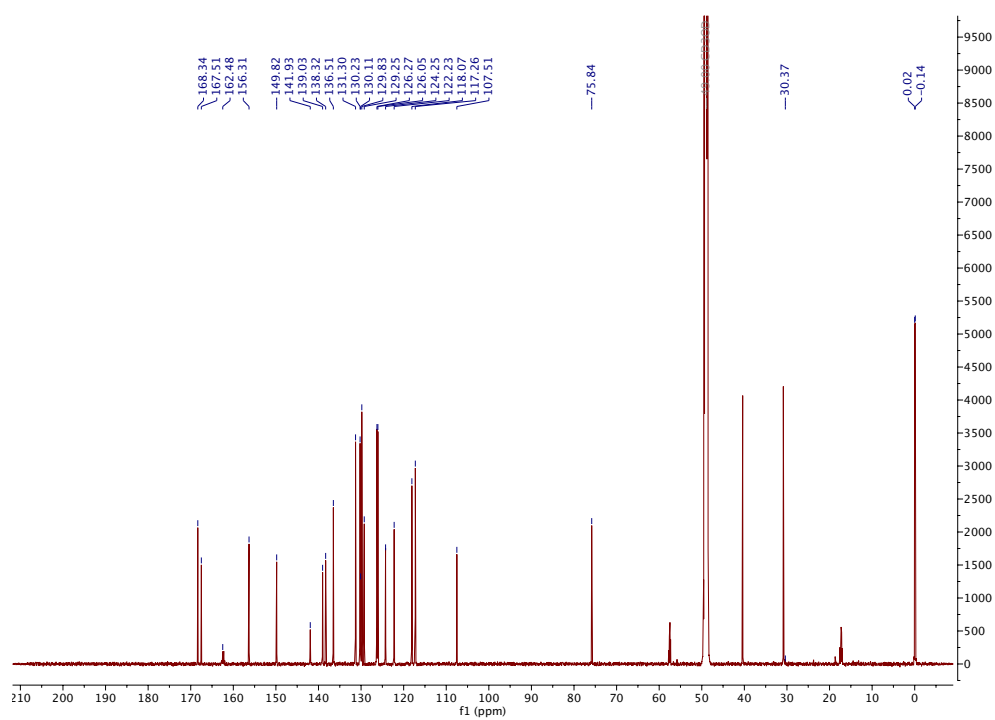
¹H-NMR (800 MHz, CD₃OD) of compound 5.



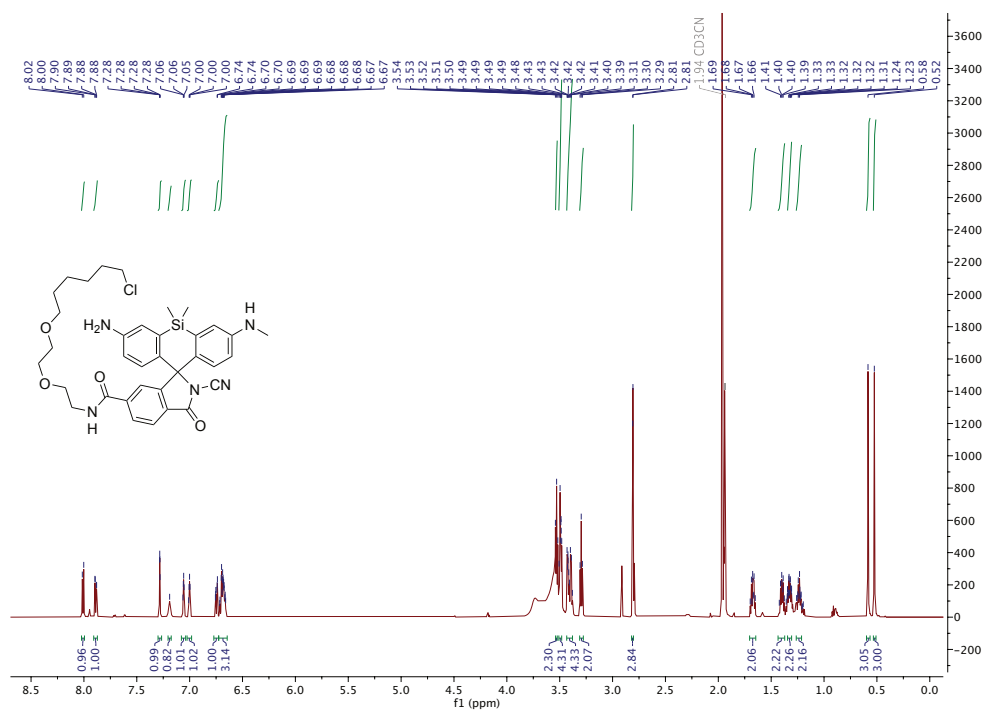
¹³C-NMR (201 MHz, CD₃OD) of compound 5.



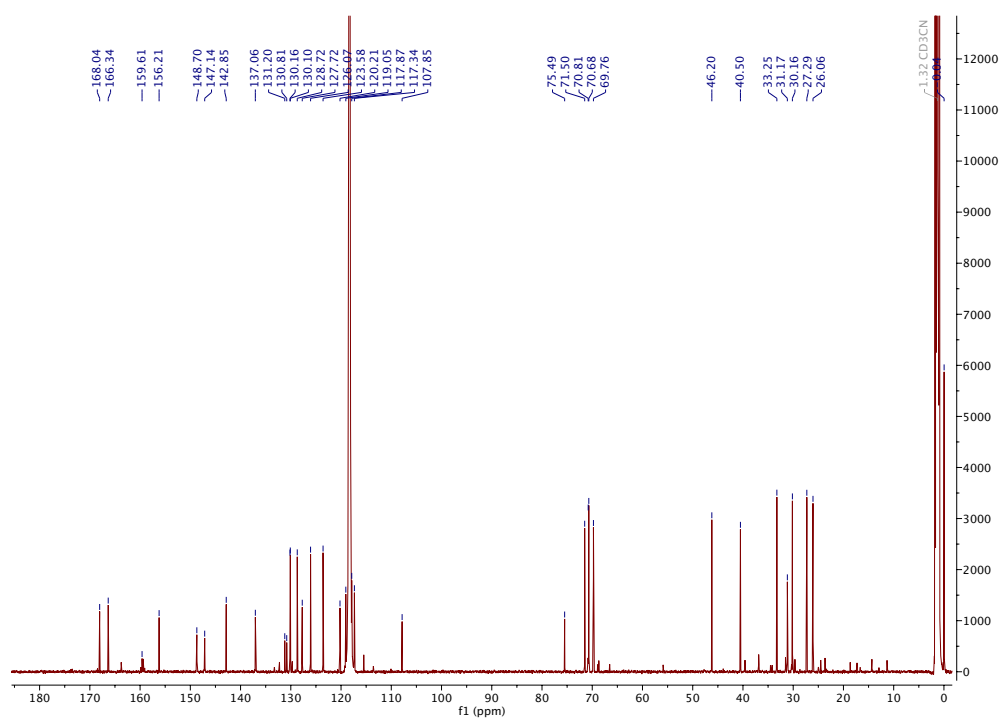
¹H-NMR (600 MHz, CD₃OD) of 7.



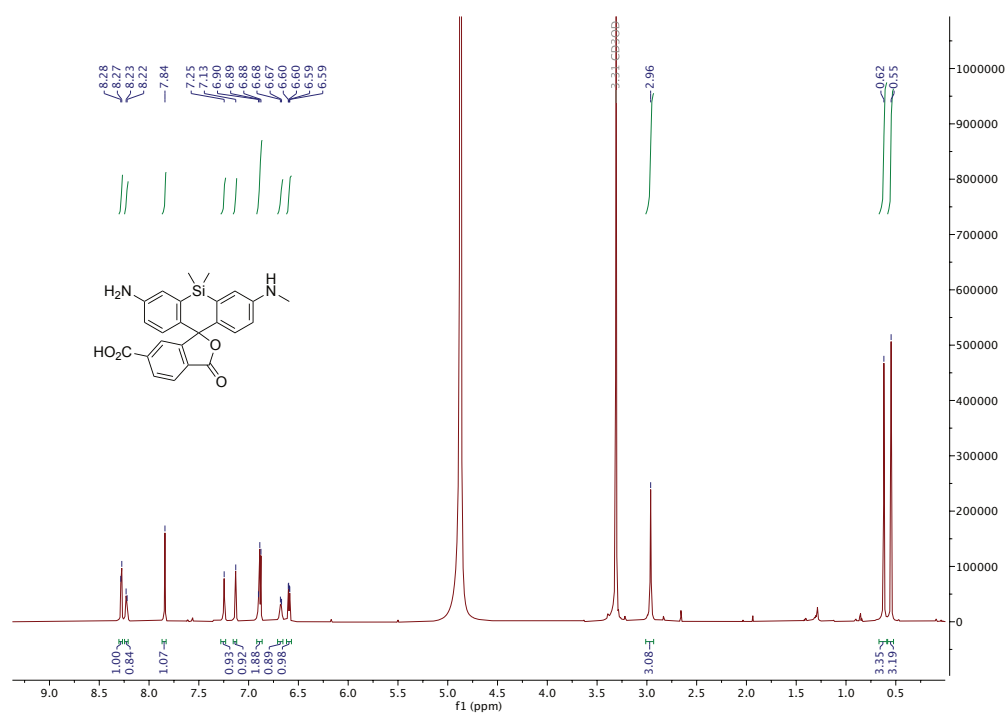
¹³C-NMR (151 MHz, CD₃OD) of compound 7.



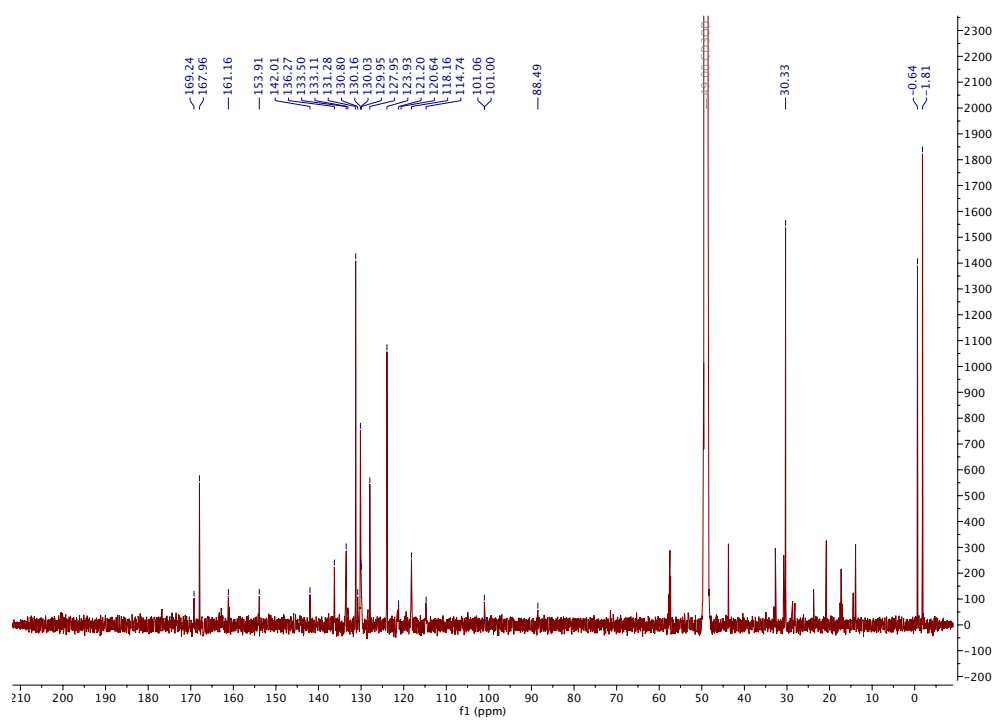
¹H-NMR (600 MHz, CD₃CN) of the TRaQ-G ligand.



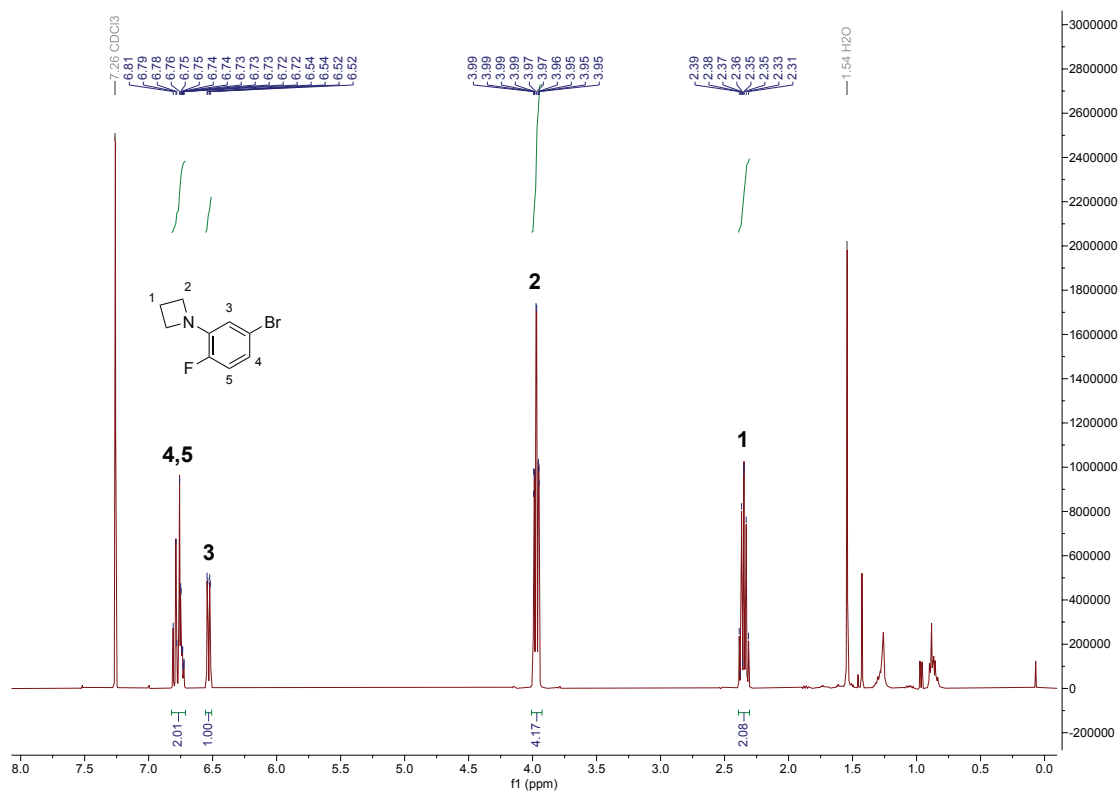
¹³C-NMR (151 MHz, CD₃CN) of the TRaQ-G ligand.



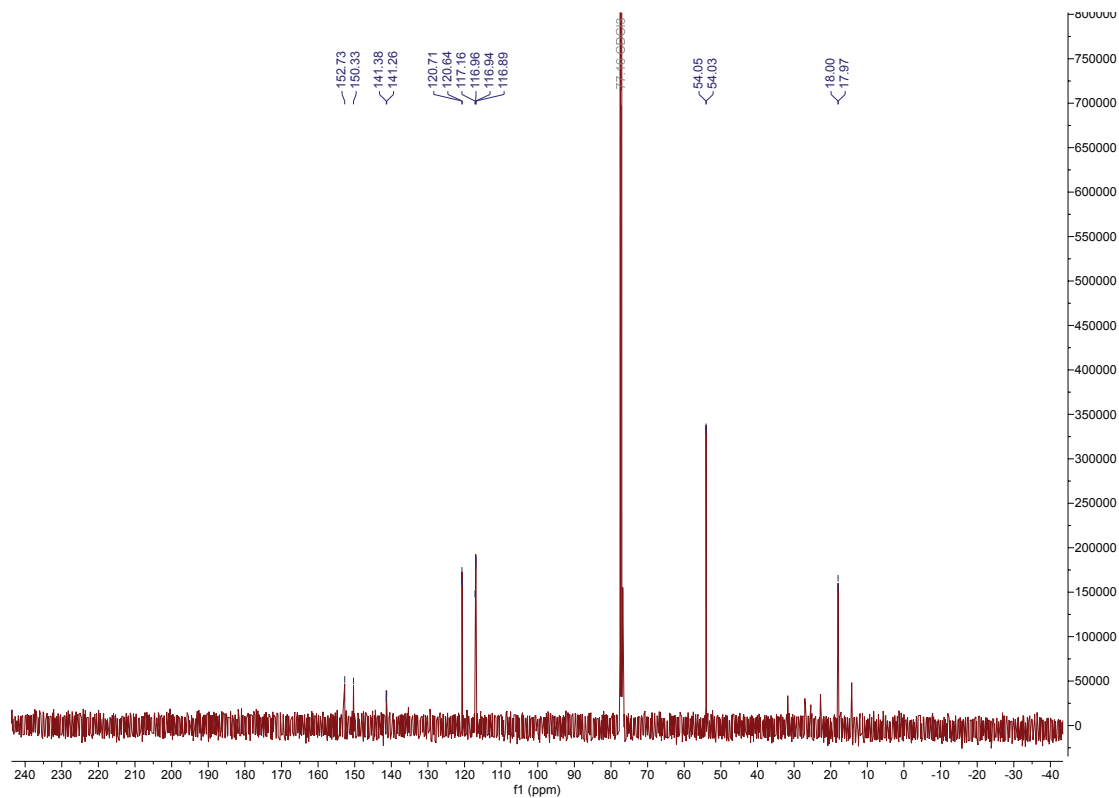
$^1\text{H-NMR}$ (800 MHz, CD_3OD) of compound **8**.



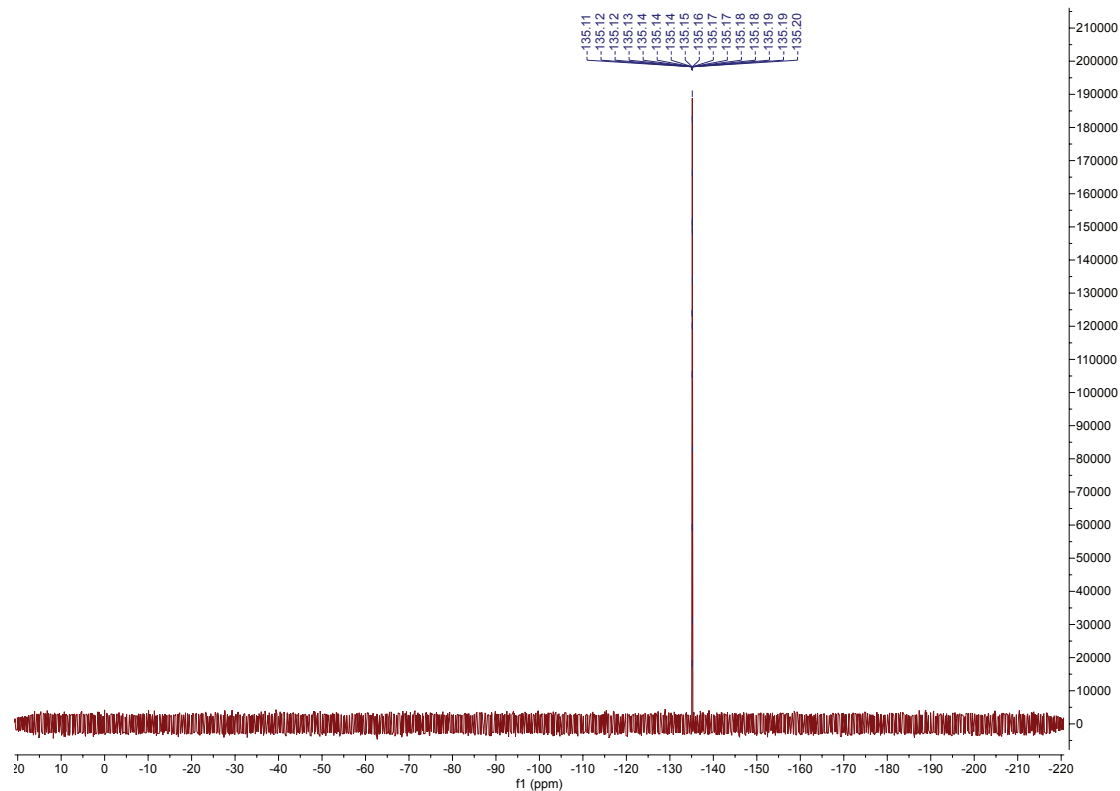
$^{13}\text{C-NMR}$ (201 MHz, CD_3OD) of compound **8**.



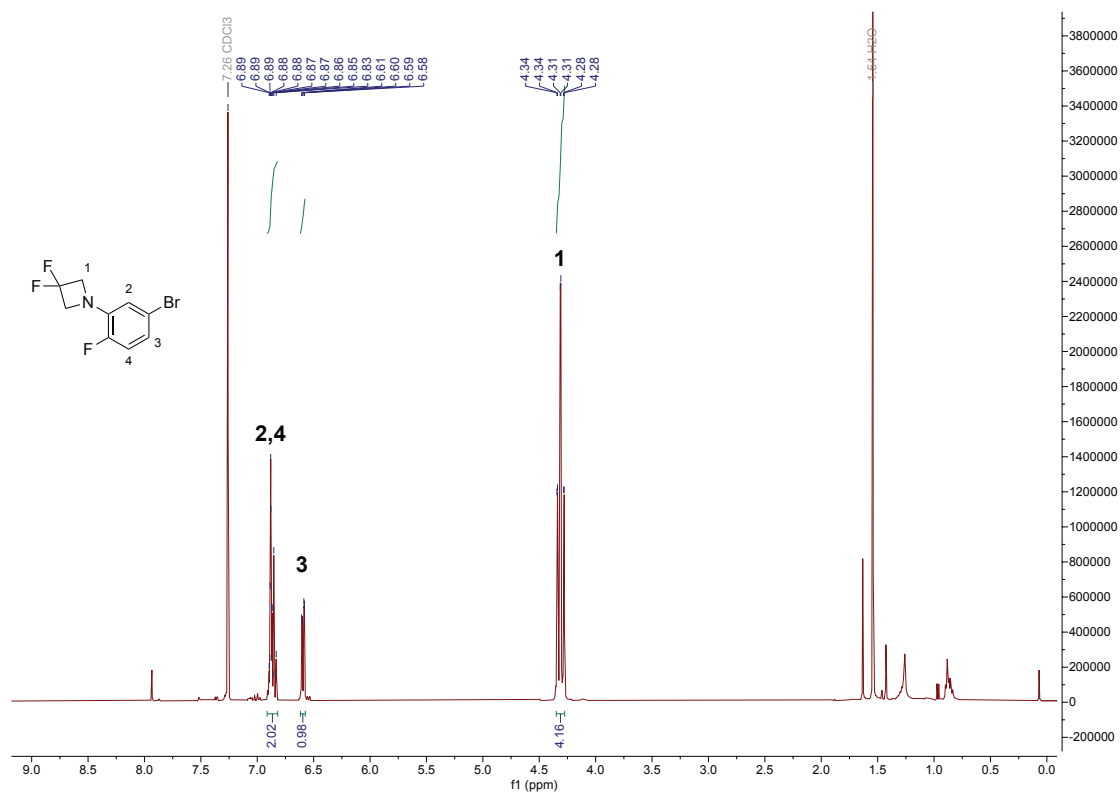
¹H NMR (400 MHz, CDCl₃) of compound **14a**.



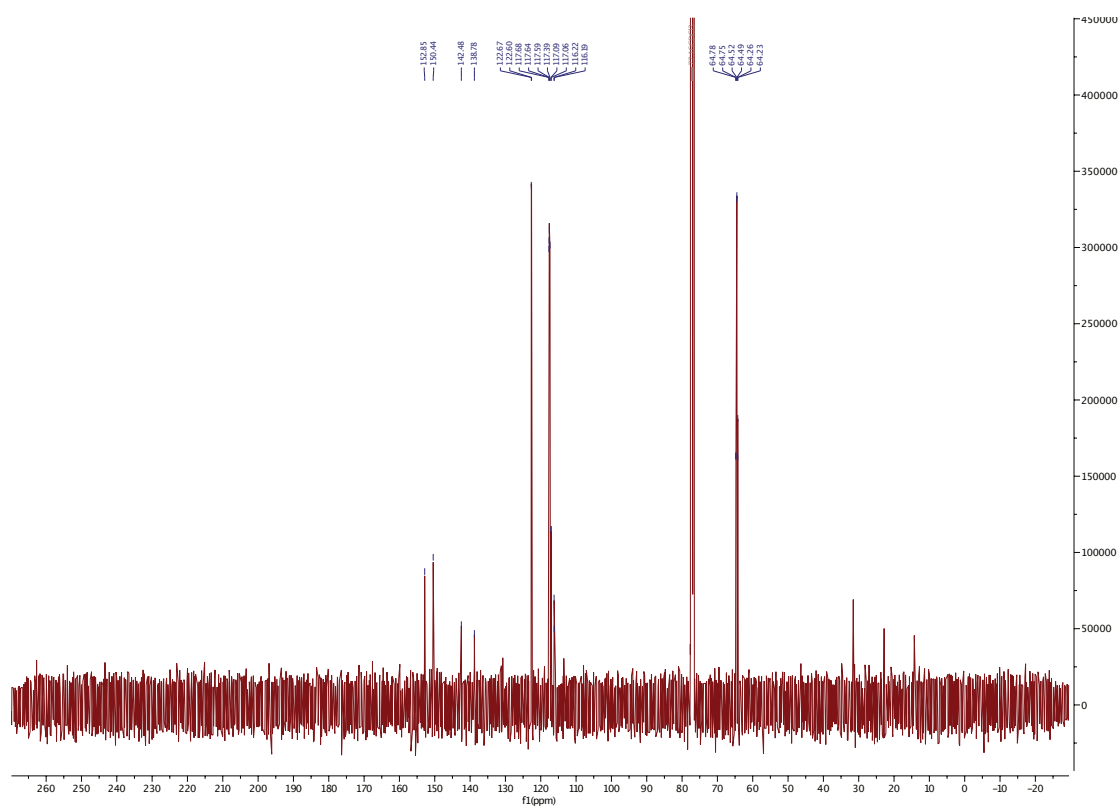
¹³C NMR (101 MHz, CDCl₃) of compound **14a**.



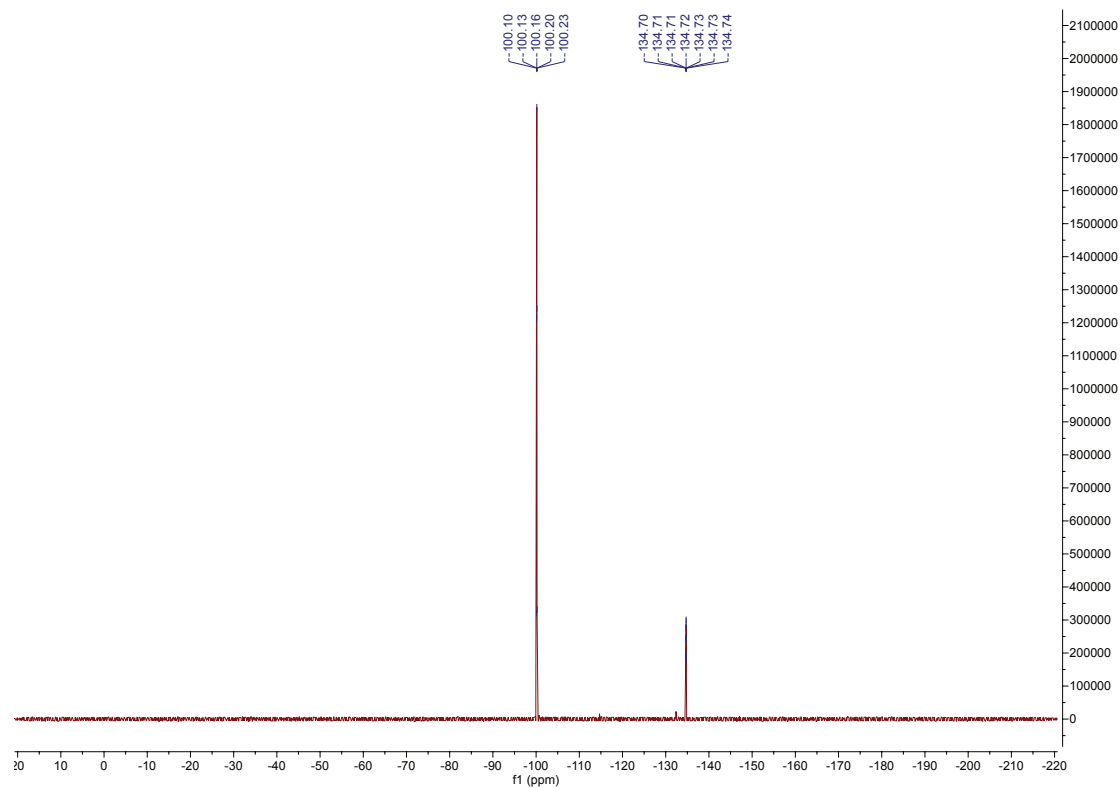
^{19}F NMR (377 MHz, CDCl_3) of compound **14a**.



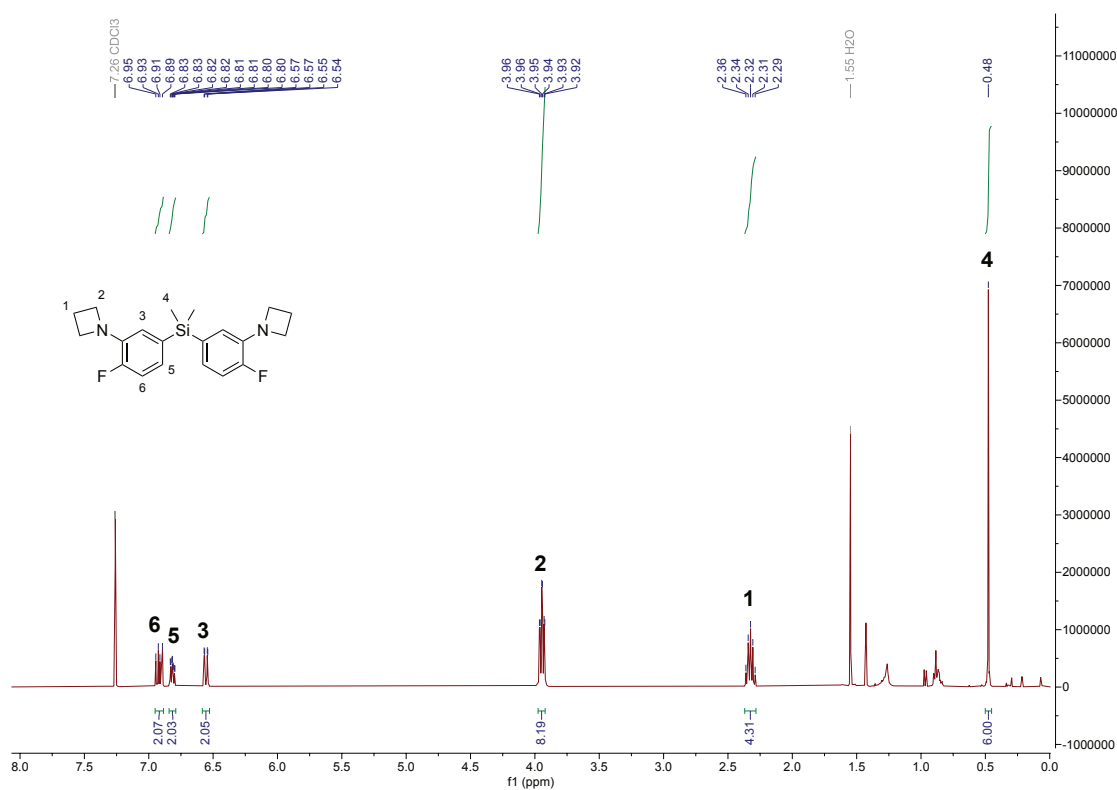
^1H NMR (400 MHz, CDCl_3) of compound **14b**.



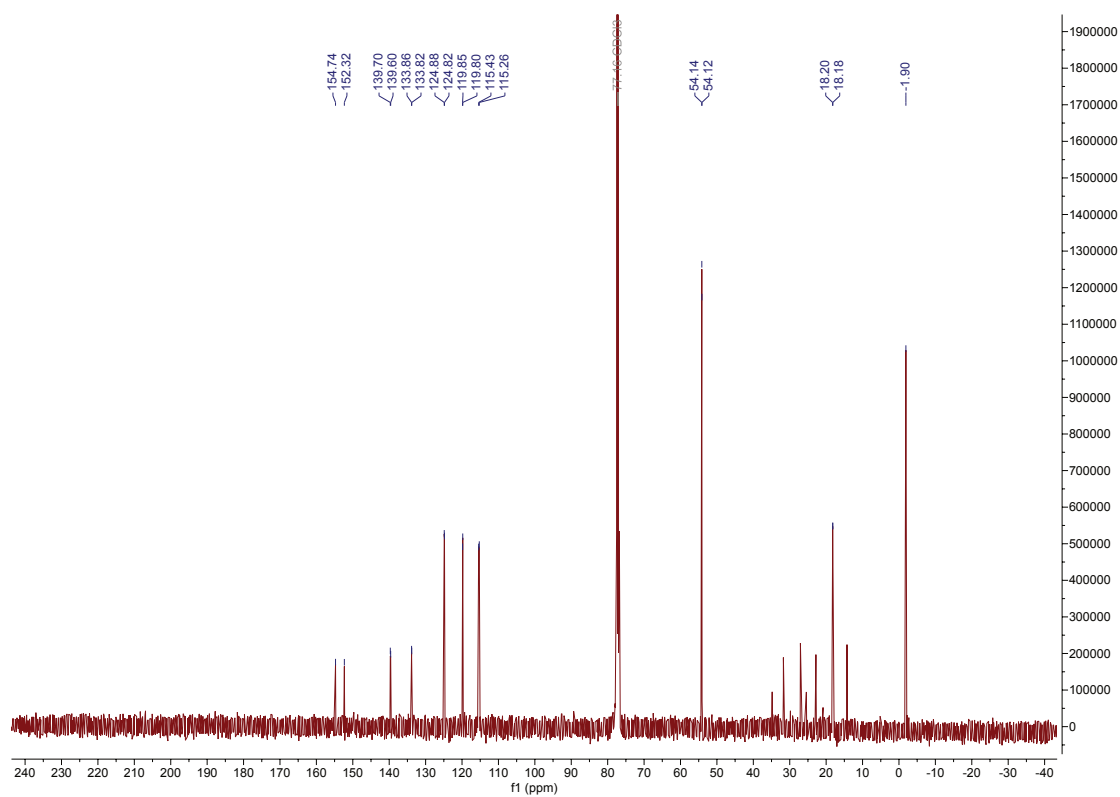
^{13}C NMR (101 MHz, CDCl_3) of compound **14b**.



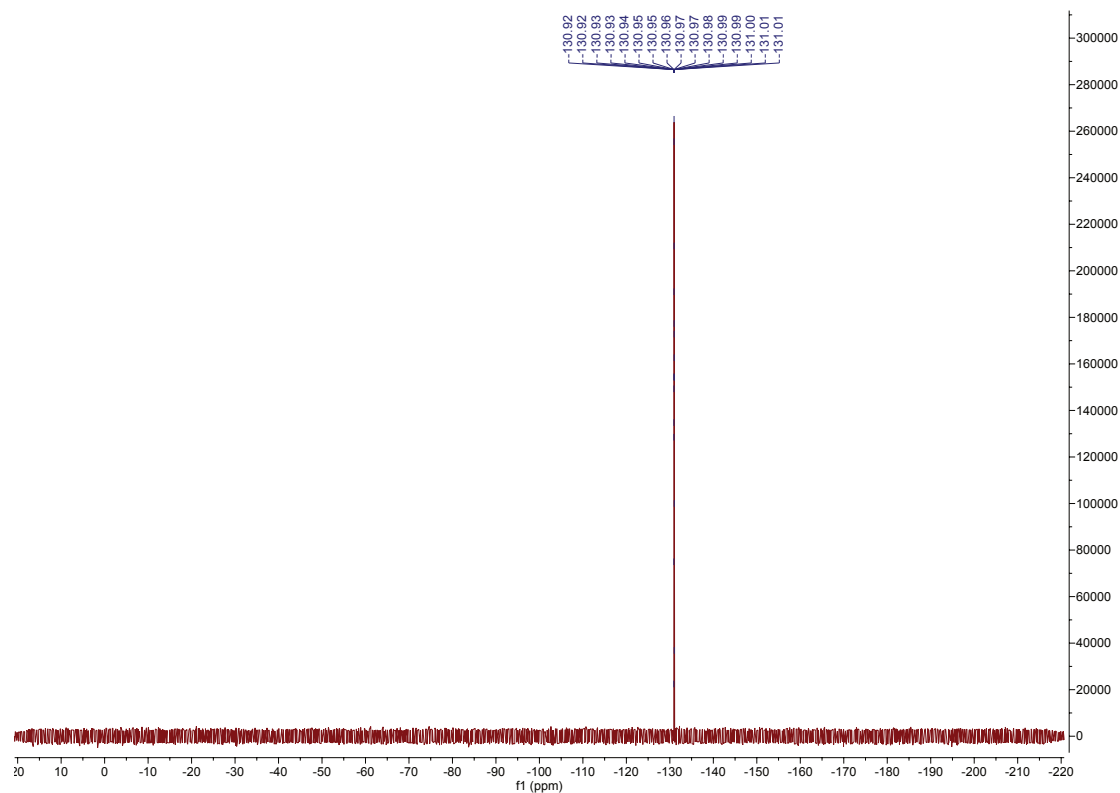
^{19}F NMR (376 MHz, CDCl_3) of compound **14b**.



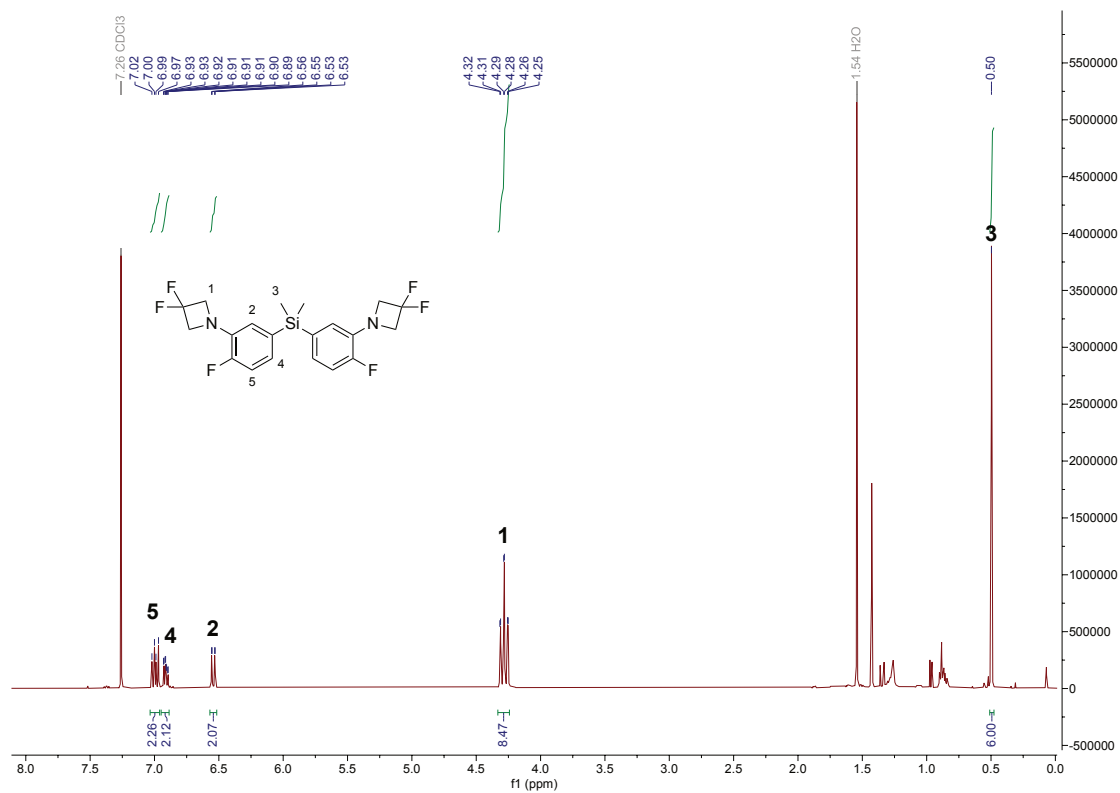
¹H NMR (400 MHz, CDCl₃) of compound **15a**.



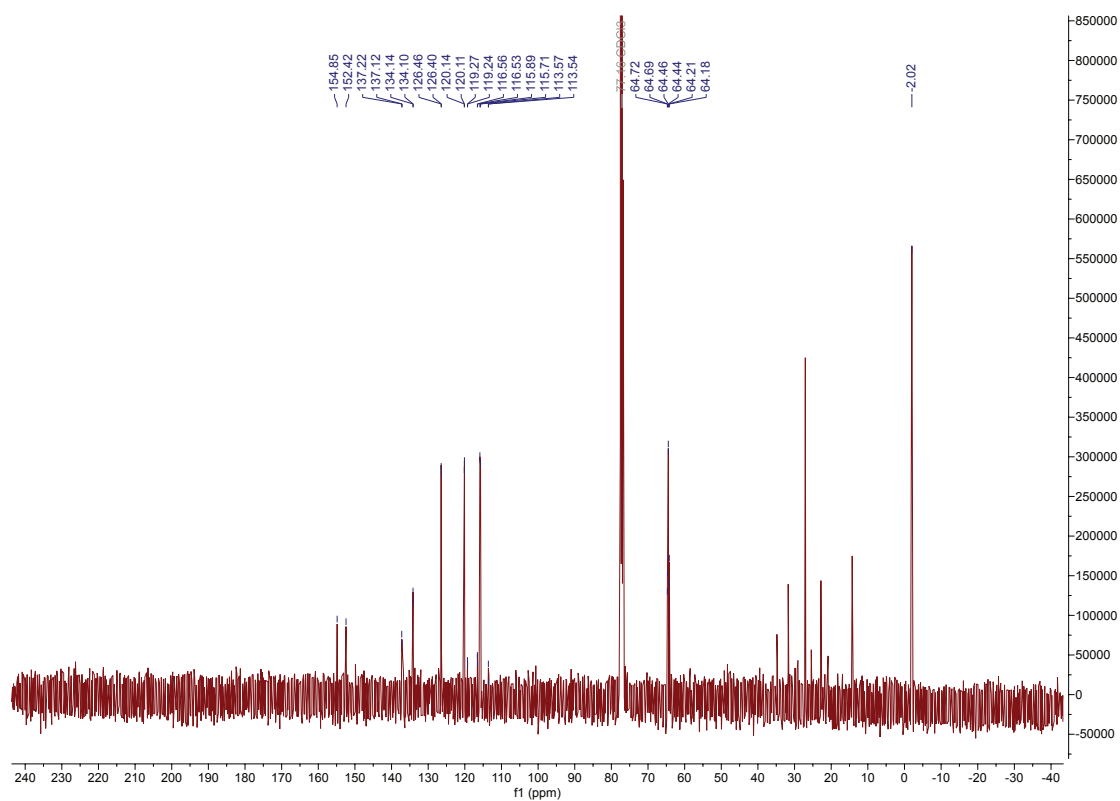
¹³C NMR (101 MHz, CDCl₃) of compound **15a**.



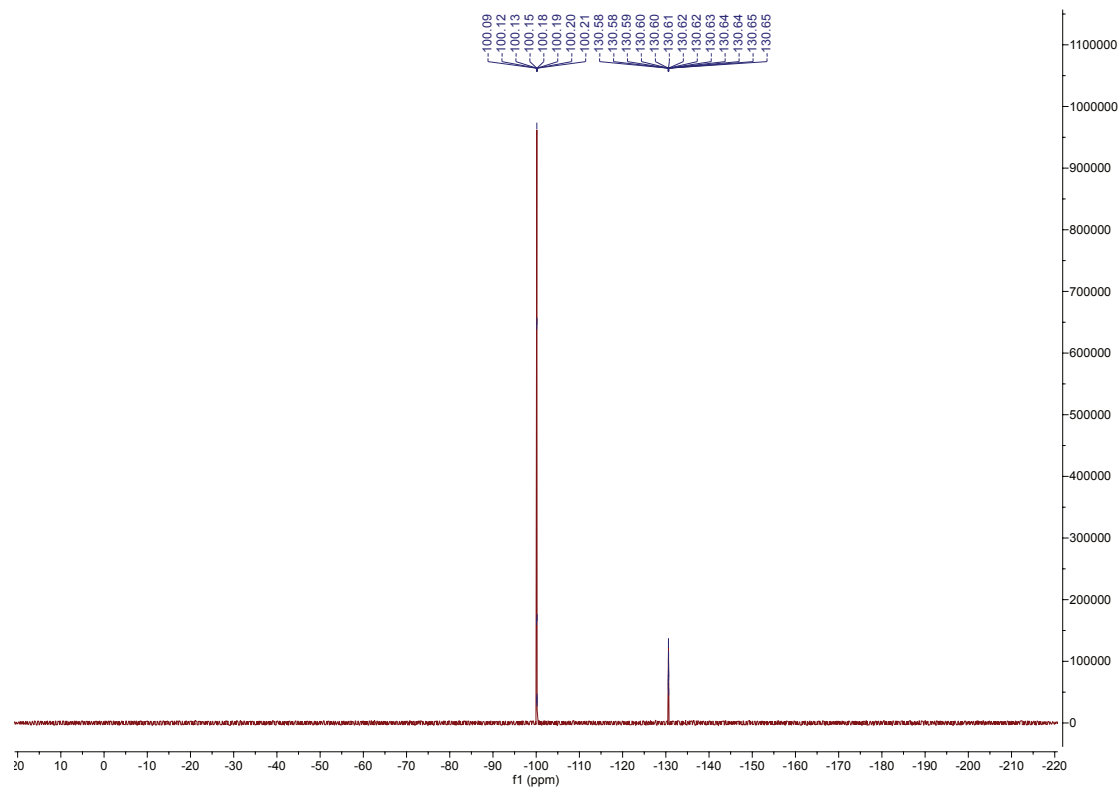
¹⁹F NMR (377 MHz, CDCl₃) of compound **15a**.



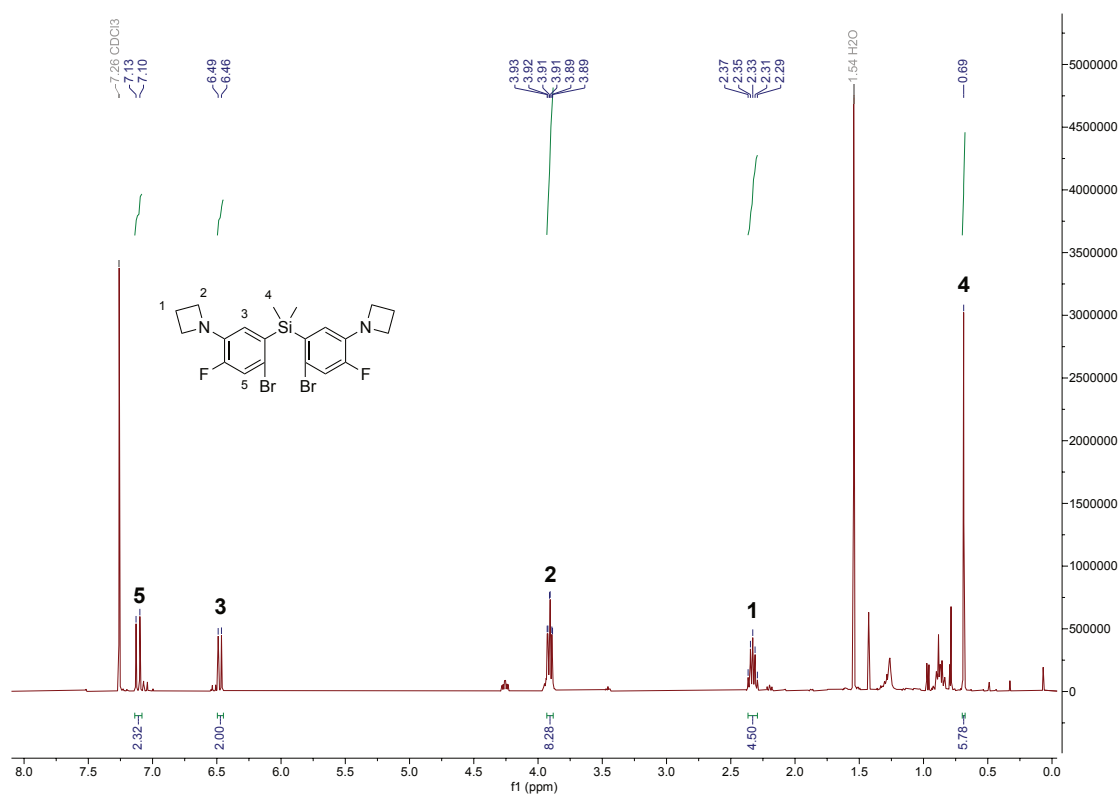
¹H NMR (400 MHz, CDCl₃) of compound **15b**.



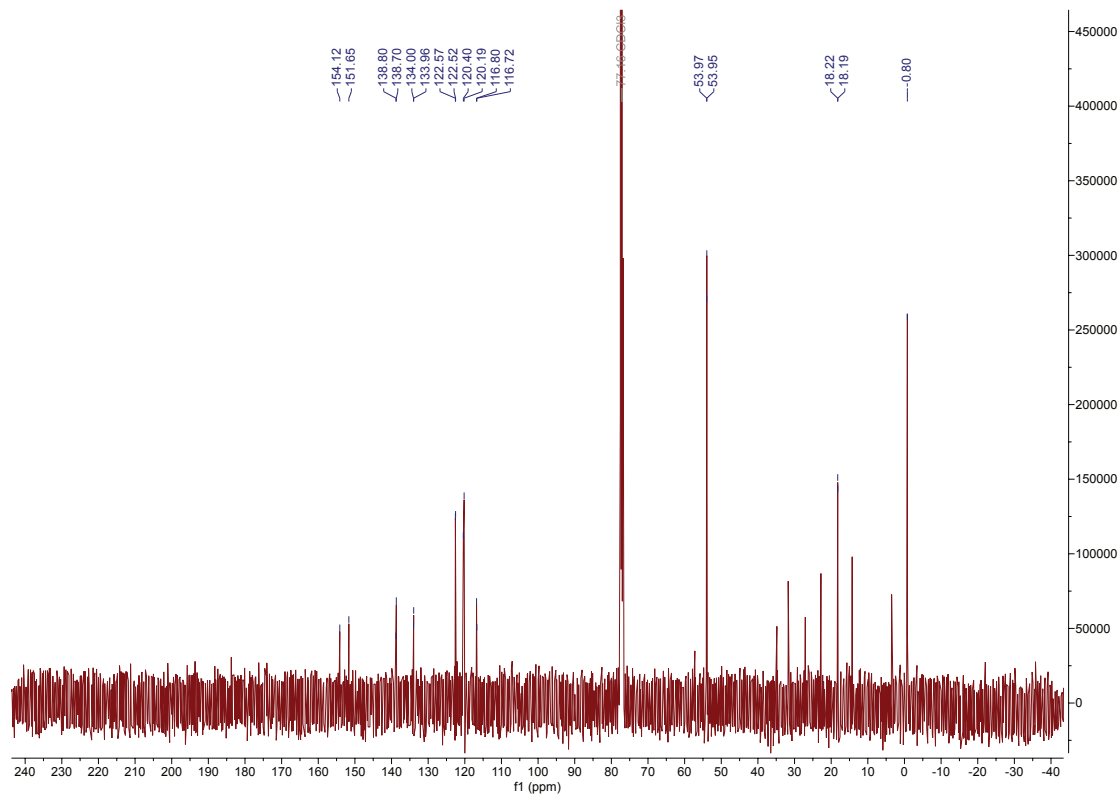
^{13}C NMR (101 MHz, CDCl_3) of compound **15b**.



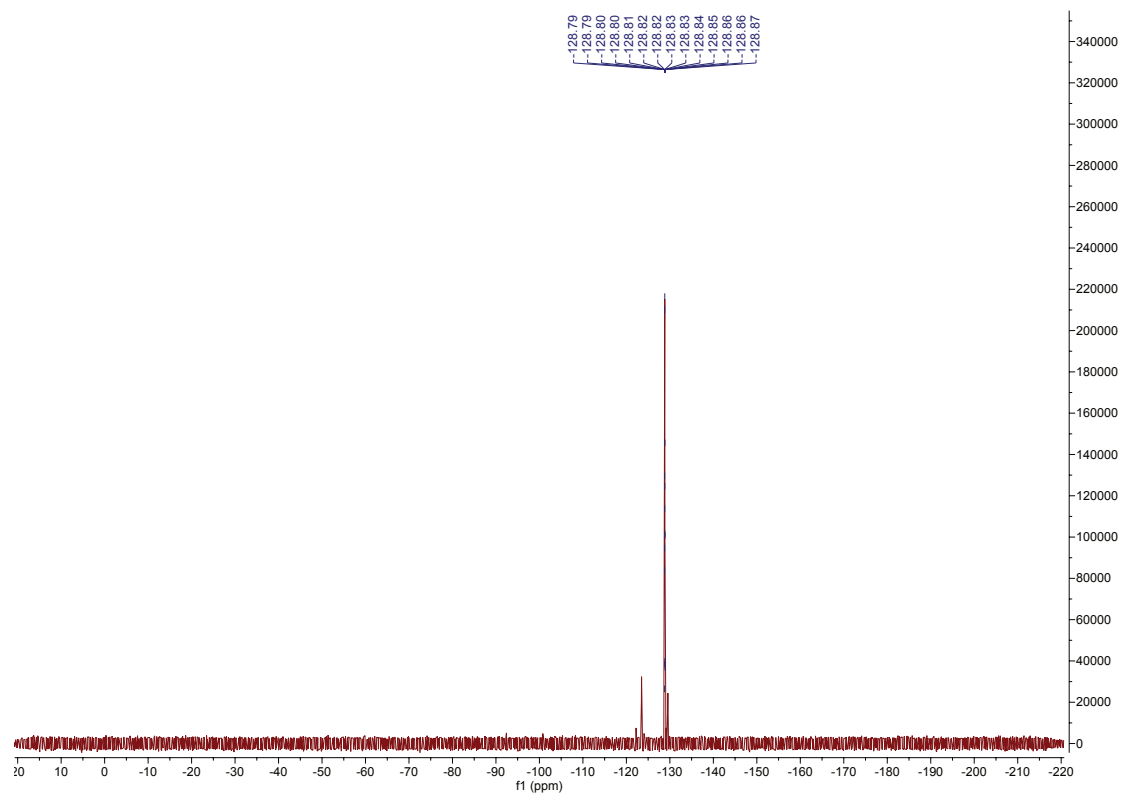
^{19}F NMR (377 MHz, CDCl_3) of compound **15b**.



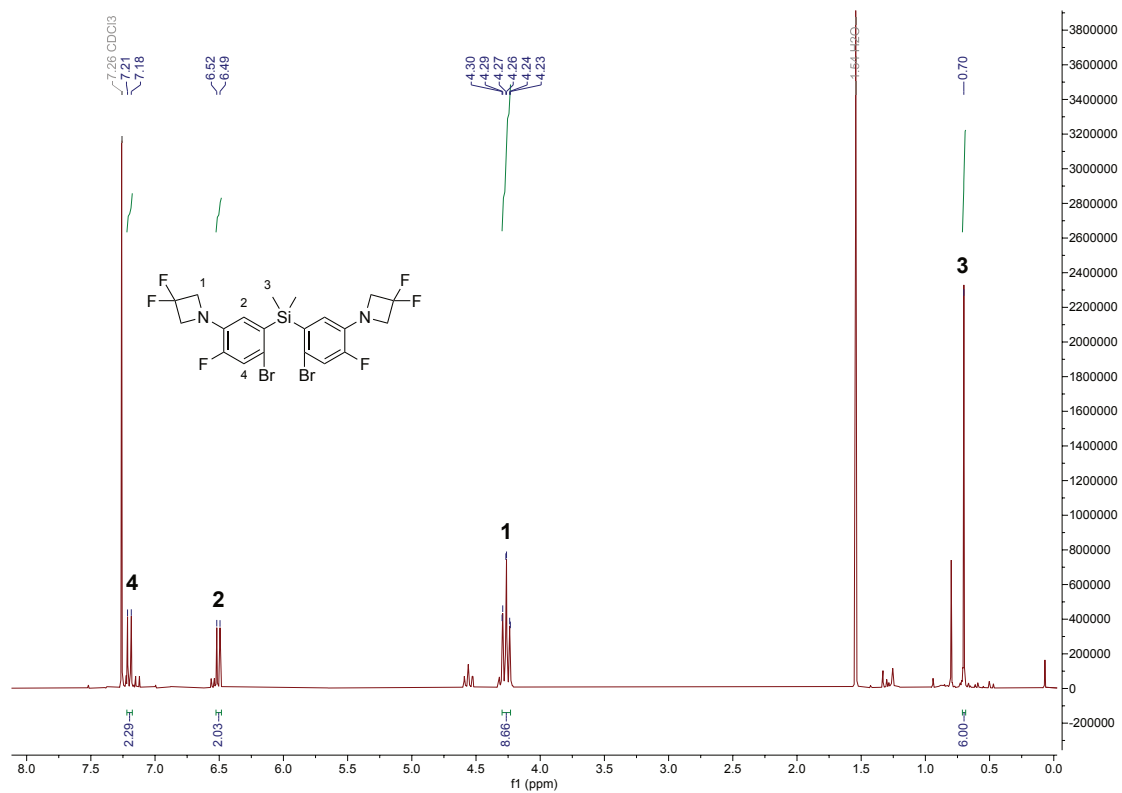
¹H NMR (400 MHz, CDCl₃) of compound **16a**.



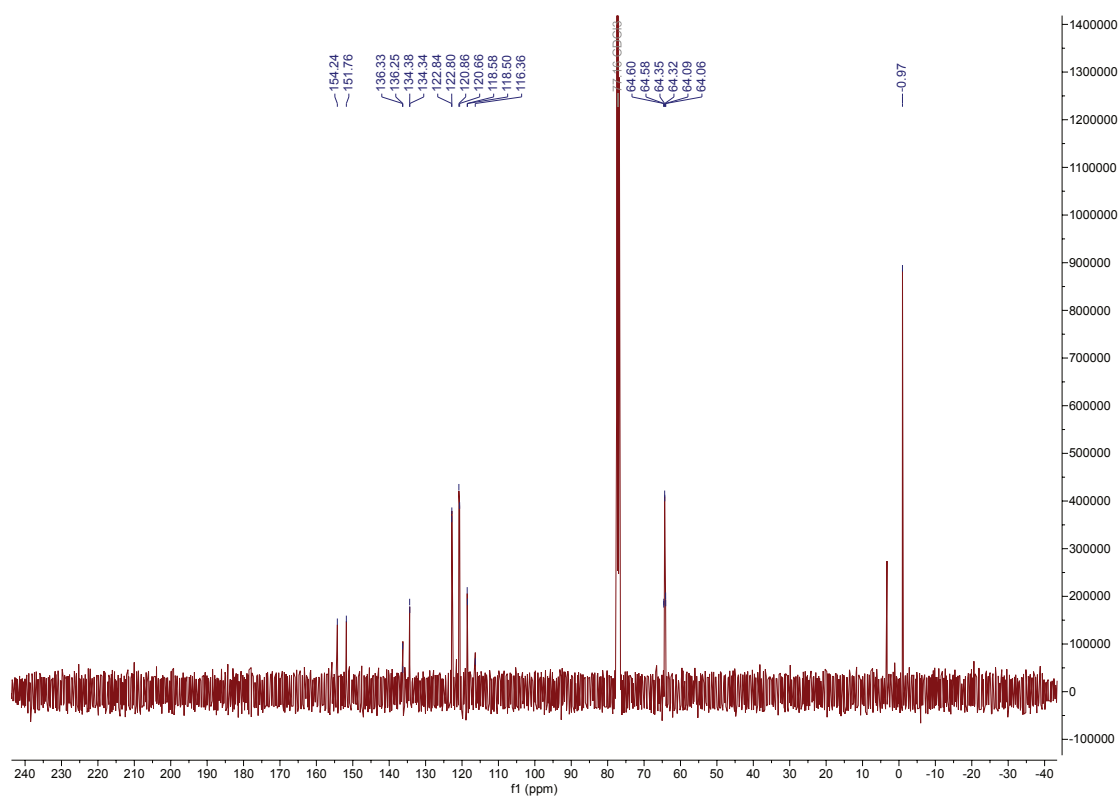
¹³C NMR (101 MHz, CDCl₃) of compound **16a**.



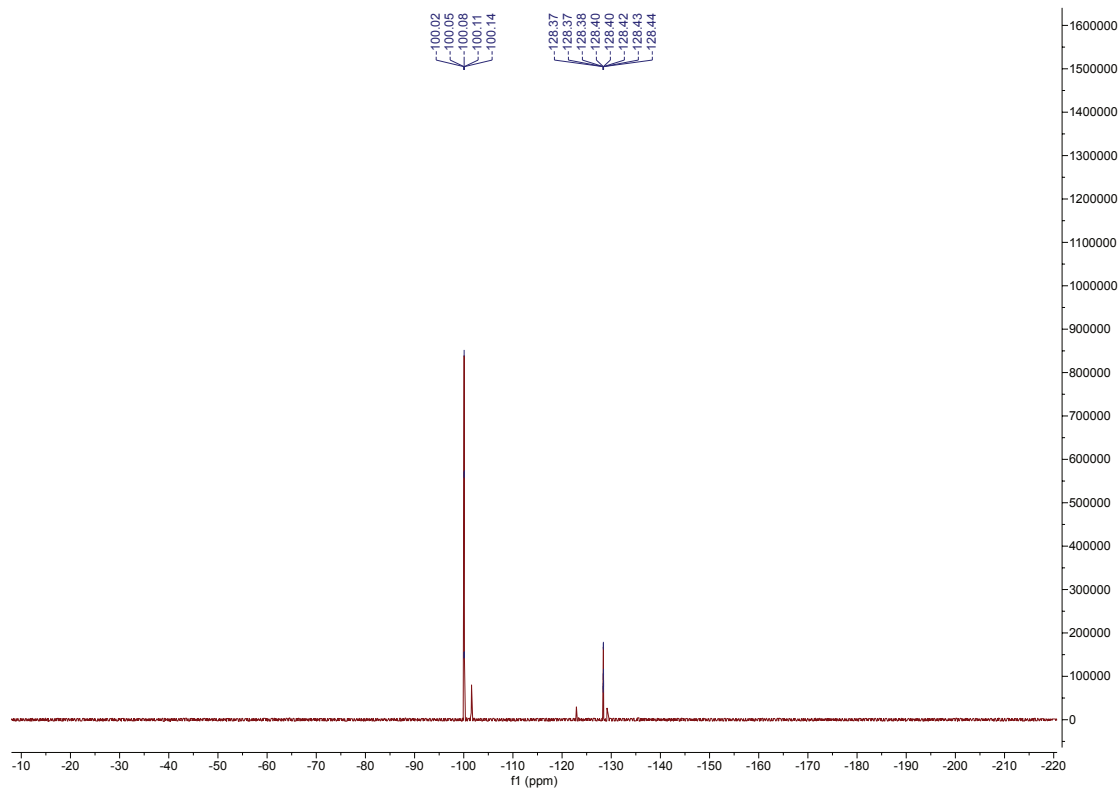
^{19}F NMR (377 MHz, CDCl_3) of compound **16a**.



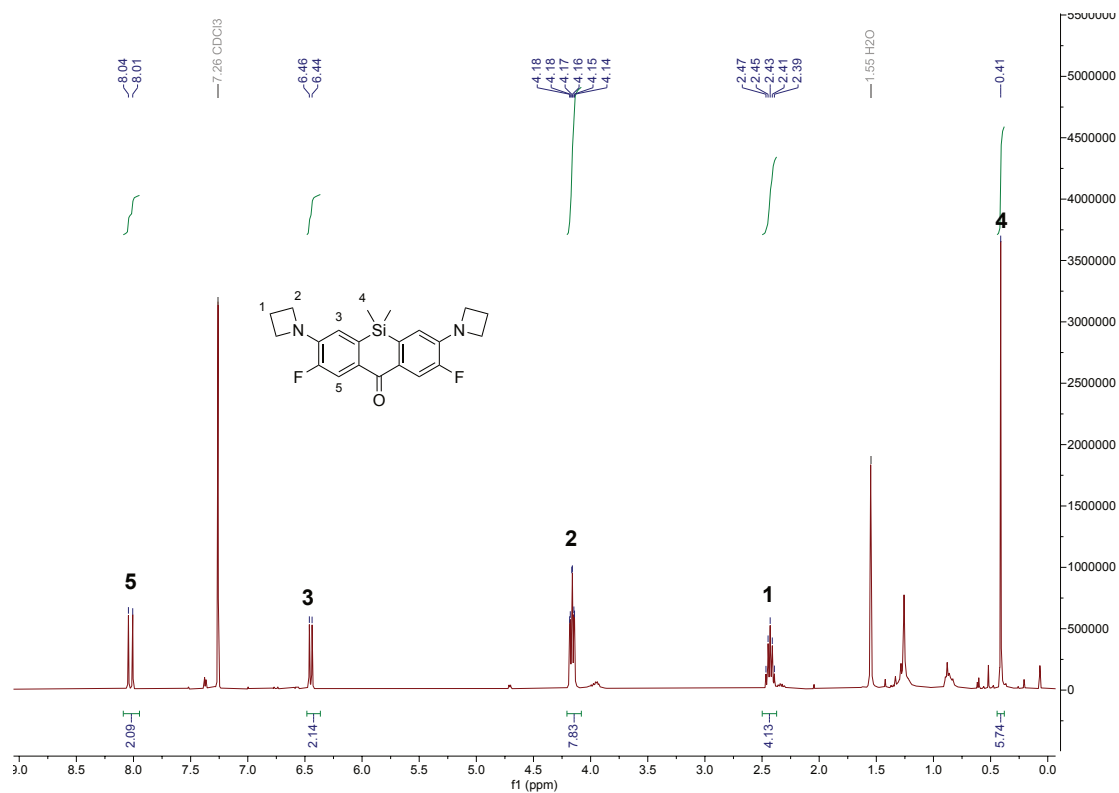
^1H NMR (400 MHz, CDCl_3) of compound **16b**.



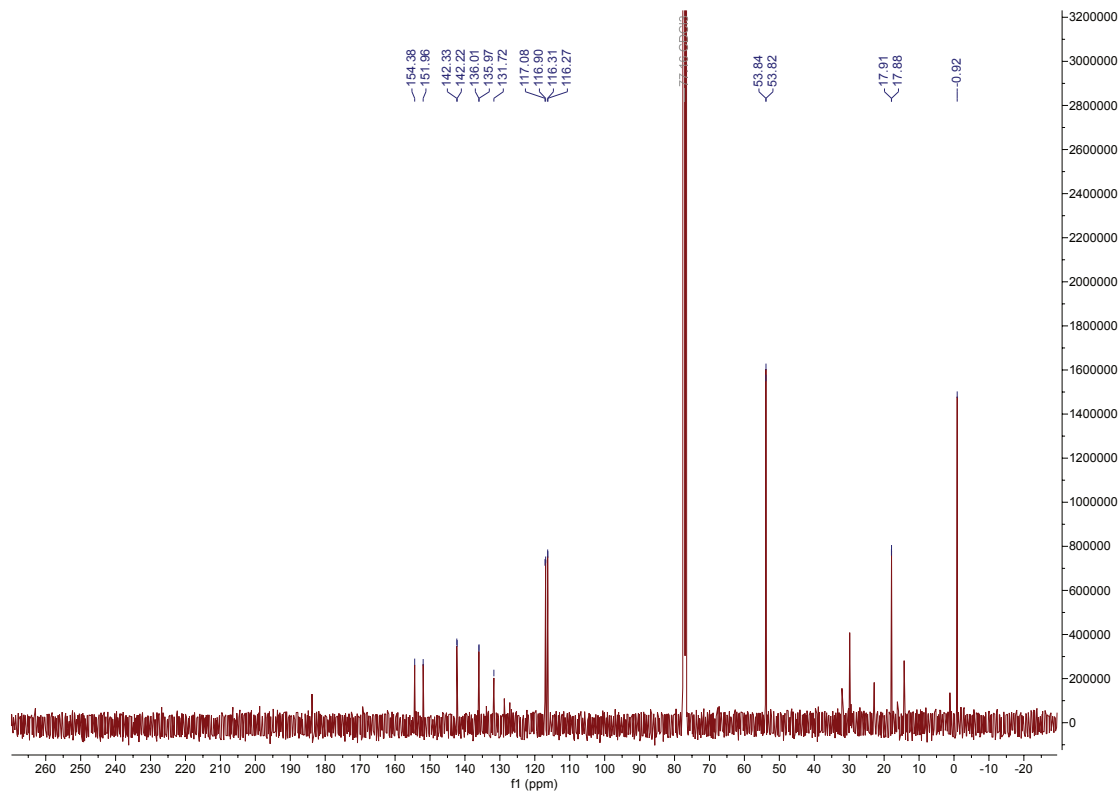
¹³C NMR (101 MHz, CDCl₃) of compound **16b**.



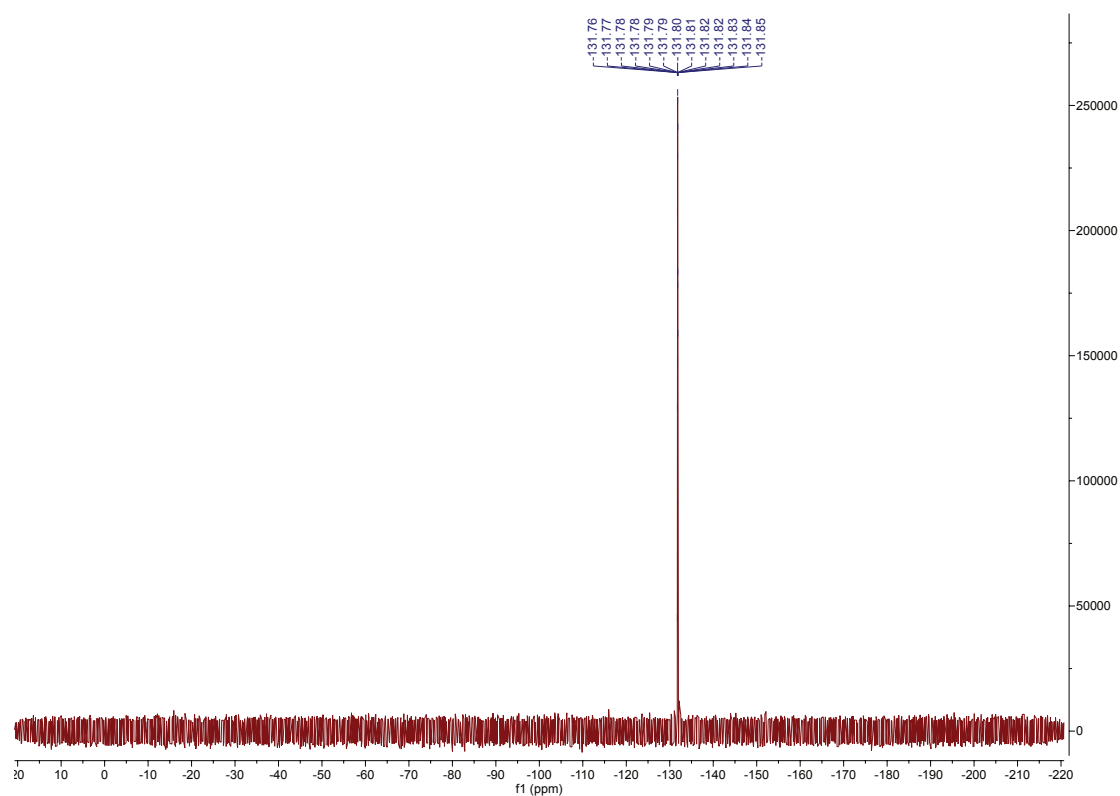
¹⁹F NMR (377 MHz, CDCl₃) of compound **16b**.



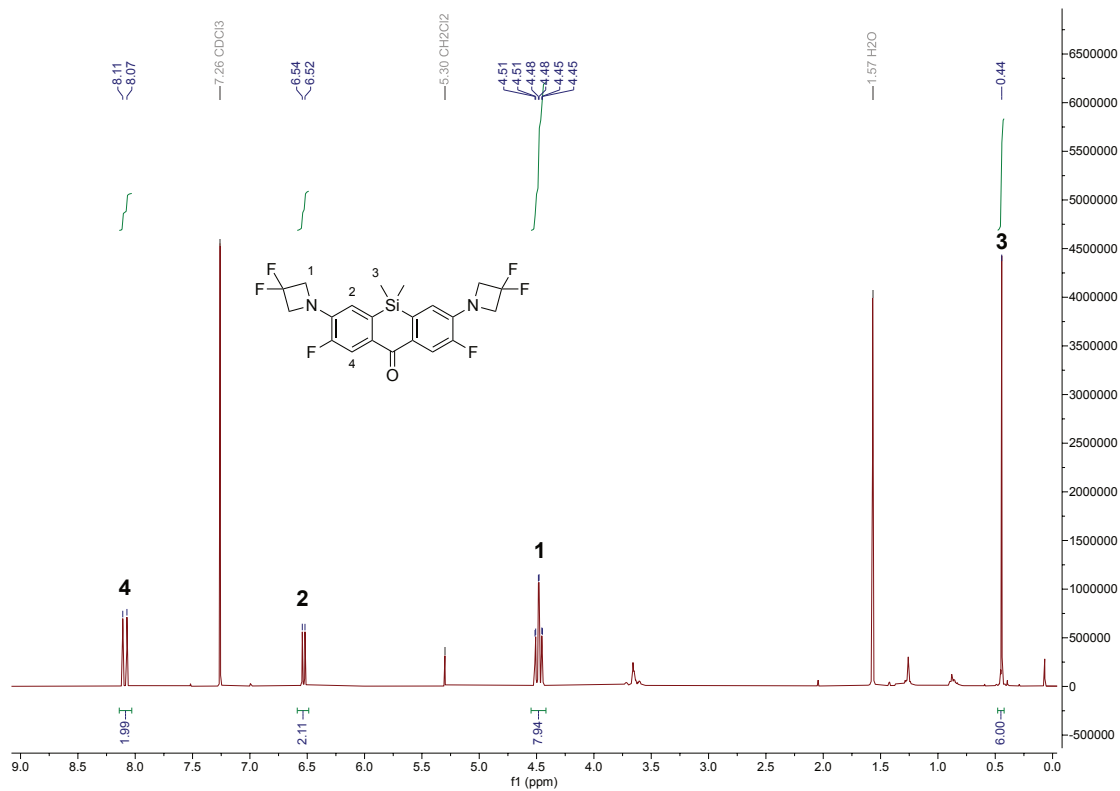
¹H NMR (400 MHz, CDCl₃) of compound **17a**.



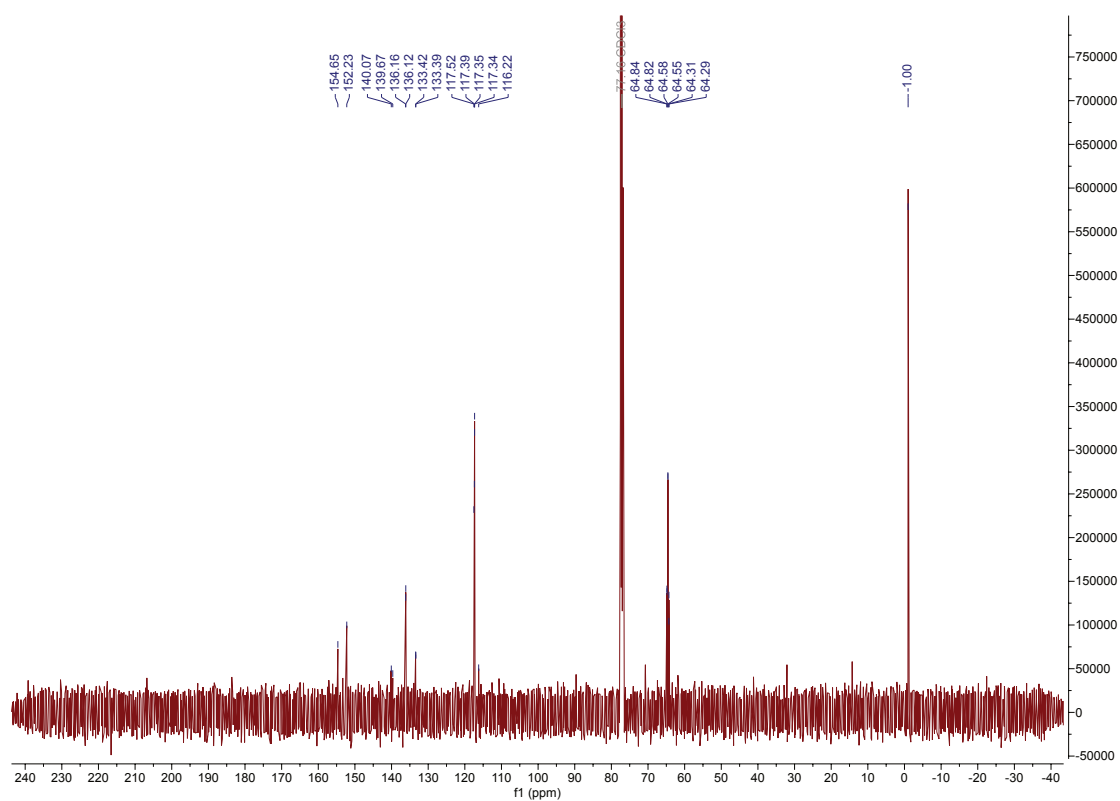
¹³C NMR (101 MHz, CDCl₃) of compound **17a**.



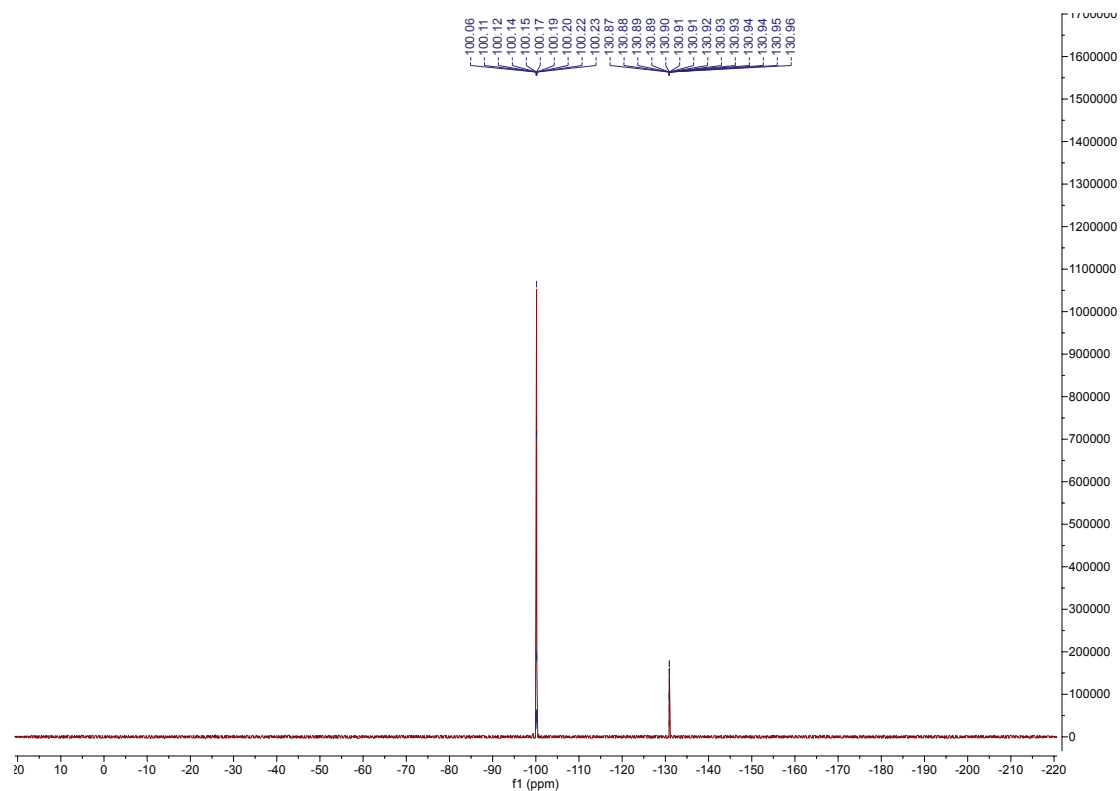
^{19}F NMR (376 MHz, CDCl_3) of compound **17a**.



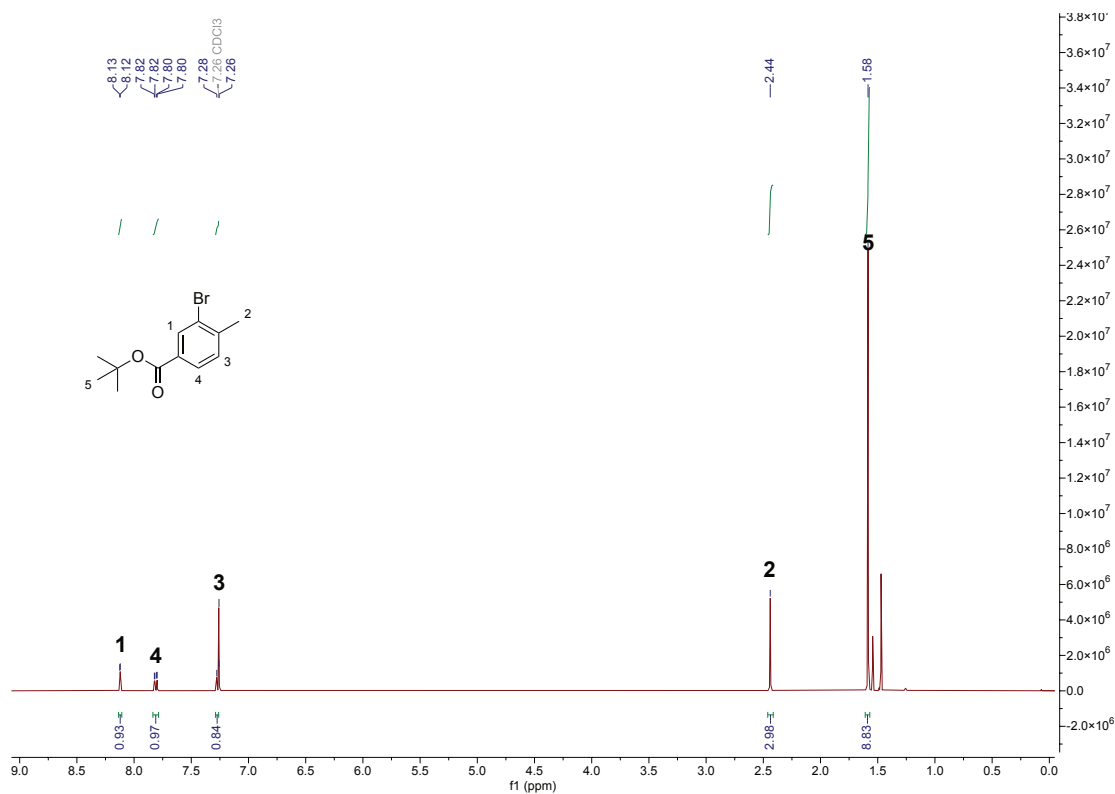
^1H NMR (400 MHz, CDCl_3) of compound **17b**.



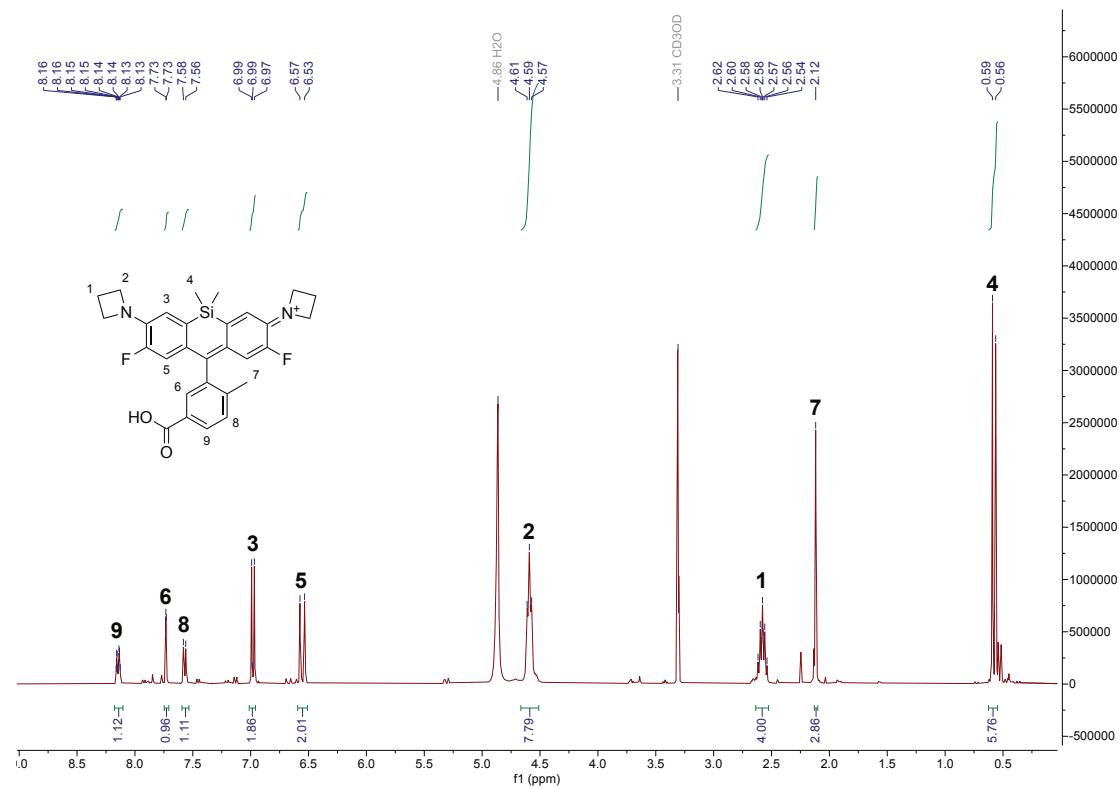
^{13}C NMR (101 MHz, CDCl_3) of compound **17b**.



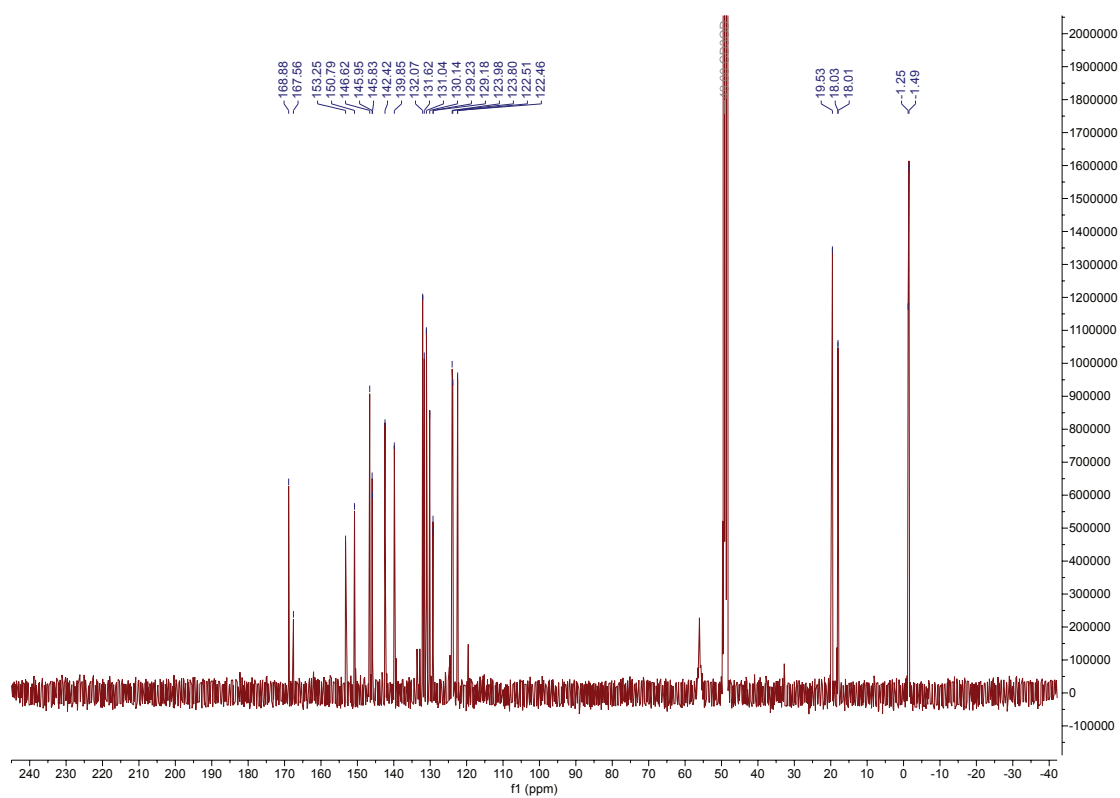
^{19}F NMR (377 MHz, CDCl_3) of compound **17b**.



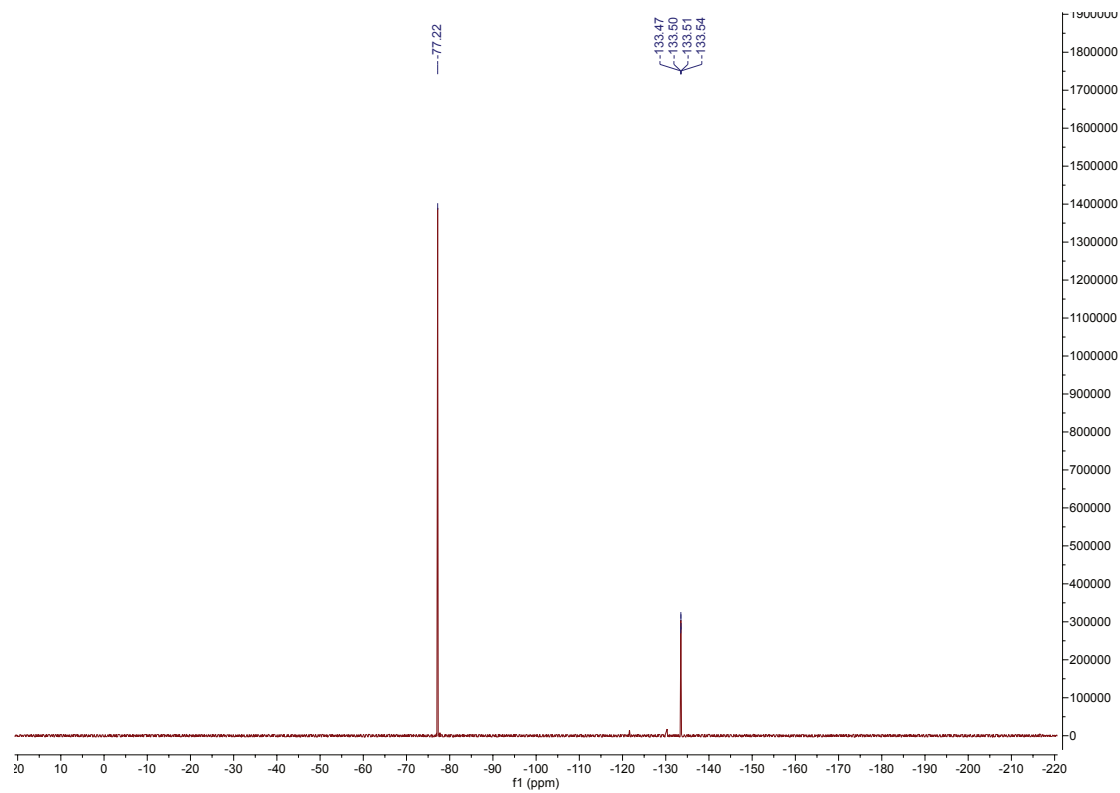
¹H NMR (400 MHz, CDCl₃) of compound **18**.



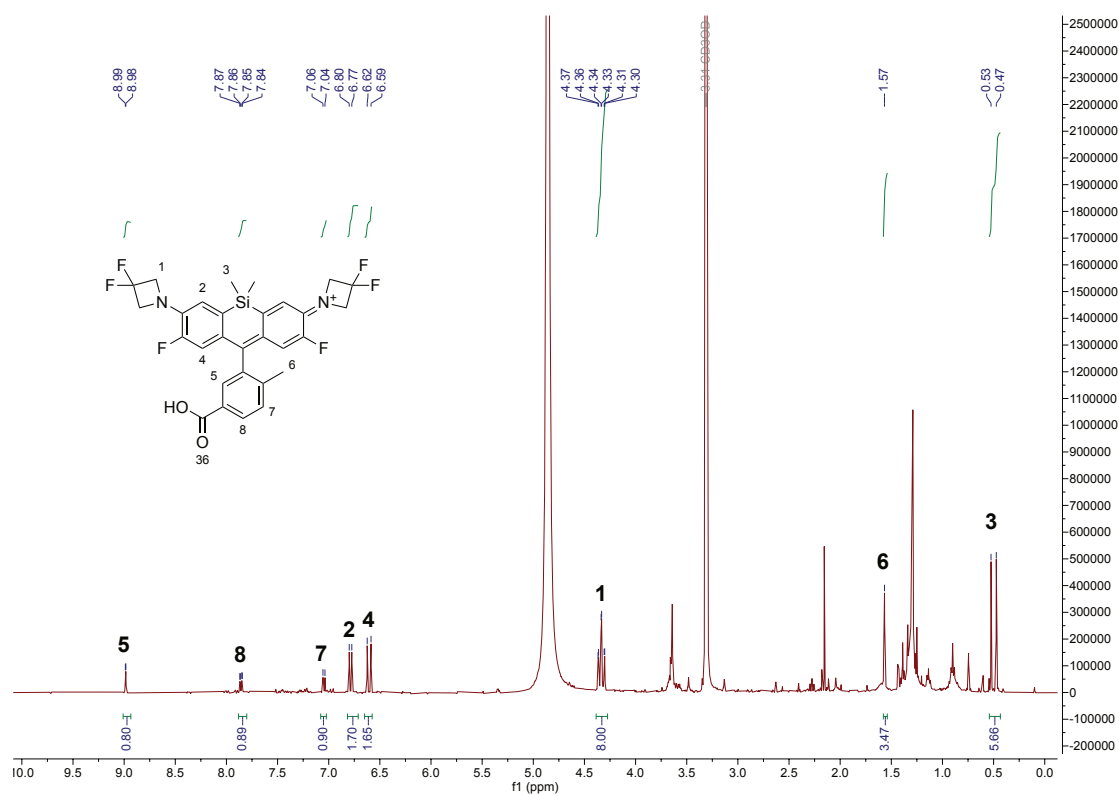
¹H NMR (400 MHz, CD₃OD) of compound **19a**.



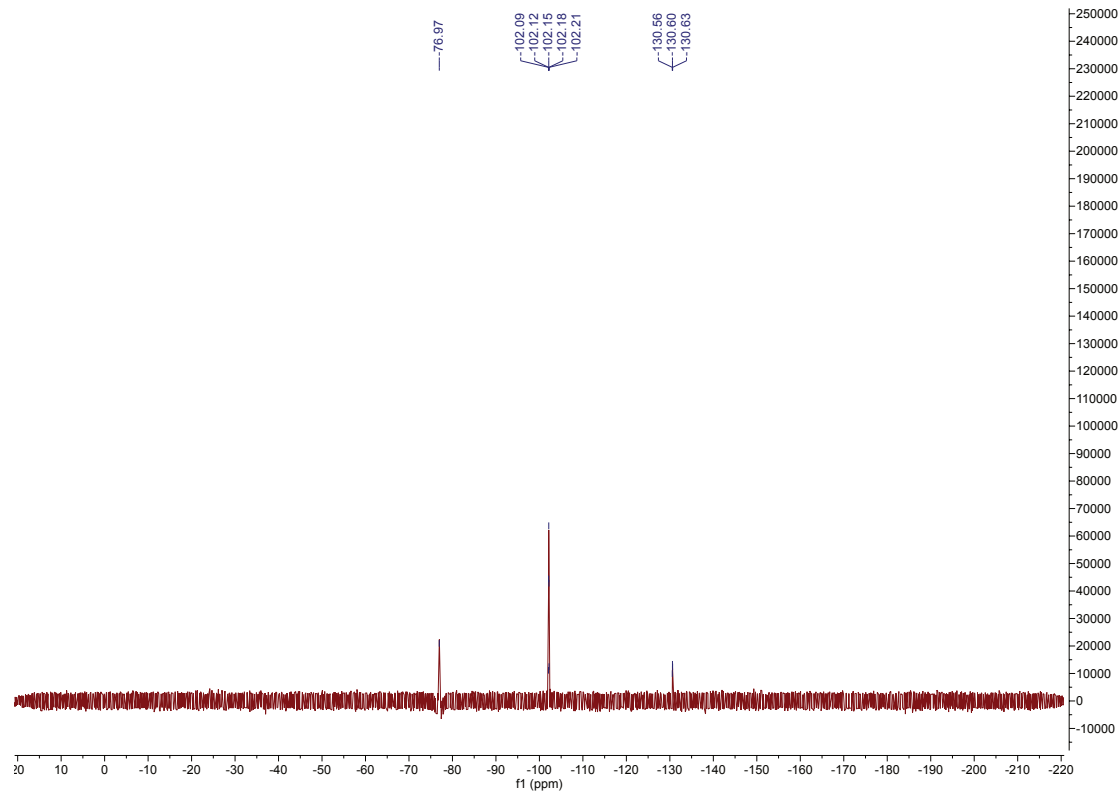
^{13}C NMR (101 MHz, CD_3OD) of compound **19a**.



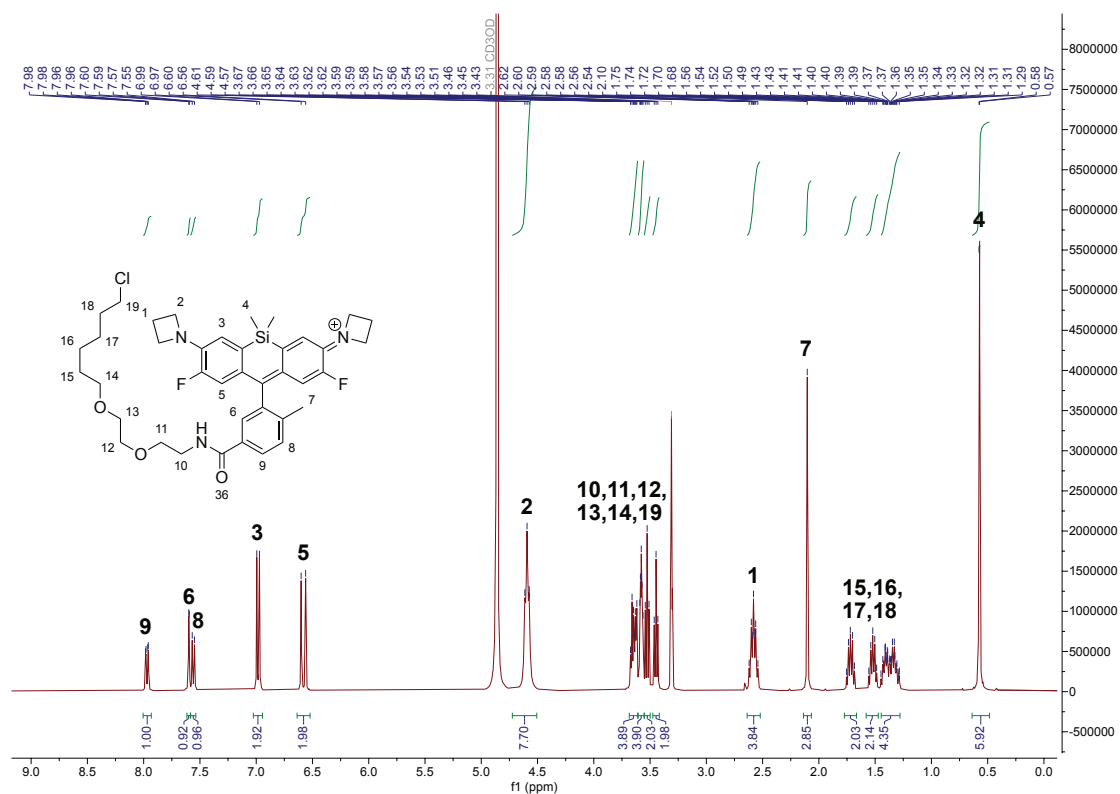
^{19}F NMR (377 MHz, CD_3OD) of compound **19a**.



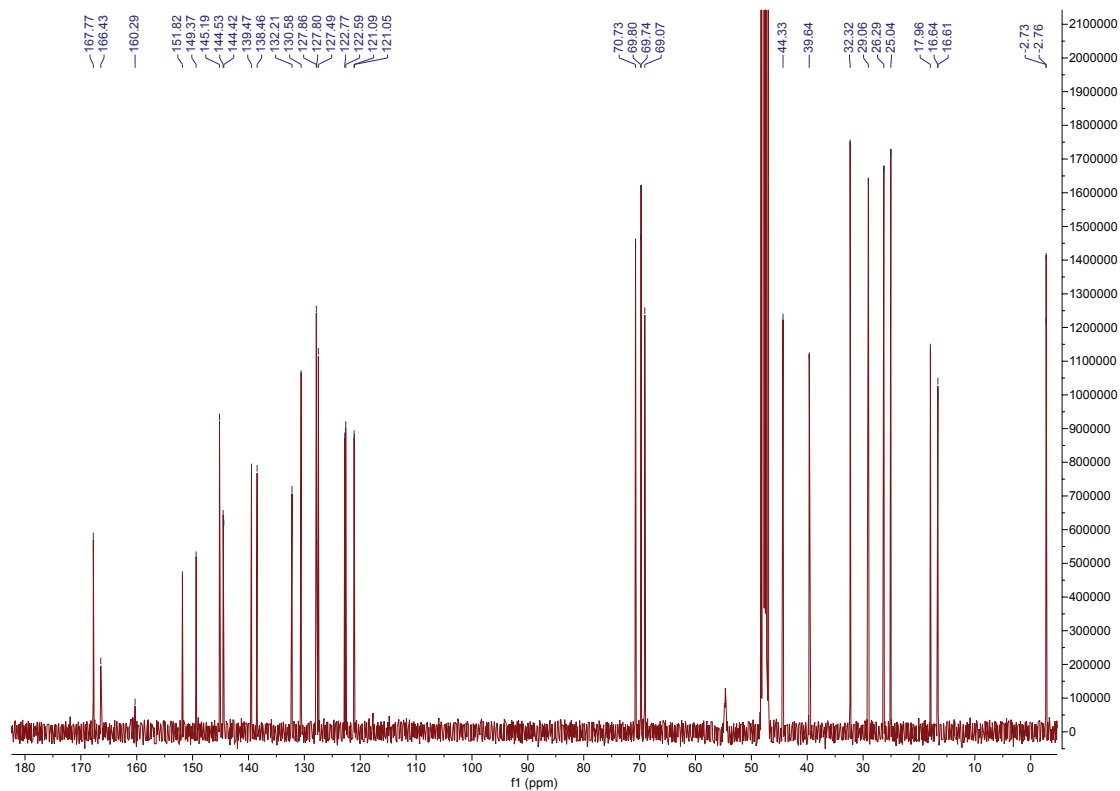
¹H NMR (400 MHz, CD₃OD) of compound 19b.



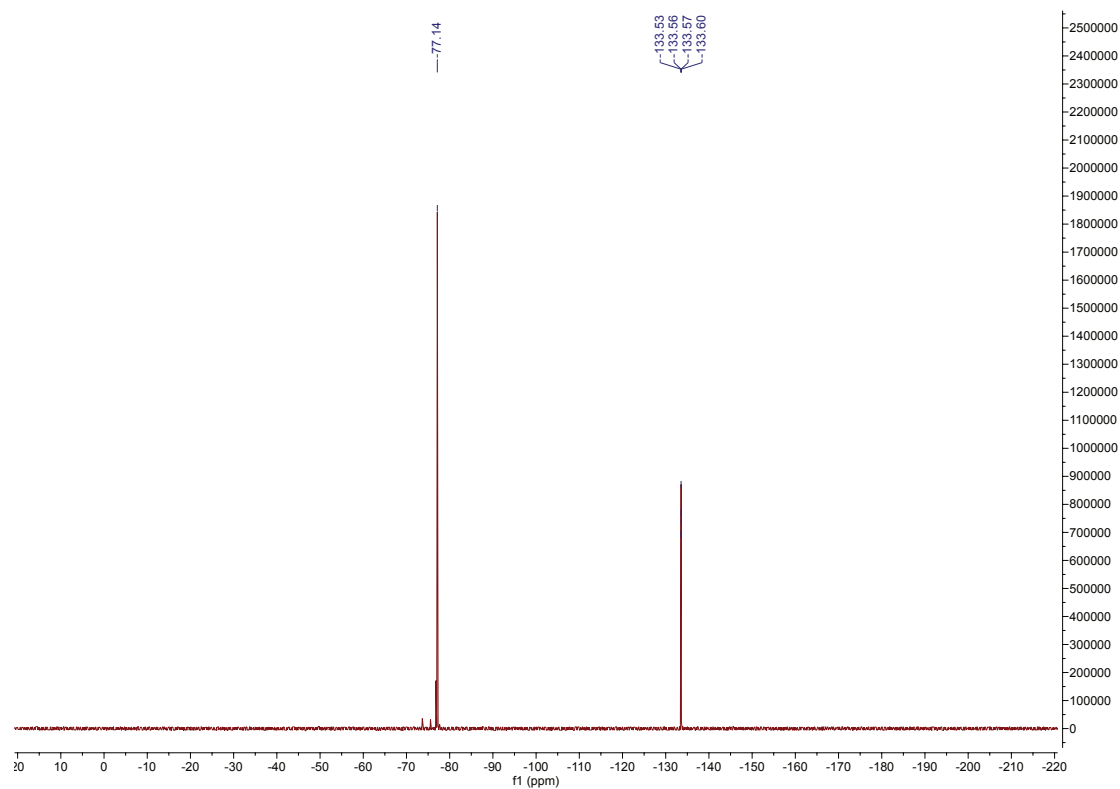
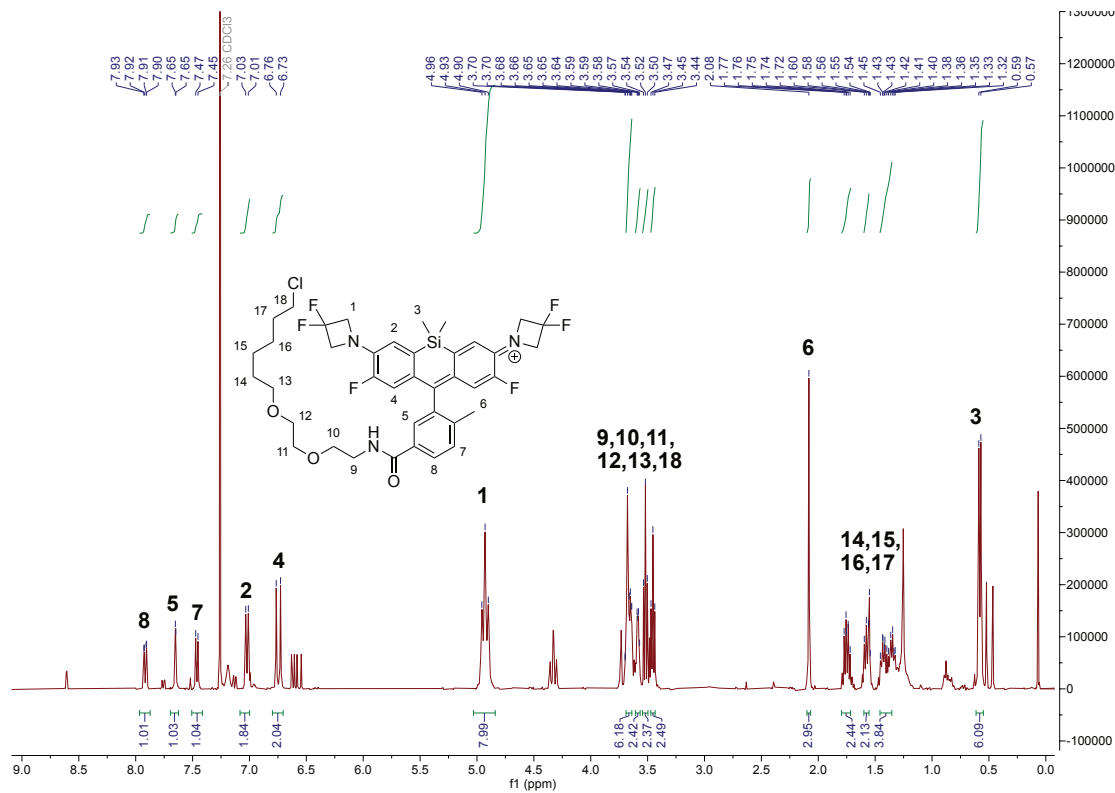
¹⁹F NMR (377 MHz, CD₃OD) of compound 19b.

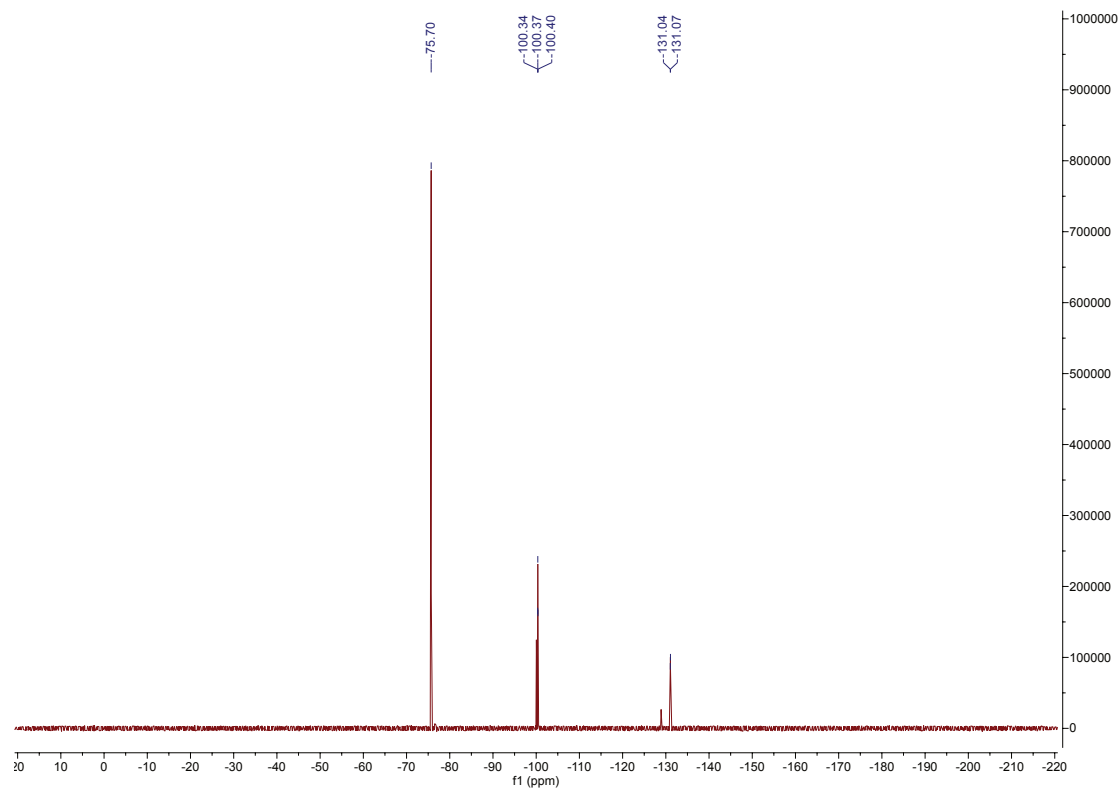


¹H NMR (400 MHz, CD₃OD) of compound **20a**.

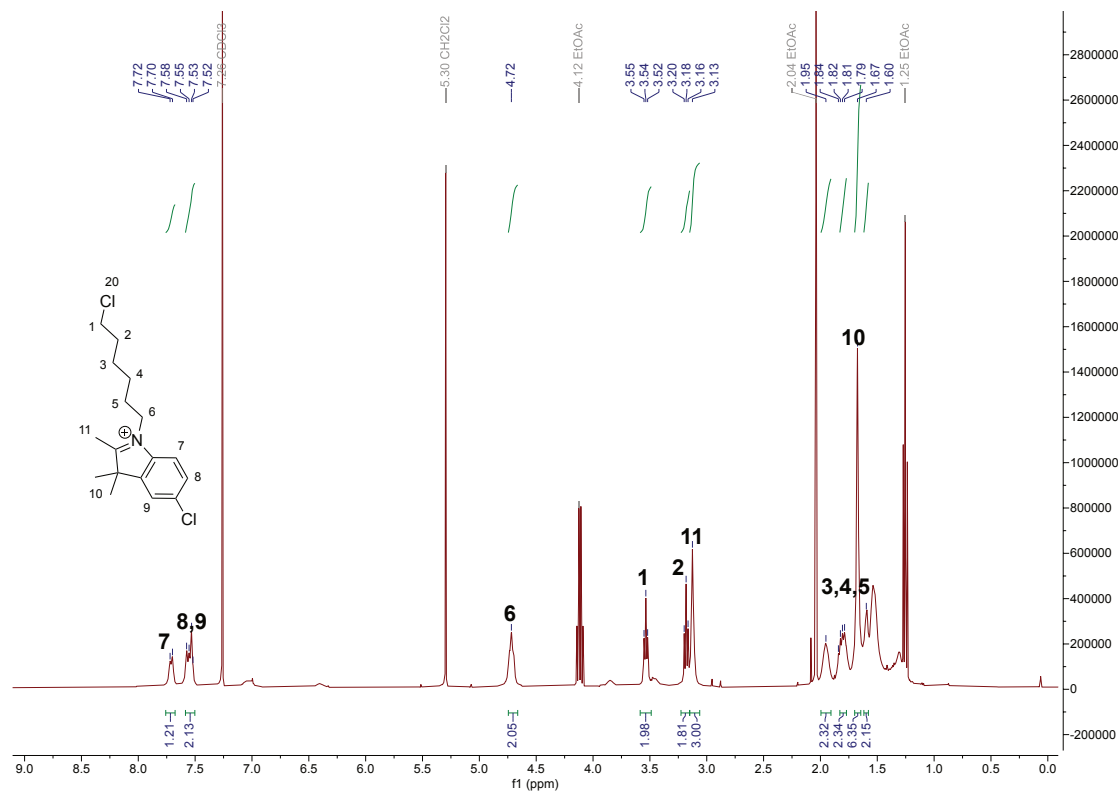


¹³C NMR (101 MHz, CD₃OD) of compound **20a**.

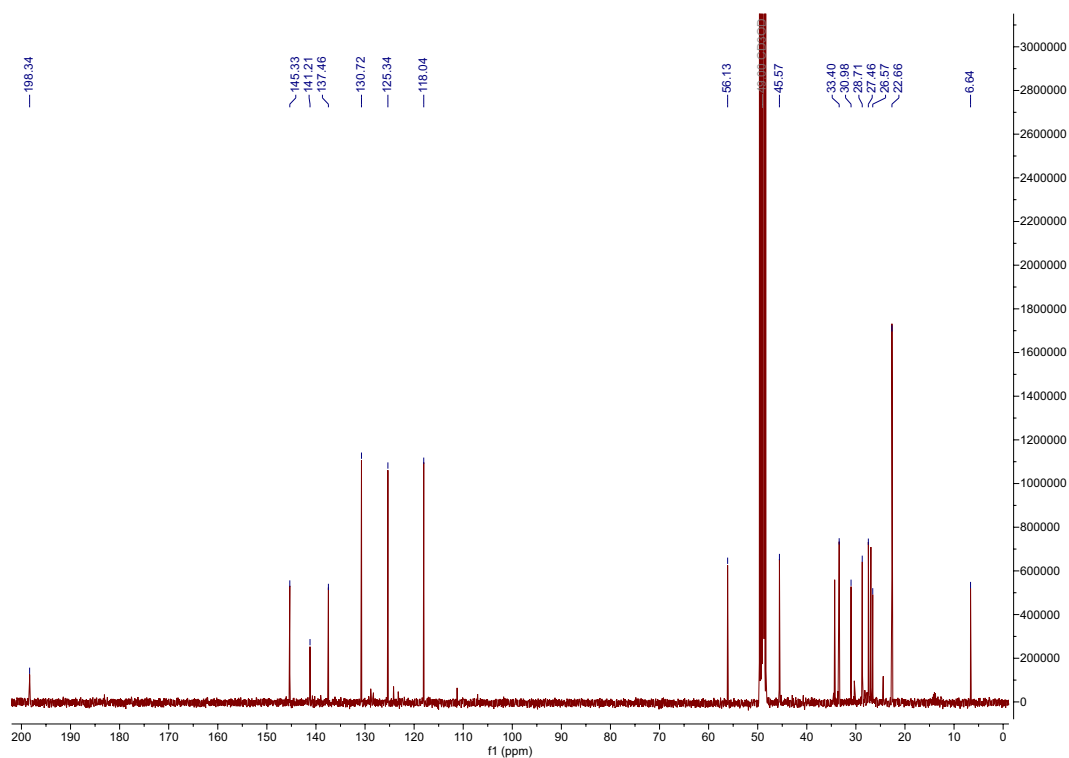
 ^{19}F NMR (376 MHz, CD_3OD) of compound **20a**. ^1H NMR (400 MHz, CDCl_3) of compound **20b**.



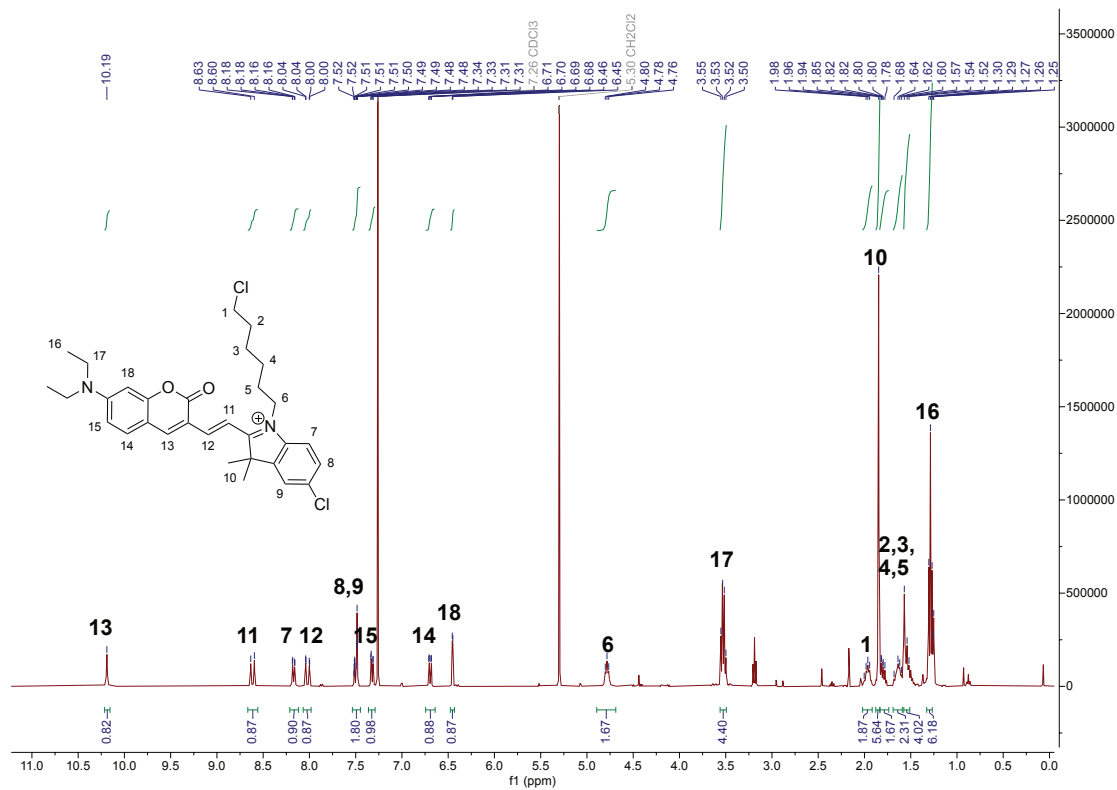
^{19}F NMR (377 MHz, CDCl_3) of compound **20b**.



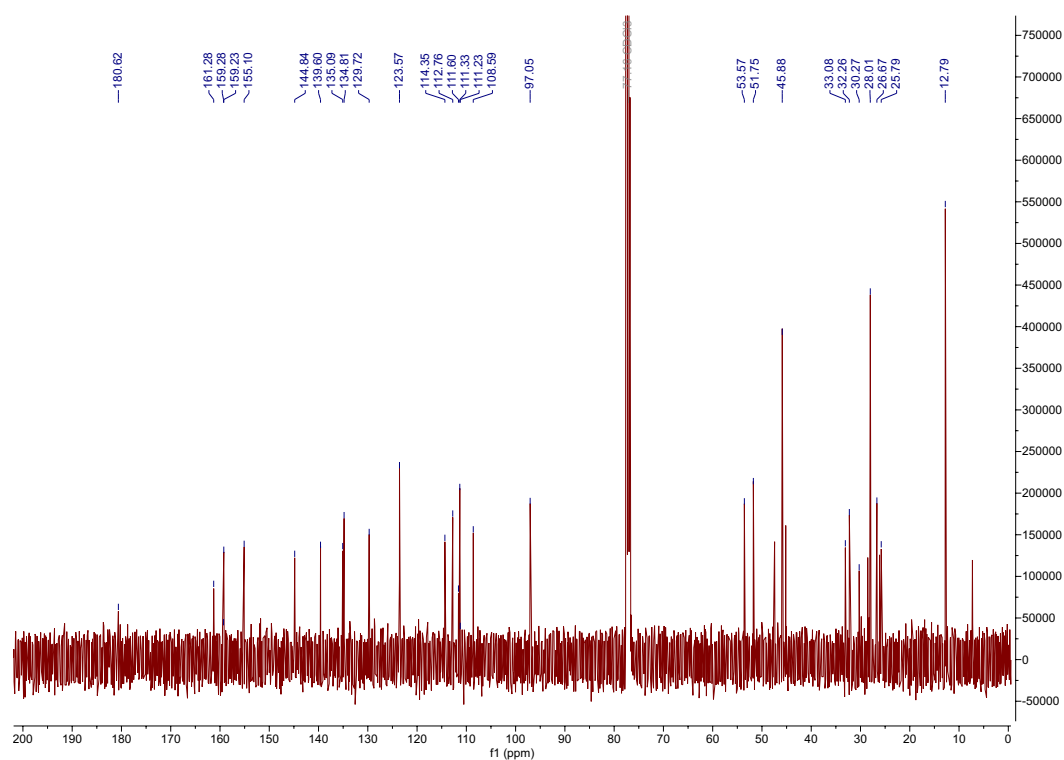
^1H -NMR (400 MHz, CDCl_3) of compound **23**.



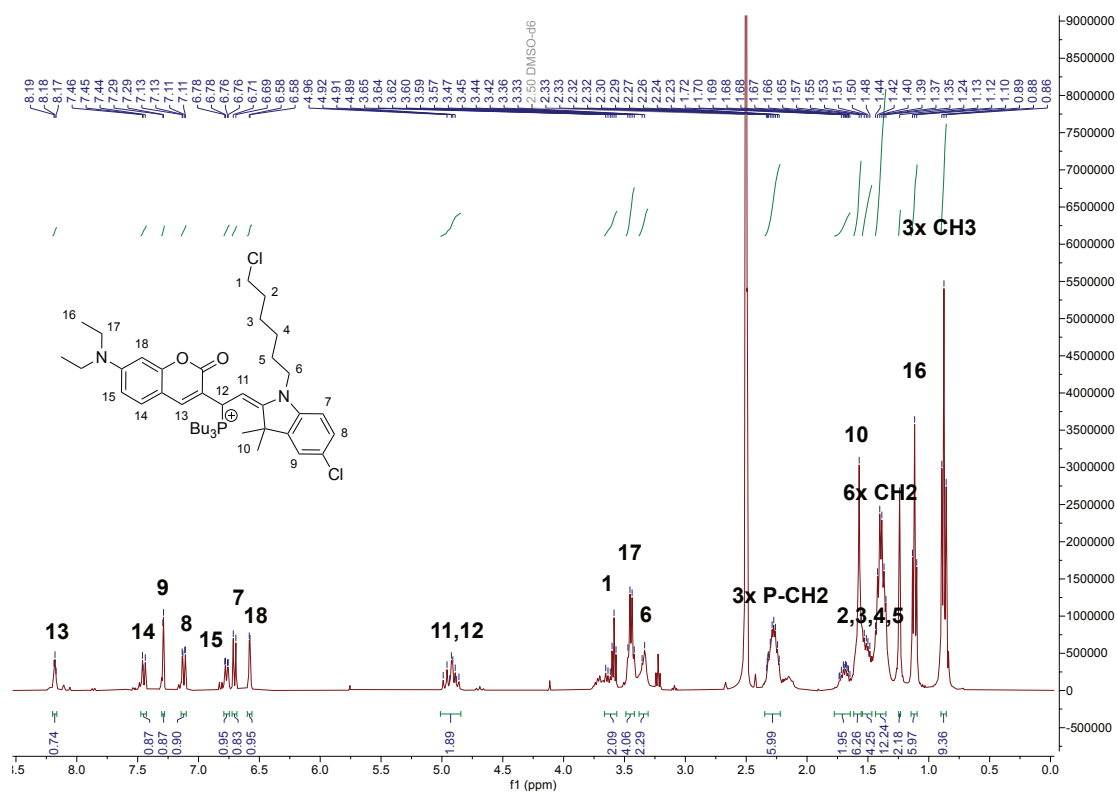
^{13}C -NMR (101 MHz, CD_3OD) of compound **23**.



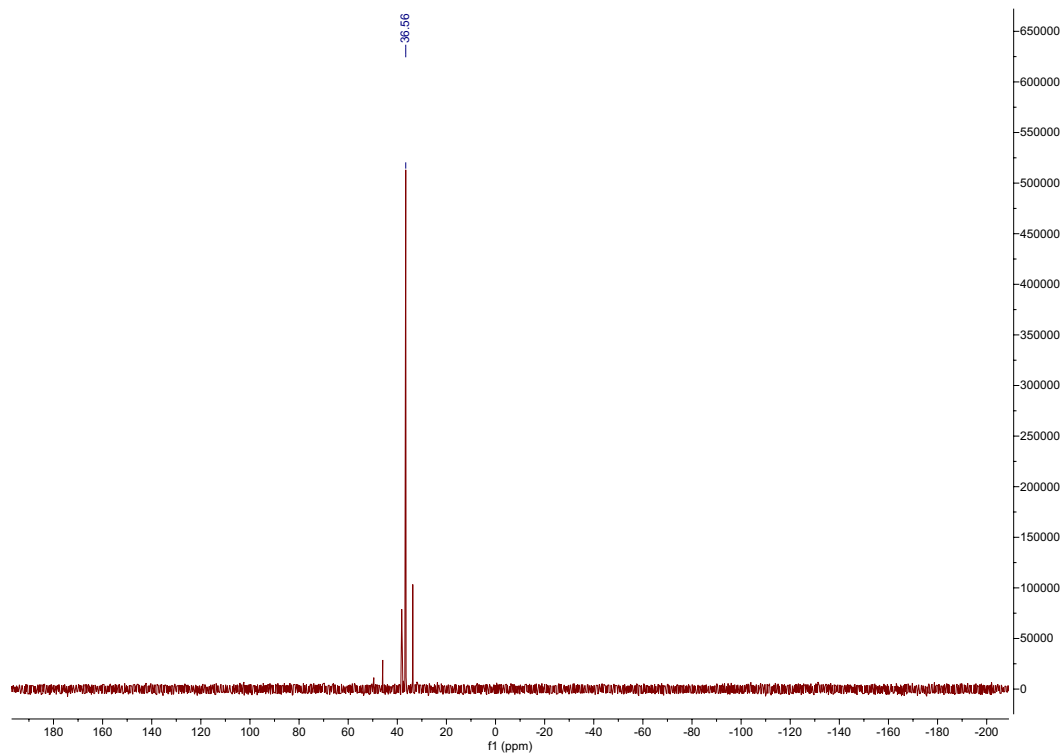
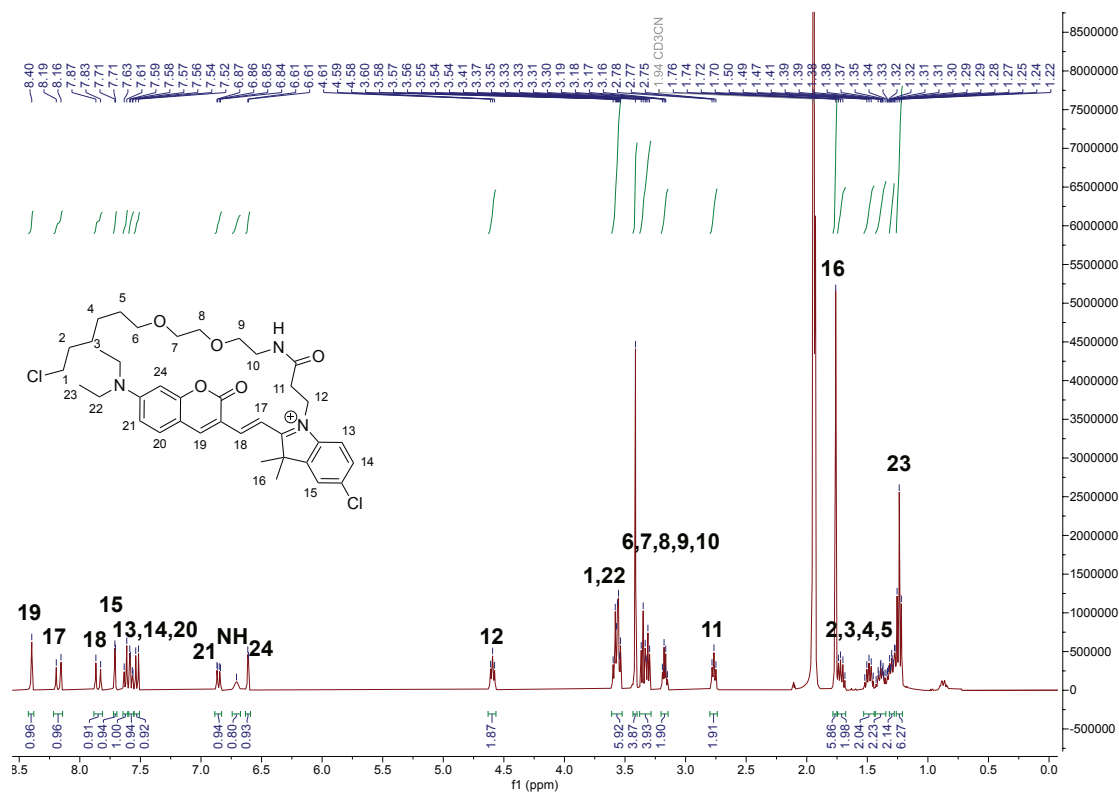
^1H -NMR (400 MHz, CDCl_3) of compound **24**.

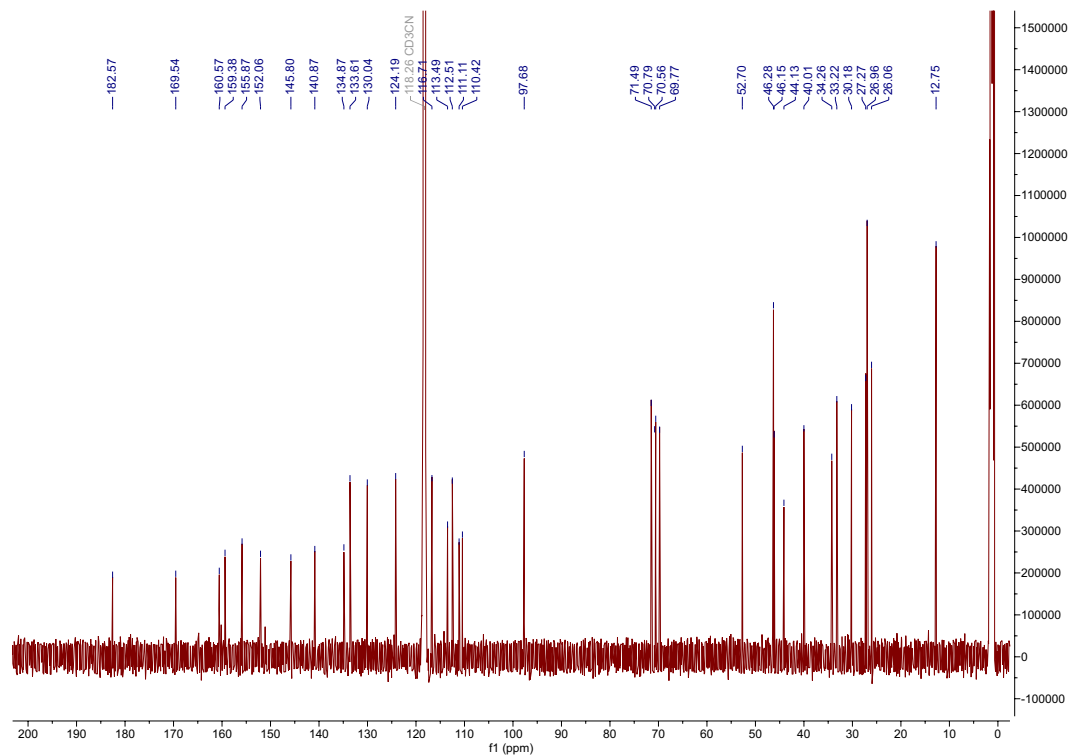


^{13}C -NMR (101 MHz, CDCl_3) of compound **24**.

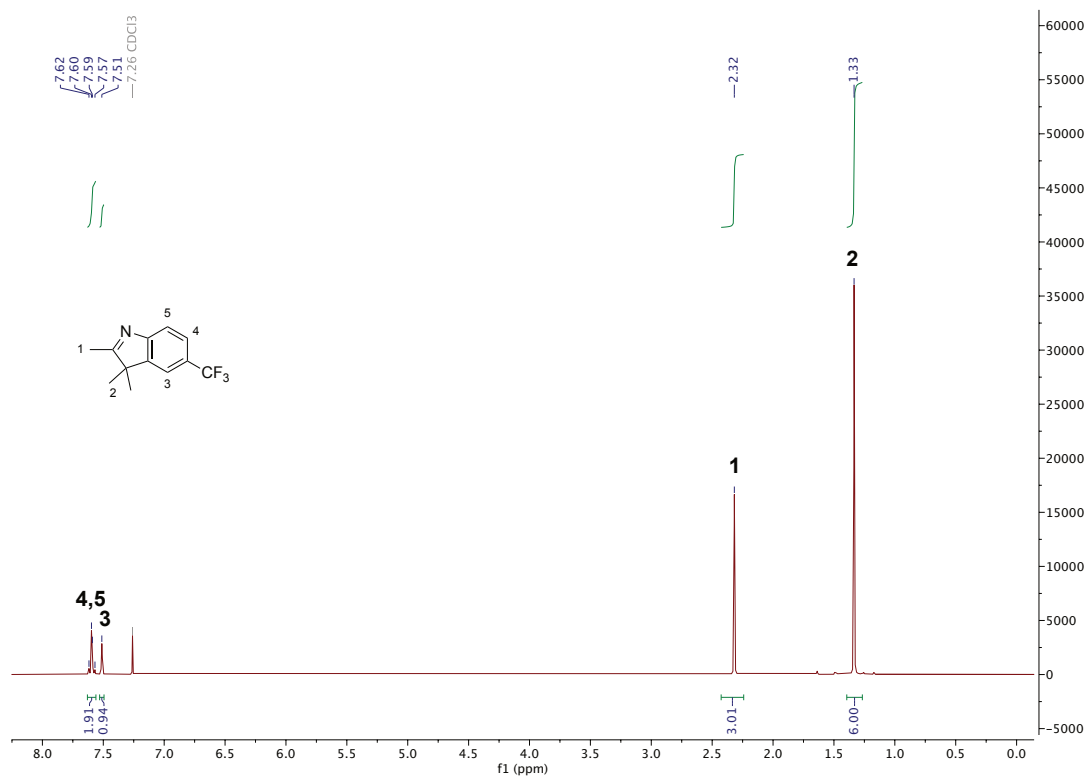


^1H -NMR (400 MHz, $\text{DMSO-}d_6$) of compound **25**.

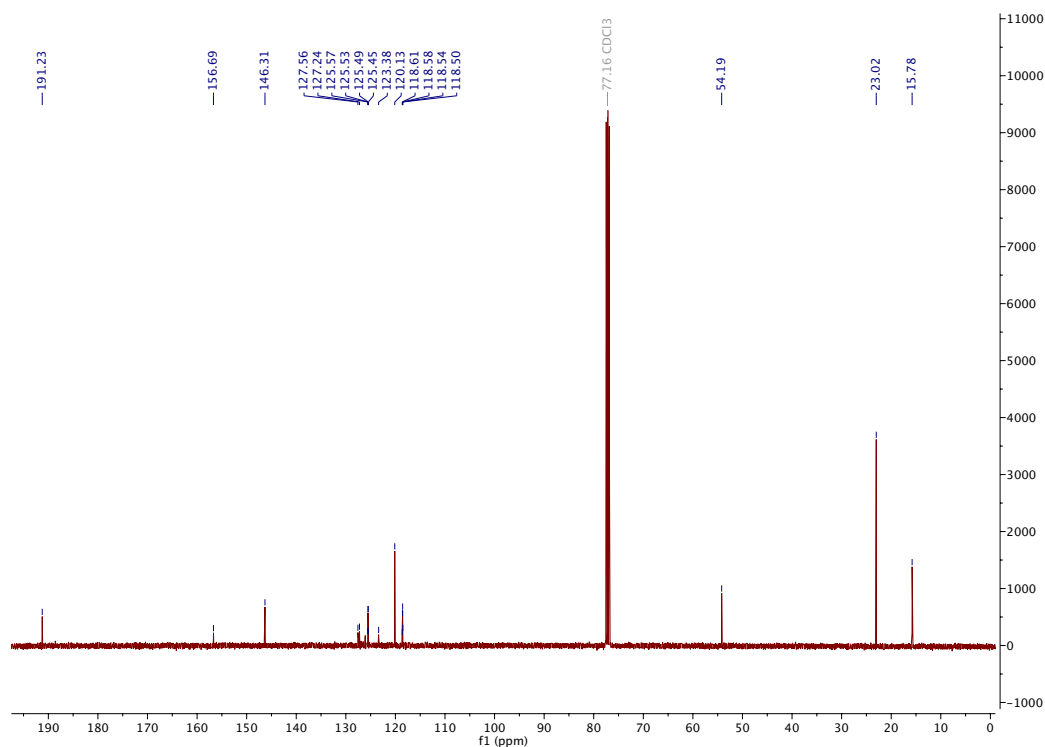
 ^{31}P -NMR (162 MHz, $\text{DMSO-}d_6$) of compound **25**. ^1H -NMR (400 MHz, CD_3CN) of compound **27**.



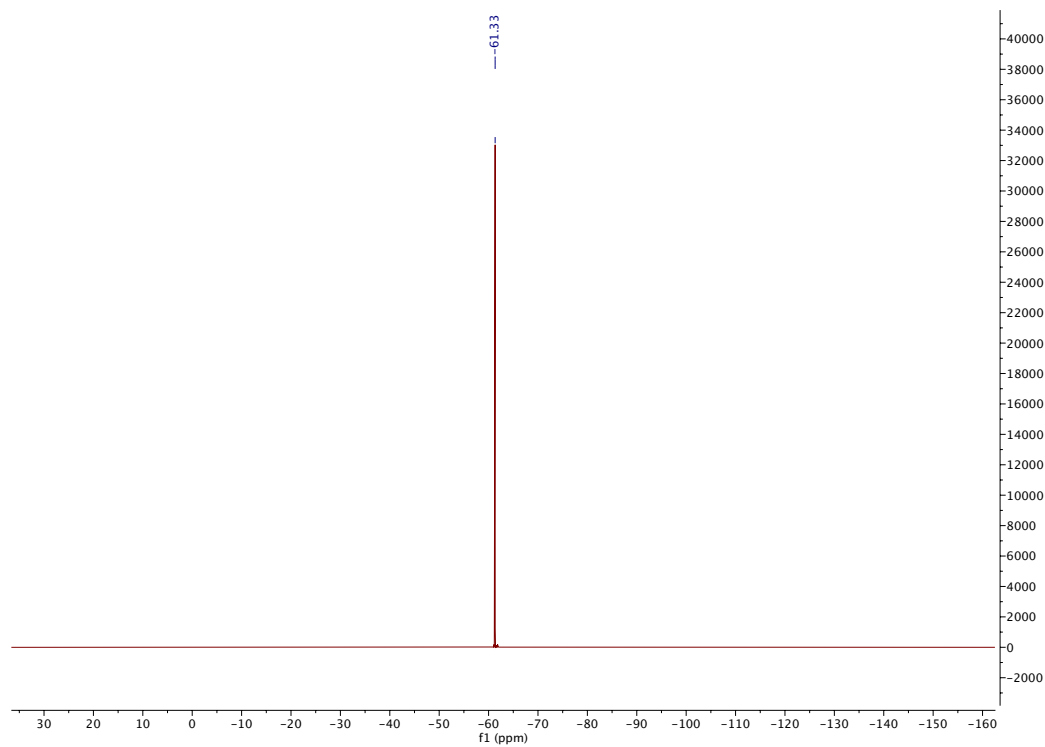
^{13}C -NMR (151 MHz, CD_3CN) of compound **27**.



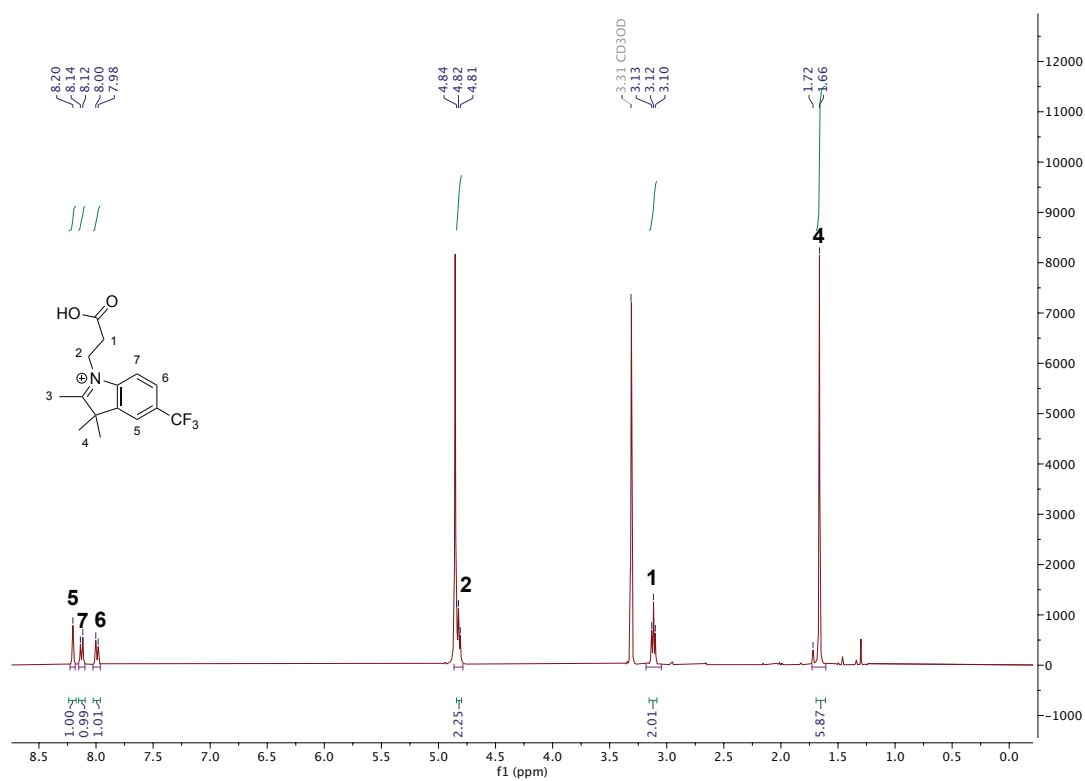
^1H NMR (400 MHz, CDCl_3) of compound **28**.



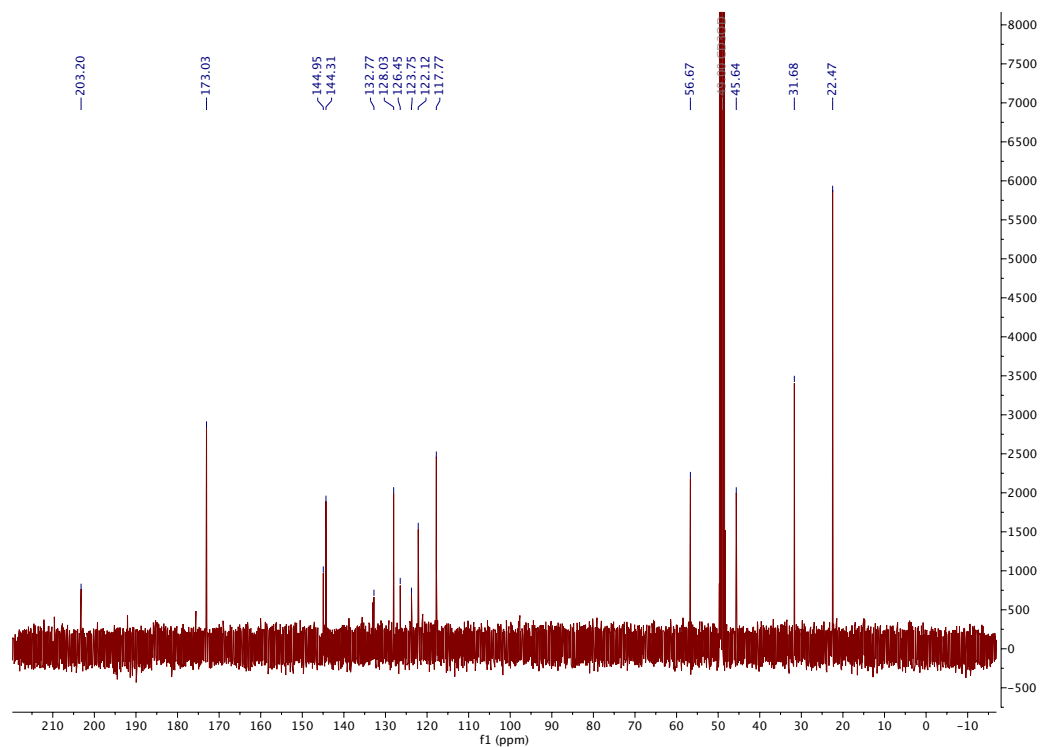
^{13}C NMR (101 MHz, CDCl_3) of compound **28**.



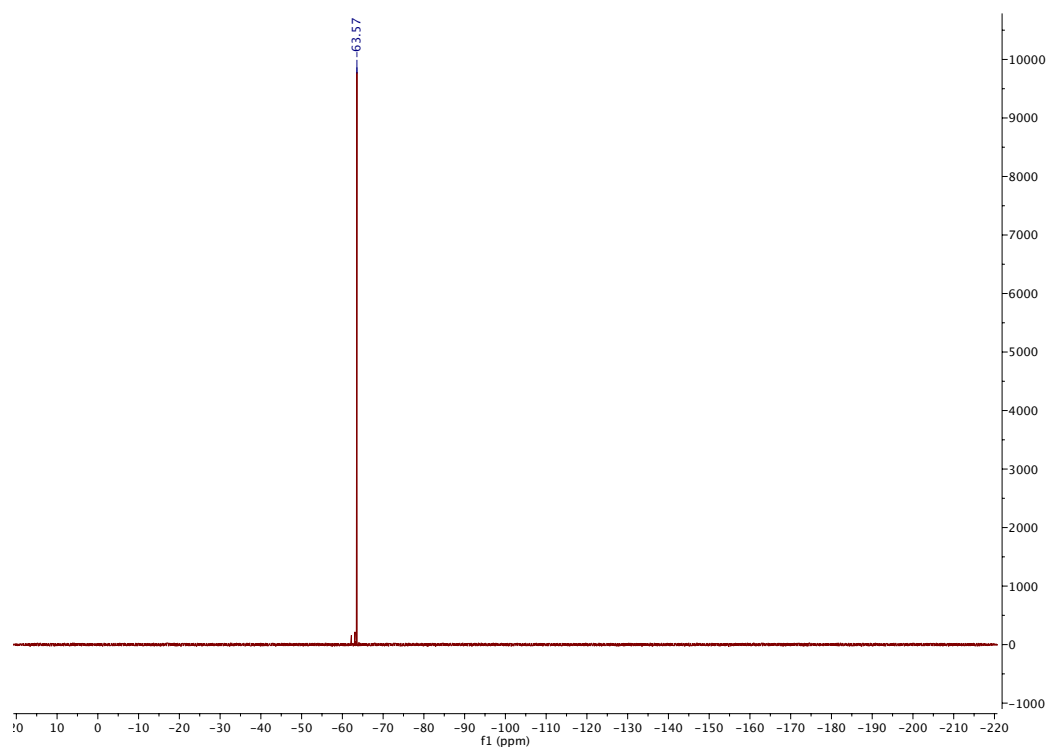
^{19}F NMR (376 MHz, CDCl_3) of compound **28**.



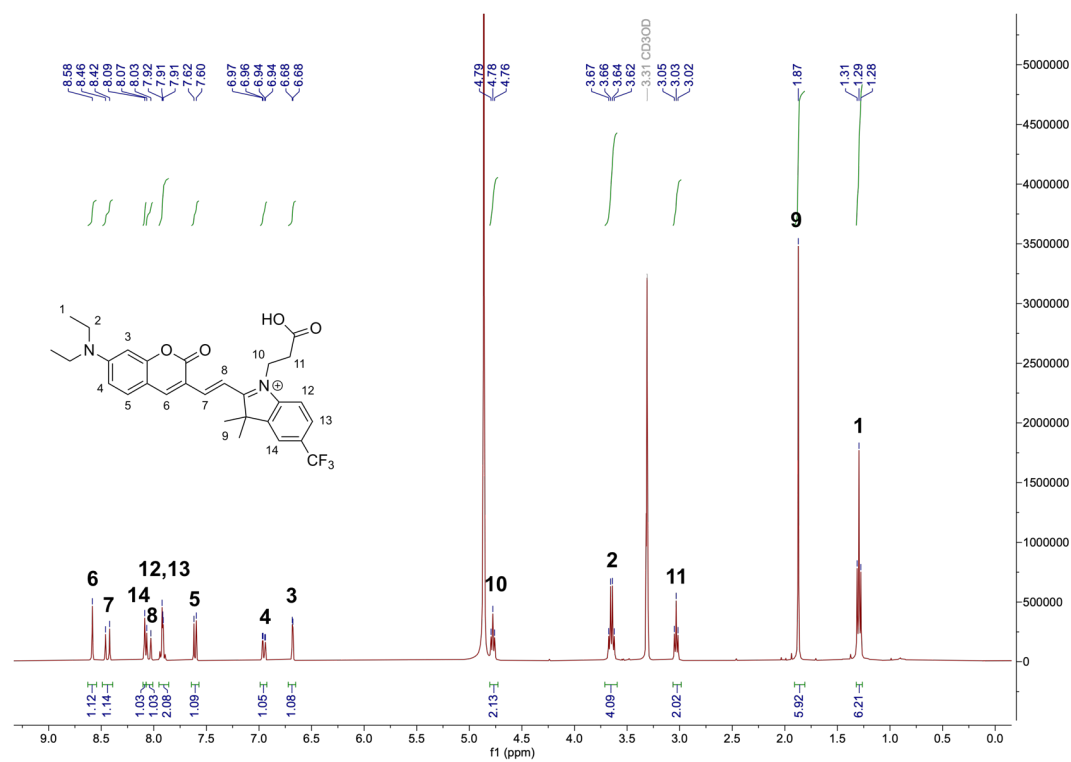
¹H NMR (400 MHz, CD₃OD) of compound **29**.



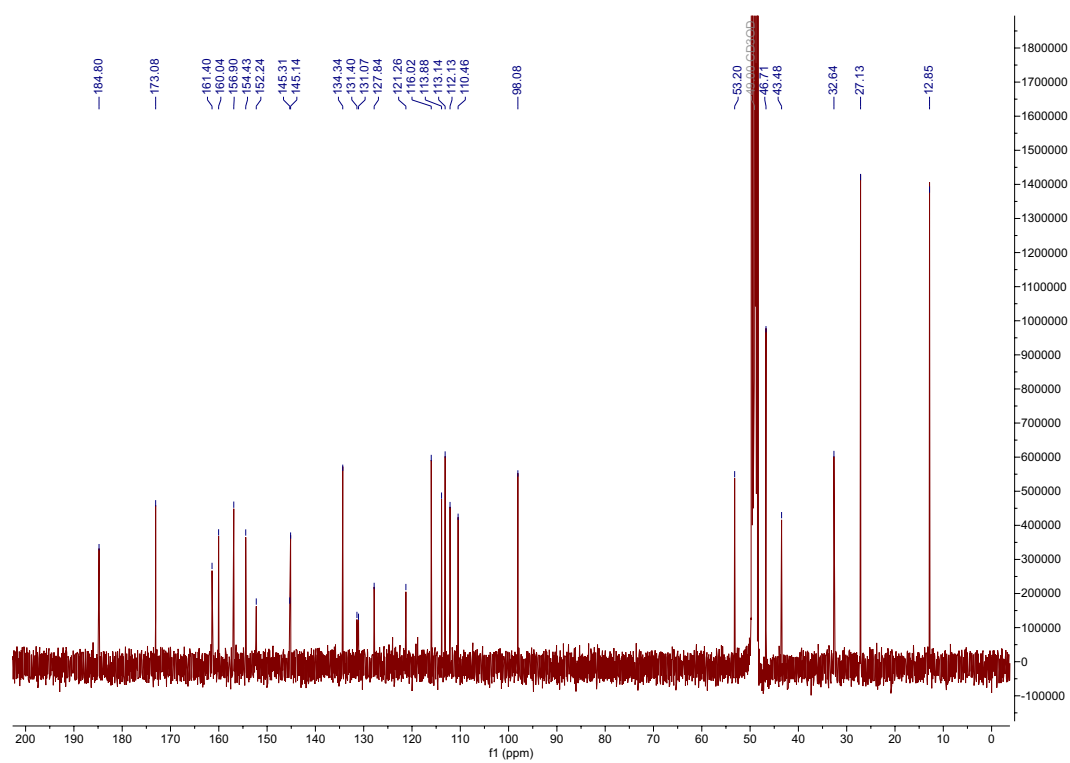
¹³C NMR (101 MHz, CD₃OD) of compound **29**.



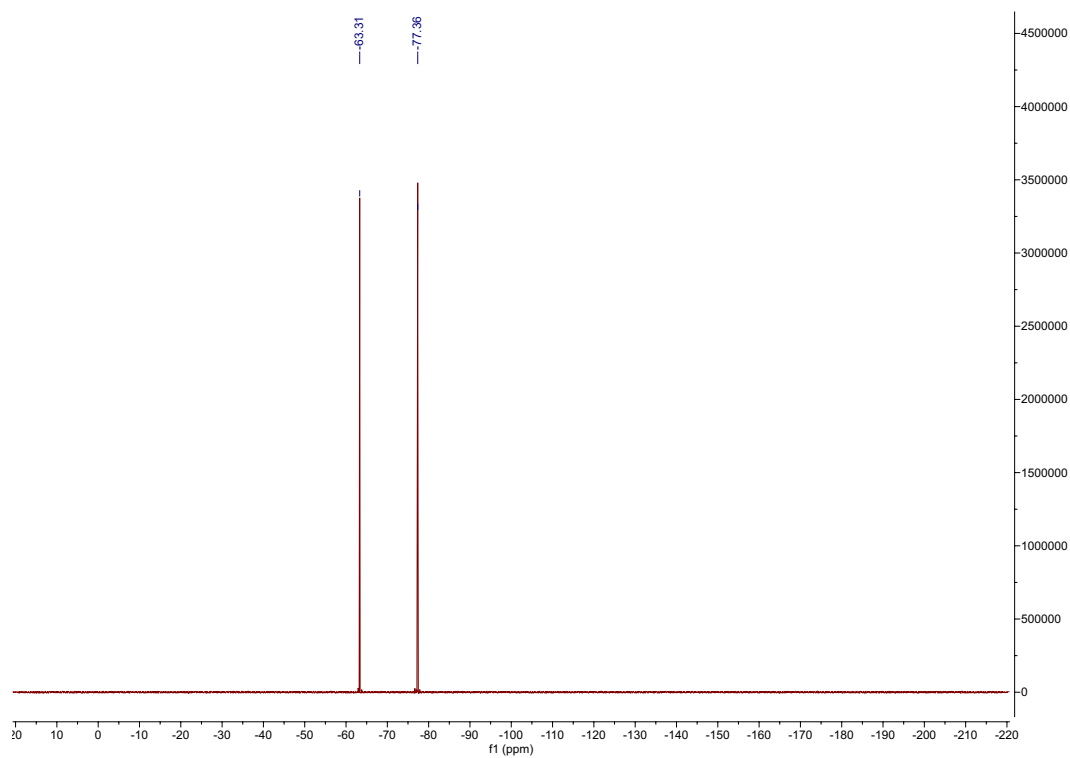
^{19}F NMR (376 MHz, CD_3OD) of compound **29**.



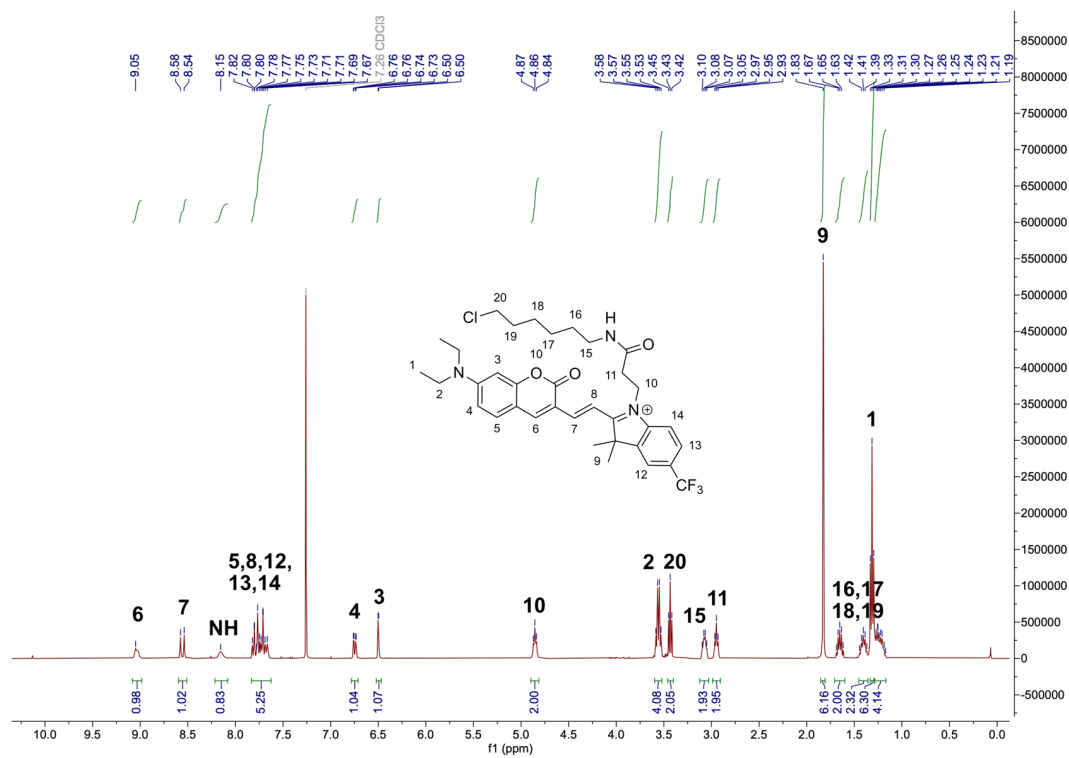
^1H NMR (400 MHz, CD_3OD) of compound **30**.



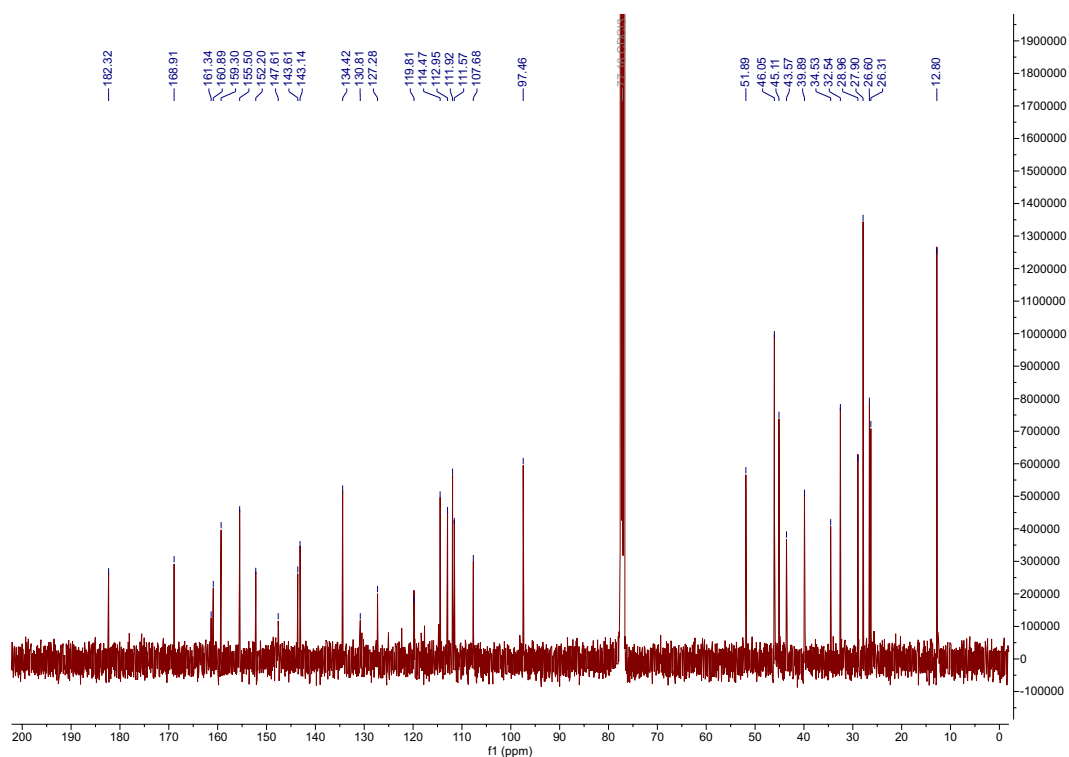
^{13}C NMR (101 MHz, CD_3OD) of compound **30**.



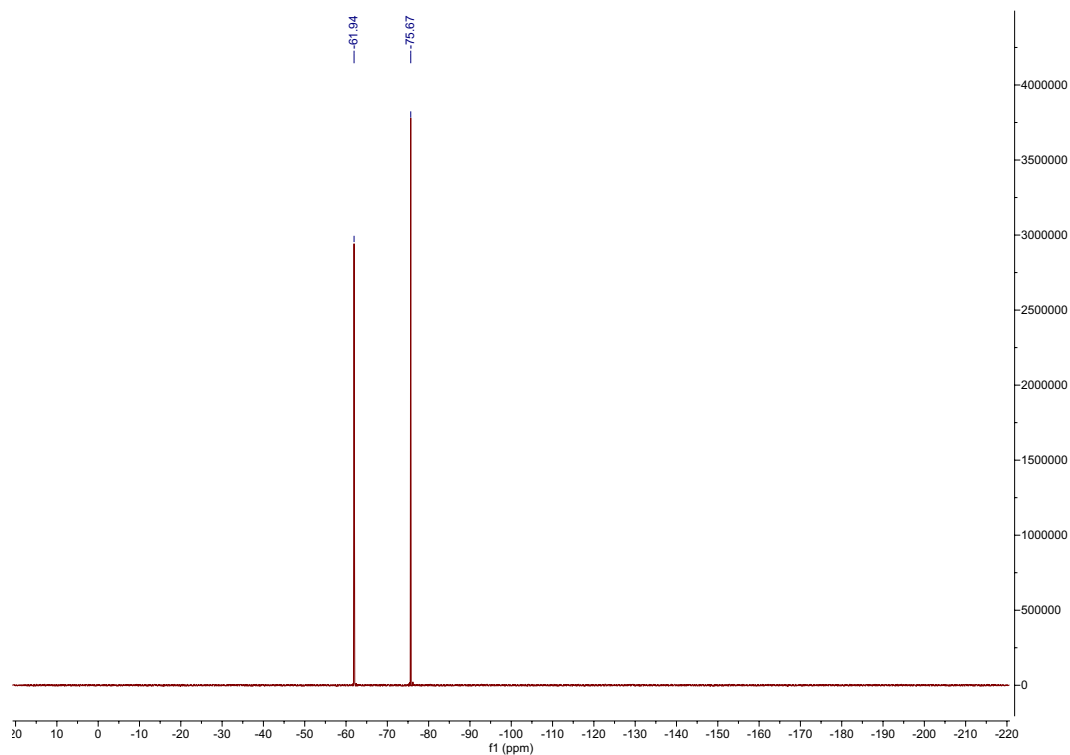
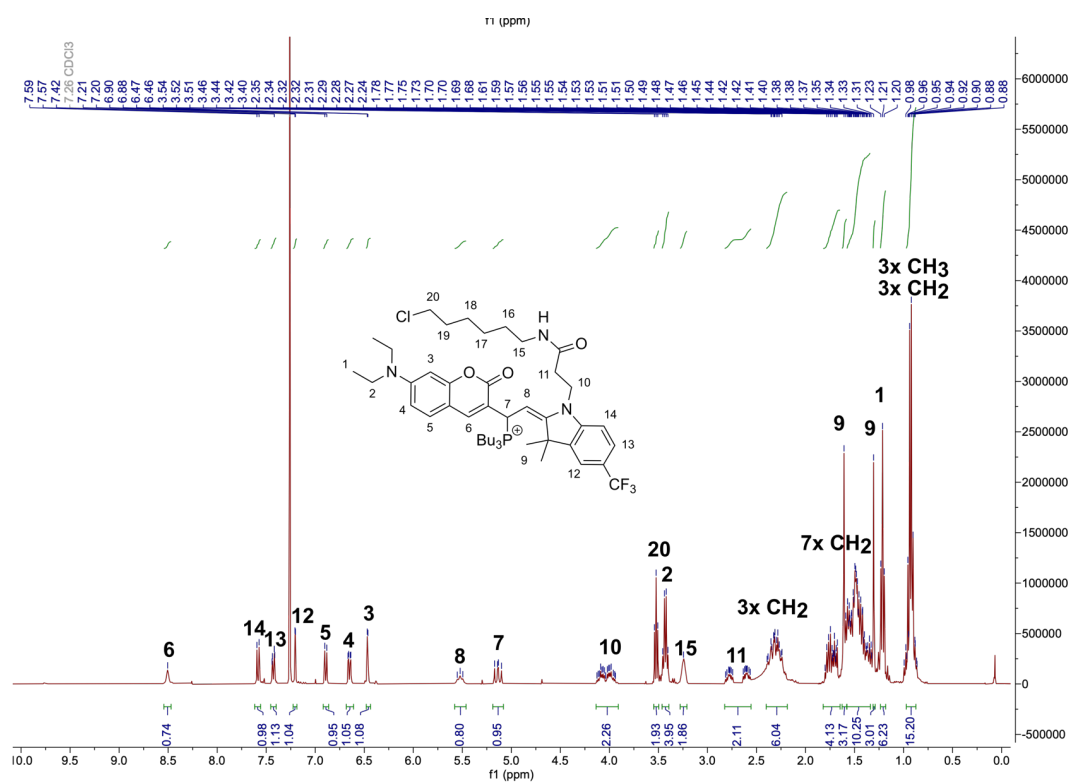
^{19}F NMR (376 MHz, CD_3OD) of compound **30**.

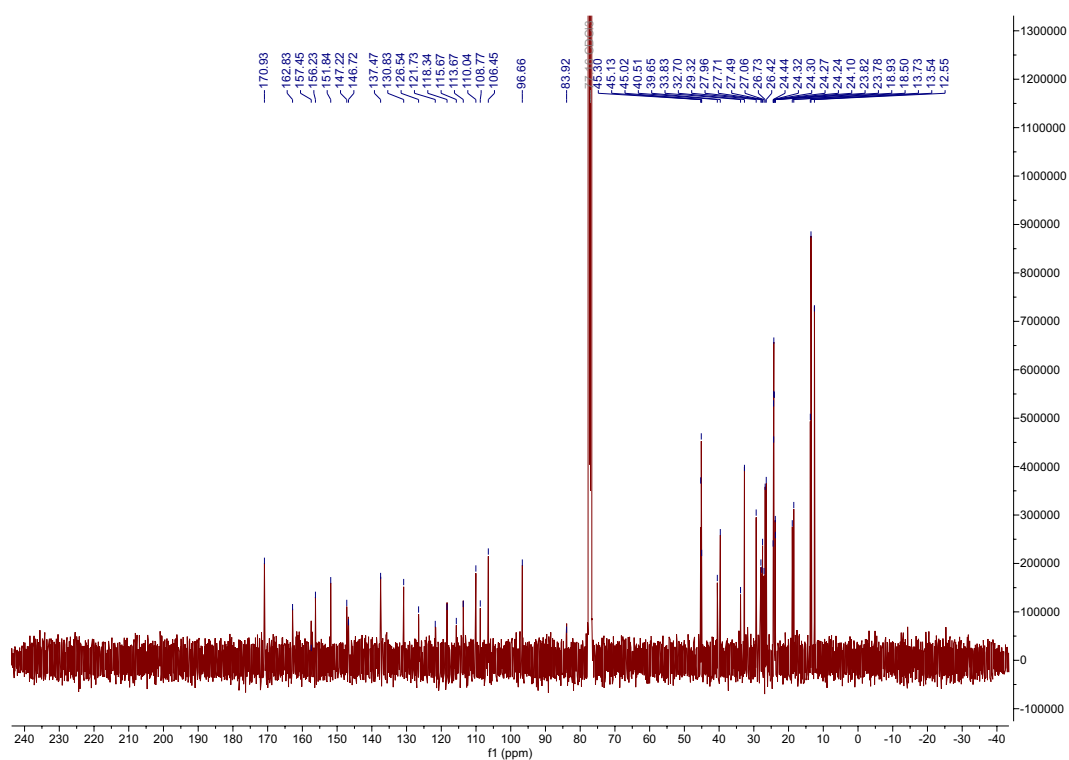


¹H NMR (400 MHz, CDCl₃) of compound **31**.

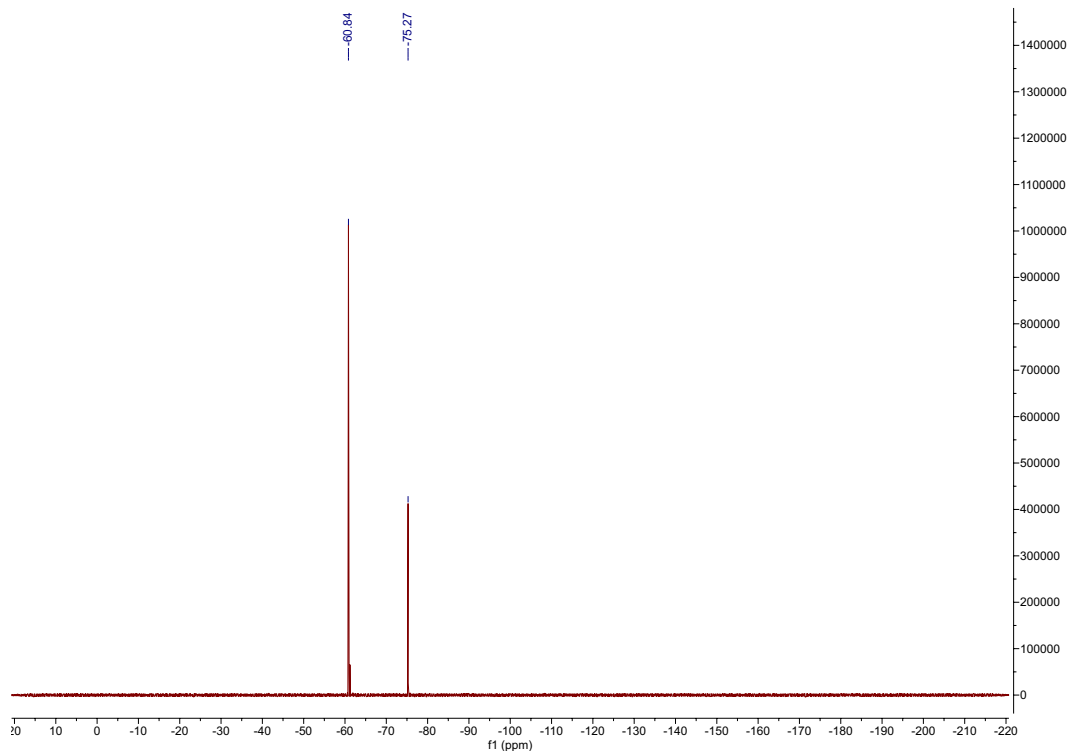


¹³C NMR (101 MHz, CDCl₃) of compound **31**.

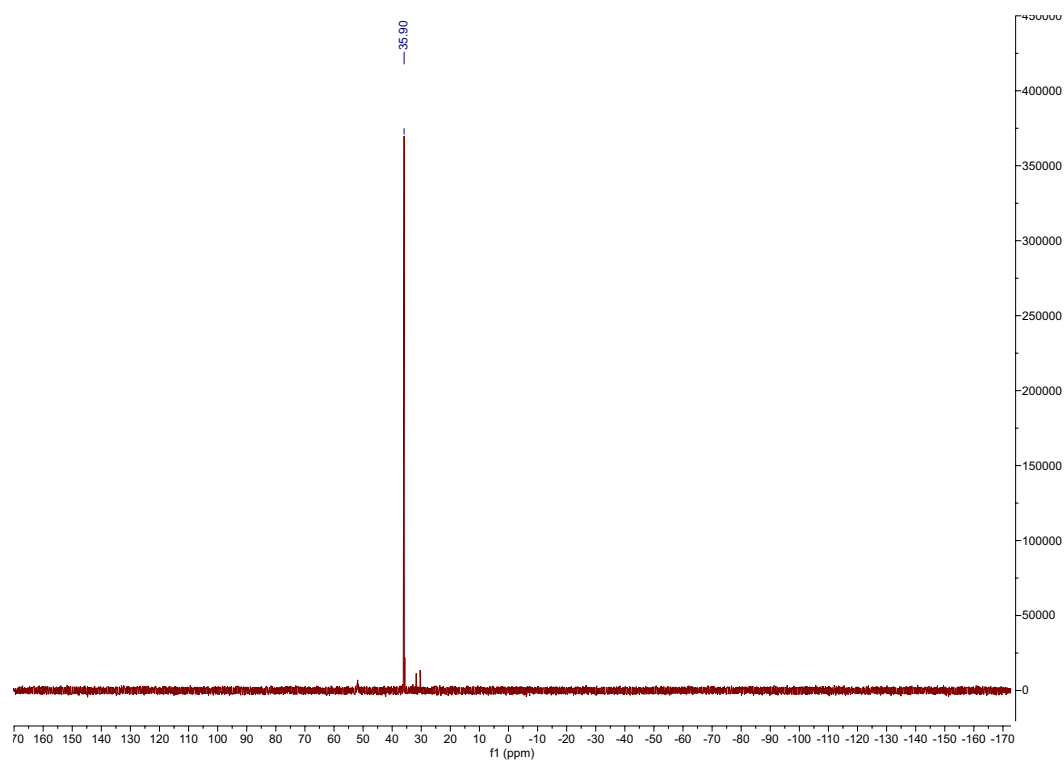
 ^{19}F NMR (376 MHz, CDCl_3) of compound **31**. ^1H NMR (400 MHz, CDCl_3) of compound **32**.



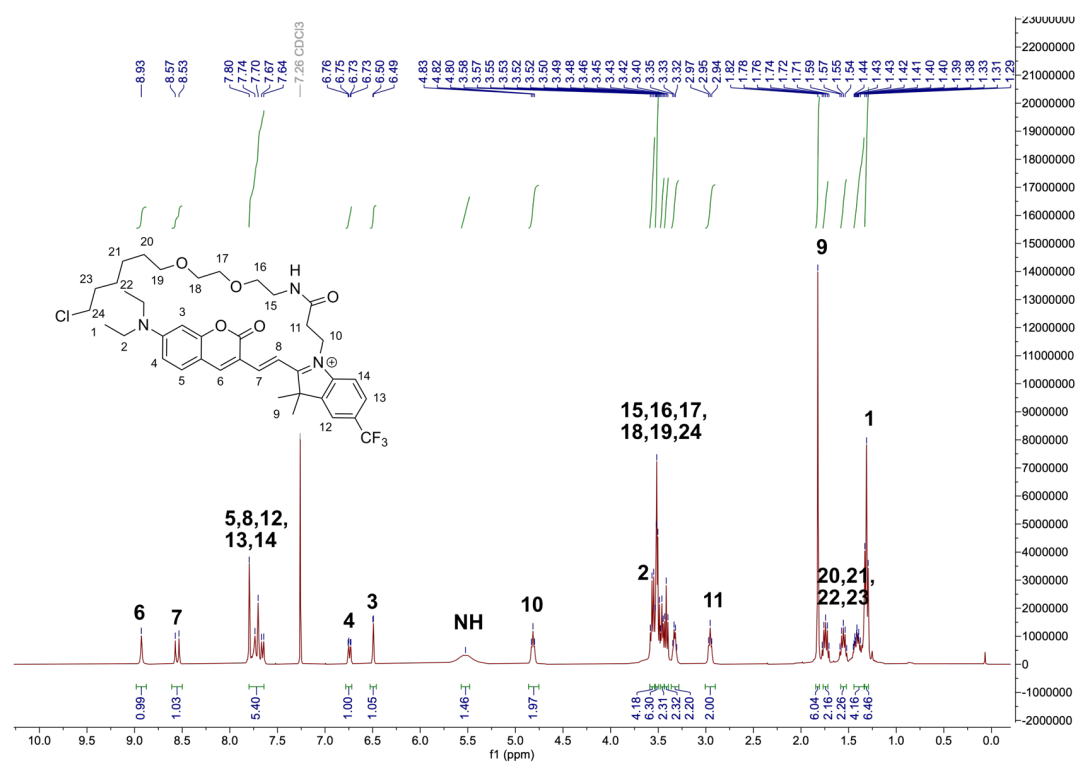
¹³C NMR (101 MHz, CDCl₃) of compound **32**.



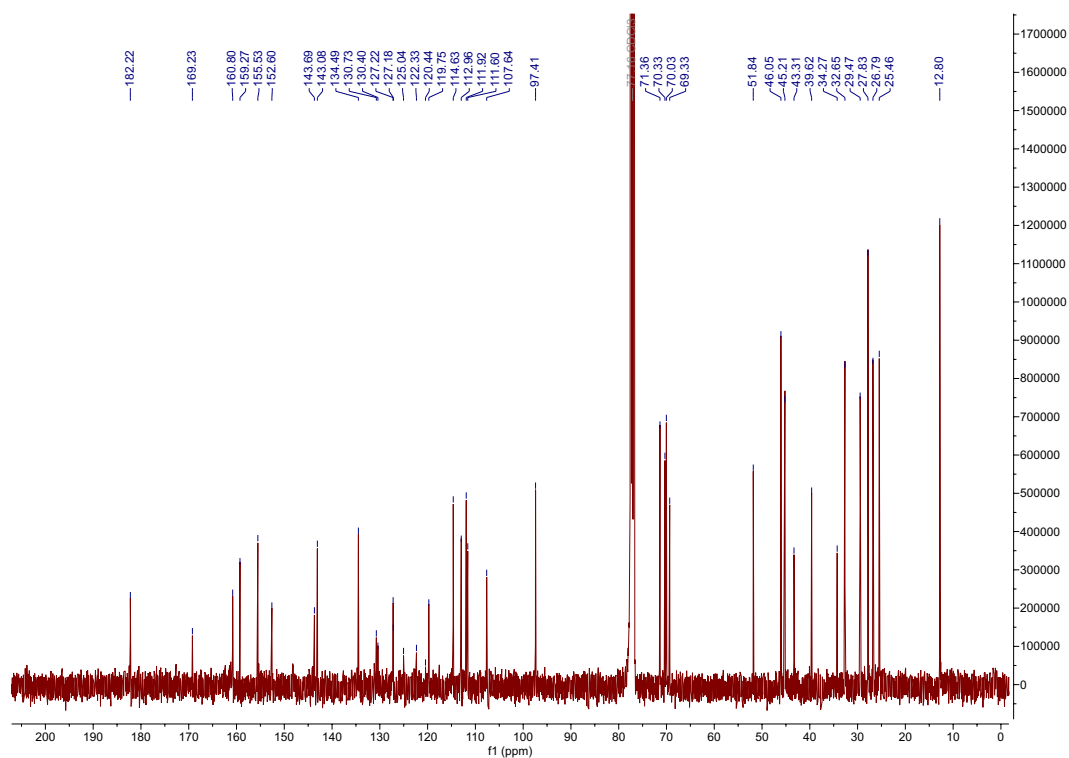
¹⁹F NMR (377 MHz, CDCl₃) of compound **32**.



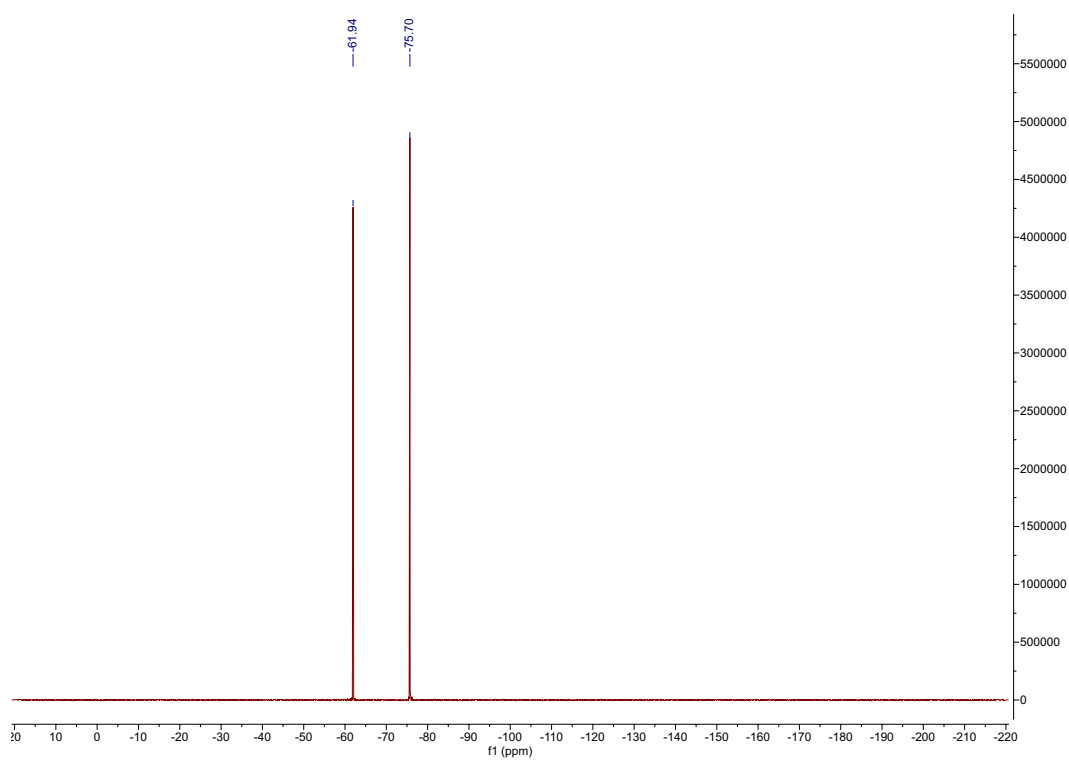
^{31}P NMR (162 MHz, CDCl_3) of compound **32**.



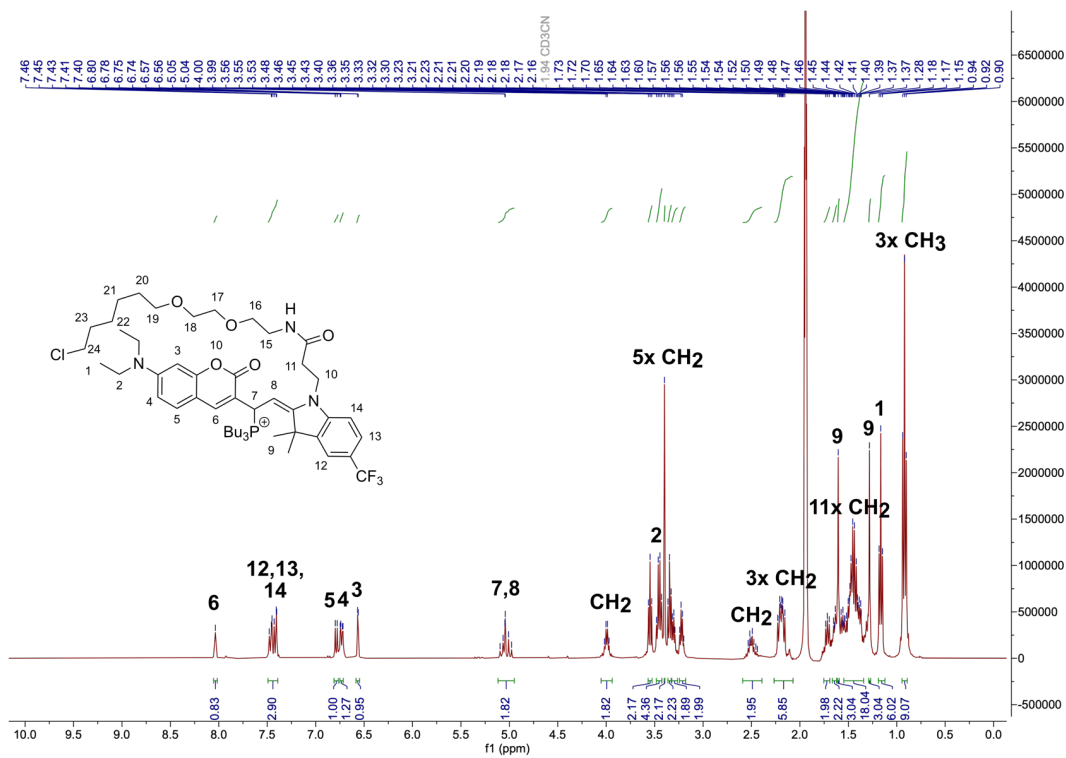
^1H NMR (400 MHz, CDCl_3) of compound **33**.



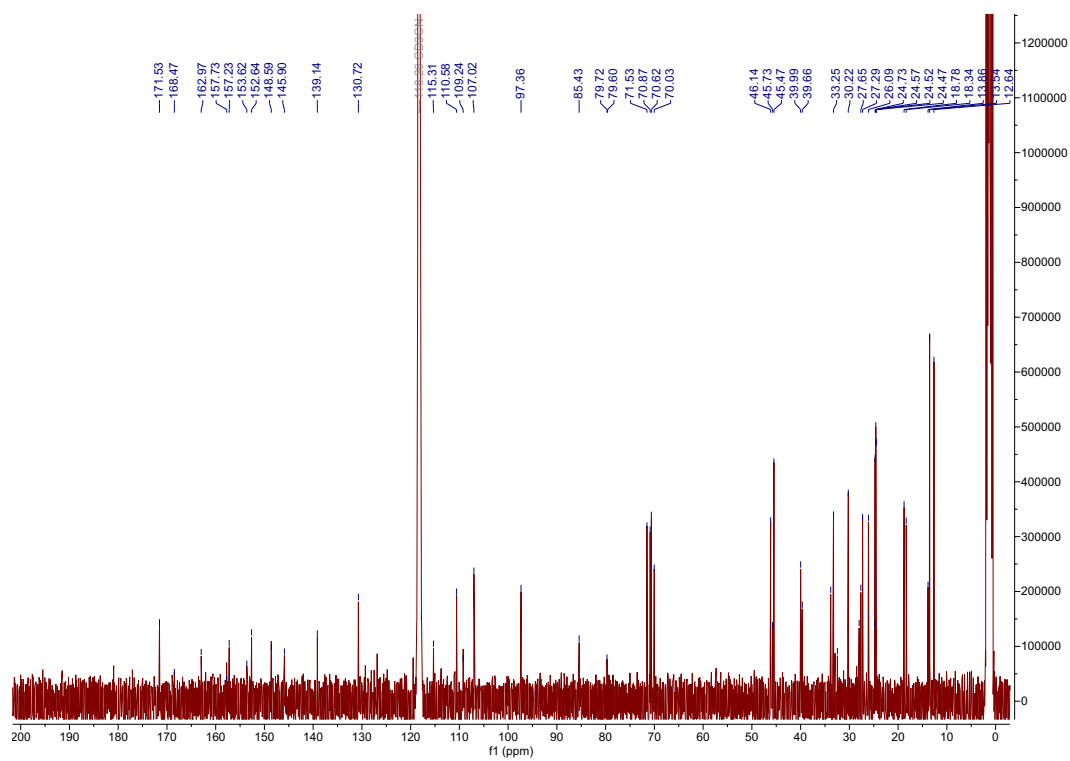
^{13}C NMR (101 MHz, CDCl_3) of compound **33**.



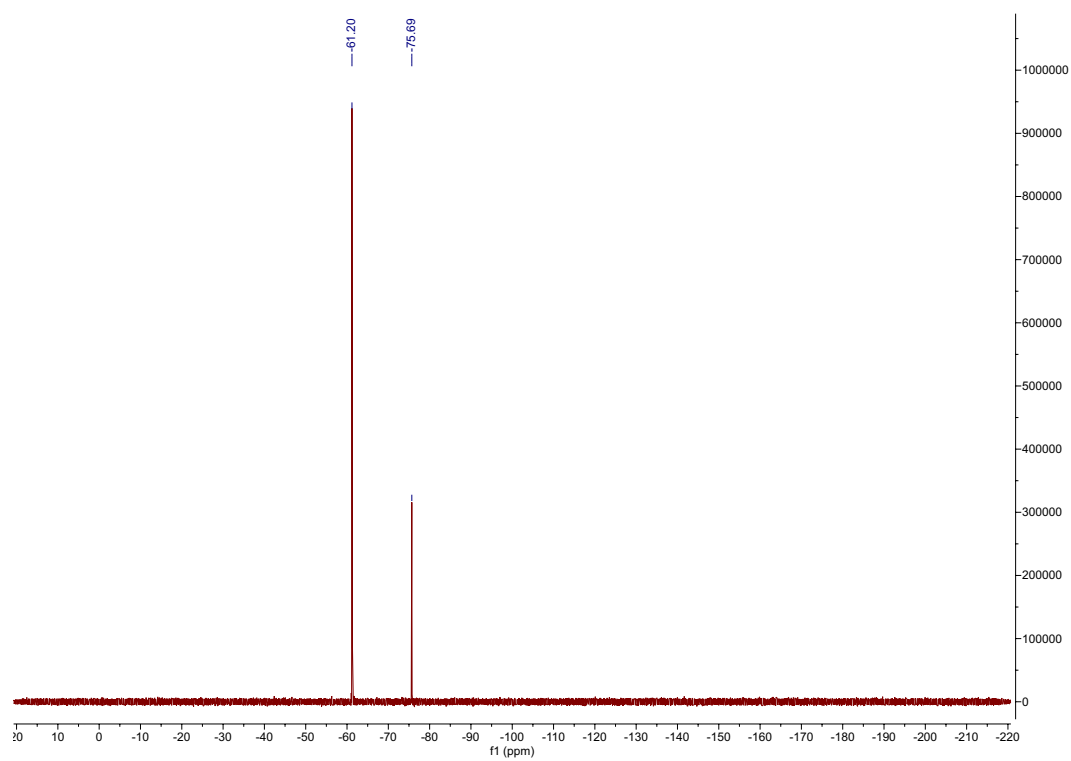
^{19}F NMR (376 MHz, CDCl_3) of compound **33**.



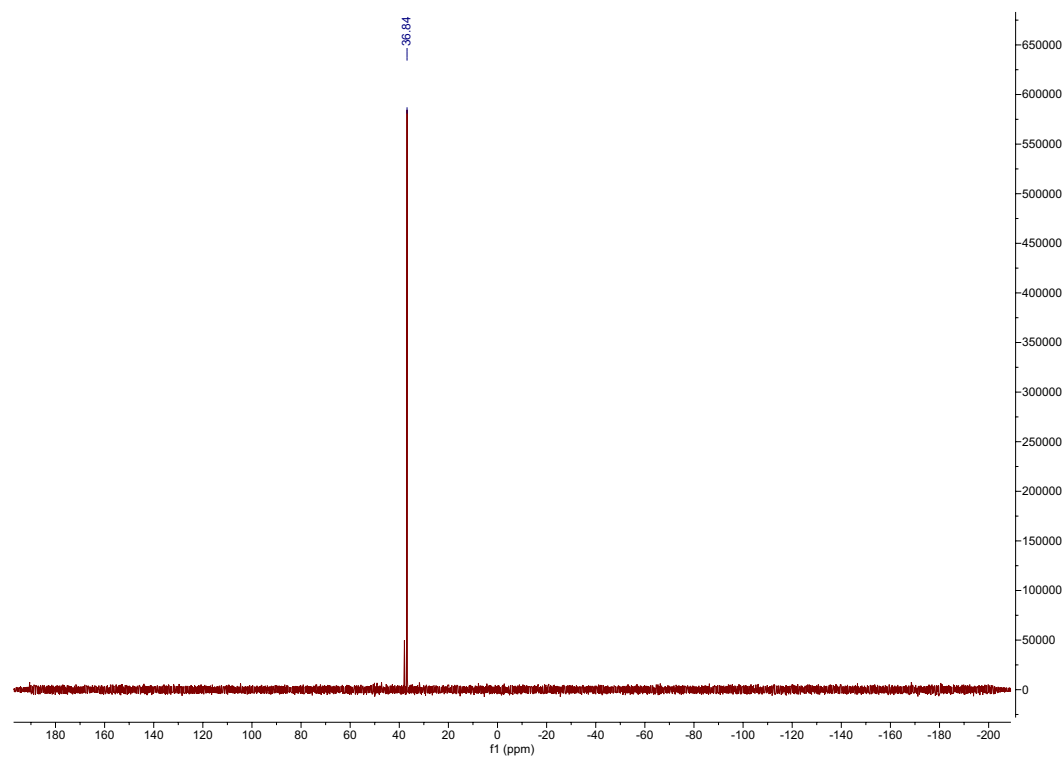
¹H NMR (400 MHz, CD₃CN) of compound **34**.



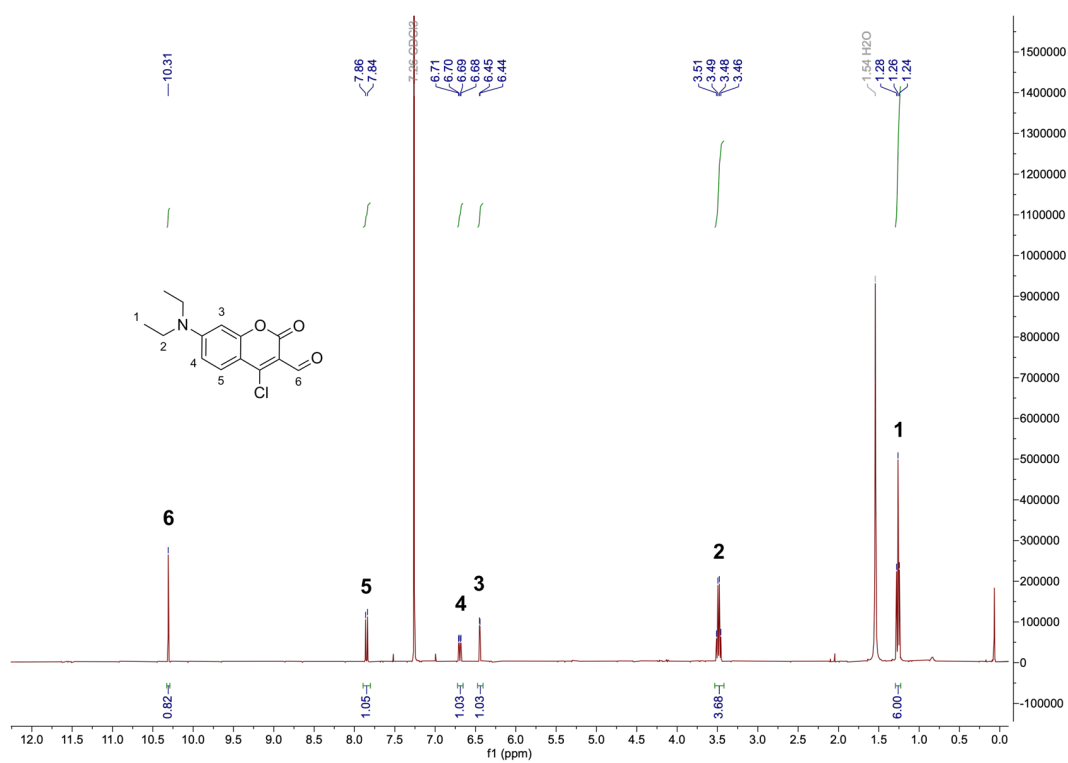
¹³C NMR (101 MHz, CD₃CN) of compound **34**.



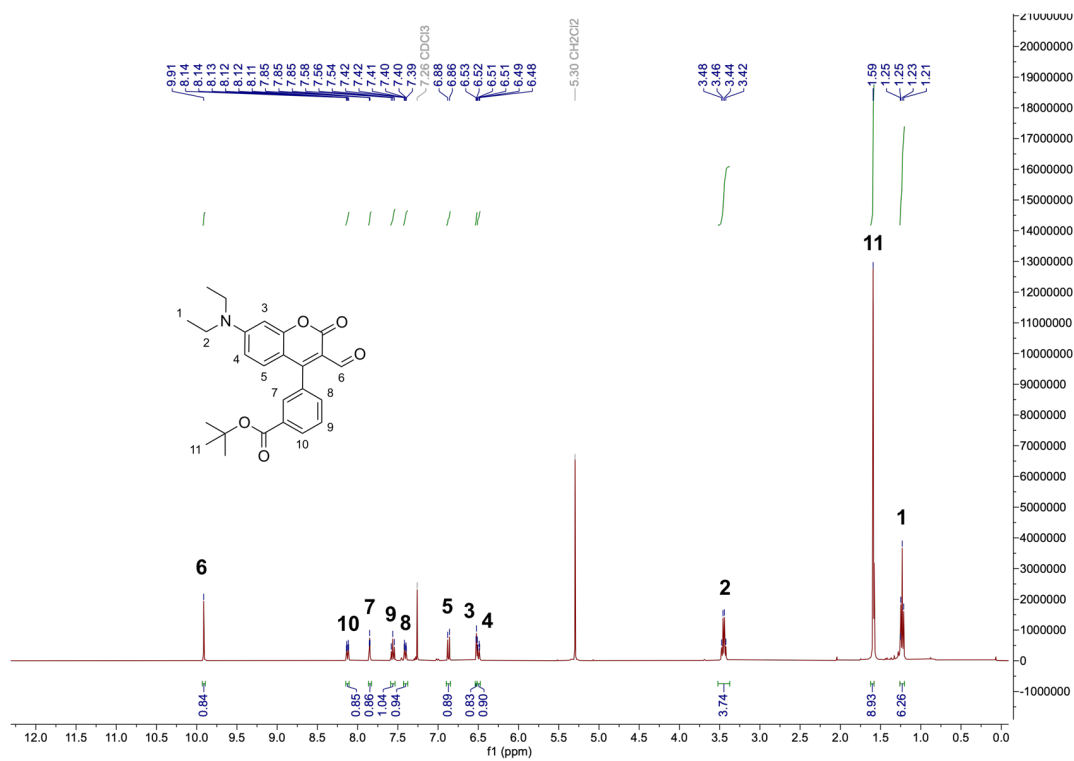
^{19}F NMR (376 MHz, CD_3CN) of compound **34**.



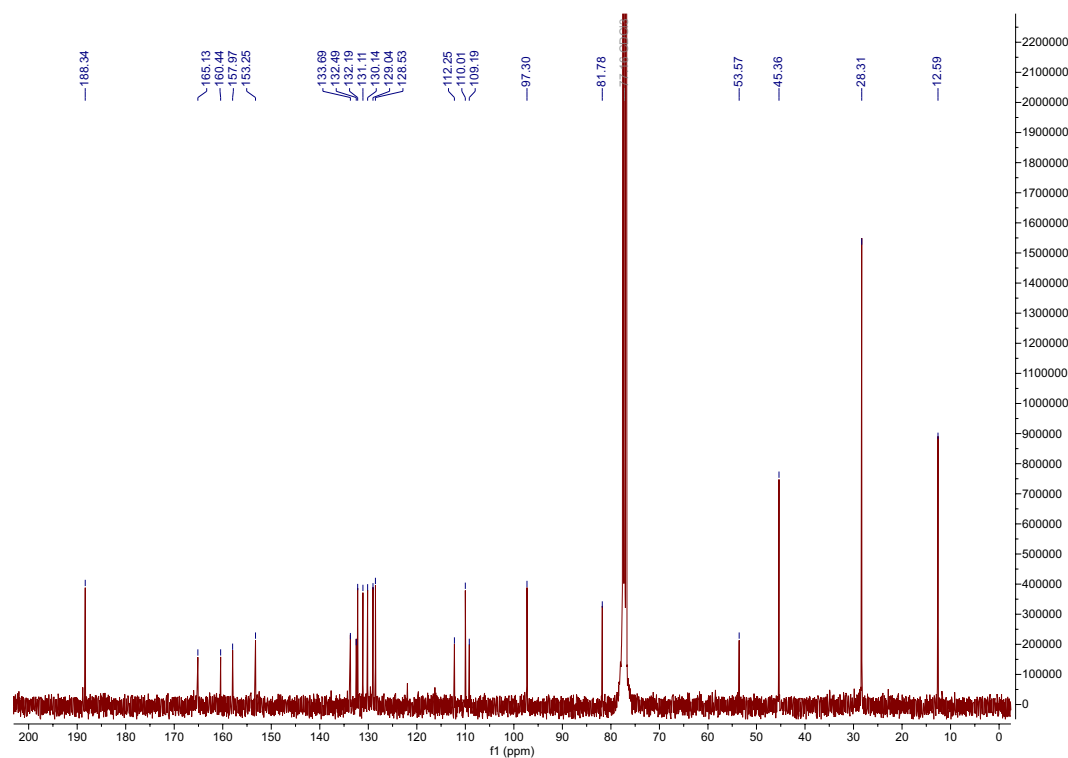
^{31}P NMR (162 MHz, CD_3CN) of compound **34**.



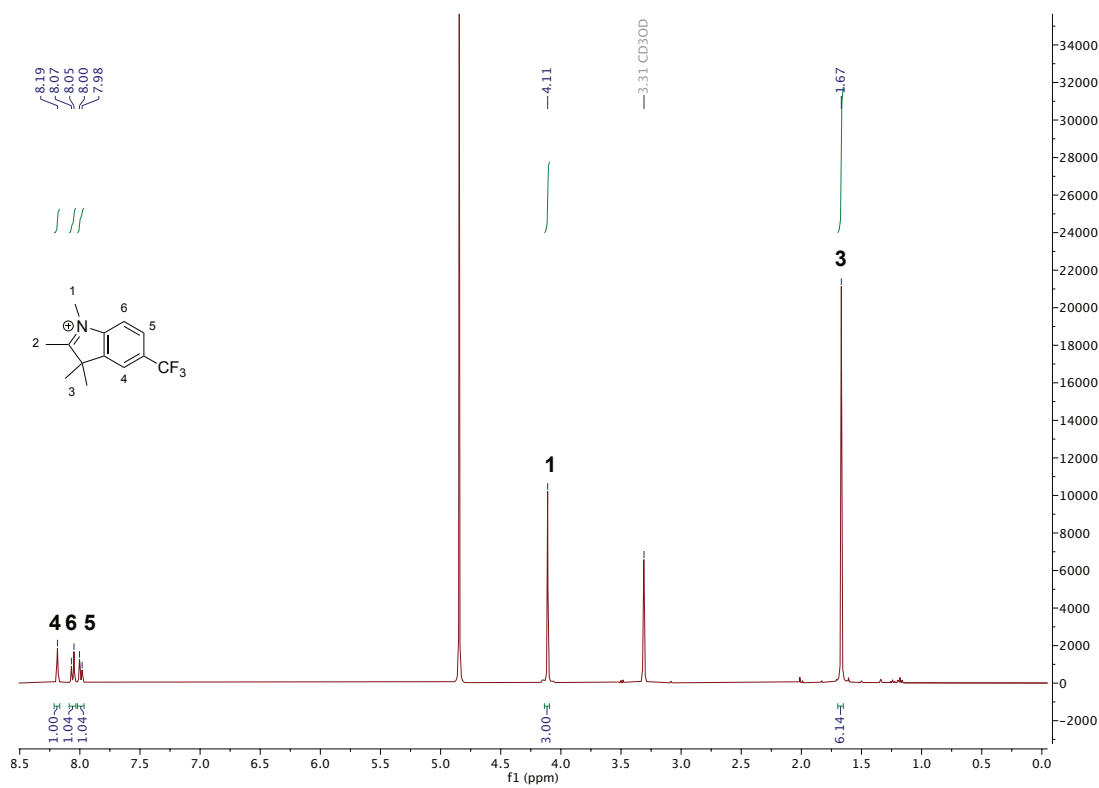
¹H NMR (400 MHz, CDCl₃) of compound **35**.



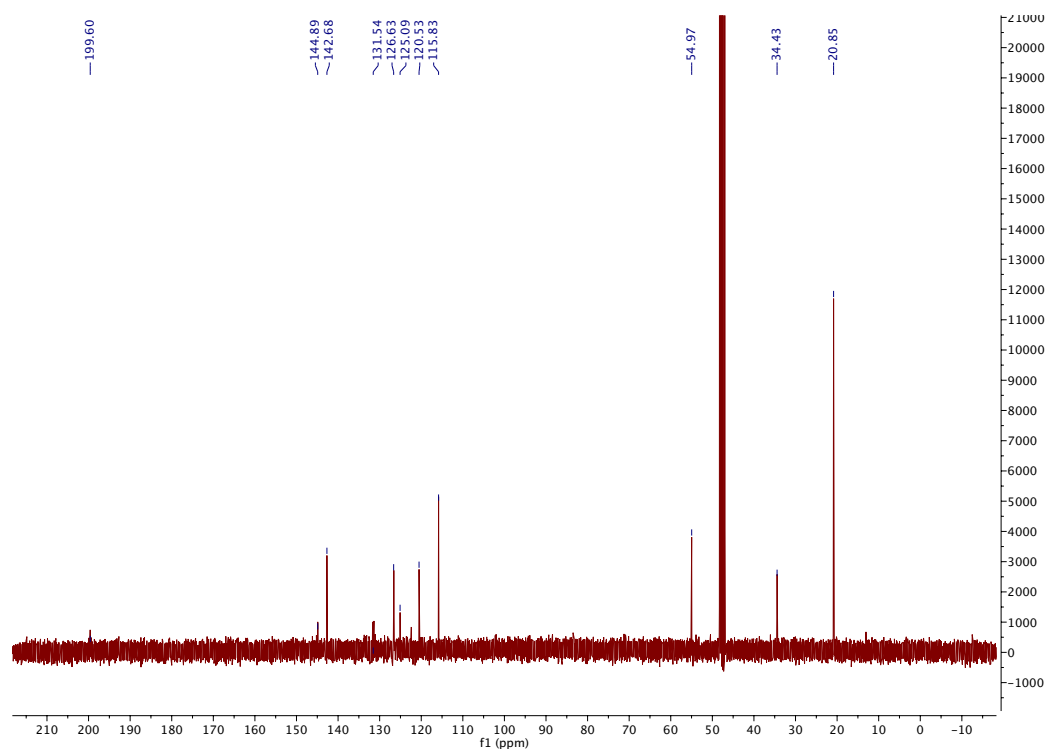
¹H NMR (400 MHz, CDCl₃) of compound **36**.



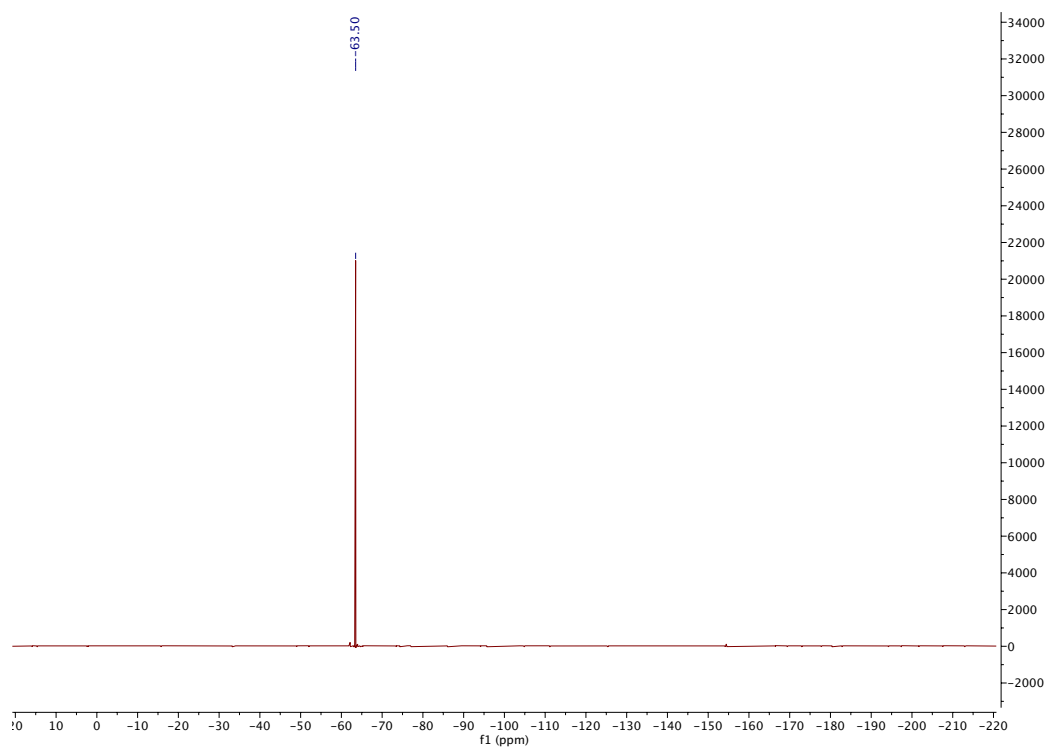
^{13}C NMR (101 MHz, CDCl_3) of compound **36**.



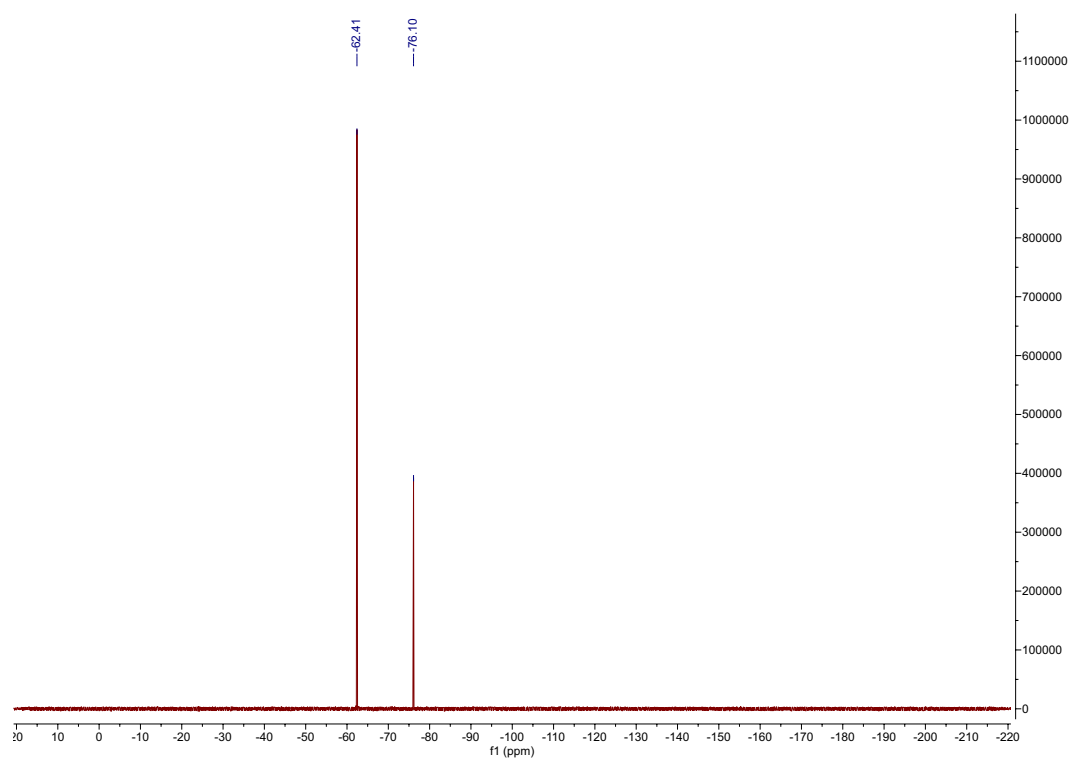
^1H NMR (400 MHz, CD_3OD) of compound **37**.



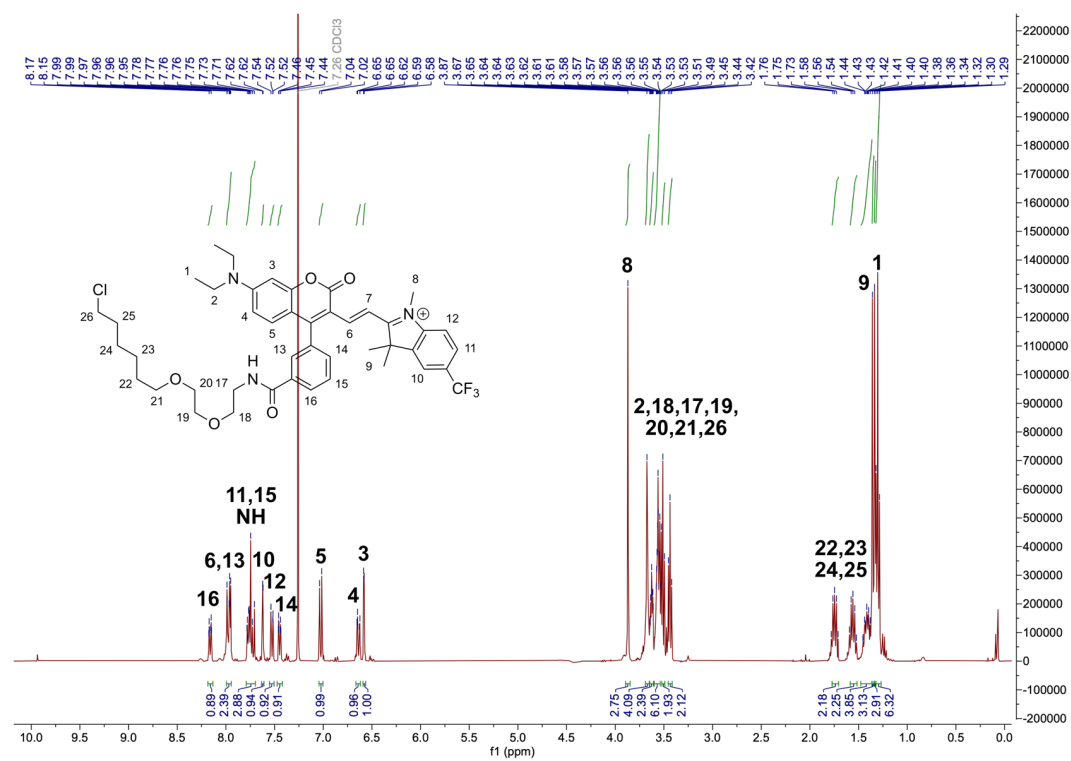
^{13}C NMR (101 MHz, CD_3OD) of compound **37**.



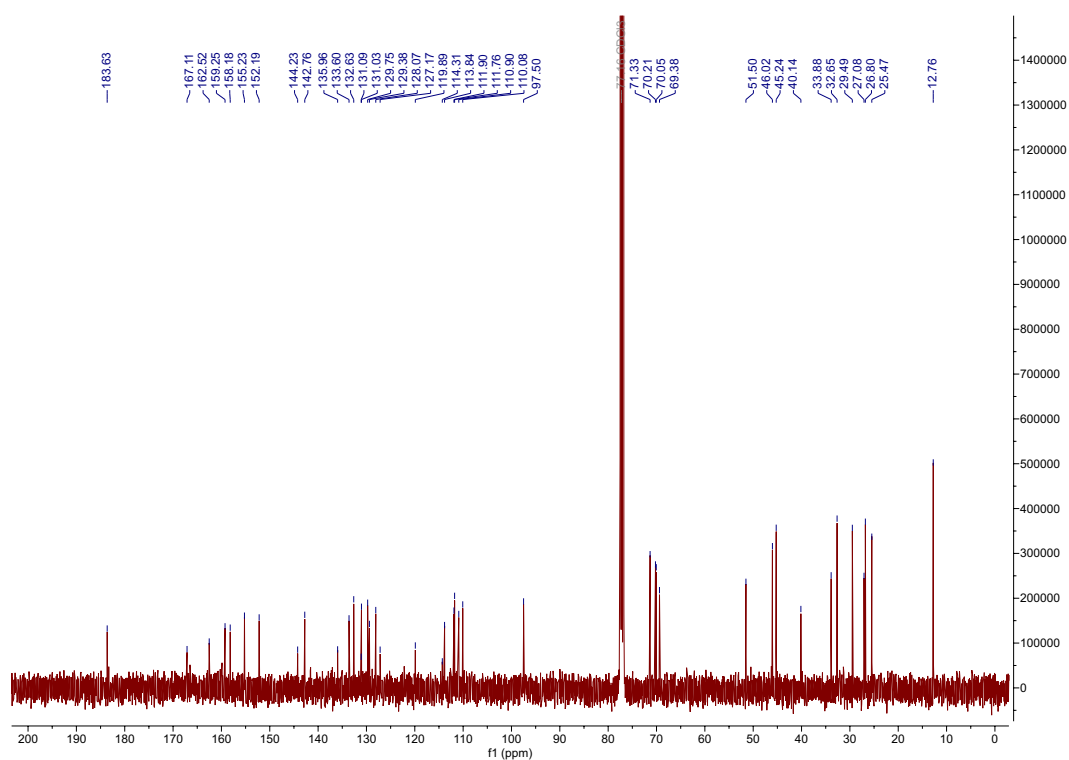
^{19}F NMR (376 MHz, CD_3OD) of compound **37**.



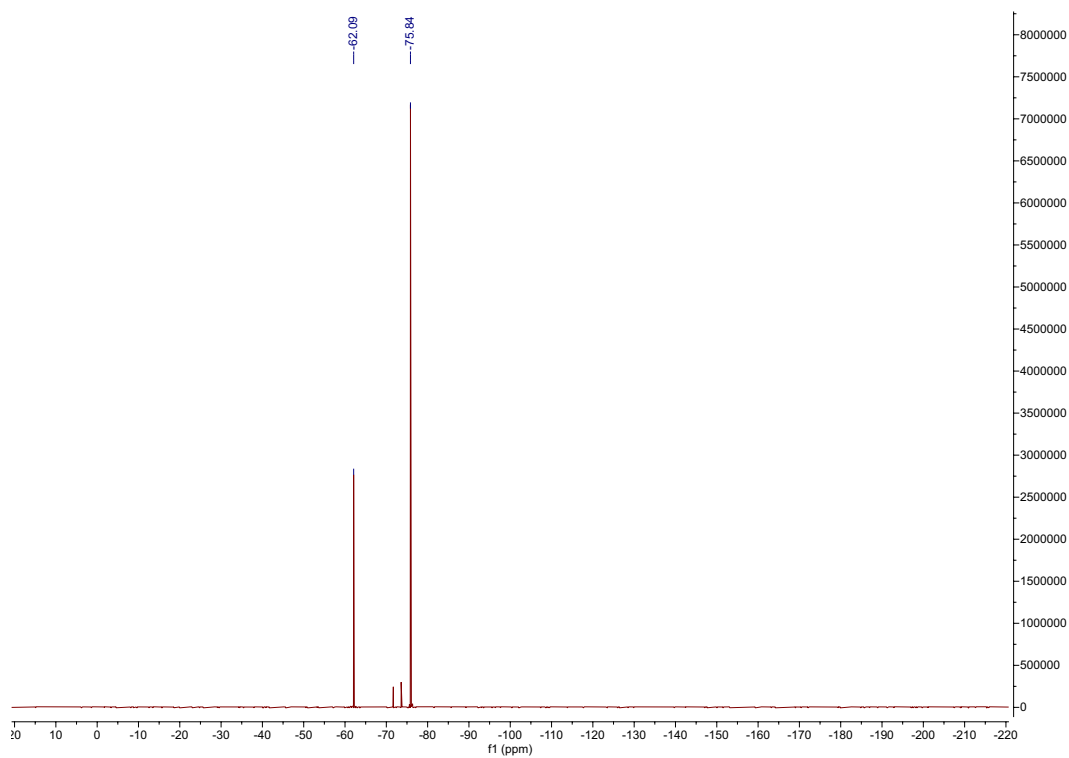
^{19}F NMR (377 MHz, CD_3CN) of compound **38**.



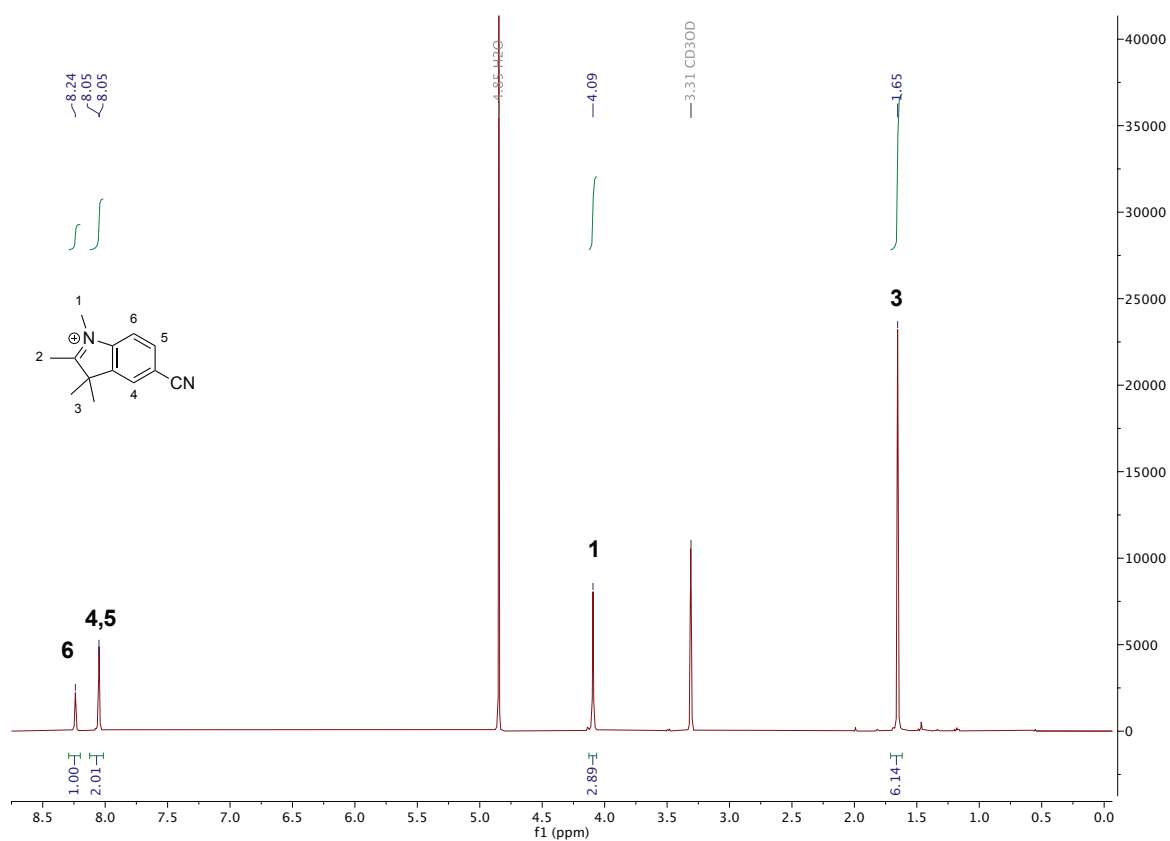
^1H NMR (400 MHz, CDCl_3) of compound **39**.



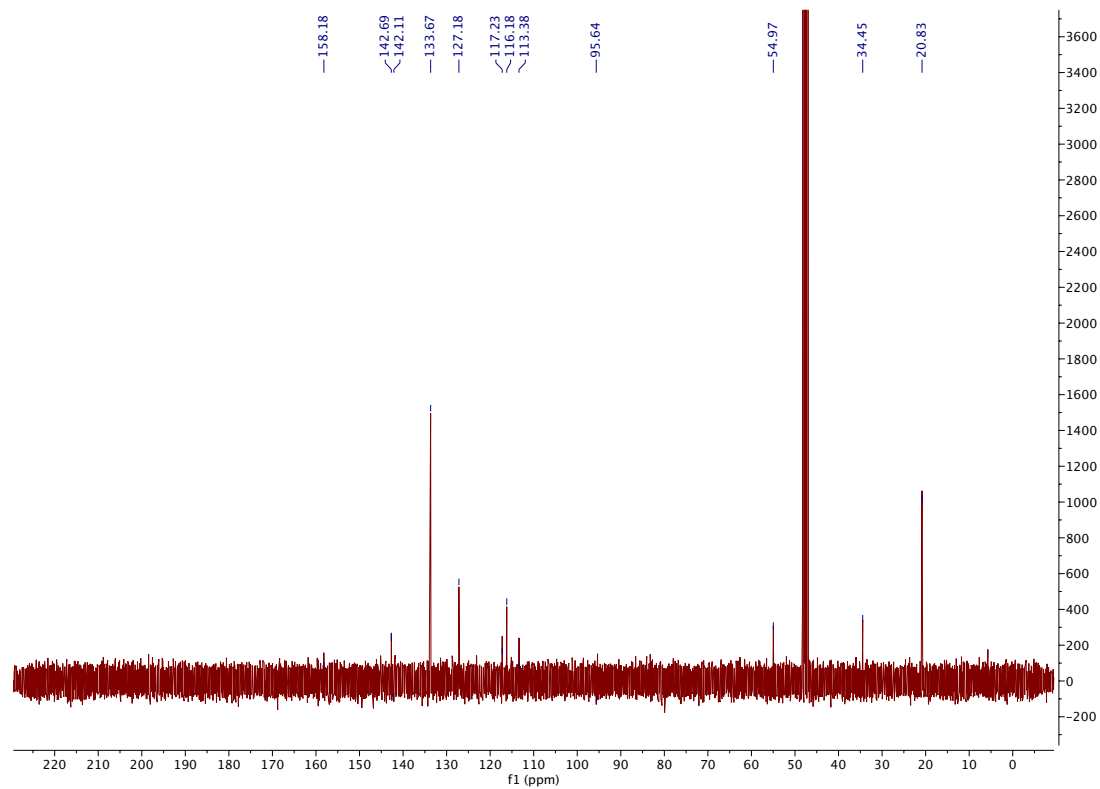
¹³C NMR (101 MHz, CDCl₃) of compound **39**.



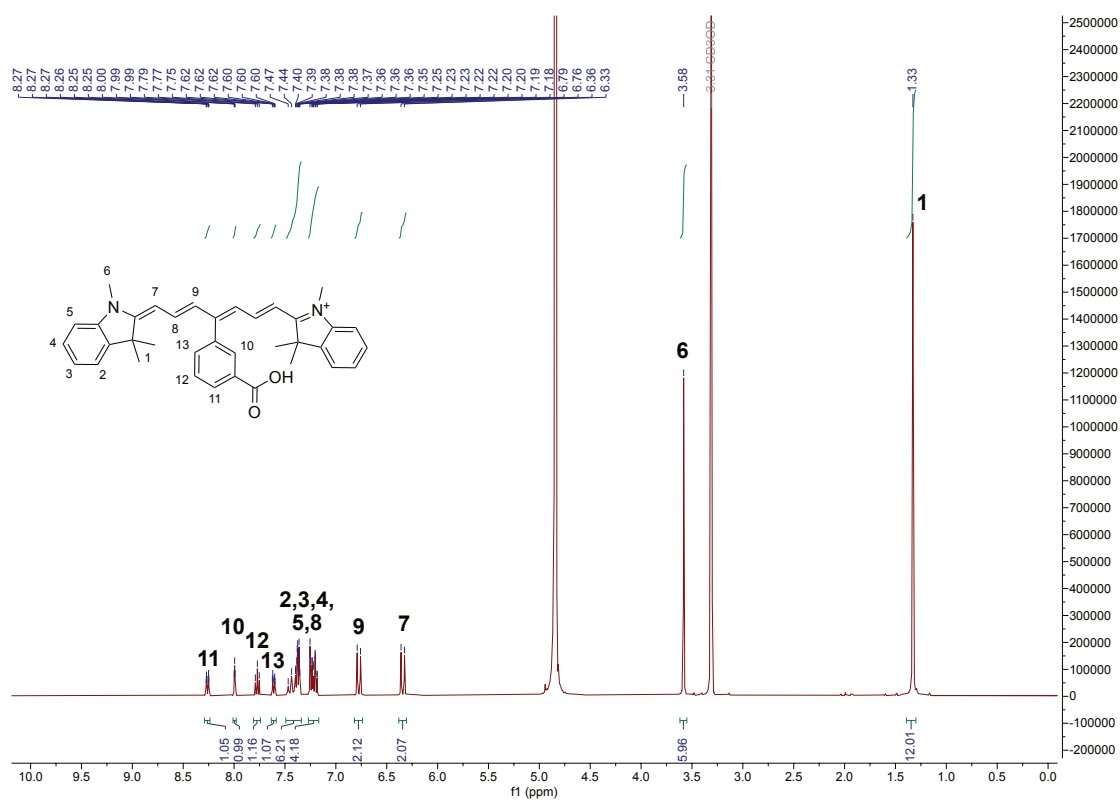
¹⁹F NMR (376 MHz, CDCl₃) of compound **39**.



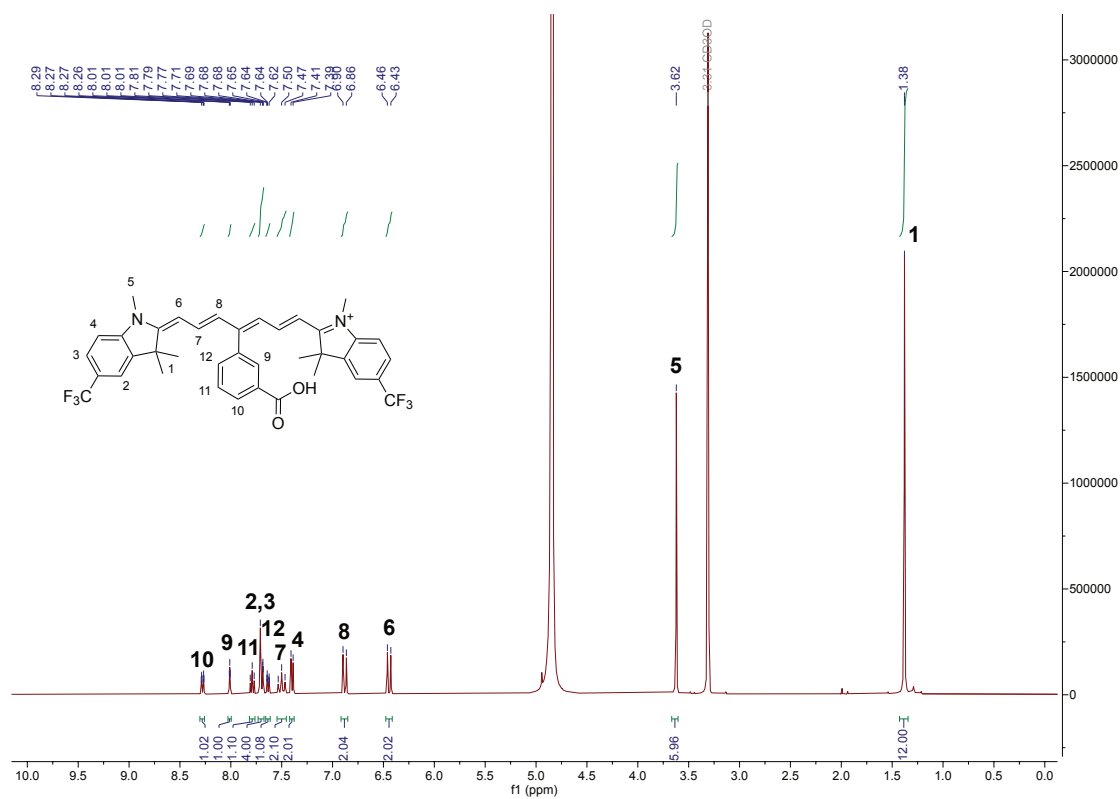
¹H NMR (400 MHz, CD₃OD) of compound **42c**.



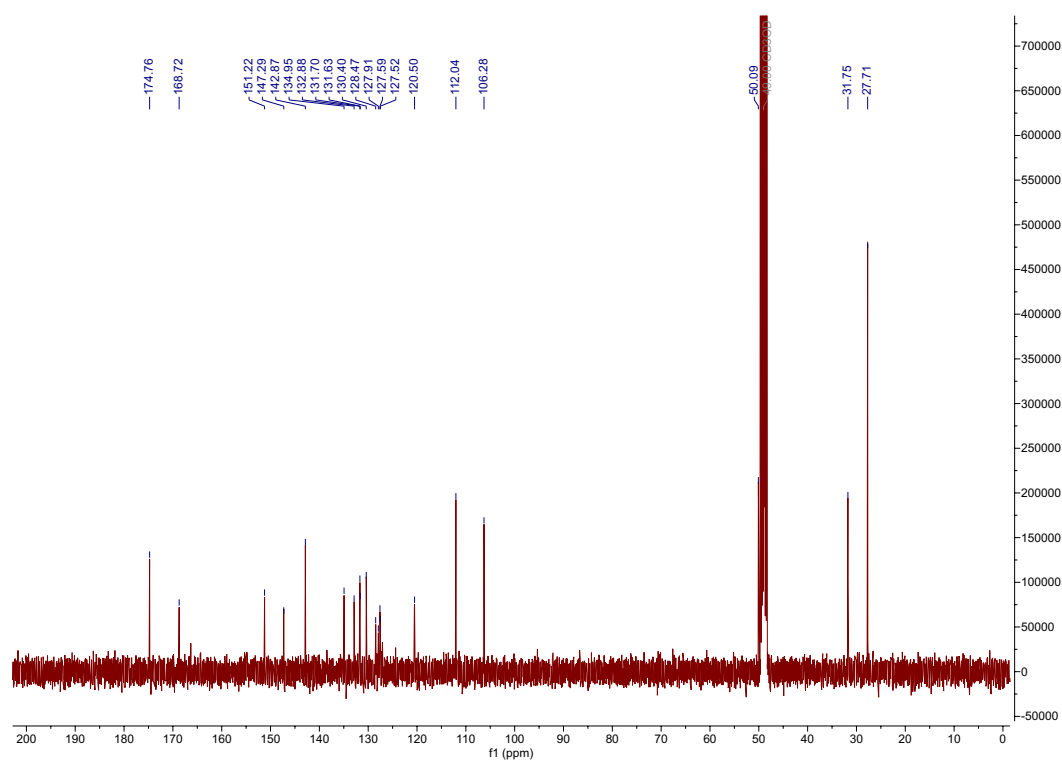
¹³C NMR (101 MHz, CD₃OD) of compound **42c**.



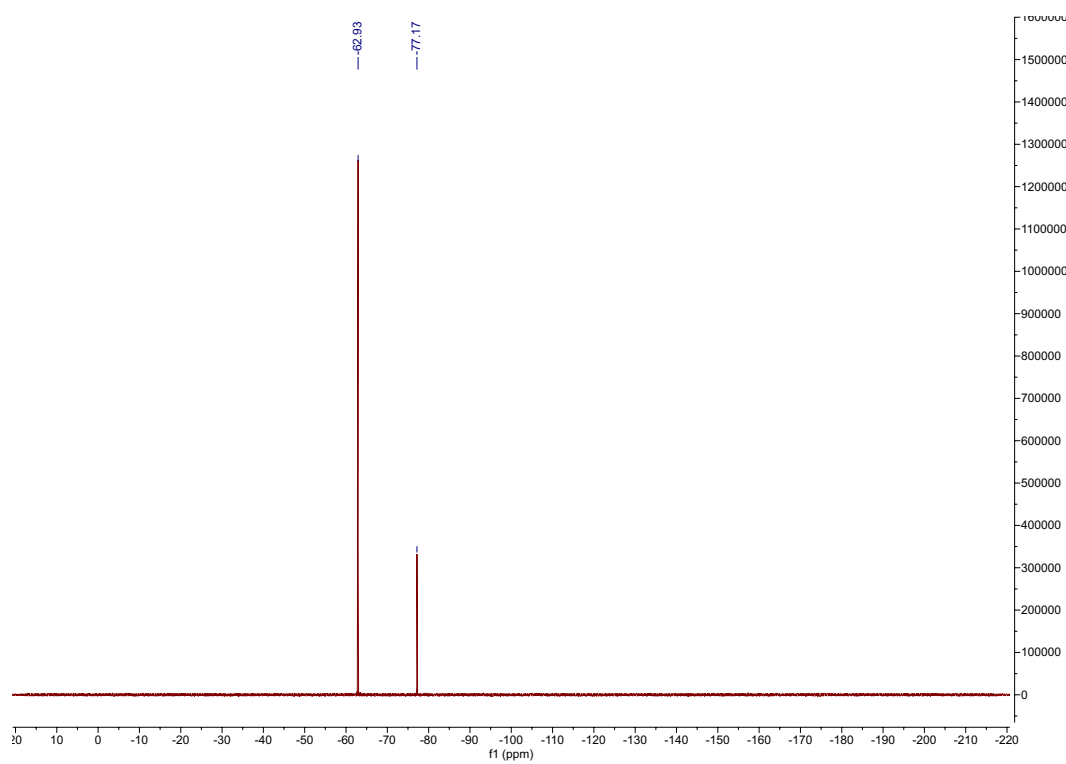
¹H NMR (400 MHz, CD₃OD) of compound **43a**.



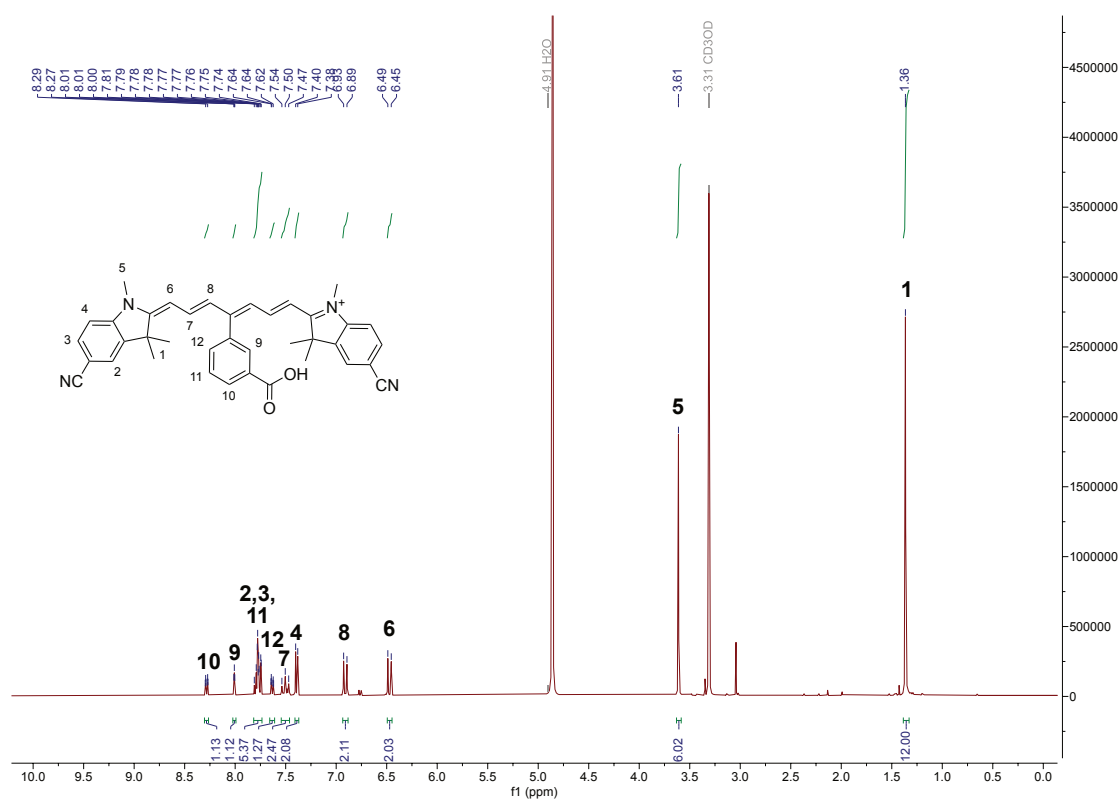
¹H NMR (400 MHz, CD₃OD) of compound **43b**.



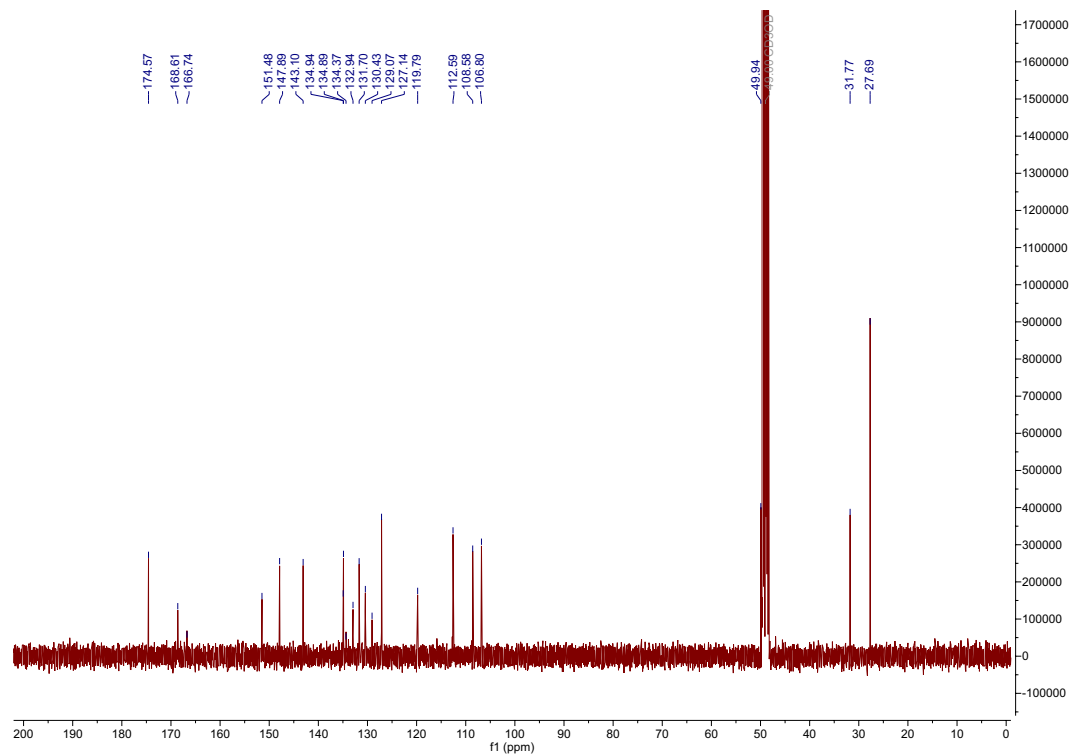
^{13}C NMR (101 MHz, CD_3OD) of compound **43b**.



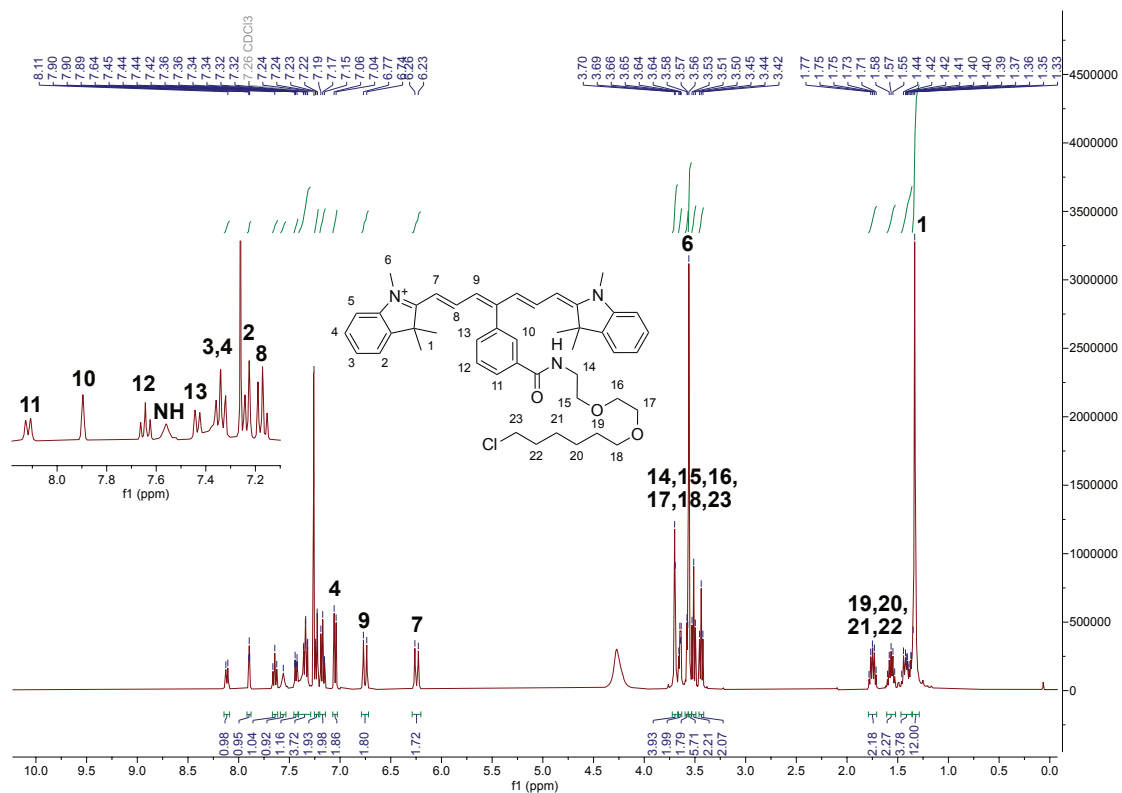
^{19}F NMR (377 MHz, CD_3OD) of compound **43b**.



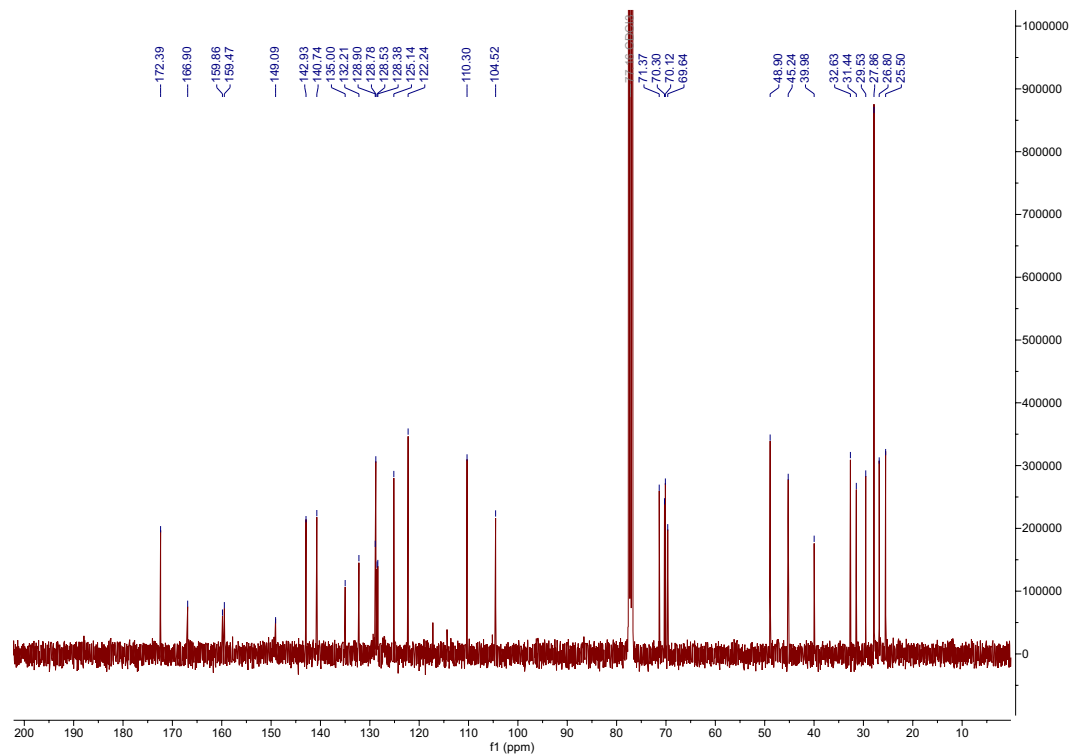
¹H NMR (400 MHz, CD₃OD) of compound 43c.



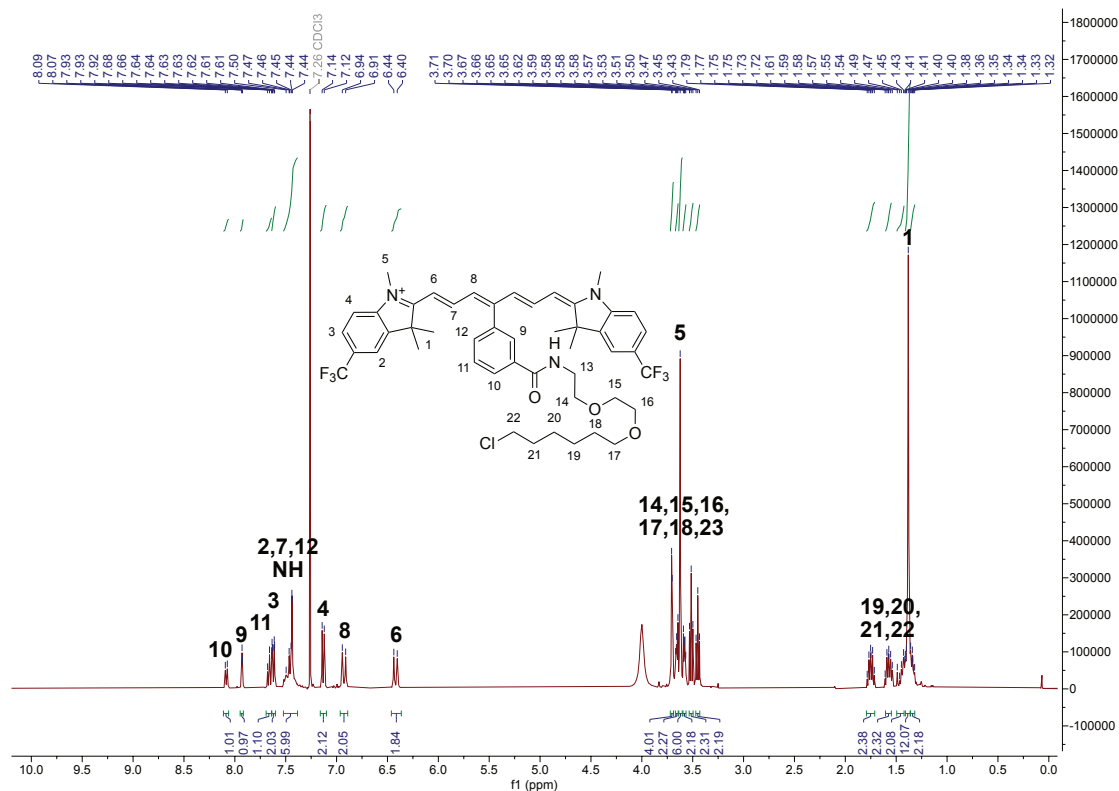
¹³C NMR (101 MHz, CD₃OD) of compound 43c.



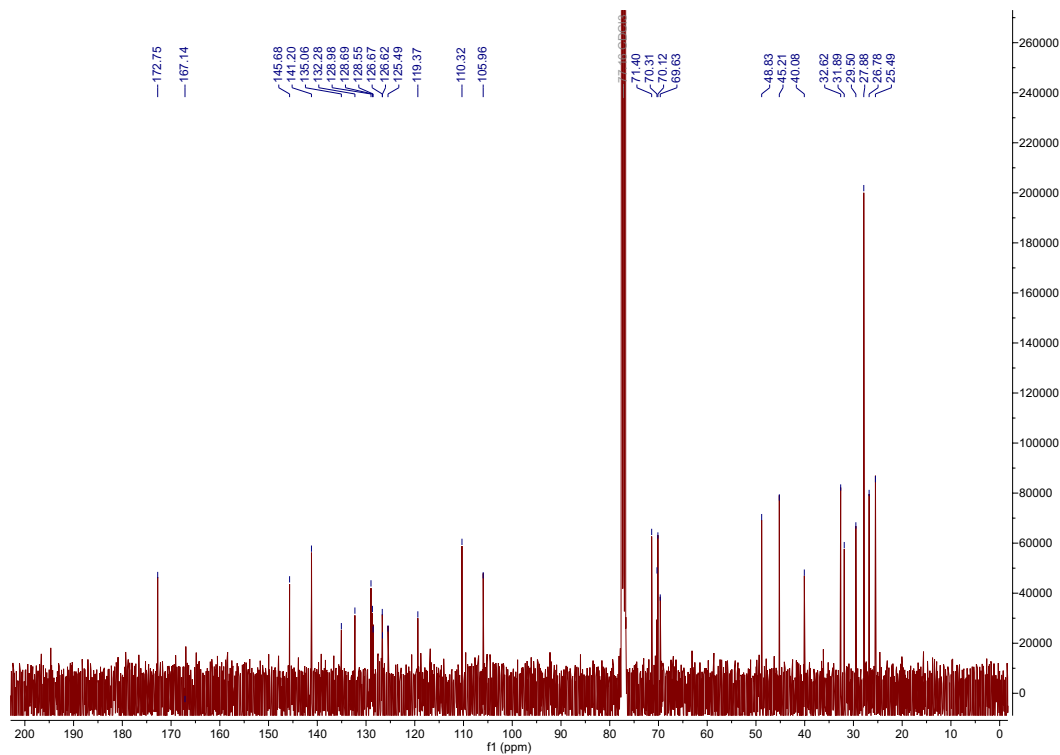
¹H NMR (400 MHz, CDCl₃) of compound **44a**.



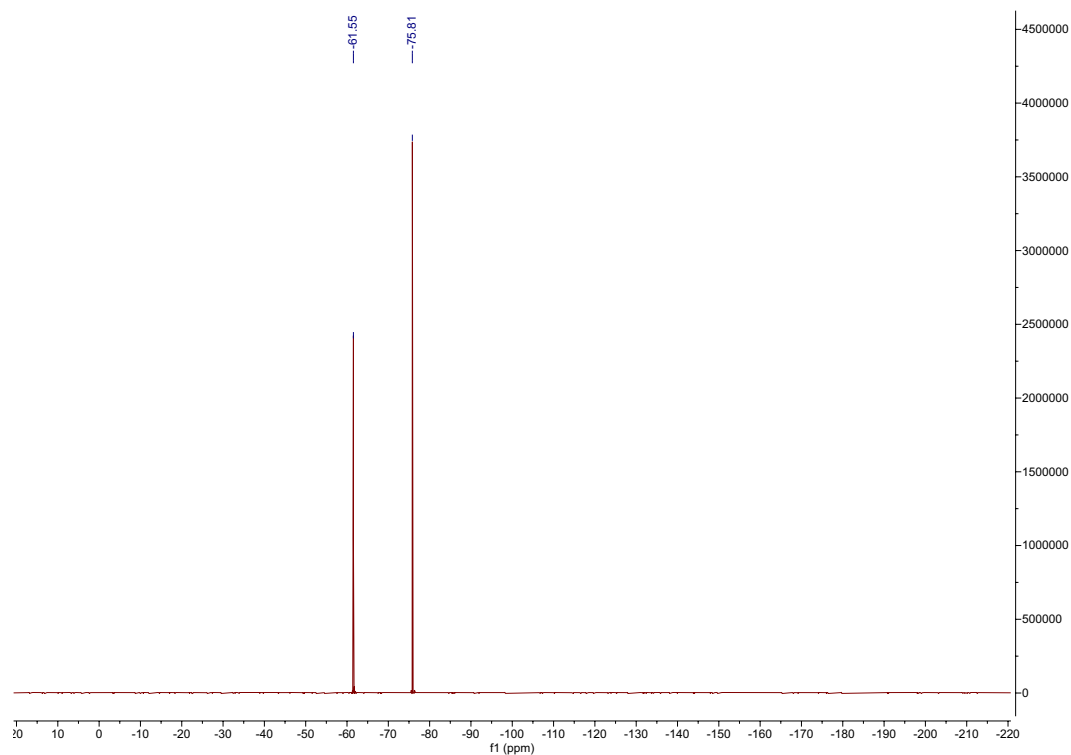
¹³C NMR (101 MHz, CDCl₃) of compound **44a**.



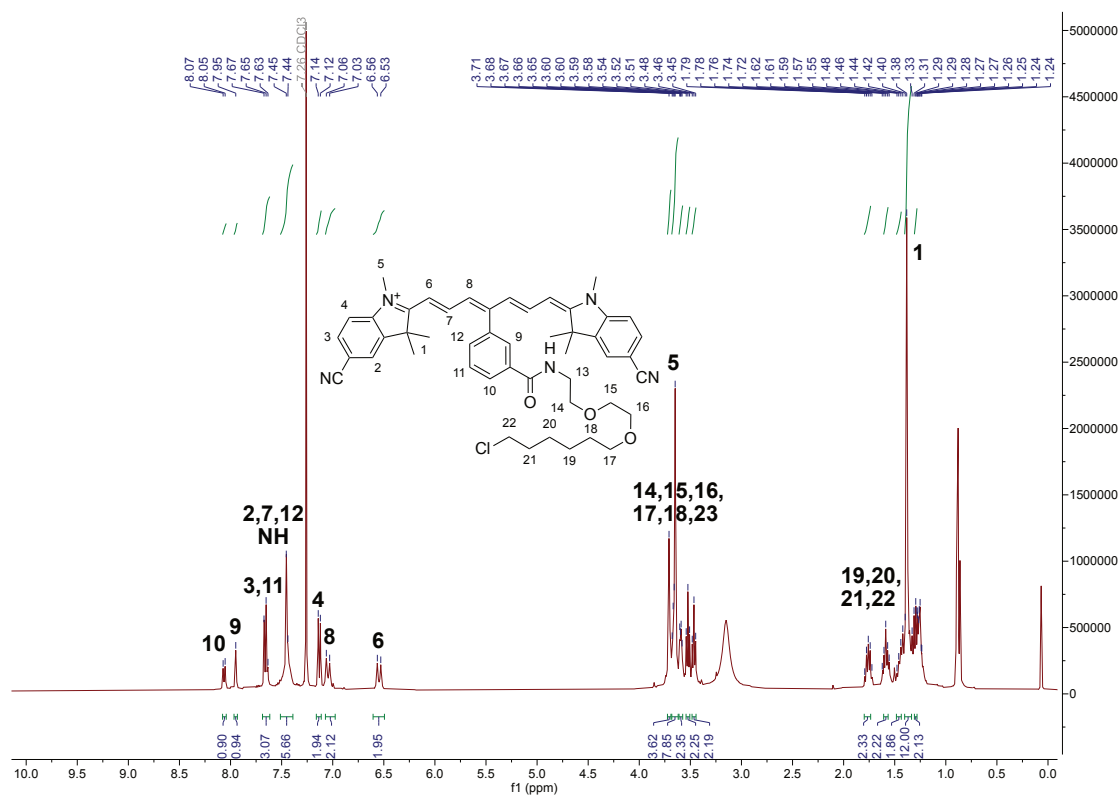
^1H NMR (400 MHz, CDCl_3) of compound **44b**.



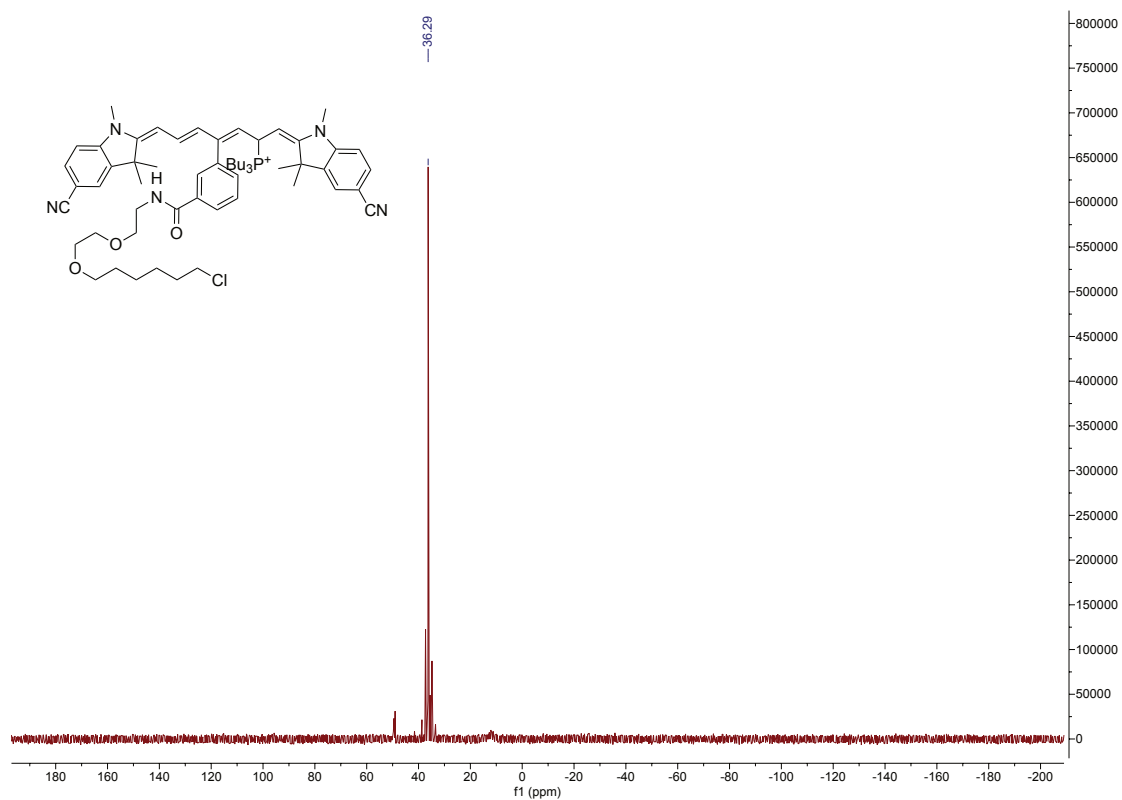
^{13}C NMR (101 MHz, CDCl_3) of compound **44b**.



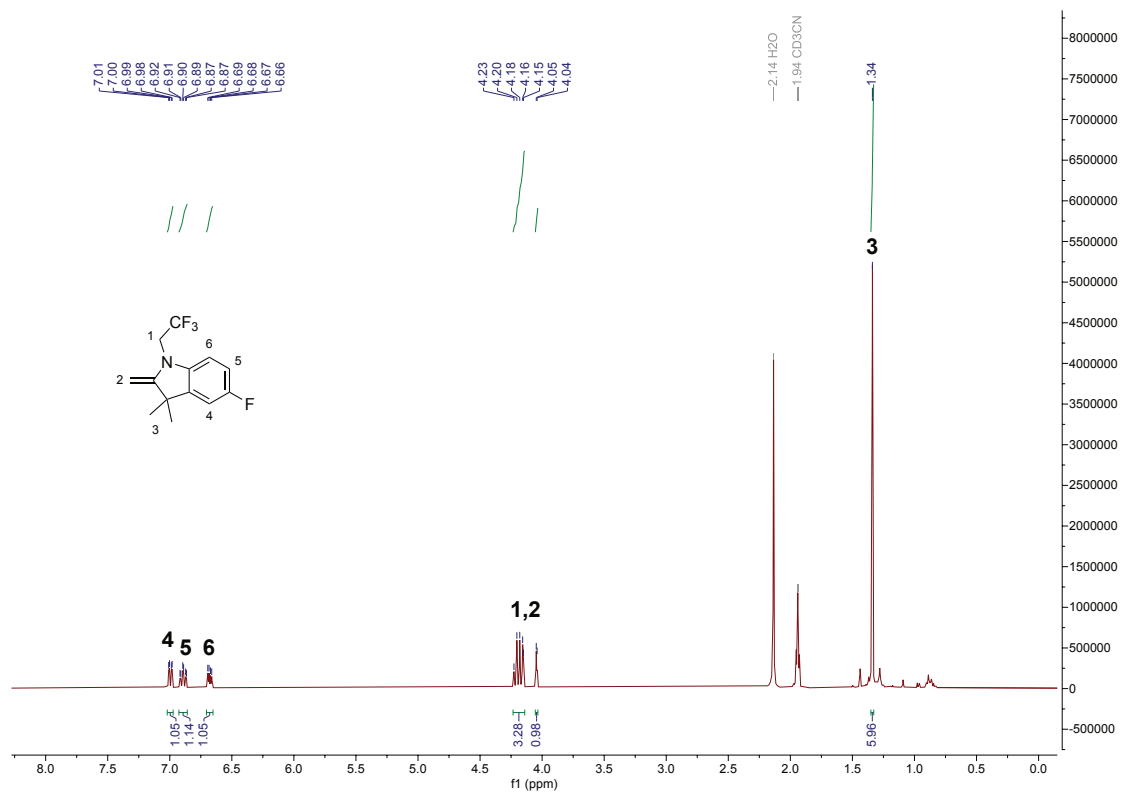
^{19}F NMR (377 MHz, CDCl_3) of compound **44b**.



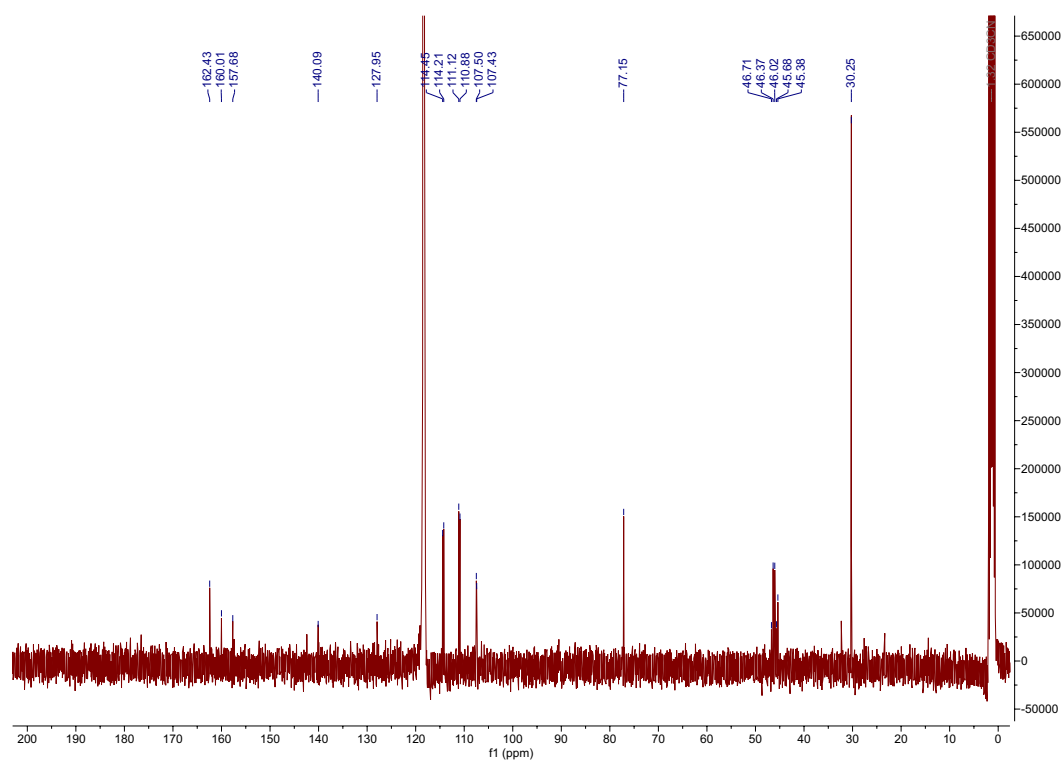
^1H NMR (400 MHz, CDCl_3) of compound **44c**.



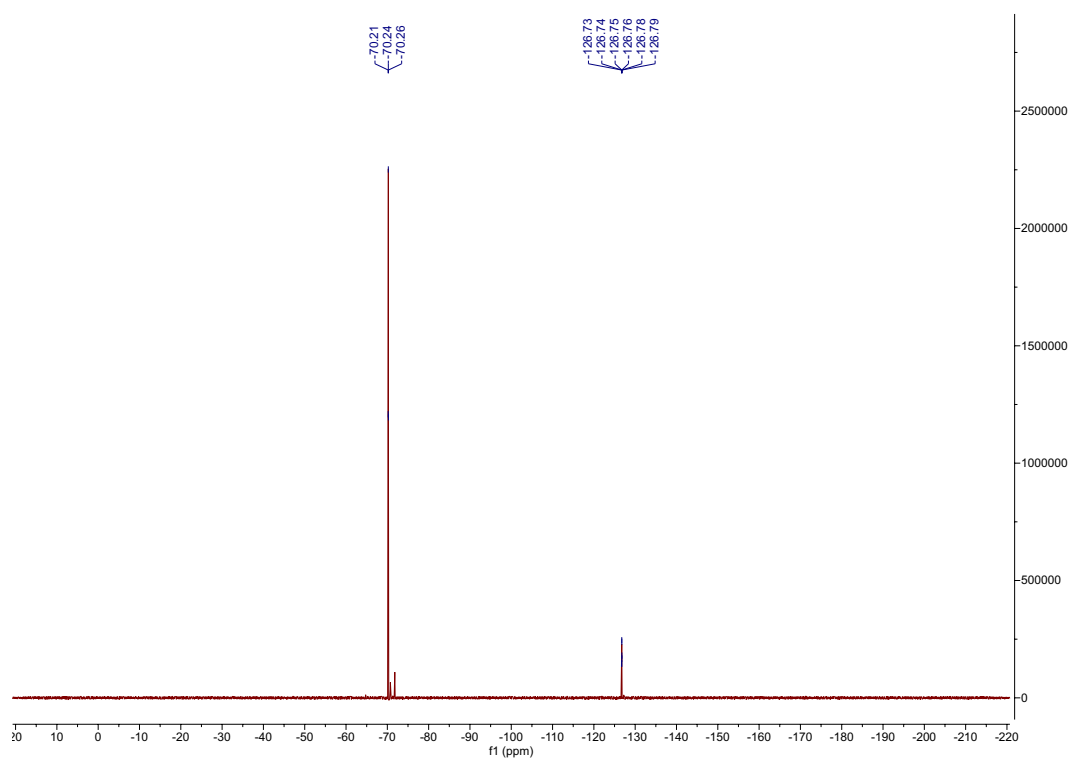
³¹P NMR (162 MHz, CD₃CN) of compound **45c**.



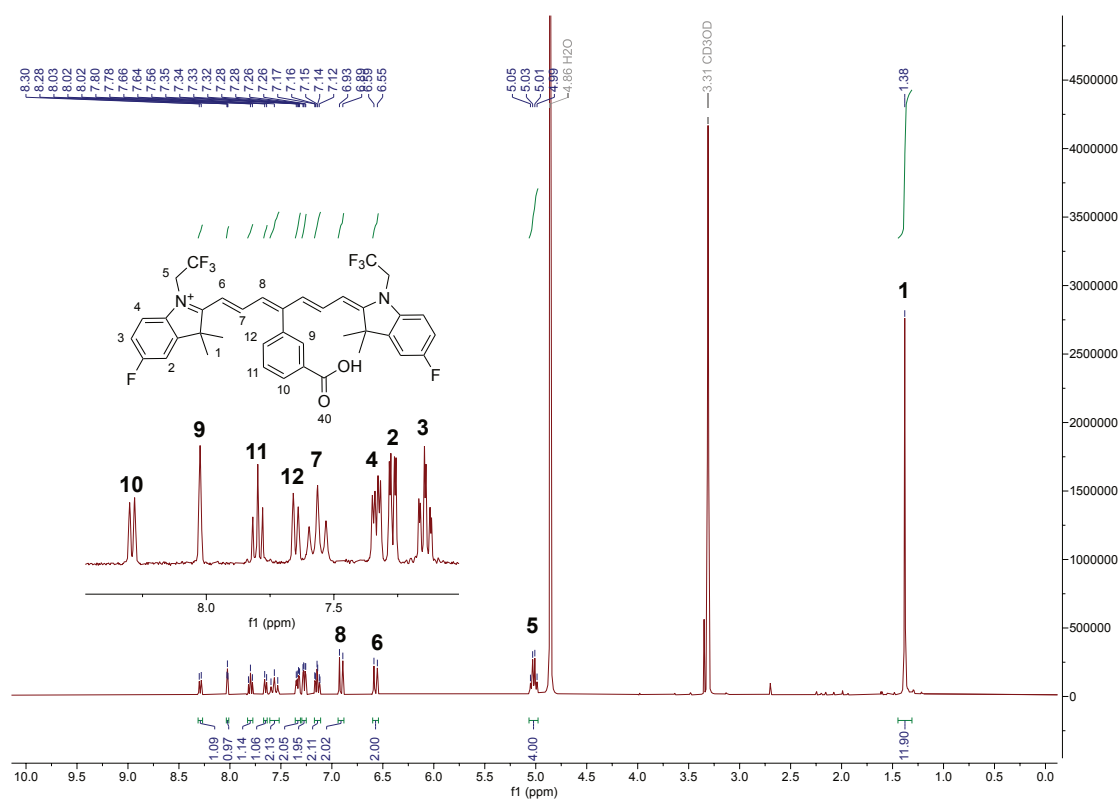
¹H NMR (400 MHz, CD₃CN) of compound **52**.



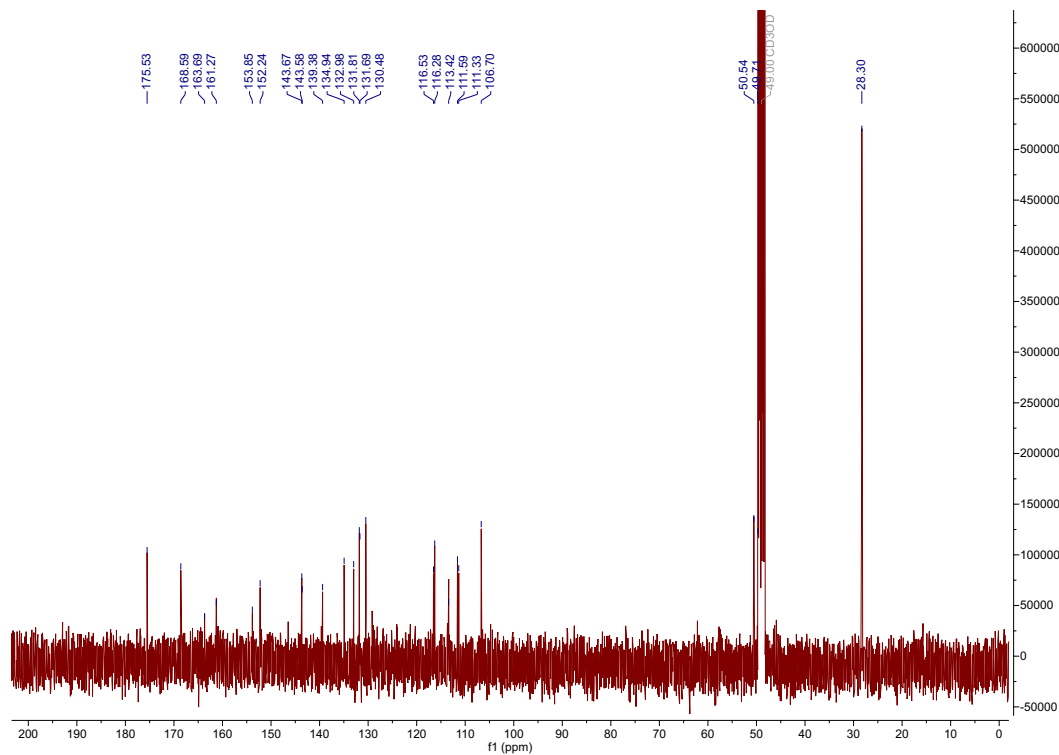
^{13}C NMR (101 MHz, CD_3CN) of compound **52**.



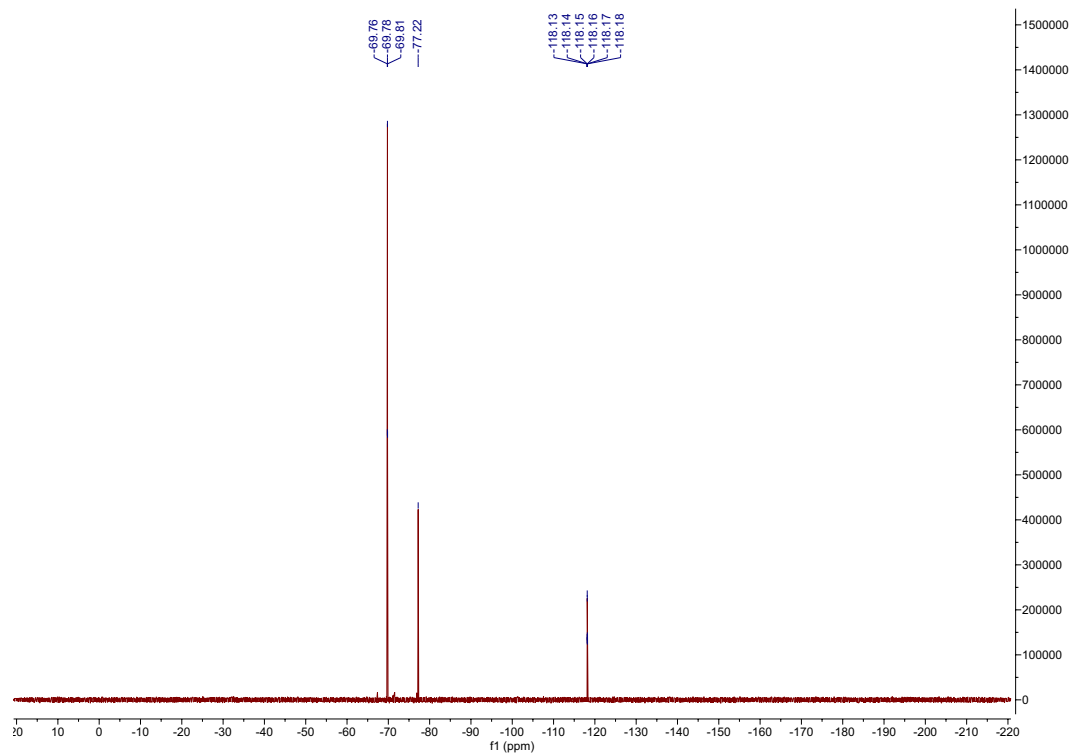
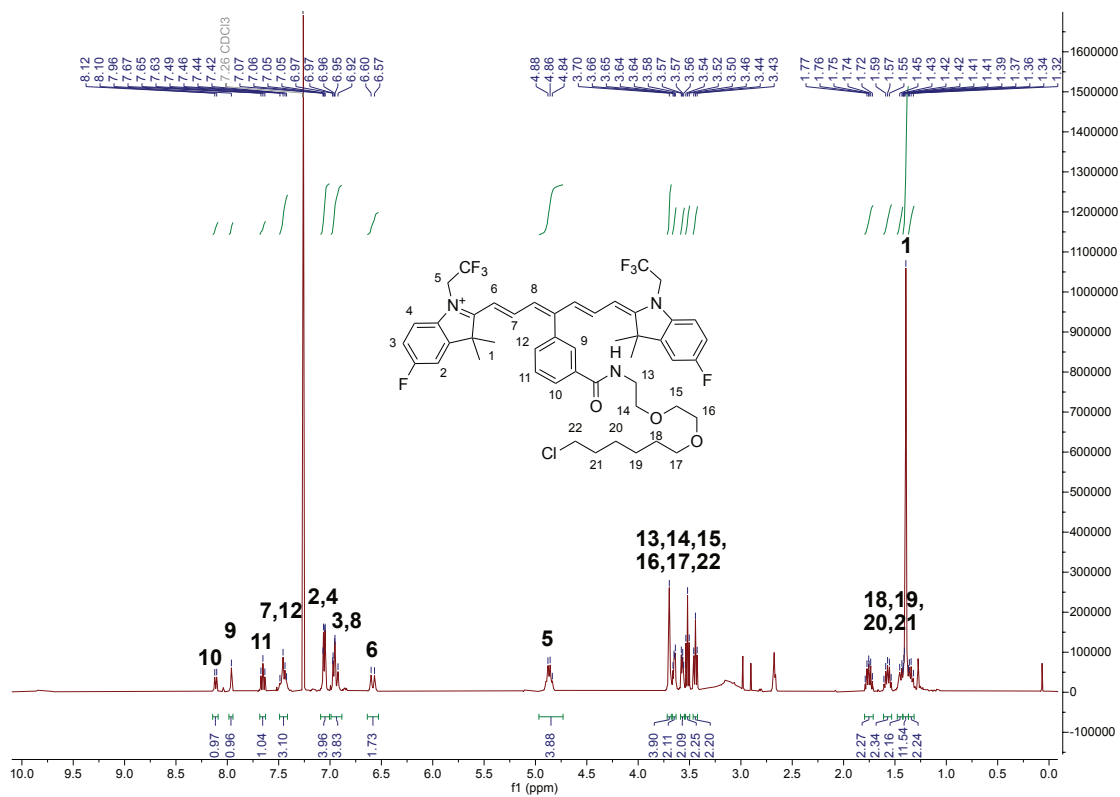
^{19}F NMR (376 MHz, CD_3CN) of compound **52**.

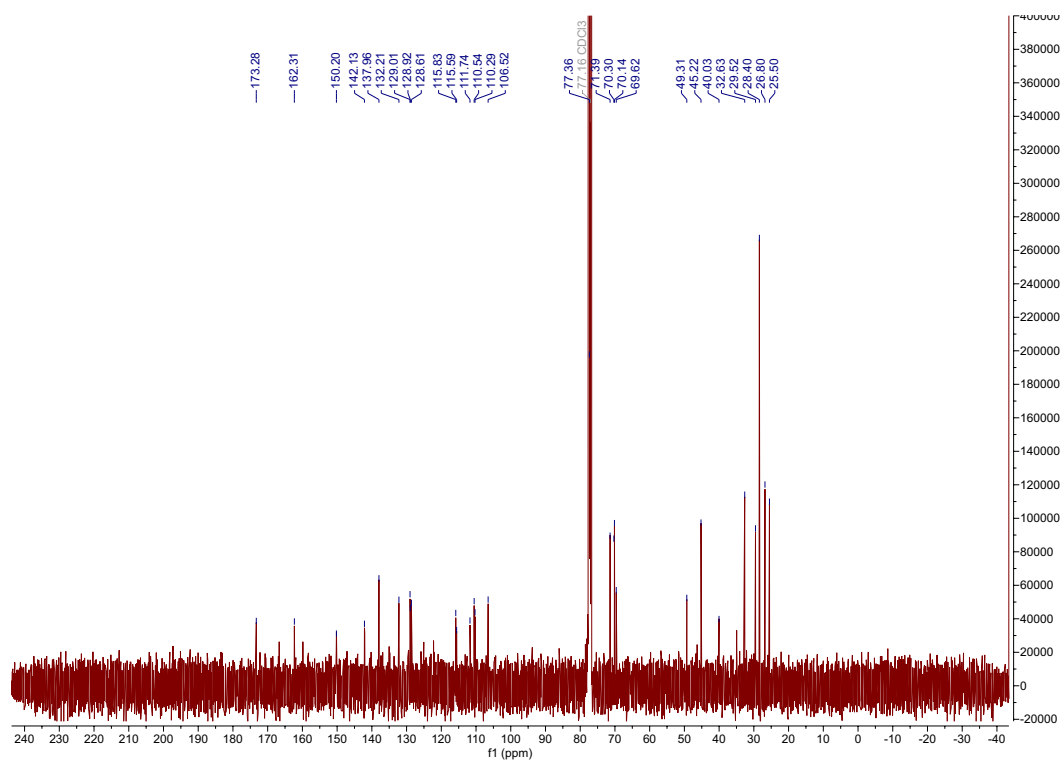


¹H NMR (400 MHz, CD₃OD) of compound **53.**

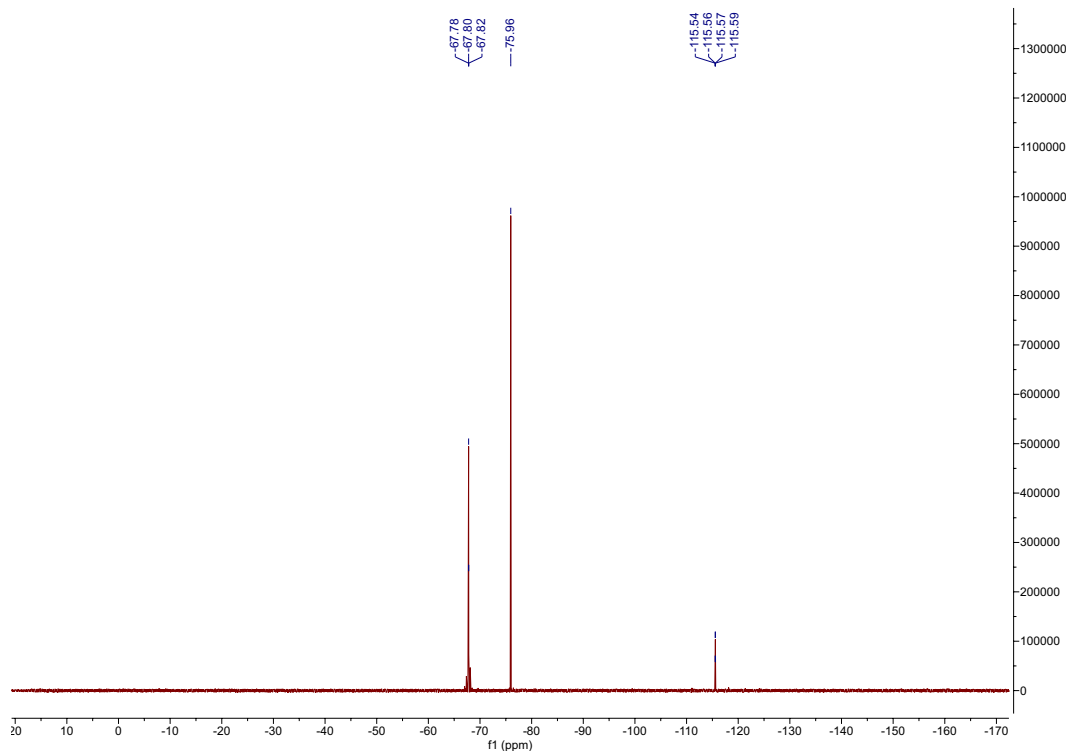


¹³C NMR (101 MHz, CD₃OD) of compound **53.**

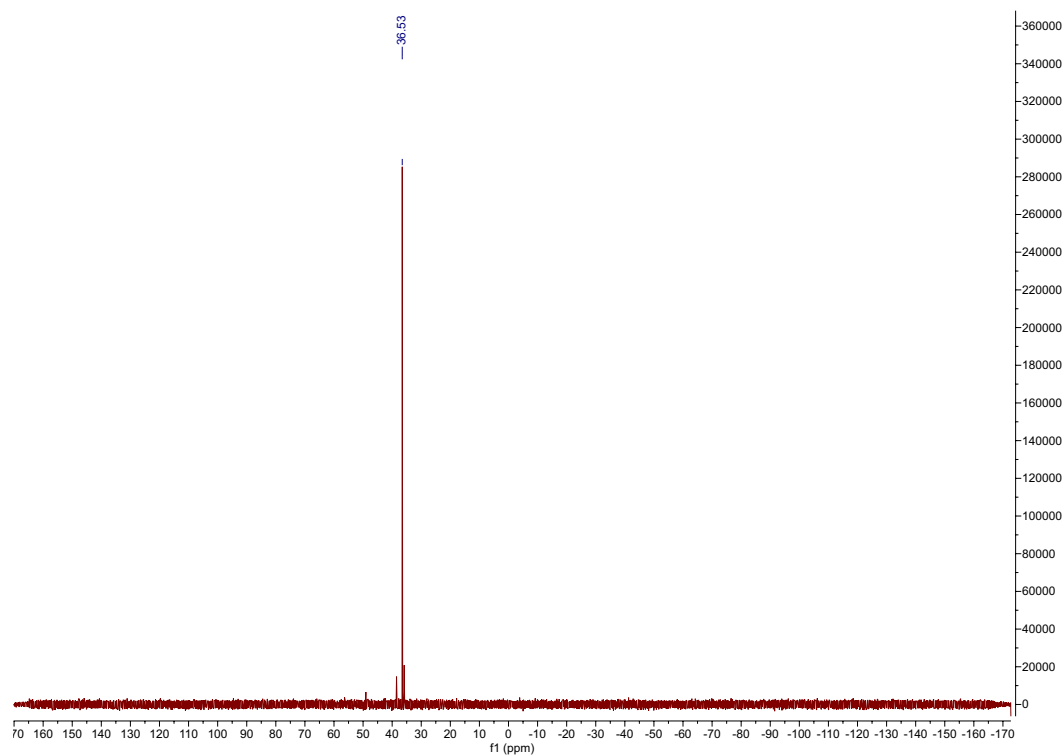
 ^{19}F NMR (376 MHz, CD_3OD) of compound **53**. ^1H NMR (400 MHz, CDCl_3) of compound **54**.



¹³C NMR (101 MHz, CDCl₃) of compound **54**.

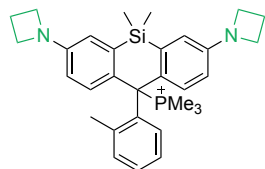


¹⁹F NMR (377 MHz, CDCl₃) of compound **54**.

 ^{31}P

^{31}P NMR (162 MHz, CD_3CN) of compound **55**.

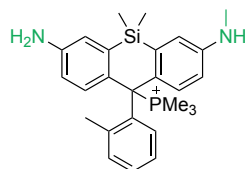
10.2 Cartesian coordinates for modeled compounds



Minimum				TS			
C	-0.003	2.431	-0.51	C	0.004	2.422	-0.677
C	-0.03	4.88	-0.574	C	0.001	4.857	-0.486
C	0.016	2.41	-1.93	C	0.011	2.544	-2.091
C	-0.01	4.858	-1.961	C	0.008	4.979	-1.869
H	-0.049	5.817	-0.031	H	-0.002	5.735	0.149
C	0.011	3.629	-2.616	C	0.012	3.827	-2.652
H	-0.012	5.781	-2.53	H	0.01	5.956	-2.338
H	0.025	3.608	-3.701	H	0.018	3.917	-3.733
C	1.335	0.349	0.019	C	1.305	0.325	-0.181
C	2.506	1.13	-0.024	C	2.481	1.118	-0.149
C	1.476	-1.048	-0.134	C	1.475	-1.087	-0.262
C	3.766	0.579	-0.191	C	3.747	0.577	-0.178
H	2.438	2.207	0.063	H	2.393	2.195	-0.092

C	2.752	-1.6	-0.301	C	2.755	-1.63	-0.296
C	3.919	-0.815	-0.328	C	3.92	-0.828	-0.247
H	4.632	1.229	-0.226	H	4.613	1.227	-0.148
H	2.854	-2.672	-0.434	H	2.882	-2.705	-0.375
C	-1.337	0.347	0.014	C	-1.3	0.323	-0.191
C	-2.509	1.126	-0.04	C	-2.477	1.115	-0.176
C	-1.476	-1.051	-0.133	C	-1.468	-1.089	-0.266
C	-3.767	0.573	-0.208	C	-3.742	0.572	-0.209
H	-2.443	2.204	0.042	H	-2.391	2.193	-0.126
C	-2.751	-1.605	-0.301	C	-2.747	-1.634	-0.303
C	-3.919	-0.821	-0.335	C	-3.913	-0.833	-0.267
H	-4.634	1.222	-0.25	H	-4.609	1.222	-0.192
H	-2.852	-2.679	-0.429	H	-2.872	-2.71	-0.377
Si	0.001	-2.205	-0.283	Si	0.005	-2.242	-0.464
C	-5.557	-2.773	-0.227	C	-5.589	-2.777	-0.155
H	-5.363	-3.487	-1.031	H	-5.39	-3.406	-1.028
H	-5.116	-3.151	0.704	H	-5.183	-3.264	0.738
C	0.004	-3.57	1.02	C	0.006	-3.635	0.806
H	-0.879	-4.206	0.901	H	-0.878	-4.266	0.678
H	0.885	-4.206	0.897	H	0.886	-4.271	0.671
H	0.006	-3.185	2.042	H	0.011	-3.261	1.832
C	0.001	-3.022	-1.985	C	0.006	-2.991	-2.196
H	0	-2.278	-2.785	H	0.005	-2.214	-2.964
H	0.885	-3.655	-2.109	H	0.892	-3.617	-2.344
H	-0.882	-3.656	-2.108	H	-0.877	-3.62	-2.344
N	-5.154	-1.386	-0.528	N	-5.145	-1.385	-0.308
N	5.154	-1.377	-0.522	N	5.152	-1.378	-0.288
C	0.041	1.145	-2.754	C	0.015	1.354	-3.021
H	-0.81	0.498	-2.531	H	-0.863	0.722	-2.872
H	0.01	1.391	-3.817	H	0.02	1.687	-4.06
H	0.946	0.561	-2.569	H	0.894	0.723	-2.864
C	-0.026	3.674	0.129	C	-0.001	3.588	0.092
H	-0.045	3.744	1.205	H	-0.006	3.517	1.169
P	-0.003	1.313	2.197	P	-0.017	1.323	2.425
C	1.458	2.163	2.885	C	1.396	2.121	3.299
H	2.357	1.599	2.64	H	2.333	1.727	2.902
H	1.555	3.181	2.514	H	1.376	3.201	3.142
C	-1.492	2.108	2.891	C	-1.525	2.005	3.234
H	-1.385	2.095	3.977	H	-1.492	1.821	4.312
H	-2.376	1.535	2.612	H	-2.409	1.522	2.815
C	0.029	-0.34	2.947	C	0.04	-0.412	3.014
H	0.932	-0.872	2.654	H	0.958	-0.89	2.673

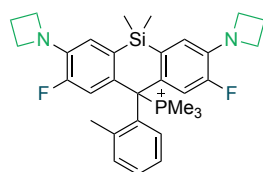
H	-0.855	-0.904	2.657	H	-0.818	-0.962	2.627
H	0.027	-0.205	4.031	H	0.011	-0.433	4.106
H	1.335	2.189	3.97	H	1.344	1.914	4.371
H	-1.605	3.136	2.555	H	-1.595	3.078	3.056
C	-0.002	1.089	0.271	C	0.002	1.009	-0.097
C	-6.461	-0.825	-0.135	C	-6.475	-0.806	-0.07
H	-6.431	-0.317	0.837	H	-6.54	-0.245	0.869
H	-6.909	-0.157	-0.874	H	-6.84	-0.179	-0.888
C	-7.017	-2.272	-0.071	C	-7.044	-2.251	-0.01
C	5.557	-2.767	-0.232	C	5.599	-2.772	-0.158
H	5.115	-3.153	0.695	H	5.198	-3.273	0.73
H	5.364	-3.474	-1.042	H	5.398	-3.387	-1.039
C	6.461	-0.82	-0.123	C	6.483	-0.8	-0.051
H	6.91	-0.145	-0.856	H	6.842	-0.163	-0.864
H	6.431	-0.32	0.853	H	6.553	-0.25	0.894
C	7.017	-2.267	-0.071	C	7.054	-2.245	-0.011
H	7.513	-2.549	0.856	H	7.548	-2.517	0.919
H	7.655	-2.516	-0.918	H	7.7	-2.489	-0.853
H	-7.514	-2.546	0.857	H	-7.535	-2.512	0.925
H	-7.654	-2.528	-0.917	H	-7.692	-2.506	-0.847



Minimum				TS			
C	-1.115	-1.852	-0.508	C	-1.169	-1.806	-0.695
C	-2.195	-4.05	-0.564	C	-2.317	-3.951	-0.491
C	-1.078	-1.852	-1.928	C	-1.215	-1.928	-2.108
C	-2.159	-4.049	-1.951	C	-2.366	-4.071	-1.874
H	-2.619	-4.884	-0.018	H	-2.736	-4.72	0.148
C	-1.603	-2.954	-2.61	C	-1.817	-3.063	-2.662
H	-2.555	-4.884	-2.518	H	-2.825	-4.937	-2.338
H	-1.573	-2.949	-3.695	H	-1.852	-3.153	-3.743
C	-1.4	0.615	-0.021	C	-1.331	0.662	-0.224
C	-2.793	0.435	-0.092	C	-2.741	0.519	-0.213
C	-0.9	1.925	-0.185	C	-0.811	1.984	-0.308
C	-3.67	1.488	-0.296	C	-3.596	1.598	-0.265
H	-3.215	-0.559	0.001	H	-3.175	-0.47	-0.15
C	-1.797	2.982	-0.388	C	-1.684	3.066	-0.368

C	-3.185	2.798	-0.438	C	-3.084	2.91	-0.341
H	-4.737	1.296	-0.348	H	-4.669	1.44	-0.249
H	-1.412	3.989	-0.525	H	-1.288	4.075	-0.447
C	0.995	-0.569	0.043	C	0.96	-0.571	-0.174
C	1.701	-1.79	0.026	C	1.621	-1.829	-0.128
C	1.743	0.615	-0.109	C	1.78	0.59	-0.24
C	3.073	-1.852	-0.117	C	2.989	-1.945	-0.126
H	1.163	-2.726	0.114	H	1.033	-2.736	-0.081
C	3.139	0.545	-0.249	C	3.166	0.464	-0.245
C	3.837	-0.674	-0.252	C	3.811	-0.792	-0.179
H	3.569	-2.817	-0.13	H	3.45	-2.926	-0.083
H	3.699	1.465	-0.373	H	3.779	1.356	-0.314
Si	0.938	2.303	-0.304	Si	1.036	2.303	-0.475
C	6.076	0.408	-0.345	C	6.102	0.189	-0.237
H	7.106	0.067	-0.447	H	7.112	-0.217	-0.219
H	5.872	1.107	-1.161	H	5.98	0.769	-1.158
H	5.981	0.949	0.605	H	5.987	0.864	0.617
C	1.514	3.549	0.99	C	1.665	3.542	0.796
H	2.591	3.722	0.892	H	2.746	3.679	0.692
H	1.013	4.51	0.836	H	1.195	4.518	0.64
H	1.316	3.226	2.014	H	1.459	3.227	1.821
C	1.335	3.006	-2.01	C	1.426	2.939	-2.207
H	1.03	2.321	-2.806	H	1.077	2.243	-2.974
H	0.82	3.959	-2.165	H	0.946	3.907	-2.378
H	2.409	3.189	-2.112	H	2.505	3.073	-2.333
N	5.2	-0.75	-0.418	N	5.162	-0.917	-0.174
H	5.621	-1.638	-0.197	H	5.543	-1.85	-0.134
N	-4.045	3.857	-0.692	N	-3.92	3.99	-0.435
H	-5.005	3.734	-0.402	H	-4.894	3.876	-0.202
H	-3.693	4.78	-0.484	H	-3.545	4.913	-0.281
C	-0.504	-0.727	-2.757	C	-0.644	-0.887	-3.043
H	0.551	-0.556	-2.531	H	0.428	-0.745	-2.882
H	-0.588	-0.965	-3.818	H	-0.791	-1.19	-4.08
H	-1.027	0.214	-2.579	H	-1.12	0.087	-2.904
C	-1.676	-2.96	0.134	C	-1.723	-2.827	0.081
H	-1.728	-3.009	1.211	H	-1.694	-2.753	1.158
P	-0.672	-0.814	2.197	P	-0.711	-0.807	2.456
C	-2.372	-0.903	2.857	C	-2.355	-0.814	3.291
H	-2.928	-0.017	2.557	H	-2.976	-0.02	2.871
H	-2.898	-1.795	2.522	H	-2.855	-1.77	3.13
C	0.278	-2.195	2.919	C	0.26	-2.112	3.321
H	0.143	-2.147	4.001	H	0.302	-1.909	4.394

H	1.334	-2.076	2.684	H	1.275	-2.131	2.921
C	0.037	0.682	2.94	C	0.058	0.753	3.038
H	-0.518	1.563	2.622	H	-0.502	1.608	2.657
H	1.087	0.778	2.671	H	1.088	0.811	2.684
H	-0.047	0.578	4.023	H	0.057	0.785	4.13
H	-2.291	-0.923	3.946	H	-2.238	-0.647	4.365
H	-0.067	-3.162	2.559	H	-0.197	-3.089	3.159
C	-0.536	-0.639	0.269	C	-0.507	-0.556	-0.127

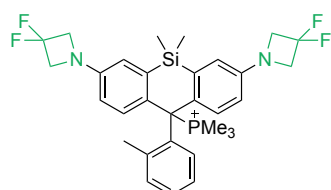


Minimum				TS			
C	-0.004	2.377	-0.482	C	0.002	2.367	-0.663
C	-0.038	4.825	-0.529	C	-0.005	4.797	-0.431
C	0.017	2.365	-1.903	C	0.009	2.512	-2.076
C	-0.016	4.813	-1.915	C	0.002	4.942	-1.813
H	-0.06	5.758	0.021	H	-0.011	5.665	0.218
C	0.01	3.589	-2.58	C	0.009	3.803	-2.614
H	-0.02	5.739	-2.478	H	0.003	5.927	-2.266
H	0.025	3.576	-3.664	H	0.015	3.912	-3.694
C	1.331	0.287	0.029	C	1.3	0.262	-0.191
C	2.498	1.074	-0.019	C	2.473	1.06	-0.16
C	1.473	-1.107	-0.127	C	1.473	-1.147	-0.272
C	3.734	0.499	-0.19	C	3.716	0.495	-0.186
H	2.458	2.153	0.054	H	2.414	2.139	-0.109
C	2.753	-1.654	-0.293	C	2.755	-1.687	-0.3
C	3.93	-0.886	-0.318	C	3.932	-0.901	-0.246
H	2.857	-2.726	-0.426	H	2.884	-2.761	-0.376
C	-1.333	0.284	0.025	C	-1.296	0.261	-0.197
C	-2.5	1.07	-0.033	C	-2.47	1.057	-0.178
C	-1.473	-1.11	-0.125	C	-1.466	-1.149	-0.27
C	-3.735	0.493	-0.204	C	-3.712	0.491	-0.205
H	-2.463	2.149	0.035	H	-2.412	2.137	-0.133
C	-2.753	-1.66	-0.29	C	-2.748	-1.69	-0.299
C	-3.93	-0.893	-0.322	C	-3.926	-0.905	-0.254
H	-2.855	-2.732	-0.418	H	-2.875	-2.765	-0.37
Si	0.001	-2.267	-0.28	Si	0.004	-2.304	-0.485
C	-5.5	-2.878	-0.331	C	-5.536	-2.879	-0.183

H	-5.311	-3.504	-1.206	H	-5.317	-3.467	-1.078
H	-5	-3.316	0.541	H	-5.098	-3.375	0.69
C	0.005	-3.634	1.018	C	0.007	-3.708	0.769
H	-0.878	-4.27	0.898	H	-0.878	-4.338	0.637
H	0.886	-4.271	0.892	H	0.886	-4.344	0.625
H	0.009	-3.253	2.041	H	0.016	-3.345	1.799
C	0	-3.074	-1.986	C	0.002	-3.025	-2.227
H	-0.002	-2.326	-2.782	H	0	-2.236	-2.983
H	0.883	-3.706	-2.114	H	0.887	-3.649	-2.386
H	-0.883	-3.709	-2.112	H	-0.882	-3.651	-2.383
N	-5.169	-1.449	-0.52	N	-5.153	-1.462	-0.293
N	5.169	-1.44	-0.518	N	5.16	-1.456	-0.286
C	0.047	1.106	-2.737	C	0.016	1.336	-3.024
H	-0.797	0.45	-2.515	H	-0.862	0.699	-2.884
H	0.006	1.36	-3.797	H	0.018	1.684	-4.057
H	0.958	0.529	-2.564	H	0.896	0.704	-2.878
C	-0.032	3.615	0.166	C	-0.005	3.52	0.126
H	-0.053	3.678	1.243	H	-0.011	3.429	1.202
P	0	1.239	2.22	P	-0.011	1.234	2.464
C	1.461	2.093	2.9	C	1.39	2.043	3.347
H	2.358	1.522	2.666	H	2.334	1.662	2.953
H	1.563	3.106	2.519	H	1.358	3.123	3.196
C	-1.493	2.026	2.912	C	-1.527	1.889	3.281
H	-1.383	2.015	3.998	H	-1.486	1.706	4.358
H	-2.374	1.448	2.637	H	-2.405	1.391	2.867
C	0.039	-0.416	2.961	C	0.068	-0.507	3.035
H	0.944	-0.944	2.664	H	0.992	-0.971	2.686
H	-0.844	-0.983	2.671	H	-0.784	-1.064	2.645
H	0.039	-0.285	4.045	H	0.043	-0.541	4.127
H	1.335	2.13	3.984	H	1.336	1.83	4.418
H	-1.613	3.054	2.575	H	-1.617	2.961	3.103
C	-0.002	1.03	0.29	C	0.002	0.947	-0.108
C	-6.47	-1.001	0.04	C	-6.51	-0.958	0.008
H	-6.382	-0.637	1.069	H	-6.575	-0.46	0.979
H	-6.989	-0.257	-0.564	H	-6.919	-0.303	-0.763
C	-6.967	-2.465	-0.056	C	-7.01	-2.427	-0.002
C	5.5	-2.87	-0.34	C	5.544	-2.874	-0.189
H	4.999	-3.315	0.529	H	5.107	-3.377	0.68
H	5.311	-3.489	-1.22	H	5.325	-3.454	-1.089
C	6.47	-0.997	0.047	C	6.516	-0.953	0.02
H	6.989	-0.248	-0.552	H	6.925	-0.291	-0.745
H	6.381	-0.64	1.078	H	6.581	-0.464	0.995

Appendix

C	6.967	-2.459	-0.061	C	7.018	-2.422	-0.004
H	7.415	-2.878	0.838	H	7.491	-2.762	0.915
H	7.627	-2.626	-0.912	H	7.658	-2.654	-0.853
H	-7.416	-2.877	0.846	H	-7.483	-2.759	0.92
H	-7.627	-2.638	-0.906	H	-7.65	-2.668	-0.849
F	-4.824	1.313	-0.289	F	-4.805	1.309	-0.194
F	4.822	1.32	-0.266	F	4.808	1.314	-0.163

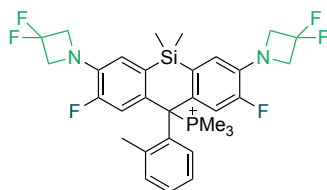


Minimum				TS			
C	-0.003	2.716	-0.485	C	0	2.733	-0.628
C	-0.032	5.165	-0.5	C	0.001	5.146	-0.263
C	0.017	2.723	-1.906	C	-0.001	2.954	-2.03
C	-0.011	5.171	-1.887	C	-0.001	5.366	-1.635
H	-0.052	6.091	0.062	H	0.001	5.977	0.432
C	0.013	3.956	-2.567	C	-0.001	4.273	-2.498
H	-0.013	6.105	-2.438	H	-0.001	6.374	-2.034
H	0.027	3.956	-3.652	H	-0.002	4.44	-3.57
C	1.336	0.623	0.001	C	1.301	0.609	-0.26
C	2.504	1.406	-0.031	C	2.474	1.402	-0.184
C	1.475	-0.77	-0.178	C	1.47	-0.798	-0.404
C	3.764	0.859	-0.211	C	3.74	0.861	-0.222
H	2.436	2.482	0.073	H	2.384	2.475	-0.079
C	2.752	-1.317	-0.358	C	2.751	-1.338	-0.446
C	3.913	-0.529	-0.368	C	3.908	-0.536	-0.346
H	4.629	1.511	-0.238	H	4.605	1.51	-0.158
H	2.854	-2.387	-0.513	H	2.879	-2.408	-0.573
C	-1.338	0.621	-0.005	C	-1.301	0.609	-0.259
C	-2.507	1.403	-0.049	C	-2.474	1.402	-0.182
C	-1.475	-0.773	-0.178	C	-1.47	-0.798	-0.404
C	-3.765	0.854	-0.23	C	-3.74	0.862	-0.22
H	-2.44	2.479	0.051	H	-2.384	2.475	-0.076
C	-2.751	-1.323	-0.359	C	-2.752	-1.338	-0.446
C	-3.913	-0.536	-0.378	C	-3.909	-0.536	-0.344
H	-4.63	1.504	-0.265	H	-4.605	1.511	-0.155
H	-2.851	-2.393	-0.509	H	-2.88	-2.408	-0.572
Si	0.001	-1.928	-0.347	Si	0	-1.939	-0.686

C	-5.536	-2.493	-0.271	C	-5.563	-2.488	-0.212
H	-5.434	-3.201	-1.095	H	-5.485	-3.114	-1.103
H	-5.07	-2.89	0.637	H	-5.103	-2.983	0.648
C	0.004	-3.311	0.935	C	0	-3.414	0.485
H	-0.878	-3.945	0.805	H	-0.882	-4.038	0.31
H	0.885	-3.945	0.802	H	0.881	-4.038	0.311
H	0.005	-2.942	1.963	H	-0.001	-3.11	1.534
C	0.001	-2.713	-2.062	C	0	-2.554	-2.469
H	0.001	-1.955	-2.849	H	0	-1.72	-3.175
H	0.885	-3.344	-2.198	H	0.884	-3.168	-2.663
H	-0.881	-3.345	-2.197	H	-0.885	-3.168	-2.663
N	-5.155	-1.1	-0.587	N	-5.151	-1.087	-0.398
N	5.156	-1.091	-0.579	N	5.15	-1.087	-0.399
C	0.044	1.475	-2.756	C	-0.002	1.83	-3.04
H	-0.805	0.822	-2.547	H	-0.881	1.19	-2.932
H	0.011	1.743	-3.813	H	-0.002	2.233	-4.054
H	0.95	0.89	-2.586	H	0.877	1.189	-2.932
C	-0.028	3.946	0.178	C	0.001	3.84	0.223
H	-0.048	3.994	1.256	H	0.002	3.688	1.293
P	-0.003	1.543	2.199	P	0.001	1.432	2.475
C	1.457	2.384	2.899	C	1.466	2.108	3.369
H	2.357	1.828	2.643	H	2.375	1.681	2.944
H	1.55	3.41	2.548	H	1.506	3.193	3.258
C	-1.494	2.325	2.903	C	-1.457	2.114	3.375
H	-1.385	2.297	3.989	H	-1.401	1.864	4.438
H	-2.376	1.753	2.619	H	-2.369	1.689	2.955
C	0.03	-0.123	2.917	C	-0.001	-0.342	2.946
H	0.934	-0.649	2.616	H	0.887	-0.833	2.544
H	-0.854	-0.682	2.617	H	-0.891	-0.83	2.547
H	0.027	-0.007	4.003	H	0	-0.442	4.034
H	1.334	2.388	3.984	H	1.414	1.858	4.432
H	-1.61	3.357	2.582	H	-1.494	3.199	3.264
C	-0.002	1.359	0.269	C	0	1.284	-0.156
C	-6.446	-0.531	-0.148	C	-6.448	-0.51	-0.007
H	-6.405	-0.015	0.817	H	-6.439	0.006	0.958
H	-6.959	0.085	-0.889	H	-6.926	0.108	-0.769
C	-6.957	-1.972	-0.019	C	-6.974	-1.952	0.082
C	5.536	-2.487	-0.276	C	5.562	-2.488	-0.212
H	5.069	-2.894	0.627	H	5.102	-2.982	0.649
H	5.435	-3.187	-1.107	H	5.484	-3.115	-1.102
C	6.447	-0.526	-0.133	C	6.447	-0.51	-0.009
H	6.96	0.096	-0.867	H	6.926	0.107	-0.772

Appendix

H	6.404	-0.02	0.837	H	6.439	0.006	0.955
C	6.957	-1.969	-0.018	C	6.973	-1.952	0.081
F	7.506	-2.312	1.185	F	7.496	-2.31	1.29
F	7.875	-2.325	-0.971	F	7.914	-2.277	-0.855
F	-7.507	-2.303	1.187	F	-7.497	-2.311	1.29
F	-7.874	-2.338	-0.969	F	-7.915	-2.276	-0.855

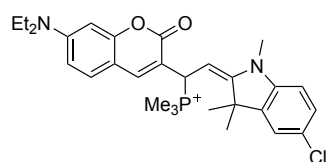


Minimum				TS			
C	-0.003	2.666	-0.454	C	-0.003	2.673	-0.628
C	-0.04	5.114	-0.462	C	0.002	5.082	-0.243
C	0.019	2.675	-1.875	C	-0.01	2.904	-2.029
C	-0.016	5.123	-1.849	C	-0.005	5.312	-1.613
H	-0.064	6.038	0.102	H	0.007	5.908	0.459
C	0.012	3.91	-2.533	C	-0.01	4.226	-2.485
H	-0.02	6.058	-2.398	H	-0.005	6.323	-2.003
H	0.028	3.914	-3.617	H	-0.016	4.403	-3.556
C	1.331	0.568	0.023	C	1.293	0.546	-0.262
C	2.496	1.357	-0.015	C	2.464	1.345	-0.197
C	1.472	-0.823	-0.155	C	1.464	-0.861	-0.391
C	3.731	0.786	-0.199	C	3.706	0.78	-0.231
H	2.455	2.435	0.074	H	2.402	2.421	-0.109
C	2.753	-1.367	-0.333	C	2.747	-1.398	-0.424
C	3.923	-0.595	-0.347	C	3.916	-0.611	-0.33
H	2.856	-2.436	-0.486	H	2.876	-2.469	-0.537
C	-1.333	0.565	0.019	C	-1.299	0.547	-0.254
C	-2.498	1.354	-0.031	C	-2.468	1.347	-0.178
C	-1.472	-0.826	-0.154	C	-1.472	-0.858	-0.39
C	-3.733	0.781	-0.215	C	-3.712	0.784	-0.208
H	-2.459	2.432	0.054	H	-2.405	2.423	-0.082
C	-2.752	-1.373	-0.332	C	-2.756	-1.394	-0.422
C	-3.923	-0.601	-0.354	C	-3.923	-0.606	-0.319
H	-2.854	-2.442	-0.48	H	-2.887	-2.464	-0.541
Si	0.001	-1.985	-0.323	Si	-0.005	-2.005	-0.671
C	-5.493	-2.582	-0.399	C	-5.534	-2.575	-0.267
H	-5.395	-3.189	-1.3	H	-5.436	-3.143	-1.194
H	-4.983	-3.058	0.445	H	-5.055	-3.104	0.563

C	0.004	-3.364	0.961	C	-0.007	-3.473	0.505
H	-0.878	-3.999	0.833	H	-0.887	-4.1	0.328
H	0.885	-3.999	0.828	H	0.876	-4.096	0.337
H	0.007	-2.995	1.988	H	-0.013	-3.165	1.553
C	0	-2.768	-2.038	C	-0.004	-2.617	-2.453
H	-0.001	-2.009	-2.825	H	-0.003	-1.783	-3.159
H	0.883	-3.399	-2.174	H	0.879	-3.232	-2.647
H	-0.883	-3.4	-2.172	H	-0.889	-3.23	-2.648
N	-5.171	-1.149	-0.571	N	-5.164	-1.153	-0.371
N	5.171	-1.141	-0.565	N	5.155	-1.16	-0.381
C	0.051	1.43	-2.729	C	-0.016	1.787	-3.046
H	-0.79	0.768	-2.517	H	-0.895	1.147	-2.939
H	0.006	1.702	-3.784	H	-0.019	2.196	-4.056
H	0.965	0.854	-2.57	H	0.863	1.144	-2.946
C	-0.034	3.894	0.213	C	0.003	3.772	0.234
H	-0.057	3.94	1.291	H	0.008	3.608	1.301
P	-0.001	1.486	2.23	P	0.017	1.372	2.523
C	1.459	2.333	2.92	C	1.54	1.971	3.371
H	2.358	1.769	2.678	H	2.414	1.494	2.925
H	1.558	3.353	2.554	H	1.634	3.051	3.252
C	-1.496	2.262	2.929	C	-1.371	2.135	3.467
H	-1.384	2.239	4.015	H	-1.302	1.874	4.526
H	-2.375	1.684	2.651	H	-2.321	1.773	3.07
C	0.041	-0.18	2.946	C	-0.068	-0.4	2.995
H	0.947	-0.703	2.643	H	0.785	-0.935	2.575
H	-0.842	-0.744	2.648	H	-0.991	-0.842	2.617
H	0.04	-0.065	4.031	H	-0.047	-0.501	4.083
H	1.332	2.354	4.004	H	1.504	1.729	4.437
H	-1.618	3.292	2.605	H	-1.342	3.221	3.363
C	-0.002	1.307	0.298	C	-0.002	1.224	-0.168
C	-6.453	-0.689	0.024	C	-6.479	-0.645	0.077
H	-6.364	-0.325	1.051	H	-6.475	-0.205	1.076
H	-7.019	0.013	-0.587	H	-6.982	0.012	-0.633
C	-6.917	-2.148	-0.032	C	-6.959	-2.105	0.064
C	5.493	-2.575	-0.404	C	5.524	-2.582	-0.265
H	4.982	-3.057	0.436	H	5.046	-3.103	0.57
H	5.394	-3.176	-1.309	H	5.426	-3.157	-1.187
C	6.453	-0.686	0.034	C	6.472	-0.649	0.061
H	7.02	0.021	-0.571	H	6.974	0	-0.655
H	6.364	-0.33	1.064	H	6.469	-0.2	1.056
C	6.917	-2.145	-0.034	C	6.95	-2.11	0.061
F	7.418	-2.669	1.122	F	7.459	-2.56	1.244

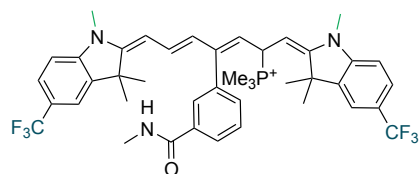
Appendix

F	7.852	-2.396	-1.004	F	7.88	-2.405	-0.896
F	-7.418	-2.663	1.129	F	-7.469	-2.565	1.243
F	-7.853	-2.407	-0.999	F	-7.889	-2.391	-0.896
F	-4.823	1.596	-0.289	F	-4.804	1.595	-0.14
F	4.822	1.602	-0.263	F	4.8	1.59	-0.175



Minimum				TS			
C	4.607	-0.63	0.85	C	4.972	-0.652	0.85
C	3.584	-1.057	-1.718	C	3.991	-1.075	-1.739
C	4.803	-1.589	-1.376	C	5.298	-1.375	-1.454
C	5.356	-1.407	-0.068	C	5.838	-1.186	-0.139
H	4.961	-0.42	1.848	H	5.303	-0.458	1.858
H	3.19	-1.22	-2.716	H	3.611	-1.235	-2.742
H	5.343	-2.155	-2.12	H	5.923	-1.759	-2.246
C	3.386	-0.104	0.475	C	3.662	-0.358	0.533
C	1.487	1.239	1.164	C	1.542	0.499	1.359
C	0.876	1.005	-0.13	C	0.956	0.25	0.049
C	2.827	-0.295	-0.802	C	3.119	-0.555	-0.753
C	1.556	0.277	-1.068	C	1.764	-0.234	-0.959
H	1.119	0.117	-2.049	H	1.339	-0.391	-1.946
O	2.711	0.643	1.407	O	2.875	0.154	1.53
O	1.031	1.924	2.063	O	0.993	0.996	2.322
N	6.551	-1.971	0.283	N	7.128	-1.517	0.152
C	7.105	-1.797	1.633	C	7.685	-1.301	1.496
H	6.296	-1.885	2.361	H	6.947	-1.611	2.239
H	7.769	-2.644	1.815	H	8.528	-1.985	1.603
C	7.875	-0.489	1.849	C	8.15	0.133	1.772
H	8.218	-0.433	2.886	H	8.52	0.205	2.798
H	8.751	-0.434	1.2	H	8.961	0.422	1.099
H	7.249	0.385	1.652	H	7.337	0.852	1.654
C	-1.541	1.205	0.648	C	-1.466	0.355	0.779
H	-1.322	1.586	1.635	H	-1.164	0.54	1.798
C	-4.575	-0.626	1.176	C	-4.935	-0.536	1.142
C	-5.638	-1.111	1.936	C	-6.096	-0.753	1.875
H	-5.75	-0.876	2.987	H	-6.151	-0.58	2.942
C	-6.584	-1.929	1.31	C	-7.224	-1.216	1.192
H	-7.419	-2.318	1.879	H	-8.144	-1.396	1.732

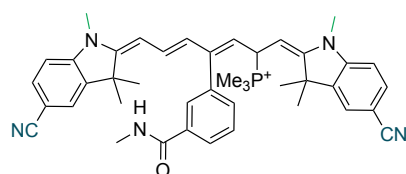
C	-6.452	-2.241	-0.037	C	-7.161	-1.447	-0.178
C	-5.385	-1.758	-0.802	C	-5.992	-1.232	-0.912
H	-5.304	-2.018	-1.851	H	-5.972	-1.424	-1.978
C	-4.451	-0.95	-0.181	C	-4.877	-0.775	-0.232
C	-2.214	-1.383	-1.238	C	-2.822	-1.753	-1.295
H	-2.675	-1.971	-2.036	H	-3.404	-2.123	-2.141
H	-1.297	-0.947	-1.636	H	-1.804	-1.568	-1.64
H	-1.945	-2.06	-0.425	H	-2.79	-2.534	-0.533
Cl	-7.661	-3.278	-0.81	Cl	-8.6	-2.032	-1.018
C	-3.317	0.729	2.889	C	-3.381	0.286	2.96
H	-2.395	0.337	3.331	H	-2.701	-0.445	3.405
H	-3.255	1.821	2.865	H	-2.923	1.275	3.002
H	-4.151	0.447	3.526	H	-4.301	0.306	3.537
N	-3.521	0.2	1.555	N	-3.684	-0.066	1.578
C	-2.653	0.451	0.489	C	-2.784	-0.003	0.555
C	-0.518	1.55	-0.402	C	-0.463	0.485	-0.21
P	-0.473	3.416	-0.766	P	-0.364	2.987	-0.756
C	-0.568	3.632	-2.567	C	-0.527	3.603	-2.485
H	-0.516	4.695	-2.807	H	-0.468	4.695	-2.512
H	0.267	3.114	-3.042	H	0.277	3.186	-3.095
H	-1.508	3.225	-2.941	H	-1.483	3.286	-2.903
C	1.048	4.225	-0.2	C	1.201	3.749	-0.162
H	1.128	4.146	0.883	H	1.323	3.548	0.903
H	1.914	3.759	-0.671	H	2.046	3.319	-0.701
H	1.001	5.275	-0.494	H	1.187	4.83	-0.324
C	-1.885	4.259	-0.006	C	-1.679	3.868	0.177
H	-2.816	3.8	-0.338	H	-2.66	3.572	-0.196
H	-1.815	4.191	1.079	H	-1.613	3.602	1.233
H	-1.865	5.308	-0.308	H	-1.568	4.95	0.071
H	-0.823	1.148	-1.367	H	-0.734	0.255	-1.231
C	-3.199	-0.296	-0.751	C	-3.478	-0.464	-0.741
C	-3.581	0.655	-1.906	C	-3.528	0.641	-1.819
H	-4.244	1.451	-1.56	H	-3.978	1.555	-1.427
H	-2.702	1.112	-2.364	H	-2.534	0.877	-2.201
H	-4.098	0.096	-2.689	H	-4.132	0.299	-2.662
C	7.349	-2.741	-0.682	C	8.031	-2.066	-0.872
H	8.001	-3.395	-0.101	H	8.799	-2.632	-0.343
H	6.687	-3.402	-1.247	H	7.484	-2.791	-1.477
C	8.195	-1.892	-1.637	C	8.695	-1.015	-1.769
H	8.929	-1.297	-1.091	H	9.326	-0.34	-1.187
H	8.734	-2.546	-2.328	H	9.326	-1.514	-2.51
H	7.576	-1.212	-2.227	H	7.955	-0.415	-2.303



Minimum				TS			
C	-6.667	-1.389	0.957	C	7.386	1.258	0.465
C	-5.904	-0.513	0.184	C	6.466	0.323	-0.004
C	-6.251	-0.232	-1.146	C	6.798	-0.586	-1.016
C	-7.352	-0.827	-1.723	C	8.06	-0.577	-1.576
C	-8.125	-1.718	-0.957	C	8.998	0.36	-1.113
C	-7.782	-1.986	0.369	C	8.66	1.261	-0.102
H	-6.424	-1.61	1.988	H	7.146	1.971	1.241
H	-7.62	-0.62	-2.753	H	8.325	-1.273	-2.363
H	-8.384	-2.669	0.955	H	9.39	1.981	0.246
N	-4.756	0.192	0.537	N	5.139	0.115	0.399
C	-0.894	2.33	-0.136	C	0.836	-1.384	0.045
H	-0.752	2.933	-1.029	H	0.778	-2.249	-0.611
C	0.161	1.595	0.293	C	-0.334	-0.719	0.318
C	1.425	1.664	-0.424	C	-1.574	-1.203	-0.222
H	1.44	2.327	-1.287	H	-1.518	-2.133	-0.784
C	-3.311	1.897	-0.573	C	3.281	-1.401	-0.269
H	-3.186	2.366	-1.543	H	3.093	-2.204	-0.974
C	-4.326	1.007	-0.512	C	4.556	-0.901	-0.323
C	-4.453	0.088	-2.883	C	5.125	-1.269	-2.776
H	-3.954	-0.825	-2.55	H	4.903	-0.221	-2.988
H	-3.695	0.774	-3.267	H	4.227	-1.859	-2.972
C	-5.245	0.743	-1.73	C	5.596	-1.457	-1.317
C	-5.935	2.032	-2.219	C	5.895	-2.945	-1.034
H	-6.493	2.511	-1.412	H	6.212	-3.096	0
H	-5.2	2.745	-2.601	H	5.01	-3.559	-1.218
H	-6.631	1.802	-3.029	H	6.692	-3.296	-1.693
C	-4.09	0.026	1.82	C	4.476	0.947	1.396
H	-4.218	0.901	2.462	H	4.057	0.336	2.193
H	-4.515	-0.833	2.335	H	5.202	1.621	1.841
H	-3.029	-0.174	1.675	H	3.688	1.546	0.936
C	2.561	0.989	-0.103	C	-2.793	-0.593	-0.094
H	2.534	0.341	0.762	H	-2.832	0.334	0.461
C	3.786	1.125	-0.844	C	-3.994	-1.143	-0.633
H	3.745	1.844	-1.657	H	-3.874	-2.101	-1.131

C	5.003	0.531	-0.691	C	-5.287	-0.69	-0.604
C	4.528	-1.174	1.12	C	-5.009	1.596	0.433
H	3.63	-1.507	0.598	H	-4.191	1.837	-0.247
H	5.044	-2.055	1.494	H	-5.641	2.476	0.523
H	4.243	-0.551	1.972	H	-4.607	1.354	1.42
C	6.558	2.41	-1.442	C	-6.567	-2.888	-0.47
H	7.462	2.638	-2.013	H	-7.442	-3.429	-0.84
H	5.745	3.023	-1.837	H	-5.684	-3.498	-0.668
H	6.728	2.691	-0.401	H	-6.669	-2.767	0.611
C	5.974	0.533	-3.043	C	-6.302	-1.71	-2.701
H	5.73	-0.527	-3.144	H	-6.215	-0.748	-3.212
H	5.149	1.118	-3.456	H	-5.415	-2.305	-2.928
H	6.869	0.739	-3.636	H	-7.174	-2.234	-3.101
C	6.219	0.909	-1.564	C	-6.455	-1.519	-1.175
N	5.4	-0.458	0.202	N	-5.794	0.494	-0.105
C	7.309	0.046	-0.957	C	-7.642	-0.632	-0.851
C	6.76	-0.731	0.075	C	-7.186	0.533	-0.22
C	8.645	-0.062	-1.277	C	-8.988	-0.816	-1.088
H	9.075	0.529	-2.078	H	-9.35	-1.711	-1.582
C	8.9	-1.723	0.48	C	-9.431	1.336	-0.045
H	9.526	-2.408	1.037	H	-10.134	2.097	0.269
C	7.548	-1.62	0.807	C	-8.07	1.528	0.195
H	7.146	-2.218	1.614	H	-7.736	2.428	0.694
C	9.449	-0.961	-0.552	C	-9.89	0.182	-0.682
H	-5.127	-0.169	-3.704	H	5.906	-1.601	-3.464
C	0.066	0.672	1.471	C	-0.338	0.533	1.14
C	-0.185	-0.69	1.266	C	0.093	1.739	0.576
C	-0.24	-1.583	2.342	C	0.07	2.929	1.312
H	-0.303	-1.045	0.248	H	0.41	1.736	-0.461
C	0.214	0.247	3.854	C	-0.817	1.711	3.204
C	-0.032	-1.104	3.64	C	-0.392	2.906	2.632
H	0.37	0.616	4.861	H	-1.168	1.696	4.229
H	-0.065	-1.799	4.469	H	-0.416	3.829	3.198
C	-0.482	-3.058	2.164	C	0.489	4.255	0.737
O	-0.06	-3.878	2.986	O	0.057	5.316	1.2
N	-1.179	-3.435	1.069	N	1.353	4.23	-0.302
C	-2.287	2.349	0.444	C	2.147	-1.035	0.532
H	-2.317	1.769	1.364	H	2.2	-0.151	1.147
P	-2.711	4.09	1.001	P	2.342	-2.573	2.475
C	-4.349	4.11	1.777	C	3.91	-2.537	3.438
H	-5.084	3.687	1.091	H	4.761	-2.548	2.755
H	-4.33	3.53	2.7	H	3.95	-1.628	4.041

C	-1.488	4.696	2.194	C	1.016	-2.644	3.747
H	-0.5	4.711	1.733	H	0.047	-2.764	3.259
H	-1.761	5.707	2.5	H	1.18	-3.488	4.422
C	0.269	1.132	2.776	C	-0.799	0.531	2.461
H	0.485	2.179	2.949	H	-1.147	-0.393	2.908
C	-2.732	5.213	-0.422	C	2.32	-4.238	1.702
H	-2.957	6.221	-0.067	H	2.453	-5.015	2.459
H	-1.759	5.218	-0.912	H	1.365	-4.393	1.196
C	-1.476	-4.833	0.783	C	1.828	5.448	-0.944
H	-1.956	-4.892	-0.192	H	2.434	5.171	-1.805
H	-0.557	-5.421	0.764	H	0.985	6.055	-1.281
H	-2.143	-5.26	1.536	H	2.434	6.049	-0.26
H	-1.603	-2.731	0.486	H	1.765	3.355	-0.583
H	-1.475	4.047	3.07	H	1.011	-1.718	4.323
H	-3.5	4.903	-1.131	H	3.124	-4.314	0.969
H	-4.62	5.141	2.008	H	3.972	-3.406	4.098
C	-9.352	-2.323	-1.555	C	10.385	0.345	-1.673
C	10.909	-1.042	-0.857	C	-11.356	-0.034	-0.885
F	-10.431	-1.482	-1.513	F	11.18	-0.594	-1.078
F	-9.193	-2.64	-2.867	F	10.407	0.054	-2.999
F	-9.745	-3.457	-0.926	F	11.028	1.526	-1.521
F	11.17	-0.966	-2.189	F	-11.635	-0.635	-2.07
F	11.625	-0.023	-0.288	F	-11.905	-0.841	0.072
F	11.481	-2.187	-0.413	F	-12.07	1.116	-0.854

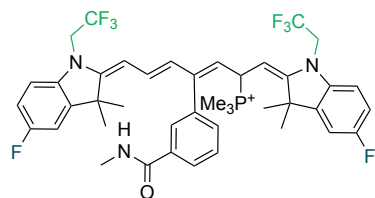


Minimum				TS			
C	-6.269	1.927	-0.611	C	-6.269	1.927	-0.611
C	-5.619	0.898	0.078	C	-5.619	0.898	0.078
C	-5.923	0.618	1.42	C	-5.923	0.618	1.42
C	-6.878	1.348	2.09	C	-6.878	1.348	2.09
C	-7.548	2.389	1.407	C	-7.548	2.389	1.407
C	-7.234	2.665	0.066	C	-7.234	2.665	0.066
H	-6.042	2.166	-1.641	H	-6.042	2.166	-1.641
H	-7.121	1.141	3.125	H	-7.121	1.141	3.125
H	-7.75	3.466	-0.449	H	-7.75	3.466	-0.449
N	-4.636	0.03	-0.38	N	-4.636	0.03	-0.38

C	-0.869	-2.247	0.162	C	-0.869	-2.247	0.162
H	-0.714	-2.896	1.021	H	-0.714	-2.896	1.021
C	0.176	-1.484	-0.238	C	0.176	-1.484	-0.238
C	1.45	-1.586	0.458	C	1.45	-1.586	0.458
H	1.479	-2.294	1.285	H	1.479	-2.294	1.285
C	-3.271	-1.797	0.635	C	-3.271	-1.797	0.635
H	-3.155	-2.31	1.584	H	-3.155	-2.31	1.584
C	-4.222	-0.839	0.635	C	-4.222	-0.839	0.635
C	-4.168	-0.11	3.081	C	-4.168	-0.11	3.081
H	-3.542	0.744	2.813	H	-3.542	0.744	2.813
H	-3.517	-0.931	3.389	H	-3.517	-0.931	3.389
C	-5.063	-0.536	1.898	C	-5.063	-0.536	1.898
C	-5.932	-1.75	2.291	C	-5.932	-1.75	2.291
H	-6.567	-2.065	1.46	H	-6.567	-2.065	1.46
H	-5.304	-2.594	2.584	H	-5.304	-2.594	2.584
H	-6.575	-1.495	3.137	H	-6.575	-1.495	3.137
C	-4.119	0.061	-1.74	C	-4.119	0.061	-1.74
H	-4.194	-0.924	-2.202	H	-4.194	-0.924	-2.202
H	-4.715	0.746	-2.337	H	-4.715	0.746	-2.337
H	-3.082	0.402	-1.764	H	-3.082	0.402	-1.764
C	2.579	-0.893	0.157	C	2.579	-0.893	0.157
H	2.539	-0.2	-0.672	H	2.539	-0.2	-0.672
C	3.814	-1.065	0.876	C	3.814	-1.065	0.876
H	3.778	-1.816	1.659	H	3.778	-1.816	1.659
C	5.032	-0.472	0.735	C	5.032	-0.472	0.735
C	4.552	1.285	-1.026	C	4.552	1.285	-1.026
H	3.669	1.626	-0.485	H	3.669	1.626	-0.485
H	5.076	2.161	-1.401	H	5.076	2.161	-1.401
H	4.245	0.673	-1.878	H	4.245	0.673	-1.878
C	6.585	-2.381	1.408	C	6.585	-2.381	1.408
H	7.491	-2.633	1.965	H	7.491	-2.633	1.965
H	5.772	-3.005	1.786	H	5.772	-3.005	1.786
H	6.747	-2.627	0.356	H	6.747	-2.627	0.356
C	6.021	-0.559	3.077	C	6.021	-0.559	3.077
H	5.784	0.498	3.217	H	5.784	0.498	3.217
H	5.197	-1.154	3.477	H	5.197	-1.154	3.477
H	6.919	-0.79	3.656	H	6.919	-0.79	3.656
C	6.252	-0.885	1.584	C	6.252	-0.885	1.584
N	5.429	0.546	-0.13	N	5.429	0.546	-0.13
C	7.341	-0.005	0.999	C	7.341	-0.005	0.999
C	6.786	0.809	-0.003	C	6.786	0.809	-0.003
C	8.678	0.085	1.311	C	8.678	0.085	1.311

H	9.118	-0.534	2.084	H	9.118	-0.534	2.084
C	8.922	1.809	-0.401	C	8.922	1.809	-0.401
H	9.551	2.507	-0.94	H	9.551	2.507	-0.94
C	7.571	1.721	-0.716	C	7.571	1.721	-0.716
H	7.163	2.344	-1.5	H	7.163	2.344	-1.5
C	9.486	1.004	0.604	C	9.486	1.004	0.604
H	-4.785	0.171	3.938	H	-4.785	0.171	3.938
C	10.873	1.113	0.907	C	10.873	1.113	0.907
C	-8.539	3.159	2.079	C	-8.539	3.159	2.079
N	12.001	1.199	1.155	N	12.001	1.199	1.155
N	-9.345	3.784	2.628	N	-9.345	3.784	2.628
C	0.06	-0.497	-1.36	C	0.06	-0.497	-1.36
C	-0.22	0.845	-1.076	C	-0.22	0.845	-1.076
C	-0.298	1.797	-2.098	C	-0.298	1.797	-2.098
H	-0.345	1.138	-0.04	H	-0.345	1.138	-0.04
C	0.192	0.068	-3.715	C	0.192	0.068	-3.715
C	-0.082	1.4	-3.422	C	-0.082	1.4	-3.422
H	0.353	-0.238	-4.742	H	0.353	-0.238	-4.742
H	-0.132	2.141	-4.21	H	-0.132	2.141	-4.21
C	-0.575	3.253	-1.834	C	-0.575	3.253	-1.834
O	-0.172	4.13	-2.603	O	-0.172	4.13	-2.603
N	-1.282	3.547	-0.719	N	-1.282	3.547	-0.719
C	-2.267	-2.239	-0.407	C	-2.267	-2.239	-0.407
H	-2.297	-1.628	-1.306	H	-2.297	-1.628	-1.306
P	-2.708	-3.96	-1.005	P	-2.708	-3.96	-1.005
C	-4.351	-3.948	-1.768	C	-4.351	-3.948	-1.768
H	-5.079	-3.545	-1.063	H	-5.079	-3.545	-1.063
H	-4.337	-3.339	-2.673	H	-4.337	-3.339	-2.673
C	-1.494	-4.542	-2.219	C	-1.494	-4.542	-2.219
H	-0.505	-4.573	-1.762	H	-0.505	-4.573	-1.762
H	-1.774	-5.543	-2.55	H	-1.774	-5.543	-2.55
C	0.268	-0.876	-2.69	C	0.268	-0.876	-2.69
H	0.502	-1.908	-2.924	H	0.502	-1.908	-2.924
C	-2.735	-5.117	0.392	C	-2.735	-5.117	0.392
H	-2.973	-6.113	0.014	H	-2.973	-6.113	0.014
H	-1.759	-5.145	0.878	H	-1.759	-5.145	0.878
C	-1.613	4.917	-0.351	C	-1.613	4.917	-0.351
H	-2.101	4.905	0.622	H	-2.101	4.905	0.622
H	-0.708	5.524	-0.288	H	-0.708	5.524	-0.288
H	-2.286	5.375	-1.082	H	-2.286	5.375	-1.082
H	-1.689	2.799	-0.181	H	-1.689	2.799	-0.181
H	-1.481	-3.868	-3.076	H	-1.481	-3.868	-3.076

H	-3.496	-4.815	1.111	H	-3.496	-4.815	1.111
H	-4.628	-4.97	-2.031	H	-4.628	-4.97	-2.031

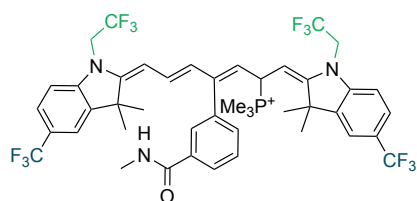


Minimum				TS			
C	-6.404	1.957	0.984	C	7.281	1.193	-1.04
C	-5.762	0.729	1.117	C	6.41	0.109	-1.025
C	-6.121	-0.177	2.114	C	6.761	-1.126	-1.565
C	-7.14	0.123	3.005	C	8.009	-1.311	-2.14
C	-7.774	1.353	2.862	C	8.873	-0.222	-2.15
C	-7.429	2.269	1.884	C	8.539	1.014	-1.622
H	-6.147	2.664	0.207	H	7.024	2.151	-0.611
H	-7.443	-0.556	3.793	H	8.319	-2.255	-2.574
H	-7.957	3.212	1.817	H	9.254	1.826	-1.656
N	-4.7	0.203	0.343	N	5.087	0.044	-0.511
C	-0.98	-2.159	-0.218	C	0.891	-1.669	0.026
H	-0.848	-3.053	0.386	H	0.834	-2.663	-0.409
C	0.099	-1.354	-0.367	C	-0.289	-0.983	0.193
C	1.361	-1.746	0.246	C	-1.527	-1.602	-0.183
H	1.334	-2.671	0.819	H	-1.46	-2.627	-0.54
C	-3.38	-1.933	0.416	C	3.319	-1.724	-0.384
H	-3.3	-2.813	1.046	H	3.156	-2.728	-0.761
C	-4.326	-1.064	0.825	C	4.554	-1.22	-0.697
C	-4.41	-1.572	3.326	C	5.08	-2.528	-2.813
H	-3.803	-0.685	3.521	H	4.784	-1.665	-3.413
H	-3.746	-2.436	3.252	H	4.22	-3.193	-2.712
C	-5.238	-1.405	2.033	C	5.603	-2.09	-1.424
C	-6.077	-2.673	1.766	C	5.995	-3.325	-0.585
H	-6.672	-2.567	0.857	H	6.39	-3.032	0.39
H	-5.432	-3.548	1.658	H	5.135	-3.979	-0.431
H	-6.757	-2.855	2.602	H	6.766	-3.896	-1.107
C	-3.897	1.079	-0.478	C	4.348	1.256	-0.224
H	-2.855	0.768	-0.478	H	3.294	1.118	-0.454
H	-3.924	2.093	-0.07	H	4.715	2.062	-0.863
C	2.543	-1.085	0.143	C	-2.76	-1.008	-0.143
H	2.559	-0.178	-0.446	H	-2.806	0.011	0.216
C	3.757	-1.576	0.741	C	-3.955	-1.693	-0.514

Appendix

H	3.655	-2.553	1.205	H	-3.811	-2.744	-0.744
C	5.018	-1.071	0.822	C	-5.259	-1.289	-0.624
C	4.778	1.309	-0.028	C	-5.139	1.228	-0.372
H	3.753	1.252	0.332	H	-4.131	1.151	-0.775
H	5.214	2.223	0.381	H	-5.659	1.995	-0.948
C	6.453	-3.164	0.629	C	-6.511	-3.359	0.162
H	7.313	-3.696	1.043	H	-7.351	-4.025	-0.054
H	5.591	-3.836	0.657	H	-5.605	-3.965	0.226
H	6.668	-2.923	-0.415	H	-6.684	-2.89	1.133
C	5.872	-2.25	2.92	C	-6.134	-2.981	-2.319
H	5.663	-1.356	3.512	H	-6.027	-2.242	-3.116
H	5.011	-2.918	2.988	H	-5.23	-3.593	-2.29
H	6.731	-2.763	3.361	H	-6.975	-3.634	-2.564
C	6.171	-1.886	1.45	C	-6.379	-2.298	-0.955
N	5.536	0.163	0.412	N	-5.833	-0.033	-0.498
C	7.331	-0.914	1.354	C	-7.601	-1.405	-1.006
C	6.906	0.265	0.739	C	-7.228	-0.089	-0.731
C	8.642	-1.051	1.781	C	-8.923	-1.717	-1.281
H	9.006	-1.95	2.265	H	-9.25	-2.726	-1.501
C	9.098	1.202	0.965	C	-9.489	0.641	-1.005
H	9.808	2.006	0.825	H	-10.247	1.414	-1.009
C	7.774	1.333	0.532	C	-8.154	0.949	-0.723
H	7.463	2.245	0.042	H	-7.881	1.971	-0.497
C	9.499	0.024	1.572	C	-9.84	-0.671	-1.273
H	-5.075	-1.729	4.179	H	5.865	-3.067	-3.348
C	0.048	-0.052	-1.108	C	-0.304	0.424	0.71
C	-0.008	1.147	-0.386	C	-0.085	1.491	-0.168
C	-0.007	2.384	-1.04	C	-0.125	2.815	0.285
H	-0.019	1.098	0.697	H	0.08	1.27	-1.217
C	0.116	1.234	-3.162	C	-0.6	2.011	2.516
C	0.064	2.419	-2.437	C	-0.387	3.067	1.636
H	0.166	1.264	-4.245	H	-0.8	2.211	3.562
H	0.078	3.377	-2.94	H	-0.424	4.092	1.982
C	-0.039	3.694	-0.299	C	0.064	3.998	-0.627
O	0.46	4.714	-0.784	O	-0.406	5.104	-0.342
N	-0.635	3.695	0.914	N	0.766	3.792	-1.764
C	-2.386	-1.94	-0.724	C	2.205	-1.18	0.336
H	-2.437	-1.054	-1.352	H	2.26	-0.184	0.746
P	-2.834	-3.347	-1.891	P	2.588	-2.209	2.625
C	-4.563	-3.223	-2.416	C	4.339	-2.226	3.187
H	-5.21	-3.231	-1.54	H	4.984	-2.528	2.361
H	-4.718	-2.303	-2.978	H	4.628	-1.226	3.511

C	-1.765	-3.322	-3.356	C	1.629	-1.746	4.129
H	-0.722	-3.412	-3.054	H	0.562	-1.855	3.929
H	-2.027	-4.165	-3.998	H	1.901	-2.395	4.966
C	0.113	0.004	-2.503	C	-0.569	0.696	2.056
H	0.182	-0.912	-3.077	H	-0.756	-0.121	2.742
C	-2.61	-4.936	-1.046	C	2.179	-3.982	2.371
H	-2.911	-5.735	-1.724	H	2.383	-4.558	3.277
H	-1.565	-5.074	-0.772	H	1.123	-4.082	2.116
C	-0.726	4.897	1.732	C	1.013	4.858	-2.725
H	-1.175	4.631	2.688	H	1.502	4.429	-3.598
H	0.267	5.315	1.909	H	0.073	5.319	-3.034
H	-1.341	5.661	1.249	H	1.657	5.635	-2.303
H	-1.131	2.874	1.222	H	1.224	2.907	-1.91
H	-1.913	-2.393	-3.908	H	1.836	-0.709	4.393
H	-3.234	-4.976	-0.152	H	2.778	-4.385	1.552
H	-4.797	-4.08	-3.05	H	4.467	-2.928	4.015
C	4.743	1.474	-1.546	C	-5.045	1.732	1.067
C	-4.36	1.182	-1.929	C	4.463	1.749	1.216
F	-5.657	1.538	-2.038	F	5.743	1.951	1.591
F	-4.222	0.015	-2.605	F	3.926	0.889	2.11
F	-3.63	2.108	-2.587	F	3.811	2.923	1.35
F	5.976	1.661	-2.071	F	-6.261	1.974	1.606
F	4.213	0.403	-2.177	F	-4.425	0.856	1.886
F	3.998	2.55	-1.883	F	-4.35	2.889	1.109
F	-8.783	1.667	3.729	F	10.108	-0.381	-2.707
F	10.797	-0.091	1.984	F	-11.148	-0.956	-1.54



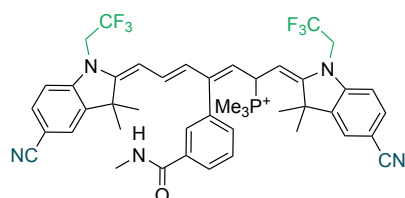
Minimum				TS			
C	-6.509	-1.752	0.482	C	7.421	1.06	-0.804
C	-5.867	-0.796	-0.303	C	6.521	0.009	-0.661
C	-6.251	-0.563	-1.626	C	6.863	-1.304	-0.988
C	-7.287	-1.28	-2.189	C	8.127	-1.595	-1.465
C	-7.945	-2.246	-1.411	C	9.047	-0.547	-1.614
C	-7.556	-2.475	-0.091	C	8.695	0.763	-1.288
H	-6.234	-1.938	1.51	H	7.171	2.079	-0.544
H	-7.585	-1.112	-3.217	H	8.404	-2.608	-1.729

Appendix

H	-8.067	-3.222	0.502	H	9.413	1.564	-1.407
N	-4.79	0.037	0.041	N	5.183	0.053	-0.21
C	-1.026	2.159	-0.822	C	0.921	-1.476	0.4
H	-0.891	2.5	-1.845	H	0.859	-2.52	0.104
C	0.031	1.548	-0.235	C	-0.253	-0.76	0.436
C	1.273	1.419	-0.987	C	-1.488	-1.415	0.116
H	1.244	1.8	-2.005	H	-1.423	-2.477	-0.108
C	-3.456	1.776	-1.194	C	3.36	-1.637	0.107
H	-3.39	2.17	-2.202	H	3.186	-2.684	-0.118
C	-4.418	0.845	-1.053	C	4.619	-1.215	-0.224
C	-4.563	-0.077	-3.429	C	5.196	-2.834	-2.096
H	-3.968	-0.942	-3.125	H	4.957	-2.062	-2.831
H	-3.89	0.675	-3.846	H	4.31	-3.453	-1.941
C	-5.358	0.498	-2.237	C	5.67	-2.208	-0.762
C	-6.181	1.726	-2.68	C	5.986	-3.314	0.267
H	-6.749	2.142	-1.846	H	6.337	-2.89	1.209
H	-5.528	2.507	-3.077	H	5.102	-3.924	0.466
H	-6.884	1.442	-3.467	H	6.767	-3.97	-0.124
C	-4.012	-0.211	1.233	C	4.471	1.313	-0.119
H	-2.965	0.038	1.073	H	3.423	1.171	-0.372
H	-4.048	-1.274	1.483	H	4.886	2.015	-0.845
C	2.438	0.899	-0.524	C	-2.718	-0.816	0.066
H	2.455	0.544	0.497	H	-2.762	0.239	0.299
C	3.633	0.856	-1.328	C	-3.908	-1.539	-0.244
H	3.521	1.325	-2.301	H	-3.754	-2.605	-0.382
C	4.881	0.366	-1.111	C	-5.213	-1.162	-0.395
C	4.668	-0.889	1.092	C	-5.139	1.373	-0.249
H	3.629	-1.052	0.814	H	-4.13	1.311	-0.648
H	5.08	-1.859	1.375	H	-5.672	2.117	-0.843
C	6.339	2.04	-2.359	C	-6.441	-3.206	0.496
H	7.184	2.147	-3.043	H	-7.271	-3.892	0.31
H	5.483	2.565	-2.79	H	-5.528	-3.797	0.596
H	6.598	2.522	-1.413	H	-6.625	-2.689	1.44
C	5.647	-0.117	-3.497	C	-6.051	-2.954	-2
H	5.409	-1.174	-3.364	H	-5.952	-2.256	-2.834
H	4.785	0.377	-3.951	H	-5.137	-3.547	-1.933
H	6.486	-0.037	-4.192	H	-6.88	-3.633	-2.213
C	6.011	0.545	-2.15	C	-6.316	-2.204	-0.674
N	5.409	-0.345	-0.022	N	-5.809	0.095	-0.354
C	7.166	-0.176	-1.484	C	-7.55	-1.332	-0.781
C	6.754	-0.674	-0.242	C	-7.194	0.005	-0.586
C	8.455	-0.391	-1.927	C	-8.863	-1.671	-1.039

H	8.781	-0.016	-2.889	H	-9.151	-2.703	-1.197
C	8.923	-1.608	0.124	C	-9.46	0.683	-0.908
H	9.612	-2.165	0.747	H	-10.208	1.463	-0.959
C	7.622	-1.392	0.578	C	-8.135	1.03	-0.644
H	7.323	-1.771	1.545	H	-7.876	2.067	-0.483
C	9.341	-1.118	-1.113	C	-9.824	-0.649	-1.106
H	-5.249	-0.392	-4.22	H	5.985	-3.469	-2.506
C	-0.022	0.967	1.145	C	-0.263	0.706	0.748
C	-0.147	-0.419	1.304	C	0.002	1.634	-0.265
C	-0.151	-1.002	2.576	C	-0.034	3.009	-0.008
H	-0.206	-1.037	0.415	H	0.198	1.265	-1.266
C	0.107	1.193	3.556	C	-0.6	2.54	2.295
C	-0.016	-0.184	3.703	C	-0.341	3.456	1.281
H	0.21	1.824	4.431	H	-0.834	2.89	3.294
H	-0.007	-0.639	4.686	H	-0.377	4.52	1.475
C	-0.258	-2.488	2.793	C	0.204	4.043	-1.076
O	0.201	-3.019	3.809	O	-0.296	5.169	-0.995
N	-0.875	-3.204	1.827	N	0.982	3.679	-2.12
C	-2.415	2.368	-0.268	C	2.23	-0.968	0.682
H	-2.485	2.006	0.755	H	2.293	0.074	0.953
P	-2.74	4.216	-0.116	P	2.495	-1.67	3.144
C	-4.435	4.525	0.444	C	4.205	-1.628	3.821
H	-5.138	4.039	-0.233	H	4.898	-2.053	3.094
H	-4.568	4.136	1.452	H	4.494	-0.596	4.02
C	-1.582	4.969	1.057	C	1.456	-0.984	4.501
H	-0.558	4.81	0.718	H	0.401	-1.109	4.253
H	-1.781	6.04	1.107	H	1.664	-1.506	5.44
C	0.11	1.766	2.285	C	-0.571	1.171	2.03
H	0.237	2.836	2.179	H	-0.796	0.465	2.82
C	-2.512	5.02	-1.727	C	2.066	-3.457	3.124
H	-2.694	6.089	-1.605	H	2.197	-3.895	4.117
H	-1.492	4.871	-2.081	H	1.026	-3.58	2.814
C	-1.039	-4.648	1.917	C	1.277	4.589	-3.219
H	-1.485	-5.004	0.99	H	1.831	4.042	-3.981
H	-0.072	-5.135	2.057	H	0.353	4.971	-3.656
H	-1.688	-4.923	2.754	H	1.877	5.439	-2.883
H	-1.327	-2.721	1.067	H	1.465	2.796	-2.093
H	-1.719	4.532	2.046	H	1.667	0.079	4.626
H	-3.218	4.621	-2.455	H	2.708	-3.983	2.416
H	-4.612	5.602	0.443	H	4.262	-2.206	4.748
C	-9.106	-2.988	-1.994	C	10.441	-0.852	-2.074
C	10.751	-1.313	-1.57	C	-11.258	-1.014	-1.335

F	-10.267	-2.27	-1.939	F	11.264	-1.198	-1.041
F	-8.926	-3.289	-3.306	F	10.485	-1.89	-2.945
F	-9.36	-4.156	-1.358	F	11.033	0.2	-2.686
F	10.83	-1.637	-2.889	F	-11.401	-2	-2.258
F	11.509	-0.185	-1.427	F	-11.865	-1.479	-0.204
F	11.399	-2.287	-0.891	F	-12.007	0.029	-1.76
C	4.702	-0.008	2.339	C	-5.066	1.904	1.181
C	-4.499	0.548	2.465	C	4.55	1.989	1.247
F	-5.79	0.287	2.758	F	5.822	2.218	1.635
F	-4.399	1.891	2.318	F	3.968	1.262	2.226
F	-3.762	0.209	3.543	F	3.919	3.181	1.203
F	5.957	0.15	2.818	F	-6.292	2.116	1.71
F	4.214	1.232	2.117	F	-4.424	1.059	2.017
F	3.963	-0.564	3.324	F	-4.406	3.081	1.207



Minimum				TS			
C	6.194	2.174	-0.688	C	7.304	1.155	-1.001
C	5.621	0.937	-0.985	C	6.429	0.072	-0.95
C	6.003	0.206	-2.116	C	6.782	-1.189	-1.436
C	6.968	0.695	-2.97	C	8.03	-1.398	-1.985
C	7.559	1.945	-2.685	C	8.932	-0.316	-2.043
C	7.165	2.671	-1.551	C	8.562	0.947	-1.557
H	5.921	2.743	0.19	H	7.044	2.131	-0.616
H	7.272	0.144	-3.851	H	8.323	-2.366	-2.371
H	7.626	3.628	-1.341	H	9.265	1.769	-1.608
N	4.625	0.249	-0.281	N	5.111	0.037	-0.451
C	1.028	-2.272	-0.017	C	0.893	-1.618	0.095
H	0.892	-3.036	-0.778	H	0.834	-2.622	-0.317
C	-0.046	-1.503	0.28	C	-0.285	-0.922	0.239
C	-1.305	-1.761	-0.408	C	-1.522	-1.548	-0.127
H	-1.279	-2.561	-1.145	H	-1.455	-2.582	-0.456
C	3.413	-1.927	-0.628	C	3.325	-1.711	-0.273
H	3.363	-2.708	-1.379	H	3.158	-2.728	-0.613
C	4.302	-0.962	-0.928	C	4.566	-1.233	-0.591
C	4.346	-1.117	-3.477	C	5.106	-2.631	-2.644
H	3.683	-0.251	-3.539	H	4.823	-1.793	-3.285

H	3.736	-2.022	-3.51	H	4.24	-3.286	-2.525
C	5.197	-1.075	-2.189	C	5.615	-2.139	-1.269
C	6.118	-2.311	-2.112	C	5.988	-3.339	-0.373
H	6.732	-2.29	-1.209	H	6.373	-3.008	0.594
H	5.53	-3.232	-2.11	H	5.121	-3.98	-0.203
H	6.784	-2.337	-2.978	H	6.76	-3.938	-0.861
C	3.859	0.911	0.752	C	4.387	1.262	-0.174
H	2.83	0.558	0.76	H	3.332	1.135	-0.403
H	3.822	1.983	0.551	H	4.763	2.057	-0.82
C	-2.478	-1.11	-0.203	C	-2.753	-0.95	-0.107
H	-2.493	-0.33	0.545	H	-2.798	0.077	0.225
C	-3.685	-1.456	-0.912	C	-3.945	-1.647	-0.467
H	-3.587	-2.338	-1.539	H	-3.796	-2.702	-0.676
C	-4.927	-0.91	-0.947	C	-5.248	-1.255	-0.591
C	-4.669	1.258	0.364	C	-5.145	1.27	-0.341
H	-3.631	1.242	0.04	H	-4.136	1.202	-0.741
H	-5.061	2.25	0.136	H	-5.665	2.039	-0.914
C	-6.424	-2.953	-1.187	C	-6.493	-3.324	0.208
H	-7.28	-3.372	-1.722	H	-7.328	-3.996	-0.007
H	-5.58	-3.637	-1.305	H	-5.584	-3.924	0.281
H	-6.675	-2.896	-0.125	H	-6.673	-2.848	1.174
C	-5.725	-1.661	-3.253	C	-6.107	-2.963	-2.275
H	-5.47	-0.682	-3.666	H	-6	-2.23	-3.077
H	-4.88	-2.334	-3.41	H	-5.2	-3.57	-2.238
H	-6.579	-2.057	-3.809	H	-6.944	-3.622	-2.519
C	-6.074	-1.559	-1.752	C	-6.361	-2.272	-0.917
N	-5.433	0.253	-0.34	N	-5.833	0.005	-0.485
C	-7.209	-0.58	-1.523	C	-7.586	-1.383	-0.98
C	-6.772	0.456	-0.688	C	-7.215	-0.06	-0.719
C	-8.499	-0.587	-2.007	C	-8.901	-1.696	-1.254
H	-8.852	-1.379	-2.657	H	-9.207	-2.714	-1.46
C	-8.917	1.501	-0.812	C	-9.47	0.666	-1.005
H	-9.593	2.303	-0.541	H	-10.214	1.453	-1.015
C	-7.617	1.505	-0.32	C	-8.144	0.98	-0.725
H	-7.297	2.303	0.336	H	-7.872	2.004	-0.511
C	-9.368	0.467	-1.648	C	-9.856	-0.658	-1.266
H	4.996	-1.117	-4.356	H	5.893	-3.199	-3.146
C	0.004	-0.372	1.262	C	-0.298	0.497	0.719
C	0.029	0.948	0.794	C	-0.055	1.541	-0.182
C	0.024	2.029	1.683	C	-0.096	2.876	0.236
H	0.017	1.117	-0.277	H	0.126	1.292	-1.222
C	-0.038	0.475	3.534	C	-0.618	2.132	2.478

Appendix

C	-0.016	1.781	3.059	C	-0.382	3.163	1.575
H	-0.066	0.287	4.601	H	-0.835	2.36	3.515
H	-0.031	2.619	3.745	H	-0.42	4.197	1.894
C	0.017	3.462	1.224	C	0.114	4.034	-0.702
O	-0.467	4.354	1.927	O	-0.365	5.146	-0.459
N	0.558	3.72	0.012	N	0.843	3.798	-1.816
C	2.439	-2.149	0.508	C	2.203	-1.128	0.399
H	2.498	-1.394	1.288	H	2.264	-0.127	0.795
P	2.915	-3.742	1.389	P	2.545	-2.119	2.772
C	4.653	-3.695	1.894	C	4.28	-2.15	3.386
H	5.285	-3.544	1.019	H	4.945	-2.484	2.588
H	4.813	-2.885	2.604	H	4.577	-1.147	3.693
C	1.878	-3.991	2.854	C	1.557	-1.604	4.24
H	0.829	-4.042	2.561	H	0.494	-1.702	4.017
H	2.163	-4.931	3.33	H	1.799	-2.235	5.101
C	-0.034	-0.597	2.641	C	-0.586	0.805	2.053
H	-0.082	-1.611	3.02	H	-0.792	0.007	2.755
C	2.682	-5.153	0.273	C	2.118	-3.894	2.557
H	2.995	-6.06	0.793	H	2.281	-4.446	3.486
H	1.632	-5.246	-0.005	H	1.069	-3.986	2.267
C	0.605	5.065	-0.546	C	1.112	4.837	-2.801
H	0.997	5.004	-1.56	H	1.625	4.384	-3.648
H	-0.396	5.5	-0.576	H	0.179	5.284	-3.147
H	1.249	5.72	0.047	H	1.742	5.628	-2.385
H	1.04	2.985	-0.48	H	1.306	2.911	-1.925
H	2.029	-3.173	3.558	H	1.774	-0.563	4.483
H	3.292	-5.03	-0.622	H	2.738	-4.33	1.772
H	4.906	-4.646	2.366	H	4.372	-2.832	4.236
C	-4.704	1.098	1.882	C	-5.065	1.758	1.104
C	4.433	0.747	2.157	C	4.512	1.761	1.263
F	5.719	1.145	2.241	F	5.796	1.955	1.63
F	4.397	-0.539	2.585	F	3.974	0.908	2.162
F	3.723	1.48	3.039	F	3.87	2.94	1.393
F	-5.956	1.213	2.38	F	-6.287	1.982	1.635
F	-4.231	-0.099	2.293	F	-4.444	0.876	1.916
F	-3.95	2.053	2.469	F	-4.379	2.919	1.164
N	-11.794	0.491	-2.535	N	-12.332	-1.2	-1.773
N	9.373	2.897	-4.26	N	11.284	-0.664	-3.056
C	-10.707	0.481	-2.136	C	-11.223	-0.956	-1.545
C	8.56	2.471	-3.553	C	10.232	-0.507	-2.602

Curriculum vitae



Sarah Emmert
(née Hübner)

emmert-sarah@web.de

www.linkedin.com/in/sarah-emmert-686089218

Research Experience

since 02/2020 **École Polytechnique Fédérale de Lausanne and University of Zurich**

PhD student in the group of Prof. Pablo Rivera-Fuentes investigating redox biology with fluorescent sensors for live-cell imaging.

09/2018 – 10/2019 **Ludwig-Maximilian University, Munich**

Several research projects in the group of Prof. Thomas Carell synthesizing modified nucleotides for solid-phase RNA synthesis.

04/2018 – 07/2018 **Institute for Stroke and Dementia Research (ISD), Munich**

Research project in the group of Prof. Dominik Paquet working on model systems for neurovascular disorders based on CRISPR-Cas9 engineered hiPSCs.

10/2017 – 03/2018 **University of California, Berkeley**

Research projects in the groups of Prof. Evan Miller and Prof. Christopher Chang developing fluorescent sensors for transmembrane voltage and intracellular copper.

02/2016 – 03/2016 **Max-Planck-Institute for Biochemistry, Martinsried**

Development of chromatography methods for the purification of hydrophilic and acidic peptides.

Education

10/2017 – 10/2019 **Ludwig-Maximilian University, Munich**

Master of Chemistry

10/2014 – 09/2017 **Ludwig-Maximilian University, Munich**

Bachelor of Chemistry and Biochemistry

Publications

1. Emmert, S., Quargnali, G., Thallmair, S. & Rivera-Fuentes, P. A locally activatable sensor for robust quantification of organellar glutathione. *Nat. Chem.* (2023). doi:10.1038/s41557-023-01249-3.
2. Xu, F., Crisp, A., Schinkel, T., Dubini, R. C. A., Hübner, S., Becker, S., Schelter, F., Rovó, P. & Carell, T. Isoxazole nucleosides as building blocks for a plausible proto-RNA. *Angew. Chem. Int. Ed.* **61**, e202211945 (2022).
3. Okamura, H., Crisp, A., Hübner, S., Becker, S., Rovó, P. & Carell, T. Proto-urea-RNA (Wöhler RNA) containing unusually stable urea nucleosides. *Angew. Chem. Int. Ed.* **58**, 18691–18696 (2019).

Conference Presentations

- 10/2023** EMBO | EMBL Symposium: Seeing is believing – Imaging the molecular processes of life, Heidelberg (Talk)
- 08/2023** Fall Meeting of the Swiss Chemical Society, Bern (Talk)
- 08/2023** GRC Chemical Imaging, Easton (Poster Award)
- 11/2022** International Symposium on Chemical Biology, Geneva (Poster Award)
- 09/2022** Fall Meeting of the Swiss Chemical Society, Zurich (Poster)
- 03/2022** European Molecular Imaging Meeting, Thessaloniki (Talk)

Scholarships and Honors

- 05/2023** **Swiss Academy of Sciences and Swiss Chemical Society**
Chemistry travel award
- 06/2022** **71st Lindau Nobel Laureate Meeting Chemistry**
Participant nominated by the Elite Network Bavaria
- 08/2020 – 06/2023** **Studienstiftung des Deutschen Volkes**
PhD fellowship
- 12/2018** **Ludwig-Maximilian University Munich**
Research award for excellent students
- 10/2017 – 03/2018** **Bayer International Fellowship Program**
Otto Bayer fellowship
- 10/2014 – 03/2020** **Max-Weber Program**
Student fellowship